

**NUMERICAL AND EXPERIMENTAL  
INVESTIGATION INTO THE  
BEHAVIOUR OF GRANULAR  
MATERIALS UNDER GENERALISED  
STRESS STATES**

By

DANIEL BARRETO GONZALEZ

September 2009

A thesis submitted to the University of London  
(Imperial College of Science, Technology and Medicine)  
in partial fulfilment of the requirements for the degree of  
Doctor of Philosophy in the Faculty of Engineering

## Abstract

The construction of any structure above or below ground level will induce a change in the stress conditions underneath and adjacent to it. These changes may affect both the magnitude and orientation of the stresses. Therefore, a sound understanding of the behaviour of soil under generalised three-dimensional conditions is important for geotechnical engineers. Previous experimental research has demonstrated that the magnitude and direction of applied stresses are important factors governing soil response. While the anisotropic response of soil in terms of stiffness and strength is well established, there are limits to detail our understanding of soil response in the three dimensional stress space. In particular a better understanding of the relationship between the particle scale interactions and the overall response would improve the available soil predictive tools.

One apparatus used to study soil anisotropy is the hollow cylinder apparatus (HCA). In this equipment, as its name indicates, a hollow cylindrical soil specimen can be vertically compressed or extended and simultaneously twisted. Therefore, the direction and magnitude of the applied stresses are independently controlled and a generalised three-dimensional stress state can always be specified. Consequently, complex loading conditions encountered in the field can be replicated in the laboratory. However, it is known that due to the boundary conditions required for HCA testing, undesirable stress and strain non-uniformities are present.

Traditionally, numerical investigations of anisotropic soil behaviour and analyses of the stress and strain non-uniformities present in the HCA have used continuum finite element analyses. The distinct element method (DEM) accounts for the true particulate nature of soil and earlier studies have demonstrated that it can simulate simple loading conditions. DEM gives additional micro-mechanical quantities and parameters that cannot be easily obtained from experimental tests or conventional continuum analyses and it can capture the particle-scale interactions underlying the observed macro-scale behaviour. However, DEM has not been used to replicate soil behaviour under more complex conditions involving rotation of the applied stresses as it occurs in the HCA.

This thesis describes high quality HCA experiments on spherical particles (glass ballotini) that can (in principle) be accurately replicated in DEM numerical simulations. Two different sample height:diameter ratios (1:1 and 2:1) were used in the physical experiments to analyse the effects of sample geometry and boundary conditions on the macro-scale response and the generation of stress and strain non-uniformities.

In order to replicate the behaviour observed in the HCA experiments, a new DEM algorithm was implemented to include principal stress rotation. This approach allows simulation of general loading conditions free from boundary effects and was quantitatively validated analytically, and gave qualitative agreement with experiments. The macro-scale response of HCA tests is directly compared with DEM simulations and additional micro-mechanical analyses are presented. From the DEM simulation results, some of the micro-mechanical parameters examined include the coordination number (average number of contacts per particle) and the evolution of soil fabric (related to the inter-particle contacts orientation). Additional sensitivity analyses to evaluate the effect of different particle characteristics are also discussed. Based on the results of detailed micro-mechanical analyses, a possible framework for the understanding of soil behaviour in terms of the evolution of soil fabric has been proposed. It has been found that the macro-scale observations can be well explained in terms of the evolution and changes in soil structure.

A new generalised axi-symmetric environment that can be used to include realistic boundary conditions has been also developed. The future use of this environment can provide invaluable insight into the sources of stress and strain in HCA testing. Furthermore, in the future it can be applied to gain further understanding of other axi-symmetric geotechnical processes (e.g. CPT testing, pile driving, etc).

## Acknowledgements

Many persons have given me enough sources of support and encouragement for the completion of this thesis. First of all, my supervisors Dr Catherine O'Sullivan and Dr Lidija Zdravkovic. They provided me with guidance and advice. Furthermore, they were able to make me use my energy and increase my confidence to complete this self-indulgent and self-imposed task, while keeping my degree of happiness at the highest level at all times. The financial support given by EPSRC and the Department of Civil and Environmental Engineering (Imperial College London) have made possible what for me always seemed impossible.

I could not have made the lines above and below available to anyone without the valuable support and discussions of other research staff at Imperial College. With no particular order, intelligent comments and arguments were gratefully received from Dr Jaimie Standing, Dr Mike de Freitas, Prof David Potts, Prof Matthew Coop, and Prof Richard Jardine from internal colloquia and interesting conversations inside and outside the corridors of the Skempton building. Obviously, they are in no way accountable for the content of what appears in these pages; any defects in the present thesis, as well as those derived from it on the past and the future, are my responsibility alone.

My special thanks also to the laboratory technicians. In particular, the friendliness and support given by Mr Alan Bolsher were invaluable. The efforts by Mr Steve Ackerley and Mr Graham Keefe were also fundamental to deliver my experimental results on time.

Many Ph.D researchers, denoted in this Chapter as friends, were instrumental for the successful delivery of this thesis. Thanks to their complete support I have found the strength to conclude this thesis after the normal and constant struggles of life. Ordered according to the number of characters in their name, special mention goes to David, Joana, Miguel, Ignazio, Giovanny, Katerina, Reinhard and many others that would make of this a never ending chapter.

This thesis would not have been finished without the unfailing assistance of my wife, who was able to tolerate the moods and demands of a student constantly obsessed by the major problems of existence and soil mechanics. Her devotion and support have been an immeasurable and incredible contribution, documented by the fact that these pages have retained a minimum of lucidity.

Before proceeding to discuss more earthly and particulate matters, I must express my gratitude to my parents. After all, this deep and solid foundation, the effective and major principal orientation towards always wanting to give my best and challenge myself, is because I followed their unique behaviour.

Dedicated to the memory of my sister, Silvia;  
and to my parents, my wife and my dog.

"I would rather be ashes than dust. I would rather that my spark should burn out in a brilliant blaze than it should be stifled by a dryrot. I would rather be a superb meteor, every atom of me in a magnificent glow, than a sleepy and permanent planet. The proper function of man is to live, not to exist. I shall not waste my days trying to prolong them. I shall use my time."

*Jack London*

# Contents

<b>Abstract</b>	i
<b>Acknowledgements</b>	iii
<b>1 Introduction</b>	1
1.1 Introduction . . . . .	1
1.2 Aim and objectives . . . . .	2
1.3 Outline of the thesis . . . . .	3
<b>2 Background Information</b>	5
2.1 Introduction . . . . .	5
2.2 Definition of anisotropy . . . . .	6
2.3 Measurement of soil anisotropy in the laboratory . . . . .	7
2.3.1 The direct shear box . . . . .	7
2.3.2 The simple shear device . . . . .	8
2.3.3 The triaxial cell . . . . .	9
2.3.4 The true triaxial apparatus . . . . .	10
2.3.5 The plain strain device . . . . .	10
2.3.6 The directional shear cell . . . . .	11
2.3.7 The hollow cylinder apparatus . . . . .	11
2.4 Previous experimental studies on the effects of soil anisotropy . . . . .	12
2.4.1 Anisotropic soil behaviour: Effects of $\alpha$ on soil behaviour . . . . .	13

## CONTENTS

---

2.4.2	Anisotropic soil behaviour: Effects of $b$ on soil behaviour . . . . .	24
2.4.3	Small-strain anisotropy . . . . .	29
2.5	A failure model for granular materials . . . . .	31
2.5.1	The deviatoric stress plane . . . . .	31
2.5.2	Failure criterion proposed by Lade & Duncan (1973) . . . . .	32
2.6	DEM Background . . . . .	34
2.6.1	Algorithm . . . . .	35
2.6.2	Time step and stability . . . . .	36
2.6.3	Boundary types in DEM simulations . . . . .	37
2.7	Micro-mechanical parameters . . . . .	38
2.7.1	Stress tensor . . . . .	38
2.7.2	Strain tensor . . . . .	40
2.7.3	Coordination number . . . . .	40
2.7.4	Fabric tensor . . . . .	41
2.8	Quantification of soil fabric . . . . .	41
2.8.1	Fourier approximations (curve fitting methods) . . . . .	42
2.8.2	Eigenvalue methods . . . . .	46
2.9	Previous DEM research considering granular material response . . . . .	48
2.9.1	Triaxial simulations . . . . .	48
2.9.2	True triaxial simulations . . . . .	54
2.9.3	DEM simulations involving principal stress rotation . . . . .	57
2.10	Summary . . . . .	59
<b>3</b>	<b>Test material, apparatus and procedures</b>	<b>63</b>
3.1	Introduction . . . . .	63
3.2	Test material . . . . .	64
3.3	Apparatus . . . . .	66
3.3.1	Triaxial stress path cell . . . . .	67

## CONTENTS

---

3.3.2	Imperial College Hollow Cylinder Apparatus (ICHCA) . . . . .	69
3.3.3	Large Imperial College Hollow Cylinder Apparatus (LICHCA) . . . . .	85
3.4	Stress and strain non-uniformities . . . . .	89
3.4.1	The origin of the non-uniformities . . . . .	90
3.4.2	Previous numerical analyses of non-uniformities . . . . .	91
3.4.3	Previous experimental results highlighting the effects of non-uniformities . . . . .	107
3.5	Sample preparation and testing procedures . . . . .	109
3.5.1	Sample preparation method for triaxial tests . . . . .	112
3.5.2	Sample preparation method for hollow cylinder tests . . . . .	115
3.5.3	Testing procedures . . . . .	126
3.6	Summary . . . . .	126
<b>4</b>	<b>Experimental results</b>	<b>128</b>
4.1	Introduction . . . . .	128
4.2	Triaxial tests . . . . .	128
4.2.1	The effect of the testing conditions on the behaviour of glass ballotini . . . . .	130
4.2.2	The effect of particle size and particle size distribution on the behaviour of glass ballotini . . . . .	137
4.2.3	Experimental determination of the $K_0$ value . . . . .	139
4.3	Hollow cylinder tests . . . . .	141
4.3.1	Tests to study the effects of the particle size distribution on soil behaviour - ICHCA . . . . .	143
4.3.2	Tests to study the effect of $\alpha$ and $b$ on soil behaviour - ICHCA	151
4.3.3	Tests to study the effect of $\alpha$ and $b$ on soil behaviour - LICHCA	160
4.4	Summary . . . . .	167

## CONTENTS

---

<b>5 Code development and its validation</b>	<b>169</b>
5.1 Introduction . . . . .	169
5.2 The periodic cell . . . . .	170
5.3 DEM algorithms for simulations involving normal loading . . . . .	171
5.3.1 Contact detection . . . . .	171
5.3.2 Simulation control . . . . .	173
5.3.3 Code validation . . . . .	175
5.4 New DEM algorithms for simulations involving principal stress rotation	184
5.4.1 Simulation control . . . . .	184
5.4.2 Contact detection . . . . .	187
5.4.3 Code validation . . . . .	188
5.5 New developments for the control of complex servo-controlled stress paths . . . . .	193
5.6 Summary . . . . .	196
<b>6 DEM simulations under normal loading</b>	<b>197</b>
6.1 Introduction . . . . .	197
6.2 Input parameters . . . . .	198
6.3 Specimen generation . . . . .	200
6.3.1 Specimen generation approach for isotropic stress states . . . . .	201
6.3.2 Specimen generation approach for anisotropic stress states . . . . .	203
6.4 Triaxial simulations . . . . .	207
6.4.1 Experimental validation . . . . .	207
6.4.2 Sensitivity analyses . . . . .	211
6.5 Constant $b$ tests . . . . .	225
6.5.1 Isotropically consolidated specimens . . . . .	225
6.5.2 Anisotropically consolidated specimens ( $K_0$ ) . . . . .	236
6.6 Summary . . . . .	246

<b>7 DEM simulations involving principal stress rotation</b>	<b>248</b>
7.1 Introduction . . . . .	248
7.2 DEM simulations of hollow cylinder tests . . . . .	249
7.2.1 Isotropically consolidated specimens . . . . .	249
7.2.2 Anisotropically ( $K_0$ ) consolidated specimens . . . . .	251
7.3 A new fabric surface to understand the behaviour of granular materials	265
7.4 Effect of pre-shearing on the anisotropic response of granular materials	267
7.5 Influence of the initial structure on the development of non-coaxiality	270
7.6 Stress path dependance of the response of granular materials . . . . .	272
7.7 Summary . . . . .	283
<b>8 Advanced modelling of hollow cylinder tests</b>	<b>284</b>
8.1 Introduction . . . . .	284
8.2 Circumferential (vertical) periodic boundaries . . . . .	284
8.3 Flexible boundaries . . . . .	292
8.4 Rigid boundaries . . . . .	298
8.5 Specimen generation . . . . .	299
8.5.1 Two-dimensional simulations . . . . .	299
8.5.2 Three-dimensional attempts . . . . .	310
8.6 Simulation control for realistic axi-symmetric HCA specimens . . . . .	317
8.6.1 Method for application of torque . . . . .	318
8.6.2 Control algorithms . . . . .	320
8.7 Preliminary results using rigid boundaries . . . . .	321
8.7.1 DEM simulation with axial translation of the top boundary .	321
8.7.2 DEM simulation with rotation of the top boundary to simulate application of torque . . . . .	323
8.7.3 Some observations about non-uniformities in HCA testing .	324
8.8 Summary . . . . .	327

<b>9 Conclusions</b>	<b>330</b>
9.1 Summary . . . . .	330
9.2 Findings . . . . .	331
9.2.1 Experimental results . . . . .	331
9.2.2 Numerical results - Implementation . . . . .	333
9.2.3 Numerical results - DEM simulations . . . . .	334
9.2.4 Evolution of soil fabric . . . . .	337
9.3 Suggestions for further research . . . . .	338
9.3.1 Experimental research . . . . .	338
9.3.2 Numerical research . . . . .	339
<b>References</b>	<b>341</b>

# List of Tables

2.1	Typical characteristics of different sands . . . . .	12
3.1	Mineral composition of type SL beads (information provided by Sig-mund Lindner on delivery) . . . . .	64
3.2	Different particle sizes of type SL beads . . . . .	64
3.3	Summary of capacity, accuracy and stability of transducers employed in the triaxial stress path cell . . . . .	67
3.4	Summary of capacity, accuracy and stability of transducers employed in the ICHCA and LICHCA . . . . .	81
4.1	Triaxial stress path cell testing programme . . . . .	129
4.2	Hollow cylinder apparatus testing programme . . . . .	141
5.1	Summary of input parameters for simulations on FCC assemblies . .	179
6.1	Input Parameters for DEM Simulations . . . . .	198
6.2	Grain size distribution for specimens with 4000 particles . . . . .	199

# List of Figures

2.1	Tilted deposition of sand samples (Oda 1972a) . . . . .	9
2.2	Effect of angle $\alpha$ on stress-strain and volume changes of a) Sand B and b) Sand D (modified after Oda 1972a) . . . . .	15
2.3	Inherent anisotropy of Leighton Buzzard sand (modified after Arthur & Menzies 1972) . . . . .	16
2.4	Induced anisotropy upon reloading with a change of principal stress direction a) $\Delta\alpha = 0$ , b) $\Delta\alpha = 30$ , c) $\Delta\alpha = 60$ and d) $\Delta\alpha = 90$ (modified after Arthur et al. 1977) . . . . .	18
2.5	Differences between a) induced and b) inherent anisotropy of Leighton Buzzard sand (modified after Arthur et al. 1981) . . . . .	20
2.6	Stress-strength anisotropy of Ham River sand (Symes 1983) . . . .	21
2.7	Development of volumetric strain in HCA test involving continuous rotation of the major principal stress (modified after Symes 1983) . .	22
2.8	Dependence of the maximum stress ratio on $b$ and $\alpha$ . (Symes 1983) .	23
2.9	Effect of $b$ on $\phi'$ for Monterrey No. 0 sand (modified after Sutherland & Mesdary 1969) . . . . .	25
2.10	Effect of $b$ on $\phi'$ for glass ballotini (modified after Haruyama 1981) .	26
2.11	Effect of $b$ on $\phi'$ for Ham river sand (modified after Green 1971) . .	27
2.12	Effect of $b$ on the major principal strain at failure . . . . .	28
2.13	Effect of $b$ on the intermediate principal strain at failure (modified after Reades & Green 1976) . . . . .	29
2.14	Description of the deviatoric plane in three-dimensional stress conditions . . . . .	32
2.15	Effect of changing the orientation of the major principal stress on the failure envelope of granular materials . . . . .	33

---

## LIST OF FIGURES

2.16 Failure envelopes of the Lade & Duncan (1973) model in a) triaxial plane and b) deviatoric plane (Lade & Duncan 1973) . . . . .	33
2.17 Schematic representation of the DEM algorithm . . . . .	36
2.18 Definition of the force and branch vectors for the determination of the stress tensor . . . . .	39
2.19 Typical unit contact normal distribution and its fitted Fourier series .	43
2.20 Variation of the magnitude of anisotropy ( $a$ ) and its effect on the distribution of contact normals . . . . .	44
2.21 Variation of the direction of anisotropy ( $\theta_a$ ) and its effect on the distribution of contact normals . . . . .	45
2.22 Two-axis ratio plot for analysis of orientation data in the eigenvalue method (Woodcock 1977) . . . . .	47
2.23 DEM simulations of axi-symmetric compression in a periodic cell. Qualitative behaviour (Thornton 2000) . . . . .	50
2.24 DEM simulations of axi-symmetric compression in a periodic cell. Critical void ratio (Thornton 2000) . . . . .	51
2.25 Evolution of the normal and tangential force contribution to the deviatoric stress during axi-symmetric compression (Thornton 2000) .	51
2.26 Evolution of induced structural anisotropy during axi-symmetric compression (Thornton 2000) . . . . .	52
2.27 Macro-scale comparison of DEM simulation results and laboratory tests (modified after Cui et al. 2007a) . . . . .	53
2.28 Sensitivity of deformed specimen shape ( $\epsilon_a = 15.3\%$ ) to particle/boundary friction coefficient. a) $\mu = 0.0$ , b) $\mu = 0.05$ and c) $\mu = 0.10$ (Cui et al. 2007a) . . . . .	54
2.29 Comparison of internal stresses in a DEM triaxial simulation (modified after Cui et al. 2007a) . . . . .	55
2.30 Network of contact forces in three zones (only forces exceeding mean force plus one standard deviation) a) $\epsilon_a = 6.2\%$ (around peak), b) $\epsilon_a = 12.3\%$ (post peak) (Cui et al. 2007a) . . . . .	56
2.31 Failure states of stress and fabric components in DEM simulations of constant $b$ tests (modified after Thornton 2000) . . . . .	57
2.32 Evolution of shear strength for all tests (modified after Ng 2004b) .	58
2.33 Unit normal strength descriptors (Ng 2004b) . . . . .	58

---

## LIST OF FIGURES

2.34	Unit normal force strength descriptors (Ng 2004 <i>b</i> ) . . . . .	59
2.35	Influence of the major principal stress orientation on the angle of shearing resistance of granular materials . . . . .	60
2.36	Influence of the intermediate stress ratio on the angle of shearing resistance of granular materials . . . . .	61
3.1	Grain size distribution for the different glass ballotini sizes . . . . .	66
3.2	Schematic representation of the triaxial stress path cell (Bishop & Wesley 1975) . . . . .	68
3.3	Schematic representation of the ICHCA (Symes 1983) . . . . .	70
3.4	The ICHCA and a test under progress . . . . .	71
3.5	Load application and stress components in the HCA . . . . .	72
3.6	Mohr's circle of stress states in the HCA . . . . .	75
3.7	Details of a pair of opposed proximity transducers to measure radial displacements (Symes 1983) . . . . .	78
3.8	Details of arrangement of the proximity transducers - top view (Zdravkovic 1996) . . . . .	79
3.9	Schematic representation of the a) single axis and b) double axis electro-levels (modified after Zdravkovic 1996) . . . . .	80
3.10	Control and data acquisition system for the ICHCA and LICHCA (Zdravkovic 1996) . . . . .	82
3.11	Load application algorithm for the ICHCA and LICHCA (Zdravkovic 1996) . . . . .	84
3.12	Comparison of set-up for the external proximity transducers in the ICHCA and LICHCA . . . . .	86
3.13	Deployment for the internal proximity transducers in the LICHCA . .	87
3.14	Outer moulds for the ICHCA and ICHCA . . . . .	88
3.15	New inner extensions for the inner mould and its deployment . . . . .	89
3.16	System for application of vacuum used to hold the outer membrane against the mould . . . . .	90
3.17	Shear stress variation with HCA radius (Porovic 1995) . . . . .	91
3.18	Vertical and shear stress distribution across the sample wall due to the application of torque (Saada & Townsend 1981) . . . . .	92

## LIST OF FIGURES

---

3.19 Definition of parameters to assess the level of non-uniformities in the HCA (Hight et al. 1983) . . . . .	93
3.20 Areas of the stress space were the level of non-uniformities is unacceptable (Hight et al. 1983) . . . . .	94
3.21 Distribution of stresses across the wall of the HCA sample using linear elastic FE analyses (Hight et al. 1983) . . . . .	95
3.22 Distribution of stresses at two different stress levels in the HCA using elasto-plastic FE analyses (Hight et al. 1983) . . . . .	96
3.23 Distribution of stresses due to the application of torque using associated and non-associated plasticity. a) Before yield and b) after yield (modified after Gens & Potts 1984) . . . . .	97
3.24 Definition of parameters for the assessment of non-uniformities (Vaid et al. 1990) . . . . .	98
3.25 Areas of the stress space were the level of non-uniformities is unacceptable added by Vaid et al. (1990) . . . . .	99
3.26 Effect of the stress and stress non-uniformities on the stress-strain relationship obtained from HCA tests (Menkiti 1995) . . . . .	100
3.27 Effect of the non-uniformities on the strain development with $b=0.5$ (Rolo 2003) . . . . .	102
3.28 Effect of the non-uniformities on the effective stress paths with $b=0.5$ (Rolo 2003) . . . . .	103
3.29 Distribution of strains across the HCA wall at a deviatoric strain level of 10% (Rolo 2003) . . . . .	103
3.30 Effect of the non-uniformities on the strain development with $b=0.3$ (Foundoukos 2006) . . . . .	104
3.31 Effect of the non-uniformities on the effective stress paths with $b=0.3$ (Foundoukos 2006) . . . . .	105
3.32 Effect of the non-uniformities on the effective stress paths with different sample geometries (modified after Zdravkovic & Potts 2005) . . . . .	105
3.33 Distribution of stress across the sample wall with different sample geometries (modified after Zdravkovic & Potts 2005) . . . . .	106
3.34 HCA experiments with samples of different height (Lade 1981) . . . . .	108
3.35 HCA experiments with samples of different height at similar $b$ and $\alpha$ values (modified after Lade et al. 2008) . . . . .	109

## LIST OF FIGURES

---

3.36 HCA experiments with samples of different height (modified after Kharchafi 1988) . . . . .	110
3.37 Effect of different sample preparation methods on soil response in the triaxial apparatus (Miura & Toki 1982) . . . . .	111
3.38 Outer mould for sample preparation in the ICHCA . . . . .	119
3.39 Inner mould for sample preparation in the ICHCA . . . . .	119
3.40 Pluviation system for the preparation of samples in the LICHCA . . .	121
3.41 Detail of pluviated ballotini during the sample preparation process in the LICHCA . . . . .	122
3.42 LICHCA sample previous to top platen connection . . . . .	125
4.1 Experimental evidence of stick-slip behaviour on sample in saturated tests on glass ballotini . . . . .	131
4.2 The behaviour of glass ballotini under triaxial conditions - Testing conditions and particle size effects on stress-strain behaviour . . . . .	133
4.3 The behaviour of glass ballotini under triaxial conditions - Testing conditions and particle size effects on shear stiffness . . . . .	133
4.4 The influence of the coefficient of inter-particle friction on the shearing resistance of granular materials (Thornton 2000) . . . . .	134
4.5 Sensitivity of calculated volumetric strain to different calculation methods . . . . .	136
4.6 The behaviour of glass ballotini under triaxial conditions - Effect of testing conditions and particle size on volumetric response . . . . .	137
4.7 Experimental determination of the $K_0$ coefficient for medium size glass ballotini . . . . .	140
4.8 Summary of HCA tests in $b - \alpha$ space . . . . .	142
4.9 Typical HCA test stress path in $t - p'$ space . . . . .	143
4.10 Consolidation stress paths in ICHCA - Exploration of the effect of particle size on the behaviour of glass ballotini . . . . .	145
4.11 Evolution of strains during $K_0$ consolidation in ICHCA - Exploration of the effect of particle size on the behaviour of glass ballotini . . . . .	146
4.12 Development of stresses during $b$ -change from 0.0 to 0.5 in ICHCA - Exploration of the effect of particle size on the behaviour of glass ballotini . . . . .	147

## LIST OF FIGURES

---

4.13 Volumetric strain development during the $b$ -change stage in ICHCA - Exploration of the effect of particle size on the behaviour of glass ballotini . . . . .	148
4.14 Development of stresses during drained shearing with $b = 0.5$ and $\alpha = 0^\circ$ . . . . .	149
4.15 Stress-strain curves during drained shear in ICHCA - Exploration of the effect of particle size on the behaviour of glass ballotini . . . . .	150
4.16 Stress paths during consolidation for ICHCA tests on glass ballotini .	152
4.17 Evolution of strains during $K_0$ consolidation - ICHCA tests on glass ballotini . . . . .	153
4.18 Development of stresses during $\alpha$ -change from $0^\circ$ to $45^\circ$ - Test IC-M- D-5 . . . . .	154
4.19 Evolution of strains during $\alpha$ -change stage - Test IC-M-D-5 . . . . .	155
4.20 Effect of the intermediate stress ratio $b$ on stress-strain response dur- ing drained shear - ICHCA tests on glass ballotini . . . . .	155
4.21 Development of stresses during drained shearing with $b = 0.0$ and $\alpha = 0^\circ$ - Test IC-M-D-4 . . . . .	156
4.22 Effect of the intermediate stress ratio $b$ on the octahedral stiffness during drained shear - ICHCA tests on glass ballotini . . . . .	157
4.23 Development of torsional shear stress during LICHCA tests with $\alpha =$ $45^\circ$ for different $b$ values . . . . .	158
4.24 Effect of the orientation of the principal stresses $\alpha$ on the stress-strain response during drained shear - ICHCA tests on glass ballotini . . . . .	158
4.25 Effect of the principal stress orientation, $\alpha$ , on the octahedral stiffness during drained shear - ICHCA tests on glass ballotini . . . . .	159
4.26 Consolidation stress paths for ICHCA and LICHCA tests on glass ballotini . . . . .	160
4.27 Sample size effects for ICHCA and LICHCA tests on glass ballotini ( $\alpha = 0^\circ$ and $b = 0.5$ ) . . . . .	161
4.28 Sample size effects for ICHCA and LICHCA tests on glass ballotini ( $\alpha = 0^\circ$ and $b = 0.0$ ) . . . . .	162
4.29 Sample size effects for ICHCA and LICHCA tests on glass ballotini ( $\alpha = 45^\circ$ and $b = 0.5$ ) . . . . .	163
4.30 Sample size effects considering the peak angle of shearing resistance - Tests performed with $b = 0.5$ . . . . .	164

## LIST OF FIGURES

---

4.31 Development of stresses during LICHCA tests with $\alpha = 45^\circ$ for different $b$ values . . . . .	165
4.32 Summary of shear strength results for LICHCA tests with different $\alpha$ and $b$ values . . . . .	166
4.33 Evolution of octahedral stiffness with deviatoric strain during LICHCA tests with $\alpha = 45^\circ$ for different $b$ values . . . . .	166
5.1 Representation of granular material using periodic boundaries in the two-dimensional space. . . . .	170
5.2 Contact detection algorithm - Binning for potential contacts . . . . .	172
5.3 Typical deformation during isotropic compression - normal loading . .	173
5.4 The FCC array: a) view along $y$ axis; b) view along $x$ axis; c) view along $z$ axis . . . . .	176
5.5 Inter-particle contact points for a typical sphere within a FCC assembly (after Thornton 1979) . . . . .	176
5.6 Stress ratios at failure for a FCC assembly for different values of the coefficient of inter-particle friction . . . . .	179
5.7 Results from a DEM simulation of a FCC specimen under triaxial loading conditions . . . . .	181
5.8 Contact force distribution for a DEM simulation of a FCC assembly under triaxial conditions . . . . .	182
5.9 Results from a DEM simulation of a FCC specimen under plane strain loading conditions . . . . .	183
5.10 Contact force distribution for a DEM simulation of a FCC assembly under plane strain conditions . . . . .	183
5.11 Comparison between analytical and numerical results for the shearing of FCC assemblies under triaxial and plane strain conditions . . . . .	184
5.12 Typical deformation during pure shear deformation - loading involving principal stress rotation . . . . .	185
5.13 Movement of particles that cross sheared boundaries . . . . .	186
5.14 Contacts occurring across the horizontal boundaries . . . . .	187
5.15 Initial arrangement of a cubic assembly of equally sized spheres . .	188
5.16 Initial and deformed states of a cubic assembly of equally sized spheres under simple shear conditions . . . . .	189

---

## LIST OF FIGURES

5.17 Total particle displacements of a cubic assembly of equally sized spheres under simple shear conditions . . . . .	190
5.18 Schematic representation of the failure mechanism under simple shear conditions (Shear in the $XZ$ direction) . . . . .	191
5.19 Direct stresses and strains for a typical DEM simulation of a FCC assembly under simple shear conditions . . . . .	192
5.20 Effective stresses and coordination number for a typical DEM simulation of a FCC assembly under simple shear conditions . . . . .	192
5.21 Contact force distribution for a DEM simulation of a FCC assembly under simple shear conditions . . . . .	194
6.1 Values of initial void ratio after isotropic compression using different inter-particle friction coefficients . . . . .	202
6.2 Example of a specimen generated with isotropic compression - Initial and final states ( $\mu = 0$ ) . . . . .	203
6.3 Anisotropic consolidation stress paths using different values of inter-particle friction . . . . .	204
6.4 Achieving a specific anisotropic stress state with different stress paths	205
6.5 Stress-strain response for triaxial compression of anisotropically consolidated specimens using different approaches . . . . .	206
6.6 Evolution of the coordination number ( $Z$ ) for triaxial compression of anisotropically consolidated specimens using different approaches . . .	207
6.7 Comparison between experimental and numerical results of triaxial tests on glass ballotini - Stress-strain response . . . . .	209
6.8 Comparison between experimental and numerical results of triaxial tests on glass ballotini - Volumetric response . . . . .	210
6.9 Effect of $\mu$ on triaxial compression - Stress-strain response . . . . .	212
6.10 Effect of $\mu$ on triaxial compression - Differences in shear stiffness . . .	213
6.11 Effect of $\mu$ on $\phi'$ . . . . .	213
6.12 Effect of $\mu$ on triaxial compression - Evolution of $Z$ . . . . .	214
6.13 Effect of $\mu$ on triaxial compression - Contact forces for three vertical slices through the DEM specimen . . . . .	216
6.14 Effect of $\mu$ on triaxial compression - Polar histograms of contact forces in the $XZ$ plane at the start of shearing and at peak . . . . .	216

## LIST OF FIGURES

---

6.15 Effect of $\mu$ on triaxial compression - Evolution of the deviatoric fabric	217
6.16 Effect of initial density on triaxial compression - Stress-strain response	218
6.17 Effect of initial density on triaxial compression - Evolution of $Z$ . . . . .	219
6.18 Effect of initial density on triaxial compression - Evolution of the deviatoric fabric . . . . .	220
6.19 Effect of the grain size distribution on triaxial compression - Stress-strain response . . . . .	221
6.20 Effect of Poisson's ratio on triaxial compression - Stress-strain response	222
6.21 Effect of Young's module on triaxial compression - Stress-strain response	223
6.22 Effect of the strain rate on triaxial compression - Stress-strain response	224
6.23 Effect of the time step on triaxial compression - Stress-strain response	224
6.24 Effect of the intermediate stress ratio $b$ - Stress-strain response . . . . .	226
6.25 Effect of the intermediate stress ratio $b$ - Development of intermediate strain ( $\epsilon_2$ ) . . . . .	226
6.26 Effect of the intermediate stress ratio $b$ on the angle of shearing resistance ( $\phi'$ ) . . . . .	227
6.27 Effect of the intermediate stress ratio $b$ on the angle of shearing resistance ( $\phi'$ ) . . . . .	228
6.28 Effect of the intermediate stress ratio $b$ on the octahedral stiffness . .	229
6.29 Effect of the intermediate stress ratio $b$ on $Z$ . . . . .	229
6.30 Effect of the intermediate stress ratio $b$ on $\Phi_d$ . . . . .	231
6.31 Effect of the intermediate stress ratio $b$ on the fabric tensor at failure	232
6.32 Effect of the intermediate stress ratio on the contact force network . .	233
6.33 Effect of $b$ on the concentration of contact force networks in the XZ plane . . . . .	233
6.34 Effect of the intermediate stress ratio on particle rotation . . . . .	235
6.35 Effect of the coefficient of inter-particle friction on the shearing resistance of constant $b$ tests . . . . .	236
6.36 Changes in the failure envelope in relation to the coefficient of inter-particle friction . . . . .	237
6.37 Effect of the initial density on constant $b$ tests . . . . .	238

---

## LIST OF FIGURES

6.38 DEM simulations of HCA tests under different intermediate stress ratio	239
6.39 Comparison of DEM simulations and LICHCA tests with $\alpha = 0^\circ$ and $b = 0.0$ . . . . .	240
6.40 Comparison of DEM simulations and LICHCA tests with $\alpha = 0^\circ$ and $b = 0.5$ . . . . .	240
6.41 Effect of the intermediate stress ratio $b$ - Comparison between the isotropically and $K_0$ consolidated response . . . . .	242
6.42 Effect of the intermediate stress ratio $b$ on $K_0$ consolidated specimens - Angle of shearing resistance ( $\phi'$ ) . . . . .	243
6.43 Effect of the intermediate stress ratio $b$ on $K_0$ consolidated specimens - Failure envelope in the $\pi$ -plane . . . . .	244
6.44 Effect of the intermediate stress ratio $b$ on $K_0$ consolidated specimens - Evolution of $Z$ . . . . .	245
6.45 Effect of the intermediate stress ratio $b$ on $K_0$ consolidated specimens - Evolution of $\Phi_d$ . . . . .	245
6.46 Schematic representation of main force carrying columns supported by lateral compressive stress that prevent chain buckling . . . . .	246
7.1 Stress-strain response for isotropically consolidated specimens sheared with different $\alpha$ values . . . . .	250
7.2 Evolution of the coordination number for isotropically consolidated specimens sheared with different $\alpha$ values . . . . .	251
7.3 Polar distribution of contact forces in the $XZ$ -plane . . . . .	252
7.4 Comparison of experiment with DEM simulations - Stress-strain re- sponse for LICHCA test with $\alpha = 45^\circ$ and $b = 0.5$ . . . . .	253
7.5 Evolution of torsional shear stress $\tau_{z\theta}$ for DEM simulation with $\alpha = 45^\circ$	255
7.6 Stress-strain response for DEM simulations of anisotropically consol- idated specimens sheared with $b = 0.5$ and different $\alpha$ values . . . . .	256
7.7 Peak shear strength for DEM simulations of anisotropically consoli- dated specimens sheared with different $\alpha$ values . . . . .	257
7.8 Effect of $\alpha$ on $K_0$ consolidated specimens - Failure envelope in the $\pi$ -plane . . . . .	258
7.9 Effect of $\alpha$ on $K_0$ consolidated specimens - Development of octahedral stiffness (for $b = 0.5$ ) . . . . .	259

## LIST OF FIGURES

---

7.10 Effect of $\alpha$ on $K_0$ consolidated specimens - Evolution of coordination number (for $b = 0.5$ ) . . . . .	260
7.11 Effect of $\alpha$ - Contact forces for three vertical slices through the DEM specimen (for $b = 0.0$ ) . . . . .	261
7.12 Effect of $b$ on the anisotropic response - Contact forces for three vertical slices through the DEM specimen ( $\alpha = 45^\circ$ ) . . . . .	262
7.13 Polar distribution of contact forces in the $XZ$ -plane for $K_0$ consolidated specimens and $b = 0.5$ . . . . .	263
7.14 Effect of $\alpha$ on $K_0$ consolidated specimens - Evolution of the deviatoric fabric, $\Phi_d$ (for $b = 0.5$ ) . . . . .	264
7.15 Deviatoric fabric in the generalised stress plane . . . . .	266
7.16 Newly proposed $\alpha$ - $b$ - $\Phi_d$ space . . . . .	267
7.17 Magnitude of anisotropy ( $a$ ) after re-consolidation for simulations assessing the effects of inherent anisotropy . . . . .	268
7.18 Influence of the inherent anisotropy in the stress-strain response for different major principal stress orientation . . . . .	269
7.19 Influence of the initial fabric in the development of non-coaxiality . .	271
7.20 Shearing stress paths - Variable mean effective stress ( $\mu = 0.325$ ) . .	273
7.21 Influence of the stress path. Stress-strain response . . . . .	275
7.22 Influence of the stress path. Normalised stress-strain response . . .	275
7.23 Influence of the stress path. Evolution of coordination number . . .	277
7.24 Influence of the stress path. Evolution of the magnitude of anisotropy ( $a$ )- All cases . . . . .	277
7.25 Influence of the stress path. Evolution of the magnitude of anisotropy ( $a$ ) . . . . .	279
7.26 Influence of the stress path. Evolution of the strength factor ( $C$ ) . .	279
7.27 Influence of the stress path. Evolution of the deviatoric fabric ( $\Phi_d$ ) .	280
7.28 Influence of the stress path. Evolution of the deviatoric fabric ( $\Phi_d$ ) for a loose specimen (Barreto et al. 2009) . . . . .	281
7.29 Different variations and multiples of the fabric invariant to quantify anisotropy . . . . .	282
8.1 Definition of angles for the generalised axi-symmetric environment .	285

## LIST OF FIGURES

---

8.2	Rotation of particles protruding circumferential periodic boundaries and their corresponding inter-particle contact forces . . . . .	287
8.3	Simulation specimens using different angles between circumferential periodic boundaries . . . . .	288
8.4	Continuity of force chain networks in a 2D simulation . . . . .	289
8.5	Rotation of particles and contact forces when $\theta_b = 90^\circ$ (Cui et al. 2007a) . . . . .	289
8.6	Reboxing algorithm for generalised DEM axi-symmetric environment - Option 1 . . . . .	291
8.7	Reboxing algorithm for generalised DEM axi-symmetric environment - Option 2 . . . . .	291
8.8	Definition of the membrane zone and identification of membrane balls (Cui et al. 2007a) . . . . .	293
8.9	Additional check to ensure that a particle can be considered as a membrane ball (Cheung & O'Sullivan 2008) . . . . .	294
8.10	Voronoi diagram for the simulation of flexible membranes - DEM simulation . . . . .	295
8.11	Projected Voronoi diagram for the simulation of flexible membranes - DEM simulation . . . . .	296
8.12	Initial configuration of specimens with a) uniform and b) non-uniform grain size distributions - Simulated section is highlighted . . . . .	301
8.13	Comparison between section simulated partially (bottom) and in full (top) after compression . . . . .	302
8.14	Arching effects in simulation with uniform specimen and $\mu = 0.22$ . .	304
8.15	Arching effects in simulation with uniform specimen and $\mu = 0.00$ . .	306
8.16	Absence of arching effects in simulation with non-uniform specimen and $\mu = 0.22$ . . . . .	307
8.17	Absence of arching effects in simulation with non-uniform specimen and $\mu = 0.00$ . . . . .	307
8.18	Arching effects in simulation with “medium” sized distribution specimen and $\mu = 0.22$ . . . . .	308
8.19	Absence of arching effects in simulation “medium” sized distribution specimen, $\mu = 0.22$ and compressed from the inner boundary . . . . .	309
8.20	Evolution of radial force on outer rigid boundary during compression	310

8.21 Example of generation for initial configuration of realistic HCA specimens . . . . .	311
8.22 Evolution of boundary stresses . . . . .	312
8.23 Effect of variable thickness on the stress distribution and coordination number . . . . .	314
8.24 Effect of section angle on the stress distribution and coordination number . . . . .	315
8.25 Effect of the height of the sample on the stress distribution and co-ordination number . . . . .	316
8.26 Single particle simulation to validate the approach to rotate the rigid top platen and allow the application of torque . . . . .	319
8.27 Stress-strain response of triaxial compression of a HCA specimen with $h = 25$ mm . . . . .	322
8.28 Stress-strain response during application of torque for of a HCA specimen with $h = 25$ mm . . . . .	323
8.29 Evolution of contact forces during application of torque on a HCA specimen with $h = 25$ mm . . . . .	325
8.30 Evolution of contact forces during triaxial compression of a HCA specimen with $h = 25$ mm . . . . .	326
8.31 Distribution of contact forces in a HCA specimen with $h = 500$ mm - Presence of stress non-uniformities . . . . .	328

# Chapter 1

## Introduction

### 1.1 Introduction

The response of soil is highly complex, in particular when a fully three dimensional stress state is considered. Furthermore, the mechanical response of granular materials is anisotropic considering strength and permeability. The *in situ* stresses felt by soil change during the construction of any geotechnical structure (i.e. pile driving, embankment construction, excavations, etc). These stress changes normally involve principal stress rotation and a variation magnitude of stresses in three orthogonal directions. A key element of soil mechanics research is to develop understanding of soil behaviour and hence advance our ability to predict response and explain failures. Advancements in understanding soil response can be achieved in physical laboratory experiments, from field observations, in theoretical or numerical models, or using a combination of these approaches.

This thesis describes a basic research study with the aim of advancing understanding of soil response under a fully three dimensional stress state. The research involved physical tests using the hollow cylinder apparatus and numerical simulations using discrete element modelling (DEM).

A number of experimental devices have been designed in order to study the anisotropic properties of soils. One of the few devices that can replicate the *in-situ* stress felt by the soil in an independent and controlled manner is the hollow cylinder apparatus (HCA). Typically numerical models used in soil mechanics consider the soil to behave as a continuum. However, this approach in many cases, ignores the particulate nature of soils and is not suited to very fundamental research that considers the

## 1. Introduction

---

particulate nature of soils. DEM models explicitly consider the particle interactions and the use of DEM is increasing in geomechanics research. It is important that a numerical model accurately simulate physical reality. Prior to this study DEM had not been validated for the simulation of complex loading conditions which involve controlled principal stress rotation. Therefore, the implementation and validation of DEM algorithms able to simulate these stress conditions are an obvious, but not simple step forward.

In this thesis, experimental results from HCA tests on glass ballotini are compared to DEM simulations that follow identical stress paths, and replicate as accurately as possible the geometrical and physical characteristics of the constituent particles. The results presented confirm that DEM is capable of reproducing the observed anisotropic behaviour of granular materials. The DEM simulations provided data to examine the particle scale mechanics underlying the observed macro-scale response.

## **1.2 Aim and objectives**

As mentioned before, the aim of the present research project is to implement and validate a new DEM algorithm capable of reproducing and explaining the observed macro-scale behaviour of granular materials. In this thesis, the following specific objectives were identified to achieve this aim

- Completion of a series of high quality HCA tests on an analogue soil (glass ballotini) suitable for DEM validation.
- Experimental assessment of the effect of the boundary conditions on the material response observed in HCA testing using two apparatuses with different geometries (aspect ratios).
- Simulation of the HCA experiments using the DEM. Two types of simulation were selected in the first instance. To simulate boundary free tests in a periodic cell new algorithms were developed. Then the tests boundary conditions could be included by developing a generalised axi-symmetric DEM environment.
- A comparison of the HCA experiments and the DEM simulations to validate the numerical model. This comparison establishes the relationship between the particle-scale interactions and the observed macro-scale behaviour.

## 1. Introduction

---

- Interpretation of the DEM data to establish the relationship between the particle scale interactions and the observed macro-scale behaviour.
- A parametric study to explore the sensitivity of the granular material response to various input parameters.

### **1.3 Outline of the thesis**

This thesis is organised into nine chapters. The first chapter presents an introduction to the subject and the objectives of the research. Chapter 2 is a review of information relevant for the understanding of the thesis. The chapter is divided into two main sections. Firstly a review of experimental procedures to assess the effects of the intermediate principal stress is given. This section also includes a description of the main findings of previous experimental research. The second part of Chapter 2 includes a description of the distinct element method (DEM), and the micro-mechanical parameters used to analyse results from DEM simulations. Particular attention is given to the quantification of soil fabric.

Chapter 3 describes the material tested and the equipment used in the research; primarily the stress path cell and hollow cylinder apparatus (HCA). The calculation of stresses and strains in the HCA is explained as well as the procedure followed to achieve testing control. The recent improvements to the HCA in order to test samples with higher aspect ratio are summarised. Previous numerical and experimental research to assess the effects of sources of stress and strain non-uniformities is considered. The last section of the Chapter describes the new sample preparation method developed and the testing procedures in detail.

Chapter 4 presents the experimental results from triaxial and HCA tests. Section 4.2 includes the results from triaxial experiments used to decide upon the testing conditions for the HCA tests and to determine the  $K_0$  coefficient for glass ballotini. Section 4.3 discusses the results from HCA tests, including the effects of the grain size distribution and sample size effects.

Chapter 5 describes the new DEM algorithms that were developed and implemented to simulate the HCA tests discussed in Chapter 4. Issues related to contact detection and simulation control are briefly summarised. Subsequently, analytical and qualitative validation of the proposed algorithms is presented.

## 1. Introduction

---

Chapter 6 includes the results of DEM simulations with periodic boundaries of tri-axial, true triaxial and constant  $b$  tests. The major principal stress is orientated in the vertical direction for all these simulations. The selection of input parameters and the specimen generation procedures are described in detail. Results from both isotropically and anisotropically consolidated specimens are analysed and compared. The DEM simulation results are analysed at the overall (macro-) and the particle (micro-) scale. Numerous sensitivity analyses are presented to provide further understanding of the material behaviour.

Chapter 7 describes DEM simulations where specimens were sheared with the major principal stress rotated with respect to the vertical direction. A new fabric surface is proposed to interpret the three-dimensional behaviour of granular materials. The effects of the initial structure and the non-coaxiality of the response are briefly discussed.

Chapter 8 explores the possibility of performing advanced DEM simulations of HCA tests including realistic boundary conditions. The issues encountered in relation to specimen generation and the potential to further assess the effects and sources of stress and strain non-uniformities are highlighted.

Finally, Chapter 9 summarises the major contributions of this research and presents suggestions for future research.

# Chapter 2

## Background Information

### 2.1 Introduction

Soil is three-dimensional and anisotropic in its nature. Its measured properties can change according to the magnitude and orientation of the stresses applied to it. Geotechnical processes involving a change in applied load can cause both the magnitude and orientation of the principal stresses to change. Both the magnitude and orientation of the principal stresses have been recognized as key factors affecting soil response.

A material is considered anisotropic if its properties are direction-dependent. Anisotropy has been studied for many years as one of the main factors affecting soil behaviour in terms of its stiffness and strength (e.g. Arthur & Menzies 1972, Vaid et al. 1990, Zdravkovic & Jardine 1997, Lade et al. 2008). Soil anisotropy arises because of the processes involved in soil deposition, stress history and composition. Additional studies also showed that the intermediate principal stress  $\sigma_2$ , plays an important role in soil behaviour. Experimental studies by Symes (1983), Shibuya (1985) and Foundoukos (2006) have confirmed that the intermediate principal stress can affect anisotropy.

A significant body of research has considered the development of models that can capture anisotropic soil behaviour for use in continuum analyses (e.g. Whittle & Kavvadas 1994, Yang et al. 2008b, Mahdi & Dafalias 2008). More recently, with the development of the distinct element method (DEM) further insight into the particle-scale interactions underlying soil behaviour has been achieved.

This chapter is divided in two main blocks: An experimental block which describes previous experimental studies on anisotropic soil behaviour and a numerical part in which DEM is briefly described and previous studies using this methodology are summarised. Although there is a substantial body of literature that considers the undrained anisotropic behaviour of granular materials, it is not discussed here as this thesis is concerned only with granular materials under drained conditions.

## 2.2 Definition of anisotropy

From the outset it is important to define two significant parameters,  $\alpha$  and  $b$ . The orientation of the major principal stress typically is measured with respect to the vertical and the angle is denoted by  $\alpha$ . The effect of the intermediate stress,  $\sigma_2$ , is normally assessed using the intermediate stress ratio  $b$ , defined as:

$$b = \frac{\sigma_2 - \sigma_3}{\sigma_1 - \sigma_3} \quad (2.1)$$

Casagrande & Carrillo (1944) made one of the earliest mentions of soil anisotropy. They characterised anisotropy into two constituent parts; *inherent* and *induced* anisotropy. They defined inherent anisotropy as a physical characteristic inherent in the material and entirely independent of the applied strains. Induced anisotropy on the other hand, was defined as a physical characteristic due exclusively to the strain associated with an applied stress. Therefore, the anisotropy of a soil element is a combination of both *inherent* and *induced* anisotropy. This combination is normally called *initial* anisotropy. This *initial* anisotropy is what determines the behaviour of the soil under general stress conditions.

There are several factors influencing the anisotropic response of soils. Particle shape, particle size, grain size distribution and stress history are amongst them. The particle size and shape of grains can create anisotropic characteristics during deposition, because individual particles tend to orientate with their longest axis orthogonally to the direction of deposition (Oda 1972a). This implies that the depositional process is also important. In fact, it has been effectively demonstrated in experimental studies (e.g. Lam & Tatsuoka (1988)) that triaxial samples tested in the laboratory with different preparation methods exhibit different response characteristics. The particle shape, particle size and the characteristics of the contacts between grains can also affect the induced anisotropy as “load carrying columns” (i.e. directional

## 2. Background Information

networks of contacting particles transmitting the applied stress) form parallel to the direction of loading (Oda 1972*b*).

Laboratory experiments have shown that stress history strongly affects the subsequent shearing behaviour of soil. For example, Arthur (1972) subjected a sand sample to a two-stage drained test in the triaxial cell in order to assess the effects of induced anisotropy. In the first stage of the test, triaxial compression was imposed until failure was approached and then in the second stage the sample was axially extended until failure occurred. The behaviour of the sample in the second stage was compared with a test performed on the same sand, with an equal initial void ratio, but only subjected to a triaxial extension stress path. Therefore the induced pre-straining of the initial compression stage is not present in the second test. The results revealed induced anisotropy in the form of large differences in the level of axial strain required to reach a given deviatoric stress. In other words, the stiffness and the mobilised angle of shearing resistance differed in both of these tests.

## **2.3 Measurement of soil anisotropy in the laboratory**

Several types of equipment can be used in the laboratory to study soil anisotropy and the effect of the intermediate stress. In general, to study anisotropy, independent control of the magnitude and direction of the principal stresses should be available. A brief description and summary of the characteristics of these apparatuses, their advantages and disadvantages, as well as the modifications that can be made in order to assess anisotropic soil response and the effect of the intermediate stress are discussed here.

### **2.3.1 The direct shear box**

The direct shear box is possibly the simplest soil laboratory test to estimate the shearing resistance of soils. It allows a sample to be  $K$  consolidated vertically and then sheared horizontally. In this apparatus, during testing a prismatic specimen is sheared by sliding one half of a box over the other half. The ease of use of this equipment is its biggest advantage, followed by its low cost. However, this method of testing is marred by numerous disadvantages.

## 2. Background Information

Firstly, in this test there is no control over the drainage conditions. Secondly, not all the stress variables can be measured, therefore assumptions about the failure state must be made in order to interpret the results. Thirdly, several studies have demonstrated that the stresses and strains in the sample are highly non-uniform. For further details, the reader is referred to the studies by Potts et al. (1987) and Cui & O'Sullivan (2006) who have analysed this problem using finite element analyses and the distinct element method, respectively. Finally, in this test the direction of the major principal stress changes, rotating from the vertical as shearing progresses but in an uncontrolled manner.

A modified version of this apparatus to study anisotropy was proposed by Guo (2008). In this modified apparatus one of the vertical sides of the two halves can be removed to pour sand while the box is tilted in any desired direction and create samples with differing particle and bedding orientations. Experimental results of the mobilised angle of shearing resistance showed that this device can reasonably capture the directional variation of the shear strength in granular materials observed in different testing devices. However, all the disadvantages in terms of non-uniformities of stress and strain as well as the uncontrolled rotation of the major principal stress noted above remain present.

### **2.3.2 The simple shear device**

The simple shear device is an improvement upon the direct shear box, developed with the aim of reducing the strain non-uniformities caused by the local displacement of the two halves in the direct shear box. Different versions of the apparatus have been proposed. Some devices use prismatic specimens such as the Cambridge simple shear apparatus initially introduced by Roscoe (1953) and its improved version by Stroud (1970), whereas others, such as the Norwegian Geotechnical Institute (NGI) design by Bjerrum & Landva (1966), use a short cylindrical sample.

Simple shear devices do not induce a shear plane in a specific location, therefore they do improve the shear box design in terms of strain non-uniformities. However, stress non-uniformities are produced due to the lack of shear stress in the side of the samples. This is particularly evident in the NGI devices as the sample is sheared with a constant perimeter boundary condition. Additionally, the simple shear device is difficult to operate, the major principal stress does not rotate in a controlled manner (as in the direct shear box) and the intermediate stress can not be measured. More

## 2. Background Information

---

differences between the direct shear box and the simple shear device are described in detail from a particulate perspective by Thornton & Zhang (2001).

### **2.3.3 The triaxial cell**

The conventional triaxial cell is widely used around the world. A common design is described by Bishop & Henkel (1962) and the principles of this apparatus are described in every soil mechanics textbook.

The interpretation of its results is not difficult as there are no shear stresses on the vertical boundary and all the stresses applied to the sample can be measured. Furthermore, its results in terms of strength and stiffness are the main parameters used in geotechnical design.

Due to the presence of the top and bottom rigid boundaries, the triaxial cell is not free from stress and strain non-homogeneities. However, one way to reduce this is to increase the aspect ratio (height/diameter) of the samples to 2 or greater. The research presented here explores the same approach to reduce the non-uniformities in the hollow cylinder apparatus.

From the perspective of this study the triaxial cell cannot be easily used to investigate soil anisotropy. Only two cases of major principal stress orientation are possible ( $\alpha = 90^\circ$  for triaxial extension when  $b = 1.0$ , and  $\alpha = 0^\circ$  for triaxial compression when  $b = 0.0$ ). Some researchers have attempted to test reconstituted samples prepared by tilted deposition (as illustrated in Figure 2.1, note that  $\theta$  is the angle of deposition) or natural samples by cutting them in an inclined manner. However, (Saada & Townsend 1981) noted that this approach is subject to errors, as undesired bending moments and shear stresses can be produced at the top and bottom boundaries if rigid platens are used.

Restricting consideration to small strain response only, the triaxial cell has provided a substantial amount of understanding about anisotropic soil behaviour. Kuwano et al. (2000) describe procedures and experimental data of anisotropic stiffness at small strains, measured using bender elements, for different granular materials including glass ballotini. These procedures are commonly used by many researchers (see Jovicic et al. 1996, Pennington et al. 2001).

## 2. Background Information

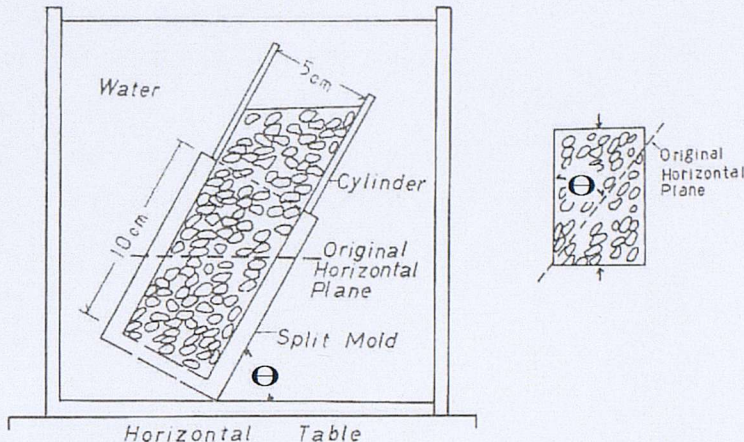


Figure 2.1: Tilted deposition of sand samples (Oda 1972a)

### **2.3.4 The true triaxial apparatus**

The true triaxial apparatus is designed upon the same concept as the conventional triaxial cell. However, it uses a prismatic specimen surrounded by six boundaries. These boundaries allow the application of three different normal stresses in fixed orthogonal directions.

This advanced feature, in contrast to the conventional triaxial cell (where the two horizontal stresses are equal), allows to evaluate the effects of the intermediate stress in soil response. However, in terms of anisotropy it possesses the same challenges as the conventional triaxial apparatus. The orthogonal and perpendicular boundaries can translate but they cannot rotate. No shear stress can be applied to the specimen and the orientation of the principal stresses cannot be controlled. The study of anisotropy is therefore limited to two situations: a)  $\alpha = 90^\circ$  and b)  $\alpha = 0^\circ$ . However, the value of  $b$  can be controlled in any of these two directions, providing another improvement over the conventional triaxial apparatus. As in the case of the conventional triaxial apparatus, there have been some attempts to test samples reconstituted by pluviation at different angles of deposition (e.g. Wong & Arthur 1985, Marachi et al. 1981).

### **2.3.5 The plain strain device**

Many versions of the plane strain apparatus have been developed (e.g. Marachi et al. 1981, Green & Reades 1975). In this device prismatic specimens are confined in one direction, therefore the intermediate strain is kept equal to zero and the intermediate

## 2. Background Information

stress can be measured if a load cell is deployed. However, that is not the best solution. To be able to measure a stress, a finite displacement is required and this violates the zero strain condition. Consequently, the influence of  $b$  in soil response can not be obtained using this apparatus. Additionally, anisotropic behaviour can not be studied because the orientation of the major principal stress can not be varied unless inclined samples are tested, but that brings the usual problems described for the triaxial devices.

### **2.3.6 The directional shear cell**

In comparison with previously described devices, the directional shear cell is a much more advanced apparatus that applies controlled changes of the magnitude and orientation of stresses. In this apparatus plane strain conditions are imposed by rigid end platens along two opposite sides of the sample. On the other four sides, direct normal and shear stresses can be applied through flexible membranes. A full description of the apparatus is provided by Arthur et al. (1981).

The possibility of application of a shear stress along four of the faces of a soil specimen is the essential feature that allows control of the orientation of the major principal stress. The application of stress and strain is relatively uniform. However, the measurement of strains is performed via photometry and/or radiography, therefore its interpretation is expensive and difficult. An essential advantage of this apparatus is that the effects of inherent and induced anisotropy under principal stress rotation can be studied independently by changing the direction in which the material is pluviated during sample preparation.

The biggest disadvantages are that while  $b$  can be measured, it cannot be controlled and the stresses in which the device can operate are low. Also sample set-up and the operation of the apparatus are difficult.

### **2.3.7 The hollow cylinder apparatus**

The hollow cylinder apparatus (HCA) subjects a hollow cylindrical specimen to four pressures that can be independently controlled. These pressures are the internal and external pressures along the vertical curved sides of the sample, a vertical load and a torque (acting over the cross-sectional area of the sample). With the indepen-

## 2. Background Information

dent application and control of these forces, the orientation and magnitude of the principal stresses can be independently measured and controlled.

Both effects of  $\alpha$  and  $b$  on soil behaviour can be easily studied, and the drainage conditions are always controlled. Consequently, this apparatus can replicate any stress path that can be followed using the previously described devices, as well as any stress path that soil can experience around different geotechnical structures. This capacity makes it easy to assess the validity of the HCA results. For example, Pradhan et al. (1988) successfully compared simple shear tests in the HCA to tests performed in the Cambridge style simple shear apparatus. Their results were comparable in terms of both strength and deformation.

The HCA presents difficulties in preparing homogeneous samples as well as measuring strain and stress under the presence of non-uniformities. The latter is due to sample geometry and boundary conditions. This non-homogeneity in stress and strain can affect the interpretation of measurements. As in the case of the triaxial apparatus, it is possible to reduce these errors to reasonable levels by selecting an appropriate geometry. Critical states are very difficult to achieve using a HCA. Additionally, inherent and induced anisotropy cannot be separated because the samples cannot be tilted (unless sand samples are frozen or they are intact clay samples) or the direction of pluviation changed. A full description of the HCA including its mode of operation and previous studies to assess the level of non-uniformities are presented in Chapter 3.

## **2.4 Previous experimental studies on the effects of soil anisotropy**

This section describes some of the findings related to the effect of the orientation of the major principal stress,  $\alpha$ , and the effects of the intermediate stress,  $b$ , on the drained behaviour of granular materials. Tests using prismatic, cylindrical and hollow cylindrical specimens are included in this summary. The characteristics of granular materials used in the quoted works are summarised in Table 2.1. Note that in Table 2.1  $C_u$  is the coefficient of uniformity obtained from the grain size distribution

## 2. Background Information

---

Sand	$G_s$	$e_{min}$	$e_{max}$	$d_{50}(mm)$	$C_u$	Reference
Ham river	2.65	0.59	0.92	0.24	1.35	Symes (1983)
Leighton Buzzard	2.64	0.50	0.92	0.67	1.31	Arthur et al (1977)
Loch Aline	2.65	0.54	0.80	0.26	1.30	Sutherland & Mesdary (1969)
Monterrey No. 0	2.65	0.53	0.86	0.43	1.53	Marachi et al (1981)
Ottawa	2.65	0.50	0.82	0.40	1.50	Vaid et al (1990)
Sand B	2.65	0.63	0.99	0.16	1.54	Oda (1972a)
Sand C	2.65	0.54	0.86	0.85	1.02	Oda (1972a)
Sand D	2.67	0.71	1.13	0.36	1.41	Oda (1972a)
Santa Monica	2.66	0.58	0.91	0.32	1.58	Lade et al (2008)
Toyoura	2.64	0.61	0.98	0.16	1.54	Lam & Tatsuoka (1988)

Table 2.1: Typical characteristics of different sands

### 2.4.1 Anisotropic soil behaviour: Effects of $\alpha$ on soil behaviour

The first attempts to study anisotropic soil behaviour involved conventional triaxial tests. A comparison was made between the response in triaxial compression and extension (e.g. Bishop 1953). In these shearing modes, the inclination of the major principal stress with respect to the vertical  $\alpha$ , is  $0^\circ$  for triaxial compression and  $90^\circ$  for triaxial extension. Note however, that the  $b$  values for these two cases are different, imposing additional limitations in the analysis of their results.

Due to the additional inherent experimental limitations imposed by the triaxial apparatus to evaluate soil anisotropy (see Section 2.3.3), more advanced studies were performed through inclining samples by pouring sand into a tilted mould to get different inclinations of the bedding plane (as outlined in Section 2.3). These tests were carried out using cylindrical and prismatic specimens under plane strain and triaxial conditions (i.e. Wong & Arthur 1985, Lam & Tatsuoka 1988, Lade & Duncan 1973). The only apparatuses that can test samples with different  $\alpha$  and  $b$  values are the hollow cylinder apparatus and the directional shear cell. Previous research evaluating the influence of  $\alpha$  on soil response using these different apparatuses is summarised in this section.

#### Effects of inherent and induced anisotropy on soil behaviour

In one of the earliest studies of soil anisotropy, Oda (1972a) tested four different sands, which were called sands A, B, C and D. Sand B had elongated particles and sand D had rounded particles. It must be recalled that the particle shape and

## 2. Background Information

the method of deposition strongly influence inherent anisotropy (see Section 2.2). Therefore, the experimental results on these two sands are of interest. In order to assess the effects of soil inherent anisotropy, samples were prepared by air-pluviation into a tilted cylindrical container that was then reoriented to have a vertical axis prior to testing, resulting on planes at  $\theta = 0, 30, 60$  and  $90$  degrees to the horizontal. The orientation of the major principal stress with respect to the vertical is denoted here as  $\alpha$ , and  $\alpha = 90 - \theta$ .

The results indicated that the effect of the tilting orientation on the mobilised deviatoric stress was more pronounced in sample B (elongated particles) than in sample D (rounded particles), (see Figure 2.2). Referring to Figure 2.2, it was observed that the axial strain to failure decreased as  $\alpha$  increased and the tendency to dilate decreased. The previous observations imply that the stiffness of soil response is the greatest when the principal stress orientation is vertical ( $\alpha = 0$ ) and that it decreases as this orientation increases. Oda concluded that the inherent fabric determines the behaviour at early stages of shearing (i.e. the difference on stiffness at small strain levels). This is because the distribution of inter-particle contacts determines the directions of stability in a soil specimen.

In a later paper by Oda (1972b), an additional test series of drained triaxial tests with different preparation methods using sand C was published. He used samples densified using two different methods. Consequently, different initial fabrics (i.e. inherent anisotropies) were created. Using image analysis at different strain levels it was shown that the initial fabric remains intact at small strains, however at large strains this initial fabric was lost, possibly due to particle rearrangement. Therefore, Oda postulated that particle sliding occurs along unstable contacts with unfavorable orientation in order to generate new contacts with better orientation. In order to confirm the previous postulate, Oda & Konishi (1974) performed two-dimensional simple shear tests on rods made of photoelastically sensitive material. They observed that as shearing progresses the contact normals rotate from 0 to 45 degrees, always towards the direction of the major principal stress.

Arthur & Menzies (1972) performed a similar study using a true triaxial apparatus, with flexible membranes all around the sample. Theoretically, this boundary configuration removes the undesired shear stresses and bending moments that are generated in tilted cylindrical specimens due to end restraint (Saada & Townsend 1981) present in the previous studies. These tests were also done with the purpose of investigating the effects of inherent anisotropy in soil behaviour. Leighton Buzzard sand was poured through air at different angles of tilt ( $\theta$ ) to produce different

2. Background Information

---

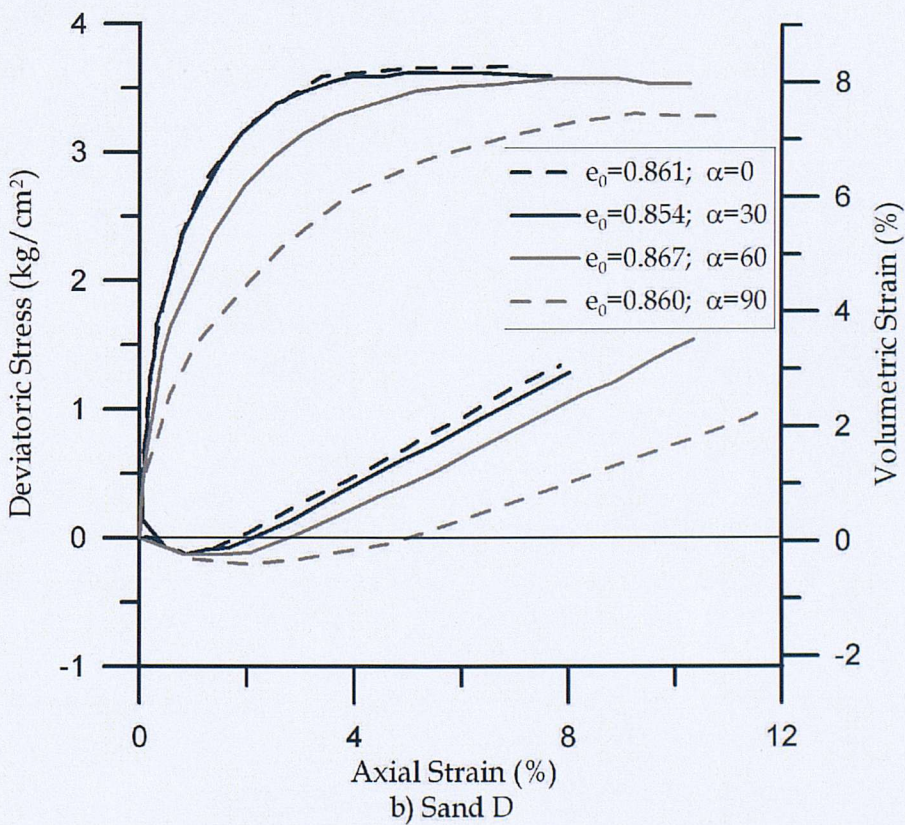
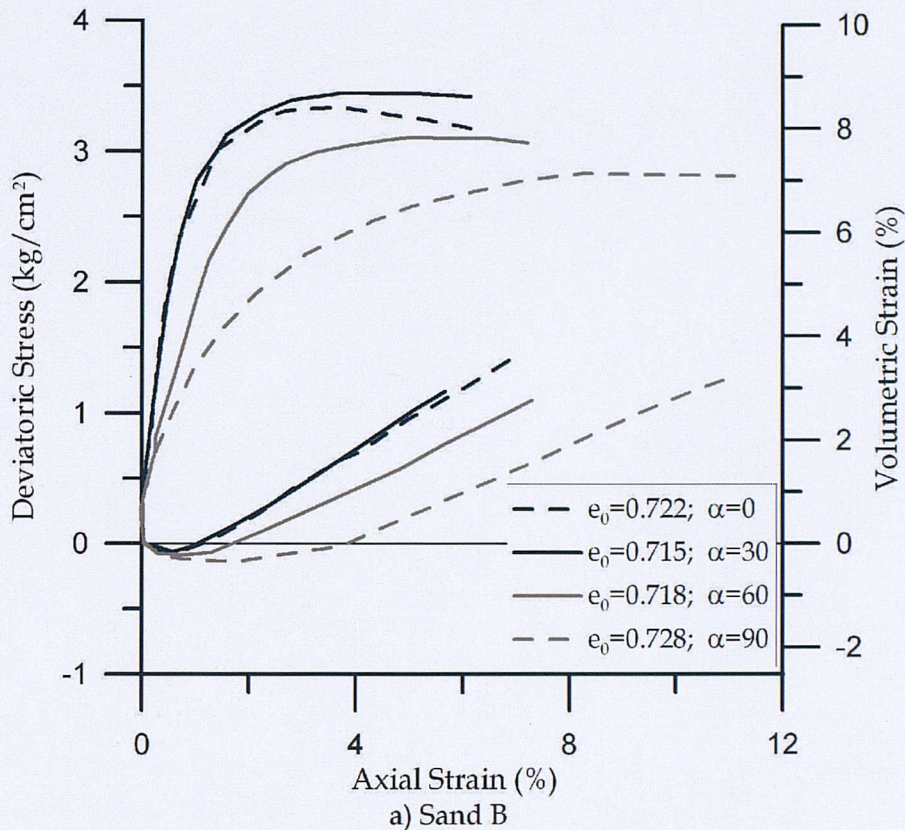


Figure 2.2: Effect of angle  $\alpha$  on stress-strain and volume changes of a) Sand B and b) Sand D (modified after Oda 1972a)

## 2. Background Information

angles in the bedding plane. Some of the results of this study are shown in Figure 2.3. It can be seen in Figure 2.3a that there is strength anisotropy in terms of the tilt angle  $\theta$  which as explained above, is related to  $\alpha$ . Although these tests did not reach a clear failure state, Figure 2.3b also confirms the results by Oda (1972a) in the sense that a different level of strain is required to get the same stress ratio as the orientation of the major principal stress ( $\alpha$ ) varies with respect to the bedding plane.

To complement the previous study, Arthur et al. (1977) used a directional shear cell to assess the effect of induced anisotropy on the behaviour of dense Leighton Buzzard sand. The effect of inherent anisotropy was eliminated in the tests by pluviating the material in the direction perpendicular to the direction of subsequent shear.

The tests consisted of several stages in order to achieve an initially induced anisotropy. First, the samples were monotonically loaded to attain a high stress ratio ( $\sigma_1/\sigma_3 = 6$ ) with a constant orientation of the major principal stress. After unloading the samples to an isotropic state, the orientation of the major principal stress was changed by a magnitude  $\Delta\alpha$ , giving the value of the orientation of the major principal stress during subsequent shearing (reloading). In this manner, an induced anisotropy was created during the first loading. Some of the results of those tests are shown in Figure 2.4.

In Figure 2.4 several plots are presented, all of which include data for the first loading and the reloading stage. Part I shows the stress-strain relationship for each of the tests in terms of the stress ratio ( $R = \sigma'_1/\sigma'_3$ ) and major principal strain  $\epsilon_1$ ; part II presents the plot of major principal strain ( $\epsilon_1$ ) against minor principal strain  $\epsilon_3$  and part III includes the stress ratio  $R$  against the incremental strain ratio ( $-\delta\epsilon_3/\delta\epsilon_1$ ). Several observations were made from these plots:

- Induced anisotropy does not significantly affect the angle of shearing resistance, being approximately equal to  $50^\circ$  in all cases. However, it must be noted that none of the tests showed a clear failure state, therefore this conclusion may be open to debate.
- Induced anisotropy can have a large influence on the strain required to achieve a given stress ratio. A larger strain is required to achieve the same stress ratio as the change in the orientation of the major principal stress ( $\Delta\alpha$ ) increases. Furthermore, the major principal strain ( $\epsilon_1$ ) increases upon reloading.

## 2. Background Information

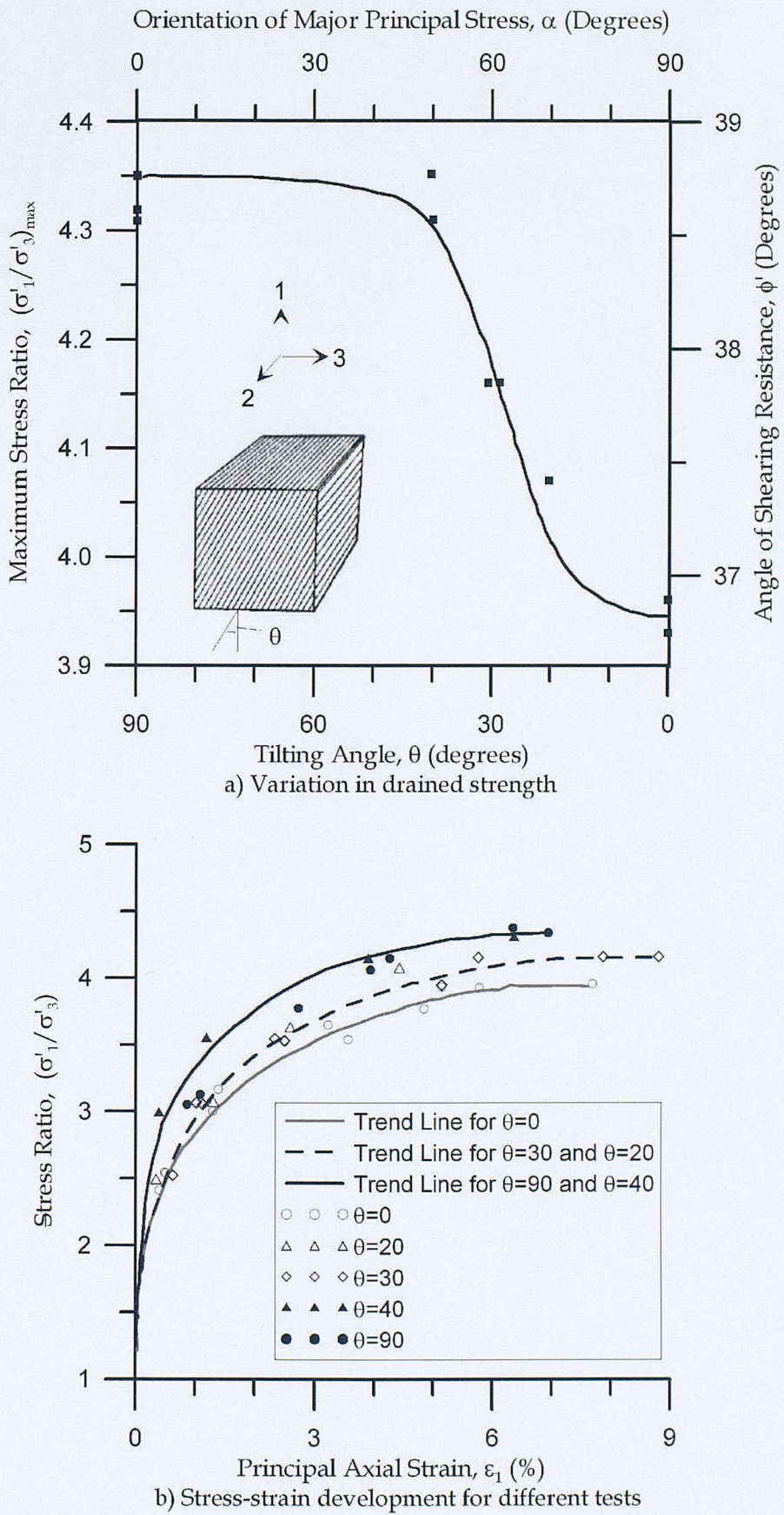


Figure 2.3: Inherent anisotropy of Leighton Buzzard sand (modified after Arthur & Menzies 1972)

## 2. Background Information

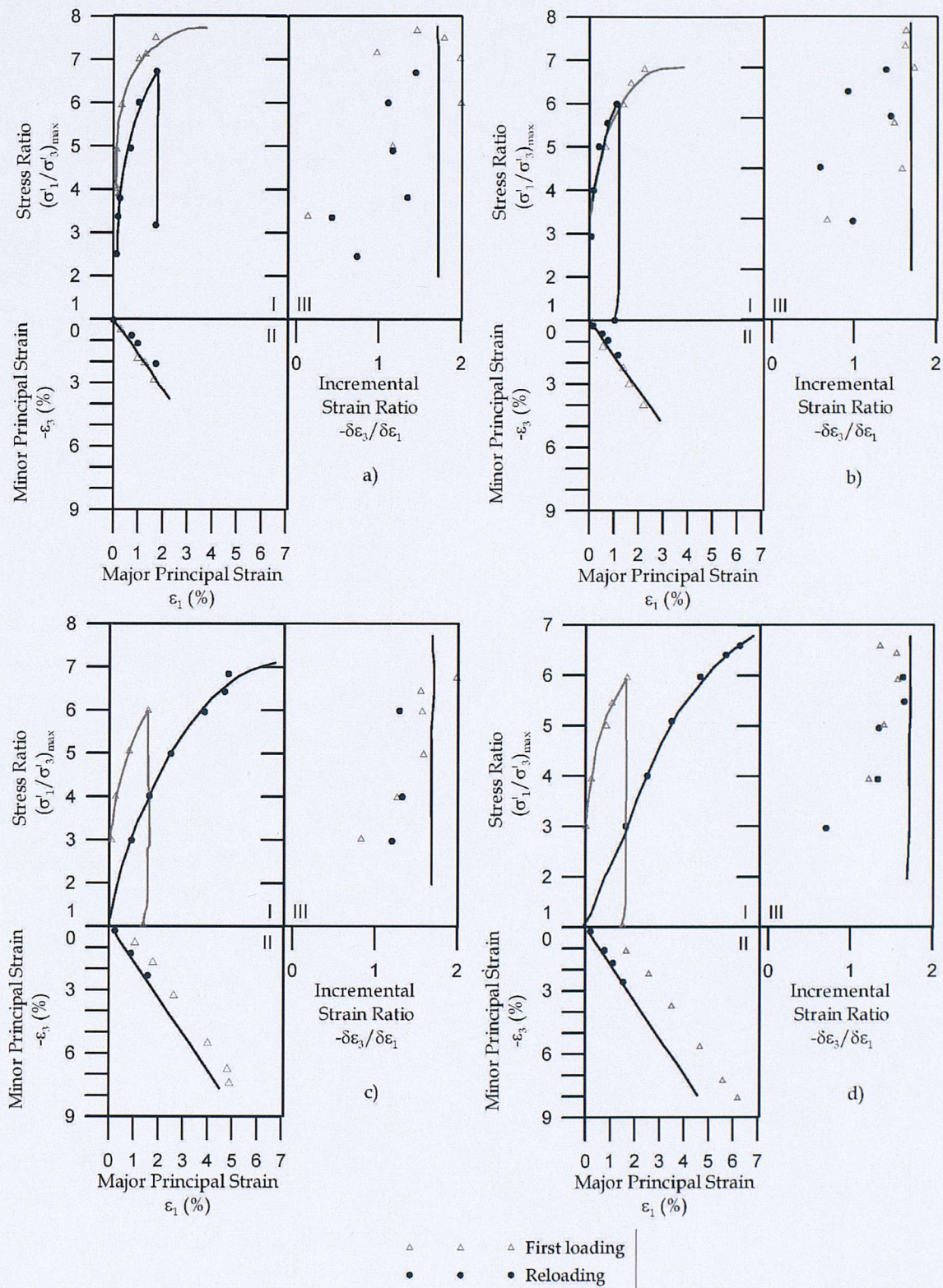


Figure 2.4: Induced anisotropy upon reloading with a change of principal stress direction a)  $\Delta\alpha = 0$ , b)  $\Delta\alpha = 30^\circ$ , c)  $\Delta\alpha = 60^\circ$  and d)  $\Delta\alpha = 90^\circ$  (modified after Arthur et al. 1977)

## 2. Background Information

Acknowledging the different effects of both inherent and induced anisotropy, Wong & Arthur (1985) and Arthur et al. (1981) extended the previous studies by performing directional shear cell tests following the same procedures as Arthur et al. (1977). However, samples were pluviated in directions both parallel and orthogonal to the direction of subsequent shearing in order to compare the effects of inherent and induced anisotropy in soil behaviour. It must be remembered that to test induced anisotropy the samples were pluviated in the direction perpendicular to the direction of subsequent shearing. To test inherent anisotropy specimens were sheared in the same direction of the pluviation.

Arthur et al. (1981) demonstrated that induced anisotropy produces a much stiffer response at small angles of the major principal stress orientation compared to the inherent anisotropy. Also larger strains as the inclination of the major principal stress increases were produced by induced anisotropy. In general, Figure 2.5 shows that the changes in stress-strain curves due to inherent and induced anisotropy are very similar. However, it can be seen that inherent anisotropy causes a continuous increase in strain as the angle of principal stress rotation increases. The induced anisotropy on the other hand, rises to a maximum when  $\alpha = 70^\circ$  and decreases slightly at  $\alpha = 90^\circ$ . These results agree with Yamada & Ishihara (1979), Oda (1972b) and Lam & Tatsuoka (1988) who said that the effects of inherent anisotropy started to disappear as the level of strain increased. It is interesting to note that Haruyama (1981) concluded that the induced anisotropy could also disappear at large stresses, based on tests on glass ballotini. Furthermore, Wong & Arthur (1985) showed that the degree of induced anisotropy is controlled by the magnitude of strain reached during the first loading stage in the directional shear cell tests.

### **Effects of initial anisotropy in soil behaviour**

As mentioned in Section 2.3, inherent and induced anisotropy cannot be separated in studies using the hollow cylinder apparatus (HCA). However, in the HCA, the effects of the orientation of the major principal stress,  $\alpha$  and intermediate stress ratio,  $b$  can be independently assessed.

Drained tests performed at Imperial College using the HCA were published by Symes (1983), Symes et al. (1982) and Symes et al. (1988) amongst others. Figure 2.6 shows the stress-strain curves and volumetric strain development for HCA experiments performed on loose Ham River sand. In these tests, the mean effective stress ( $p' = (\sigma'_1 + \sigma'_2 + \sigma'_3)/3$ ) was kept constant at 200 kPa as was the value of  $b$  (= 0.5)

## 2. Background Information

---

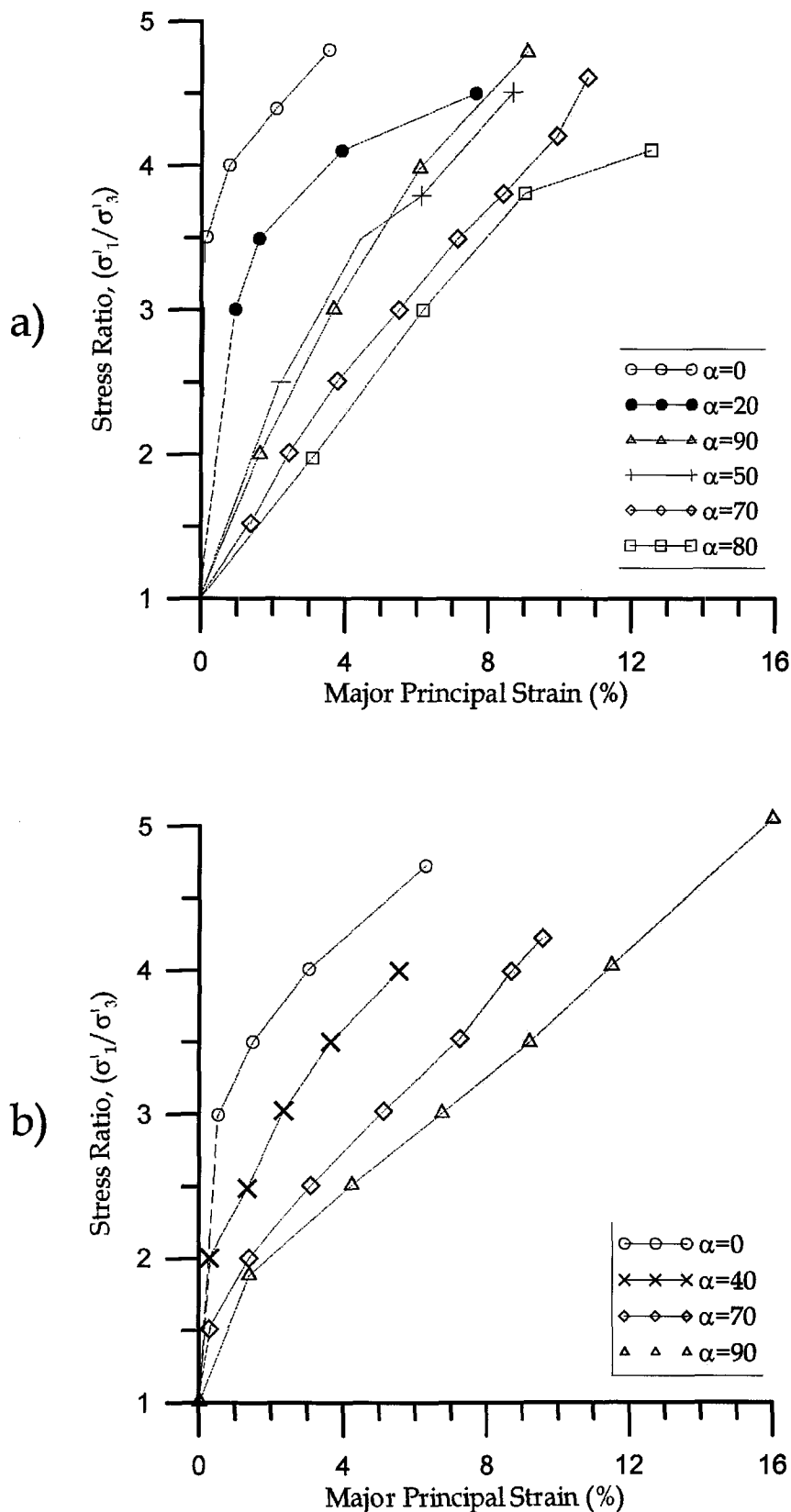


Figure 2.5: Differences between a) induced and b) inherent anisotropy of Leighton Buzzard sand (modified after Arthur et al. 1981)

## 2. Background Information

and  $\alpha$ , while the deviatoric stress ( $t = (\sigma'_1 - \sigma'_3)/2$ ) was monotonically increased during shearing. It can be seen that the maximum deviatoric stress, the maximum volumetric strain and the volumetric strain rate increase with an increment of  $\alpha$ , while the stiffness reduces with increasing  $\alpha$  value. These results were confirmed by Miura et al. (1986) and Gutierrez et al. (1991) who tested Toyoura sand sheared under different  $\alpha$  values,  $b = 0.5$  and  $p' = 98$  kPa.

Using the HCA, the effects of constant principal stress rotation can also be studied. This is important because this type of loading can occur in-situ, but also, because in HCA tests, a stage prior to shearing in which the  $\alpha$  value is rotated while  $b$ ,  $p'$  and  $t$  are kept constant can be performed. Figure 2.7 shows the volumetric strains of a multi-stage test including rotation of principal stress at constant level of deviatoric stress. Referring to Figure 2.7, the two stress paths LR1 and LR3 are described as follows: After isotropic compression to a mean effective stress,  $p'$  of 200 kPa, the deviatoric stress,  $t$  is increased to a desired value (LR1=43 kPa, LR3=89 kPa) while keeping a constant value of  $p'$ ,  $b(= 0.5)$  and  $\alpha(= 0^\circ)$ . Then, the value of  $\alpha$  is increased from  $0^\circ$  to  $45^\circ$  while the values for  $p'$ ,  $b$  and  $t$  are kept constant. Finally the deviatoric stress is increased keeping  $\alpha = 45^\circ$  constant as well as  $b$  and  $p'$ .

As mentioned above, the stage in which the angle of the major principal stress is rotated is of particular interest. From inspection of Figure 2.7 it can be seen that samples show a higher contraction with a higher value of deviatoric stress during principal stress rotation. Symes (1983) performed similar tests in which  $\alpha$  is rotated in the opposite direction ( $45^\circ$  to  $0^\circ$ ) at the same stress levels and observed that this volumetric response was lower than that shown for tests LR1 and LR3. This indicated that volumetric response was dependant not only on the current stress level, but also on the direction of stress rotation. Similar observations were done by Vaid et al. (1990) for loose and dense specimens of Ottawa sand.

### **Effect of $b$ on the assessment of $\alpha$ effects**

Oda et al. (1978) performed one of the earliest studies highlighting the effect of the intermediate principal stress on anisotropic soil response. They used tilted samples of Toyoura sand as described in similar tests in Section 2.4.1. They compared the behaviour of plane strain tests ( $b \cong 0.5$ ) in tilted prismatic samples to that of triaxial compression ( $b = 0.0$ ) in cylindrical samples.

Although the cylindrical specimens suffered from the non-uniformities as stated by

## 2. Background Information

---

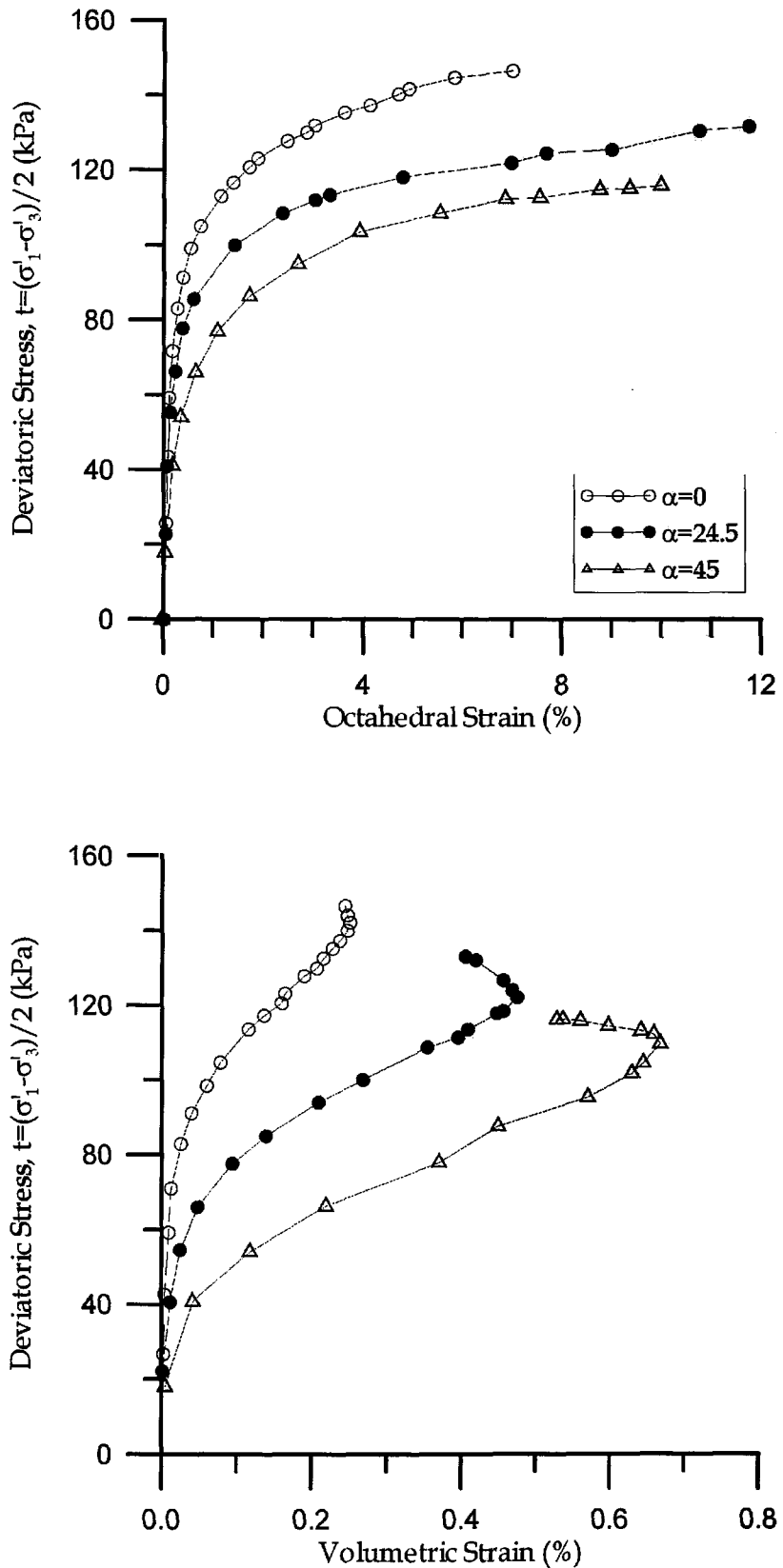


Figure 2.6: Stress-strength anisotropy of Ham River sand (Symes 1983)

## 2. Background Information

---

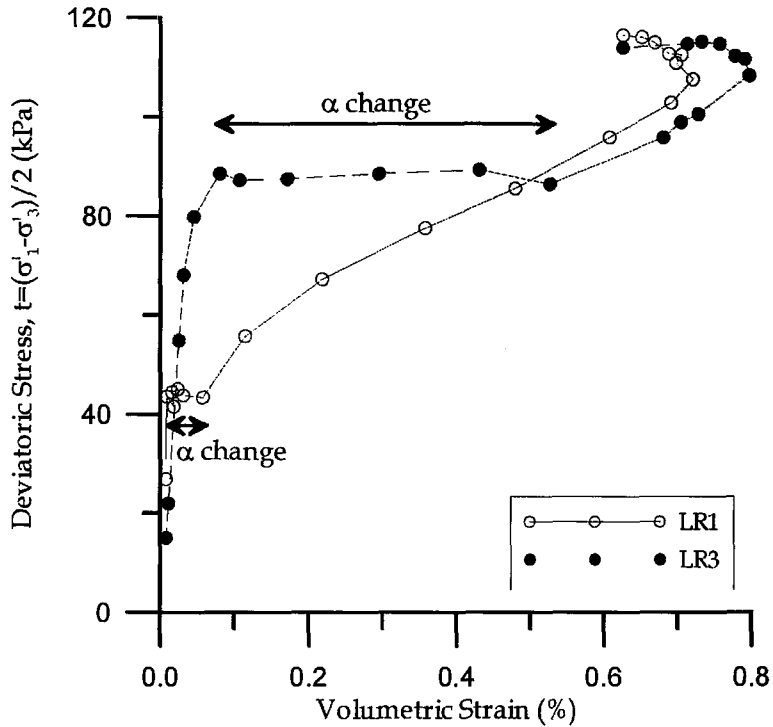


Figure 2.7: Development of volumetric strain in HCA test involving continuous rotation of the major principal stress (modified after Symes 1983)

Saada & Townsend (1981), similar trends were obtained using both sample geometries. However, the failure in plane strain tests was more brittle and the angle of shearing resistance at peak was higher than in triaxial compression.

Yamada & Ishihara (1979) performed true triaxial tests on samples of sand sheared in the directions parallel ( $\alpha = 90^\circ$ ) and perpendicular ( $\alpha = 0^\circ$ ) to the direction of deposition under different  $b$  values. The results show that the specimen was less compressible when sheared in the direction of its deposition. The conclusion is then that a specimen formed by vertical deposition is more resistant when compressed in the vertical direction ( $b = 0.0$ ). When the specimen is undergoing expansive strain ( $b = 1.0$ ), the specimen is more resistant to deformation in the horizontal direction. These results agree with the trends described in Section 2.4.1. However, all these researchers recognised that the degree of anisotropy also depends on the value of  $b$ . This fact was also identified by Lam & Tatsuoka (1988) from results on triaxial extension, triaxial compression and plane strain tests on Toyoura sand, by Symes (1983) (see Figure 2.8), Foundoukos (2006) on HCA tests of Ham River sand, and Haruyama (1981) in triaxial tests of glass ballotini.

The results of the previous experiments show that it is difficult to isolate the effects

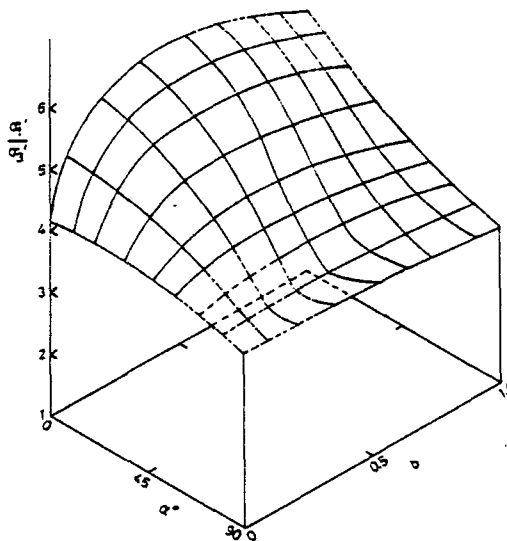


Figure 2.8: Dependence of the maximum stress ratio on  $b$  and  $\alpha$ . (Symes 1983)

of  $b$  and  $\alpha$  to understand the anisotropic behaviour of soil. This fact emphasizes the advantage of the hollow cylinder apparatus to gain further insight into these important parameters.

#### 2.4.2 Anisotropic soil behaviour: Effects of $b$ on soil behaviour

As seen in the previous section, it is generally well established that the magnitude of the intermediate stress has an effect on soil behaviour. The effect of the intermediate stress is normally assessed in terms of the intermediate stress ratio  $b$ .

The simplest comparison to highlight the influence of  $b$  on soil behaviour is a direct comparison of triaxial and plane strain tests under the same initial density and stress conditions. It must be noted that  $b = 0.0$  for triaxial compression and  $b$  varies typically between 0.3 to 0.5 under plane strain conditions. As mentioned in Section 2.4.1, different researchers (e.g. Marachi et al. 1981, Oda et al. 1978, Cornforth 1964) have found that peak strengths for all bedding plane inclinations are higher when soil is tested under plane strain than when tested under triaxial compression. Furthermore, they have demonstrated that this difference of peak strengths is higher in dense samples than in loose samples.

A different and improved approach to study the influence of  $b$  on soil behaviour

## 2. Background Information

is to test prismatic specimens in true triaxial devices. In such a study, specimens of equal initial void ratio are tested by shearing using strain control in the major principal stress direction while the remaining stresses are continuously changed to keep a constant value of  $b$ . The  $b$  value is varied systematically from 0 to 1 in different tests (one specific  $b$  value for each test) in order to have an overall picture of soil behaviour. Obviously, as mentioned before, the effects of  $b$  can also be tested using a hollow cylinder apparatus (HCA).

This section describes previous research on the effects of  $b$  on soil behaviour obtained by different types of experiment. Special attention is given to the effects on the shear strength,  $\phi'$ , assessed by the maximum mobilised angle of shearing resistance. The volumetric response with different  $b$  values is also discussed.

### **Effects of $b$ on the peak angle of shearing resistance**

The peak angle of shearing resistance seems to be affected not only by the intermediate stress ratio  $b$ , but also by the initial density and the confinement stress. Sutherland & Mesdary (1969) used cubical samples of Loch Aline sand. Different porosities and  $b$  values were tested. The results indicated that the peak angle of shearing resistance increases starting from  $b = 0.0$  to a maximum around plane strain conditions ( $b \approx 0.3 - 0.5$ ) and then decreases to a value in triaxial extension ( $b = 1.0$ ), which is very close to the value of triaxial compression ( $b = 0.0$ ). This observation was valid for all the different initial porosities (see Figure 2.9). However, Marachi et al. (1981) tested Monterrey No. 0 sand under triaxial and plane strain compression using prismatic specimens with different initial void ratios and found that the difference of shearing resistance between triaxial compression and plane strain decreases as the void ratio increases. The statement of Marachi et al. (1981) is also supported by simpler tests highlighted in Section 2.4.2. Furthermore, the results by Marachi et al. (1981) show a dependence of the difference between triaxial compression and plane strain strength on the confining stress. This difference decreases as the confinement increases.

A slightly different trend was observed by Haruyama (1981) who used dense samples of glass ballotini to assess the effects of  $b$  on the angle of shearing resistance. The trends observed (see Figure 2.10) agree with those obtained by Symes (1983) on Ham River sand tested in the HCA for constant  $\alpha$  values (see Figure 2.8) and Lade et al. (2008) using Santa Monica Beach sand also in HCA tests.

## 2. Background Information

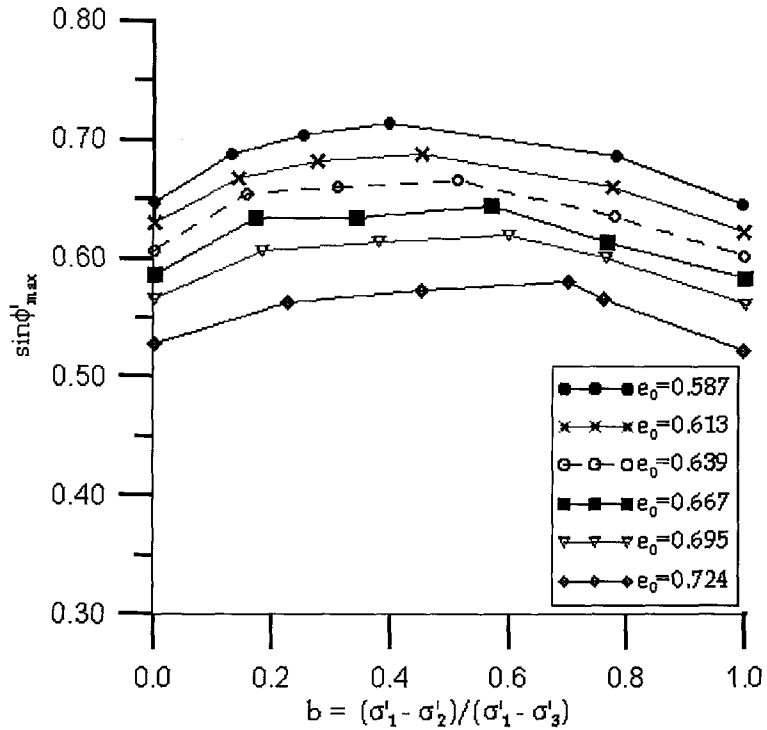


Figure 2.9: Effect of  $b$  on  $\phi'$  for Monterrey No. 0 sand (modified after Sutherland & Mesdary 1969)

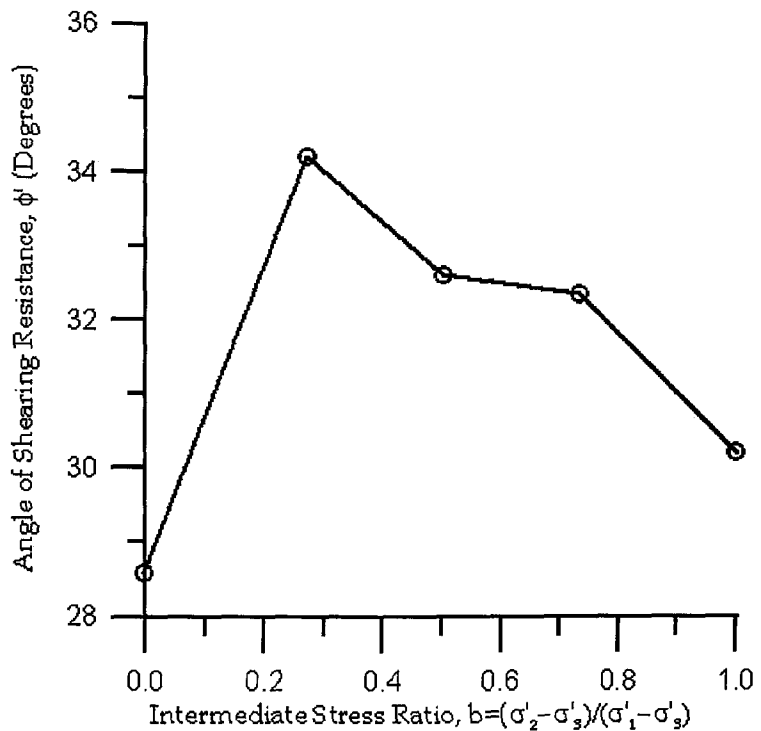


Figure 2.10: Effect of  $b$  on  $\phi'$  for glass ballotini (modified after Haruyama 1981)

## 2. Background Information

The tests performed by Green (1971) and Shapiro & Yamamuro (2003) showed a different trend in the angle of peak shearing resistance with increasing  $b$  value. It is clear from Figure 2.11 that the shear strength increases from triaxial compression to plane strain ( $b = 0.28$  for these tests). However, the scatter in the results may indicate that after the plane strain conditions ( $b > 0.28$ ) there is no effect of the intermediate stress on the angle of shearing resistance.

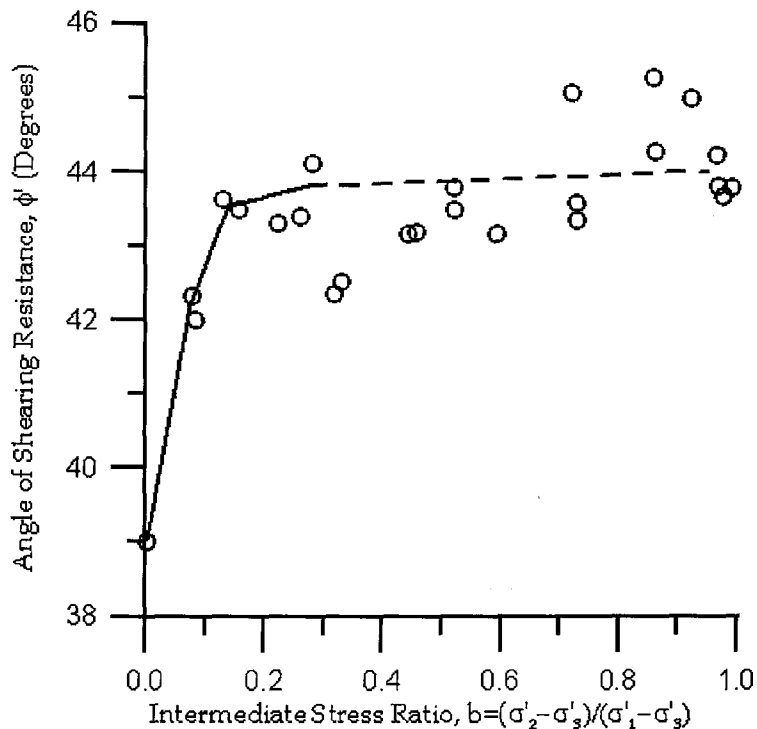


Figure 2.11: Effect of  $b$  on  $\phi'$  for Ham river sand (modified after Green 1971)

Knowing these different observations, and knowing that different researchers had equipment with different boundary conditions, it is reasonable to think that the results may be affected by this fact. In order to try to solve this dilemma Lam & Tatsuoka (1988) compared triaxial compression ( $b = 0.0$ ), plane strain ( $b = 0.2-0.6$ ) and triaxial extension ( $b = 1.0$ ) tests on Toyoura sand with different boundary conditions, sample geometries (prismatic and cubical specimens with different bedding planes) and sample sizes. From their results they concluded that the differences in the trends of the maximum angle of shearing resistance against the intermediate stress ratio found by different researchers may be caused by different sample dimensions or boundary conditions. They also observed a relation between the orientation of the major principal stress and the  $b$  value (as confirmed by Symes (1983), see Figure 2.8). More recently, Wang & Lade (2001) and Lade et al. (2008) mentioned that this relationship between the angle of shearing resistance and the intermediate

## 2. Background Information

stress ratio could also be affected by the formation of shear bands. This is a conclusion that does not contradict the study by Lam & Tatsuoka (1988), since some sample dimensions can develop shear bands more freely than others. Clearly, the expected tendency for a  $\phi'-b$  relationship is still open to debate.

### **Effects of $b$ on the volumetric response**

The volumetric response of soils is assessed by the volume changes as shearing progresses. These changes are related to the initial density of the specimen tested. Typically, a loose specimen is expected to compress and a dense specimen should dilate, or dilate after an initial amount of compression. The development of the principal strain components ( $\epsilon_1$ ,  $\epsilon_2$  and  $\epsilon_3$ ) can be evaluated, as well as the evolution of rate of dilation, during shearing. Some experimental observations considering these issues are described in this summary.

Most researchers agree with the fact that the axial strain (major principal strain,  $\epsilon_1$ ) to failure decreases when the  $b$  value increases. (e.g. Sutherland & Mesdary 1969, Green 1971, Lade & Duncan 1973, Symes 1983, Wang & Lade 2001). Although there are variable results, this behaviour can be inferred from the different tests presented in Figure 2.12. However, Reades & Green (1976) found that the axial strains to failure reduce from  $b = 0.0$  to  $b = 0.5$  and then increase slightly for both loose and dense samples as  $b$  increases. Interpretations also differ in the sense that they are dependent on the initial density. Lade & Duncan (1973) demonstrated that the axial strain to failure for loose samples initially decreases and remains essentially constant for  $b > 0.6$ . The same behaviour was not observed for the dense samples they tested.

The response of the intermediate principal strain ( $\epsilon_2$ ) cannot be discussed since plane strain conditions are forced to occur when there is no lateral deformation ( $\epsilon_2 = 0$ ). The differences between researchers are then simply given by the  $b$  value at which plane strain occurs. It is expected that when  $b$  is between triaxial compression and plane strain, the value of the intermediate strain should be negative (indicating dilation) and this amount of dilation should be reduced with increasing  $b$  value. Consequently, after the plane strain condition, and approaching the  $b$  value for triaxial extension ( $b = 1.0$ ), the intermediate strain should be positive (indicating compression), and its value should increase when  $b$  increases. This behaviour has been highlighted by Green (1971), Lade & Duncan (1973), Yamada & Ishihara (1979), Haruyama (1981), and can be confirmed in Figure 2.13 from the tests re-

## 2. Background Information

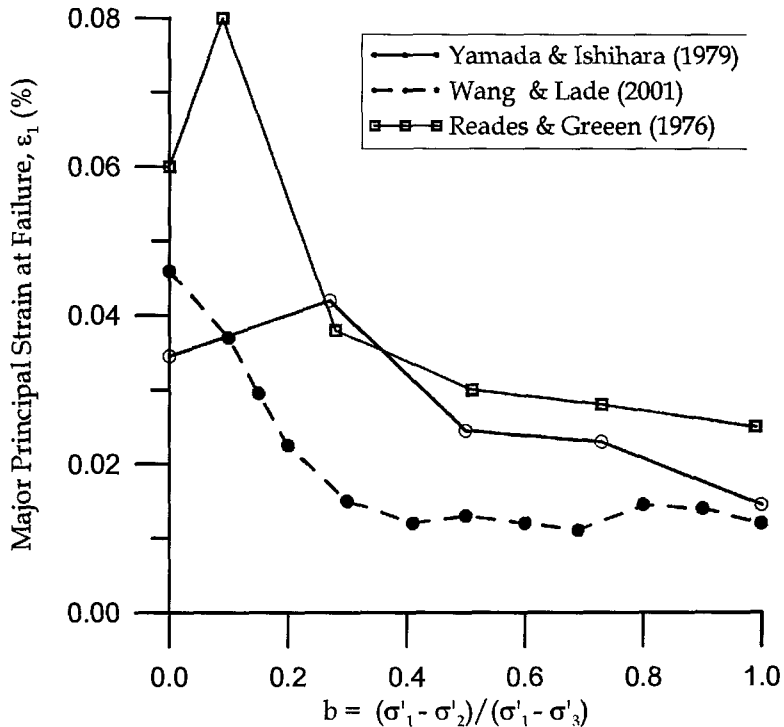


Figure 2.12: Effect of  $b$  on the major principal strain at failure

ported by Reades & Green (1976) on prismatic specimens subjected to constant  $b$  tests.

In terms of the overall volumetric strain rate, it can be said that Green (1971) observed that it increases as  $b$  is increased. This is confirmed by the results of Lade & Duncan (1973) and Symes (1983). However, it must be mentioned that Green (1971) and Reades & Green (1976) reported that the volumetric strain rate was nearly constant in the range of  $b$  values between triaxial compression and plane strain. This is an important statement because, as outlined in Section 2.4.2, the same range of  $b$  values presents the highest change in the peak angle of shearing resistance.

### 2.4.3 Small-strain anisotropy

Normally, the observed anisotropy in the macro-scale response is defined according to the level of strains. The anisotropy effects described above concern large strain response. However, in many practical applications, the operational strains lie in a very small range. Consequently, characterization of small strain response is important.

## 2. Background Information

---

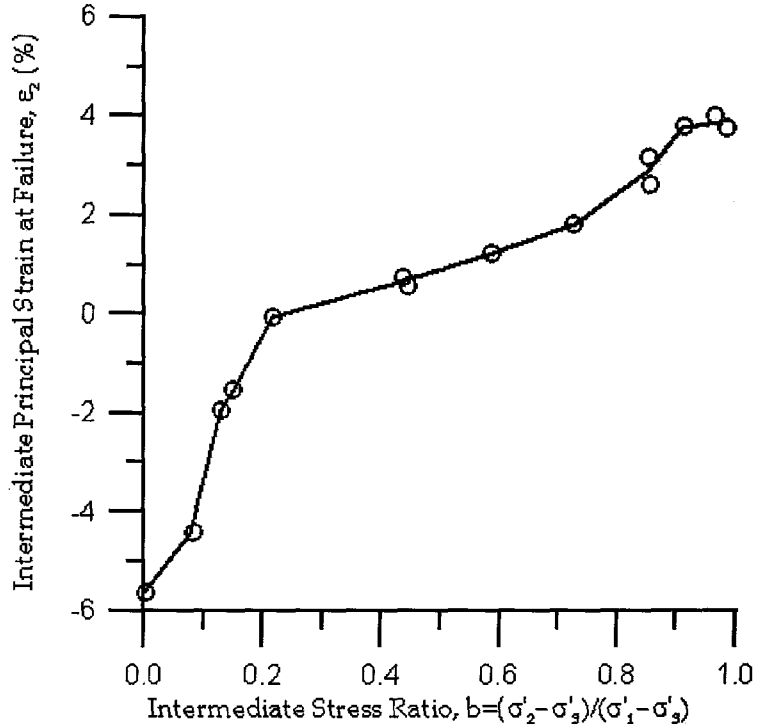


Figure 2.13: Effect of  $b$  on the intermediate principal strain at failure (modified after Reades & Green 1976)

The small-strain anisotropy deals with the behaviour of soils in the elastic region. In order to describe soil behaviour a compliance matrix is needed. This compliance matrix links the strain and stress vectors and its form depends on the constitutive behaviour of the material being studied. Thirty six elastic constants are used to describe an anisotropic continuous solid material (see Equation 2.2).

If a soil is elastic and isotropic, only two constants are required to describe the compliance matrix (Young's modulus,  $E$  and Poisson's ratio,  $\nu$ ). For a soil that is considered to be generally anisotropic and elastic the compliance matrix is defined as:

$$\begin{bmatrix} \Delta\epsilon_{xx} \\ \Delta\epsilon_{yy} \\ \Delta\epsilon_{zz} \\ \Delta\gamma_{xz} \\ \Delta\gamma_{yz} \\ \Delta\gamma_{xy} \end{bmatrix} = \begin{bmatrix} C_{11} & C_{12} & C_{13} & C_{14} & C_{15} & C_{16} \\ C_{21} & C_{22} & C_{23} & C_{24} & C_{25} & C_{26} \\ C_{31} & C_{32} & C_{33} & C_{34} & C_{35} & C_{36} \\ C_{41} & C_{42} & C_{43} & C_{44} & C_{45} & C_{46} \\ C_{51} & C_{52} & C_{53} & C_{54} & C_{55} & C_{56} \\ C_{61} & C_{62} & C_{63} & C_{64} & C_{65} & C_{66} \end{bmatrix} \begin{bmatrix} \Delta\sigma_{xx} \\ \Delta\sigma_{yy} \\ \Delta\sigma_{zz} \\ \Delta\tau_{xz} \\ \Delta\tau_{yz} \\ \Delta\tau_{xy} \end{bmatrix} \quad (2.2)$$

where the diagonal terms are equal for loading and unloading and cross coupling

terms (off-diagonal terms) may exist between any pair of stress and strain components. If the material is  $K_0$  consolidated, the soil is horizontally layered, and its initial structure is isotropic in the horizontal bedding plane. Such a material is considered to be cross-anisotropic. Only five constants of the compliance matrix are required, the compliance matrix of a cross-anisotropic material is defined as:

$$\begin{bmatrix} \Delta\epsilon_{zz} \\ \Delta\epsilon_{xx} \\ \Delta\epsilon_{yy} \\ \Delta\gamma_{zx} \end{bmatrix} = \begin{bmatrix} \frac{1}{E_{zz}} & \frac{\nu_{xz}}{E_{xx}} & \frac{\nu_{yz}}{E_{yy}} & 0 \\ \frac{\nu_{xz}}{E_{zz}} & \frac{1}{E_{xx}} & \frac{\nu_{yx}}{E_{yy}} & 0 \\ \frac{\nu_{yz}}{E_{zz}} & \frac{\nu_{xy}}{E_{xx}} & \frac{1}{E_{yy}} & 0 \\ 0 & 0 & 0 & \frac{1}{G_{zz}} \end{bmatrix} \begin{bmatrix} \Delta\sigma_{zz} \\ \Delta\sigma_{xx} \\ \Delta\sigma_{yy} \\ \Delta\tau_{zx} \end{bmatrix} \quad (2.3)$$

where all constants are related to the Young's modulus ( $E$ ) and Poisson's ratio ( $\nu$ ) that is relevant for each direction. Clearly, only five constants are required to describe a cross-anisotropic material. These constants can be determined using in-situ or laboratory tests and are dependent on void ratio, stress level, stress history and stress rates. Numerous examples of experimental studies can be found in the literature about the behaviour of soil at very small strains, which assess the factors that can affect these anisotropic parameters and the methods for its measurement (e.g. Hardin 1978, Yu & Richart 1984, Jamiolkowski et al. 1991).

Using the hollow cylinder experiments these constants can be easily evaluated. However, as stated by Foundoukos (2006) and Symes (1983), a better resolution of the current local instrumentation of the ICHCA and LICHCA is required for that purpose. Consequently, behaviour at very small strains is not discussed in this thesis.

## 2.5 A failure model for granular materials

This section introduces the concept of the deviatoric stress plane and a failure model frequently used to model the behaviour for granular materials. This specific model (and the deviatoric stress plane) are particularly important, partly because they have been constantly used for the interpretation of hollow cylinder experiments and discrete element simulations under three-dimensional stress states.

### 2.5.1 The deviatoric stress plane

Soil behaviour is three-dimensional, therefore the magnitudes of the three principal stresses are required to represent a certain stress state. Normally, the following combinations of the principal stresses (stress invariants) are used:

$$p' = \frac{\sigma'_1 + \sigma'_2 + \sigma'_3}{3} \quad (2.4)$$

$$J = \frac{1}{\sqrt{6}} \sqrt{(\sigma'_1 - \sigma'_2)^2 + (\sigma'_2 - \sigma'_3)^2 + (\sigma'_3 - \sigma'_1)^2} \quad (2.5)$$

$$\theta = \tan^{-1} \left[ \frac{1}{\sqrt{3}} \left( 2 \frac{\sigma'_2 - \sigma'_3}{\sigma'_1 - \sigma'_3} - 1 \right) \right] \quad (2.6)$$

These stress invariants are called mean effective stress, deviatoric stress and Lode's angle respectively. This choice of stress invariants has a geometric significance in the three-dimensional generalised stress plane. Referring to Figure 2.14, the value of  $p'$  is a measure of the distance along the space diagonal (line where  $\sigma'_1 = \sigma'_2 = \sigma'_3$ ) starting from the origin of the generalised stress plane to the deviatoric plane. Note that the deviatoric plane is any plane perpendicular to the space diagonal where the mean effective stress is constant. Also note that the value of  $J$  provides a measure of the distance from the space diagonal to the current stress state. The magnitude of  $\theta$  defines the position of the stress state within the deviatoric plane.

It is easy to see in Equation 2.6 that the Lode's angle is a function of the intermediate stress ratio ( $b$ ). Consequently constant  $b$  tests performed in the hollow cylinder apparatus or true triaxial devices are represented in the deviatoric plane as radial stress paths terminating at the stress state that corresponds to failure. Each value of  $b$  corresponds to a different value of  $\theta$ . For purposes of clarity, if only failure states are considered, the variation of a particular failure envelope in the deviatoric plane with a change of orientation of the major principal stress is shown in Figure 2.15.

### 2.5.2 Failure criterion proposed by Lade & Duncan (1973)

This model has been used by many researchers. For example Thornton (2000) and Ng (2004a) showed that this model agrees very well with the results of DEM

## 2. Background Information

---

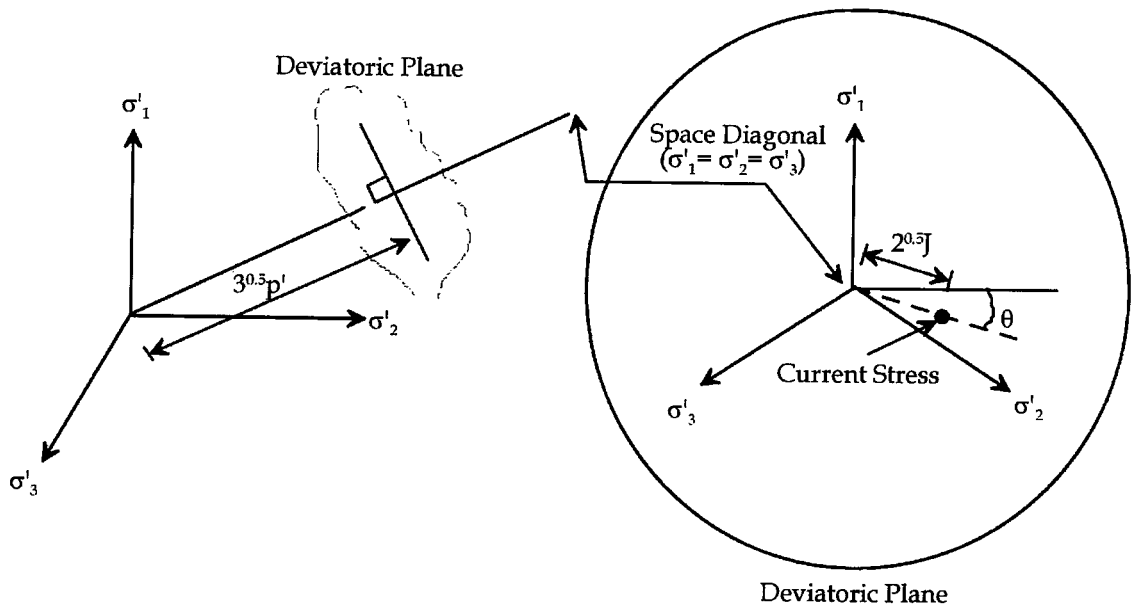


Figure 2.14: Description of the deviatoric plane in three-dimensional stress conditions

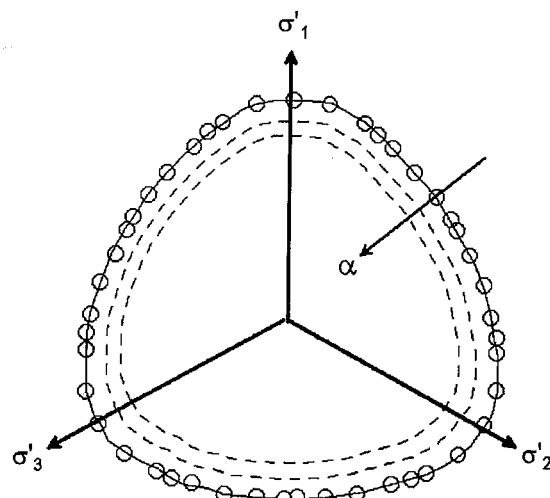


Figure 2.15: Effect of changing the orientation of the major principal stress on the failure envelope of granular materials

## 2. Background Information

simulations of true triaxial tests in which the value of  $b$  is kept constant. In this thesis the model will be used with that same comparative purpose.

The model originates from experimental evidence showing that the failure envelope of granular materials in the deviatoric stress plane approaches an equilateral triangle for high angles of shearing resistance, and approaches a regular hexagon for small values. Evidence also indicates that the failure surfaces are curved in planes containing the hydrostatic axis (i.e. at the corners of the  $\pi$ -plane (deviatoric plane)). For clarity, a representation of this model in both the deviatoric and the triaxial stress plane is shown in Figure 2.16.

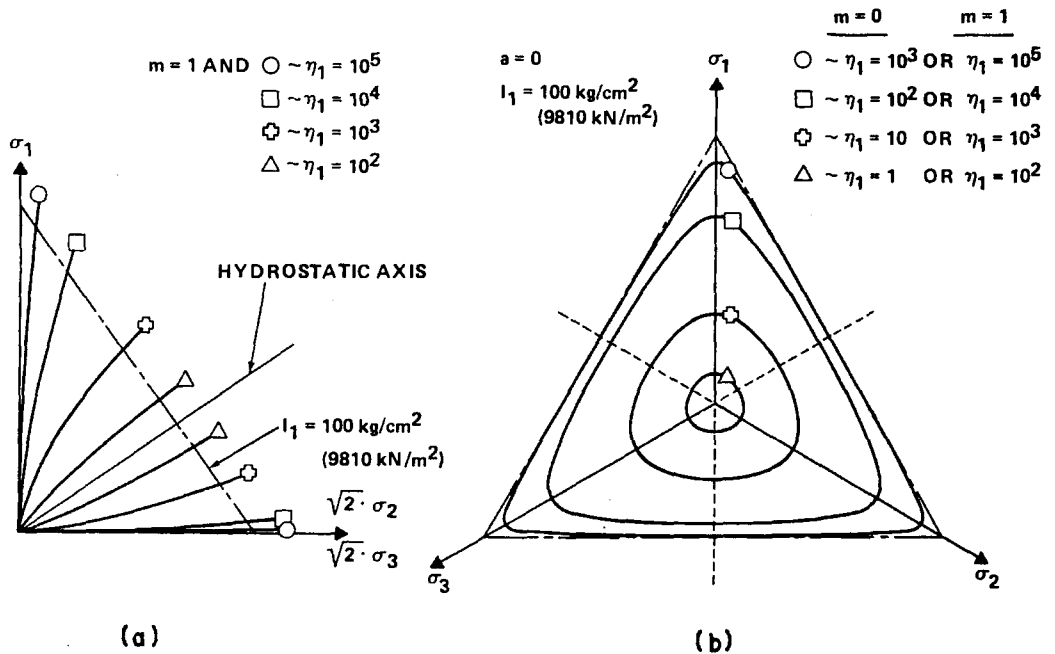


Figure 2.16: Failure envelopes of the Lade & Duncan (1973) model in a) triaxial plane and b) deviatoric plane (Lade & Duncan 1973)

The criterion is expressed in terms of the first and third invariants of the stress tensor as follows:

$$\left( \frac{I_1^3}{I_3} - 27 \right) \cdot \left( \frac{I_1}{p_a} \right)^m = \eta_1 \quad (2.7)$$

where

$$I_1 = \sigma'_1 + \sigma'_2 + \sigma'_3 \quad (2.8)$$

$$I_3 = \sigma'_1 \cdot \sigma'_2 \cdot \sigma'_3 \quad (2.9)$$

and  $p_a$  is the atmospheric pressure expressed in the same units as the stress. The value of  $I_1^3/I_3$  is 27 at the hydrostatic axis where  $\sigma'_1 = \sigma'_2 = \sigma'_3$ . The parameters  $\eta_1$  and  $m$  can be determined by plotting  $(I_1^3/I_3 - 27)$  versus  $(p_a/I_1)$  at failure in a log-log diagram and locating the best fitting straight line. The intercept of this line with  $p_a/I_1 = 1$  is the value of  $\eta_1$  and  $m$  is the slope of the line.

As the position of the  $\pi$ -plane (deviatoric plane) moves from the origin of the generalised stress plane, the failure surface defined by this criterion is shaped like an axi-symmetric bullet with the pointed apex at the origin of the principal stress axes. The apex angle increases with the value of  $\eta_1$ . The surface is concave towards the hydrostatic axis, and its curvature increases with the value of  $m$ . For  $m = 0$  the failure surface is straight. As  $\eta_1$  increases, the cross-sectional shape in the deviatoric stress plane changes from circular to triangular.

## 2.6 DEM Background

The distinct element method (DEM), originally created by Cundall & Strack (1979a) for the solution of rock mechanics problems, accounts for the particulate nature of soil. Earlier studies have demonstrated that it can reproduce the observed macro-scale response for simple loading conditions. Additionally, DEM provides micro-mechanical quantities and parameters that cannot be easily obtained from experimental tests or conventional continuum analyses and it can capture the particle-scale interactions underlying the observed macro-scale anisotropy of soils. However, DEM has not been used to replicate soil behaviour under more complex conditions that can involve rotation of the applied stresses, as it happens in the HCA. That is one of the main motivations for this study. In this section DEM is briefly described and some micro-mechanical parameters that will be used for the analysis of the simulations are presented.

### 2.6.1 Algorithm

In DEM, the interaction between particles is viewed as a transient problem, with states of equilibrium developing whenever the internal forces balance. The numerical

## 2. Background Information

---

scheme is based on an explicit time-centred finite difference system. In DEM, the equilibrium contact forces and displacements of a stressed assembly of particles are found through a series of calculations tracing the movements of the individual particles. These movements are the result of the propagation through the medium of disturbances originating at the boundaries and are a dynamic process. The speed of propagation is a function of the physical properties of the discrete medium. The method is based upon the idea that the time step chosen may be so small that during a single time step disturbances cannot propagate from any particle further than its immediate neighbours. Numerical stability considerations, and the contact detection algorithm also impose a constraint on the time-step, as discussed below.

The calculations alternate between the application of Newton's second law to the particles and a force-displacement law at the contacts. Newton's second law gives the motion of a particle resulting from the forces acting on it. The force-displacement law is used to find contact forces from particle displacements. A schematic representation of the DEM algorithm is shown in Figure 2.17.

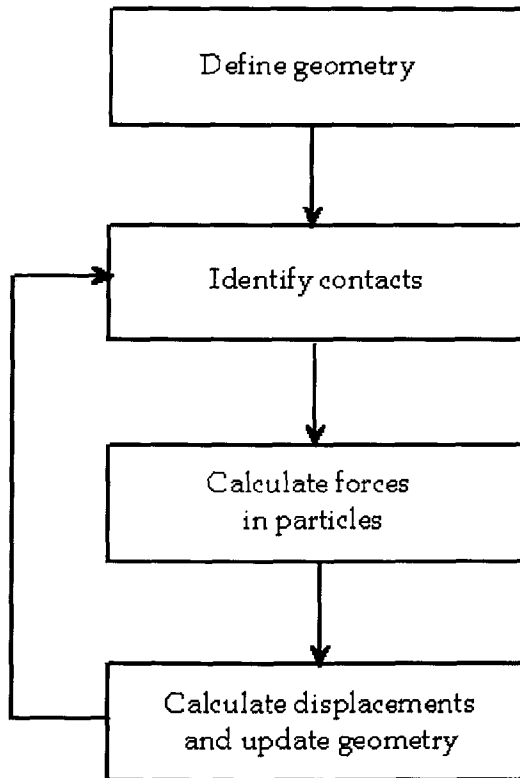


Figure 2.17: Schematic representation of the DEM algorithm

The use of Newton's second law implies that global damping can be used. This damping operates on the absolute velocities of the particles, specifically in the veloc-

## 2. Background Information

---

ity vector components, and on the rotational velocity of the particles. It is important to note that real granular materials can dissipate energy by different mechanisms including plastic deformation at the contacts and inter-particle friction. It is assumed that for granular materials most of the dissipated energy is due to frictional effects. Therefore, the value of global damping used in DEM simulations of this study was always very small.

For the simulations presented in this thesis, the force-displacement law used for the contact forces is a Hertz-Mindlin contact model (Mindlin & Deresiewicz 1953). This model considers rigid spherical particles or disks and does not allow for plastic deformation at the contacts. However, in DEM the deformations of the individual particles are small in comparison to the deformation of an assembly as a whole. Particles are allowed to overlap at contact points to account for their deformation, but this overlap is very small compared to the particle size. It is important to note that the tangential contact force is calculated incrementally to reflect the influence of changing normal contact force on the tangential stiffness (Lin & Ng 1997).

### 2.6.2 Time step and stability

As DEM uses a finite-difference integration scheme, it is conditionally stable, and one must make sure that the time step is sufficiently small. Different approaches have been proposed to define the critical time step.

Cundall & Strack (1979a) use a critical time step estimated on the basis of the single degree of freedom system of a mass  $m$  connected to ground by a spring of stiffness  $K$ , and the critical time step equals

$$\Delta t_{crit} = 2\sqrt{\frac{m}{K}} \quad (2.10)$$

Additionally, Itasca (1998) suggests that the critical time step should be multiplied by a safety factor of 0.8. However, O'Sullivan (2004) recalculated this critical time step by using the Rayleigh theorem for a Face-Centred Cubic (FCC) assembly with all the degrees of freedom in three-dimensional conditions. This was found to be

$$\Delta t_{crit} = 0.22\sqrt{\frac{m}{K}} \quad (2.11)$$

It is important to note from the previous equations that the time-step can be increased by scaling the mass of the particles. This gives additional inertia to the particles. However, if high frequency response is important, mass scaling is not recommended (O’Sullivan 2004). In this thesis, mass or density scaling was never used. Substantial efforts were made to find the fastest strain rates and the most suitable time-step using parametric studies.

The suitable selection of the time step is also related to the ability of the contact detection algorithm to efficiently recognize the creation and destruction of inter-particle contacts. With a big value of time step, the changes in the existing contact of an assembly of particles may change radically and the contact detection algorithm may not be able to detect them. Consequently, the calculated response of the particles may be affected. More details of the implementation of the contact detection algorithm are given in Chapter 5.

### 2.6.3 Boundary types in DEM simulations

Several types of boundary can be used to replicate the boundary conditions felt by a soil specimen in-situ or in laboratory testing. In this research, boundaries present in the laboratory for element testing are of particular interest. Rigid boundaries that can be strain or stress controlled, such as the top platens of a conventional triaxial cell or a hollow cylinder apparatus, need to be simulated. Additionally, accurate simulation of element tests is very challenging without an appropriate stress controlled membrane that can replicate the flexible latex membranes in standard laboratory testing.

Rigid boundaries (planar or curved) are simulated as geometrical entities with no inertia that can be displaced and rotated to allow for strain-controlled tests. Servo-control algorithms are normally used to perform stress-controlled tests.

In order to simulate flexible membranes several approaches exist. Segments of interconnected particles or segments of rigid boundaries have been used by many researchers (e.g. Evans & Zhao 2008). A more successful approach consists of applying a particular force to the boundary balls that would be in contact with the membrane in a physical experiment (e.g. Cui et al. 2007a). The latter approach is adopted in this thesis and details of its implementation are included in Chapter 8.

An additional boundary type that is often used by researchers is the periodic boundary (e.g. Thornton 2000). These boundaries intend to simulate element tests without

the influence of boundary effects. This boundary type is very important, not only because it can be used as the equivalent to a single element finite element study, but also because it allows to simulate soil behaviour in an infinite space with a substantially reduced number of particles. Details and implementation of these boundaries for this research are also presented in Chapter 5.

## 2.7 Micro-mechanical parameters

The output of the DEM simulations consists of data related to inter-particle forces, particle positions and velocities (translational and rotational). This imposes the necessity of homogenization theories in order to convert inter-particle forces and particle displacements to the more common stresses and strains used in continuum mechanics. On the other hand, this output also gives several micro-mechanical parameters that can be used to gain further insight into the behaviour of granular materials. This section includes all those parameters that are frequently used in the analysis of DEM simulations and need to be understood.

### 2.7.1 Stress tensor

The stress tensor is based on discrete contact forces, a spherical volume is normally considered for its calculation, but in fact, this volume can have any shape. The stress tensor is determined by the force vectors,  $f$ , and the branch vectors,  $l$ , as shown in Figure 2.18.

The force vector is defined by the normal and tangential contribution of a particular contact force. Since this natural division between tangential and normal forces exists, it is possible to evaluate the contribution of each of these components of the force vector to the overall stress state at any stage during a DEM simulation. The branch vector on the other hand is a vector joining the centroid of the two particles in contact.

The expression used for the calculation of the stress tensor is equivalent to the average stress of an equivalent continuum volume and it is evaluated as:

$$\overline{\sigma_{ij}} = \sum_{k=1}^{N_c} f_i^k l_j^k \quad (2.12)$$

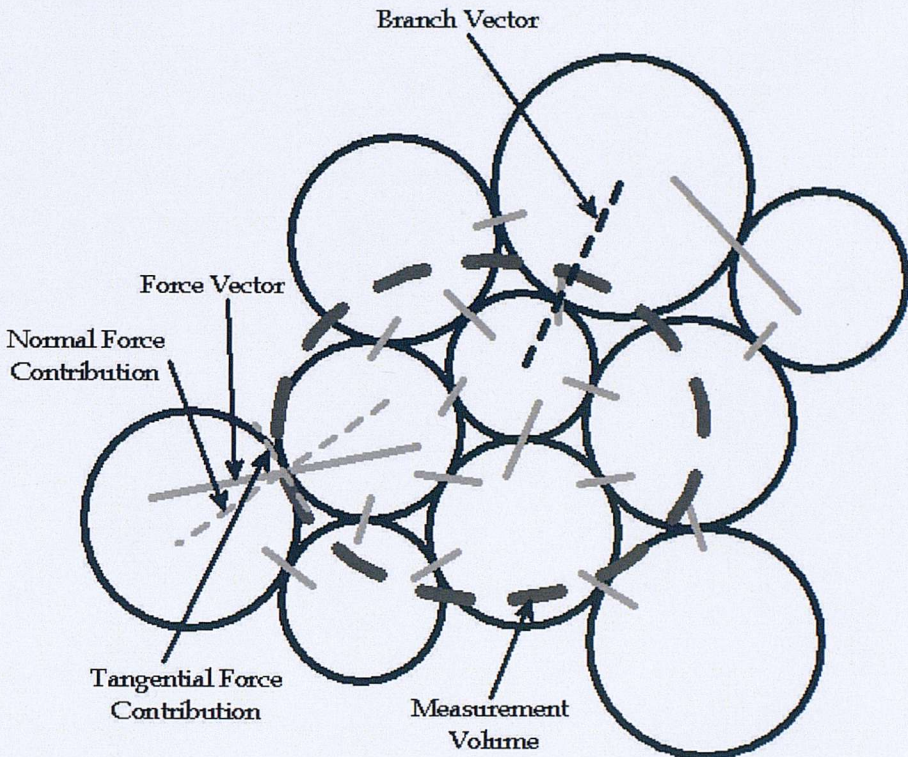


Figure 2.18: Definition of the force and branch vectors for the determination of the stress tensor

where  $N_c$  is the number of contacts,  $f$  and  $l$  are the force and branch vector of the  $k$ -th contact, and  $i$  and  $j$  correspond to the three orthogonal directions in Cartesian coordinates. This definition of stress facilitates the comparison of DEM simulations with experimental and numerical continuum analyses. The definition of strain to allow the same type of comparison is the topic of the next section.

### 2.7.2 Strain tensor

When rigid boundaries or periodic boundaries are used, the global strains in a DEM simulation can be determined in the same way as in physical experiments. That is, by monitoring the movement of the boundaries and relating these movements to their initial configurations. However, engineering applications where localized deformations occur require a more complex definition for a finite strain tensor. This definition depends on whether the deformation measure is related to the reference (original) configuration or the current configuration. When the deformation measure is related to the reference configuration, the Green strain tensor (for finite strain),  $E_{ij}$ , is often used. It can be expressed as

$$E_{ij} = \frac{1}{2}(u_{j,i} + u_{i,j} + u_{k,i}u_{k,j}) \quad (2.13)$$

where  $u_{i,j}$  is the displacement gradient tensor. The undeformed particle coordinates are selected as the reference configuration.

A number of additional homogenization approaches have been proposed. For example, O’Sullivan et al. (2003b) proposed a non-linear approach capable of capturing high deformation gradient fields. However, since all the strains could be defined in terms of the boundary conditions, these approaches are not discussed here.

### 2.7.3 Coordination number

The coordination number is probably the simplest parameter that can be evaluated from DEM simulations. It is a number related to the average number of contacts per particle. It is normally defined as:

$$Z = \frac{2N_c}{N_p} \quad (2.14)$$

where  $N_c$  is the number of contacts and  $N_p$  is the number of particles. Thornton (2000) uses an alternative definition based on the fact that in every assembly the particles having less than two contacts do not contribute to the more heavily loaded chains of force columns in granular materials. He called it the mechanical coordination number and it is defined as:

$$Z_m = \frac{2N_c - N_1}{N_p - N_0 - N_1} \quad (2.15)$$

where  $N_0$  and  $N_1$  are the number of particles with 0 or 1 contacts. DEM simulations performed by different researchers, that can highlight the importance of the coordination number, are presented in Section 2.9.

### 2.7.4 Fabric tensor

The second rank fabric tensor as defined by Satake (1982) is given by

$$\Phi_{ij} = \frac{1}{N_c} \sum_{k=1}^{N_c} n_i^k n_j^k \quad (2.16)$$

where  $N_c$  is the number of contacts and  $n_i$  denotes the unit contact normal for the  $k$ -th contact.

It was demonstrated by Satake (1982) that this is the most general form to describe fabric. However, he stated that the fabric tensor in the presence of a large number of contact normals can be expressed as a function of probability density function of contact normals. This fact is used in many methods employed for quantification of soil fabric anisotropy, as discussed in the next section.

## 2.8 Quantification of soil fabric

Yang et al. (2008b) mentioned that while there is abundant evidence of the impact of fabric anisotropy on granular behaviour, it remains a challenging task to take anisotropic effects into account in geotechnical analysis and design. Part of this problem is because there are different ways to quantify the evolution of soil fabric. There might possibly be as many as authors going into this type of micro-mechanical study. But the main problem is that the determination of fabric in a real soil is an extremely challenging task. The methods normally used to quantify soil fabric vary from very simple graphical representations in the form of stereographical projections of geological data, to very complex mathematical expressions. Some of these different ways to assess soil fabric are presented here.

### 2.8.1 Fourier approximations (curve fitting methods)

As mentioned by Satake (1982), the fabric tensor can be expressed in terms of the statistical distribution of unit contact normals. Oda (1972b) defined the second order fabric tensor as:

$$F_{ij} = \int_0^{2\pi} \int_0^\pi n_i n_j E(\mathbf{n}) \sin \gamma d\gamma d\beta \quad (2.17)$$

where  $F_{ij}$  is the fabric tensor,  $n_i$  is the component of the contact normal ( $\mathbf{n}$ ) in the  $i$  direction,  $E(\mathbf{n})$  is the distribution function of contact normals and  $\beta$  and  $\gamma$  are the

## 2. Background Information

---

angles in the spherical coordinate system. In this coordinate system, the contact normal vector can be defined as:

$$\mathbf{n}_i = \begin{bmatrix} \sin \gamma \cos \beta \\ \sin \gamma \sin \beta \\ \cos \gamma \end{bmatrix} \quad (2.18)$$

while in the Cartesian coordinate system the contact normal vector is expressed by:

$$\mathbf{n}_i = \frac{1}{|\mathbf{f}|} \begin{bmatrix} f_x \\ f_y \\ f_z \end{bmatrix} \quad (2.19)$$

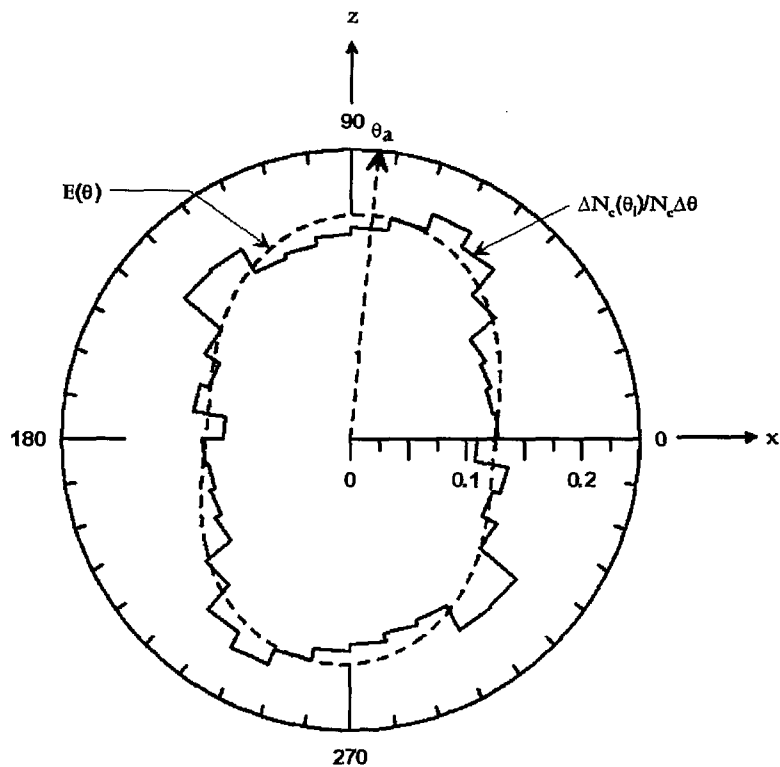


Figure 2.19: Typical unit contact normal distribution and its fitted Fourier series

The key step in quantifying fabric is then to approximate the distribution of contact normals,  $E(\mathbf{n})$  by a Fourier series. In the case of a cross anisotropic fabric under triaxial conditions, with its axis of symmetry along the vertical axis, Chang et al. (1989) suggested the following approximation using the spherical coordinate system:

## 2. Background Information

---

$$E(\mathbf{n}) = \frac{3(1 + a \cos 2\gamma)}{4\pi(3 - a)} \quad (2.20)$$

where  $a$  is the degree of fabric anisotropy, ranging between -1.0 and 1.0. This value controls the directional distribution of the contacts (i.e. positive values indicate vertical concentration and negative values horizontal concentration).

In this thesis, the Fourier approximation used was proposed by Rothenburg & Bathurst (1989). The distribution of contact normals (in the cartesian coordinate system) is then given by:

$$E(\theta) = \frac{1}{2\pi} [1 + a \cos 2(\theta - \theta_a)] \quad (2.21)$$

where  $a$  is a parameter defining the magnitude of anisotropy and  $\theta_a$  defines the direction of the fabric anisotropy or the principal fabric. Opposite to the approximation proposed by Chang et al. (1989), the latter approximation includes two coefficients of the Fourier series. Clearly, one can use as many coefficients as desired. However, the interpretation is less elegant and/or cumbersome.

The contact information, including the contact orientations, can be obtained from the DEM simulation results. Each contact can then be “binned” into an angular interval  $\Delta\theta$ , centred around an angle  $\theta_i$ . If the fabric is symmetric around the vertical (z) axis, the angle  $\theta_i$  is then given by

$$\theta_i = \tan^{-1} \frac{n_3}{n_1} \quad (2.22)$$

where  $n_3$  and  $n_1$  are the components of the contact normal in the z- and x-coordinate directions respectively. The number of contacts ( $N_c$ ) in each bin is then calculated as  $\Delta N_c(\theta_i)$  and normalized by the product  $N_c \cdot \Delta\theta$ . A discrete least squares approximation is used to determine the parameters  $a$  and  $\theta_a$  that best fit the following system of linear equations:

$$\frac{\Delta N_c(\theta_i)}{N_c \Delta\theta} = \frac{1}{2\pi} [1 + a \cos 2(\theta_i - \theta_a)] \quad (2.23)$$

To illustrate this process, the curve given by Equation 2.21 is compared with a DEM simulation data in Figure 2.19 for a representative specimen.  $\theta_a$  may give the major

## 2. Background Information

---

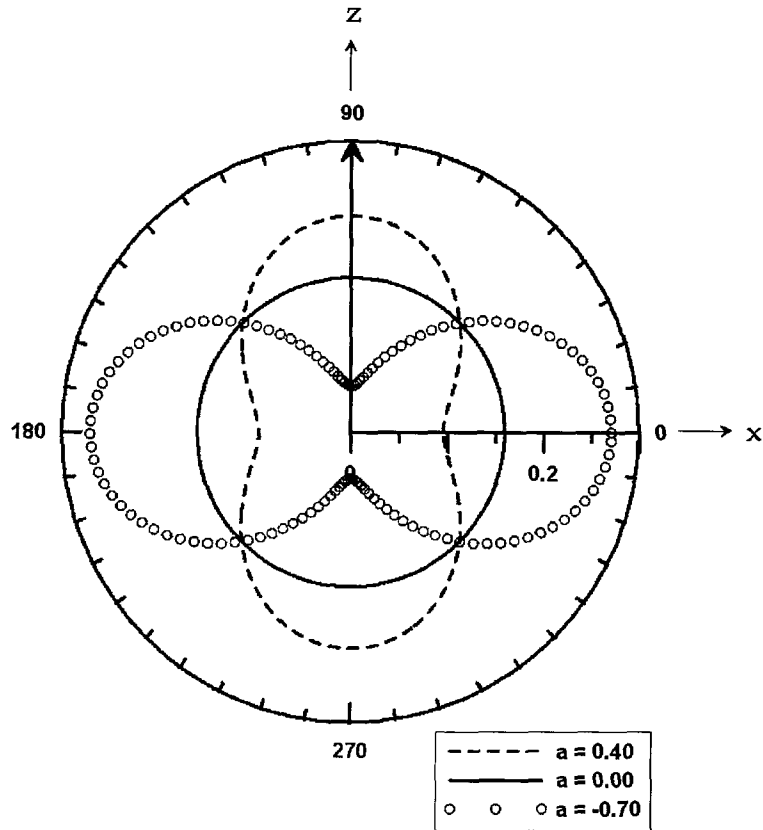


Figure 2.20: Variation of the magnitude of anisotropy ( $a$ ) and its effect on the distribution of contact normals

or minor principal fabric direction. For  $a > 0$ ,  $\theta_a$  obtained from Equation 2.23 gives the major principal fabric direction and for  $a < 0$   $\theta_a$  gives the minor principal fabric orientation. The magnitude of  $a$  is 0 when the contact distribution is isotropic, and increases as the anisotropy increases.

Figures 2.20 and 2.21 are included to clarify the significance of the values of  $\theta_a$  and  $a$ . If  $\theta_a = 90^\circ$ , a negative value of  $a$  indicates a concentration of contact normals in the horizontal direction. The effect of varying  $a$  is shown in Figure 2.21. This figure emphasizes the fact that two fabrics given by  $\theta_a = 0^\circ$ ,  $a = -0.22$  and  $\theta_a = 90^\circ$ ,  $a = 0.22$  are equivalent, therefore the continuous line ( $\theta_a = 90^\circ$ ,  $a = 0.22$ ) is identical to the dotted line ( $\theta_a = 0^\circ$ ,  $a = -0.22$ ).

It is important to note that these methods using Fourier approximations are two-dimensional and, therefore, their use in three-dimensional problems must be done with caution. A similar curve fitting approach that is three-dimensional was used by Evans & Zhao (2008). They fitted orientation data corresponding to unit contact normals to the equation of an ellipsoid whose axes are coincident with axes defining

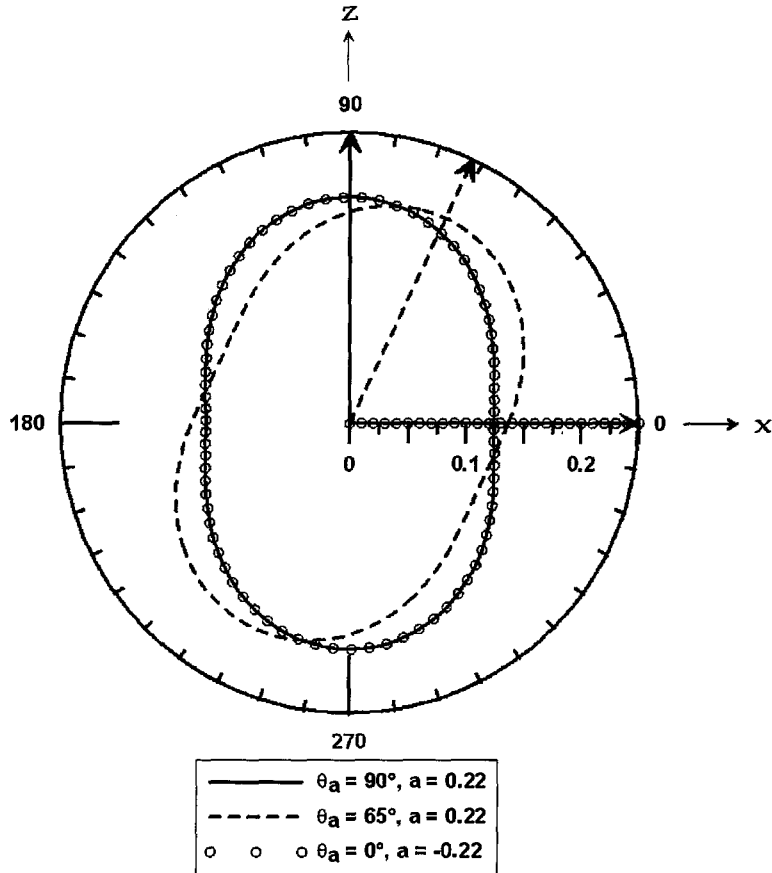


Figure 2.21: Variation of the direction of anisotropy ( $\theta_a$ ) and its effect on the distribution of contact normals

the Cartesian coordinate system as:

$$\frac{x^2}{a^2} + \frac{y^2}{b^2} + \frac{z^2}{c^2} = 1 \quad (2.24)$$

where  $a$ ,  $b$  and  $c$  are the lengths of the ellipsoid semi-axes. However, this method is not easily used in three-dimensional problems where the principal axes do not coincide with the axes of the coordinate system. Consequently, this approach is not suitable for problems involving rotation of the principal stress direction, such as those presented in this thesis.

### 2.8.2 Eigenvalue methods

In these methods, individual observations are regarded as unit vectors. The orientation tensor is defined by the sum of the cross products of the direction cosines,  $l_i$

## 2. Background Information

---

in the cartesian axes  $x$ ,  $y$  and  $z$  as follows:

$$A = \frac{1}{N} \begin{bmatrix} \sum l_x l_x & \sum l_x l_y & \sum l_x l_z \\ \sum l_y l_x & \sum l_y l_y & \sum l_y l_z \\ \sum l_z l_x & \sum l_z l_y & \sum l_z l_z \end{bmatrix} \quad (2.25)$$

where  $N$  is the number of observations. Note that the orientation tensor is equivalent with the fabric tensor defined in Section 2.7.4. Therefore, the descriptors here derived can be easily applied to the analysis of soil fabric. The eigenvectors  $\vec{v}_1, \vec{v}_2$  and  $\vec{v}_3$  of  $A$  give the principal directions of the orientation data, and the eigenvalues  $S_1, S_2$  and  $S_3$  are a measure of the degree of clustering data about the respective eigenvectors. The eigenvalues  $S_1, S_2, S_3$  have the property

$$S_1 + S_2 + S_3 = 1 \quad (2.26)$$

The eigenvalues are related to fabric shape and can be plotted in a two-axis ratio plot for their analysis. In this plot the abscissa is  $\ln(S_2/S_3)$  and the ordinate is  $\ln(S_1/S_2)$ . It must be stated that this plot is adequate and does not involve loss of the three dimensional information because only two of the three variables,  $S_1, S_2, S_3$ , are mutually independent. Watson (1966) noted that distributions described as clusters tend to have  $S_1 > S_2 \cong S_3$ , and distributions described as girdles to have  $S_1 \cong S_2 > S_3$ .

A representation of such a plot is shown in Figure 2.22. As it can be seen, the orientation data (fabric) is characterised by a shape factor  $K$  and a strength factor  $C$ .

The shape factor,  $K$  is defined as

$$K = \frac{\ln(S_1/S_2)}{\ln(S_2/S_3)} \quad (2.27)$$

and gives the gradient of straight lines in Figure 2.22. The strength factor  $C$  is defined as

$$C = \ln(S_2/S_3) \quad (2.28)$$

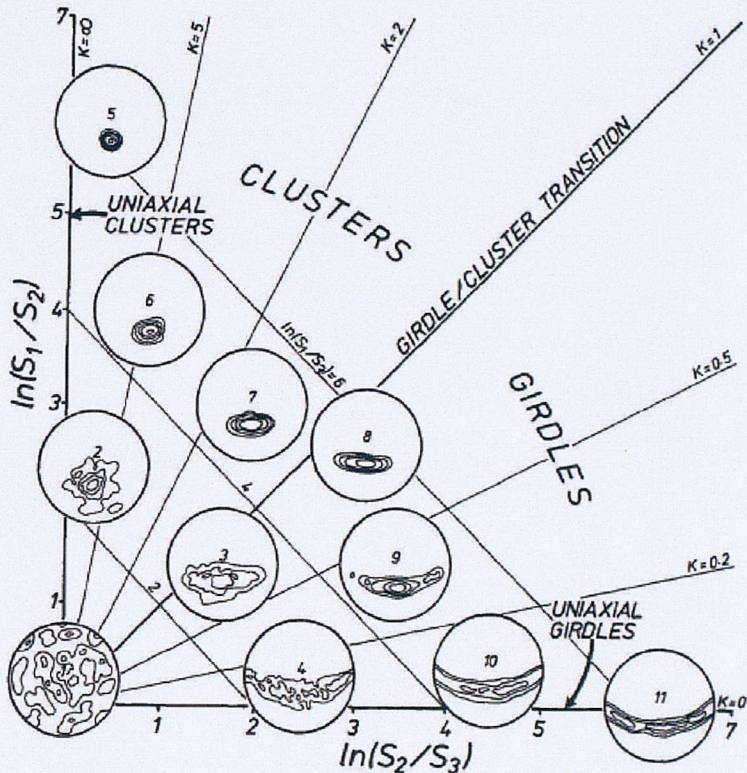


Figure 2.22: Two-axis ratio plot for analysis of orientation data in the eigenvalue method (Woodcock 1977)

and it is a measure of the strength of the preferred orientation. Uniform distributions plot at the origin of the plot, random distributions near the origin, and those with increasingly strong preferred orientation progressively further from the origin.

The suitability of these methods to describe the evolution of soil fabric had not been assessed consistently under varied and complex loading conditions. An assessment of these different quantification methods is presented in Chapter 7 for a set of simulations under different stress paths.

## 2.9 Previous DEM research considering granular material response

In this section, a review of three-dimensional DEM simulations performed in previous research is presented. This summary is presented with the aim of showing that DEM has helped to gain a further insight into the particle scale interactions that govern the macro-scale soil response and to show with examples all the additional

## 2. Background Information

information that can be gained from DEM simulations.

Despite the wide recognition of the three-dimensional behaviour of soil, the number of 3D DEM simulations is, in fact, very limited. Furthermore, simulations involving principal stress rotation are limited to simulations of the direct shear box (e.g. Cui & O'Sullivan (2006)) as well as to comparisons of plane strain, triaxial compression and triaxial extension results. This is a phenomenon similar to what happened before advanced equipment such as the directional shear cell and the hollow cylinder apparatus were introduced for experimental research. The simulations presented here and the conclusions derived from them must be compared with the experimental results presented in Section 2.4.

### **2.9.1 Triaxial simulations**

A number of three-dimensional triaxial simulations have been performed by various researchers (e.g. Tsunekawa & Iwashita 1993, Ng 2005, Evans & Zhao 2008). The use of boundary conditions in all these studies varies significantly. Periodic boundaries, rigid boundaries and flexible boundaries were used. In particular, different algorithms for the simulation of flexible membranes were implemented by different researchers. The results of previous research that is relevant for this thesis are briefly summarised in this section.

A detailed study of axi-symmetric compression tests on loose and dense specimens of spherical particles was published by Thornton (2000). These simulations were performed using three-dimensional periodic boundaries. A grain size distribution was represented using 3620 spheres with five different diameters ( $d_{50} = 0.258$  mm). The spheres were randomly generated within a cuboidal periodic cell. The assembly was then isotropically compressed using a servo-control, until equilibrium was reached under an isotropic stress of 100 kPa. Dense and loose specimens were created by isotropic compression to 100 kPa using a coefficient of inter-particle friction of 0.0 and 0.3, respectively.

During axi-symmetric compression a servo-control algorithm was used to maintain a constant effective stress ( $p'$ ) of 100 kPa. The samples were then sheared with a coefficient of inter-particle friction of 0.3. The behaviour of both samples, as shown in Figure 2.23, is qualitatively similar to physical experiments in sands. The dense sample is stiffer than the loose sample and the dense sample dilates while the loose one contracts. Additionally, both samples achieve a very similar critical void ratio at

## 2. Background Information

---

large strains (see Figure 2.24). Furthermore, the mechanical average coordination number  $Z_m$  showed a rapid change during the initial 3% of deviatoric strain and then a critical value was attained and kept constant irrespective of the volumetric behaviour of the samples.

Thornton (2000) also observed that the normal force contribution is the dominant contribution to the deviatoric stress (see Figure 2.25). Thornton (2000) also observed that the ratio of contacts which are sliding increases to a constant value after about 1% of deviatoric strain and it is independent of the initial density. Additionally, the evolution of the deviatoric fabric, determined using the principal values of the fabric tensor, showed qualitative agreement to the evolution of the deviatoric stress (see Figure 2.26 in comparison to Figure 2.23).

The results of axi-symmetric compression tests using a different coefficient of friction during shearing were also performed by Thornton (2000). It was demonstrated that an increment in the angle of shearing resistance (peak and constant volume) exists with an increase in the coefficient of friction. Further discussion related to this issue is presented in Chapter 4. The critical void ratio also depended on the friction value, getting higher void ratios for higher values of friction. Finally, the increase in friction increased the critical ratio of sliding contacts and the critical mechanical coordination number decreased when the friction was increased.

Earlier simulations performed by Thornton & Sun (1993) confirm the previous conclusions about the effect of the inter-particle friction. This study by Thornton & Sun (1993) is mentioned here because, while two coefficients of inter-particle friction were used (0.3 and 0.6) with the same simulation characteristics of the study above, it was postulated that the behaviour of these two simulations replicated the behaviour of physical experiments on glass ballotini and real sands, respectively. The DEM simulations were compared to physical experiments performed by Parikh (1967). However, experimental data was not provided for comparison in either case. Although no definite conclusion was given, it was mentioned that the DEM simulations of glass ballotini resulted in lower angles of shearing resistance than the real experiments due to boundary effects in the experiments and deviations from sphericity in the shape of the particles. For the real sands on the other hand, they mentioned the same difference, but it was attributed to the effects of particle shape in real experiments.

Of special interest for this thesis is the DEM simulation of triaxial tests performed by Cui et al. (2007a), as they accurately replicated the boundary conditions present

## 2. Background Information

---

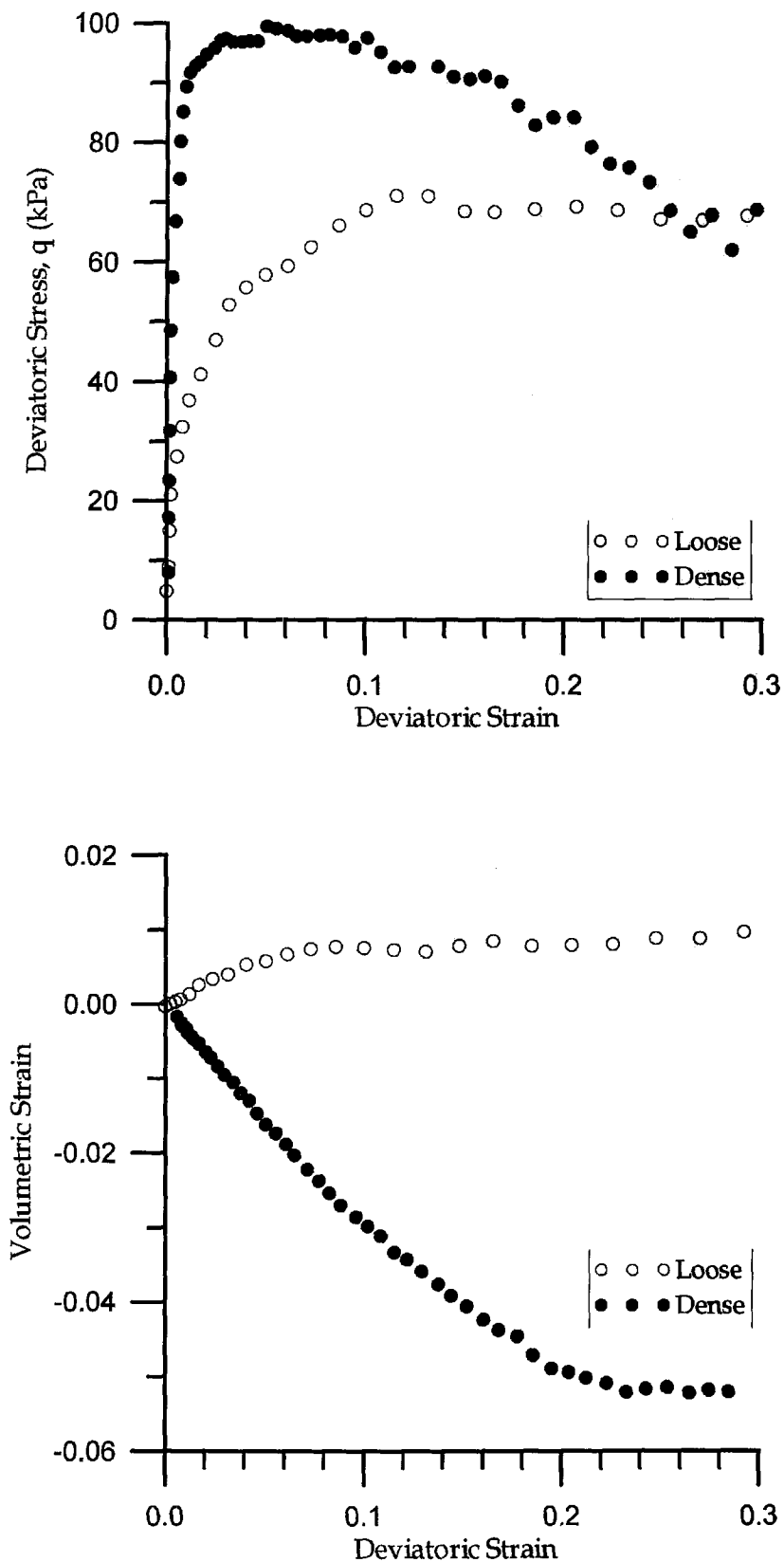


Figure 2.23: DEM simulations of axi-symmetric compression in a periodic cell. Qualitative behaviour (Thornton 2000)

## 2. Background Information

---

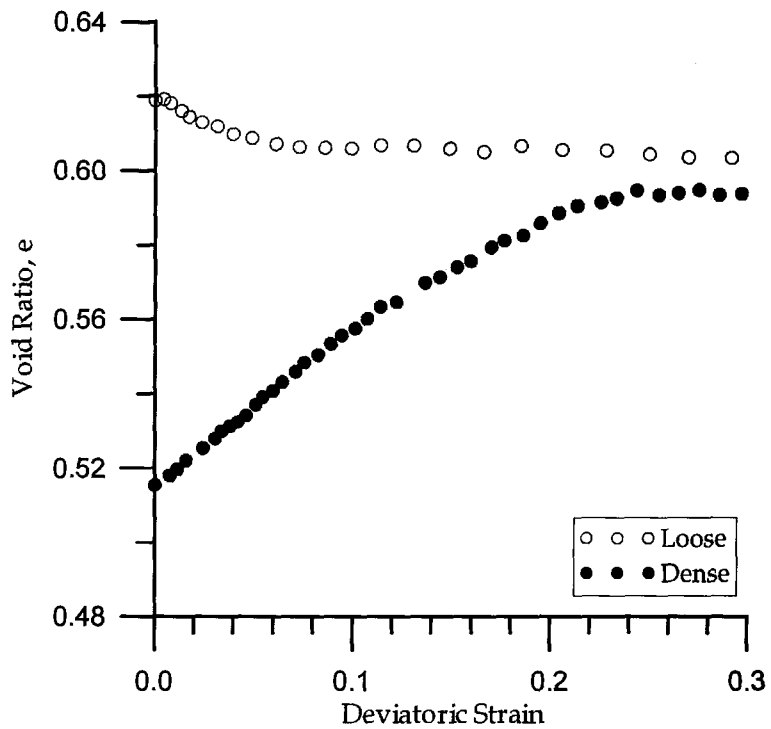


Figure 2.24: DEM simulations of axi-symmetric compression in a periodic cell. Critical void ratio (Thornton 2000)

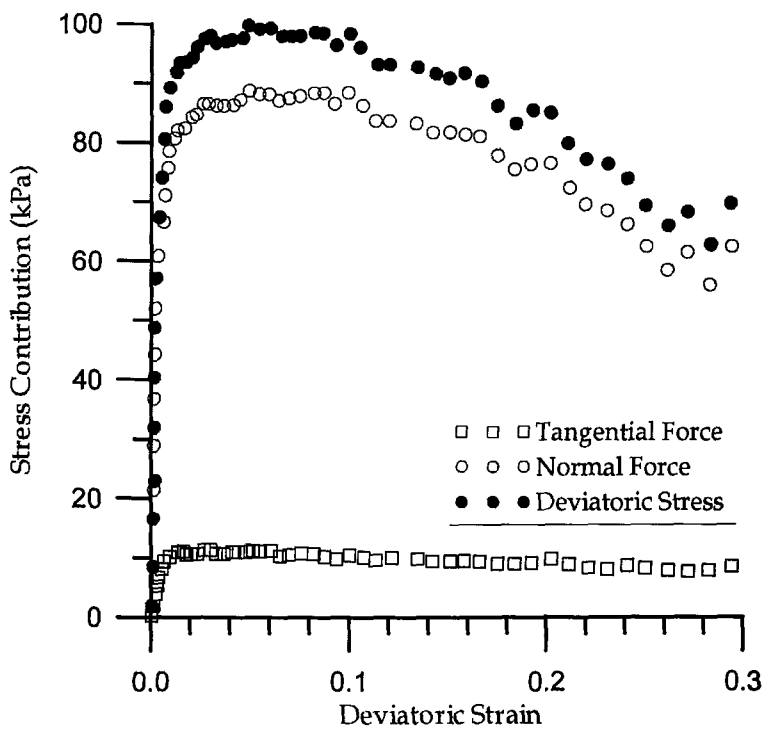


Figure 2.25: Evolution of the normal and tangential force contribution to the deviatoric stress during axi-symmetric compression (Thornton 2000)

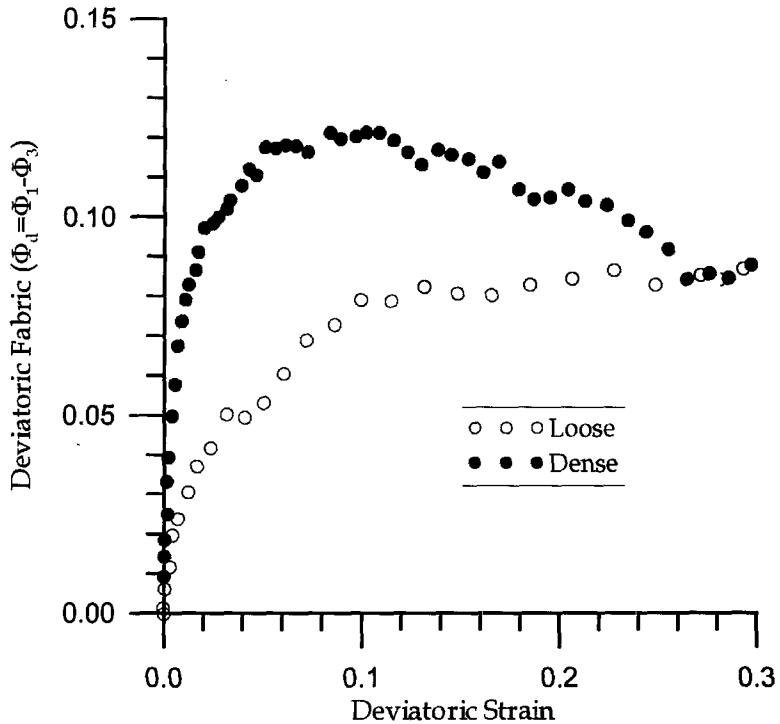


Figure 2.26: Evolution of induced structural anisotropy during axi-symmetric compression (Thornton 2000)

in the laboratory tests. The top and bottom platens were modeled as planar rigid boundaries. The flexible latex membrane was simulated by calculating the forces that should be acting in the balls in contact with the membrane. In order to reduce computational cost and taking advantage of the axi-symmetric nature of the triaxial test, vertical circumferential periodic boundaries were used to simulate only a 90 degree section of the tests. Details of these boundaries are described by Cui (2006) and will also be described in Chapter 5. The major advantage of these periodic boundaries is that the internal system of particle-to-particle contacts is maintained throughout the specimen.

This approach to simulate triaxial tests was validated with simulations of FCC assemblies as reported by Cui & O'Sullivan (2005). However, it was also validated by replicating the behaviour of physical tests on steel spheres. Figure 2.27 shows the comparison between experiments and simulations at similar void ratios. It must be noted that in order to reach this void ratio in the DEM simulation, the assembly was isotropically compressed to a stress of 3MPa. Therefore, the comparisons are in terms of stress ratios. The agreement is notable in the stress-strain curves.

Parametric studies to assess the effect of the particle-boundary friction in the re-

## 2. Background Information

---

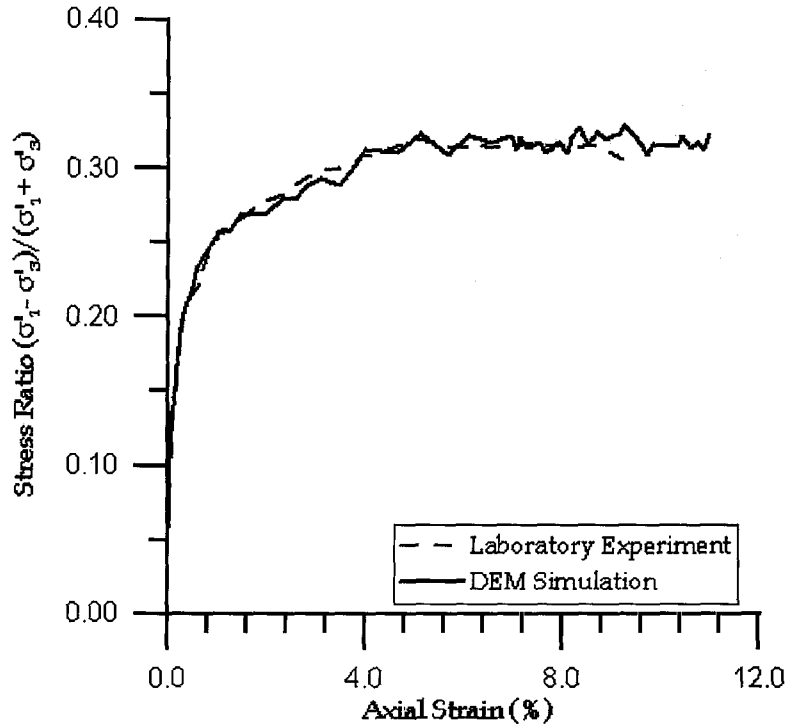


Figure 2.27: Macro-scale comparison of DEM simulation results and laboratory tests (modified after Cui et al. 2007a)

sponse of the soil were also carried out. Figure 2.28 shows that a high value of boundary friction imposes conditions of end-restraint that generate bulging in the samples as observed in real tests.

It is also important to mention the analysis of the non-uniformities present in the triaxial test presented by Cui et al. (2007a). A similar approach could be followed for the analysis of HCA non-uniformities in the DEM simulations of HCA tests in the generalised axi-symmetric environment implemented in this thesis. As mentioned in Section 2.7.1, with DEM data the value of the stress tensor can be calculated using any volume of reference. Figure 2.29 shows the different volumes at different heights of the triaxial specimen and their respective values of stress during shearing as calculated by Cui et al. (2007b). The non-homogeneity of the stress is evident. Furthermore, the value of stress calculated from the forces acting on the boundaries (as measured in a physical experiment) was lower than the average measure for the whole volume of the sample in the DEM simulation.

The effects of the internal variables, such as inter-particle forces, on the non-uniform response were also studied. Figure 2.30 shows the contact forces that have a magnitude bigger than the average of all the contact forces. Despite the difficulty in

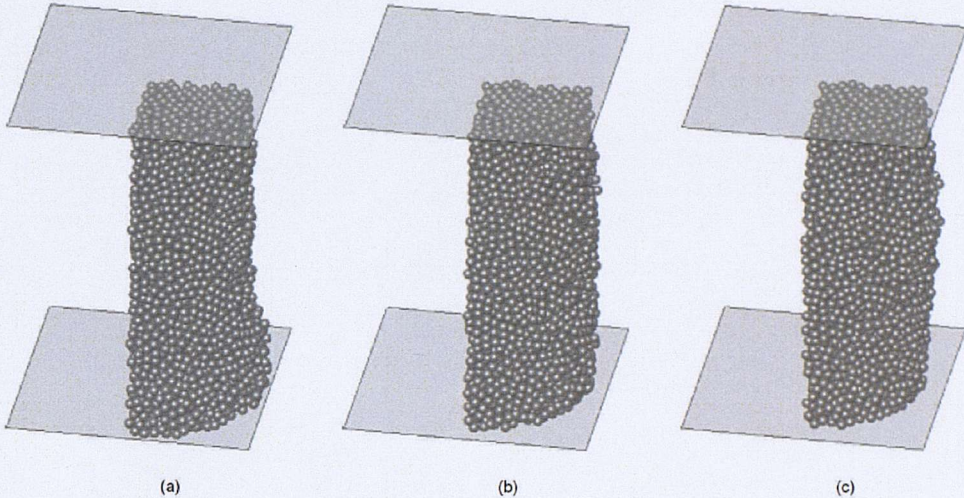


Figure 2.28: Sensitivity of deformed specimen shape ( $\epsilon_a = 15.3\%$ ) to particle/boundary friction coefficient. a)  $\mu = 0.0$ , b)  $\mu = 0.05$  and c)  $\mu = 0.10$  (Cui et al. 2007a)

visualizing three-dimensional distributions of contact forces, it can be seen that the force chains are definitely stronger for the areas closer to the rigid boundary. These figures emphasize two things, the need of quantitative methods for fabric analysis, such as those presented in Section 2.8, and the usefulness of internal variables from DEM simulations to study the evolution of non-uniformities.

### 2.9.2 True triaxial simulations

True triaxial experiments, such as those described in Section 2.4, have been qualitatively replicated by DEM researchers. Thornton (2000) subjected the same assembly of spheres described in Section 6.4 to constant  $b$  tests. The failure state for each of these tests are shown in Figure 2.31 as points in the deviatoric plane. In this figure, the outer most circle plotted above the failure states corresponds to the failure criterion proposed by Lade & Duncan (1973). Interestingly, in the same plot the inner circle represents the fabric stress at failure for each of those tests. The fabric stress contribution was also represented by an inverted Lade & Duncan (1973) failure criterion.

In terms of internal variables, Thornton (2000) postulated that the average ratio of sliding contacts and the critical mechanical average coordination number were both independent of the intermediate principal stress. The rate of dilation, on the other

## 2. Background Information

---

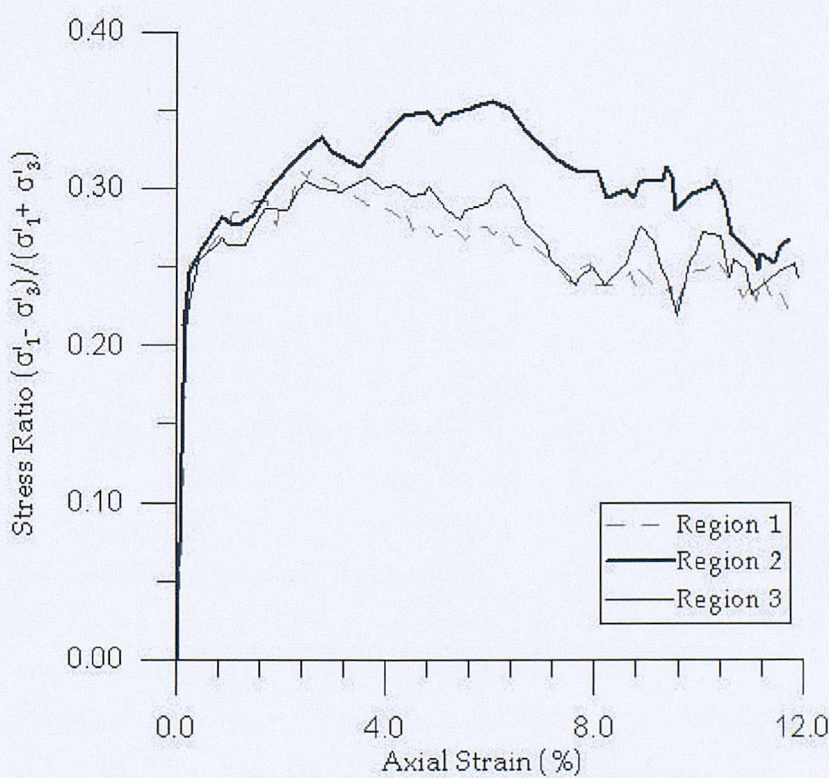
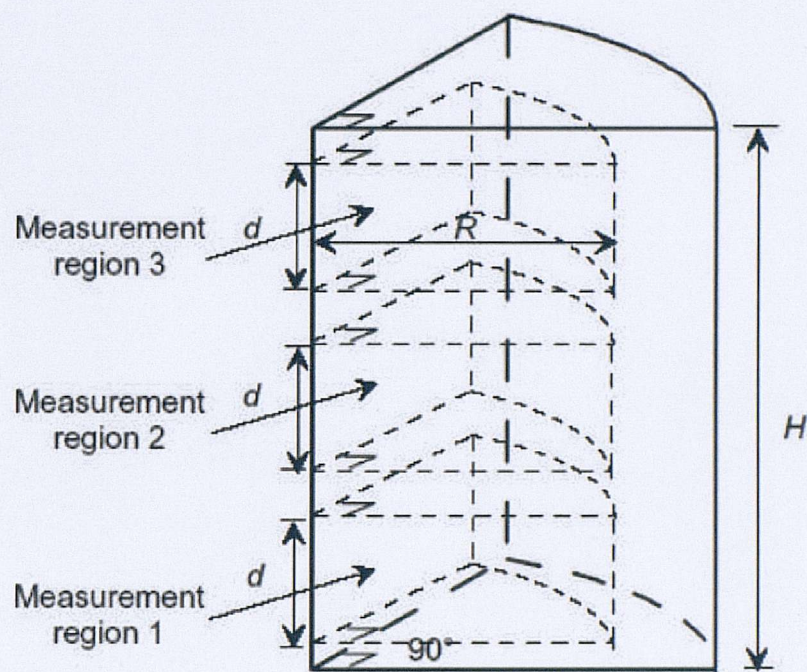


Figure 2.29: Comparison of internal stresses in a DEM triaxial simulation (modified after Cui et al. 2007a)

## 2. Background Information

---

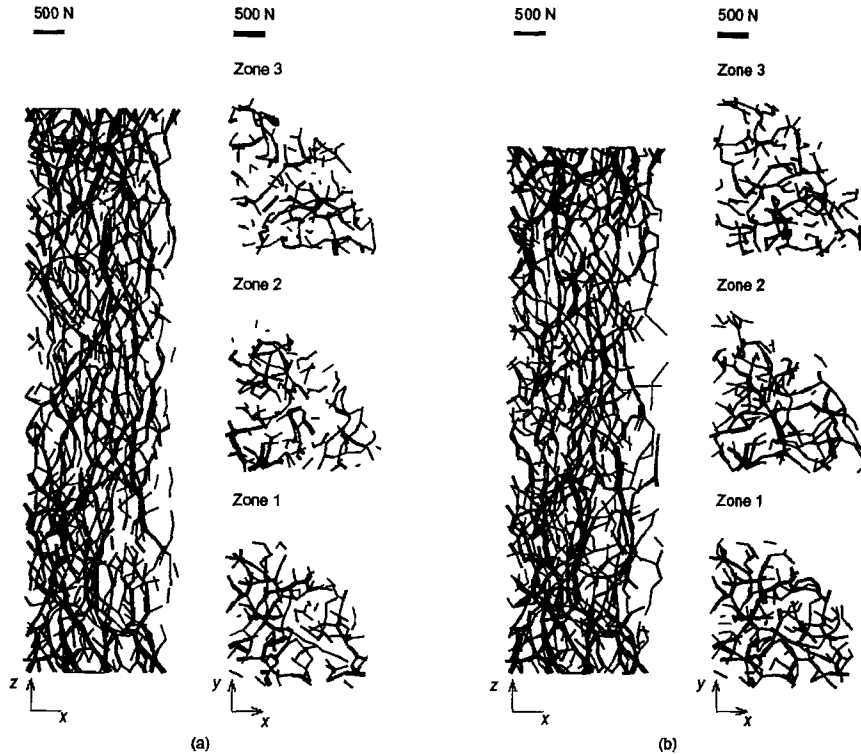


Figure 2.30: Network of contact forces in three zones (only forces exceeding mean force plus one standard deviation) a)  $\epsilon_a = 6.2\%$  (around peak), b)  $\epsilon_a = 12.3\%$  (post peak) (Cui et al. 2007a)

hand, was also insensitive to the variation of  $b$ . This contrasts with the experimental results presented in Section 2.4.2.

A substantial number of DEM simulations of different stress paths with different initial fabrics originated by different particle shapes and specimen generation methods have been performed (e.g. Ng 2000, 2001, 2004a, 2005). Most of these publications evaluate the effects of particle shape under different stress paths using ellipsoidal particles with different aspect ratios. An example of those simulations is presented here to show that his results of true triaxial simulations follow the same trend of those performed by Thornton (2000). Ng (2004b) created three samples (A, B and C) made of two types of ellipsoidal particles. In order to create different initial fabrics, a different method of specimen generation was used for each sample. Several constant  $b$  tests were simulated using  $b$  equal to 0.0, 0.2, 0.4, 0.6, 0.8 and 1.0. Some results of those simulations are discussed here.

The evolution of the angle of shearing resistance can be seen in Figure 2.32. Clearly, the trend is qualitatively similar to experimental tests discussed before and agrees

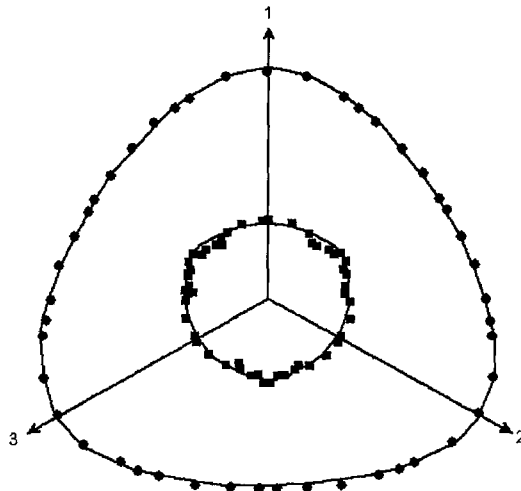


Figure 2.31: Failure states of stress and fabric components in DEM simulations of constant  $b$  tests (modified after Thornton 2000)

with the results of Thornton (2000) using a periodic cell.

The methodology of Woodcock (1977) was used by Ng (2004b) to analyse the unit contact normals and the normal contact forces (including magnitude). As it can be seen from Figure 2.33 and Figure 2.34, the strength descriptors for axial compression show a trend that could be correlated to the observed macro-scale behaviour.

Ng (2004b) postulates that the normal force strength descriptor is related to the stress ratio ( $\sigma_1/\sigma_3$ ) but shows this relationship in a logarithmic plot. This procedure introduces some doubt in the correlations. However, it demonstrates that different approaches are indeed useful to evaluate the evolution of soil fabric.

### 2.9.3 DEM simulations involving principal stress rotation

Three-dimensional DEM simulations with the objective of improving the understanding of soil behaviour under principal stress rotation are limited. Furthermore, they correspond to simulations of direct shear tests (i.e Cui & O'Sullivan 2006), comparisons between triaxial compression and extension (i.e Yimsiri & Soga 2008), or simple shear tests (i.e Thornton & Zhang 2001).

As in the physical experiments, none of the previous simulations has introduced an absolute and independent control of the orientation of the major principal stress during shearing. Consequently, they are not presented here. However, they will be quoted later because they can be useful for comparison purposes when DEM

## 2. Background Information

---

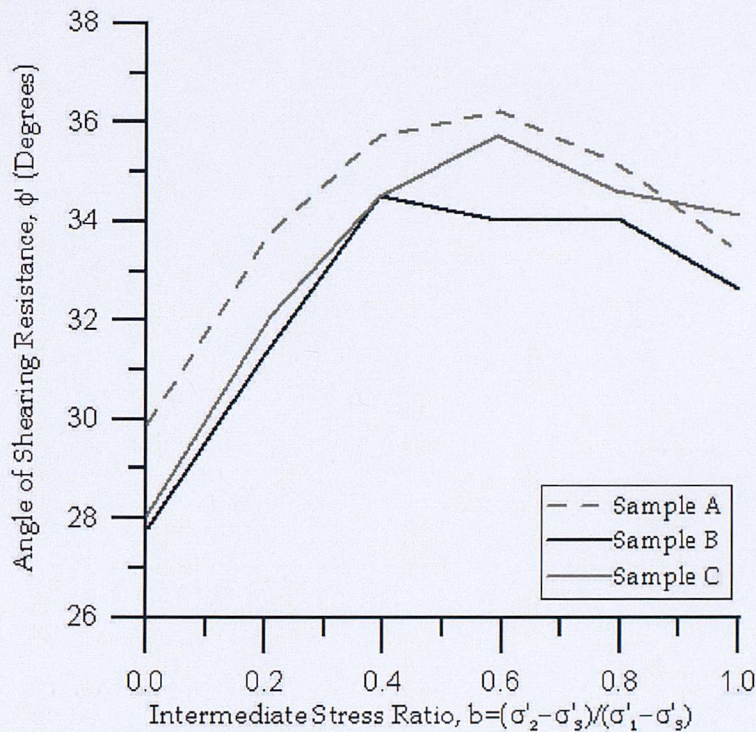


Figure 2.32: Evolution of shear strength for all tests (modified after Ng 2004b)

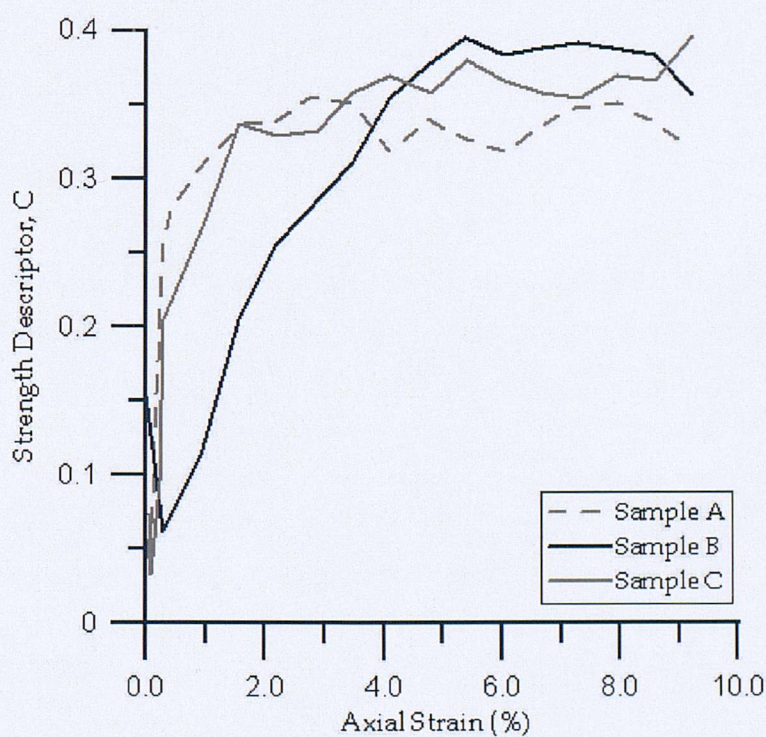


Figure 2.33: Unit normal strength descriptors (Ng 2004b)

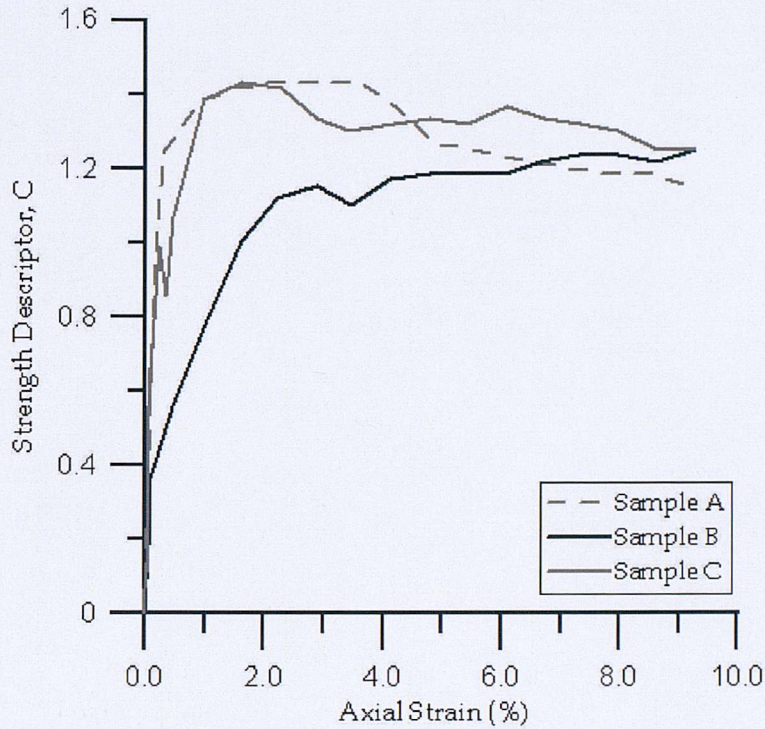


Figure 2.34: Unit normal force strength descriptors (Ng 2004*b*)

simulations involving independent principal stress rotation are introduced in this thesis.

## 2.10 Summary

This chapter reviews issues of soil anisotropic behaviour and the three-dimensional nature of the stress states felt by soil in-situ. Previous experimental research on the drained response of granular materials under generalised stress states were described and compared with numerical simulations. Special attention was given to the further insight offered by DEM simulations into the particle scale interactions, underlying the observed macro-scale response of soils. The two main objectives of this chapter were: *a*) to provide the background information necessary for the understanding of the thesis, and *b*) to highlight the need for further DEM research to gain further understanding into the micro-mechanics governing soil behaviour under complex and realistic stress conditions.

After a brief definition of anisotropy and its causes, the equipment that can be used to measure soil anisotropy in the laboratory was described. It was confirmed

## 2. Background Information

---

that the most suitable apparatus to study three-dimensional behaviour of soil with independent control of the magnitude and orientation of the principal stress is the hollow cylinder apparatus.

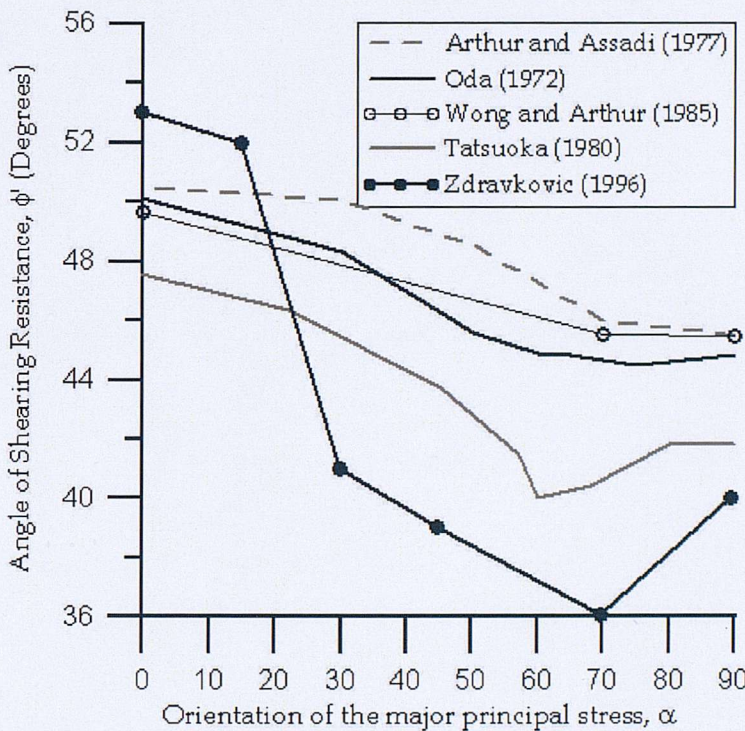


Figure 2.35: Influence of the major principal stress orientation on the angle of shearing resistance of granular materials

From previous experimental studies on the effects of the orientation of the principal stresses on soil response the following conclusions must be mentioned:

- The stress-strain response is affected by the orientation of the major principal stress. This anisotropy is also affected by the magnitude of the intermediate principal stress.
- Soil strength, measured in terms of the maximum mobilised angle of shearing resistance, is affected by the orientation of the major principal stress. For future reference, Figure 2.35 shows the results obtained by some of the studies presented in this chapter.
- In general terms, the shear stiffness of granular materials reduces as  $\alpha$  increases, while the volumetric strains increase when  $\alpha$  increases.

## 2. Background Information

---

- During shearing, the inter-particle contacts tend to orientate towards the same direction of the major principal stress because this provides a more stable configuration to withstand the current stress.

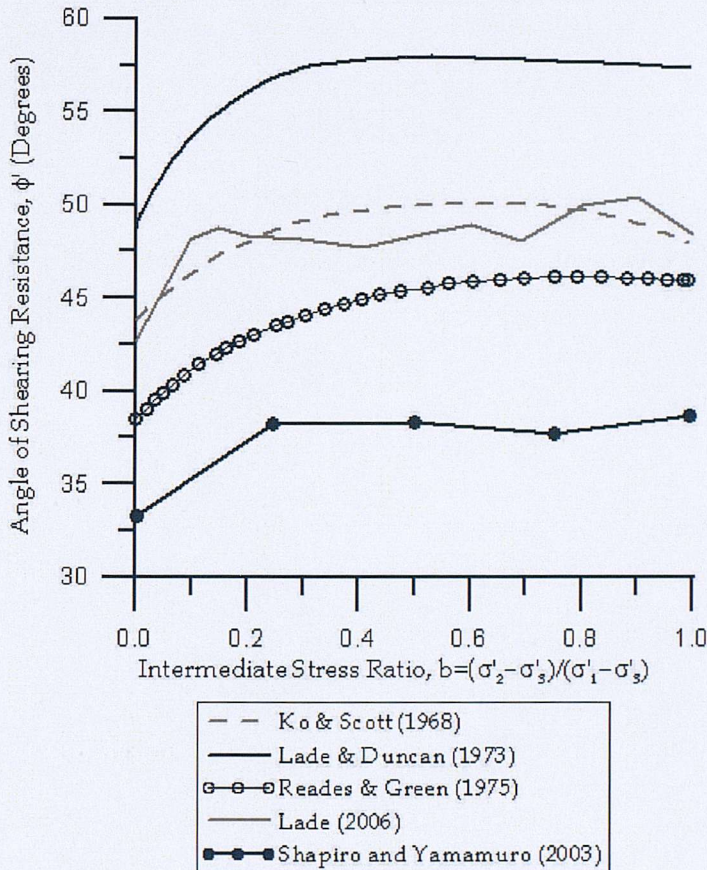


Figure 2.36: Influence of the intermediate stress ratio on the angle of shearing resistance of granular materials

Highlighting now the effects of the intermediate principal stress in soil response, the following statements can be made:

- The maximum mobilised angle of shearing resistance is affected by the value of the intermediate stress ratio, however the trend is still under discussion. For future reference, Figure 2.36 shows the results obtained by some of the studies presented in this chapter.
- Experimental evidence is not conclusive in terms of the volumetric response when  $b$  is varied. Different results in terms of stiffness and strain development were shown.

## 2. Background Information

The details of a constitutive model for granular materials proposed by Lade & Duncan (1973) were presented. This model will aid the interpretation of the experiments and simulations performed in this research.

The rest of the chapter deals with the DEM algorithm and the variables that can be obtained from these simulations. By showing recent numerical research using DEM it was demonstrated that there are no studies involving independent control of the magnitude and orientation of the principal stresses.

Previous DEM research also demonstrated the potential of this numerical tool to understand the micro-mechanical phenomena that underlies in the observed macro-scale behaviour of granular materials.

# **Chapter 3**

## **Test material, apparatus and procedures**

### **3.1 Introduction**

This chapter is divided in four major parts. These sections are about the test material, apparatus description, stress and strain non-uniformities and testing procedures. In the first section, the classification characteristics of the test material are described. The parameters that were used in DEM simulations are also listed.

The second part includes a description of the equipment used, and the process of how stresses and strains are applied and calculated is described. The section concludes with a summary of algorithms and equations used to control the equipment during the experiments. The necessary changes done to perform tests on bigger HCA samples are also described in this section.

A brief summary of previous research on the effects of non-uniformities in HCA testing is presented in Section 3.4. After some numerical analyses are described, a limited body of available experimental data related to the effects of the non-uniformities is presented.

Finally, in the last part of the chapter the sample preparation methods used are described and the procedures followed during testing are summarised. A consistent sample preparation method was devised in order to systematically compare tests under dry and saturated conditions for different sample geometries.

### 3. Test material, apparatus and procedures

---

Mineral	Content (% by weight)
SiO <sub>2</sub>	54.70
CaO	22.50
Al <sub>2</sub> O <sub>3</sub>	14.50
B <sub>2</sub> O <sub>3</sub>	5.45
MgO	1.33
K <sub>2</sub> O	0.56
TiO <sub>2</sub>	0.37
Fe <sub>2</sub> O <sub>3</sub>	0.30
Others	0.29

Table 3.1: Mineral composition of type SL beads (information provided by Sigmund Lindner on delivery)

Particle Size	$d_{50}$ (mm)	Sizes Range (mm)	$C_c$	$C_u$
Small	0.6	0.45 - 0.82	0.945	1.167
Medium	1.1	1.00 - 1.43	0.992	1.207
Big	2.5	2.43 - 3.10	1.006	1.112

Table 3.2: Different particle sizes of type SL beads

## 3.2 Test material

The material used in this study was comprised of glass spherical particles (glass ballotini). They are commercially marketed by Sigmund Lindner as type SL beads. The mineral composition of the material is given in Table 3.1. Three particle sizes were used in the tests presented in this thesis. They are referred to as small, medium and big glass ballotini, as indicated by Table 3.2. Note that in Table 3.2,  $C_c$  ( $= d_{30}^2/d_{10}d_{60}$ ) and  $C_u$  ( $= d_{60}/d_{10}$ ) are the curvature and uniformity indices of the grain size distribution, and  $d_{10}$ ,  $d_{30}$  and  $d_{60}$  are the particle diameters corresponding to the fraction finer than 10%, 30% and 60% by weight.

This material was chosen as an analogue soil because its sphericity makes possible to replicate particle geometry in an accurate way using DEM. Furthermore, as outlined in Chapter 2, glass ballotini is a material that has been used by many researchers in geotechnical engineering. The viability of using analogue soils to understand real soil behaviour was assessed by Ishibashi et al. (1991). They compared the behaviour of Ottawa sand (a sand with rounded grains with the characteristics presented in Table 2.1) and the behaviour of glass spheres in torsional shear HCA tests. They analysed stress-strain relationships and degradation of stiffness at very small strains, and demonstrated that the behaviour of both materials was very similar.

For this thesis the following physical properties of glass ballotini were found exper-

### 3. Test material, apparatus and procedures

---

imentally:

- A specific gravity of 2.57.
- A grain size distribution that was very uniform for all particle sizes (see Figure 3.1). These grain size distribution curves were found using the segmentation software (Axiovision by Carl-Zeiss-Microlmaging (2007)) attached to an optical microscope with a digital camera. In order to ensure a statistically representative sample size, the variation of the grain size distribution with the number of particles was analysed. If a minimum of 900 particles were used to calculate the grain size distribution, no changes were produced in the curves when an increasing number of particles was taken into account.
- The maximum and minimum void ratios were 0.63 and 0.54. These void ratios were obtained experimentally according to the British standard - BS 1377-4:1990.
- The roundness of the particles prior to testing, measured as the ratio between the minor and major diameter of particles, was always bigger than 0.95. This ratio was also measured using the Axiovision software attached to an optical microscope (Carl-Zeiss-Microlmaging 2007).

The values of Poisson's ratio, Young's modulus and coefficient of inter-particle friction used in DEM simulations were obtained from experimental tests performed by Cavarretta (2009). The reference values used are as follows:

- Poisson's ratio = 0.22
- Young's modulus = 70 GPa
- Coefficient of inter-particle friction = Varies between 0.079 and 0.351.

Further details related to the choice of these input parameters are discussed in Chapter 6.

## **3.3 Apparatus**

The principal pieces of equipment used for this study were the triaxial stress path cell and the hollow cylinder apparatus. The description and functionality of the

### 3. Test material, apparatus and procedures

---

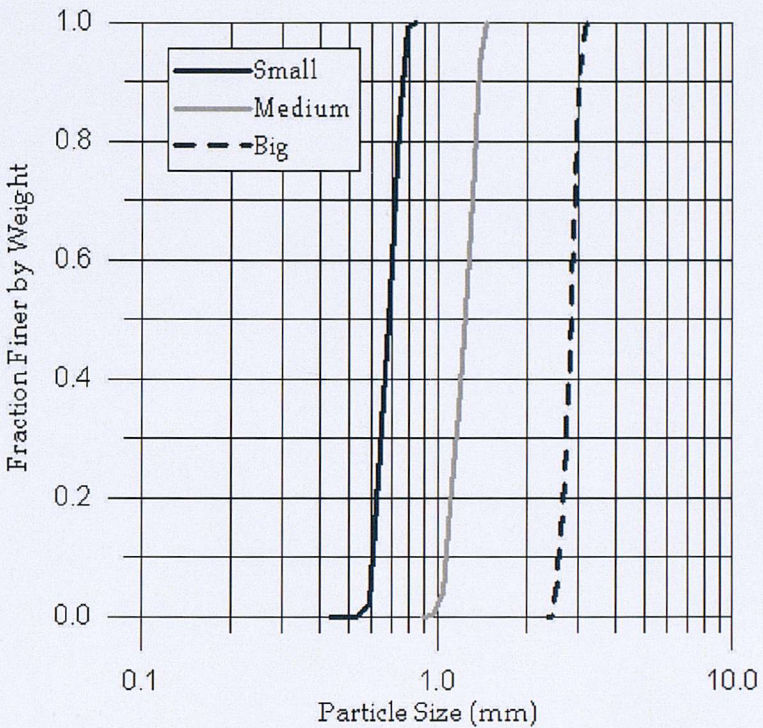


Figure 3.1: Grain size distribution for the different glass ballotini sizes

Imperial College Hollow Cylinder Apparatus (ICHCA) have been presented in detail by numerous researchers (Hight et al. 1983, Shibuya 1985, Zdravkovic 1996, Rolo 2003, Foundoukos 2006). Therefore, only a brief description of this apparatus is included in Section 3.3.2. However, the ICHCA was modified during the period of this research project, specifically, the sample height was increased. As a consequence, new moulds for sample preparation also had to be manufactured. For purposes of clarity, the now old version of the HCA will continue to be called ICHCA and the new version including the increased sample size and latest improvements will be referred to as Large Imperial College Hollow Cylinder Apparatus (LICHCA).

All the changes implemented in the development of the LICHCA are described in detail in Section 3.3.3. Note that both saturated and dry specimens were tested in this study under drained conditions. The tests of dry specimens were not common at Imperial College before the start of this study, in particular in the ICHCA, and additional changes had to be implemented in order to perform these tests. These changes are also described in detail.

### 3. Test material, apparatus and procedures

Transducer Type	Capacity	Accuracy	Stability
Load Cell	$\pm 4.5$ kN	$\pm 0.016$ kN	0.002 kN
Pressure Transducer	1.0 MPa	$\pm 0.06$ kPa	0.03 kPa
External Displacement	25 mm	$\pm 0.052$ mm	0.005 mm
Volume Gauge	50 cc	$\pm 0.032$ cc	0.001 cc
Electro-Level	17 mm	$\pm 0.028$ mm	0.006 mm
LVDT (Radial)	30 mm	$\pm 0.003$ mm	0.001 mm

Table 3.3: Summary of capacity, accuracy and stability of transducers employed in the triaxial stress path cell

#### **3.3.1 Triaxial stress path cell**

The Bishop & Wesley (1975) stress path cell has been widely used at Imperial College and it is described in detail by Smith (1974) and others. Consequently, just a brief description is included here.

A schematic cross-section of the apparatus is shown in Figure 3.2. The triaxial cell used in this study can accommodate samples 38 mm in diameter and 80 mm in height. The pedestal for the sample is mounted on top of a loading ram which is connected to a piston and a pressure chamber. The vertical load is applied by moving the sample pedestal upwards or downwards from below.

The water pressures within the perspex test chamber, loading ram and back pressures (if saturated samples are tested) are controlled by air-valves acting through air/water interfaces. By varying these pressures, any desired triaxial stress path can be easily applied to a sample. During shearing, the ram pressure is controlled by a constant rate of strain pump. This is done with the purpose of performing strain controlled tests on materials that exhibit brittle failure.

Having mentioned the mechanisms for operation of the triaxial cell, the instrumentation used for the measurement of stress and strain can be described. The instrumentation used is summarised in Table 3.3. Note that the values for accuracy are based on the mean deviation from the regression lines obtained during calibration. The stability on the other hand, is based on the scatter observed in the readings over a period of time longer than 24 hours, prior to calibration.

The deviatoric force at the top of the sample is measured with the Imperial College immersible load cell. The output of this load cell is insensitive to changes in cell water pressure. Standard Bell and Howell pressure transducers are used to measure the water pressures in the cell, as well as in the back pressure lines. These measurements

### 3. Test material, apparatus and procedures

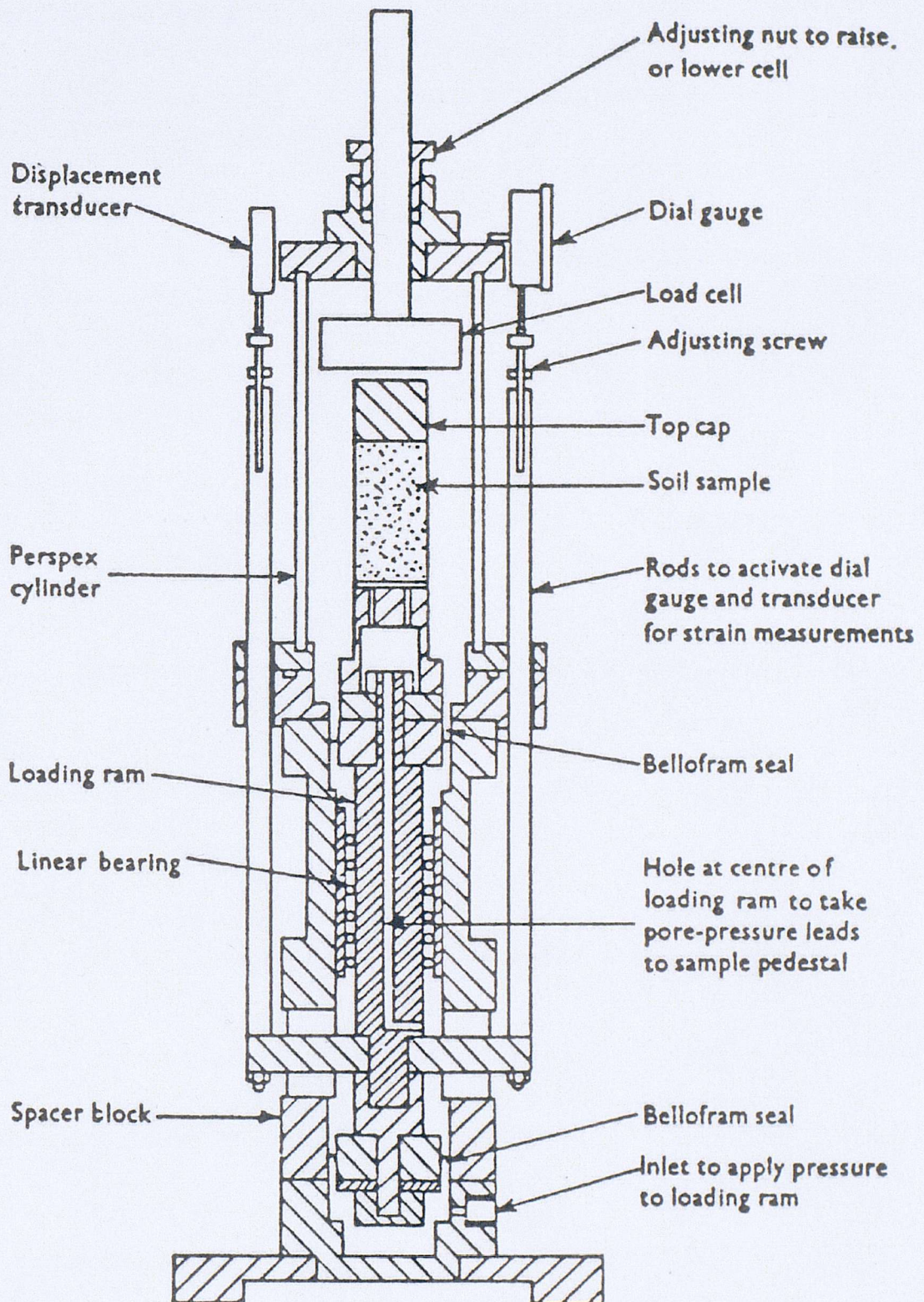


Figure 3.2: Schematic representation of the triaxial stress path cell (Bishop & Wesley 1975)

### 3. Test material, apparatus and procedures

are done independently of the type of experiment (dry or saturated).

During the tests strains are measured by different means. Firstly, a standard displacement transducer is mounted on a crosshead to provide external axial strain measurement. Secondly, two pendulum local axial strain electro-level devices (Ackerley et al. 1987), are mounted on each sample. Lastly, an Imperial College volume gauge is used to measure flow in and out of the sample (and hence the volumetric strain) when saturated samples are tested. Note that the volumetric strain of samples tested under dry conditions cannot be measured using a volume gauge device. Consequently a standard LVDT transducer is deployed in the middle of the sample to measure radial strains. In this way, the volumetric changes can be calculated using the axial and radial deformation together with an assumption about the deformation mode of the sample.

The equipment is controlled via a computer system called TRIAX which was developed by Toll (1988). All data is recorded and stored on the computer's hard disk before being transferred for subsequent post processing.

#### **3.3.2 Imperial College Hollow Cylinder Apparatus (ICHCA)**

The layout of the ICHCA is given in Figure 3.3. A picture of the apparatus is shown in Figure 3.4. The dimensions of the sample in this apparatus are 254 mm in height, 254 mm in outer diameter and 200 mm in inner diameter. The sample is contained within two latex membranes (thickness approximately 0.5 mm) and surrounded by water both internally and externally. The top cap is rigid and a 50 mm diameter loading ram transmits the axial load and torque on the top cap and the sample itself.

The outer chamber, enveloping the soil specimen and the external cell water, is made of perspex. This chamber is contained in a stainless steel frame. The perspex cylinder is suspended from a movable frame, together with the torque and axial load pistons. The loading frame can be raised or lowered using a motor to leave a clear work area below for sample set-up. A similar motorised platform is located below the base pedestal and is used for positioning the base plate of the inner chamber.

### 3. Test material, apparatus and procedures

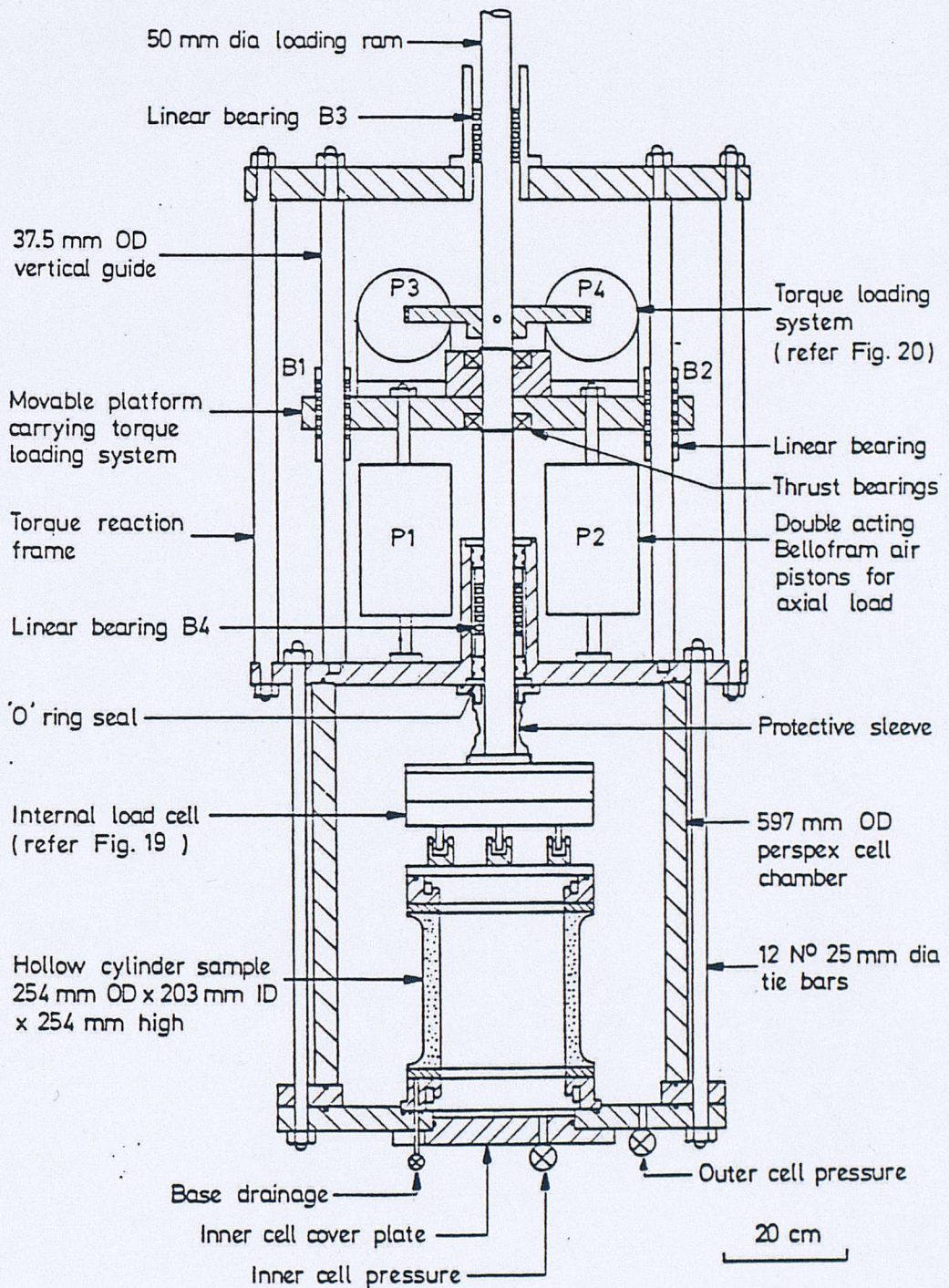


Figure 3.3: Schematic representation of the ICHCA (Symes 1983)

### 3. Test material, apparatus and procedures

---

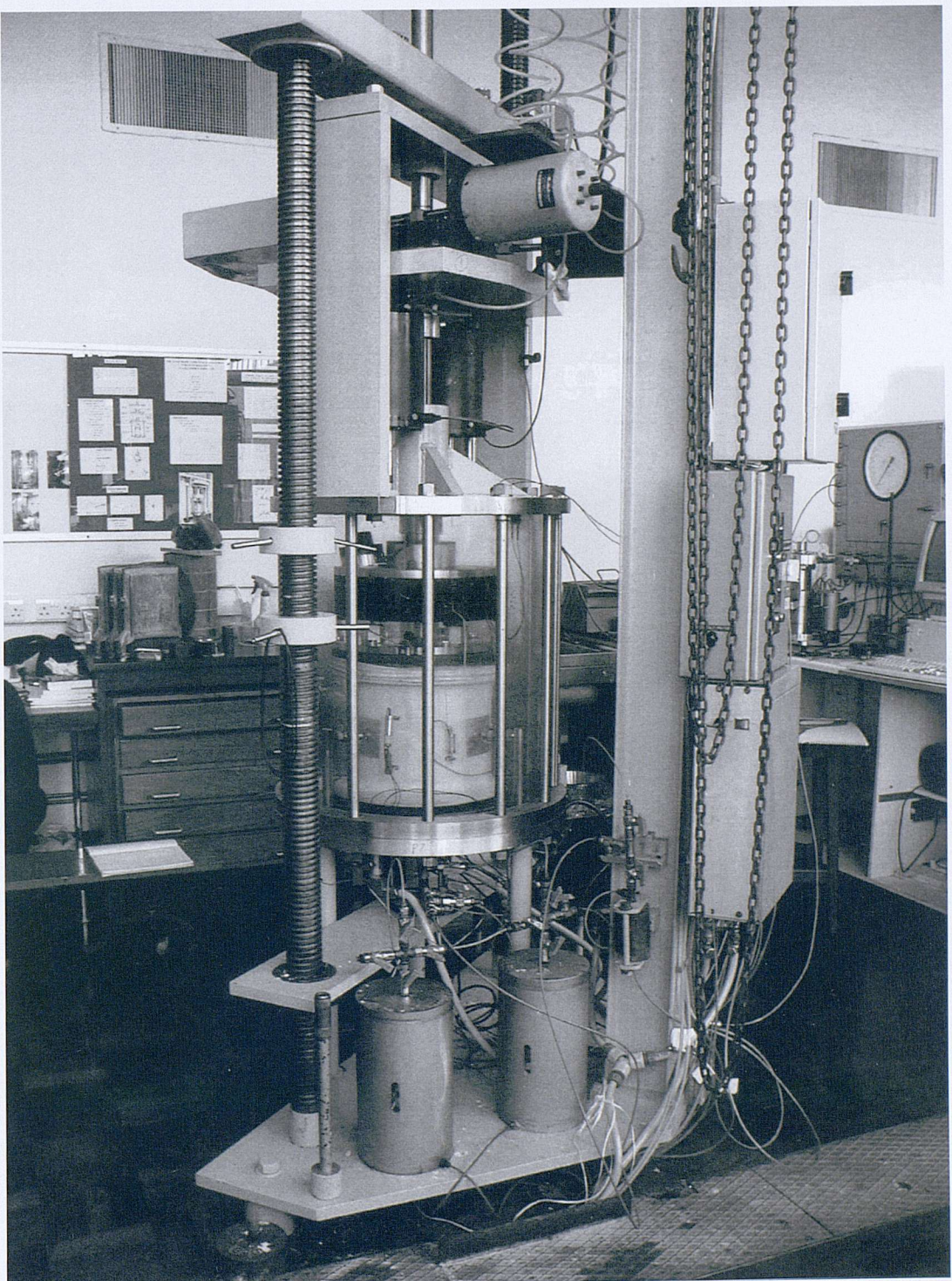


Figure 3.4: The ICHCA and a test under progress

### Load application

As mentioned in Chapter 2, the hollow cylinder apparatus is designed to study soil anisotropy. In order to perform a global study of soil anisotropy, all the components of the stress tensor should be capable of variation. In the hollow cylinder apparatus (HCA) a cylindrical coordinate system is used, furthermore, the stress tensor of a soil element in equilibrium must be symmetric. Therefore, control is required over the  $\sigma_z$ ,  $\sigma_r$ ,  $\sigma_\theta$ ,  $\tau_{z\theta}$ ,  $\tau_{r\theta}$  and  $\tau_{rz}$  components. However, the HCA can apply and independently control only four boundary conditions.

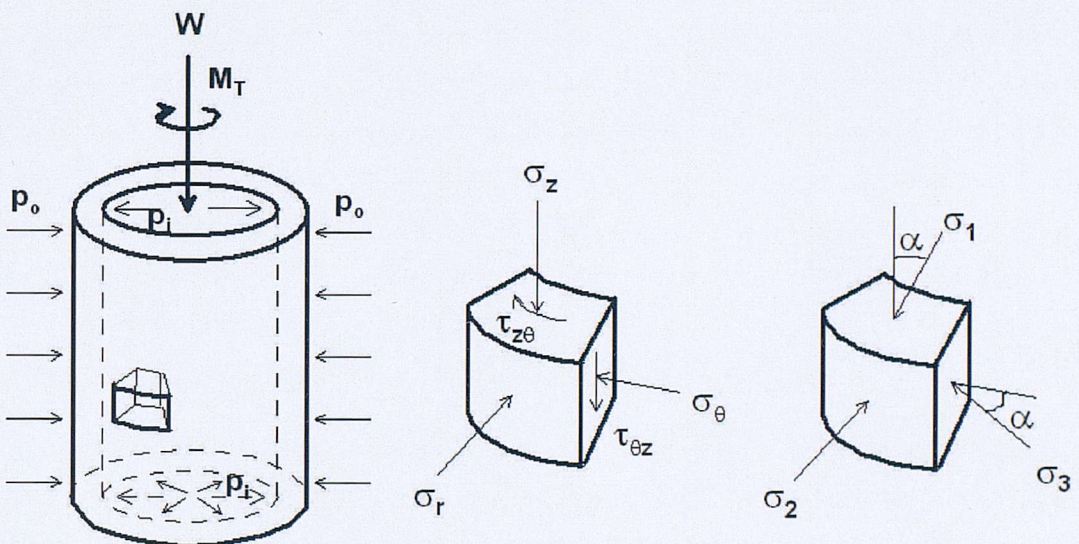


Figure 3.5: Load application and stress components in the HCA

Referring to Figure 3.5 the four boundary conditions are:

- Inner cell pressure,  $p_i$
- Outer cell pressure,  $p_o$
- Axial load,  $W$
- Torque,  $M_T$

Neglecting the undesired effects of non-uniformities of stress and strain discussed in Section 3.4, the boundary conditions of the HCA lead to  $\tau_{r\theta} = \tau_{rz} = 0$ . This is because it is not possible to have shear stresses along the vertical faces of the specimen due to the presence of flexible latex membranes surrounding the specimen. This condition forces the radial stress,  $\sigma_r$ , to remain as a principal stress.

### 3. Test material, apparatus and procedures

The remaining stress components ( $\sigma_z$ ,  $\sigma_\theta$  and  $\tau_{z\theta}$ ) can be independently controlled. Consequently, the study of soil anisotropy is thus restricted to rotations of the major and minor principal stress directions in the  $z\theta$  plane. Note that this characteristic is also present in other existing devices such as the directional shear cell described in Section 2.3.6.

The axial load and torque are applied through a loading ram connected to the top platen of the sample. This platen is rigid and rough. These conditions are necessary for the load application, as slippage between the sample and the platen must be avoided for the application of torque. However, these conditions provide non-uniformities that are discussed in Section 3.4. Note that there are different approaches to provide roughness to this boundary for the adequate application of torque. Lade (1981) coated the surface of the platen with epoxy and pressed in sand of the type to be tested. A different approach has been used by Porovic (1995), Nishimura (2005) and Minh (2006) who all used metallic blades that penetrated into the top of the sample. None of these approaches are needed in the ICHCA as it has an enlarged area of contact with the platens provided by an increase of the sample thickness via the flares observed in Figures 3.3 and 3.4.

The inner and outer cell pressures, as well as the back pressure (if saturated specimens are tested), are applied through standard air/water interfaces. As in the triaxial stress path cell, these interfaces convert air pressure into hydraulic pressure, which is then applied onto the sample through flexible latex membranes.

Axial load and torque are applied to the top platen using pairs of double acting Bellofram pistons, as shown in Figure 3.3. The user can produce a pressure difference in the upper and lower chambers of the two axial pistons ( $P_1$  and  $P_2$ ), resulting in the movement of the top platen upwards or downwards according to this pressure difference. The same principle applies for the application of torque through pistons  $P_3$  and  $P_4$ .

Samples can be tested in the ICHCA and LICHCA under stress or strain-controlled conditions. The strain control tests involve a mixed system in which one or more components of the system are driven by strain control, with the other components remaining under stress controlled conditions. A computer system keeps the specified stress conditions or stress path direction required, while maintaining a specified strain rate using a Constant Rate of Strain Pump (CRSP).

### 3. Test material, apparatus and procedures

#### **Stress calculation**

It is important to note that stresses in the HCA are calculated using certain assumptions. The equations used in this study for calculation of stress are based on the studies by Hight et al. (1983). Note that the average axial and circumferential stresses are based on equilibrium considerations and are valid irrespective of the constitutive law chosen (Hight et al. 1983). However, since the stresses can vary across the wall of the specimen, the average radial and shear stresses are calculated based on a choice of constitutive law. Hight et al. (1983) used an average value calculated assuming a linearly elastic solution, Vaid et al. (1990) used an average solution based on the linearly plastic solution. Yang et al. (2007) and Miura et al. (1986) even proposed an average between the elastic and full plastic solutions to calculate the average shear stress. However, Yang et al. (2008a) showed that unless the material has a very brittle response (such as rocks, concrete and cemented soils), the difference in the interpreted shear stresses is insignificant. Consequently, the equations proposed by Hight et al. (1983), which are used for the experimental results presented in this thesis, are presented below:

- Average axial stress:

$$\overline{\sigma_z} = \frac{W}{\pi (r_o^2 - r_i^2)} + \frac{p_o r_o^2 - p_i r_i^2}{r_o^2 - r_i^2} \quad (3.1)$$

- Average radial stress:

$$\overline{\sigma_r} = \frac{p_o r_o + p_i r_i}{r_o + r_i} \quad (3.2)$$

- Average circumferential stress:

$$\overline{\sigma_\theta} = \frac{p_o r_o - p_i r_i}{r_o - r_i} \quad (3.3)$$

- Average shear stress:

$$\overline{\tau_{z\theta}} = \frac{3M_T}{2\pi (r_o^3 - r_i^3)} \quad (3.4)$$

where  $r_o$  and  $r_i$  are the current outer and inner radii of the sample, respectively. The principal stresses can be calculated based on the average values given by Equations 3.1, 3.2, 3.3 and 3.4 (see Figure 3.6):

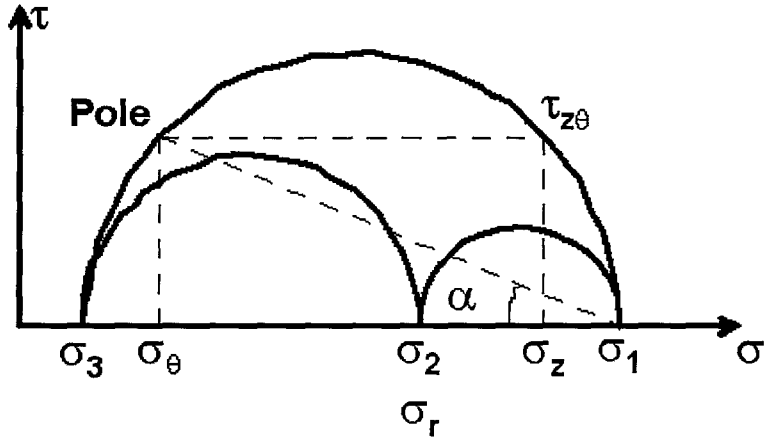


Figure 3.6: Mohr's circle of stress states in the HCA

$$\sigma_1 = \frac{\sigma_z + \sigma_\theta}{2} + \sqrt{\left(\frac{\sigma_z - \sigma_\theta}{2}\right)^2 + \tau_{z\theta}^2} \quad (3.5)$$

$$\sigma_2 = \sigma_r \quad (3.6)$$

$$\sigma_3 = \frac{\sigma_z + \sigma_\theta}{2} - \sqrt{\left(\frac{\sigma_z - \sigma_\theta}{2}\right)^2 + \tau_{z\theta}^2} \quad (3.7)$$

Note that according to the standard soil mechanics convention, compressive stresses are considered positive.

### Strain calculation

The average strains are calculated from boundary conditions. The strains are calculated as

- Average axial strain:

$$\epsilon_z = \frac{w}{l_0} \quad (3.8)$$

- Average radial strain:

$$\epsilon_r = -\frac{u_o - u_i}{r_{oz} - r_{iz}} \quad (3.9)$$

### 3. Test material, apparatus and procedures

- Average circumferential strain:

$$\epsilon_\theta = -\frac{u_o + u_i}{r_{oz} + r_{iz}} \quad (3.10)$$

- Average shear strain:

$$\gamma_{z\theta} = \frac{2\theta(r_o^3 - r_i^3)}{3H_0(r_o^2 - r_i^2)} \quad (3.11)$$

where  $w$  is the axial deformation,  $l_0$  is the length of the initial local reference (gauge length),  $u_o$  and  $u_i$  are the radial deformations of the outer and inner walls, respectively,  $r_{oz}$  and  $r_{iz}$  are the initial outer and inner radii,  $\theta$  is the circumferential angular deformation and  $H_0$  is the initial height of the sample.

The corresponding principal strains, which can also be found using a Mohr's circle of strain are:

$$\epsilon_1 = \frac{\epsilon_z + \epsilon_\theta}{2} + \sqrt{\left(\frac{\epsilon_z - \epsilon_\theta}{2}\right)^2 + \left(\frac{\gamma_{z\theta}}{2}\right)^2} \quad (3.12)$$

$$\epsilon_2 = \epsilon_r \quad (3.13)$$

$$\epsilon_3 = \frac{\epsilon_z + \epsilon_\theta}{2} - \sqrt{\left(\frac{\epsilon_z - \epsilon_\theta}{2}\right)^2 + \left(\frac{\gamma_{z\theta}}{2}\right)^2} \quad (3.14)$$

### Instrumentation

Axial load and torque are measured using a dual axis strain gauged load cell located inside the cell. The cell is immersed in water and it is filled with oil, water proofed and pressure compensated (i.e. as in the triaxial cell, it is insensitive to pressure changes within the chamber). Because of its double action (e.g. it measures axial load and torque), there is a small cross-sensitivity between axial and torque action (typically 0.06% to 0.75% for the effect of the axial load on the torque output and 0.5% to 1.47% for the effect of the torque on the axial load output). This load cell is calibrated by applying combinations of axial load and torque similar to those applied during tests and the best fit matrix of calibration coefficients includes some off-diagonal terms.

### 3. Test material, apparatus and procedures

---

The inner and outer cell pressures, back pressure and pore pressure at the base of the sample are measured by a set of standard pressure transducers. Note that when samples are tested under dry conditions the pore pressure is also measured, but not controlled.

A volume gauge of 100 cc capacity is used to measure the volume of pore fluid leaving and entering the samples when saturated samples are tested. When samples are tested under dry conditions volume changes must be calculated assessing the measurements of local and global instrumentation described below.

A range of local displacement transducers are mounted on, or near to, the inner and outer surfaces of the sample wall. These transducers measure radial, axial and torsional deformations.

The radial displacements are measured using encapsulated Kaman KD-2310 proximity transducers (see Figure 3.7). These transducers are a non-contacting type of transducer which operates on the principle of impedance variation. The sensor induces an eddy current in a remote metal foil target attached to the sample wall, which in turn interacts with a coil within the sensor. The output is a function of the gap between target and sensor. Two sets of transducers are used: 3 outer and 3 inner devices, which are arranged as shown in Figure 3.8 at 120 degrees intervals around the sample. As noted by Foundoukos (2006) the proximity transducers impose some restrictions in the analysis of tests due to their accuracy and resolution. Furthermore, the accuracy and resolution depend on the type of target. Consequently, different types of metallic targets were tried in an attempt to improve resolution of the measurements. A brass target glued to the sample, and a foil target glued to the smooth side of sand paper and then to the sample were assessed. Problems related with the ability of the target to stay in position during the whole duration of the test, and reinforcement of the sample restraining its movement, arose with a non-significative improvement in the resolution. Hence, for all the tests presented in this study, the usual foil targets attached to the sample with high vacuum grease were used.

Axial and torsional shear deformations are measured locally using electrolytic tilt transducers. These devices were first developed at Imperial College for use in the ICHCA by Burland & Symes (1982), and their design was later modified by Shibuya (1985). The device comprises a stainless steel protective cylinder casing holding a glass capsule, half filled with an iodine based electrolyte, and containing a set of three electrodes. When the sensor is at its zero position, the electrical resistance of

### 3. Test material, apparatus and procedures

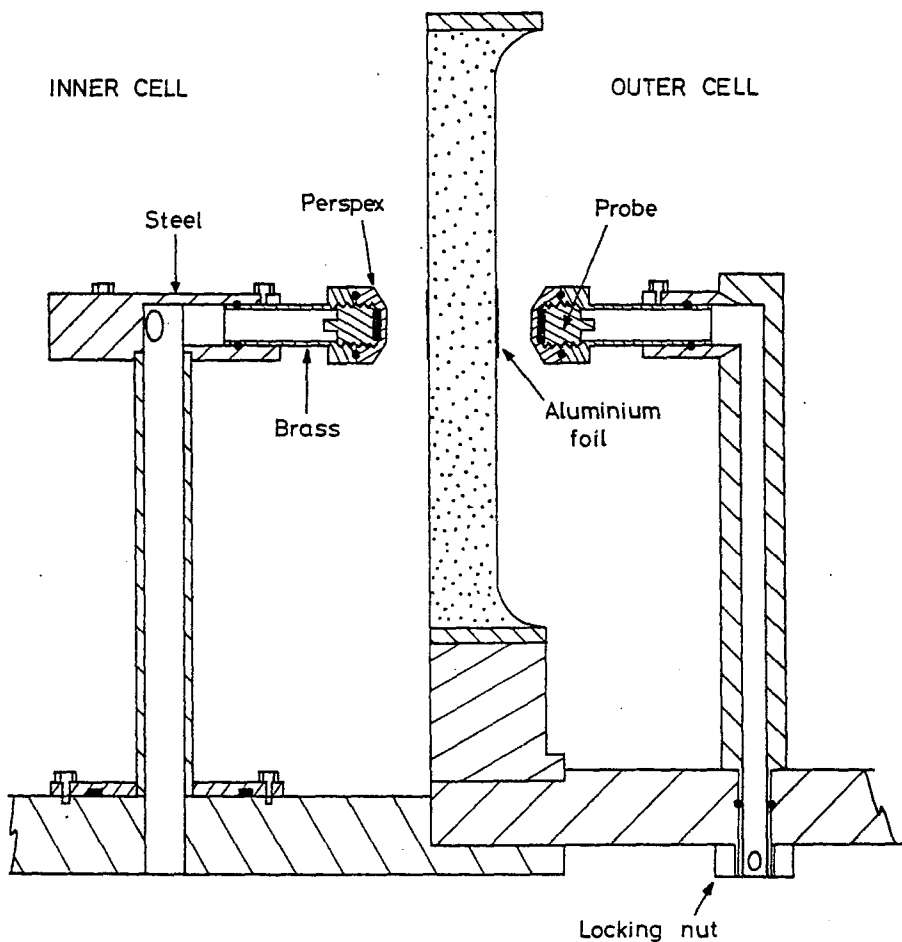


Figure 3.7: Details of a pair of opposed proximity transducers to measure radial displacements (Symes 1983)

the fluid from the central electrode to each outside electrode is equal. Tilting the sensor disturbs this balanced condition and the resistance changes, in proportion to the angle of tilt. Such devices can be either of the single axis type (with one set of electrodes), measuring only torsional shear or axial displacement, or the double axis variety (with two orthogonal sets of electrodes), which measure both axial and torsional displacement. The double axis type device, apart from having two sets of electrodes, is also comprised of two cylinders, each of them with one glass capsule and two sets of orthogonal electrodes. The two cylinders have a joint connection, allowing only one degree of freedom for the measurement of the axial strain. When the shear deformation occurs, the two cylinders behave as a rigid body. It is important to note however, that due to its double capabilities, the double axis transducers lose part of their accuracy and resolution due to electrical noise and cross interference. The different types of electro-level devices are presented in Figure 3.9.

### 3. Test material, apparatus and procedures

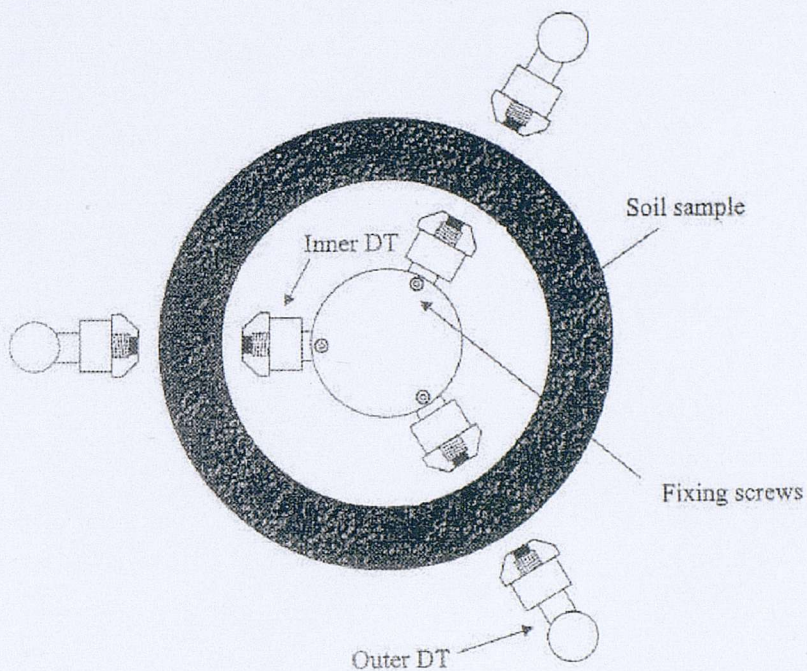


Figure 3.8: Details of arrangement of the proximity transducers - top view (Zdravkovic 1996)

All the local instrumentation is deployed in the central portion of the sample, as far away as possible from top and bottom boundaries, to reduce boundary effects and avoid the effects of strain non-uniformities. Global displacement transducers are also mounted outside the cell to record overall axial and torsional shear strain. The use of local instrumentation in the strain calculations is preferred, as global instrumentation is affected by system compliance and sample tilting and bedding errors. It is also important to mention that the angular distortion measured by the local instrumentation must be analysed with caution because the shear distortion measured corresponds to the outer boundary of a hollow cylinder sample. This distortion may be very different from the average shear strain deformation.

Table 3.4 summarizes the characteristics of the instrumentation in terms of range, stability and accuracy. Standard calibration techniques as described by Symes (1983), Shibuya (1985) and Menkiti (1995) were periodically performed for all the local and external transducers. The load cell on the other hand, was calibrated before each of the test series (i.e. before all tests using the ICHCA and before all the LICHCA tests). All the previously quoted researchers give detailed descriptions of the instrumentation calibration. Therefore, this topic is not included in this section.

### 3. Test material, apparatus and procedures

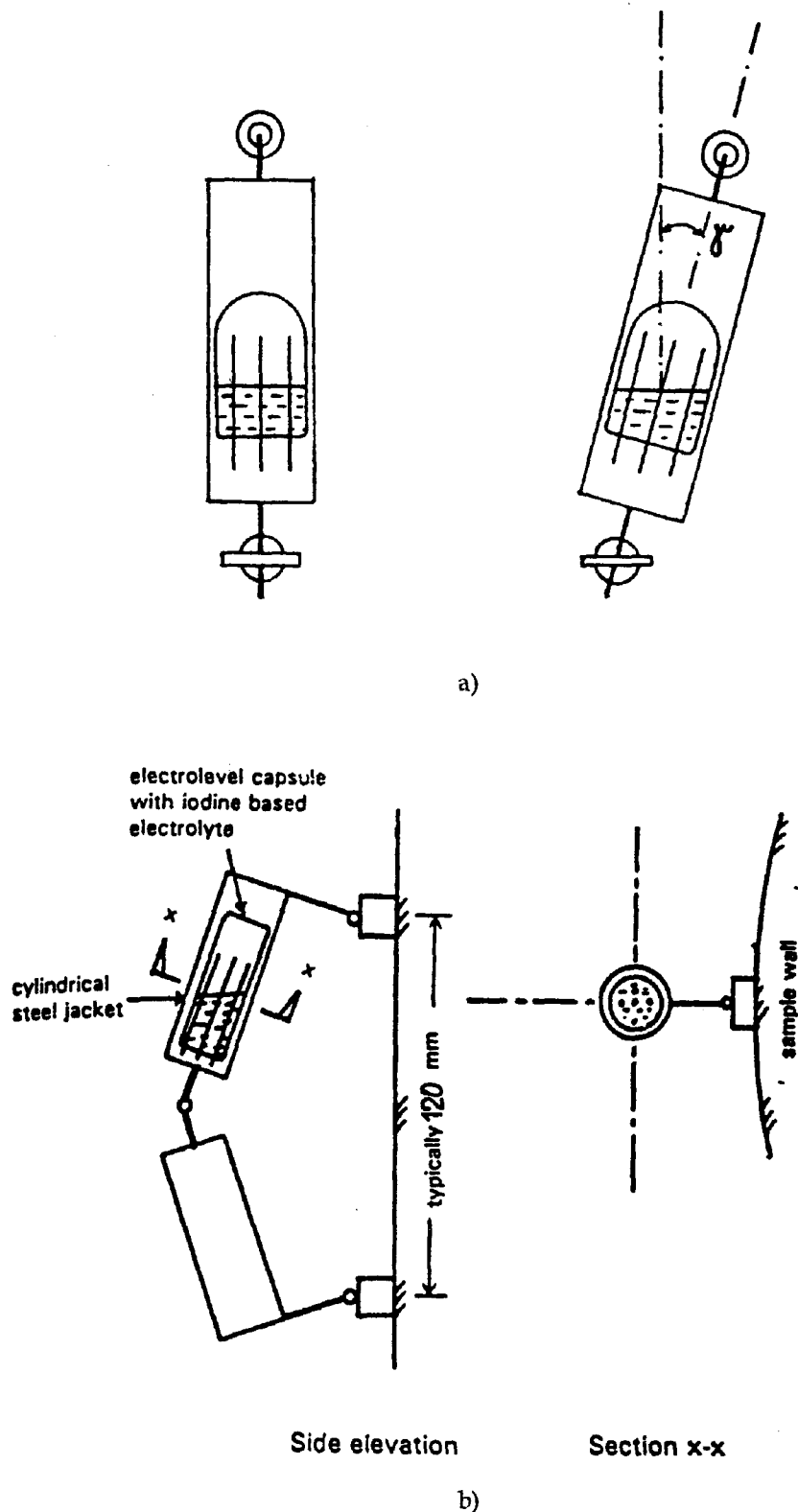


Figure 3.9: Schematic representation of the a) single axis and b) double axis electrolevels (modified after Zdravkovic 1996)

### 3. Test material, apparatus and procedures

Transducer Type	Range	Accuracy	Stability
Load Cell	-7.5 to 9.0 kN	$\pm 0.04$ kN	0.006 kN
	-0.8 to 0.8 kN.m	$\pm 0.004$ kN.m	0.0003 kN.m
Pressure Transducer	0 to 1.0 MPa	$\pm 0.3$ kPa	0.03 kPa
External Displacement	0 to 25 mm	$\pm 0.01$ mm	0.002 mm
Volume Gauge	0 to 100 cc	$\pm 0.03$ cc	0.001 cc
Electro-Level	-15 to 15 mm	$\pm 0.03$ mm	0.002 mm
	-30° to 30°	$\pm 0.013$ °	$6 \times 10^{-3}$ °
Proximity Transducer	-3 to 3 mm	$\pm 0.07$ mm	0.005 mm

Table 3.4: Summary of capacity, accuracy and stability of transducers employed in the ICHCA and LICHCA

It is important to emphasize, however, that all the tests described in this study were carried out in a temperature controlled room ( $20^\circ \pm 0.2^\circ$ ) and therefore the effect of temperature on the instrumentation was kept to a minimum.

### **Computer control and data acquisition**

The hardware used in both the ICHCA and LICHCA has been unchanged for this research. A schematic figure of the hardware is shown in Figure 3.10. The hardware consists of:

- A PC with an input/output card (I/O card), used to address and drive the stepper motors for load application
- Two analogue to digital converters (A/D), used to convert the analogue signal of the transducers to digital and vice versa
- Two modulator/demodulator boxes (M/D), used to provide a high frequency AC signal to the AC devices and then to convert back the AC to DC signal that can be then read by the A/D converter

A computer control software for the ICHCA was first developed by Zdravkovic (1996), when the whole system was changed from a micro-computer to a PC based system. This software was subsequently updated by Rolo (2003), to enable performance of strain-controlled experiments using the CRSPs for axial and torque loading. Takahashi (2003) then used this software as basis to produce a unified control program for all hollow cylinder devices in the Soil Mechanics Laboratory at Imperial College (there are two smaller devices in addition to the ICHCA used in this thesis). The author performed saturated tests on Leighton Buzzard sand under drained conditions

### 3. Test material, apparatus and procedures

---

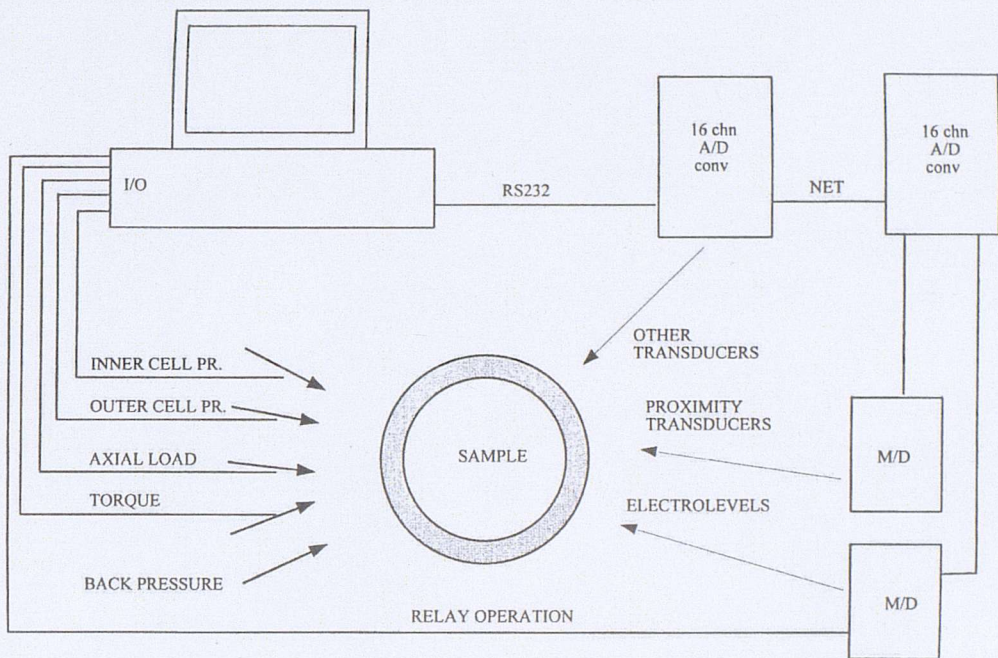


Figure 3.10: Control and data acquisition system for the ICHCA and LICHCA (Zdravkovic 1996)

in order to test the repeatability and consistency between the different programs. It was observed that the response obtained using them was identical. Consequently, this latest software was used to perform both ICHCA and LICHCA experiments in this study.

The software uses four control parameters to drive the desired stress path:

$$b = \frac{\sigma_2 - \sigma_3}{\sigma_1 - \sigma_3} \quad (3.15)$$

$$t = \frac{\sigma_1 - \sigma_3}{2} \quad (3.16)$$

$$p = \frac{1}{3} (\sigma_1 + \sigma_2 + \sigma_3) \quad (3.17)$$

$$\alpha = \frac{1}{2} \arctan \left( \frac{2\tau_{z\theta}}{\sigma_z - \sigma_\theta} \right) \quad (3.18)$$

### 3. Test material, apparatus and procedures

---

where  $\alpha$  is the angle between the major principal stress and the vertical. The target stresses are calculated from these control parameters as:

$$\sigma_z = p - t \left( \frac{2b - 1}{3} - \cos 2\alpha \right) \quad (3.19)$$

$$\sigma_r = p - t \left( \frac{2(1 - 2b)}{3} \right) \quad (3.20)$$

$$\sigma_\theta = p - t \left( \frac{2b - 1}{3} + \cos 2\alpha \right) \quad (3.21)$$

$$\tau_{z\theta} = t \sin 2\alpha \quad (3.22)$$

Knowing the target stresses from the equations above, the actual forces to be applied to the sample can be calculated as:

$$p_o = [\sigma_r(r_o + r_i) + \sigma_\theta(r_o - r_i)] \frac{1}{2r_o} \quad (3.23)$$

$$p_i = [\sigma_r(r_o + r_i) - \sigma_\theta(r_o - r_i)] \frac{1}{2r_i} \quad (3.24)$$

$$M_T = \frac{1}{3} 2\pi (r_o^3 - r_i^3) \tau_{z\theta} \quad (3.25)$$

$$W = \pi (\sigma_z(r_o^2 - r_i^2) - (p_o r_o^2 - p_i r_i^2)) \quad (3.26)$$

where  $p_o$  and  $p_i$  are the outer and inner cell pressures,  $M_T$  is the applied torque,  $W$  is the applied vertical force and  $r_o$  and  $r_i$  are the current outer and inner radii,

A schematic representation for one stress increment is shown in Figure 3.11. The algorithm for software control can be listed as follows:

1. Select a leading parameter considering one of  $b$ ,  $t$ ,  $p$  and  $\alpha$ . For example, in a shearing stage the leading parameter is  $t$ , for a  $b$ -change stage the leading parameter is  $b$  and for an  $\alpha$  rotation it is  $\alpha$ .

3. Test material, apparatus and procedures

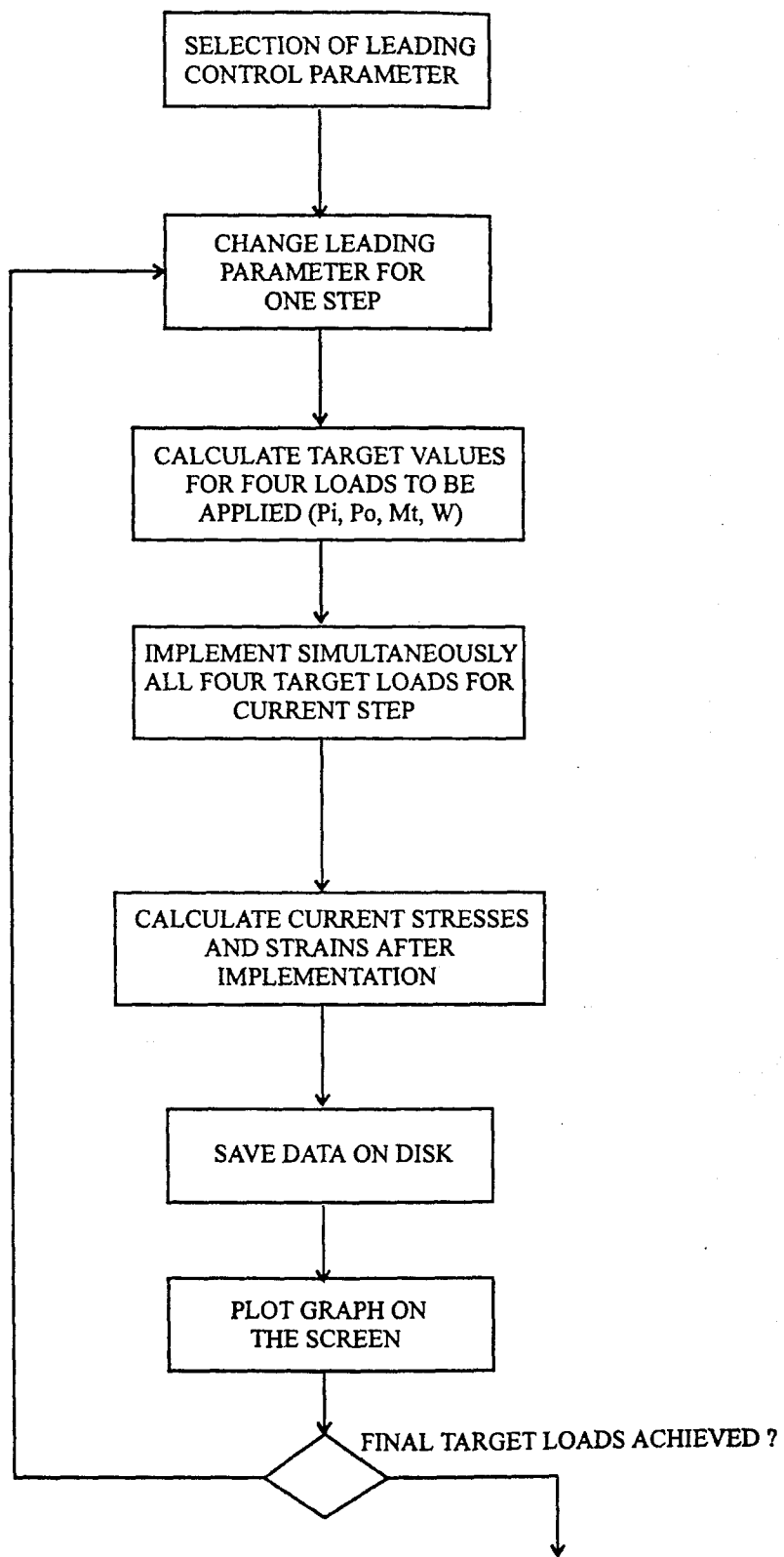


Figure 3.11: Load application algorithm for the ICHCA and LICHCA (Zdravkovic 1996)

### 3. Test material, apparatus and procedures

---

2. Select a small increment for varying the leading parameter. Typical values are  $\Delta t = 0.5 \text{ kPa}$ ,  $\Delta b = 0.05$   $\Delta\alpha = 0.1^\circ$
3. Calculate the associated changes in the remaining control parameters using the selected increment and applying equations 3.19, 3.20, 3.21 and 3.22.
4. Translate these changes in stresses to the required pressure changes using equations 3.23, 3.24, 3.25 and 3.26.
5. Read the response on transducers and calculate new stresses and strains that must be saved on the data file.
6. Steps 1 to 5 are repeated until the required stress path is completed.

#### **3.3.3 Large Imperial College Hollow Cylinder Apparatus (LICHCA)**

Based on the results of numerical analyses discussed in Section 3.4, to test samples with a height/outer diameter (H/OD) ratio of 2, the height of the ICHCA was increased, having a new sample height of approximately 50 cm. Although inner and outer radii, the local instrumentation, loading frame and the computer control and data acquisition system remained unchanged for the LICHCA, several other changes had to be done. These changes are briefly summarized in this section.

In order to accommodate a bigger sample, the most evident change was the size of the perspex chamber and the twelve steel bars that are used to support it and attach it to the base pedestal. A new perspex cell with the same diameter and a height of 92 cm was manufactured. The twelve bars were also manufactured to account for this increase in chamber size. All these changes were requested to an external provider.

In order to continue measuring the radial deformation at the middle of the sample using the proximity transducers, their support also had to be extended. These extensions were manufactured by the technicians at the Imperial College Soil Mechanics Laboratory. For the outer proximities new stainless steel tubes were manufactured that can be easily changed if smaller samples need to be tested. Figure 3.12 compares the old tubes with the new extended version. In the case of the internal proximities a simple extension such as the one described for the external proximities was not possible. The reason for that is the reduced space available to locate the

### 3. Test material, apparatus and procedures

---

base plate of the inner chamber in position. Figure 3.13 shows the solution that was also manufactured at Imperial College. It consists of a collar extension that rises the old proximities support to the required height. This extension has a middle section where the cables for the instrumentation are kept isolated from all hydrostatic pressures. Furthermore, the support of the old proximities must be separated from the extension during set-up. Further details of set-up are given in Section 3.5.1.

In order to set-up a bigger sample changes in the outer and inner moulds were also required. A new outer mould, keeping the same volume of flares at the bottom and top of the sample, was requested to an external provider. As it can be seen in Figure 3.14 it consists of three stainless steel segments that are joined together with the use of pairs of clamps. In the case of the inner mould, the old version was used for the new set-up and two new split perspex sections that can be expanded and collapsed with the use of screws were manufactured at Imperial College (see Figure 3.15).

When saturated samples are tested in the HCA, no vacuum pressure is required to hold the membranes against the moulds and give the adequate shape to the samples. This is because the large size of the sample gives a water column high enough such that its self-weight holds the membrane against the moulds. The tests presented in this thesis are the first HCA tests performed at the ICHCA/LICHCA under dry conditions, therefore a vacuum pressure was required in the moulds. Figure 3.16 shows the system set-up to do that. The system shown is connected to the vacuum pressure application points in the outer mould. This system includes a Venturi type converter to produce a negative pressure from a positive pressure source. Initially, only three vacuum application points were drilled in the middle of the moulds. Subsequent tests evidenced that it was not possible to hold the membrane in position once half of the sample was deposited. This created samples that were not uniform in terms of the void ratio across the sample height. Consequently, during shear, undesired bulging was obtained in the top part of the sample and not in the middle of the sample. The problem was solved by inserting two additional vacuum application points in the top of one of the outer mould sections (see detail in Figure 3.14). Lastly, an extension had to be added to the siphon tube. A preliminary practice period of two months was required to develop a consistent sample preparation method with adequate control of the initial void ratio for both the ICHCA and LICHCA set-ups.

### 3. Test material, apparatus and procedures

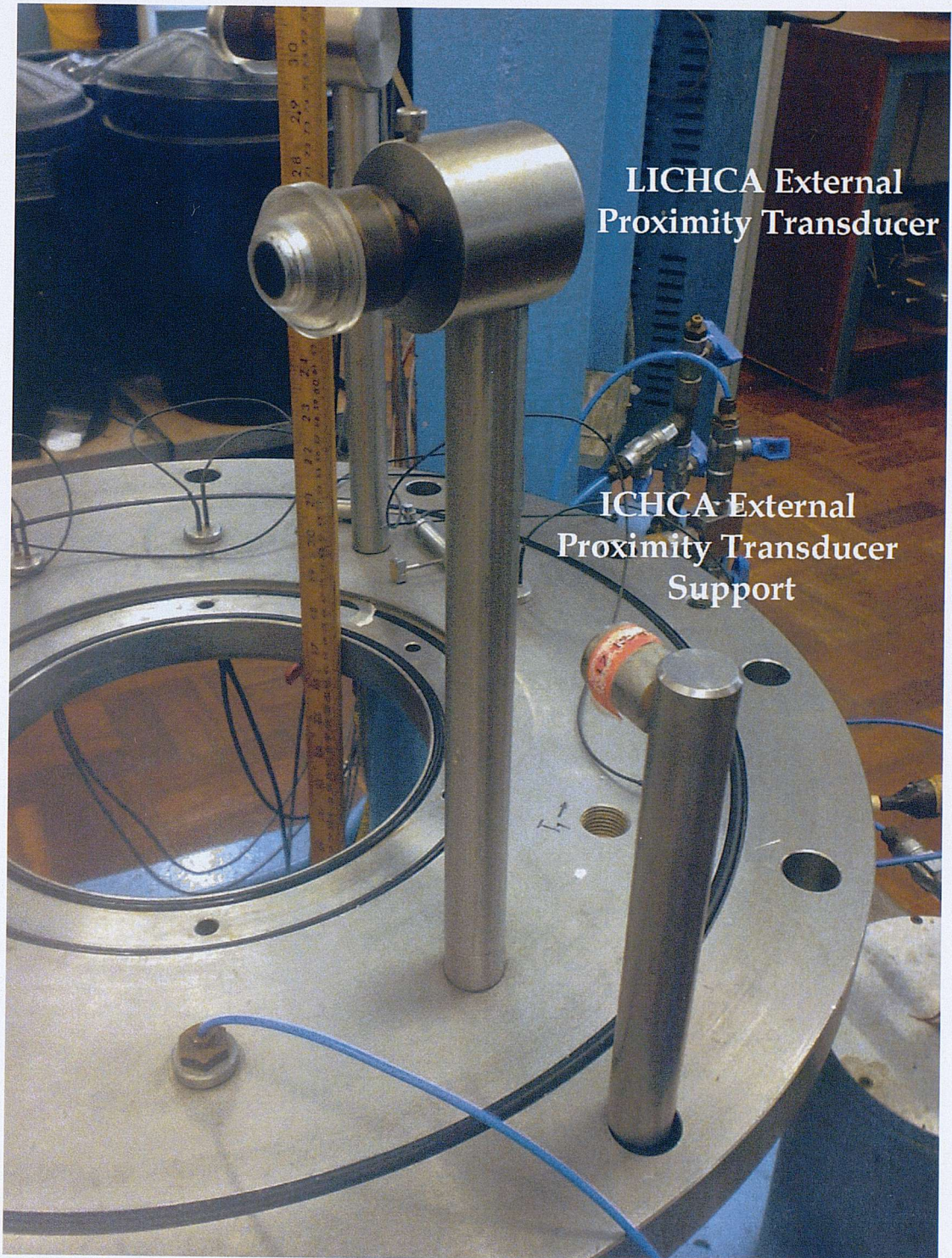


Figure 3.12: Comparison of set-up for the external proximity transducers in the ICHCA and LICHCA



Figure 3.13: Deployment for the internal proximity transducers in the LICHCA

### 3. Test material, apparatus and procedures

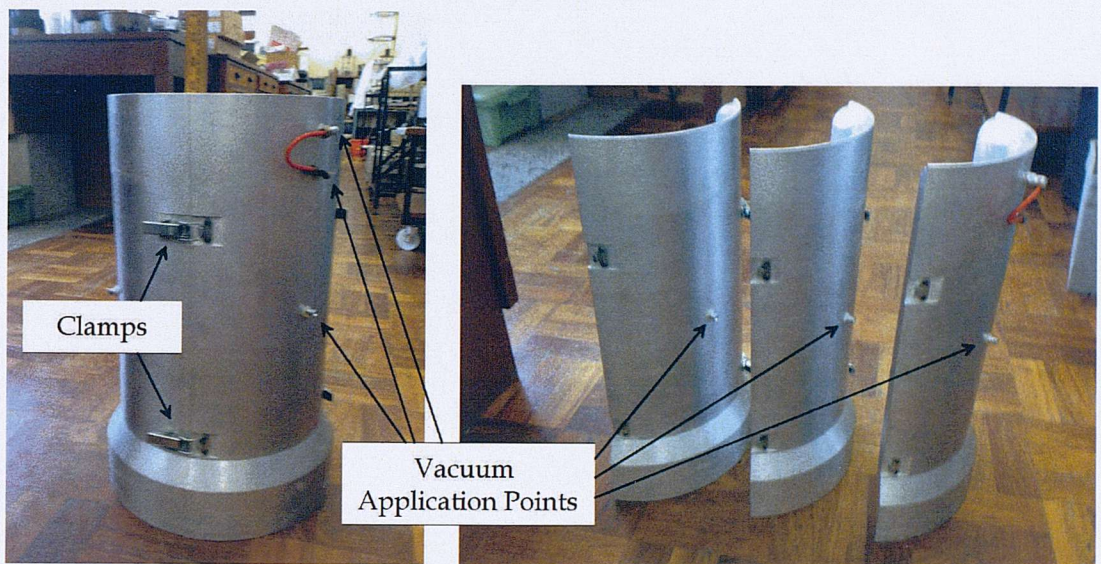


Figure 3.14: Outer moulds for the ICHCA and ICHCA

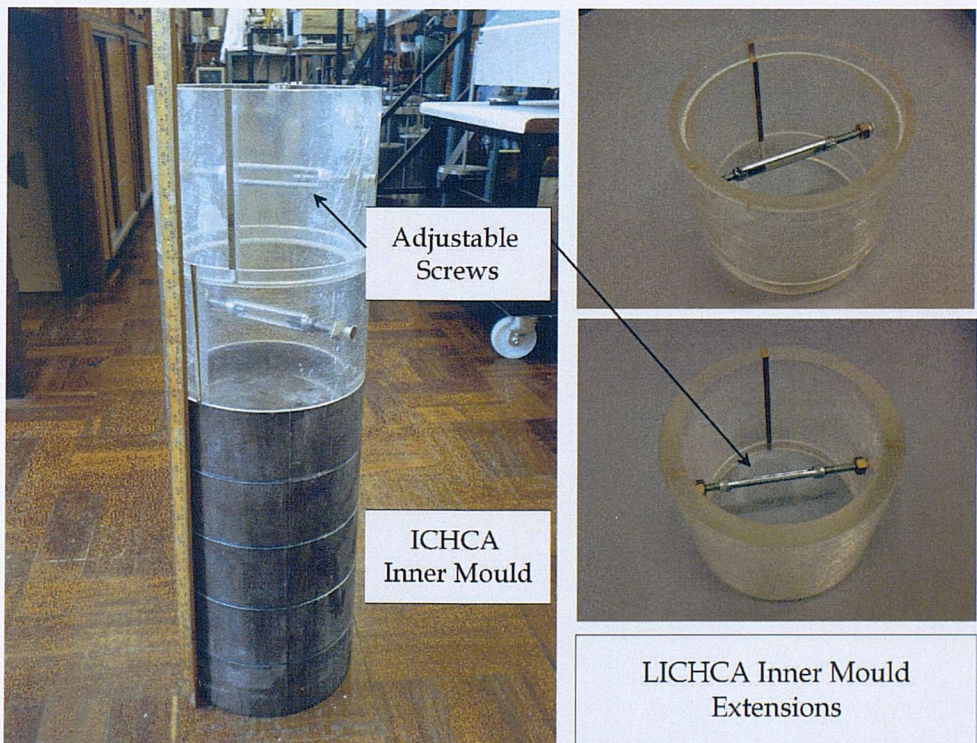


Figure 3.15: New inner extensions for the inner mould and its deployment

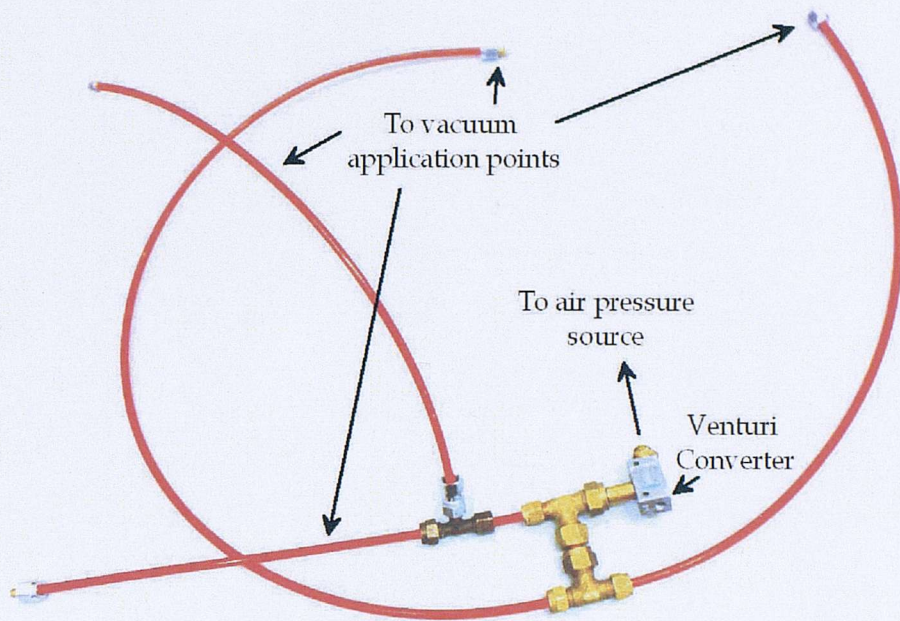


Figure 3.16: System for application of vacuum used to hold the outer membrane against the mould

### 3.4 Stress and strain non-uniformities

It is well recognized that the stress and strain conditions in a HCA during testing are non-uniform. These non-uniformities have been found to depend on the boundary conditions, the stress path applied and the constitutive law of the material (Hight et al. 1983, Zdravkovic 1996, Rolo 2003). Several numerical studies and a reduced number of experimental studies have been carried out in order to assess the effects of non-uniformities on HCA tests. All the numerical analyses to date have been performed for HCA tests under undrained conditions. Furthermore, all of these numerical analyses have used continuum finite element formulations. A brief summary of the conclusions of these studies is presented here. These studies highlight the need to perform numerical simulations using DEM in order to be able to understand the particle scale interactions that produce such non-uniform behaviour.

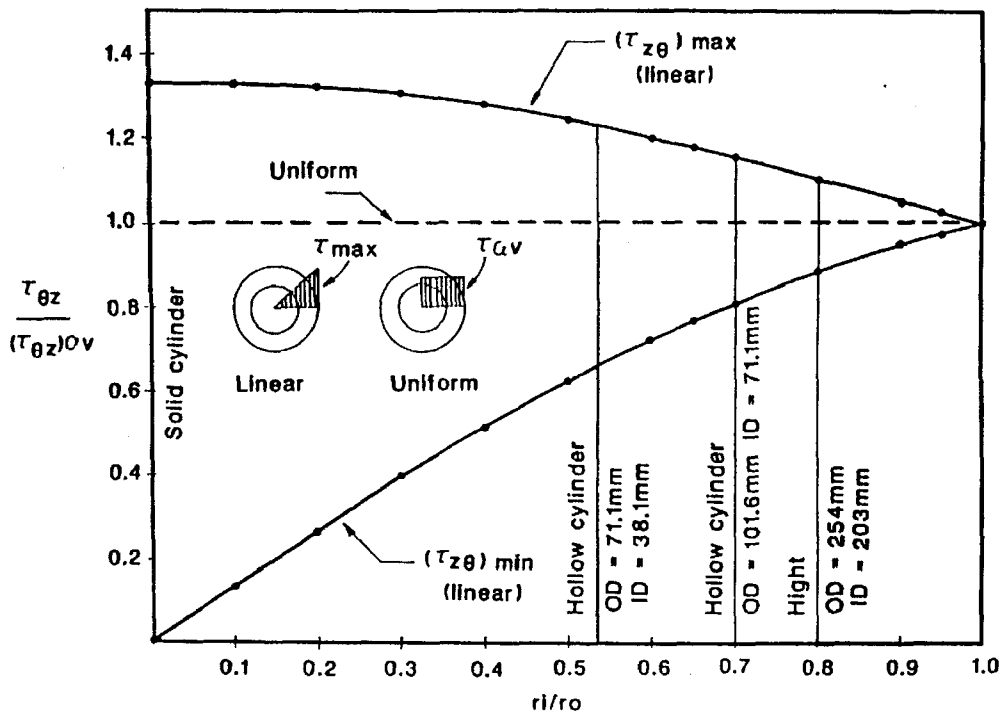


Figure 3.17: Shear stress variation with HCA radius (Porovic 1995)

### 3.4.1 The origin of the non-uniformities

Non-uniformities in HCA testing originate from rough end platens and from the way the stress is applied on the sample (e.g. different inner and outer cell pressures and torque). The torque is applied to the sample through a top cap. This produces a variation of the shear strain  $\gamma_{z\theta}$  along the sample wall. Also the shear stress  $\tau_{z\theta}$  varies across the sample wall as shown in Figure 3.17, where the maximum and minimum shear stress are plotted against the ratio of inner to outer radius. When the inner and outer cell pressures are equal, the distribution of radial stress across the wall of the sample is uniform. However, if these pressures differ, the values of the radial and circumferential stresses vary across the sample wall. Another source of non-uniformities are the rough end restraints at the top and bottom of the sample. The platens need to be rough in order to be able to apply torque to the sample. This necessary restraint constrains the ideal free radial movement of the walls of the sample, producing non-uniformities even when the inner and outer pressures are equal. Furthermore, the axial and shear stress across the wall of the sample vary due to the application of torque, as shown in Figure 3.18.

### 3. Test material, apparatus and procedures

The effects and presence of non-uniformities can not be avoided, but they can be reduced to acceptable levels with the appropriate selection of the HCA geometry. The numerical studies presented in the next section give some insight about the ideal geometry for a HCA.

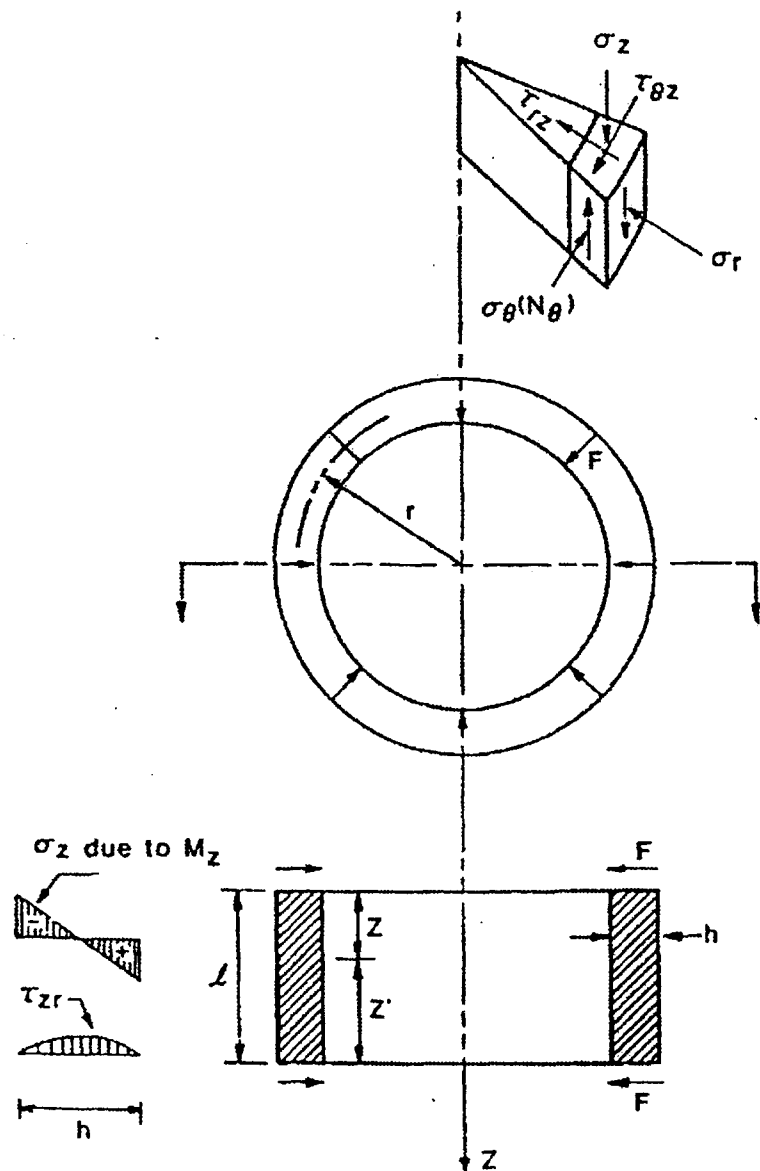


Figure 3.18: Vertical and shear stress distribution across the sample wall due to the application of torque (Saada & Townsend 1981)

### 3.4.2 Previous numerical analyses of non-uniformities

One of the earliest finite element studies to assess the effects of non-uniformities in HCA tests was presented by Hight et al. (1983). They proposed the following parameter to assess the level of non-uniformities:

$$\beta_3 = \frac{\int_{r_i}^{r_o} |\sigma_{(w)} - \bar{\sigma}^*|}{(r_o - r_i) \sigma_L} \quad (3.27)$$

where  $r_o$  and  $r_i$  are the outer and inner radii,  $\sigma_{(w)}$  is the distribution of the stress across the wall sample,  $\bar{\sigma}^*$  is the true average from the distribution of stress across the wall of the sample and  $\sigma_L$  is a measure of the average stress level. All these definitions are shown in Figure 3.19.

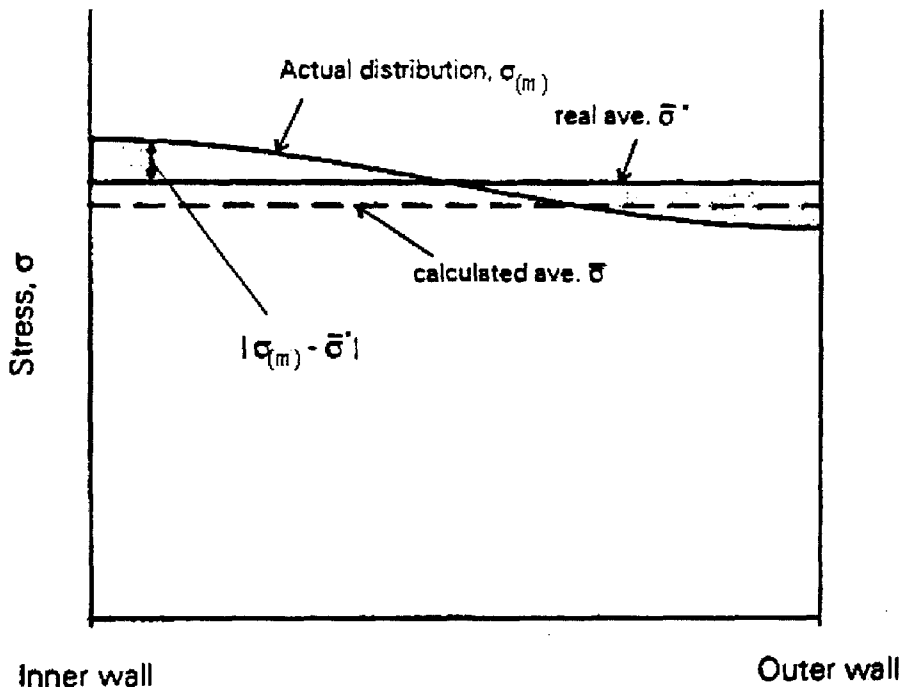


Figure 3.19: Definition of parameters to assess the level of non-uniformities in the HCA (Hight et al. 1983)

Hight et al. (1983) studied the stress variation across the sample wall. However, their study was two-dimensional, therefore the application of torque on non-uniformities was not considered (only axi-symmetric loading was assessed). In their analyses they used linear elasticity and a strain hardening modified Cam Clay model. The dimensions of the sample used were an inner diameter of 20 cm, outer diameter of 25 cm and the height was varied. The differences obtained between the linear

### 3. Test material, apparatus and procedures

elastic and the modified Cam Clay model allowed determination of the ideal sample dimensions for the ICHCA. Hight et al. (1983) suggested that if dimensions such that  $r_i/r_o = 0.8$  were used and a restriction on the difference between the inner and outer cell pressure was imposed ( $0.9 < p_o/p_i < 1.2$ ), the level of non-uniformities was reduced. The previous recommendation implied that for the ICHCA a value  $\beta_3 < 11\%$  was acceptable. With that basis, they defined two “no-go” areas in the stress space where the samples would present unacceptable non-uniformities (see Figure 3.20). Saada & Townsend (1981) also suggested that the ideal HCA geometry should be governed by the following expressions:

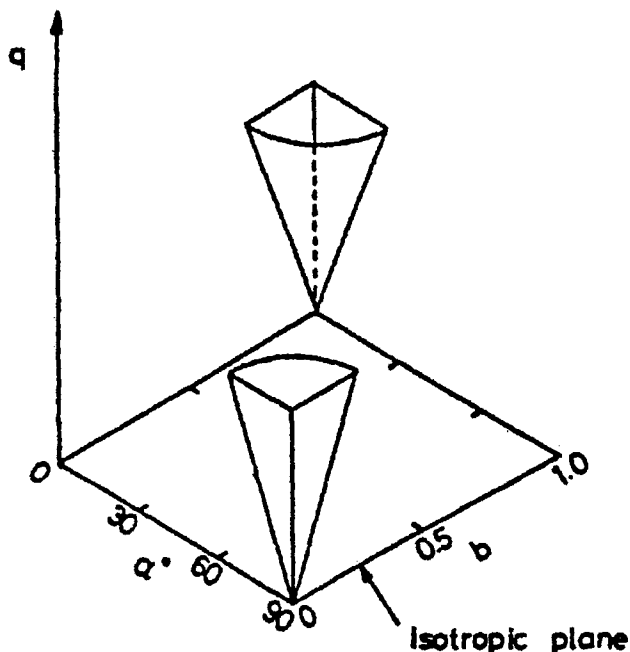


Figure 3.20: Areas of the stress space where the level of non-uniformities is unacceptable (Hight et al. 1983)

$$h \geq 5.44 \sqrt{r_o^2 - r_i^2} \quad (3.28)$$

$$\frac{r_i}{r_o} \geq 0.65 \quad (3.29)$$

The dimensions of the ICHCA satisfy the criterion imposed by Equation 3.29. But Equation 3.28 indicates that a height bigger than 408 mm would be needed for the ICHCA. It is important to note however, that these suggestions were derived using linear elastic theories for thin cylindrical shells.

### 3. Test material, apparatus and procedures

Further finite element analyses were carried out by Hight et al. (1983) to investigate the effects of end-restraint. They also used linear elastic and modified Cam Clay type constitutive models for this study. The results presented in the form of contours showed that there was a concentration of non-uniformities towards the ends of the sample (see Figure 3.21). Figure 3.22 also shows that the middle third of the sample contains acceptable levels of non-uniformities at low stress levels, but the level of non-uniformities increases as the stress level increases. Note that in Figure 3.22 the distribution for the radial stresses is not presented. This is because for the stress path analysed (undrained shearing with  $p_o = 400$  kPa and  $p_i = 350$  kPa) this distribution was not significantly affected.

A study to assess the effect of the application of torque was simulated by Gens & Potts (1984). They used the same curvature of the ICHCA, but only the central part of the sample was analysed, therefore the effect of end restraint was neglected. A stress path in which the torque is applied with constant inner and outer pressures was analysed using an elasto-plastic model with both associated and non-associated plasticity. The results presented in Figure 3.23 show the stress distribution at two stages (before yield, and after yield). It is demonstrated that when associated plasticity is used,  $\sigma_\theta = \sigma_r$  at both stages. In this case, the level of non-uniformities is small and becomes negligible as the soil elements yield. In the non-associated plasticity case the opposite is observed, non-uniformities are large and increase as the material yields.

Studies by Vaid et al. (1990), Sayao & Vaid (1991) and Wijewickreme & Vaid (1991) re-examined the stress distributions in HCA samples by using the dimensions of the HCA from the University of British Columbia (inner diameter 102 mm, outer diameter 152 mm and height 305 mm). They used isotropic elastic and incremental hyperbolic elastic models in their analyses. They also observed an increment of non-uniformities with an increase of stress ratio and sample initial density. A new parameter for the assessment of non-uniformities was suggested by Vaid et al. (1990), defined as:

$$\beta_R = \frac{R_{max} - R_{min}}{R_{av}} \quad (3.30)$$

where  $R_{max}$ ,  $R_{min}$  and  $R_{av}$  are the maximum, minimum and average stress ratios as shown in Figure 3.24. They suggested that  $\beta_R < 0.2$  would give an acceptable level of non-uniformities. This led them to define a new "no-go" area around the  $\alpha = 45^\circ$  line (see Figure 3.25). However, they mentioned that different results would

### 3. Test material, apparatus and procedures

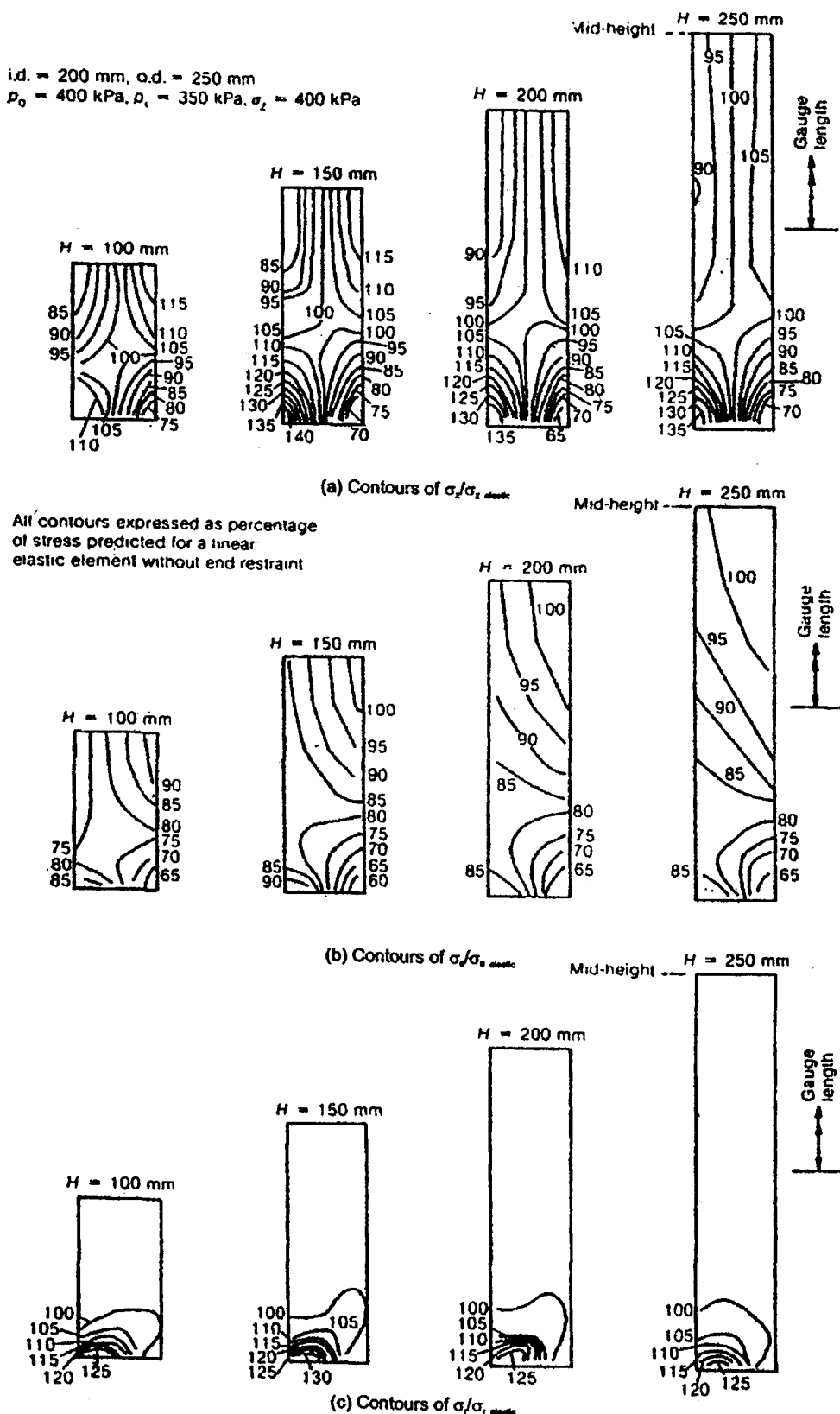


Figure 3.21: Distribution of stresses across the wall of the HCA sample using linear elastic FE analyses (Hight et al. 1983)

3. Test material, apparatus and procedures

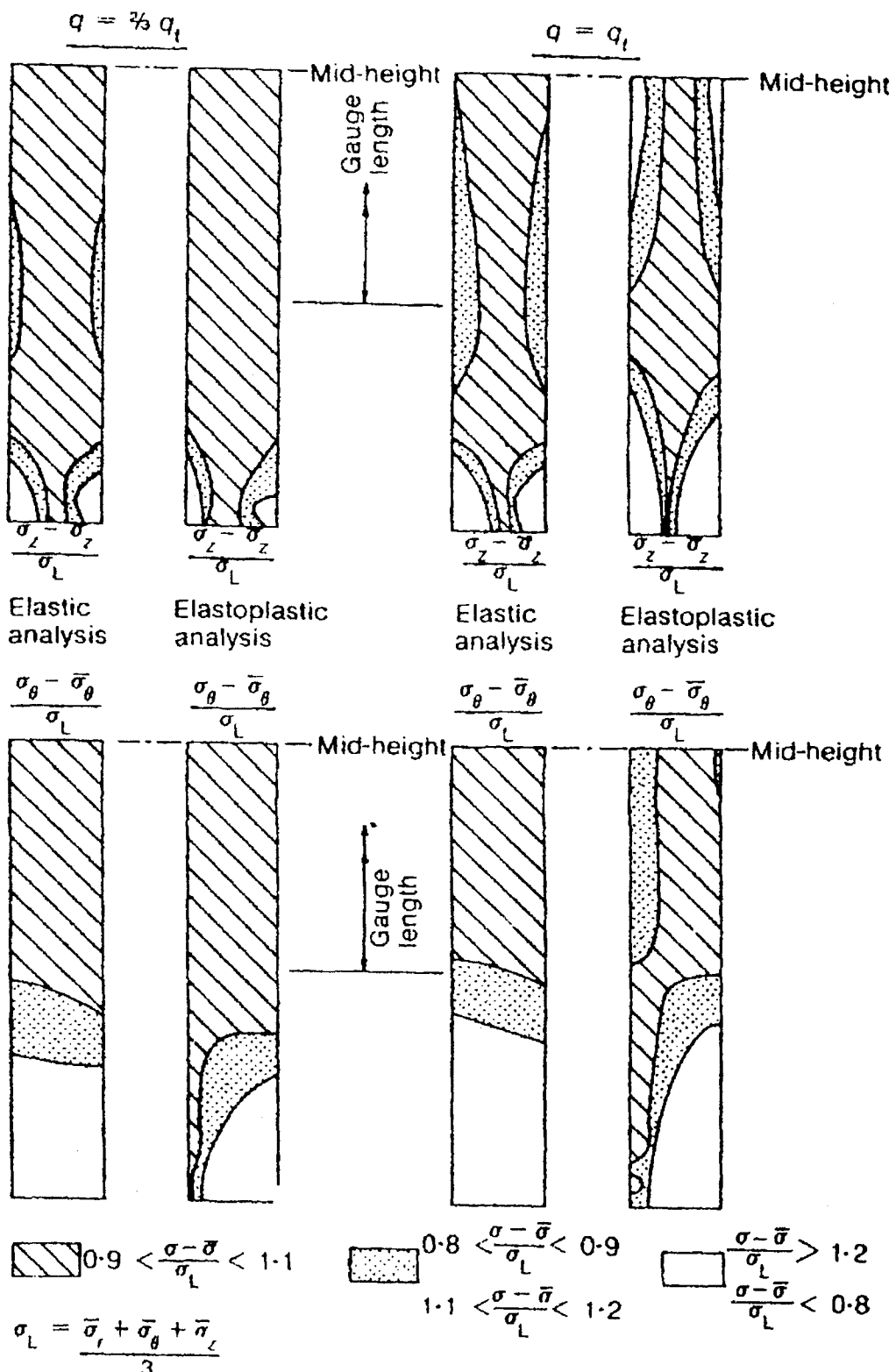


Figure 3.22: Distribution of stresses at two different stress levels in the HCA using elasto-plastic FE analyses (Hight et al. 1983)

### 3. Test material, apparatus and procedures

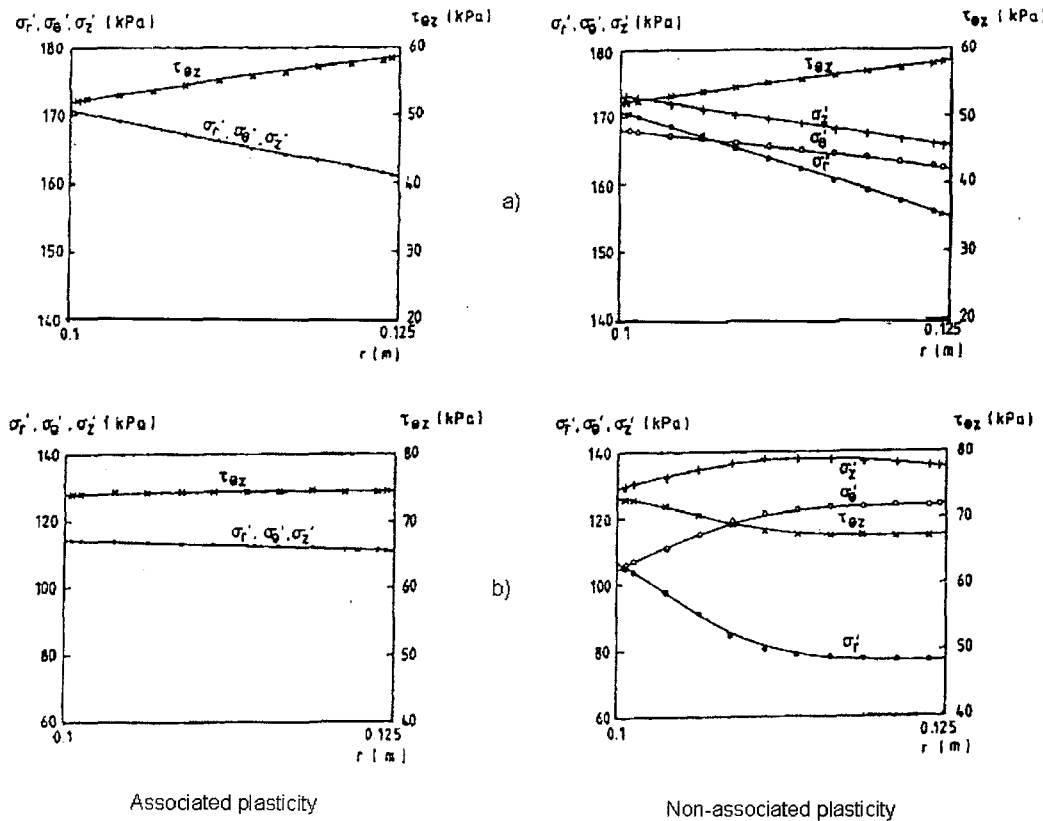


Figure 3.23: Distribution of stresses due to the application of torque using associated and non-associated plasticity. a) Before yield and b) after yield (modified after Gens & Potts 1984)

be anticipated using more realistic constitutive soil models. It is also important to note that the height requirement imposed by Saada & Townsend (1981) in Equation 3.28 is not satisfied by the dimensions of their HCA (as it is the case of the ICHCA).

All the numerical studies described above give an insight into the distribution of stresses across the sample wall, but they do not consider the effects of the non-uniformities on the interpreted stress-strain response of soils. Menkiti (1995) used a different approach in his finite element analyses to consider this effect. He used the same constitutive model and boundary conditions as Gens & Potts (1984), but in addition, he performed an analysis using a single finite element subjected to the same stress path. This element behaves uniformly and free from boundary effects providing the “true” soil response corresponding to the constitutive law used. The results from those analyses are shown in Figure 3.26 in terms of the stress-strain response. The stress path followed for both analyses consisted of undrained shearing with  $b = 0.5$  and  $\alpha = 45^\circ$  under a constant mean effective stress,  $p'$  of 200 kPa. Solid circles represent the single finite element study. Open circles are calculated values

### 3. Test material, apparatus and procedures

---

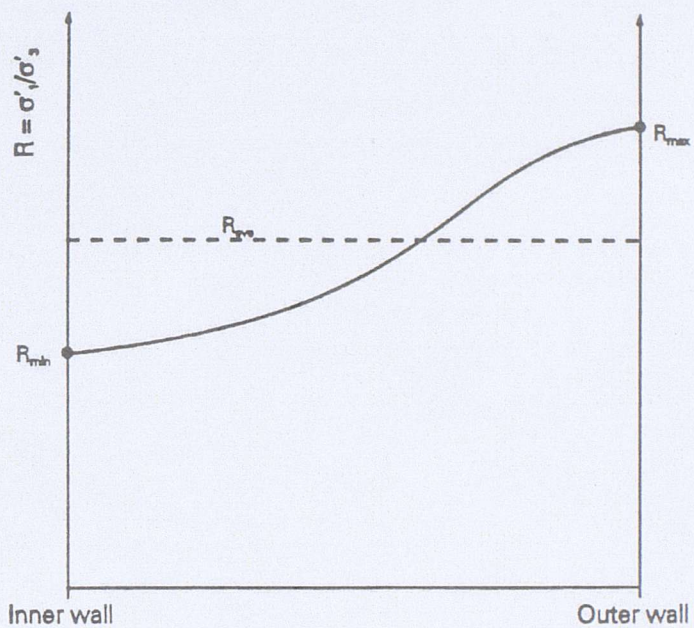


Figure 3.24: Definition of parameters for the assessment of non-uniformities (Vaid et al. 1990)

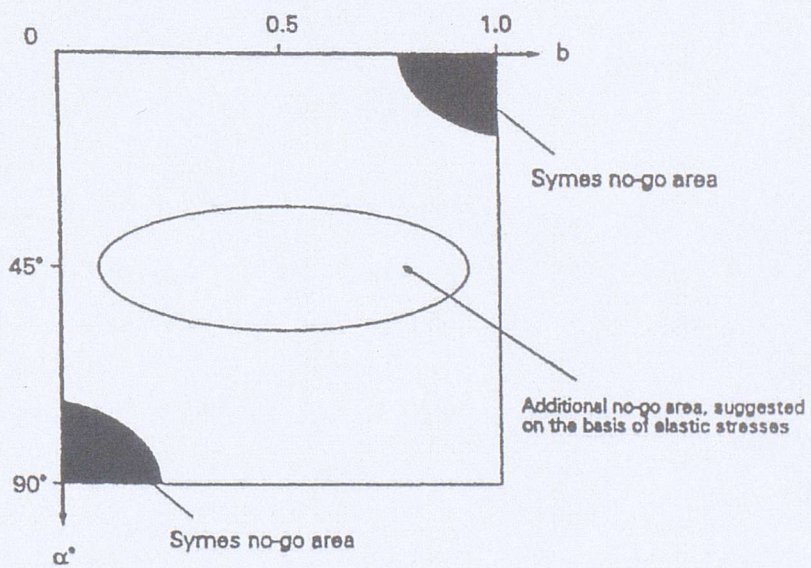


Figure 3.25: Areas of the stress space where the level of non-uniformities is unacceptable added by Vaid et al. (1990)

### 3. Test material, apparatus and procedures

from the analysis with boundary conditions. The calculated and the real behaviour show good agreement, indicating a negligible effect of the non-uniformities on the stress-strain response for samples in the ICHCA. Nevertheless, it is important to remember that Gens & Potts (1984) and Menkiti (1995) only modeled the central portion of the specimen, therefore only the effect of curvature was considered and end effects were neglected.

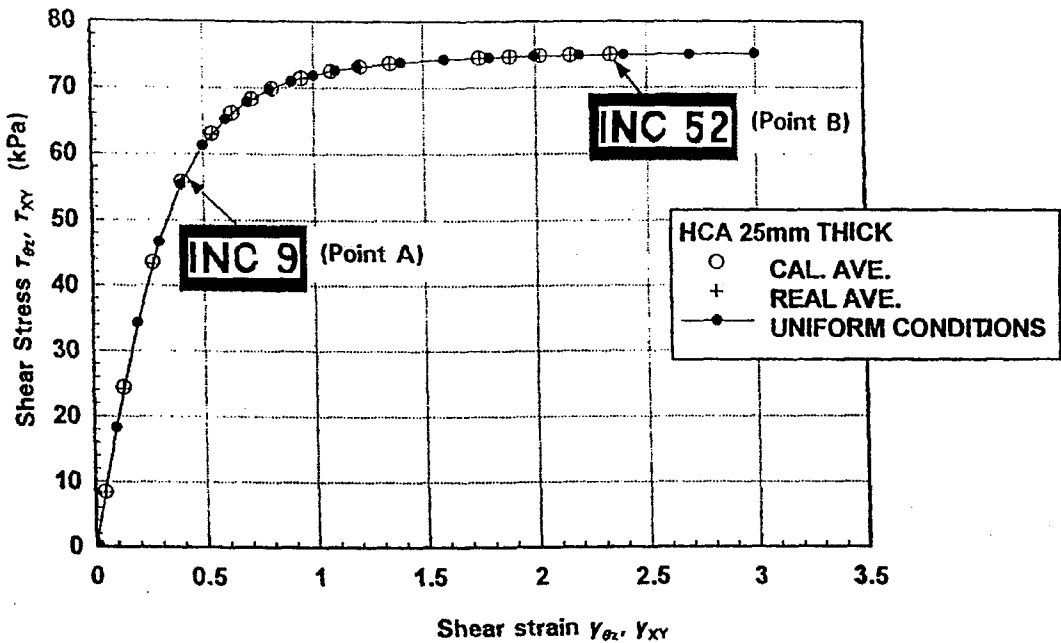


Figure 3.26: Effect of the stress and stress non-uniformities on the stress-strain relationship obtained from HCA tests (Menkiti 1995)

In the previous studies, the non-uniformities have been assessed for different sample dimensions, end restraints, constitutive models and stress paths, but not all of these variables were considered in the same analysis. Rolo (2003), Zdravkovic & Potts (2005) and Foundoukos (2006), published numerical analyses using 3D finite element analysis in terms of the Fourier Series Aided Finite Element Method (FSAFEM) proposed by Potts & Zdravkovic (1999). This method can be used for problems with geometric axi-symmetry and non-symmetric boundary conditions and/or material properties. In this type of analysis, the finite element mesh remains two-dimensional and therefore the computational time is reduced considerably. All three studies used the same two-dimensional mesh and different sample geometries, end restraints, stress paths and constitutive models. The stresses and strains were interpreted in the same way as in the physical experiments. These authors compared the behaviour of these analyses to the response of a single finite element study which is free from

### 3. Test material, apparatus and procedures

boundary effects and represents the true soil behaviour.

Rolo (2003) used a modified Cam Clay model with non-associated plasticity in the deviatoric plane to study the effects of different stress paths, sample geometries, end restraints and different inner and outer cell pressures. Two sample dimensions were used, corresponding to the dimensions of the ICHCA and the LICHCA, including both free and rough ends. The analyses included typical undrained stress paths followed in the laboratory. These stress paths involved  $K_o$  consolidation to a mean effective stress of 200 kPa and a change in the intermediate stress ratio  $b$  under drained conditions. The drained stages were followed by undrained stages including undrained unloading to the isotropic axis, an  $\alpha$ -change and undrained shearing under constant  $p$  (total mean effective stress),  $b$  and  $\alpha$ . His simulations examined the cases in which  $b = 0.5$  and  $\alpha$  values of  $0^\circ$ ,  $30^\circ$  and  $45^\circ$  were used.

The results obtained by Rolo (2003) indicated that the dimensions of the ICHCA gave rise to bigger non-uniformities compared to the LICHCA. Consequently, the trends described by Rolo (2003) are summarized here in terms of the ICHCA. Figure 3.27 indicates that the differences between the single element (ideal) response and the HCA are bigger for the smallest values of  $\alpha$ . Although Figure 3.27 highlights the difference at a deviatoric strain of 30%, which is never obtained in the experiment, the same trends are observed at smaller strain levels. Figure 3.28 shows the results in terms of stress paths. The increase in  $p'$  due to unloading indicates a clear effect of non-uniformities that was not observed in the single element study. A difference in the ultimate deviatoric stress was also observed in the different analyses, which is very marked in the case of  $\alpha = 0^\circ$ . In conclusion, it is evident that the non-uniformities are most likely to be significant when  $b = 0.5$  and  $\alpha = 0^\circ$ . Consequently, the strains across the sample wall for those conditions are presented in Figure 3.29 for a deviatoric strain of 10%, although this is also a large strain level. It is clear that the axial and circumferential strains differ significantly from the single element (ideal) behaviour for this level of strain.

The aim of the study by Foundoukos (2006) was to verify if the same trends observed by Rolo (2003) with  $b = 0.5$  could be found at different  $b$  values. Therefore, Foundoukos (2006) repeated the analyses of Rolo (2003), but applied  $b$  values during undrained shearing of 0.0 and 0.3. Figure 3.30 indicates that the same trends are observed ( $b = 0.3$ ), however the effects are less significant than those observed by Rolo (2003). Similar conclusions can be derived from Figure 3.31 in terms of stress paths, as the same tendency was observed in terms of the ultimate deviator stress and distribution of stresses across the sample wall for different  $b$  values. It is

### 3. Test material, apparatus and procedures

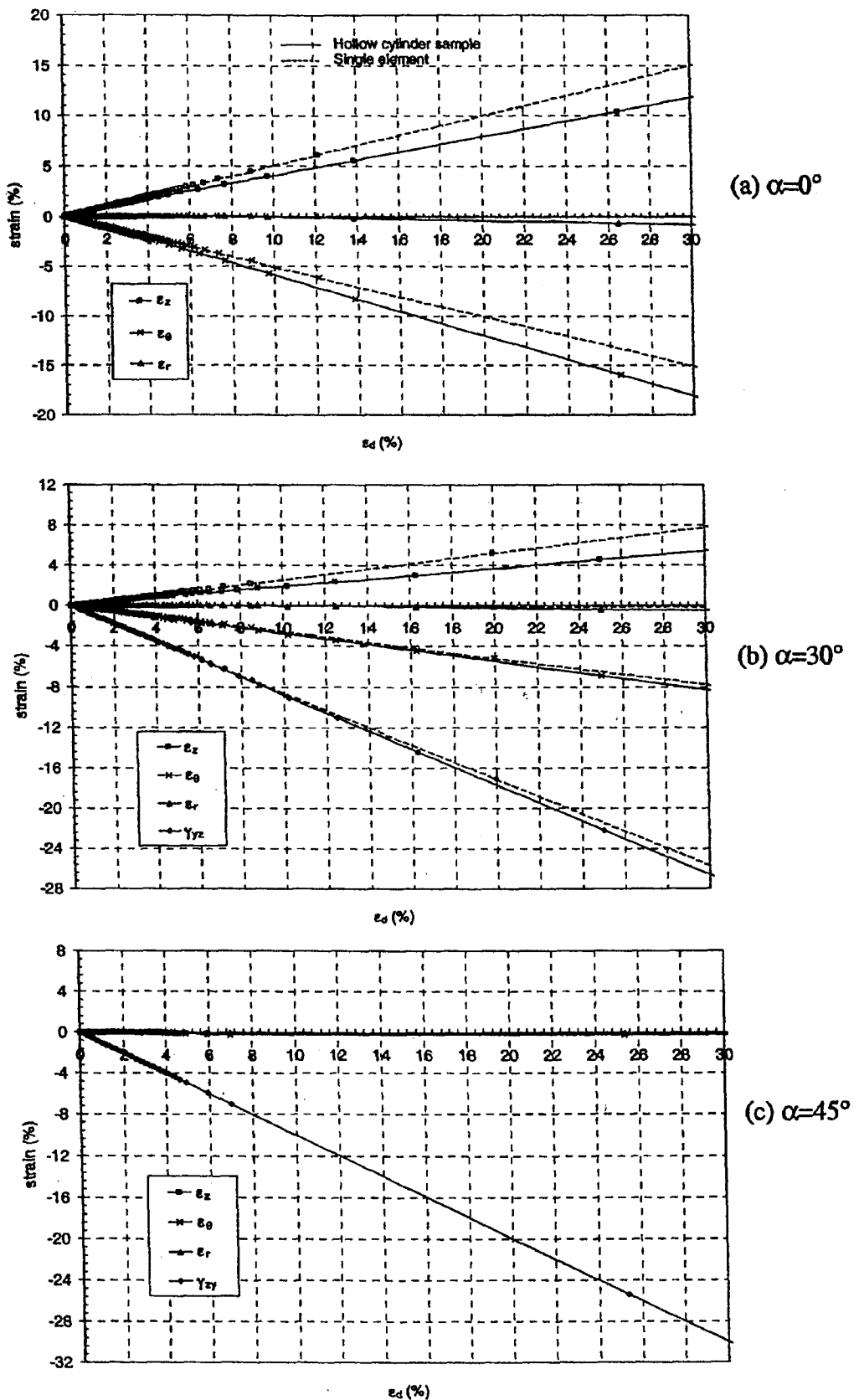


Figure 3.27: Effect of the non-uniformities on the strain development with  $b=0.5$  (Rolo 2003)

### 3. Test material, apparatus and procedures

---

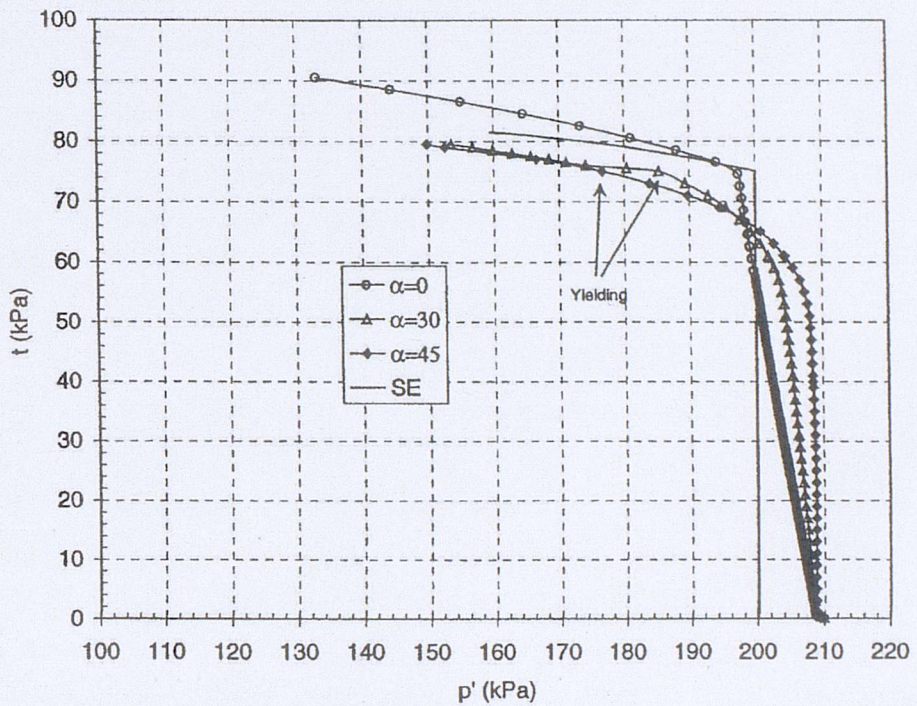


Figure 3.28: Effect of the non-uniformities on the effective stress paths with  $b=0.5$  (Rolo 2003)

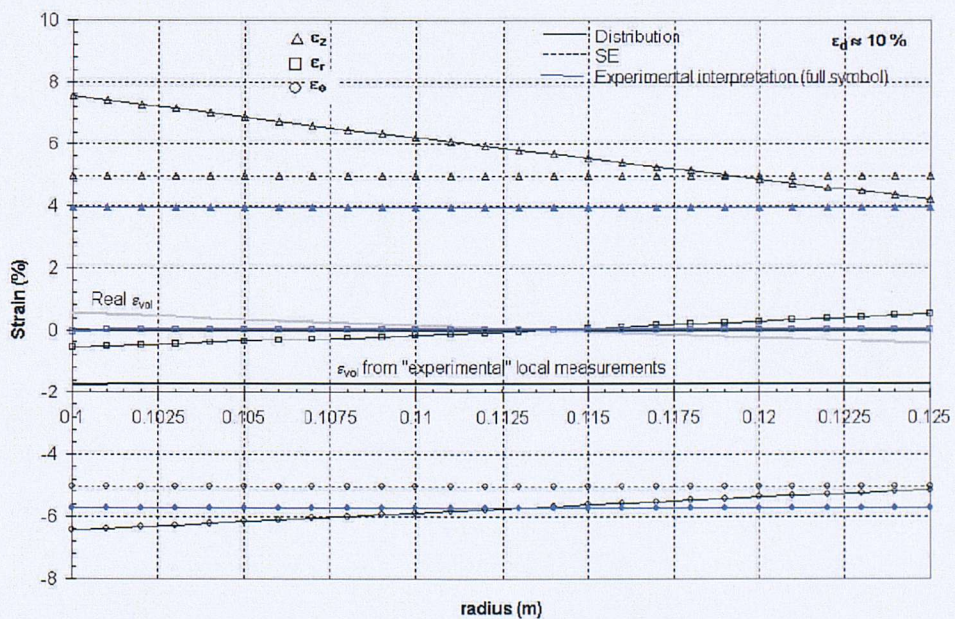


Figure 3.29: Distribution of strains across the HCA wall at a deviatoric strain level of 10% (Rolo 2003)

### 3. Test material, apparatus and procedures

---

important to note that the effects of the non-uniformities when  $b = 0$  were present but further reduced in comparison to the  $b = 0.3$  case.

The study performed by Zdravkovic & Potts (2005) considered a slightly different stress path, with the undrained unloading only reaching a deviator stress  $t$  of 45 kPa (from the initial 75 kPa) instead of 0 kPa as in the studies by Rolo (2003) and Foundoukos (2006). Also a double hardening Lade (1988) model was used instead of the modified Cam Clay, and additional geometries to those of the ICHCA and LICHCA were modelled. However, the finite element mesh, boundary conditions and use of the FSAFEM method remained similar. The results for a stress path following undrained shearing with  $b = 0.5$  and  $\alpha = 30^\circ$  are presented in Figure 3.32 where RCHCA corresponds to the analysis of a Resonant Column Hollow Cylinder Apparatus (RCHCA), with a bigger sample thickness than the LICHCA. Figure 3.33 also shows the stress distribution across the sample wall for  $t = 60$  kPa using rough platens. Note that in Figure 3.33 the real average is the average calculated from the resultant stress distribution, which is also presented in the figure. In figures 3.32 and 3.33, the trends observed by Rolo (2003) and Foundoukos (2006) were confirmed, and the advantage of having a reduced curvature in the ICHCA and LICHCA was emphasized.

The studies by Rolo (2003), Zdravkovic & Potts (2005) and Foundoukos (2006) were fundamental in the process of deciding to update the sample geometry from the ICHCA to the LICHCA. Although these studies were performed for stress paths under undrained conditions, they were also determinant in the design of the testing programme of this thesis.

In conclusion, previous numerical research indicates that the ideal HCA geometry must have the smallest possible ratio of wall thickness to sample diameter, hence a reduced curvature, and under those conditions a H/OD (height/outer diameter) ratio of 2 gives a middle section where the effects of stress and strain non-uniformities are negligible. The dimensions adopted for the LICHCA, described in Section 3.3.3 were chosen based on such criteria. The previous numerical analyses showed that the stress path presenting the worst case in terms of stress and strain uniformity is when  $\alpha = 0^\circ$  and  $b = 0.5$ . The testing programme of this thesis included this scenario in order to provide a point of comparison with DEM simulations.

### 3. Test material, apparatus and procedures

---

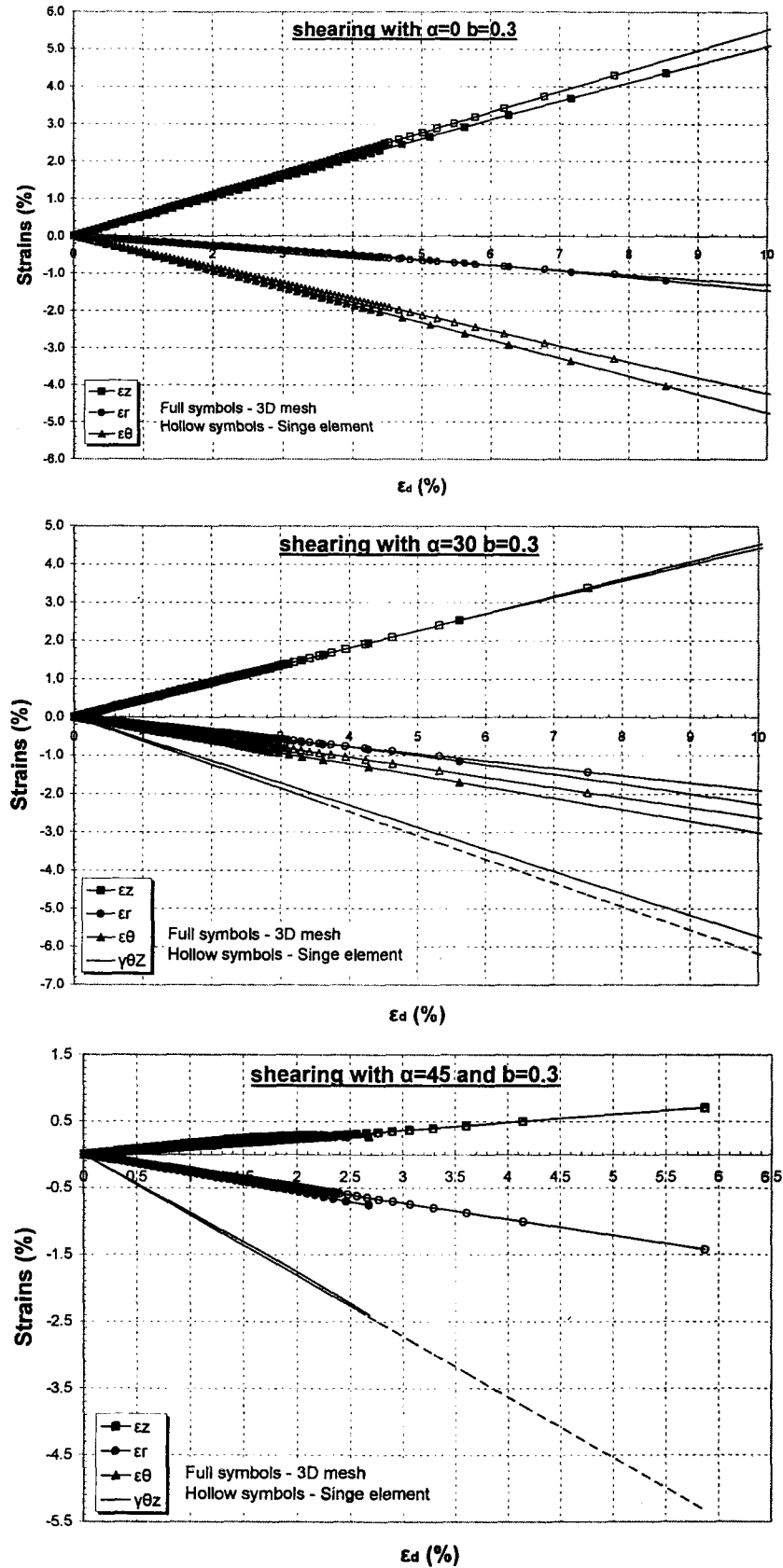


Figure 3.30: Effect of the non-uniformities on the strain development with  $b=0.3$  (Foundoukos 2006)

### 3. Test material, apparatus and procedures

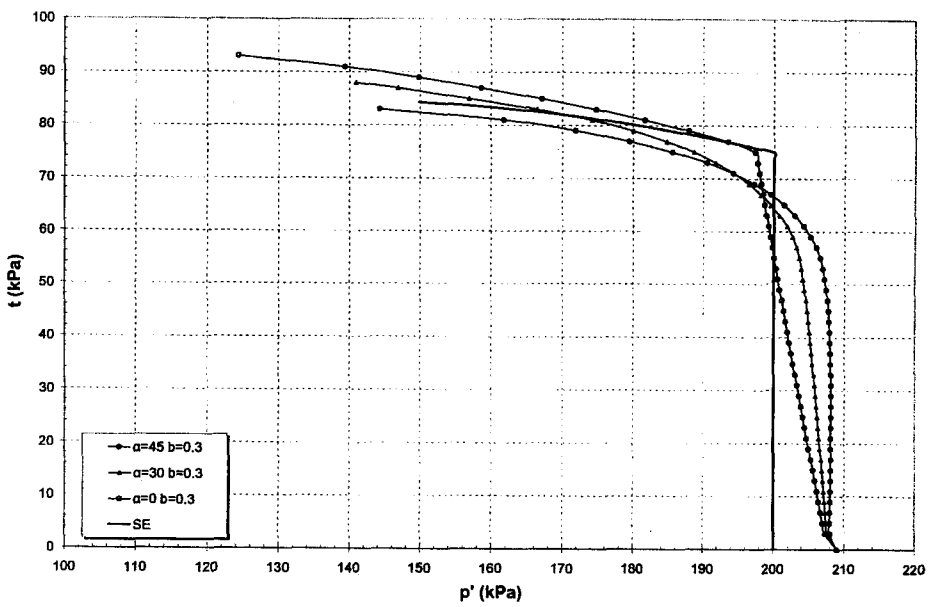


Figure 3.31: Effect of the non-uniformities on the effective stress paths with  $b=0.3$  (Foundoukos 2006)

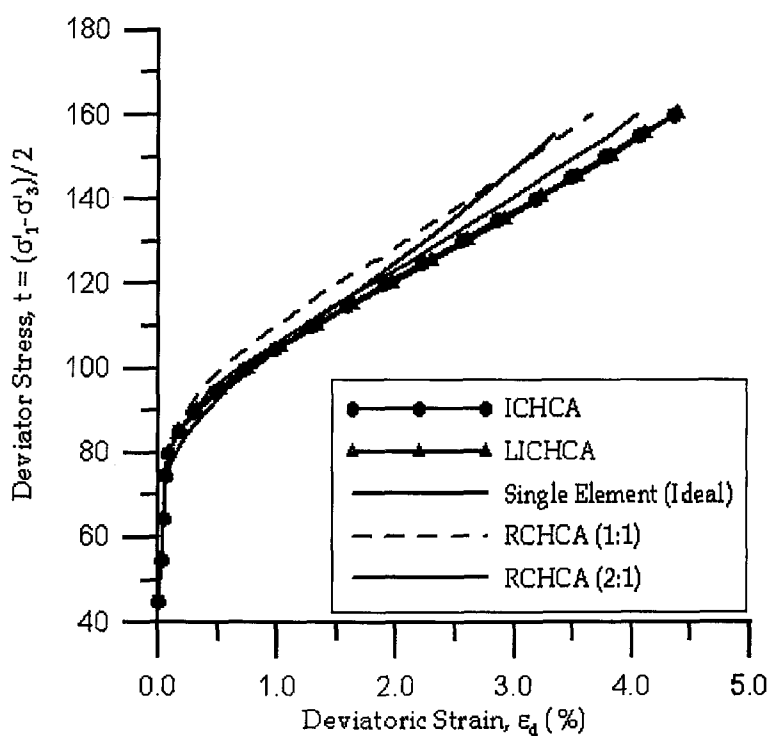


Figure 3.32: Effect of the non-uniformities on the effective stress paths with different sample geometries (modified after Zdravkovic & Potts 2005)

### 3. Test material, apparatus and procedures

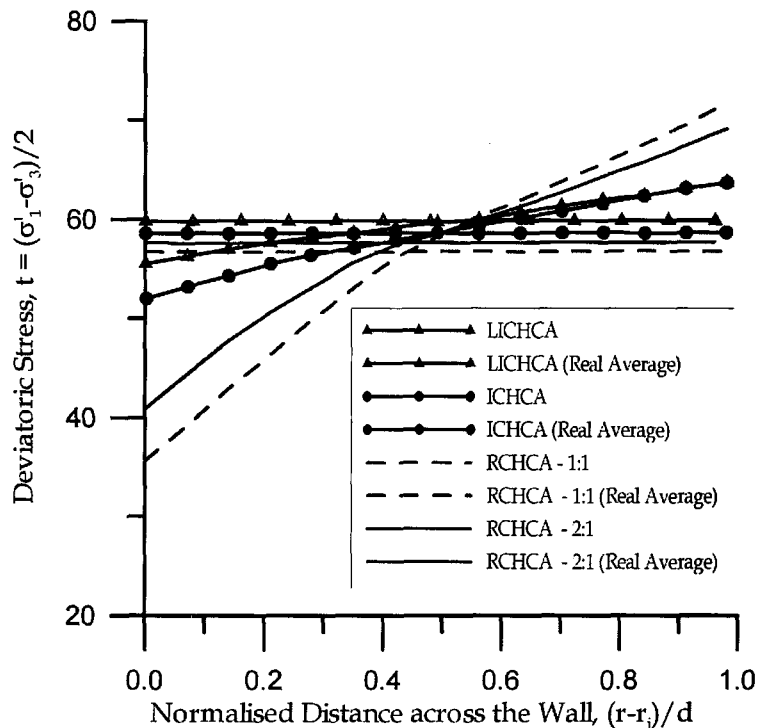


Figure 3.33: Distribution of stress across the sample wall with different sample geometries (modified after Zdravkovic & Potts 2005)

#### **3.4.3 Previous experimental results highlighting the effects of non-uniformities**

The number of previous and fully documented experimental studies where the presence of non-uniformities was studied is limited. Some of the conclusions that were derived from those small number of studies are described here.

Although the actual results and detailed experimental data were not published, Lade (1981) assessed the presence of non-uniformities in terms of the ratio  $\sigma_{\theta_{average}}/\sigma_{cell}$  for HCA tests on Monterrey No. 0 and Santa Monica Beach sands. Equal external and internal cell pressures were maintained in these tests. The HCA specimen had external and internal diameters of 22 cm and 18 cm respectively. For tests on loose samples of Monterrey No. 0 sand using a sample height of 5 cm he found that the stress ratio at failure was 1.8. This stress ratio was then compared with tests on Santa Monica Beach sand with the same external and internal radii, but using sample heights of 10 cm and 40 cm. The results are presented in Figure 3.34. These results clearly indicate that for the bigger sample sizes the effect of the presence of non-uniformities becomes negligible. Note that an assumption was required to

### 3. Test material, apparatus and procedures

produce this plot. It is assumed that for the sample of 40 cm height there is no end restraint effect on  $\sigma_\theta$  because the angle of shearing resistance ( $\phi'$ ) was comparable to the true triaxial case. By knowing the value of ( $\phi'$ ) and the stresses measured in the cases with sample height 5 and 10 cm, the stress ratio can be then calculated.

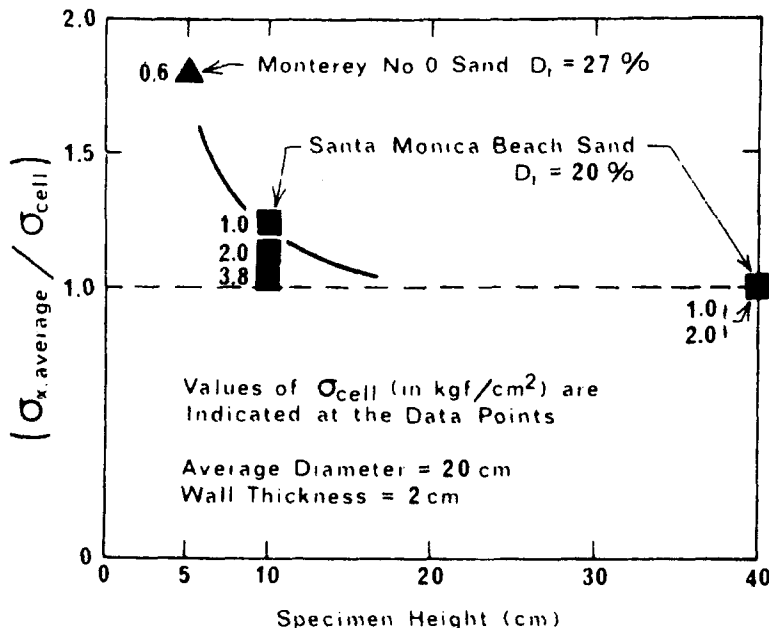


Figure 3.34: HCA experiments with samples of different height (Lade 1981)

A year later, Fukushima & Tatsuoka (1982) considered HCA tests on Toyoura sand with external radius 10 cm, internal radius 6 cm, and sample heights of 2 cm, 4 cm, 10 cm and 20 cm. While the data itself was not presented, some important findings were stated in this paper. The results indicated that the volumetric strains were unreasonably small for the smallest specimen. Fukushima & Tatsuoka (1982) also found that the angle of shearing resistance ( $\phi'$ ) increased with a decrease in sample height. These differences were attributed to the radial restraint at the bottom and top of the sample. Pradel et al. (1990) reported that the shear strength changed when tests on Toyoura sand was tested in a HCA with inner radius of 3 cm, outer radius of 5 cm and sample heights of 10 cm and 5 cm. But yet again, no data was presented to support this conclusion.

More recently Lade et al. (2008) presented HCA tests on Santa Monica Beach sand using a HCA with inner radius of 9 cm and outer radius of 11 cm with sample height of 25 and 40 cm in order to study shear band formation. Interestingly, although the paper mentions that there is no change in the shear strength with sample size, Figure 3.35 highlights that such a difference may exist. The boxes drawn surrounding

### 3. Test material, apparatus and procedures

---

data points indicate that the small samples ( $h = 25$  cm) produced higher angles of shearing resistance than the big samples ( $h = 40$  cm). Additionally, the tests with height of 40 cm seem to form an upper bound for the data using the HCA with height of 25 cm.

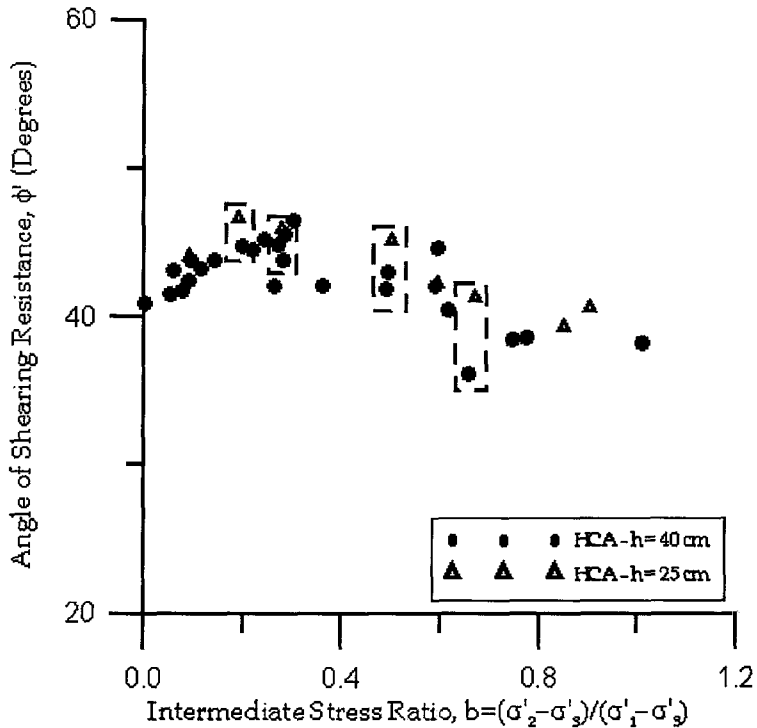


Figure 3.35: HCA experiments with samples of different height at similar  $b$  and  $\alpha$  values (modified after Lade et al. 2008)

The final experimental study considered here is the work of Kharchafi (1988). Khar-chafi (1988) tested fine Hostun sand in a HCA with the following dimensions: inner diameter 15 cm, outer diameter 18 cm and sample heights 9 cm and 18 cm. The results in terms of stress-strain curves are presented in Figure 3.36 and show tests for the two sample geometries under two conditions ( $b = 0.0$ ,  $\alpha = 0^\circ$  and  $b = 0.5$ ,  $\alpha = 45^\circ$ ). It is clear that for the case in which  $b = 0.0$  and  $\alpha = 0^\circ$  the response of the taller sample is weaker than that of the shorter one. The calculated angles of shearing resistance are  $35^\circ$  and  $37^\circ$  degrees for the big and small samples, respectively. In the second case, with  $b = 0.5$  and  $\alpha = 45^\circ$  the stress-strain response of both sample geometries was the same up to a point in which a shear plane was developed and the deviator stress started to decrease in the big sample. It is important to note, that in this study, the height/outer diameter (H/OD) ratio of the taller sample is 1.

Although the data presented in this section is limited, the experimental results broadly agree with the numerical analyses presented in the previous section. It is

3. Test material, apparatus and procedures

---

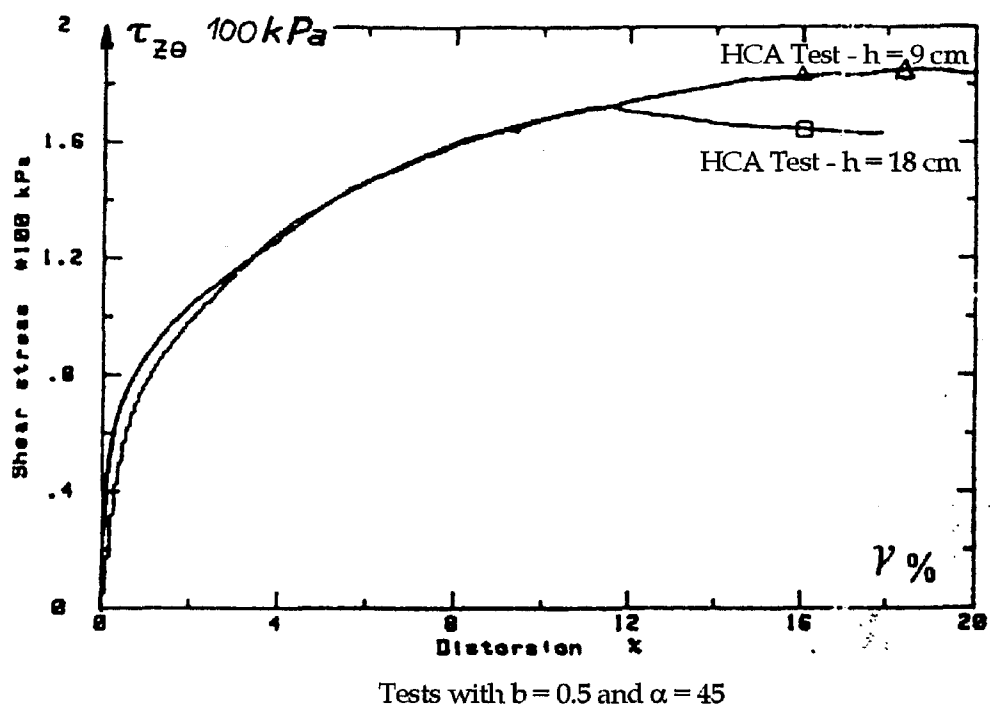
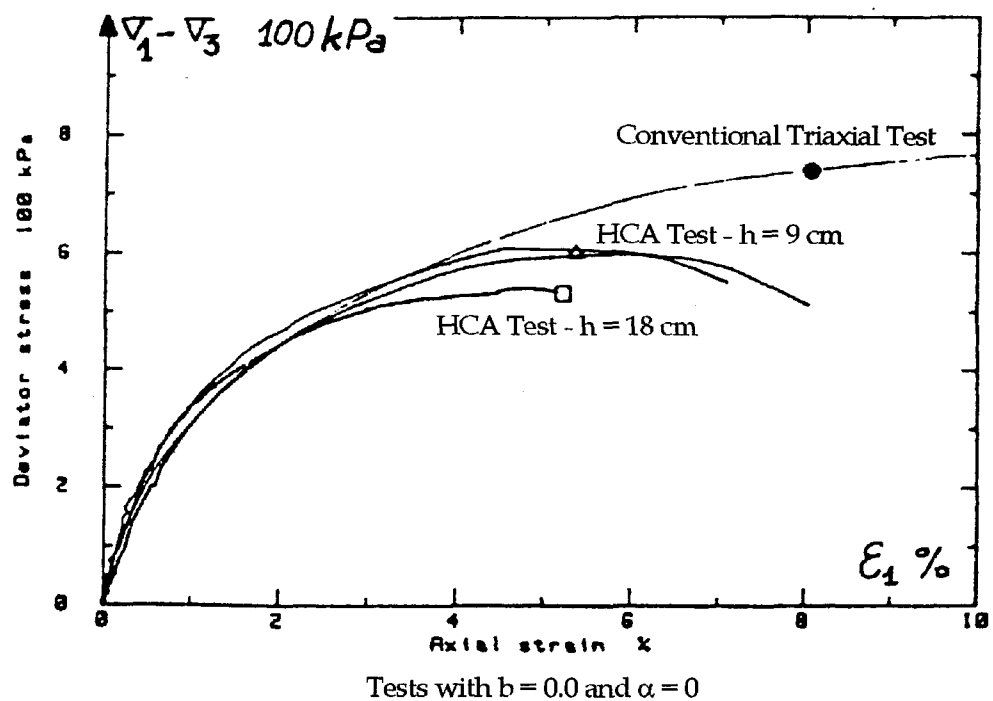


Figure 3.36: HCA experiments with samples of different height (modified after Khar-chafi 1988)

### 3. Test material, apparatus and procedures

---

clear that HCA samples with the same inner and outer radii, but with different height may give smaller shear strength for taller specimen heights.

## **3.5 Sample preparation and testing procedures**

All experimental tests described in this study were performed using reconstituted specimens of glass ballotini. It is well known that the sample preparation method affects the stress-strain response of granular materials. For example, tests on Toyoura sand performed by Miura & Toki (1982) showed that the strain stress relationship as well as the volumetric response during triaxial extension and compression was different for several sample preparation methods (see Figure 3.37). In this section a review of the methods for sample preparation used for tests on reconstituted granular materials is presented. Subsequently, the sample preparation methods used for the present study are described in detail.

Several experimental studies have been carried out to evaluate the effect of the preparation method on granular soil response (e.g. Okamoto & Fityus 2006, Vaid & Negussey 1988, Oda 1972a). Kuerbis & Vaid (1968) proposed the following criteria to assess the suitability of different techniques for preparation of reconstituted sand samples:

1. The method must be able to produce loose to dense samples in the density range expected within the soil deposit
2. The samples must have uniform void ratio throughout
3. The samples should be well mixed without particle segregation
4. The method should simulate the mode of soil deposition commonly found in the soil deposit being modeled.

The author would also add to the previous list that the preparation method must be repeatable.

Several sample preparation methods have been used in geotechnical laboratories. Each of these methods simulate a particular mode of deposition. Generally, the dry deposition method is considered suitable for modeling the natural deposition process of wind blown aeolian deposits, whereas the moist tamping method can model the

### 3. Test material, apparatus and procedures

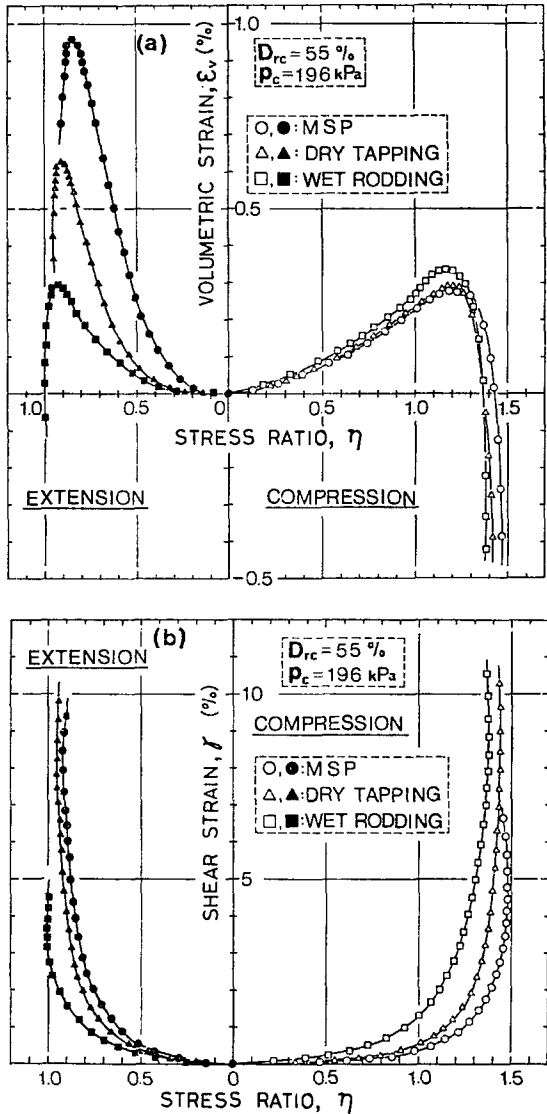


Figure 3.37: Effect of different sample preparation methods on soil response in the triaxial apparatus (Miura & Toki 1982)

soil fabric of rolled construction fills better, and has the advantage of preventing segregation of well graded materials. The water pluviation simulates deposition through water. The slurry deposition method, on the other hand, models hydraulic fill or fluvial deposition (Kuerbis & Vaid 1968).

In terms of uniformity of void ratio and relative densities, some methods give better results than others. Miura et al. (1984) showed that a high degree of uniformity may be achieved in air pluviated samples while tamped sand shows considerable non-uniformity. Furthermore, James (1967) showed, by using radiographic methods, that a mesh diffuser considerably improves the uniformity of dry sand prepared by pouring the sand through air. The major factors that affect relative density

### 3. Test material, apparatus and procedures

---

of air pluviated samples are height of particle drop (Vaid & Negussey 1988) and rate of deposition (Miura & Toki 1982). Okamoto & Fityus (2006) found that the higher densities achieved under slower rates of deposition are more repeatable. The pluviation method has many advantages over the vibration methods that are frequently used because it avoids particle crushing, and gives better repeatability (Lo Presti et al. 1992). The influence of segregation in the present study is not significant because the material used is very uniformly graded in terms of particle size.

Given the objective of this research, and the observations noted above, the most appropriate method of sample preparation chosen was the pluviation. Nevertheless, different types of tests were performed in this study. These include triaxial and hollow cylinder tests in saturated and dry specimens of glass ballotini. Even though pluviation was used, the preparation method used for the different kinds of equipment and moisture conditions (dry or saturated) involves minor changes that are detailed below.

#### **3.5.1 Sample preparation method for triaxial tests**

A preliminary investigation of the behaviour of glass ballotini was carried out using the triaxial stress path cell in both dry and saturated specimens in order to decide the ideal conditions for subsequent hollow cylinder testing. The methods of sample preparation used for both dry and saturated glass ballotini samples are described in this section. The differences between the two procedures are highlighted where necessary.

##### **Preliminary tasks**

Approximately 160 g of material were used in each triaxial test. Initially, the material was washed with distilled water using a sieve with a mesh opening smaller than the smallest particle size. The material was washed in order to remove dust and impurities produced in the manufacturing process or under prolonged storage. The clean material was then oven-dried over a period of 24 hours and its weight was then determined on a scale with a precision of  $\pm 0.01$  grams.

If the test was performed under dry conditions the porous stones to be used were also oven dried separately. Under saturated conditions, the cleaned material was

### 3. Test material, apparatus and procedures

then submerged under water and de-aired in a vacuum chamber with a pressure of -90 kPa for approximately 30 minutes. The soil sample was de-aired together with the porous stones that were previously boiled in water for 15 minutes.

Before starting the sample set-up, all the air/water interfaces were re-set and put in the adequate position for subsequent use. The loading ram and the CRSP were also adjusted to give the maximum possible axial displacement during shearing. If the tests were under saturated conditions, additional checks were performed to ensure that all the tubing corresponding to the cell pressure and back pressure lines were saturated during testing. Under dry conditions, moisture and humidity needed to be avoided. Consequently, for these tests, the back pressure line was isolated several days before testing and a reduced amount of air pressure was blown (not directly) through it prior to sample set-up. These procedures left the material and the equipment ready for sample set-up.

#### **Sample set-up**

Having prepared the material and the equipment for testing, the steps used to set up the sample are listed below. As before, the general procedure is described and when differences for dry and saturated samples arise, they are highlighted.

- A porous stone was placed on the sample pedestal.
- A latex membrane was stretched around the porous stone and pedestal to hold the sample using a pair of rubber O-rings.
- The sample mould was placed around the pedestal (surrounding the latex membrane) to form the shape and size of the sample. A 3-piece metal mould which forms a cylindrical 38 × 76 mm (diameter × height) sample was used.
- The latex membrane was stretched over the top of the mould and a suction of -20 kPa was used to hold the latex membrane against the mould.

The previous procedure left a cylindrical cavity where the material was deposited. The method of deposition varied according to the testing method (dry or saturated). The different procedures are described below:

- For saturated specimens the inner cylindrical cavity was filled with water after opening the back pressure line. The material was then slowly spooned

### 3. Test material, apparatus and procedures

---

ensuring the procedure was always performed under water to ease subsequent saturation.

- For dry specimens a funnel with a hose which has drawn marks with 1 cm spacing was deployed inside the cylindrical cavity. The material was then slowly spooned into the funnel. The spooning process was performed using an approximately similar (and very reduced) amount of material each time to ensure that an intended constant falling height was indeed kept constant.

Although the previous deposition methods were very consistent after significant practice, they provided different initial relative densities. In general, the dry preparation method produced higher densities than the wet method. To get a denser sample in the wet method, slight vibration of the mold at different and equally spaced intervals of the sample deposition was performed. This allowed to obtain dry and saturated samples with the same initial relative density, to be able to compare their results directly. The following procedures were then performed when the inner cylindrical cavity was filled to the desired height with the material.

- A porous stone was placed on top of the sample. On the porous stone a perspex platen was deployed and the latex membrane was carefully stretched over the sample, stone and platen using two rubber O-rings.
- The sample was then subjected to a suction of 30 kPa through the back pressure line to hold the sample. At this point the mould was removed and the dimensions of the sample were measured.
- The local radial and axial instrumentation was then deployed ensuring that its calibrated linear range could be used during most of the test.
- The perspex chamber was placed over the sample, fixed to the pedestal and filled with water.
- A cell pressure of 50 kPa was slowly applied to the sample, while simultaneously reducing the applied suction.

For saturated samples, full saturation was achieved by applying a back pressure of 400 kPa and a cell pressure of 450 kPa. These pressures were applied in increments of 50 kPa/hr, keeping a constant value of mean effective stress (= 50 kPa). In the case of dry samples, the back pressure line was then open to the atmosphere to keep

### 3. Test material, apparatus and procedures

---

a constant mean effective stress of 50 kPa. Note that by doing this the back pressure cannot be controlled as in saturated tests, however, it could always be monitored and the presence of leaks or humidity inside the sample were easily detected.

#### **3.5.2 Sample preparation method for hollow cylinder tests**

The results of a preliminary series of tests on triaxial specimens under dry and saturated conditions helped to conclude that the hollow cylinder tests should be performed under dry conditions. The results of these preliminary tests are described in Chapter 4. In this section the sample preparation procedures for hollow cylinder tests are described. In contrast to the triaxial tests there is no difference in the procedures due to testing conditions, but there are differences due to the two different sample dimensions used (ICHCA and LICHCA). As above, the general procedure is described and differences highlighted when necessary.

##### **Preliminary tasks**

The duration of sample set-up in the hollow cylinder apparatus, including all the preliminary tasks described below could take more than 2 days, while only 2-3 hours were needed for each triaxial test. Consequently, additional measures were taken before each test to ensure the lack of leaks both in the apparatus and in the latex membranes used. As in the triaxial tests, the material and porous stones were prepared washing them with water and in a sieve, but using approximate amounts of 9 kg for the ICHCA and 18 kg for the LICHCA. After the material was cleaned, it was oven-dried during a period of 24 hours. The apparatus was also filled with water and the zero readings of the load cell were written down previous to sample set-up.

In order to avoid leaks in the outer and inner membranes, the presence of holes, imperfections or weak zones were visually inspected before set-up. Each membrane was stretched manually against a bright background. This allowed to identify holes or any other imperfection that could produce a leak during testing. Leaks needed to be avoided at all costs, not only due to the time required for set-up but also to keep the material under dry conditions during the whole test. In the case that such imperfection or failure was found during inspection, the following tasks were performed:

### 3. Test material, apparatus and procedures

---

- The area under consideration was cleaned using butanone and allowed to dry.
- The cleaned area was covered with a thin layer of liquid latex that was then allowed to dry.
- The dried liquid latex layer produced a sticky surface that could adhere to the material or the sample preparation moulds. Therefore, talcum powder was used to cover this area after the liquid latex was dried.
- The same procedure was followed on the other side of the membrane to ensure that the imperfection was fully reinforced and/or covered.

Having checked the membrane, additional tasks had to be performed prior to sample set-up. These tasks are listed below:

- A set of vertical and horizontal grid lines (with a separation of 2.5 cm) were drawn on the outer membrane to illustrate the specimen deformation mode during subsequent shearing. These grid lines were also very useful for identifying the deformation patterns of each sample.
- All the surfaces of the hollow cylinder apparatus were rigorously cleaned using butanone and a piece of cotton. Air pressure was used to remove dust that could interfere with the numerous O-rings and generate leaks during the tests.
- All the O-rings were cleaned using a clean damp cloth and soap. The excess of soap was then removed using a different damp cloth.
- All the surfaces of the local instrumentation that needed to be in contact with the sample were cleaned using sand paper to remove super-glue applied in the previous test.
- Six aluminium foil targets of dimension  $8 \times 8$  cm were cut to be used in conjunction with the proximity transducers.

Finally, the perspex chamber and loading system were raised to the upper limits of the crosshead frame. This allowed maximum available space during sample set-up.

### 3. Test material, apparatus and procedures

---

#### **Sample set-up**

When the material was ready and the previous tasks were finished, the following steps were applied in order. Once again, differences between the ICHCA and LICHCA set-up procedures will be highlighted.

- Silicon grease was used to lubricate the small O-ring that seals the inner latex membrane.
- The inner membrane was then positioned in the inverted lip of the base platen including the bottom porous stone and sealed tightly against the O-ring mentioned in the previous step.
- The rubber O-rings that isolate the sample from the inner and outer chamber were lubricated and deployed in the base pedestal.
- The base platen, complete with membrane was then transferred to the base pedestal of the apparatus. The appropriate alignment of this platen was verified by marks that were previously carved in both the base plate and pedestal.
- The outer latex membrane was stretched over the base platen and fixed using three O-rings.

The deployment of the inner and outer moulds differs for the ICHCA and the LICHCA. In the case of the ICHCA two sets of wooden moulds were used internally and externally. In the LICHCA two perspex extensions and the wooden mould of the ICHCA were used internally, while a aluminium outer mould was used. The procedures for both apparatuses are described below.

In the ICHCA:

- The outer mould system, which consists of three wooden segments joined together by six tapered pins (see Figure 3.38), was positioned on the pedestal surrounding the outer membrane.
- The outer membrane was then stretched over the top of the moulds. This membrane was held in place and the outer mould was covered using pieces of recycled membrane.
- Suction was then applied to the mould in order to hold the membrane against the mould. A single vacuum pressure application point was used in this mould.

### 3. Test material, apparatus and procedures

- The inner mould was positioned in the apparatus so that it was perpendicular to the base plate and concentric with the porous stone. It was then covered with the inner membrane, the bottom of which was fixed to the base pedestal. The inner mould was set-up from the top of the inner membrane and was supported by a metallic ring attached to the base pedestal.
- The mould was then expanded as desired, using the conical taper shown in Figure 3.39.
- Additional PVC extensions to the inner and outer mould were then added to provide an adequate pluviation height without loosing any material.

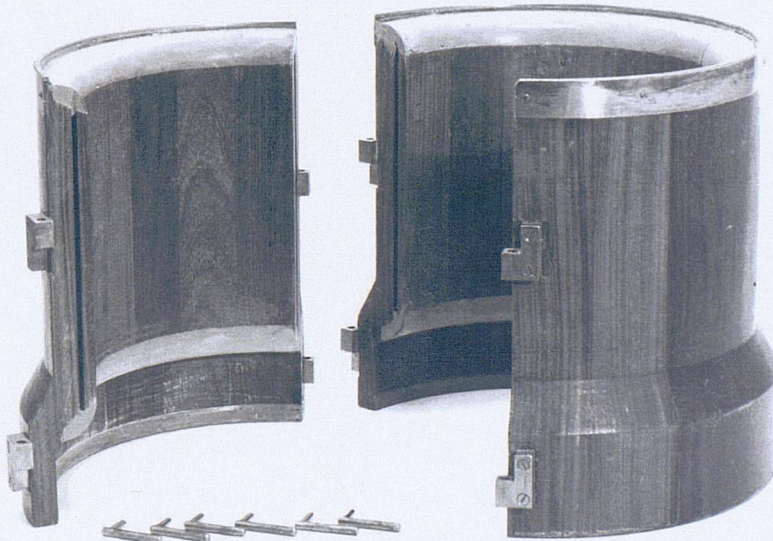


Figure 3.38: Outer mould for sample preparation in the ICHCA

In the LICHCA:

- The outer mould system consists of three aluminium segments joined together by six clamps. It was positioned on the pedestal surrounding the outer membrane as in the ICHCA.

### 3. Test material, apparatus and procedures

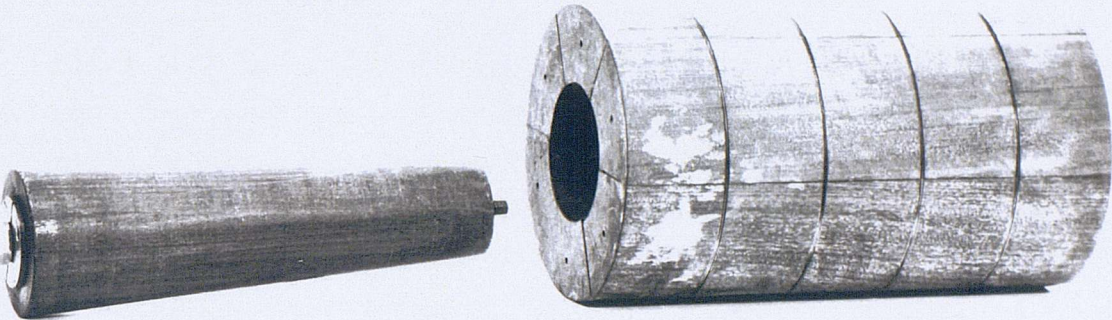


Figure 3.39: Inner mould for sample preparation in the ICHCA

- The outer membrane was then stretched over the top of the moulds. This membrane was held in place and the outer mould was covered using pieces of recycled membrane.
- Suction was then applied to the mould. In order to hold the membrane against the mould a pressure of 30 kPa was provided through the five vacuum pressure points.
- The inner wooden mould used for the ICHCA tests was positioned in the apparatus so that it was perpendicular to the base plate and concentric with the porous stone. It was then covered with the inner membrane, the bottom of which was fixed to the base pedestal. The inner mould was set-up from the top of the inner membrane and was supported by a metallic ring attached to the base pedestal.
- The mould was then expanded as desired, using the conical taper shown in Figure 3.39.
- As the height of the LICHCA is the double the height of the ICHCA, the two perspex extensions were added through the top of the inner membrane. Chalk was previously added to their surface to ease their removal after sample pluviation.
- Additional PVC extensions to the inner and outer mould were then added to provide an adequate pluviation height without losing any material.

### 3. Test material, apparatus and procedures

---

The previous procedures established an annular cavity between two latex membranes where the material was deposited using the following procedures:

- The pluviating device was deployed on top of the inner mould extension. A funnel and a pipe with a siphon tube were attached to a frame to pluviate the sample. An “earth” cable was connected to this frame to reduce electrostatic forces within particles. This avoided excessive bouncing of the particles as well as adherence of material to the surfaces of the siphon tube. A baffle board fixed at the end of the siphon tube of 15 mm diameter ensured that a concentrated jet of ballotini did not disturb the existing ballotini surface, and that the grains would gently rain downwards on an individual basis. This baffle also contributed with the role intended for mesh diffusers as discussed in Section 3.5. Figure 3.40 illustrates the different parts described here.
- In this way small amounts (approximately 80 g) of material were successively rained into the funnel. The frame was used to rotate the funnel and pipe around the annular cavity.
- In order that the sand grains should consistently fall from the same height the frame allows the siphon tube to be simultaneously rotated and raised. Note that in the LICHCA an extension pipe was added to this siphon because the frame has the same height of the ICHCA (25 cm).

As discussed in Section 3.5, the density of the resulting sample is primarily controlled by the fall height and the rate of discharge which in turn is governed by the diameter of the siphon and the length of the siphon. The faster the rate of discharge, the looser the resulting sample. To ensure repeatable results, it was essential to maintain the same fall height level when pluviating the sand. Uniform samples of repeatable initial densities were consistently obtained using this method only after six to eight weeks of continuous practice before starting the actual tests. The uniformity of the void ratio across the sample height were checked visually. Non-uniformities were normally clearly observed when they occurred due to membrane penetration. However, this issue was also checked by performing a grain size distribution analysis at three different heights using an optical microscope with software capable to perform segmentation analyses as discussed in Section 3.2. A picture of the sample during preparation is illustrated in Figure 3.41

After finishing the sample pluviation the following procedures were carried out:

### 3. Test material, apparatus and procedures

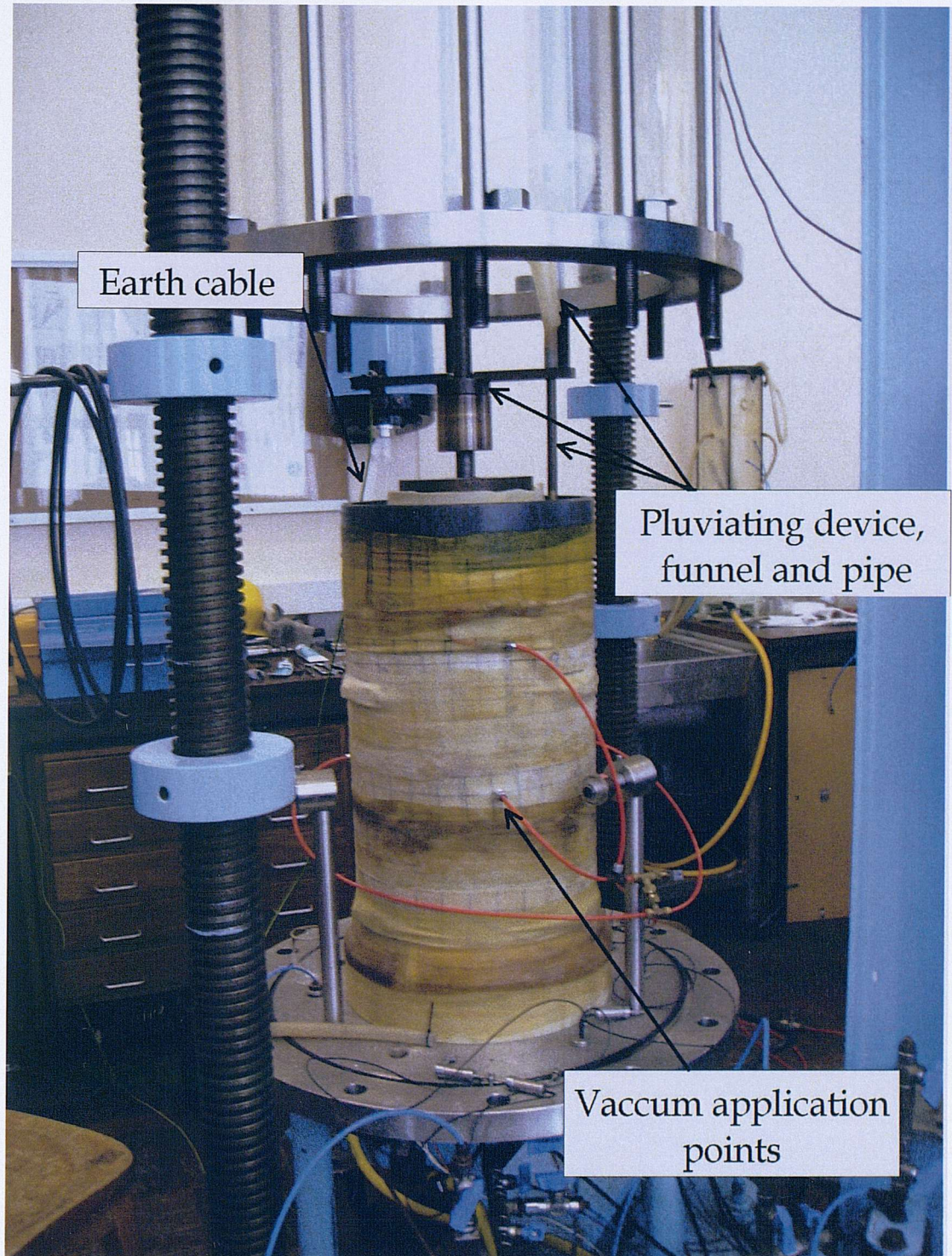


Figure 3.40: Pluviation system for the preparation of samples in the LICHCA

### 3. Test material, apparatus and procedures



Figure 3.41: Detail of pluviated ballotini during the sample preparation process in the LICHCA

### 3. Test material, apparatus and procedures

---

- The inner and outer membranes were sealed using the top porous stone and three O-rings. At this point, a suction of 50 kPa was applied to the top-cap of the sample.
- When the suction was fully developed and remained stable, the moulds were removed. The inner mould (and extensions in the LICHCA) were removed first. The inner extensions were removed by unscrewing slightly the rotating bolt that expands the extension, allowing the removal of the brass piece, consequently the perspex mould collapses, contracts and becomes easily removed. The inner wooden mould was extracted by releasing the conical taper which causes the six segments to contract.
- The outer mould was removed by undoing the tapered pins or clamps and separating the three segments. The sample was at this stage entirely supported by suction and as mentioned before, the presence of non-uniformities in void ratio could be easily checked.
- The sample dimensions were then measured accurately. A profiling adjustable device was used to determine the outer radii at different heights at four positions around the circumference of the sample. The inner dimensions were obtained using a specially developed adjustable probe. The ends of the probe are spherical in shape in order to avoid perforation of the membrane. The probe can be extended until contact is made in opposite diameters of the inner wall, whereupon the arm was locked and the length measured using a vernier micrometer. The sample height was measured using a high precision measuring tape along different circumferential positions.
- After the sample dimensions were taken, three foil targets were deployed on the inner membrane where the inner proximity transducers had to be set-up.
- The base plate of the inner chamber was then set-up in the apparatus, raised and positioned. The raise of this base plate brings the inner proximity transducer into position. The inner cell was then filled with water. Note that in the LICHCA an extension for the base of the proximity transducers needed to be added to the base plate.
- The inner cell was then isolated using a stainless steel top-platen. This platen includes three pots used to join the sample to the rest of the apparatus.
- With the inner chamber filled with water the local instrumentation was attached to the outer surface of the sample. Care was taken to have the linear

### 3. Test material, apparatus and procedures

range of the transducers for the longest possible time and also to locate the instrumentation on opposite sides for ease of analysis of the experimental data.

At this stage (Figure 3.42), the sample was ready to be connected to the rest of the apparatus and the perspex chamber had to be closed and filled with water. Three threaded studs protrude from the bottom of the load cell. The load cell is gently lowered so that these studs gradually become submerged in the resin which is contained in the three pots attached to the sample top-plate. When the resin has set a high strength junction exists between the sample and the apparatus. This junction is capable of transmitting torsional, compressive and tensile forces to the sample. The next procedures had to be followed in order to do that connection:

- About 90 g of resin were mixed with a catalyst to control the speed of hardening. If 1% by weight was added to the resin a period of 40 minutes elapses before the onset of hardening. This gave enough time to perform the tasks described below.
- After the resin was poured into the pots, the loading frame and perspex chamber were lowered into position. This allows the studs protruding from the load cell to be carefully inserted into the resin pots. The vertical movement of the loading frame was restricted from the top of the perspex chamber once the studs were in the appropriate position.
- The zero positions of the load cell had to be read well before the resin set. As the resin hardens, it gets warmer and expands, affecting the readings.
- The twelve nuts joining the outer cell to the base plate were tightened.
- When the resin was fully hardened (after approximately 1.5 hours), the condition of zero movement of the load cell was then relaxed and a condition of zero axial force was imposed.
- Now the outer cell was filled with water, and the inner and outer cell pressures were allowed to equalise.
- At this stage the suction that held the sample in place was gradually reduced with the simultaneous increment of the inner and outer cell pressures.
- When the inner and outer cell pressures were equal to 50 kPa the suction was completely disconnected from the back pressure line and the back pressure valve was open to atmospheric pressure. This brought the samples to a constant mean effective stress of 50 kPa.

### 3. Test material, apparatus and procedures

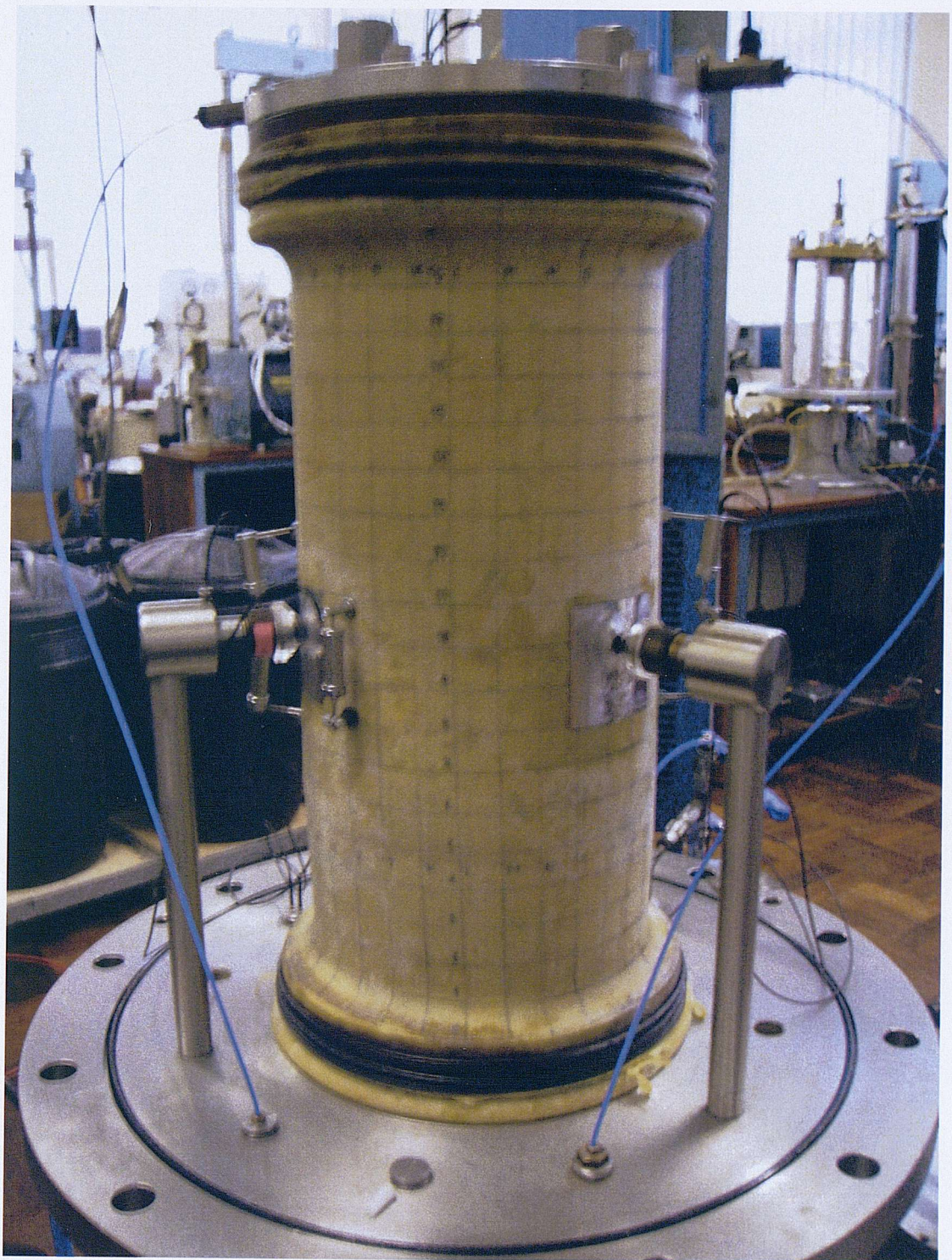


Figure 3.42: LICHCA sample previous to top platen connection

### 3. Test material, apparatus and procedures

At this point the sample dimensions and other parameters could be input into the software and the test was started. As in the triaxial tests, drained stress paths were followed without controlling the pore (back) pressure but measuring it during the whole duration of the test.

#### **3.5.3 Testing procedures**

All triaxial tests were isotropically consolidated to a mean effective stress of 200 kPa and sheared under drained conditions from the final consolidation state. The drained stress paths were followed at a controlled and constant rate of axial strain applied by a CRSP. Further details about the stress paths and calculations to obtain stresses and strains are described in Chapter 4.

HCA tests on the other hand, were  $K_0$  consolidated, with the value of  $K_0$  determined from triaxial tests with local axial and radial instrumentation in which the radial deformation was equal to zero. In the HCA tests the radial deformation was not controlled but it was directly measured. Results presented in Chapter 4 confirm the validity of the chosen  $K_0$  value. These tests were performed under  $K_0$  with the aim of highlighting the effects of stress and strain non-uniformities.

All HCA tests were sheared under strain control as in the triaxial tests. Further details of the stress paths followed are presented in Chapter 4.

## **3.6 Summary**

This chapter presented the test material, the apparatus for physical experiments, the effects of stress and strain non-uniformities in HCA tests, and the test procedures.

Section 3.2 described the test material. The bulk properties of the material were characterised using standard soil mechanics procedures. Newer techniques, including microscopy, were used to describe the material at the particle scale.

Section 3.3 presented the equipment used in this thesis. The methods for stress and strain calculation were discussed in detail. The instrumentation used for the measurement of stress and strain was described. The last part of the section presented the changes that were necessary to perform HCA tests with a H/OD ratio of 2 to diminish the effect of stress and strain non-uniformities.

### 3. Test material, apparatus and procedures

---

Stress and strain non-uniformities are discussed in Section 3.4. It was shown with previous numerical analyses that these non-uniformities depend on sample geometry, boundary conditions, load application and the constitutive law of the material. Furthermore, the previous numerical research provided the optimum sample geometry for the LICHCA (outer diameter: 25 cm, inner diameter: 20 cm and height: 50 cm) and indicated the worst case in terms of presence of non-uniformities ( $\alpha = 0^\circ$  and  $b = 0.5$ ). The numerical research presented was performed using finite element analyses. This highlights the potential benefits of performing DEM simulations to understand the particle scale interactions giving origin to these non-uniformities. Limited experimental research on the effect of the non-uniformities was also presented in this section. These limited experimental results indicated that for a variety of granular materials, HCA tests with equal inner and outer radii but different heights provided weaker strengths when taller sample heights were used.

Section 3.5 described the sample preparation methods and testing procedures for all tests presented in this thesis. A consistent method for the preparation of reconstituted granular soils for both dry and saturated conditions, as well as for different sample geometries was described in detail.

# Chapter 4

## Experimental results

### 4.1 Introduction

This chapter presents the experimental results that serve as the framework of comparison for the DEM simulations presented in Chapters 6 and 7. Both triaxial tests as well as hollow cylinder tests performed with different sample sizes are described.

The triaxial tests were part of a preliminary test series to determine the testing conditions for the subsequent hollow cylinder tests. Together with the HCA tests, and the DEM simulations in Chapters 6 and 7, they also provide understanding of the effects of the particle size and size distribution on soil behaviour.

The HCA tests explore the effects of the principal stress orientation and the intermediate stress ratio on the behaviour of glass ballotini. Tests using two sample geometries are presented to highlight, from an experimental perspective, the effects of stress and strain non-uniformities present in hollow cylinder testing.

### 4.2 Triaxial tests

In this section results from a series of drained triaxial tests on glass ballotini are presented. These tests were performed in the triaxial stress path cell described in Section 3.3.1. The tests were carried out to provide basic information on the behaviour of glass ballotini and to decide upon the testing conditions for the hollow cylinder tests presented in Section 4.3.

#### 4. Experimental results

---

Test ID	Particle size	Testing condition	Initial void ratio ( $e_0$ )	Purpose
TX-S-W-1	Small	Saturated	0.601	Size and condition effect
TX-B-W-2	Big	Saturated	0.601	Size and condition effect
TX-S-D-3	Small	Dry	0.598	Size and condition effect
TX-S-D-3R	Small	Dry	0.598	Experimental repeatability
TX-B-D-4	Big	Dry	0.598	Size and condition effect
TX-M-W-5	Medium	Saturated	0.618	Volume change calculations
TX-M-D-6	Medium	Dry	0.598	$K_0$ determination

Table 4.1: Triaxial stress path cell testing programme

The triaxial test series included tests performed on isotropically consolidated samples of “small”, “medium” and “big” size ballotini (see Table 3.2). The mean diameter of these sizes correspond to 0.6, 1.1 and 2.5 mm, respectively. A confining pressure of 200 kPa was used for all tests. Additional tests were performed using medium size ballotini in order to determine the value of  $K_0$  to be used in the hollow cylinder tests. The summary of triaxial tests performed for this thesis is presented in Table 4.1.

In Table 4.1 tests are identified by a consistent coding system that is used to reference all the tests presented in this thesis. The test ID is divided in four descriptors separated by hyphens. The first part tells the type of test performed (TX=Triaxial, IC=ICHCA, LIC=LICHCA), the second identifier indicates the particle size used (S=Small, M=Medium, B=Big), the third item describes the testing condition (W=Saturated, D=Dry) and the last one is the test number.

After set-up and saturation as described in Chapter 3, the first five tests listed in Table 4.1 were isotropically consolidated to a mean effective stress of 200 kPa. A constant pore (back) pressure of 400 kPa was used in the saturated tests, while atmospheric pressure (0 kPa) was used for the dry tests. This consolidation stage was performed using stress increments of 25 kPa/hr. This ensured that there was no increase in pore water pressure during consolidation. After consolidation the samples were allowed to creep, usually overnight. This gave enough time (at least 4 hours) to get stable volumetric strain readings at the end of each creep period.

In Sections 4.2.1 and 4.2.2 tests TX-S-W-1, TX-B-W-2, TX-S-D-3 and TX-B-D-4 are compared in terms of the testing conditions (saturated or dry) and grain size distribution effects. Test TX-M-W-5 was performed to compare volumetric strain calculation using local instrumentation, with strains calculated using volume gauge measurements. Results for this analysis are given in Section 4.2.1. The measurement

## 4. Experimental results

of the  $K_0$  coefficient (test TX-M-D-6), is summarized in Section 4.2.3. Test TX-S-D-3R is a test with exact conditions to test TX-S-D-3 carried out in order to verify experimental repeatability.

### **4.2.1 The effect of the testing conditions on the behaviour of glass ballotini**

The effect of the testing conditions on the behaviour of glass ballotini was assessed using triaxial testing of samples under dry and saturated conditions. The effects of the test conditions on shear strength and development of volumetric strains are discussed below. However, rather surprisingly, the test conditions also influenced the extent of the observed stick-slip behaviour as also detailed in this section.

#### **Interpretation of test results**

Referring to Figure 4.1 it can be seen that the stress-strain curves are represented in terms of the deviatoric stress ( $t$ ) and deviatoric strain ( $\epsilon_d$ ) calculated with the equations given below:

$$t = \frac{\sigma'_1 - \sigma'_3}{2} \quad (4.1)$$

$$\epsilon_d = \frac{2}{\sqrt{6}} \sqrt{(\Delta\epsilon_1 - \Delta\epsilon_2)^2 + (\Delta\epsilon_2 - \Delta\epsilon_3)^2 + (\Delta\epsilon_1 - \Delta\epsilon_3)^2} \quad (4.2)$$

All stress-strain curves presented in this chapter use the same definitions. The use of these equations enables comparison of the triaxial and HCA tests in the deviatoric plane and also correlating the results to those found in the literature. For both triaxial and HCA tests the octahedral stiffness,  $G_{oct}$  is used for all the analyses.

$$G_{oct} = \frac{\Delta J}{\epsilon_d} \quad (4.3)$$

where  $J$  is calculated using Equation 2.5 which was presented in Section 2.14. The deviatoric strain,  $\epsilon_d$  is calculated as above.

### Stick-slip behaviour

Figure 4.1 shows the stress-strain response for tests TX-S-W-1 and TX-B-D-4. These two tests were performed on samples of different particle sizes, in addition different testing conditions. However, they are the best example to contrast and highlight the observed existence of stick-slip behaviour in the saturated tests. Note, however, that in some dry tests the stick-slip behaviour was also found.

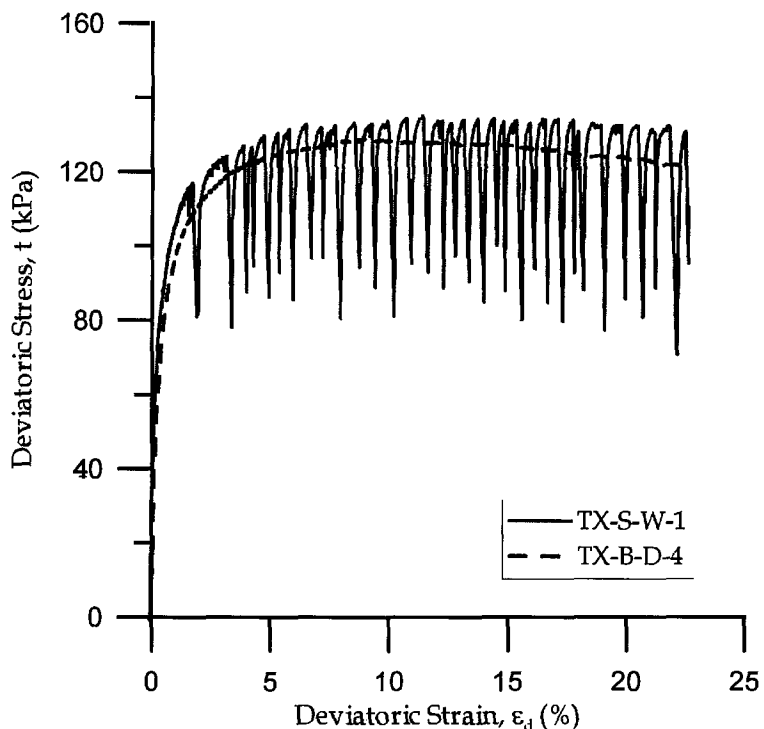


Figure 4.1: Experimental evidence of stick-slip behaviour on sample in saturated tests on glass ballotini

An early study by Haruyama (1969) reported the existence of stick-slip behaviour in triaxial compression tests on steel spheres. As it can be seen for tests TX-S-W-1 in Figure 4.1, stick-slip is characterised by a sudden drop in the deviatoric stress which is gradually recovered as the deviatoric strain increases. This cycle is repeated successively. This abnormal behaviour, nevertheless, does not change the analysis of experimental results. As proposed by Haruyama (1969), the standard interpretation of such stress-strain response is to adopt the maximum envelope of the stress-strain curve including the stick-slip behaviour.

The study by Haruyama (1969) postulated that the stick-slip behaviour was dependent on the surface roughness of the steel spheres and also on the confining

#### 4. Experimental results

---

stress. Experimental studies performed at Imperial College subsequent to the preliminary study by the author confirmed this dependance of the stick-slip behaviour of glass ballotini on the surface roughness of the particles (Cavarretta 2009, Wu 2008, Kwan 2007). The studies by Cavarretta (2009), Wu (2008) and Kwan (2007) also confirmed the observations by Haruyama (1969), stating that the stick-slip behaviour was present in all dry and saturated samples. Additionally, they highlighted that stick-slip was more evident on dry samples. These recent experimental results from Imperial College contrast the experiments by Adjemian & Evesque (2004) who stated that stick-slip was present only in dry tests.

The presence of stick-slip behaviour was one of the factors that contributed to the decision to perform the HCA tests under dry conditions, as described in Section 4.3. It is hoped that the experiments performed in this research provide further insight into this issue.

#### **Stress-strain and stiffness behaviour**

The effect of testing conditions on the strength of glass ballotini was assessed by comparison of tests TX-S-W-1 and TX-B-W-2 (saturated samples) with tests TX-S-D-3 and TX-B-D-4 (dry samples). These four tests had an almost identical initial void ratio as it is shown in Table 4.1.

Figure 4.2 shows the results of these four tests in terms of their stress-strain relationship and Figure 4.3 demonstrates the results in terms of the stiffness degradation curves. In these figures, gray is used for saturated tests, black for dry tests, empty circles for tests on big size ballotini, and filled circles for tests on small size ballotini.

Referring to Figure 4.2, it can be seen that the saturated samples (gray) give a mobilised angle of shear resistance that is slightly higher than the resistance for the dry tests. Note that some tests finished at a deviatoric strain lower than the others. This is due to difficulties encountered in deploying the radial strain belt, which as a result produced a lack of range in the radial strain belt movement. Consequently, the tests were stopped at the point when radial local instrumentation started to contact with the axial instrumentation or the sample itself (due to bulging). In addition to these comments, it can be seen that test TX-S-D-3R shows a repeatable behaviour in comparison to test TX-S-D-3 which was performed under identical testing conditions and initial void ratio for particles with the same grain size distribution.

The evolution of shear stiffness illustrated in Figure 4.3 also shows that the response

#### 4. Experimental results

---

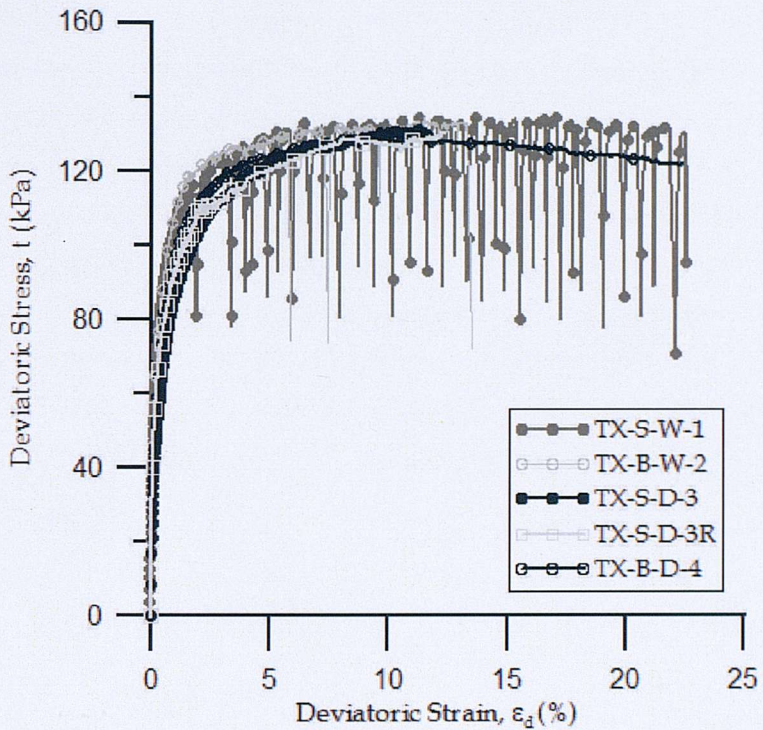


Figure 4.2: The behaviour of glass ballotini under triaxial conditions - Testing conditions and particle size effects on stress-strain behaviour

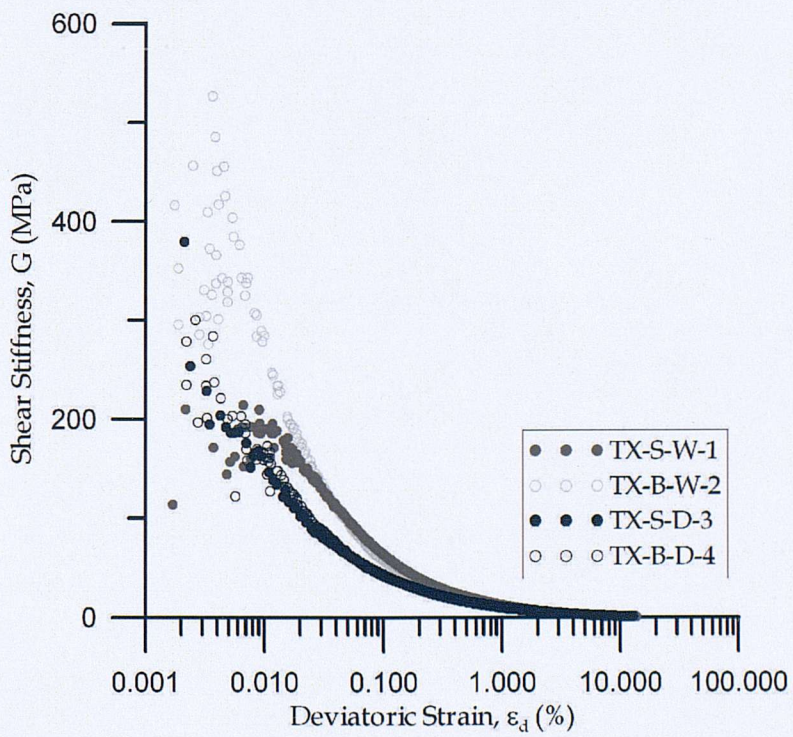


Figure 4.3: The behaviour of glass ballotini under triaxial conditions - Testing conditions and particle size effects on shear stiffness

#### 4. Experimental results

of the saturated samples is moderately stiffer than the dry samples. These results imply that the shear strength is dependent on the coefficient of inter-particle friction. This is a consequence of the change of inter-particle friction depending on the condition of the particles. Experimental measurements of inter-particle friction performed by Cavarretta (2009) under dry conditions friction differ to those measured under submerged conditions. The dependence of the shear strength on the angle of inter-particle friction is a topic that remains controversial. Skinner (1974) performed direct shear box experiments coupled with the measurement of the inter-particle friction of different materials. He concluded that the angle of shearing resistance was independent of the coefficient of inter-particle friction (see Figure 4.4).

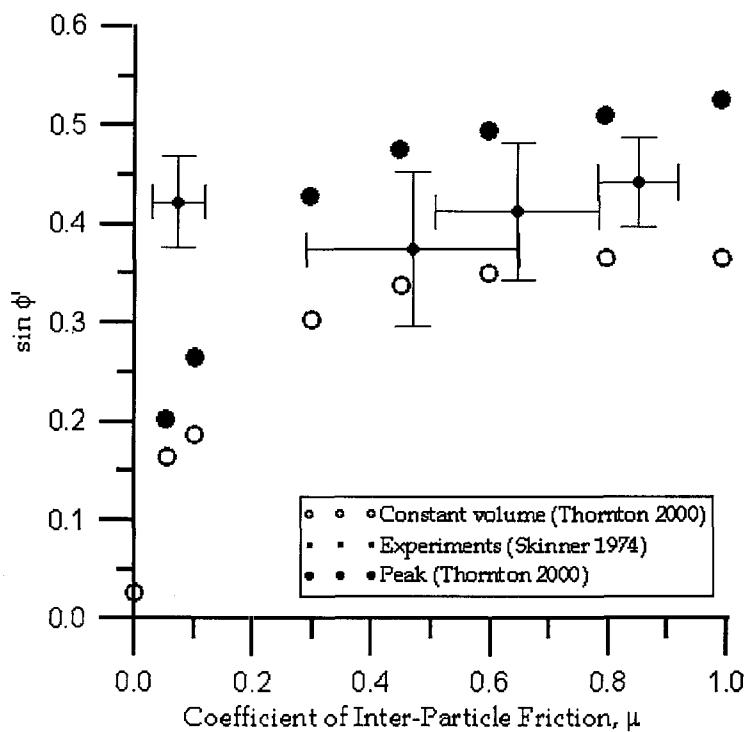


Figure 4.4: The influence of the coefficient of inter-particle friction on the shearing resistance of granular materials (Thornton 2000)

Clearly, the most recent experimental evidence presented in this thesis disagrees with the evidence presented by Skinner (1974). On the other hand, these results agree with more recent triaxial tests performed by Kwan (2007) and Cavarretta (2009), and also with the trends shown by many DEM studies such as the one by Thornton (2000) which is also illustrated in Figure 4.4.

### Volumetric response

When testing samples under dry conditions there is a lack of volume gauge measurements. Hence, the volumetric strains have to be determined using local instrumentation. All the triaxial tests presented here had local radial and axial instrumentation deployed on the middle of the sample. The volumetric changes are then calculated using the longitudinal changes measured by axial electro-level devices, and the diameter changes monitored by the radial strain belt. These calculations require assumptions to be made and consequently, the analysis are somewhat subjective.

The lack of accurate volumetric strain data for dry tests might seem to preclude their use. However, the tests presented in this thesis were performed for comparison with numerical simulations using DEM. The coefficient of inter-particle friction is a very important input parameter in DEM simulations, and the sensitivity of the DEM results to this input value is significant (see Figure 4.4). The experimental measurement of this coefficient is easier under dry conditions. Furthermore, as pointed out Cavarretta (2009), the measurement under wet conditions of inter-particle friction is difficult, and requires extra care as it is also affected by the moisture conditions of the surrounding environment. Additionally, other researchers have found an influence of the fluid contamination on the inter-particle friction measurements. For this reason, the possibility of testing under dry conditions had to be considered.

Triaxial test TX-M-W-5 was a test performed under saturated conditions, using medium size ballotini. This test was used to compare directly the volume gauge measurements with volumetric strain changes calculated from the local instrumentation. Figure 4.5 illustrates how different the volumetric strains can be depending on the initial assumption that is made about the mode of deformation.

Considering Figure 4.5, all the assumptions agree initially, at small level of deviatoric strain (up to 0.5%). As the local radial strain belt measures changes of diameter in the middle of the sample, several assumptions can be made about the mode of deformation as shearing progresses and the sample bulges around its middle section. Several assumptions were tested as illustrated in Figure 4.5. First was the commonly used right cylinder assumption. In this case, as it would be expected, severe overestimation of the volumetric strain occurred as the sample bulged. Another option was to assume a parabolic deformation considering that there was no change in diameter at the top and bottom of the sample due to the presence of the porous stones. These assumptions are represented in Figure 4.5 and it is observed that the parabola assumption reasonably agreed with the global measurement using volume

#### 4. Experimental results

---

gauge. Based on this result, all the volumetric strains corresponding to triaxial tests presented in this thesis were calculated using the parabolic assumption.

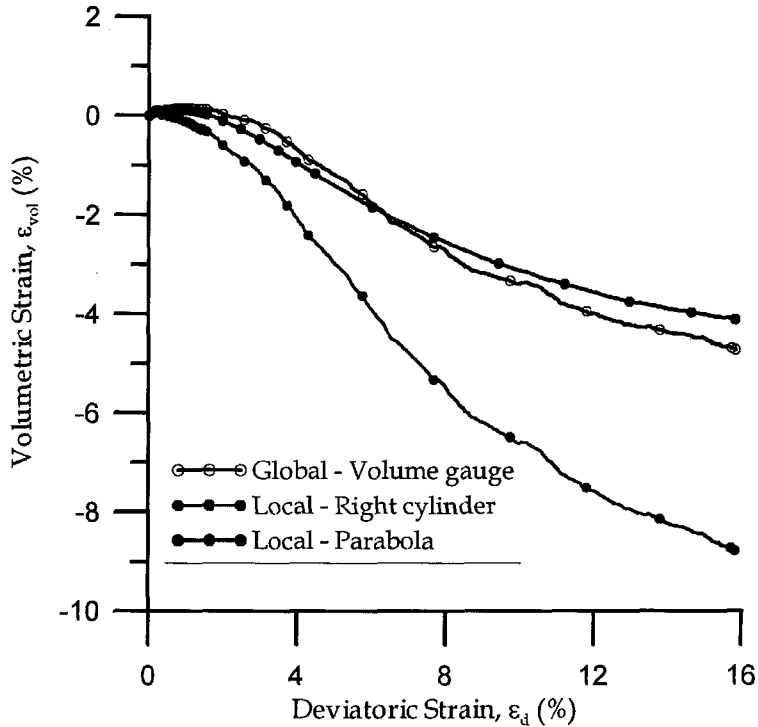


Figure 4.5: Sensitivity of calculated volumetric strain to different calculation methods

Note that the volumetric strain calculations also include corrections due to the effects of membrane penetration (when tests were performed under saturated conditions). Several analytical and experimental methods have been proposed to account for membrane penetration when volumetric changes are calculated in triaxial tests. The results of these volume changes rely heavily on the mode of deformation assumed for the membrane in contact with the individual particles. Kramer et al. (1990) developed the following expression for the volume change ( $w_o$ ) based on spheres of equal size:

$$w_o = 0.395d_s \left( \frac{1 - \alpha_m}{5 + 64\alpha_m^2 + 80\alpha_m^4} \right)^{\frac{1}{3}} \left( \frac{p_{net}d_s}{E_m t} \right)^{\frac{1}{3}} \quad (4.4)$$

where  $d_s$  is the sphere radius,  $p_{net}$  is the net pressure acting on membranes,  $E_m$  is the Young's modulus of the membrane,  $t$  is the thickness of the membrane and  $\alpha_m$  is given by

#### 4. Experimental results

---

$$\alpha_m = 0.15 \left( \frac{p_{net} d_s}{E_m t} \right)^{0.34} \quad (4.5)$$

This expression was chosen because the particle size distribution of the glass ballotini is very uniform and therefore the assumptions for its deduction are not in disagreement with the actual experiments. It must be emphasized however, that the corrections due to this penetration were not significant (less than 0.001%).

Knowing the corrections and assumptions involved in the volumetric strain calculations, the effect of testing conditions on the volumetric response can be discussed. The results of the triaxial tests discussed in the previous section in terms of stress-strain and stiffness are illustrated in Figure 4.6 in terms of volumetric strains.

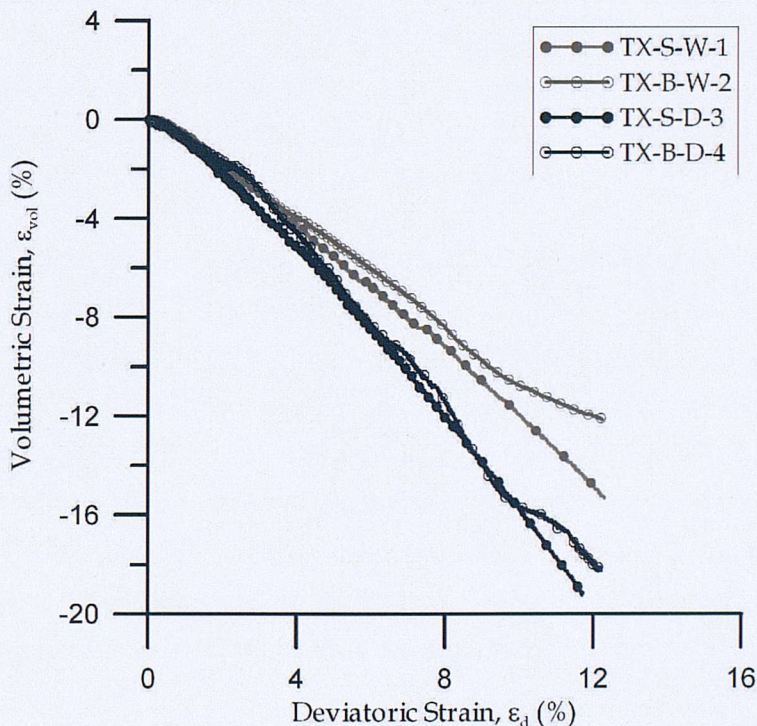


Figure 4.6: The behaviour of glass ballotini under triaxial conditions - Effect of testing conditions and particle size on volumetric response

It can be seen that all tests have a very similar response at small strain levels (up to 2%) with a very slight initial compression before extensive dilation at larger strains. The results shown in Figure 4.6 are coincident with those in Figures 4.2 and 4.3 as the stiffest samples (under saturated conditions) experienced the lowest volumetric changes.

#### 4.2.2 The effect of particle size and particle size distribution on the behaviour of glass ballotini

The effects of the particle size distribution on the behaviour of glass ballotini can also be assessed with reference to Figures 4.2, 4.3 and 4.6. In Chapter 3 it was mentioned that the different particle sizes for small, medium and big glass ballotini were very uniform. Furthermore, the coefficients characterising the grain size distribution were very similar ( $C_u$  and  $C_c$ , Table 3.2). However, the range of sizes differed. The aim of this section is to experimentally assess the possible effects of this.

##### Stress-strain and stiffness behaviour

Referring to Figure 4.3, it can be seen that for both dry and saturated conditions, the big ballotini samples are slightly stiffer than the small ballotini samples. Referring to Figure 4.2, big ballotini samples also give rise to slightly higher mobilised angles of shearing resistance.

The conclusions mentioned above are, at least by intuition, expected. It may be thought that it could be a small sensitivity to sample size. This is because in the samples with big ballotini, a maximum number of 16 particles can be expected across the sample diameter. Additionally, the total number of particles in the representative element volume may be considered to be low. However, it is believed that there is a bigger sensitivity in the response due to the fact that the grain size distribution differs between the samples, not only there are differences in the mean particle size, but also between the minimum and maximum particle size for each of the samples. This hypothesis will be revisited in Section 4.3 and Chapter 6.

##### Volumetric response

The big ballotini samples exhibited smaller volumetric strains than the small ballotini samples, as illustrated in Fig 4.6. It is believed that this response is also a consequence of the small differences in grain size distribution as hypothesized above, and discussed further in Section 4.3 and Chapter 6.

At this stage it must be stated that, in accordance with the results and discussions presented in the previous sections, it was decided to perform the HCA tests under dry conditions. In summary, the decision was based on the following arguments:

## 4. Experimental results

- The measurement of inter-particle friction is easier under dry conditions.
- The volumetric strains could be calculated using reasonable assumptions.
- The dry tests seemed to be less affected by stick-slip behaviour.
- The volumetric response of dry specimens was bigger, a fact that would be an advantage in presence of the current resolution of the instrumentation in the ICHCA and LICHCA, as discussed in Chapter 3.

An additional decision taken at this stage of the research was to perform the HCA tests consolidated under  $K_0$  conditions. This is because in this way the effects of the stress-strain non-uniformities would be more evident (Zdravkovic 1996, Foundoukos 2006). The experimental determination of the  $K_0$  for glass ballotini is the subject of the next section.

### **4.2.3 Experimental determination of the $K_0$ value**

There are several empirical relationships used to estimate the  $K_0$  coefficient, the most popular of them is the well-known formula of Jaky (1944):

$$K_0 = 1 - \sin \phi' \quad (4.6)$$

Kuwano (1999) used this equation to estimate the  $K_0$  value of glass ballotini. After several triaxial tests, she concluded that this formula underestimated the  $K_0$  value. Consequently, it was decided to measure  $K_0$  experimentally prior to HCA testing.

In triaxial testing,  $K_0$  conditions are achieved only if the radial deformation is zero during consolidation. Previous studies by Bishop & Henkel (1962) advised that in triaxial testing, the condition of no radial deformation is only ensured if the sample is homogeneous, and if loading is performed in series of large steps separated by intervals to allow time for consolidation to be achieved and ensure that any gradients of pore pressure that may have been generated disappear. Therefore, a slow but continuous increase in the cell pressure, with a corresponding increase in the axial load being increased accordingly as required was recommended. Daramola (1978) followed this recommendations and suggested an experimental approach suitable for the available local instrumentation at Imperial College to determine the  $K_0$  in

#### 4. Experimental results

---

sands. Due to similarities in the instrumentation used here with this earlier study, the approach proposed by Daramola (1978) was largely followed here.

In Daramola's approach, an initial anisotropic  $K_0$  state is guessed and consolidation is started using the guessed  $K_0$  value. Normally, Jaky's formula is used for the initial guess. If the initial guess is correct, after following the  $K_0$  stress path with the computer controlled servo system, the sample will consolidate with no radial deformation. On the contrary, if the sample bulges, a loading interval keeping a constant deviatoric stress  $q$ , while the mean effective stress  $p'$  increases is followed to eliminate the radial deformation. Once the sample has its initial diameter, an interval at constant  $p'$  while  $q$  increases would produce further radial deformation that must be reset to 0 as before. Such approach, when carried out for medium size ballotini (test TX-M-D-6), produces an stress path as illustrated in Figure 4.7.

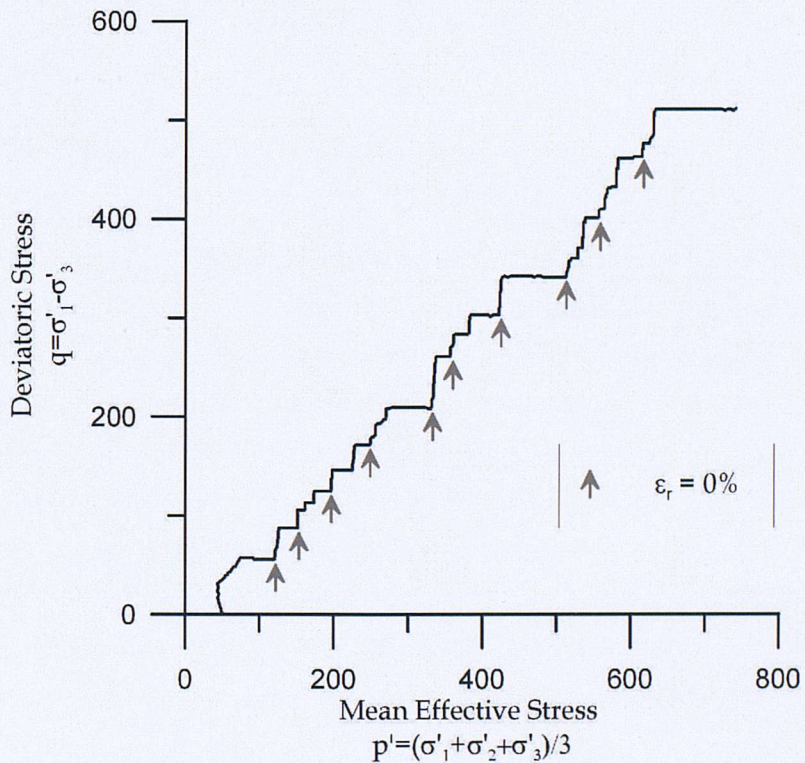


Figure 4.7: Experimental determination of the  $K_0$  coefficient for medium size glass ballotini

In addition to the recommendations by Bishop & Henkel (1962) and Daramola (1978), the advice by Okochi & Tatsuoka (1984) was also followed in this thesis. Okochi & Tatsuoka (1984) stated that for stiff sands, a variation in the radial deformation bigger than 0.005% would produce significant errors in the measured  $K_0$  value. Therefore, for the experiment in Figure 4.7 the allowed radial deformation

#### 4. Experimental results

for each constant  $q$  loading interval was never bigger than 0.005%. The gray arrows in Figure 4.7 indicate some of the specific points where the radial deformation is zero. Using these points, and assuming an intercept with the origin in  $q - p'$  space, a least squares approximation gives the equation of the line used to find the  $K_0$  value. That is because

$$q = \frac{3(1 - K_0)}{1 + 2K_0} p' \quad (4.7)$$

In order to get confidence in the results, three experiments were performed on medium size ballotini. The results of the least squares regression gave a  $K_0$  of 0.51. This confirmed Kuwano's finding that the formula by Jaky (1944) underestimates  $K_0$  for this material. The value of 0.51 was used for the HCA tests described in the next section.

### **4.3 Hollow cylinder tests**

This section presents results from a series of tests that were performed in the ICHCA and LICHCA to investigate the effects of the intermediate principal stress and the orientation of the principal stresses on the behaviour of  $K_0$  consolidated glass ballotini. In particular, tests were performed to identify the influence of the particle size distribution and sample size under different stress paths in which the orientation of the major principal stress  $\alpha$ , the intermediate stress ratio  $b$ , and the mean effective stress  $p'$ , are kept constant during drained shearing. As a consequence of the preliminary triaxial study discussed in the previous section, the tests presented in this section were performed under dry (and drained) conditions. Hence, excess pore water pressures are not generated and the effective stresses are equivalent to the total stresses.

The testing programme for the HCA experiments performed in this research is presented in Table 4.2, and they are also represented in the  $b - \alpha$  space in Figure 4.8. Note that in Table 4.2 the test ID follows the convention used for the triaxial tests in Section 4.2. Additionally, the particles sizes are defined in Table 3.2.

The testing programme was planned to cover a wide area of the  $b - \alpha$  space, avoiding the "no-go" areas proposed by Symes (1983), but also including the most non-homogeneous case in terms of stress and strain distribution as concluded by

#### 4. Experimental results

Test ID	Particle size	Testing condition	Initial void ratio ( $e_0$ )	$\alpha$ -value (°)	$b$ -value
IC-S-D-1	Small	Dry	0.551	0	0.5
IC-M-D-2	Medium	Dry	0.553	0	0.5
IC-B-D-3	Big	Dry	0.554	0	0.5
IC-M-D-4	Medium	Dry	0.553	0	0.0
IC-M-D-5	Medium	Dry	0.553	45	0.5
LIC-M-D-1	Medium	Dry	0.552	0	0.5
LIC-M-D-2	Medium	Dry	0.554	0	0.0
LIC-M-D-3	Medium	Dry	0.553	45	0.5
LIC-M-D-4	Medium	Dry	0.553	45	0.0
LIC-M-D-5	Medium	Dry	0.552	45	1.0

Table 4.2: Hollow cylinder apparatus testing programme

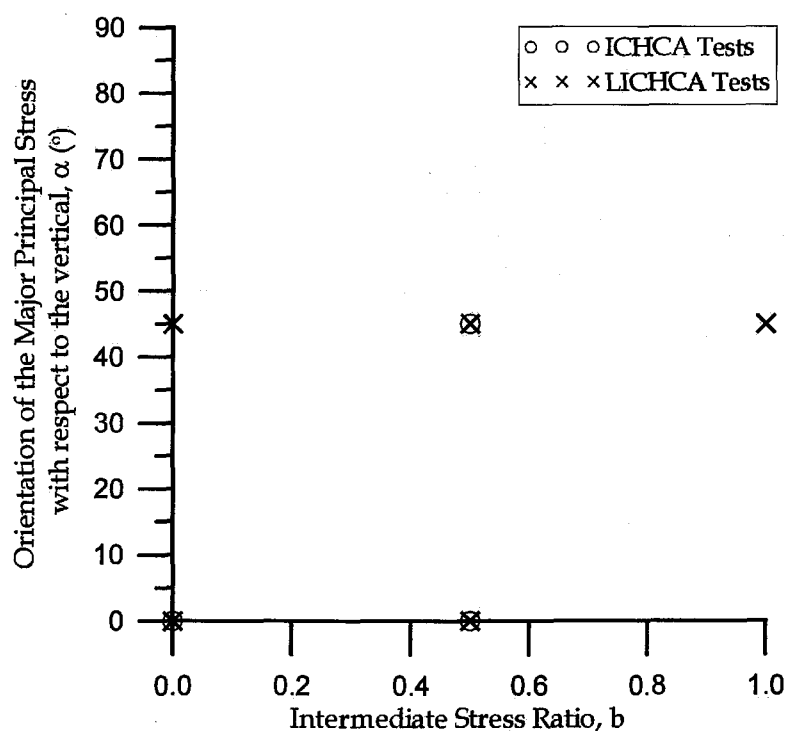


Figure 4.8: Summary of HCA tests in  $b - \alpha$  space

#### 4. Experimental results

Foundoukos (2006). For this specific case (i.e.  $b = 0.5$  and  $\alpha = 0^\circ$ ), three samples with differing particle sizes were used to assess the effects of mean particle size and grain size distribution on the anisotropic behaviour. The remaining tests were considered to provide a wider range of situations to independently assess the effects of  $b$  and  $\alpha$  on the behaviour of glass ballotini, and to aid as an additional guidance in the interpretation of the DEM results presented in Chapters 6 and 7.

The HCA test samples were prepared using the same procedure explained in Chapter 3. Therefore, they have similar initial void ratios (see Table 4.2). It is then expected that the arrangement of the particles (fabric) after  $K_0$  consolidation is the same for all tests.

All the tests presented in this section were initially  $K_0$  consolidated with  $\alpha = 0^\circ$  and  $K_0 = 0.51$ , the value obtained in the preliminary triaxial study.  $K_0$  consolidation was carried out up to a mean effective stress  $p' = 200$  kPa. For tests in which  $b \neq 0.0$ , the  $b$  value was changed from 0.0 to 0.5 (or 1.0) under drained conditions. This “ $b$ -stage” plots as a single point (A) in the  $t - p'$  space at the end of the  $K_0$  line (see Figure 4.9) because both the deviatoric stress  $t$  and the mean effective stress  $p'$  are held constant during this change of  $b$  value. After the “ $b$ -stage”, the  $\alpha$  value was changed from  $0^\circ$  to  $45^\circ$  where required, also under drained conditions, while maintaining a constant value for  $b$ ,  $t$ , and  $p'$ . After rotating the orientation of the principal stress with respect to the vertical ( $\alpha$ ), each sample was sheared by increasing the deviatoric stress  $t$  from point A, while keeping  $\alpha$ ,  $b$  and  $p'$  constant. Note that between  $K_0$  consolidation and the  $b$  and  $\alpha$  stages, a suitable period for creep was allowed. The duration of each of these stages including the time allowed for creep was approximately 24 hours. Shearing normally lasted approximately 48 hours. Hence a test including  $b$  and  $\alpha$  changes took 5 days, excluding the time required for sample set-up and dismantling.

##### **4.3.1 Tests to study the effects of the particle size distribution on soil behaviour - ICHCA**

Tests IC-S-D-1, IC-M-D-2 and IC-B-D-3 were performed to evaluate the effects of the mean particle diameter and the grain size distribution on the behaviour of glass ballotini. Note that these three tests involved shearing where  $b = 0.5$  and  $\alpha = 0^\circ$ , the most non-homogeneous case in terms of stress and strain distribution as stated by extensive prior numerical research performed at Imperial College using

#### 4. Experimental results

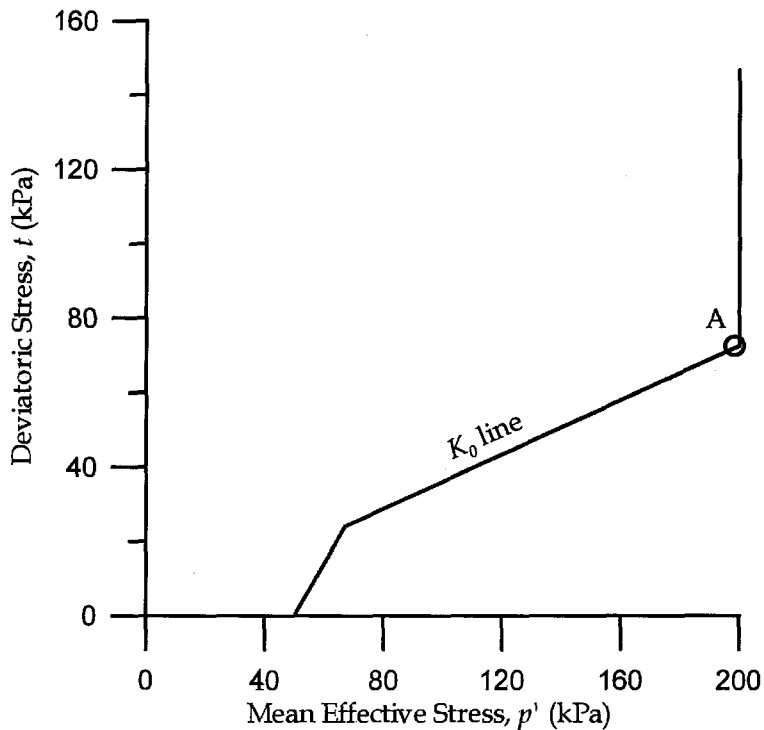


Figure 4.9: Typical HCA test stress path in  $t - p'$  space

the finite element method. A summary of the previous studies on stress and strain non-uniformities was presented in Chapter 3.

Unpublished studies by Shibuya (1985) had suggested that due to the sample thickness of the ICHCA (2.5 cm), the maximum mean particle diameter that could be tested reliably was 0.6 mm. It was stated by Shibuya (1985) that particle sizes bigger than that would create kinematic constraint in the HCA tests, implying that approximately 50 particles across the sample thickness were the minimum requirement to obtain reliable results. Hence, in the present study, three tests including mean particle sizes of 0.6 mm (Small), 1.1 mm (Medium) and 2.6 mm (Big) were systematically tested under the same conditions and identical preparation methods to assess the ICHCA capabilities.

The current experimental study is also important for numerical simulations using DEM. The use of bigger particle sizes, such as 1.1 mm instead of 0.6 mm diameter, would imply a considerable reduction in the number of particles that would need to be simulated using DEM if realistic boundary conditions and the actual ICHCA and LICHCA sample geometries were used. Consequently, the computational time required for these simulations could be significantly reduced by the selection of a specific particle size.

#### 4. Experimental results

##### Effects observed during $K_0$ consolidation

$K_0$  consolidation stress paths for the three tests are shown in Figure 4.10. These paths show that the consolidation process is well controlled and followed the expected  $K_0$  path in an accurate and repeatable manner. Note however, that test IC-B-D-3 (with big ballotini) seems to have experienced less stable readings than the other two tests, specially at the beginning of the  $K_0$  line. It is possible that this effect may be result of the lack of accuracy in the measurement of the radial deformation by the radial proximity transducers. The samples with big ballotini produced a rough surface in the aluminium foil targets, which in turn reduced the resolution of the transducers significantly. As a consequence, the calculation of stress and strain is not as precise for the “big” ballotini in comparison to the other specimens.

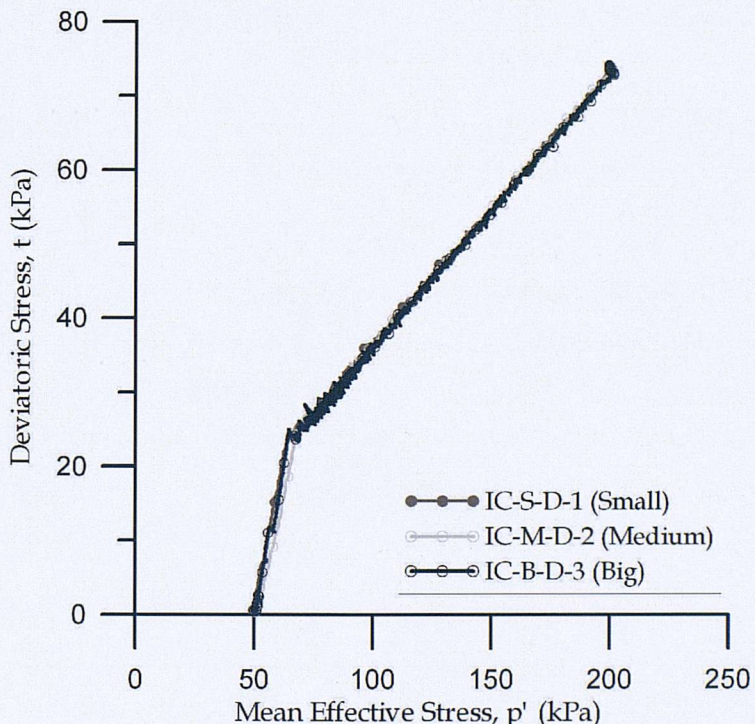


Figure 4.10: Consolidation stress paths in ICHCA - Exploration of the effect of particle size on the behaviour of glass ballotini

It must be noted that in the HCA tests presented in this thesis, the radial deformation was not controlled. However, the radial strains were directly measured. During  $K_0$  consolidation, radial strains are supposed to be zero, and furthermore, the volumetric strains are expected to be approximately equal to the vertical strains. Figure 4.11 shows the evolution of these strains measured along the  $K_0$  line as depicted in Figures 4.9 and 4.10.

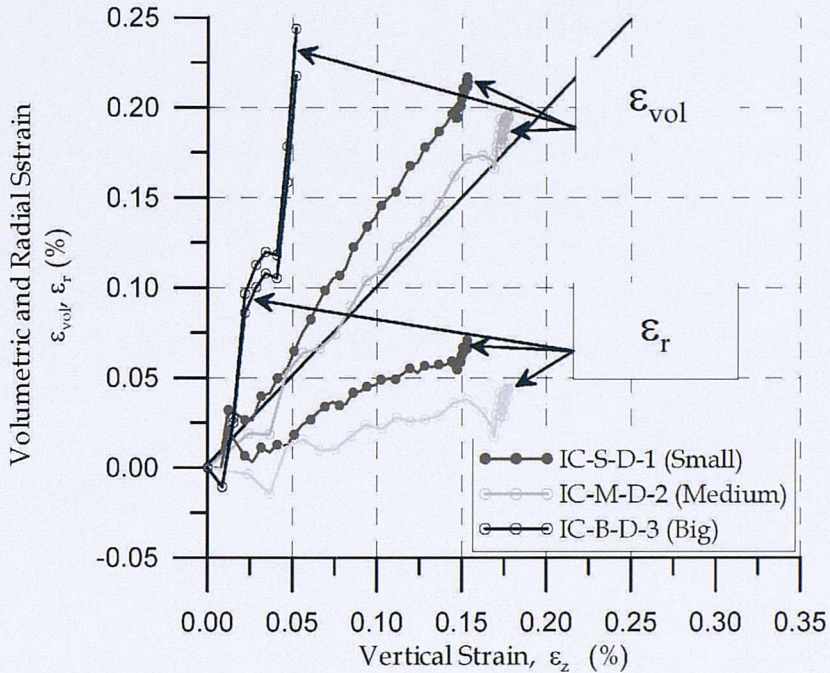


Figure 4.11: Evolution of strains during  $K_0$  consolidation in ICHCA - Exploration of the effect of particle size on the behaviour of glass ballotini

Referring to Figure 4.11, it can be seen that the tests on the small and medium ballotini were very repeatable and that the  $K_0$  conditions were closely satisfied ( $\epsilon_{vol} \cong \epsilon_z$  and  $\epsilon_r \cong 0$ ). However, it must be noted that the radial strains were smaller for the medium sized ballotini. Further experimental and numerical research is needed to determine whether this difference is related to the different relative size ranges (grain size distributions) used.

It is clear that for the test on big ballotini,  $K_0$  conditions were not at all satisfied. The data for this test goes out of scale. Therefore, for clarity, not all data corresponding to this test (IC-B-D-3) was plotted in Figure 4.11. Nevertheless, it is clear that the volumetric strains are higher than those observed in the other tests, and very similar to the radial strains. These observations may indicate that the test using big ballotini was affected by the lack of adequate resolution in the transducers, which recorded an unrealistic volumetric response.

#### Effects observed during the $b$ -change stage

After  $K_0$  consolidation and a sufficient period of creep, the three samples were subjected to stress changes such that,  $t$ ,  $p'$  and  $\alpha$  remained constant, while  $b$  changed

#### 4. Experimental results

gradually from 0.0 to 0.5. The three samples were subjected to the same changes of direct stresses ( $\sigma'_z$ ,  $\sigma'_r$  and  $\sigma'_{\theta}$ ), as shown in Figure 4.12.

Figure 4.13 shows the evolution of the volumetric strain with respect to the change in  $b$  value for the three tests with different particle sizes. It is clear that the volumetric strain is very small for all tests. However, the test on big ballotini experienced a total volumetric strain than is more than double to that observed in the tests on small and medium ballotini (0.22% and 0.47%, respectively). Note that the tests on small and medium ballotini are very repeatable and also, as remarked in the previous section, the stability of the measurements in the test on big ballotini is lower than in the other two tests.

Clearly, the response in all tests is non-linear. Furthermore, the test performed on big ballotini is stiffer than the other two tests when  $b$  is less than 0.10. This gives some evidence of the possible constraint that may be present for the test on big ballotini, considering that for this case, there was an average of only 10 particles across the sample thickness. It is also important to note that the presence of compressive volumetric strains confirms that the material is not isotropic and linearly elastic. In such a case, the volumetric strain should be zero, since there is no change in the mean effective stress  $p'$ .

The three tests described in this section were sheared with constant values for  $b$ ,  $\alpha$  and  $p'$  of 0.5, 0° and 200 kPa, respectively. Therefore, an  $\alpha$ -change stage was not required. The effects of the particle size and grain size distribution during drained shearing are the topic of the next section.

#### **Effects observed during drained shearing**

At the end of the  $b$ -change stage, the three samples had a creep period in which the volumetric strain rates of change were negligible. Subsequently, the samples were sheared under drained conditions while  $p'$ ,  $b$  and  $\alpha$  remained constant.

Figure 4.14 shows the variation of the direct stresses ( $\sigma'_z$ ,  $\sigma'_r$  and  $\sigma'_{\theta z}$ ) with deviatoric strain during the drained shear stage. Note that the radial stress ( $\sigma'_r$ ) stayed constant while the vertical stress ( $\sigma'_z$ ) increased at the same rate that the circumferential stress ( $\sigma'_{\theta}$ ) decreases in order to maintain the  $b = 0.5$  condition. On the other hand, the torsional shear stress ( $\tau_{z\theta}$ ) remained at zero because there is no stress rotation and the direction of the major principal stress is aligned with the vertical ( $\alpha = 0^\circ$ ).

#### 4. Experimental results

---

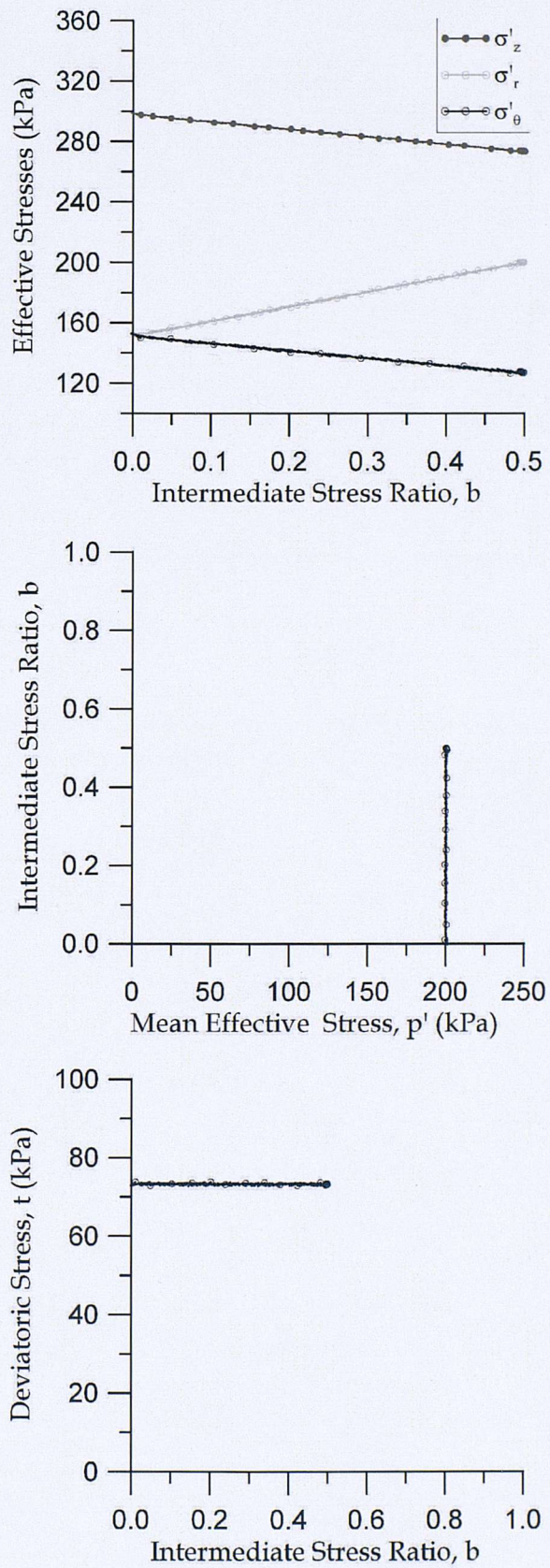


Figure 4.12: Development of stresses during  $b$ -change from 0.0 to 0.5 in ICHCA - Exploration of the effect of particle size on the behaviour of glass ballotini

#### 4. Experimental results

---

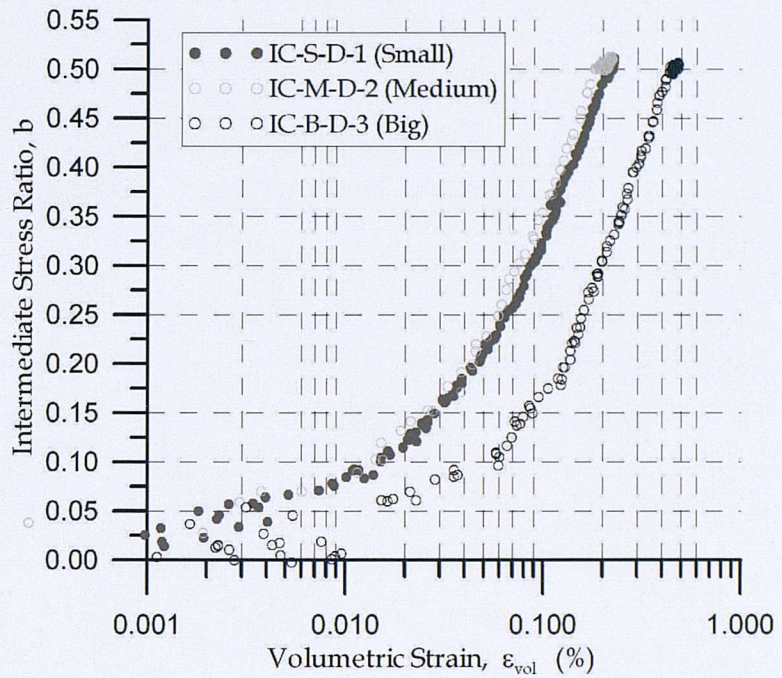


Figure 4.13: Volumetric strain development during the  $b$ -change stage in ICHCA - Exploration of the effect of particle size on the behaviour of glass ballotini

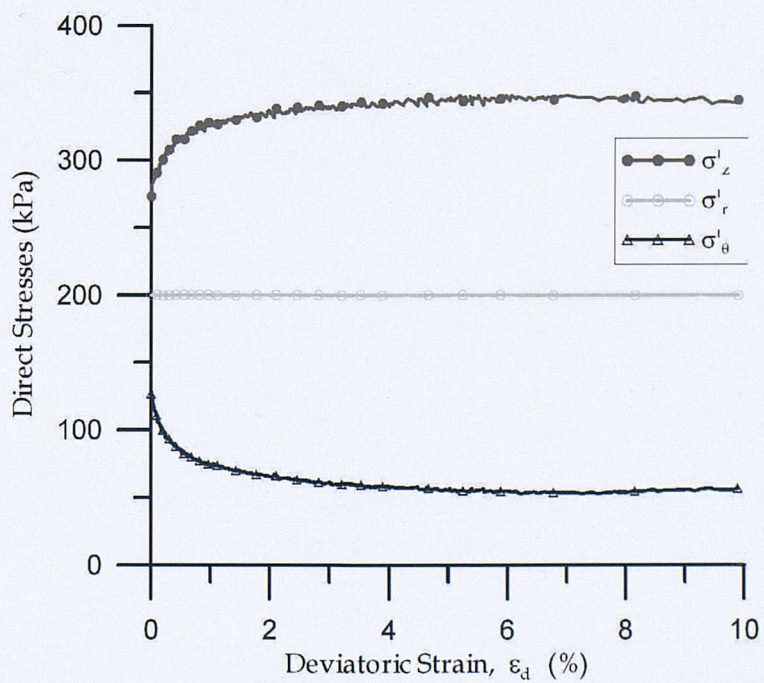


Figure 4.14: Development of stresses during drained shearing with  $b = 0.5$  and  $\alpha = 0^\circ$

#### 4. Experimental results

Figure 4.15 shows the stress-strain curves for the three tests. Please note the following:

- The curves presented include data that has been “smoothed”. This was done for ease of comparison and to omit the majority of stress fluctuations produced by the stick-slip behaviour.
- The data included here corresponds to measurements performed while the local instrumentation was on its appropriate position. After considerable bulging of the samples, the local radial instrumentation must be removed to avoid its damage. When the local radial instrumentation is removed the dimensions of the sample are not reliable. Consequently, the determination of the stresses on the sample cannot be performed with confidence.

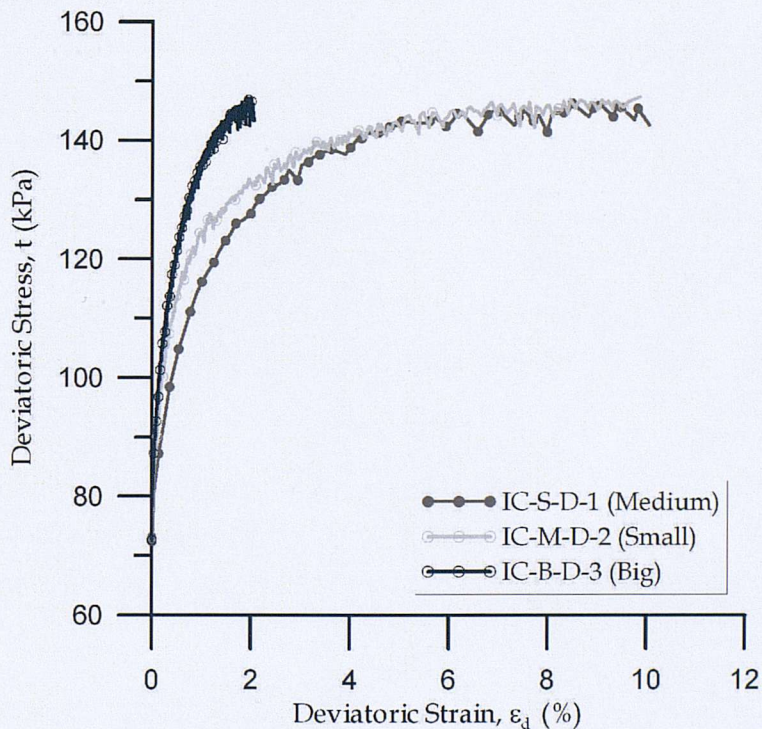


Figure 4.15: Stress-strain curves during drained shear in ICHCA - Exploration of the effect of particle size on the behaviour of glass ballotini

Referring to Figure 4.15, it can be seen that, as expected, the test performed on big ballotini is significantly stiffer than the other two tests. Considerable bulging of the middle of the sample made necessary to remove the local radial instrumentation at about 2% of deviatoric strain. Consequently, a distinctive stress point defining the peak mobilised strength cannot be identified for test IC-B-D-3. This

#### 4. Experimental results

---

excessive bulging on the big ballotini might be considered as further evidence of the kinematic constraint imposed by a reduced number of particles across the thickness of the sample. A kinematic constraint would inhibit radial deformation, therefore when a vertical strain is introduced, the sample must buckle in the middle section, generating the excessive bulging observed for this experiment.

Tests IC-S-D-1 and IC-M-D-2 allowed an easier interpretation of the peak mobilised shear strength because bulging was significant only after larger strains. Furthermore, the peak strength was equal for both tests. In terms of the peak angle of shearing resistance, the strength was  $47.1^\circ$ .

Careful observation of Figure 4.15 also reveals a small difference in the stress-strength curves of tests IC-S-D-1 and IC-M-D-2. In the deviatoric strain range between 0.5 and 4.0% the test on the medium ballotini seems to be less stiff than the test on small ballotini. It may be argued that this difference of stiffness is due to a partial constraint in the medium size ballotini. However, the difference is mainly due to the difference in the grain size and grain size distribution, as shown in Chapter 6 using DEM simulations.

Note that both tests, IC-S-D-1 and IC-M-D-2 developed several sets of two complementary shear bands at an average angle of approximately  $57^\circ$  with respect to the horizontal. In contrast, test IC-B-D-3 did not develop any shear bands, possibly due to the kinematic constraint imposed by the reduced number of particles across the sample's thickness.

These results led to the conclusion that the rest of the ICHCA and LICHCA testing programmes would be performed using medium size ballotini. As mentioned above, this reduces significantly the number of particles in the DEM simulations.

#### **4.3.2 Tests to study the effect of $\alpha$ and $b$ on soil behaviour - ICHCA**

The results of tests IC-M-D-4 and IC-M-D-5 in comparison to IC-M-D-2 allow the effects of the principal stress rotation (in terms of  $\alpha$ ) and the intermediate principal stress (in terms of  $b$ ) on the behaviour of glass ballotini to be assessed. The stress conditions for these tests were selected because they represent extreme conditions in the  $\alpha$ - $b$  stress space as explained below.

Test IC-M-D-4 ( $\alpha = 0^\circ$ ,  $b = 0.0$ ) is similar to the triaxial compression tests of Section

#### 4. Experimental results

4.2, however in this case the mean effective stress  $p'$  is kept constant during shearing. Test IC-M-D-2 ( $\alpha = 0^\circ$ ,  $b = 0.5$ ) is a test which is meant to be close to the nominal plane strain compression. As discussed in Chapter 2, for plane strain conditions  $b$  is somewhere in between 0.3 and 0.5 for many natural sands. The comparison of tests IC-M-D-4 and IC-M-D-2 then gives a comparison of two extreme cases in terms of the intermediate principal stress ratio: triaxial compression and plane strain compression.

On the other hand, test IC-M-D-5 ( $\alpha = 45^\circ$ ,  $b = 0.5$ ) involves shearing in such conditions that the predominant mode of deformation is torsional shear. In a sense, this conditions are similar to simple shear, the other extreme condition in the  $\alpha$ - $b$  stress space. Note however, that tests IC-M-D-4 and IC-M-D-5 are both sheared while the inner and outer pressures remained equal. Hence, that source of non-uniformities is eliminated for these two tests, while it is present in test IC-M-D-2.

Figures 4.16 and 4.17 are presented to demonstrate the repeatability of the tests. The observations made for the tests to assess the effects of particle size and grain size distribution are also valid here. Figure 4.17 also shows that the  $K_0$  conditions are closely followed. Since the experimental observations relative to the consolidation and  $b$ -change stages have been discussed in detail, this section concentrates on the effects seen during the  $\alpha$ -change stage for test IC-M-D-5, and the effects of  $\alpha$  and  $b$  during drained shearing.

Note that test IC-MD-4 is sheared starting from the end of the  $K_0$  consolidation with no further  $b$  or  $\alpha$  change stages required. Test IC-M-D-5 includes an  $\alpha$ -change from  $0^\circ$  to  $45^\circ$  (prior to the drained shear stage) which is performed after a substantial creep period following the  $b$ -change stage.

After a creep period following the corresponding previous stage ( $K_0$  consolidation,  $b$ -change or  $\alpha$ -change), the different samples were sheared while  $p'$ ,  $\alpha$ ,  $b$  remained constant. A comparison of the results of test IC-M-D-2 ( $\alpha = 0^\circ$ ,  $b = 0.5$ ) and IC-M-D-4 ( $\alpha = 0^\circ$ ,  $b = 0.0$ ) allows the evaluation of the effects of  $b$ . A comparison of the results of test IC-M-D-2 ( $\alpha = 0^\circ$ ,  $b = 0.5$ ) and IC-M-D-5 ( $\alpha = 45^\circ$ ,  $b = 0.5$ ) allows the evaluation of the effects of  $\alpha$  on the response.

#### **Effects observed during the $\alpha$ -change stage**

Figure 4.18 shows the variation of the direct stresses ( $\sigma'_z$ ,  $\sigma'_r$  and  $\sigma'_\theta$ ), and the torsional shear stress ( $\tau_{z\theta}$ ) with deviatoric strain for tests IC-M-D-5 during the  $\alpha$ -change

#### 4. Experimental results

---

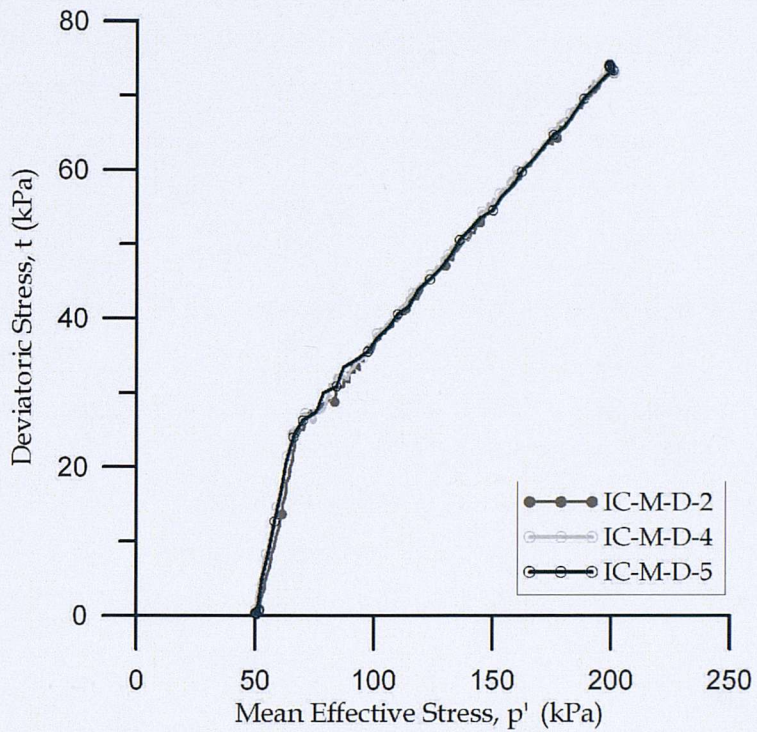


Figure 4.16: Stress paths during consolidation for ICHCA tests on glass ballotini

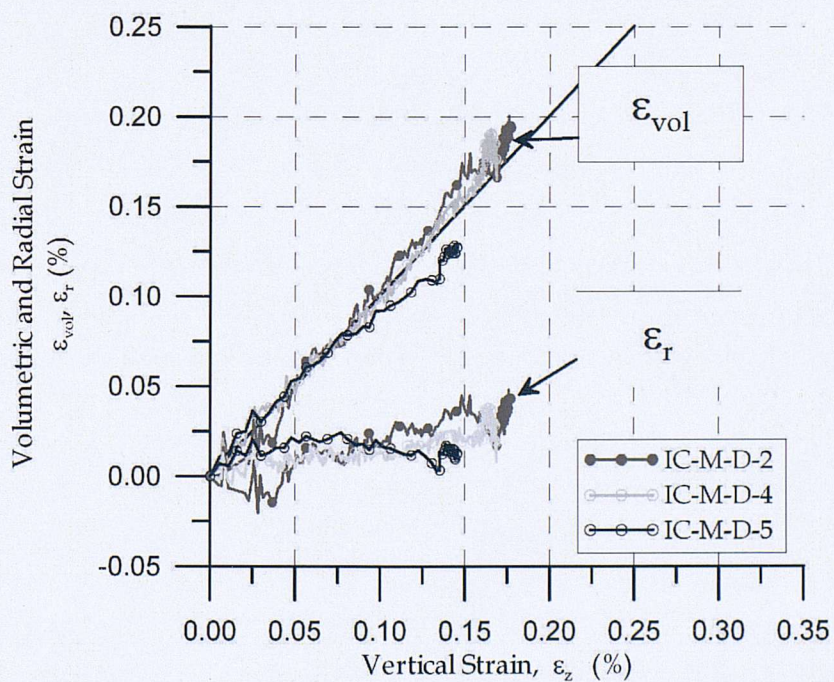


Figure 4.17: Evolution of strains during  $K_0$  consolidation - ICHCA tests on glass ballotini

#### 4. Experimental results

stage. It should be noted here that  $\tau_{z\theta}$  is drawn negative, as it acts in clockwise direction on an element of the sample's wall. The dominant mode of deformation during the  $\alpha$ -change is torsional shear ( $\gamma_{\theta z}$ ), as it is shown in Figure 4.19 which illustrates the variation of strain components with deviatoric strain during the  $\alpha$ -change stage.

#### **Effects of the intermediate stress ratio ( $b$ ) during drained shearing**

The effect of the intermediate stress ratio  $b$  is immediately seen in the stress-strain response for tests IC-M-D-2 and IC-M-D-4. Figure 4.20 illustrates that the test with  $b = 0.0$  mobilises a lower strength than the test with  $b = 0.5$ . The stress-strain curve for test IC-M-D-4 is the result of the evolution of the direct stresses as illustrated in Figure 4.21. Note that  $\sigma'_z$  increases at a rate that is twice as fast as the rate of decrease of  $\sigma'_r$  and  $\sigma'_{\theta}$ . Yet again,  $\tau_{z\theta} \approx 0$  due to the lack of stress rotation during shearing.

Although stick-slip will be discussed in more detail later, it must be noted that the stress-strain curve of test IC-M-D-4 has purposely not been smoothed as explained in the previous section to demonstrate that the stress fluctuations also exist when the sample is subjected to stress conditions when the effect of the intermediate principal stress is considered.

The angle of shearing resistance at peak for the test with  $b = 0.0$  was  $29.6^\circ$ , a substantial reduction from the  $47.1^\circ$  value of the test with  $b = 0.5$ . It is also observed from Figure 4.20 that the strain to failure for test IC-M-D-4 is reduced in comparison with that for test IC-M-D-2. Additionally a more brittle response is observed for the test with  $b = 0.0$ . These observations are in agreement with the experiments by Reades & Green (1976), but in opposition to other researchers as commented in Chapter 2.

Both Menkiti (1995) and Zdravkovic (1996) postulated that during the  $b$ -change stage from 0.0 to 0.5 there is a re-accommodation of the particles to withstand a different stress state, resulting in the creation of more and stronger contacts in the radial direction ( $\sigma'_2 = \sigma'_r$ ). Consequently, the samples sheared with  $b = 0.5$  were significantly stiffer and stronger than the samples with a smaller  $b$  value. This issue is also evident in the tests on glass ballotini, and DEM simulations can validate this hypothesis.

Figure 4.22 shows the development of the octahedral stiffness with deviatoric strain

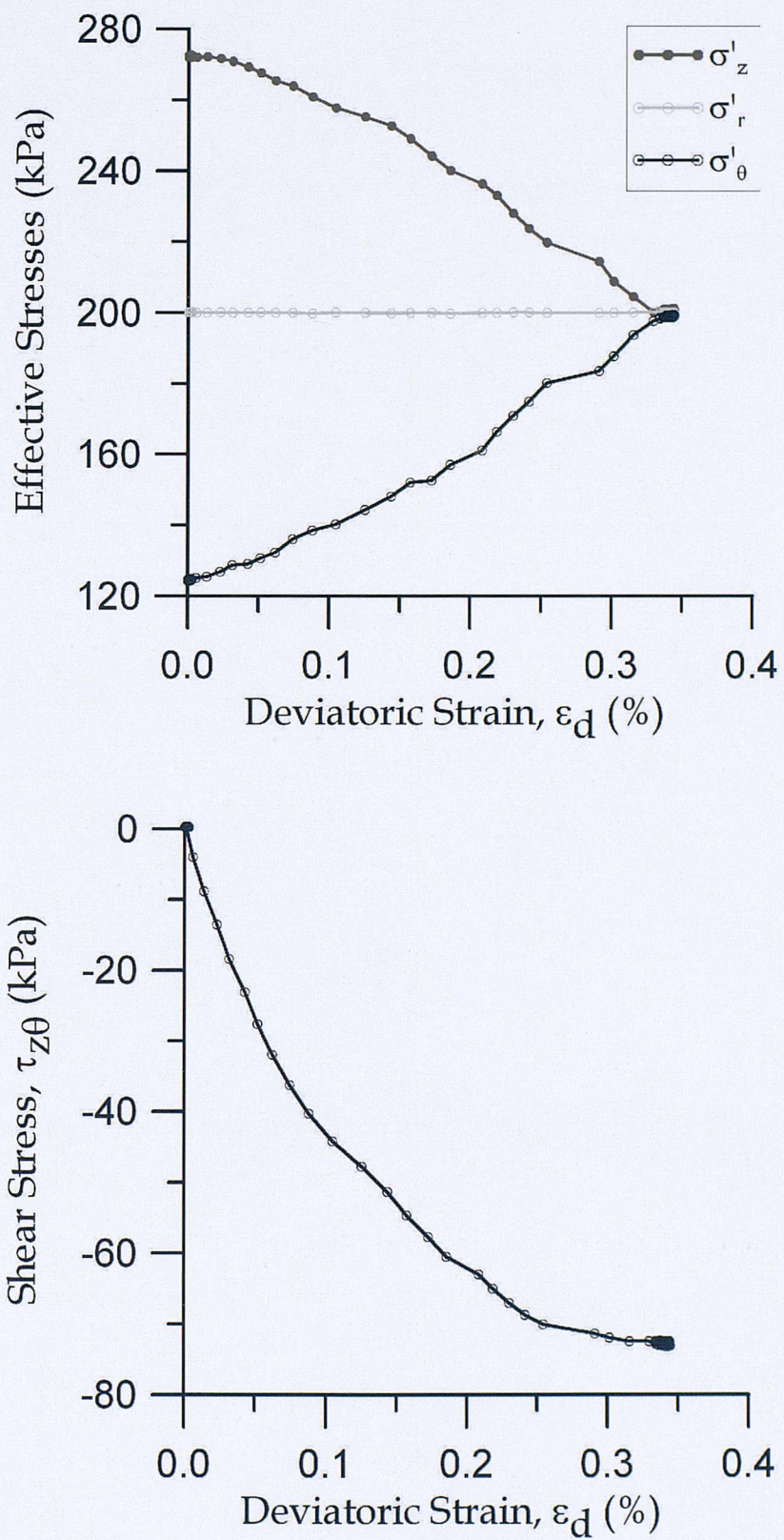


Figure 4.18: Development of stresses during  $\alpha$ -change from  $0^\circ$  to  $45^\circ$  - Test IC-M-D-5

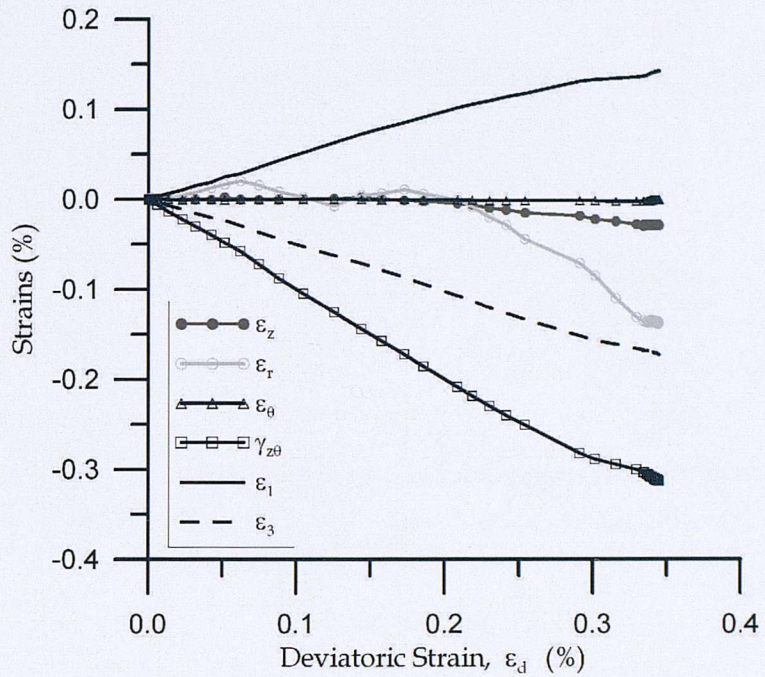


Figure 4.19: Evolution of strains during  $\alpha$ -change stage - Test IC-M-D-5

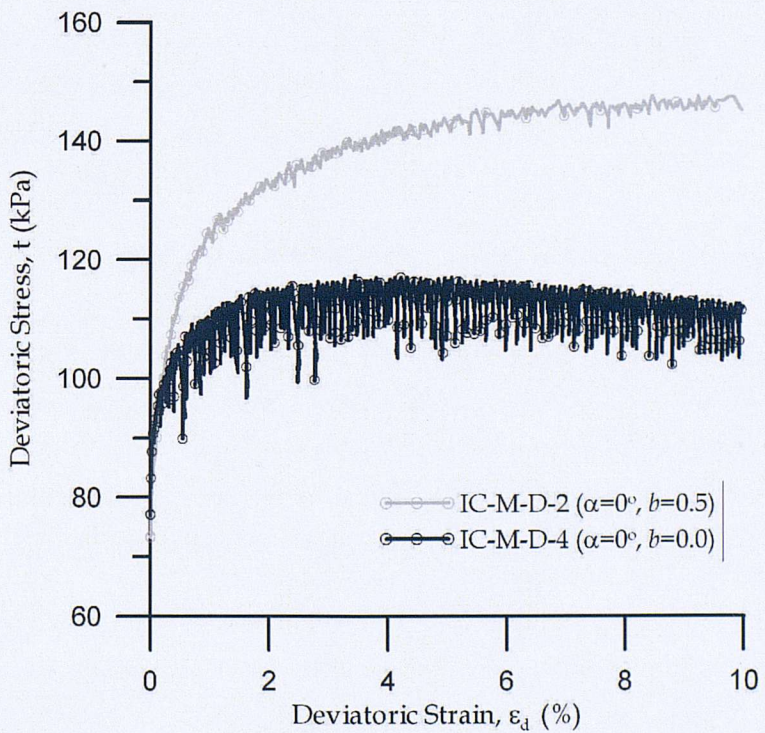


Figure 4.20: Effect of the intermediate stress ratio  $b$  on stress-strain response during drained shear - ICHCA tests on glass ballotini

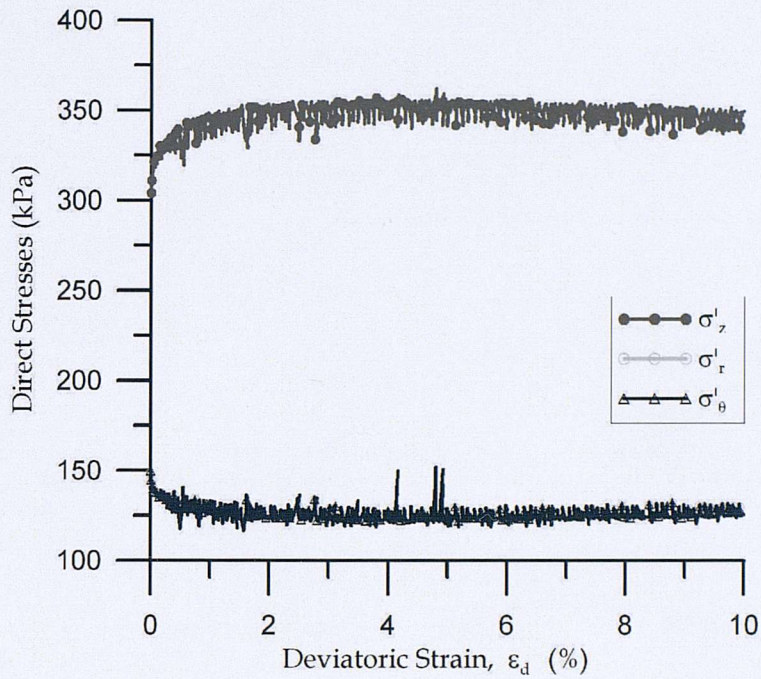


Figure 4.21: Development of stresses during drained shearing with  $b = 0.0$  and  $\alpha = 0^\circ$  - Test IC-M-D-4

for both tests. It is not clear which of the tests is stiffer at the smallest strain levels where the stiffness could not be measured with confidence due to the capabilities of the ICHCA instrumentation. However, once  $\epsilon_d$  is bigger than 0.10%, the test with  $b = 0.5$  is definitely stiffer than the test with  $b = 0.0$ .

#### Effects of the principal stress orientation ( $\alpha$ ) during drained shearing

The effect of the orientation  $\alpha$  of the principal stresses on soil behaviour can be observed from the stress-strain response for tests IC-M-D-2 and IC-M-D-5 illustrated in Figure 4.24. For test IC-M-D-5, the stress-strain curves are the result of keeping the direct stresses constant ( $\sigma'_z = \sigma'_r = \sigma'_\theta = 200$  kPa) while varying the torsional shear stress ( $\tau_{z\theta}$ ) as illustrated in Figure 4.31.

Clearly, the test with  $\alpha = 0^\circ$  is considerably stronger and stiffer than the test with  $\alpha = 45^\circ$ . Once again, the stress-strain curve of test IC-M-D-4 has not been smoothed as explained in the previous section to demonstrate that the stress fluctuations also exist when principal stress rotation is involved.

In contrast with observations of the effects of  $b$ , in the case of the different  $\alpha$  values there is no distinctive pattern in terms either of the brittleness of failure or the

#### 4. Experimental results

---

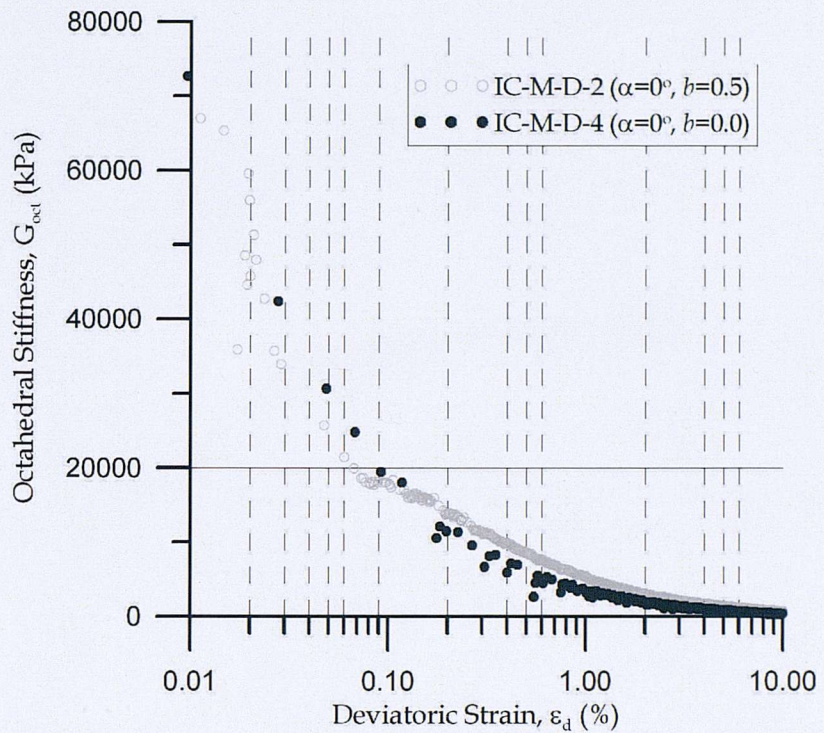


Figure 4.22: Effect of the intermediate stress ratio  $b$  on the octahedral stiffness during drained shear - ICHCA tests on glass ballotini

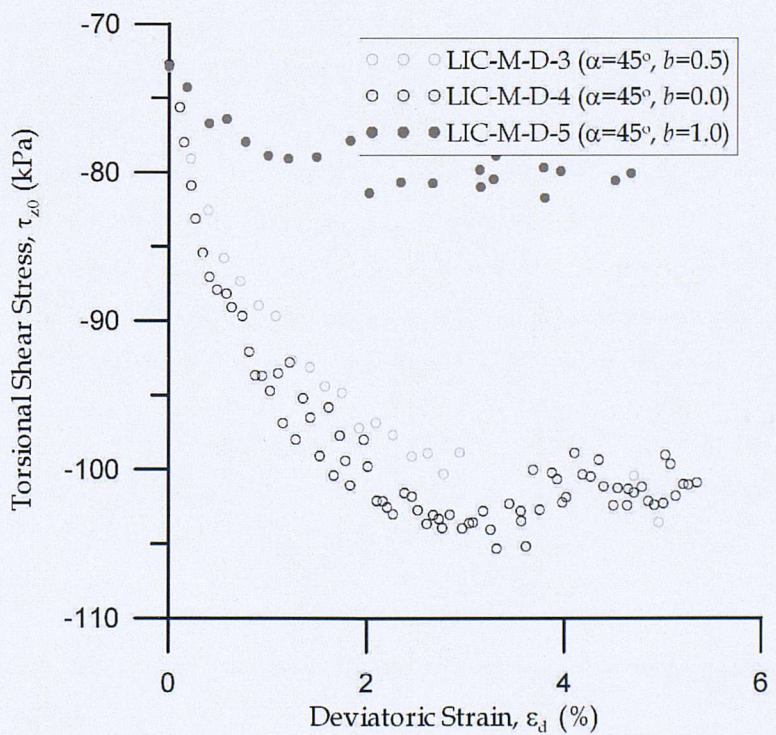


Figure 4.23: Development of torsional shear stress during LICHCA tests with  $\alpha = 45^\circ$  for different  $b$  values

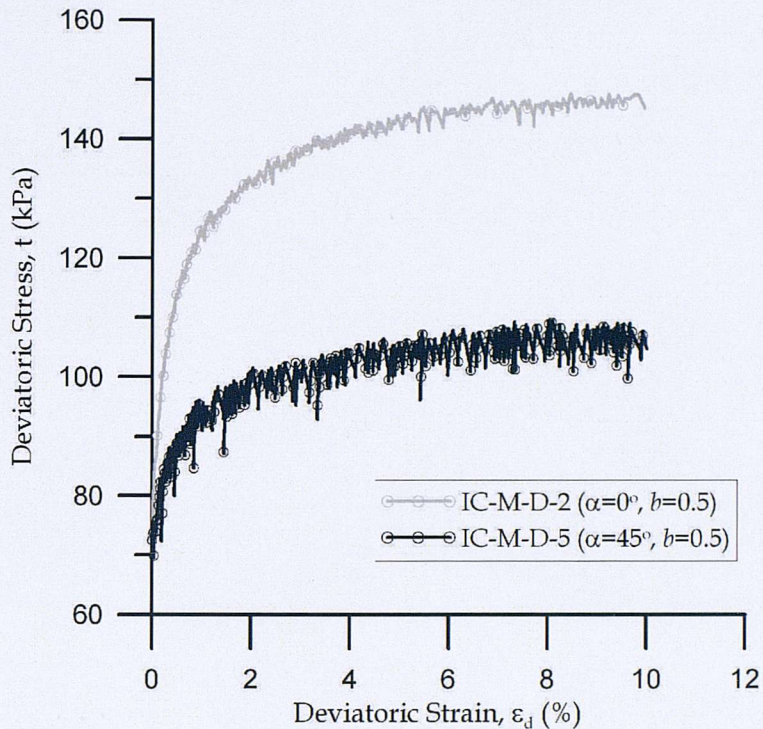


Figure 4.24: Effect of the orientation of the principal stresses  $\alpha$  on the stress-strain response during drained shear - ICHCA tests on glass ballotini

strain required to attain failure conditions. Both stress-strain curves presented in Figure 4.24 show similar trends. However, the stress conditions at peak are easier to identify for test IC-M-D-5. The difference between both conditions shows a smaller effect of the principal stress orientation on the peak strength when compared to the intermediate stress ratio. The  $\phi'_{peak}$  for the test with  $\alpha = 45^\circ$  is  $32.5^\circ$ ,  $14.6^\circ$  lower than for the test with  $\alpha = 0^\circ$ . This difference in terms of the peak angle of shearing resistance are consistent with previous experiments performed by Symes (1983), Shibuya (1985) and others as discussed in Chapter 2.

There are substantial differences in terms of the stiffness behaviour of both samples. As shown in Figure 4.25 the test with  $\alpha = 45^\circ$  is significantly softer than the test with  $\alpha = 0^\circ$ . This conclusion that can be confidently stated for all strain levels.

### 4.3.3 Tests to study the effect of $\alpha$ and $b$ on soil behaviour - LICHCA

As discussed in Chapter 3, the LICHCA is a modified version of the ICHCA. Particularly, the height/outer diameter ratio was increased from 1 to 2. This change

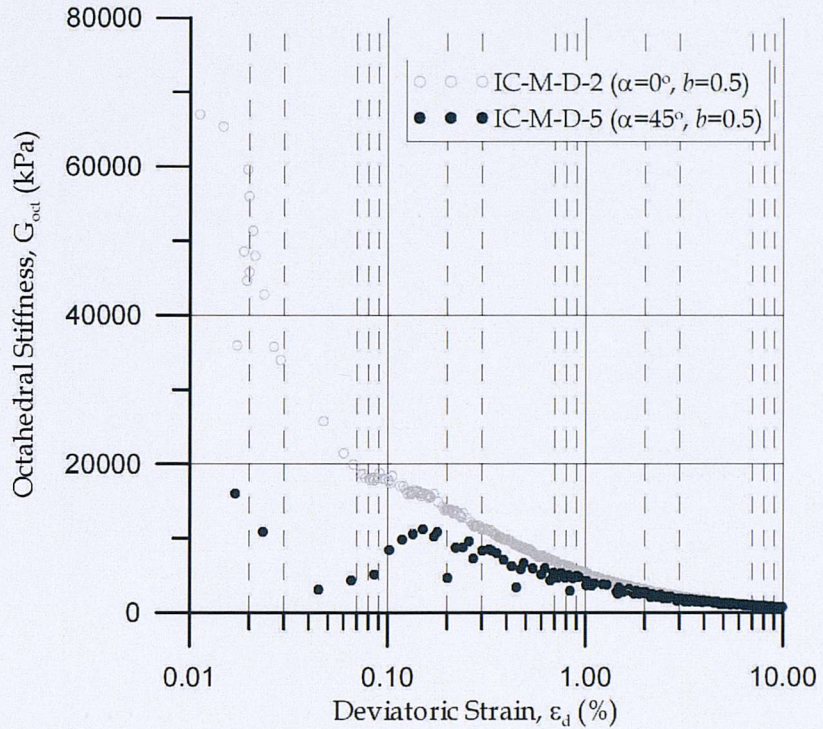


Figure 4.25: Effect of the principal stress orientation,  $\alpha$ , on the octahedral stiffness during drained shear - ICHCA tests on glass ballotini

of geometry was intended to further reduce the effects of strain and stress non-uniformities in hollow cylinder testing. The aim of the tests presented in this section is to assess experimentally the effect of such non-uniformities.

#### Sample size effects on the response of glass ballotini

Three tests that were performed in the ICHCA were repeated under identical conditions in the LICHCA to evaluate the effect of the sample geometry on the anisotropic response of glass ballotini. As for the ICHCA tests, the tests in the LICHCA were very repeatable and well controlled, as illustrated in the consolidation stress paths in Figure 4.26 for both apparatuses.

As it would be expected under repeatable tests,  $K_0$  conditions (i.e.  $\epsilon_r \cong 0$  and  $\epsilon_z \cong \epsilon_{vol}$ ) are satisfied for the LICHCA test as demonstrated in the case of the ICHCA tests. The effects found during consolidation,  $b$ -change and  $\alpha$ -change were discussed before. Furthermore, these tests are meant to be a guidance for comparison with the results of numerical simulations. Consequently, the discussion related to the sample size effects is in relation to the effects observed during drained shear.

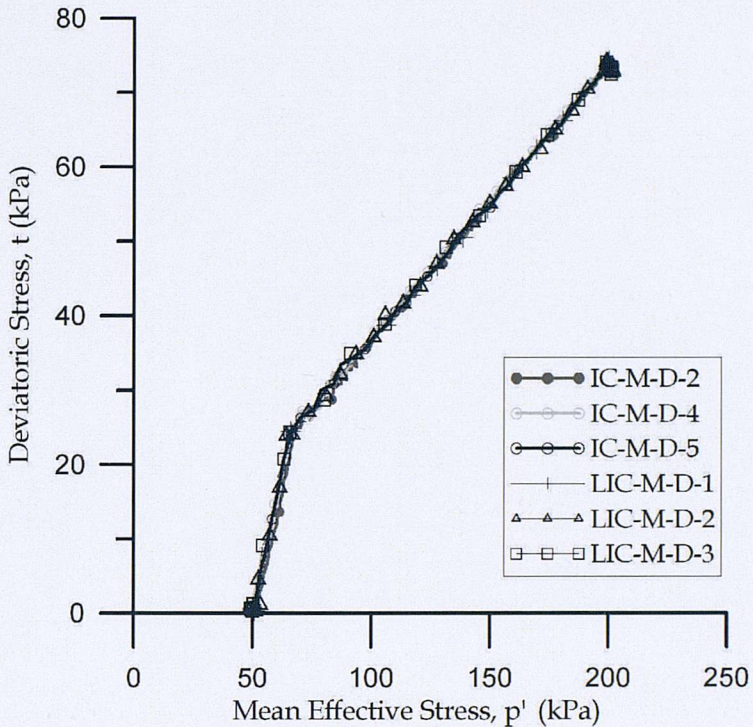


Figure 4.26: Consolidation stress paths for ICHCA and LICHCA tests on glass ballotini

Note however, that similar observations to those described in the case of the ICHCA tests were also observed in the LICHCA tests.

Figures 4.27, 4.28 and 4.29 show the stress-strain curves from the three tests performed in the LICHCA in comparison with the equivalent tests in the ICHCA. As it can be seen, there are some gaps in the available data in some of the plots relevant to the LICHCA tests. This was caused by accidental errors during those tests when the data was not recorded to a file in these specific intervals. Also note that the stress-strain curves for the LICHCA terminate at approximately half of the deviatoric strains for the tests in the ICHCA. This is a consequence of the increase in sample size of the apparatus. While the sample size was doubled, the maximum range in which the ram can provide axial or torsional shear strain remained unchanged.

Figure 4.27 compares the tests with  $\alpha = 0^\circ$  and  $b = 0.5$  in both apparatuses. Both tests experienced a very similar behaviour in terms of stiffness when  $\epsilon_d$  was smaller than 0.2%. After this point the test with the big sample becomes significantly softer and a marked difference in the mobilised angle of shearing resistance can be observed. The  $\phi'_{peak}$  values differ by  $10.9^\circ$ . Recall that  $\phi'_{peak}$  for the ICHCA test was  $47.1^\circ$ . The LICHCA test gave a  $\phi'_{peak}$  value of only  $36.2^\circ$ .

#### 4. Experimental results

---

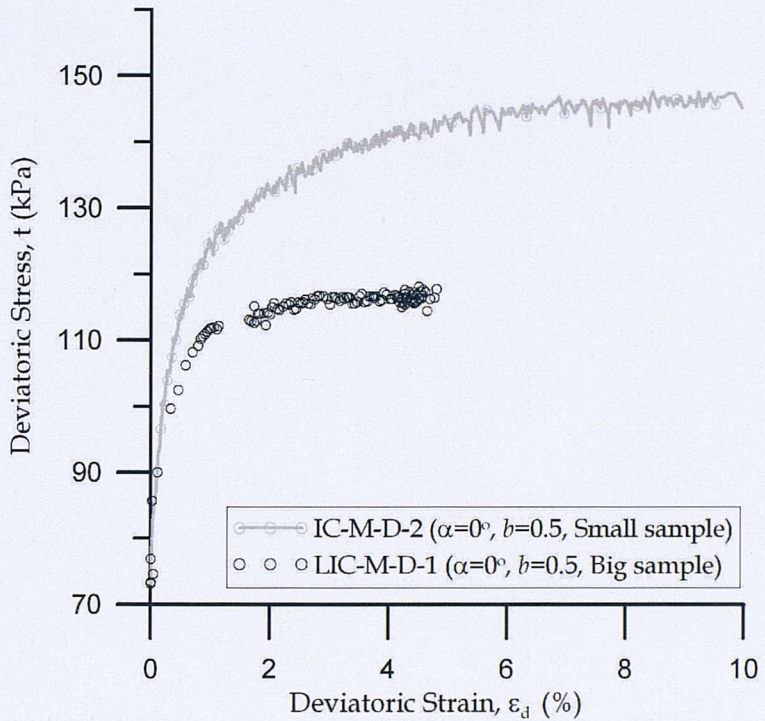


Figure 4.27: Sample size effects for ICHCA and LICHCA tests on glass ballotini ( $\alpha = 0^\circ$  and  $b = 0.5$ )

It is believed that this difference of results is due to the presence of strain and stress non-uniformities, particularly in these tests which are performed under the most extreme conditions in terms of non-homogeneities. Note however, that Lade et al. (2008) found differences in tests performed on Santa Monica sand of approximately 8 degrees. The tests by Lade et al. (2008) are not as non-uniform as the case presented here (i.e.  $p_i = p_o$ , refer to Section 3.4). Furthermore, their tests were performed with a HCA with different dimensions and height/outer diameter ratios compared to the ICHCA. Nevertheless, the agreement between both studies is reasonable.

Figures 4.28 and 4.29 illustrate the sample size effects for the other two stress conditions (i.e.  $\alpha = 0^\circ$ ,  $b = 0.0$  and  $\alpha = 45^\circ$  and  $b = 0.5$ ). In contrast with Figure 4.27, the stress-strain curves for these two stress conditions are much more similar for the two sample geometries. Note however, that the taller samples experienced a moderately weaker response in both cases. These results are in agreement with the experimental observations by Kharchafi (1988) as described in Chapter 3.

Figure 4.30 shows a summary of results in  $\alpha - \phi'_{peak}$  plane for both sample sizes. It can be seen that sample size affects significantly the condition of  $\alpha = 0^\circ$  and  $b = 0.5$ . This was also confirmed in studies by Rolo (2003) and Foundoukos (2006). Further

#### 4. Experimental results

---

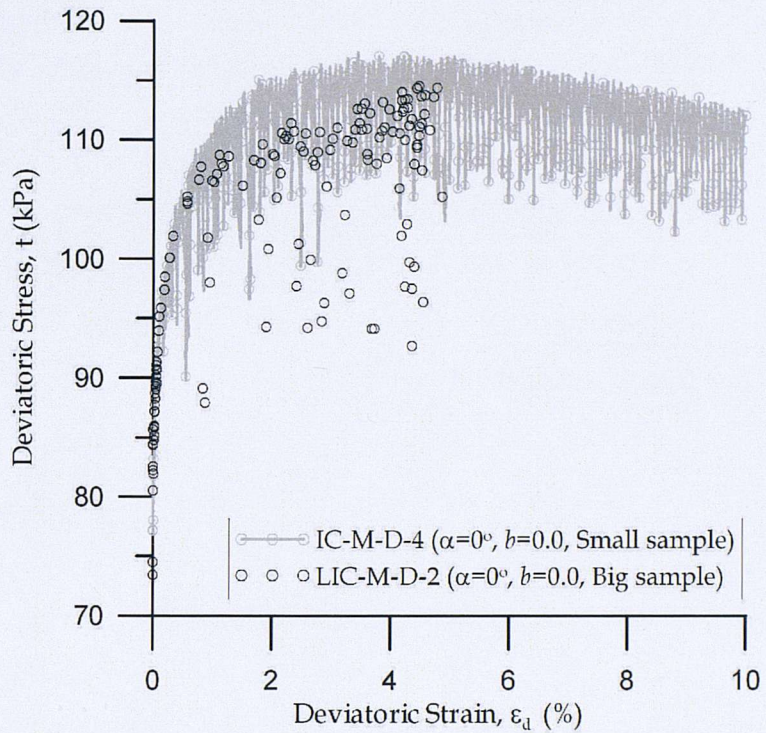


Figure 4.28: Sample size effects for ICHCA and LICHCA tests on glass ballotini ( $\alpha = 0^\circ$  and  $b = 0.0$ )

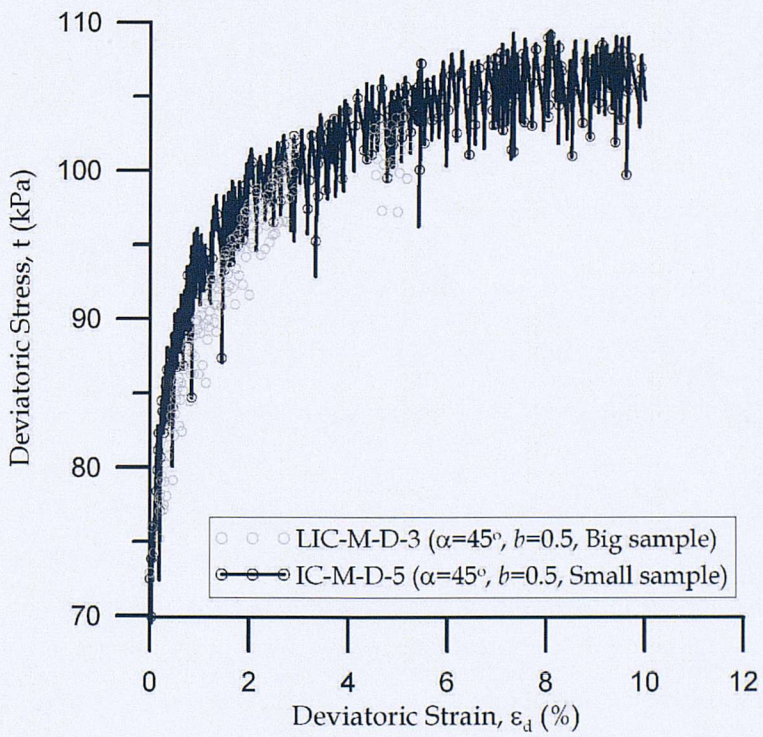


Figure 4.29: Sample size effects for ICHCA and LICHCA tests on glass ballotini ( $\alpha = 45^\circ$  and  $b = 0.5$ )

#### 4. Experimental results

---

to this, the limited set of results indicates that once  $\alpha > 0^\circ$  when  $b = 0.5$ , the two sample sizes produce similar behaviour, hence reducing the effect of non-uniformities in a smaller sample. Ultimately, the total anisotropy, expressed as a difference in strength between  $\alpha = 0^\circ$  and  $\alpha = 45^\circ$  is smaller in the larger sample. In terms of stiffness and strain development, these tests behaved in a very similar way to the tests in the ICHCA. Consequently, details are not included here.

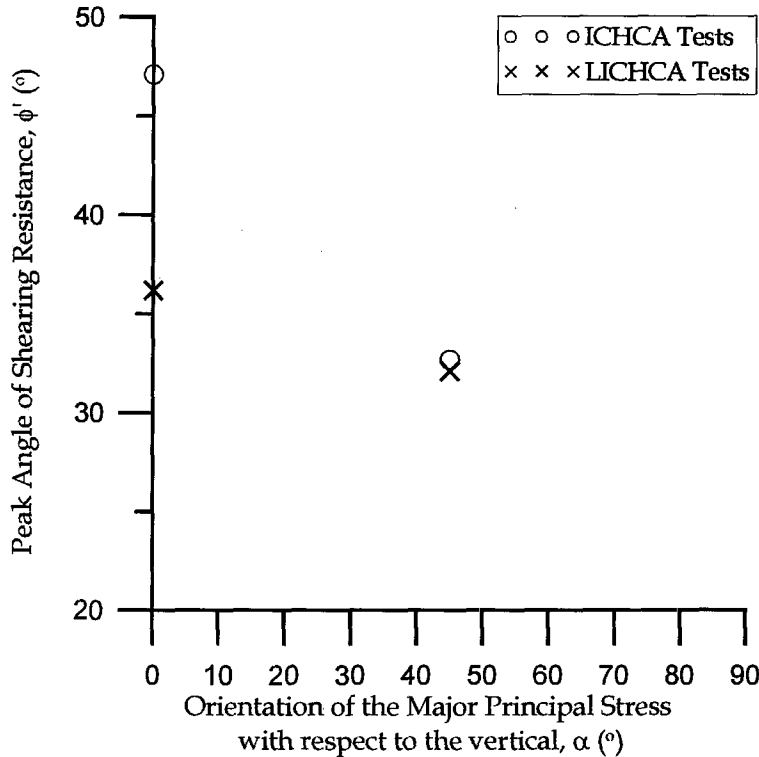


Figure 4.30: Sample size effects considering the peak angle of shearing resistance - Tests performed with  $b = 0.5$

#### Tests examining granular material response for $\alpha = 45^\circ$ , $b$ varied

For all the tests presented here  $\alpha = 45^\circ$ . Test LIC-M-D-4 was carried out with  $b = 0.0$  and test LIC-M-D-5 with  $b = 1.0$ . These tests and test LIC-M-D-3 ( $b = 0.5$ ) described in the previous section provide further understanding of soil behaviour when the orientation of the major principal stress is  $45^\circ$  for different  $b$  values. Furthermore, this area of the  $\alpha$ - $b$  space is far from the “no-go” areas defined by Symes (1983) and has been studied in detail by several researchers at Imperial College (e.g. Symes 1983, Shibuya 1985, Zdravkovic 1996).

The tests are compared in Figures 4.31 and 4.23. Considering the tests with  $b = 0.0$

#### 4. Experimental results

---

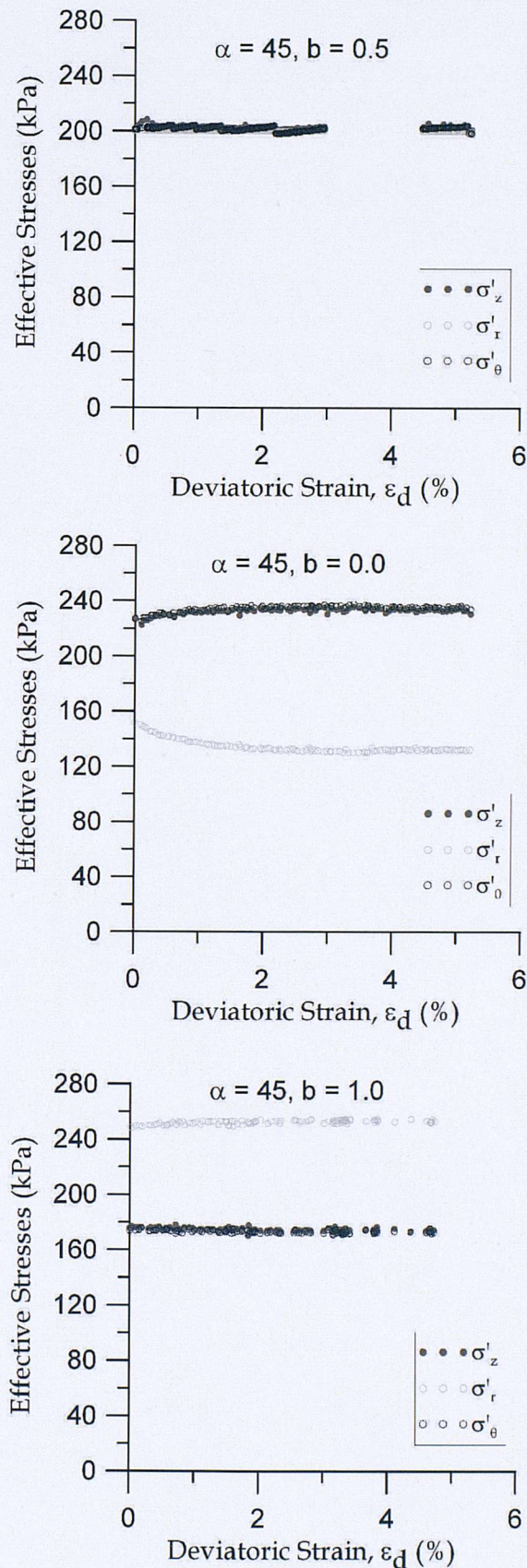


Figure 4.31: Development of stresses during LICHCA tests with  $\alpha = 45^\circ$  for different  $b$  values

#### 4. Experimental results

---

and  $b = 0.5$ , both showed similar stress-strain responses which significantly differ from the test with  $b = 1.0$ . The test with  $b = 0.5$  had the strongest response with a peak angle of shearing resistance of  $32.1^\circ$ .

A summary of results for the peak shearing resistance is presented in figure 4.32 in terms of the intermediate stress ratio for all the tests performed in the LICHCA. The trends obtained for both values of the orientation of the major principal stress show similar patterns. However, it can be seen that the effect of the intermediate stress ratio is slightly higher in the case of  $\alpha = 0^\circ$ . These results agree fairly well with previous research performed by Symes (1983) and Lade et al. (2008) for different sands (see Chapter 2). The trends for  $\alpha = 0^\circ$  are also consistent with numerical simulations performed by Ng (2004b) and Thornton (2000).

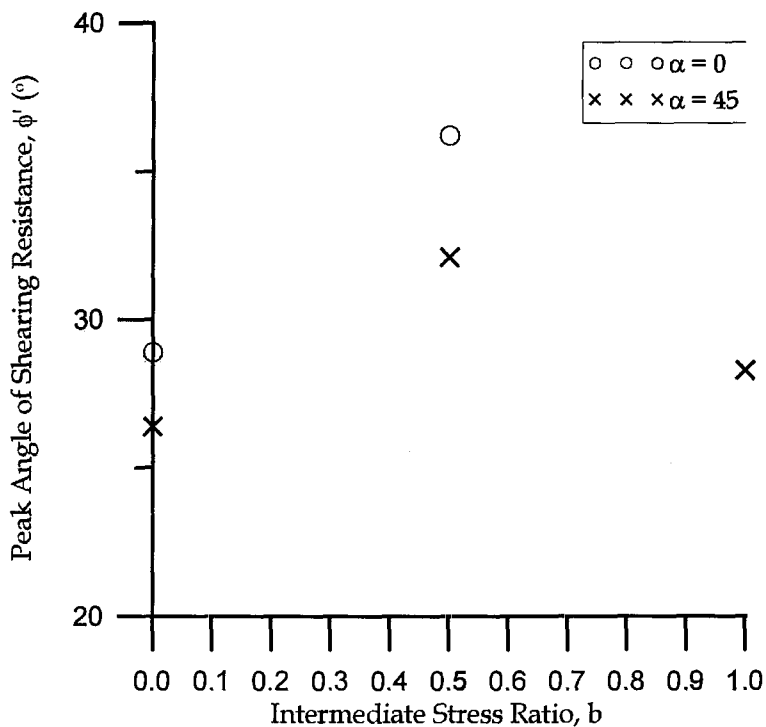


Figure 4.32: Summary of shear strength results for LICHCA tests with different  $\alpha$  and  $b$  values

In terms of the degradation of stiffness as illustrated in Figure 4.33, it is clear that the stiffest response corresponds to the test with  $b = 0.5$ . This test is close to the nominal plane strain conditions, and in that sense provides additional restraint in the radial direction. As a result the response is stiffer.

It is important to note that for all these three tests the main mode of deformation is torsional shear as  $\alpha = 45^\circ$ . Under these circumstances, the applied torque to the

#### 4. Experimental results

---

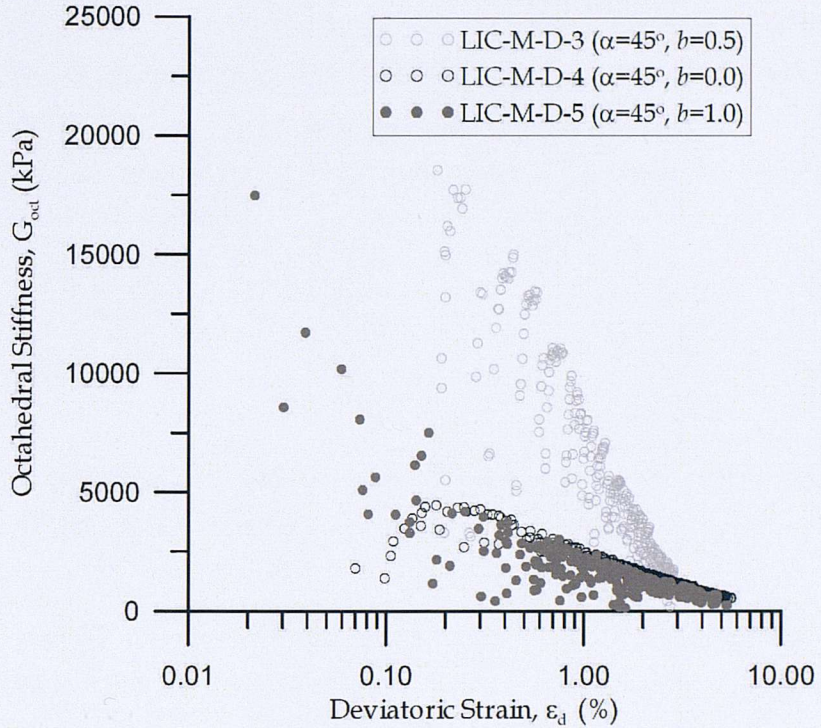


Figure 4.33: Evolution of octahedral stiffness with deviatoric strain during LICHCA tests with  $\alpha = 45^\circ$  for different  $b$  values

sample is significant. As mentioned before, the test with  $b = 0.5$  is close to the nominal plane strain scenario, which is located somewhere between  $0.3 \leq b \leq 0.5$ . Consequently the radial strain for this experiment (LIC-M-D-3) is the smallest when compared to the other two tests.

Comparing —Figures 4.28 and 4.29 as well as the other stress-strain curves presented in this chapter, the following observations can be made in relation to the observed stick-slip behaviour.

- Stick-slip appears for all the tests before the peak shearing resistance is reached.
- The stress fluctuations may be related to local instabilities. Stick-slip could be related to the local collapse of load carrying columns between grains. It is clear that the magnitude of the stress fluctuations is significantly bigger for the tests with the major principal stress orientation of  $45^\circ$ .
- The observation above can be explained as  $K_0$  consolidated specimens develop an internal structure aimed to withstand the principal stress in the vertical direction. Therefore, when sheared at a different inclination, the destruction of contacts orientated in an unfavourable manner becomes easier.

Although the above observations seem clear from the experimental data obtained during this thesis, they are not conclusive and further research is needed for a better understanding of this interesting phenomenon. Particulary, the effect of inter-particle friction as well as particle geometry, could be easily investigated both numerically and experimentally.

## 4.4 Summary

This Chapter presents the results of triaxial and hollow cylinder tests. The main conclusions of the triaxial triaxial tests are:

- The triaxial tests provided the required information to decide upon the testing conditions for the subsequent HCA tests. As a result, the HCA tests were performed under dry conditions.
- The triaxial tests also give further understanding into the effects of inter-particle friction on the shearing resistance of granular materials and the phenomenon of stick-slip behaviour.
- The analyses of the results showed the importance of making appropriate assumptions regarding the deformation mode for the calculation of volumetric strains.
- The  $K_0$  was experimentally measured. The value obtained was used in the subsequent HCA tests.

The hollow cylinder tests considered a variety of stress conditions, and two different sample heights were used in order to assess the effects of the stress and strain non-uniformities in the anisotropic response of granular materials. The main conclusions from this series of tests are:

- A comparison of HCA tests using three different particles sizes gave some understanding about the importance of a minimum number of particles across the thickness of the sample in order to avoid kinematic constraints. At this point, it is emphasized that this result may differ for other granular materials with more complex particle shapes, which give more complex contact patterns.

#### 4. Experimental results

- The previous analysis also provided some evidence of the possible effects of the grain size distribution on the stress-strain response of granular materials. This fact is further examined using DEM in the following chapter.
- The analysis of the test results using different sample geometries provided some guidance on the effect of the stress and strain non-uniformities in the shear strength of granular materials. In particular, it was shown that the  $\alpha = 0^\circ$ ,  $b = 0.5$  stress state involves the highest effect of non-uniformities in a smaller sample.

# Chapter 5

## Code development and its validation

### 5.1 Introduction

The DEM code used in this thesis is a modified version of ELLIPSE3D (Lin & Ng 1997) which follows the algorithm proposed by Cundall & Strack (1979a) on their code called TRUBAL. This DEM code was subsequently modified and extended by O'Sullivan (2002) and Cui (2006). For this thesis a new rectangular cell with periodic boundaries was implemented in order to perform the DEM simulations. Periodic boundaries have been used in DEM simulations by many researchers (e.g Cui et al. 2007a, Thornton 2000). However, as mentioned in Chapter 2, previous DEM research has not involved stress paths involving shear deformation, which experience controlled changes in the orientation of the principal stresses.

This chapter describes the properties of the periodic cell and discusses the recent code developments that were implemented in order to carry out the DEM simulations presented in Chapters 6 and 7. Specifically, changes related to the contact detection algorithm and the improvements in order to be able to simulate shear deformation and include controlled principal stress rotation. These changes are validated using analytical solutions for packings of equal spheres with a specific geometrical configuration.

## 5.2 The periodic cell

When periodic boundaries are used, the material is assumed to be infinite in extent. The material is represented by repeated and identical representative volume elements made of particles subjected to uniform strain fields (see Figure 5.1). Note that Figure 5.1 represents a two-dimensional periodic cell. However, the concept is easily extrapolated to three-dimensions.

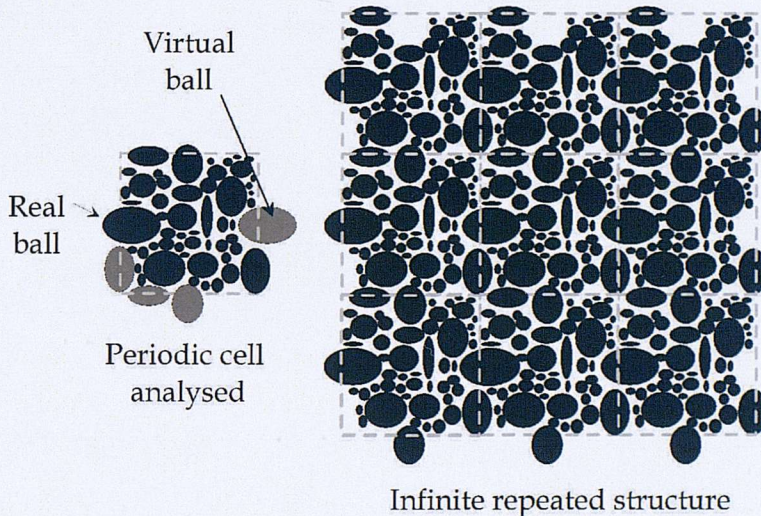


Figure 5.1: Representation of granular material using periodic boundaries in the two-dimensional space.

Periodic boundaries are normally used to simulate response without influence of boundary effects. Furthermore, due to the existence of a representative volume element, an infinite material can be simulated using a reduced number of particles. The fundamental principle that allows to do this is the conservation of mass. In order to simulate an infinite space, the movement of each particle is tracked at all times during a DEM simulation. If the centroid of a particle protrudes from one of the boundaries illustrated in Figure 5.1, then the particle is moved to the opposite boundary, with the same  $x$  (or  $y$ ) coordinate as the “real” ball. On the other hand, if a ball is close to a boundary, a virtual ball is introduced just outside the opposite periodic boundary in order to generate a continuous network of contact forces. This is illustrated in Figure 5.1.

This periodic cell concept has been applied to simulate triaxial, plane strain and true triaxial tests by a number of researchers (e.g Thornton 2000, Ng 2004b). This approach is considered in Section 5.3. In this thesis, the approach has been extended

to consider the case where there is principal stress rotation as described in Section 5.4.

## 5.3 DEM algorithms for simulations involving normal loading

Simulations which involve normal loading in a periodic cell include standard triaxial tests, plane strain tests on prismatic specimens and constant  $b$  tests (where  $\alpha = 0^\circ$  or  $90^\circ$ ), such as those discussed in Chapter 2 (e.g Thornton 2000, Ng 2004b). This section explains different code requirements in order to be able to perform these simulations. Recent developments to the contact detection algorithm are presented first. These changes are followed by the description of the algorithms related to the operation of the periodic boundaries.

### 5.3.1 Contact detection

There is a high probability that a single particle will interact only with its immediate neighbors, and not with particles that are very far from it. Therefore, in DEM simulations it is possible to reduce the computational cost and reduce the use of memory if contact detection is only performed for a particle and its possible area (2D) or volume (3D) of influence. Munjiza & Andrews (1998) and Williams et al. (2003) proposed binning algorithms based on that principle. The code used for the present thesis also included a similar approach. While a binning algorithm did exist in the code already, it was complex and a new algorithm was implemented to facilitate the implementation of stress rotation and generalised axi-symmetric stress conditions. Consequently, the contact detection algorithm is described here with the aim of justifying the changes and decisions made to implement the DEM algorithms for simulations involving shear deformation.

In such approach, which is illustrated in Figure 5.2, the periodic volume is divided in cells (bins) with a size slightly larger than the size of the biggest particle. The algorithm is based on the fact that it is very easy to allocate each particle to a bin knowing its centroid coordinates. A contact between two particles exists if the distance between the centroids of two particles is less than the sum of their radii. The test to identify a contact needs to be performed only between particles that are allocated to the same bin or adjacent bins to the particle under consideration.

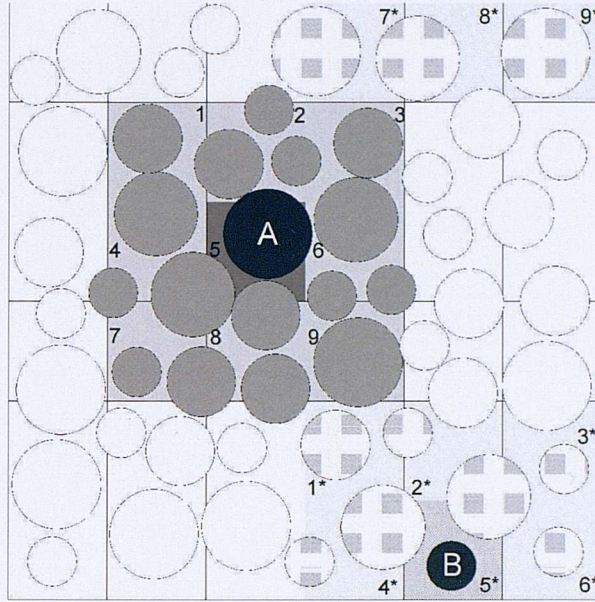


Figure 5.2: Contact detection algorithm - Binning for potential contacts

Considering particle A in Figure 5.2, only particles in bins 1-9 will be considered when contacts need to be identified. Since one of the objectives of the periodic cell is to have an infinite space with a continuous network of particle contacts, contact detection requires further considerations when a particle is allocated to a bin which is close to the boundaries. As illustrated in Figure 5.2, particle B would need to be tested for contact with spheres within the bins 1\* to 9\* only.

Care must be taken when considering contacts across periodic boundaries (i.e. between particles in bins 6\* and 9\*). Consider two particles, 1 and 2, with coordinates  $x_1, y_1, x_2, y_2$  and radii  $r_1$  and  $r_2$ . If the  $x$ -direction is evaluated, these particles are located in a periodic cell bounded by the planes  $x = 0$  and  $x = x_{max}$ . If  $l_x = x_1 - x_2$ , and  $|l_x|$  is bigger than the grid size (periodic cell size), the overlap at the contact point is calculated as:

$$\Delta n = \sqrt{\left(x_1 - x_2 - \frac{l_x}{|l_x|} x_{max}\right)^2 + (y_1 - y_2)^2} - (r_1 - r_2) \quad (5.1)$$

In the opposite case (i.e.  $|l_x|$  is smaller than the grid size), the overlap is calculated as:

$$\Delta n = \sqrt{(x_1 - x_2)^2 + (y_1 - y_2)^2} - (r_1 - r_2) \quad (5.2)$$

### 5.3.2 Simulation control

When normal loading is applied (e.g. triaxial and true triaxial tests), stress and strain-controlled loading paths can be simulated. The periodic cell is a cubic box extending from the origin of the axes. (i.e. the planes  $x = y = z = 0$  form three sides of the periodic cell). The positions of the other three sides are defined by values specified by the user and denoted as  $x_{max}$ ,  $y_{max}$  and  $z_{max}$ . It must be emphasized that these dimensions should be determined carefully in order to maintain a specific centre-to-centre spacing between particles if lattice type structures of particles are used. Such lattice packings are useful for code validation purposes.

To perform numerical simulations tests along different stress paths, the deformation of the periodic cell is controlled by specifying the grid strain rate tensor,  $\dot{\epsilon}_{ij}$ . The indexes  $i, j = 1, 2, 3$  correspond to the Cartesian coordinate axes  $x, y, z$ , respectively.

During the simulation, the position boundaries in the  $x, y$  and  $z$  planes are varied according to the strain rate specified by  $\dot{\epsilon}_{ij}$ , while the boundaries in the  $x = y = z = 0$  planes remain stationary. Specifying appropriate values for the grid velocity allows to perform any strain-controlled stress path. A typical example of idealised periodic cell deformation is shown in Figure 5.3

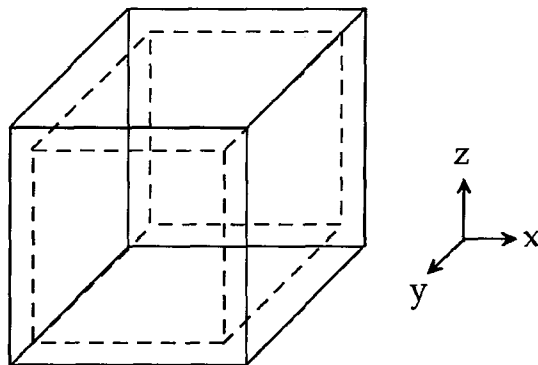


Figure 5.3: Typical deformation during isotropic compression - normal loading

In Figure 5.3, the case of isotropic compression, the strain rate tensor is given by (considering compressive strains to be positive):

$$\dot{\epsilon}_{ij} = \begin{bmatrix} 1 & 0 & 0 \\ 0 & 1 & 0 \\ 0 & 0 & 1 \end{bmatrix} \quad (5.3)$$

## 5. Code development and its validation

---

During a simulation, the limits of the periodic cell are adjusted according to the strain rate tensor,  $\dot{\epsilon}_{ij}$ . For example, in the  $x$ -direction, the deformation of the periodic cell in a given time increment,  $\Delta t$ , is given by

$$\Delta x_{max} = \dot{\epsilon}_{11} \cdot x_{max} \cdot \Delta t \quad (5.4)$$

where  $\dot{\epsilon}_{11}$  is the strain rate in the  $x$ -direction. Similar definitions are formulated for each direction of the three dimensional space.

For stress-controlled stress paths, the grid strain rate is modified according to a servo-control algorithm that ensures that the stress specified by the user is maintained within the assembly. Then the strain rate  $\dot{\epsilon}_{ij}$  is given by

$$\dot{\epsilon}_{ij} = \dot{\epsilon}_{ij}^{user} + \dot{\epsilon}_{ij}^{serv} \quad (5.5)$$

where  $\dot{\epsilon}_{ij}^{user}$  is the user specified strain rate tensor, and  $\dot{\epsilon}_{ij}^{serv}$  is a servo-controlled strain rate calculated to satisfy stress requirements. In a given time increment the servo-controlled strain rate is adjusted. The servo-controlled strain rate is calculated as:

$$\dot{\epsilon}_{ij}^{serv} = \dot{\epsilon}_{ij}^{serv} - g (\sigma_{ij}^{req} - \sigma_{ij}^{meas}) \quad (5.6)$$

where  $\sigma_{ij}^{req}$  is the required stress,  $\sigma_{ij}^{meas}$  is the measured stress inside the representative volume element and  $g$  is a user-specified gain parameter. In this way, if strain-controlled tests are simulated, the term  $\dot{\epsilon}_{ij}^{serv}$  is equal to zero.

As one of the objectives of the periodic boundaries is to introduce a uniform strain field, the particles in the assembly must move according to the grid velocity as if they were part of a continuum. This particle movement due to the grid velocity modifies the inter-particle contact forces, in turn producing new particle displacements. Particle movement in a periodic cell simulation is then the result of two interacting movements. Firstly, particles interact with each other by changing, creating and destroying contacts, and consequently, producing additional displacements. Additionally, the strain rate tensor governs the movement of the particles. For example in the  $x$ -direction, the coordinate change  $\Delta x_i$ , for a particle  $i$ , during a time step equal to  $\Delta t$  is:

$$\Delta x_i = \dot{\epsilon}_{11} \cdot x_i \cdot \Delta t + v_i^{t+\Delta t} \Delta t \quad (5.7)$$

where  $x_i$  are the coordinates of the sphere centroids and  $v_i$  is the resultant velocity obtained from the interaction between particles. Clearly, the overall movement of a particle in any time step is the sum of the strain rate movement and the movement calculated from the resultant force acting on the particle.

### 5.3.3 Code validation

There are several ways to validate a DEM code. Amongst them are qualitative, experimental and analytical validations. An analytical validation is very important as the validation of numerical calculations using experimental measurements can be affected by boundary effects and differences in particle geometry (O'Sullivan 2002). O'Sullivan et al. (2003a) highlighted the importance of analytical validation in addition to comparison with experimental measurements.

Close-packed regular arrays of uniform rigid spheres are commonly studied as their strain-increment and stress tensors at failure can be analytically found. Consequently, they have been used for the validation of DEM codes (e.g. Cundall & Strack 1979b).

A particular type of lattice type assembly is the face-centered cubic (FCC) arrangement as depicted in Figure 5.4. This type of particle arrangement has been studied by many researchers (e.g. Rennie 1959, Parkin 1965). Of particular interest is the study by Thornton (1979) that considered a failure mechanism resulting from gap formation along two sets of rows of contiguous spheres perpendicular to each other.

The initial contact points (P, Q, R, S, T and U) for a typical sphere within a FCC assembly are shown in Figure 5.5. Note that each contact in Figure 5.5 is matched on a contact located diametrically opposite it. Consequently, a typical sphere within a FCC assembly has a total of 12 contact points. For the failure mechanism considered by Thornton (1979), failure results in the formation of gaps at contacts T and/or U. Therefore, at failure 4 (or 2) contacts are lost in each of the spheres within the assembly.

In order to calculate the average stress tensor at failure for the FCC assembly, the strain-increment tensor associated with the failure mechanism is required. This strain-increment tensor was obtained by Parkin (1965) and it corresponds to:

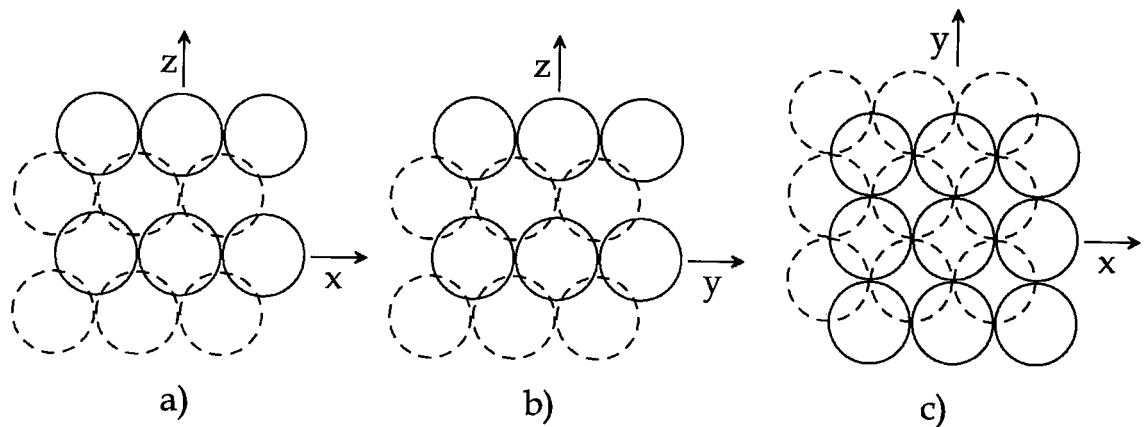


Figure 5.4: The FCC array: a) view along  $y$  axis; b) view along  $x$  axis; c) view along  $z$  axis

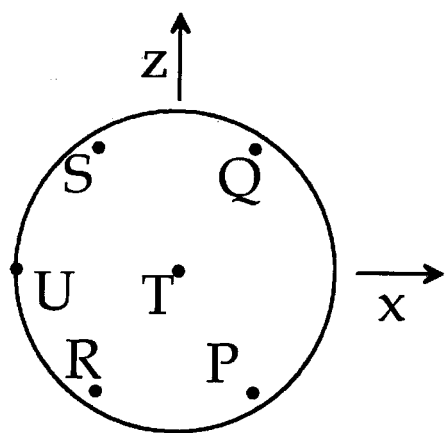


Figure 5.5: Inter-particle contact points for a typical sphere within a FCC assembly (after Thornton 1979)

$$S = \begin{bmatrix} d\epsilon_{xx} & d\epsilon_{xy} & d\epsilon_{xz} \\ d\epsilon_{yx} & d\epsilon_{yy} & d\epsilon_{yz} \\ d\epsilon_{zx} & d\epsilon_{zy} & d\epsilon_{zz} \end{bmatrix} = \begin{bmatrix} -2a & 0 & 0 \\ 0 & -2b & 0 \\ 0 & 0 & (a+b) \end{bmatrix} \quad (5.8)$$

where  $a + b = 1$ . The term  $(a + b)$  is equivalent to a unit strain-increment in the  $z$ -direction, which as a result of the packing geometry, is the direction of the major principal strain-increment at failure. The values of  $a$  and  $b$  therefore indicate the ratio of the other two principal strain-increments. In this way, under standard triaxial conditions where  $\sigma'_2 = \sigma'_3$  we would have a strain increment tensor where  $a = b = 0.5$ .

Each of the contact points  $P, Q, R, S, T$  and  $U$  is associated with a contact force  $p, q, r, s, t$  and  $u$ . Additionally, these forces are composed of a tangential and a normal component. The stress tensor at failure for the failure mechanism analysed by Thornton (1979) is found by calculating the contribution of the normal and tangential forces to the stress tensor. The contribution of these forces to the average stress tensor is obtained by multiplying the orthogonal components of these forces by the coordinates of their contact points. The calculation of these contributions involves the strain increment tensor indicated above.

In the case of triaxial compression ( $0 \leq a \leq 1, t = u = 0$ ) as derived by Parkin (1965) there are no forces at the T and U contacts. Note that this triaxial compression range includes the range of true triaxial conditions where  $\sigma'_2 \neq \sigma'_3$  and therefore  $a \neq b$ . The average stress tensor for this condition within a typical sphere of the FCC assembly is a multiple of

$$\begin{bmatrix} 1 - 2af/F & \tau_{xy} & \tau_{xz} \\ \tau_{yx} & 1 - 2bf/F & \tau_{yz} \\ \tau_{zx} & \tau_{zy} & 2 + 2(a+b)f/F \end{bmatrix} \quad (5.9)$$

where  $f = \mu n$ ,  $F = \sqrt{3a^2/2 + ab + 3b^2/2}$  and  $n$  is the smallest of the contact forces at contacts P, Q, R and S. Those forces can be calculated as:

$$p = 1 - \tau_{yx} + \tau_{zx}/\sqrt{2} - \tau_{zy}/\sqrt{2} \quad (5.10)$$

$$q = 1 - \tau_{yx} - \tau_{zx}/\sqrt{2} + \tau_{zy}/\sqrt{2} \quad (5.11)$$

$$r = 1 + \tau_{yx} - \tau_{zx}/\sqrt{2} - \tau_{zy}/\sqrt{2} \quad (5.12)$$

$$s = 1 + \tau_{yx} + \tau_{zx}/\sqrt{2} + \tau_{zy}/\sqrt{2} \quad (5.13)$$

Since triaxial conditions are considered here, all the shear stress components in the equations are 0 ( $n = 1$ ). Consequently, all the contact forces are equal and  $f = \mu$ .

Note that triaxial compression and plain strain conditions in these studies refer to situations in which the major principal stress direction remains in the vertical direction, therefore, they are denominated as irrotational cases. For plane strain conditions ( $b = 0$  (or  $a = 0$ ),  $t \geq 0$ ), the average stress tensor at failure is given by Rennie (1959).

$$\begin{bmatrix} 1 - 2f/F & \tau_{xy} & \tau_{xz} \\ \tau_{yx} & 1 + t & \tau_{yz} \\ \tau_{zx} & \tau_{zy} & 2 + 2f/F \end{bmatrix} \quad (5.14)$$

where  $F = \sqrt{3/2}$ . For this mechanism, Rennie (1959) stated that such a stress tensor is only valid for small values of inter-particle friction. However he did not mention what value is considered to be “small”.

In these “irrotational” conditions, the strain-increment orientations necessarily coincide with the stress increment orientation. This is because the shear stress components are zero, therefore the components of the average stress tensor at failure correspond to the principal stresses. The principal stress ratios at failure found from Equations 5.9 and 5.14 are of particular interest for validation purposes.

The evolution of the major and minor principal stress ratios for the irrotational case for different values of the coefficient of inter-particle friction  $\mu$  can be obtained varying the values of  $a$ ,  $b$  and  $\mu$  in Equations 5.9 and 5.14. This is illustrated in Figure 5.6. As it can be seen for the failure mode under consideration, the strength is unaffected by the intermediate principal stress under plain strain conditions. Additionally, a higher shear strength is observed for higher values of coefficient of inter-particle friction, a fact that has been observed in many DEM simulations as discussed in the previous chapter.

Since the analytical stress ratios that should be expected for the failure of a FCC assembly of spheres are known, the results of DEM simulations using the DEM code can be contrasted to the analytical solution in order to validate the code performance. An extensive series of DEM simulations was performed with that purpose.

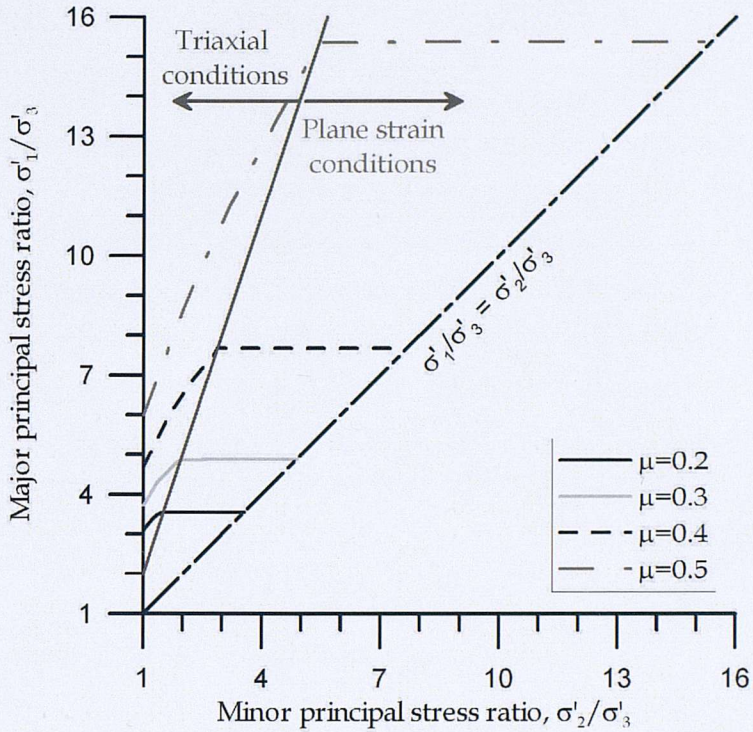


Figure 5.6: Stress ratios at failure for a FCC assembly for different values of the coefficient of inter-particle friction

Different stress conditions, coefficients of inter-particle friction and particle densities were considered. Table 5.1 summarizes the input parameters for these simulations.

Simulations were performed using an assembly of 2600 spherical particles with a radius of 0.75 mm. The FCC geometry of the assembly is schematically presented in Figure 5.4. Therefore rows of  $10 \times 10$  particles in plan view and 26 rows in height were used. Simulations were performed to replicate standard triaxial, true triaxial and plane strain conditions. For each of these shearing modes, the assemblies were first isotropically compressed to attain a specific confining stress, and a range of stress levels was considered as indicated in Table 5.1. Subsequent to this

Description	Parameter	Input value
Particle density	$\rho$	$2.56 \times 10^{-4}$ to $2.56 \times 10^{-8} \text{ kg/mm}^3$
Poisson's ratio	$\nu$	0.22
Shear modulus	$G$	28688 N/mm <sup>2</sup>
Inter-particle friction	$\mu$	0.2-0.5
Confinement stress	$\sigma_c$	25 - 800 kPa

Table 5.1: Summary of input parameters for simulations on FCC assemblies

consolidation process, the assemblies were sheared along the different stress paths.

For standard triaxial conditions the specimens were sheared in the vertical direction under strain control while the horizontal stresses were kept constant and equal. True triaxial simulations were performed in a similar manner, but the two horizontal stresses differed. Similarly, in the plane strain compression, the minor horizontal stress was kept constant, the deformation in the other horizontal direction remained as zero, and the specimen was sheared under strain controlled conditions in the vertical direction. All simulations were carried out until a peak stress state could be easily identified from the stress-strain curves. Once the peak is identified, the stress ratios can be calculated and compared with the theoretical values calculated analytically.

### **DEM results for triaxial conditions**

Figure 5.7 shows the results of a typical triaxial simulation with a coefficient of inter-particle friction of 0.3 and a constant (horizontal) confining isotropic stress of 200 kPa. The peak stress is easily identifiable and there is a sudden drop in the coordination number from 12 contacts to 8 contacts per particle once this peak stress state is mobilised. This reduction of the coordination number by 4 is expected, because as the analytical solution predicts, gaps are formed at the T and U contacts (4 in total) under triaxial compression conditions. Further confirmation that the failure mechanism is as expected is obtained by considering the changes in the specimen's normal contact force network. Figure 5.8 illustrates the plan (*XY*) and lateral (*ZX*) views of a section of the simulated FCC assembly. The state of the contact force network is presented at the initial state (after isotropic consolidation) and at the failure state. In Figure 5.8 the contact force networks are drawn by connecting the centroids of each particle in contact. It is clear then, that prior to shearing each sphere has the 12 contact points expected. Furthermore, it is evident that under triaxial conditions the contacts at the T and U contact points were lost at the moment of failure. The loss of these contacts is easily identified from Figure 5.8 since they correspond to the force chains parallel to the *x* and *y* axes.

### **DEM results for plane strain conditions**

A typical stress-strain response for a plane strain simulation is presented in Figure 5.9. In this case, the coefficient of inter-particle friction is 0.3 and there is a confining

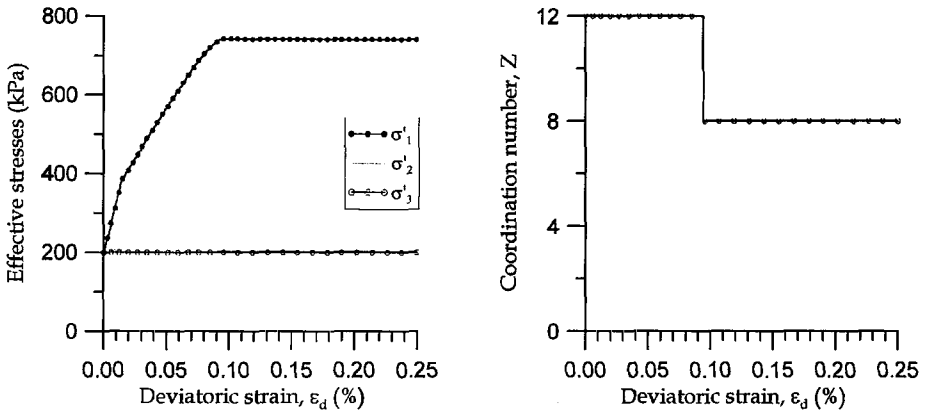


Figure 5.7: Results from a DEM simulation of a FCC specimen under triaxial loading conditions

stress of 200 kPa in the  $x$ -direction. The constraint imposed in the deformation in the  $y$ -direction (inhibiting dilation) produces an increase in the intermediate principal stress during shearing. A sudden drop in the coordination number by 2 is observed. This loss of contacts does not however coincide with the maximum point for the mobilised peak axial stress. The two contacts that are lost correspond to the U contacts in Figure 5.5, as illustrated in Figure 5.10, where it is seen that all the contacts lost at the failure state are located in the  $x$ -direction.

### Comparison of DEM simulations and theoretical strength

The stress ratios at failure from some of the DEM simulations performed in this extensive series are compared with the analytical peak stress ratios in Figure 5.11. Note that standard triaxial ( $\sigma'_2 = \sigma'_3$ ), true triaxial ( $\sigma'_2 \neq \sigma'_3$ ) and plane strain loading conditions are included in the comparison. The agreement between the DEM results and the theoretical values is very good.

From Figure 5.11, it seems to be a slightly higher difference in the results at higher values of coefficient of inter-particle friction, especially under plane strain conditions. These differences might be caused by the fact mentioned by Rennie (1959) that the stress ratios analytically derived may not be the most accurate for higher values of inter-particle friction. It is worth nothing however, that the errors here obtained (maximum of 1.1% for triaxial conditions and 3.0% for plane strain conditions), are smaller than those reported in the validation simulations by other researchers (e.g. Itasca 1998, Cundall & Strack 1979b).

It is also observed from Figure 5.11 that the shearing strength of the FCC assemblies,

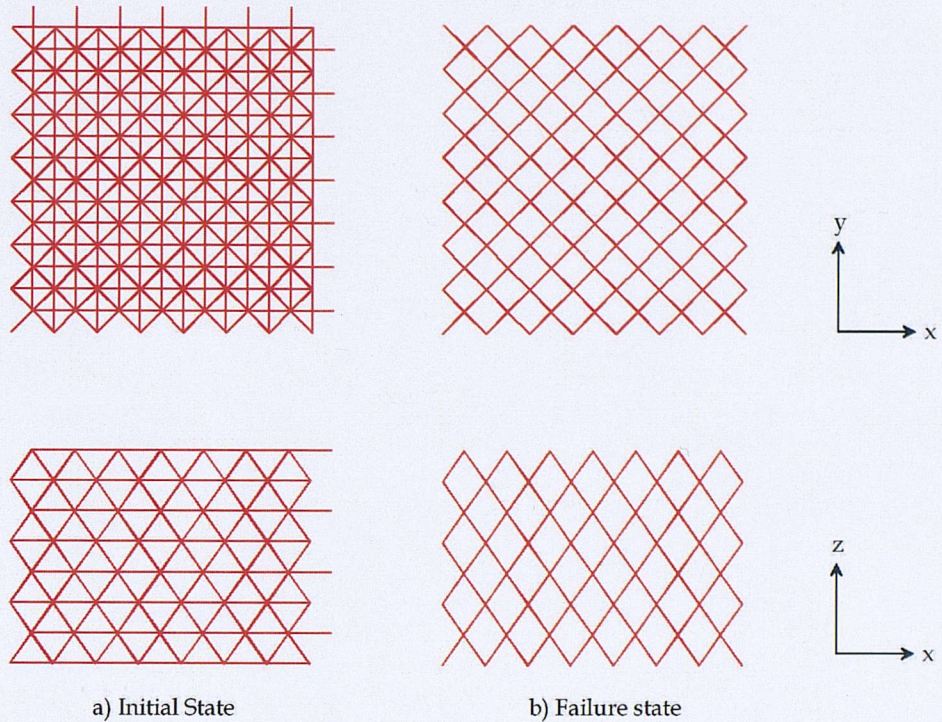


Figure 5.8: Contact force distribution for a DEM simulation of a FCC assembly under triaxial conditions

independently of the loading conditions, is dependent on the coefficient of inter-particle friction. This fact confirms the results of many DEM simulations by others researchers (e.g. Ng 2004*b*, Thornton 2000), as well as the experimental triaxial results presented on Chapter 4 for dry and wet samples. As it is seen in Table 5.1, further DEM simulations were performed to assess the effects of particle density. It was corroborated, that as the analytical theory indicates, the stress ratios were independent of this parameter. The same conclusion was found in terms of the effect of the confinement stress on the stress ratios at failure. Further details of the behaviour of FCC assemblies under different loading conditions are reported by Cummins (2008), who performed some of the simulations presented in this section. His support in this task is greatly acknowledged.

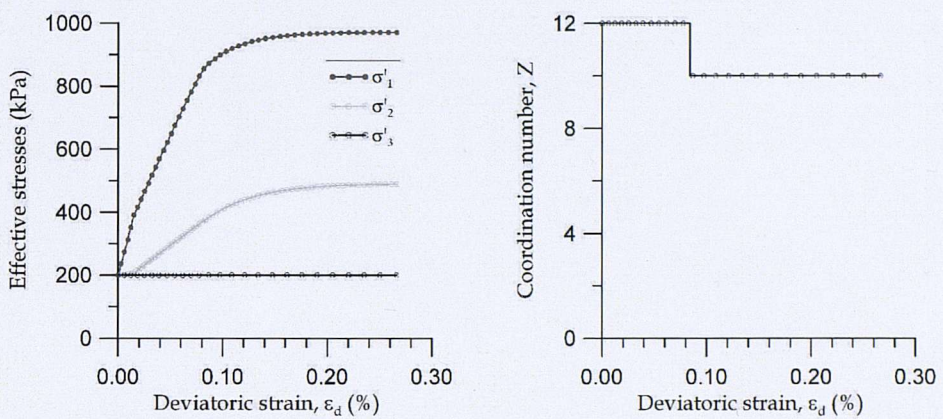


Figure 5.9: Results from a DEM simulation of a FCC specimen under plane strain loading conditions

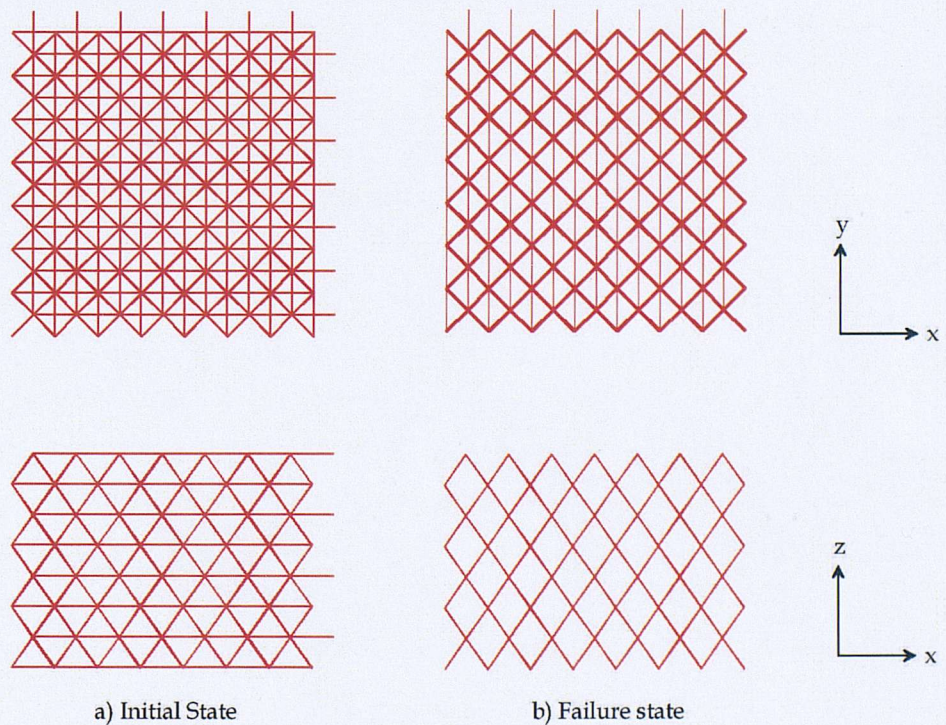


Figure 5.10: Contact force distribution for a DEM simulation of a FCC assembly under plane strain conditions

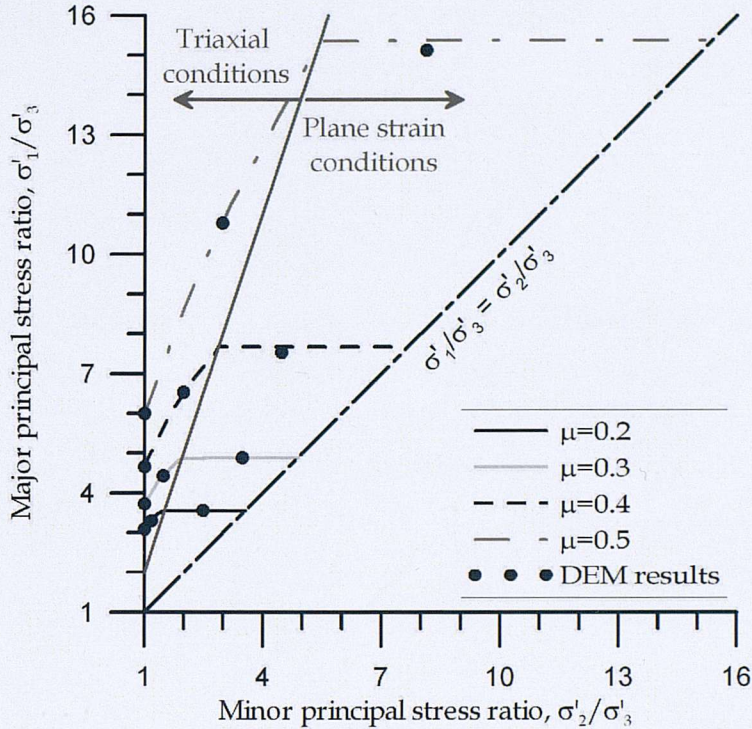


Figure 5.11: Comparison between analytical and numerical results for the shearing of FCC assemblies under triaxial and plane strain conditions

## 5.4 New DEM algorithms for simulations involving principal stress rotation

Conventional periodic cell simulations such as those described in Section 5.3 do not involve principal stress rotation. A completely new algorithm was implemented into the DEM code in order to perform this type of simulations. This new implementation allows simulation of the loading conditions present in the HCA tests presented in Chapter 4. Although most of the calculations performed in periodic cell simulations involving principal stress rotation are the same as those described for normal loading, there are further details that must be taken into consideration. These additional and new requirements are described in this section.

### 5.4.1 Simulation control

Principal stress rotation occurs when a combination of normal and shear stresses are applied. Therefore, in order to perform DEM simulations involving principal stress rotation, a way to have non-zero entries for the off-diagonal terms of the strain rate

tensor ( $\dot{\epsilon}_{ij}$ ) is needed. Conceptually, a strain rate tensor of the form:

$$\dot{\epsilon}_{ij} = \begin{bmatrix} 0 & 0 & 1 \\ 0 & 0 & 0 \\ 1 & 0 & 0 \end{bmatrix} \quad (5.15)$$

would produce a shear deformation as illustrated in Figure 5.12. With this type of loading, the contraction (or expansion) in the vertical direction depends on the response of the material and also in the type of normal load imposed in that direction. A normal stress or deformation constraint can be imposed.

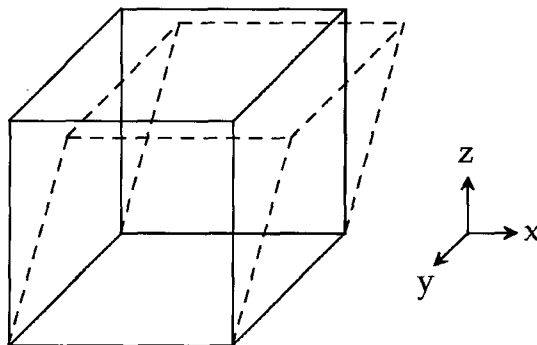


Figure 5.12: Typical deformation during pure shear deformation - loading involving principal stress rotation

Knowing this ideal shear deformation, it is straightforward to specify a strain rate tensor for the deformation of the grid and to update the positions of the particles according to the grid velocity. Considering the  $x$ -direction, and taken into consideration the change due to the grid position only, the change in particle position is calculated as:

$$\Delta x_i = \dot{\epsilon}_{ij} \cdot x_j \cdot \Delta t \quad (5.16)$$

Although the definition of the strain rate tensor and calculation of particle positions are easy, there is challenge with this type of simulation. It is related to the control of the periodic boundaries and the movements of particles across them.

Intuitively, a possible option is to deform the periodic boundaries just as the conceptual deformation illustrated in Figure 5.12. However, referring to Section 5.3.1, if a rectangular grid is used, the grid indices to assign each particle to a bin can be calculated by taking the integer value of the ratio:

$$\frac{x_i}{\Delta x_i^{grid}} \quad (5.17)$$

As the cell deforms, and the cell deviates from its rectangular geometry, this simple mapping becomes complicated. Consequently, a second option is to keep the sheared periodic boundaries (vertical boundaries in Figure 5.12) stationary and keep track of the corner movement at a given time step  $t$  ( $\Delta x_{max}^t$ ) as illustrated in Figure 5.13.

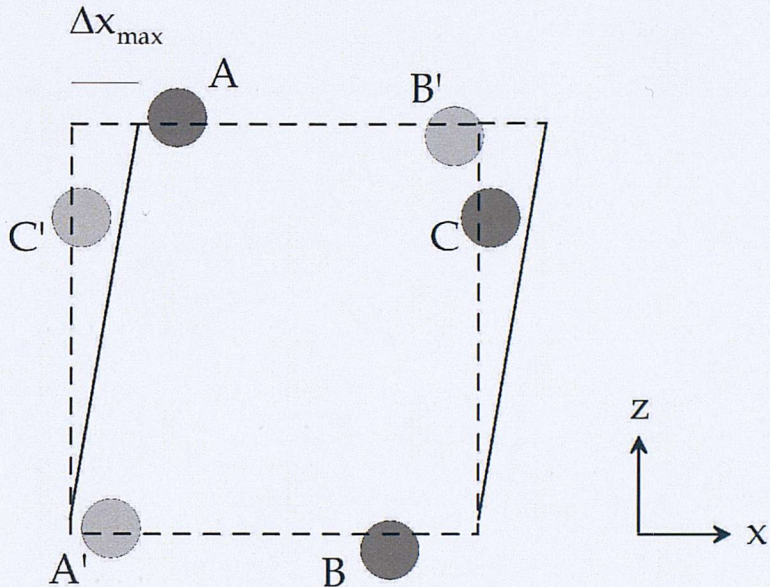


Figure 5.13: Movement of particles that cross sheared boundaries

With this assumption, the mapping rule that assigns each sphere to a bin is simple. Furthermore, it is identical to that used during simulations that use normal loading only (as in Section 5.3). However, care must be taken when considering the movement of particles and calculating inter-particle contacts across boundaries.

Figure 5.13 considers the case of spheres at different positions close to a periodic boundary. The movement of particles protruding from a periodic boundary depends on their position relative to them. Referring to Figure 5.13, the following cases are considered, for ball starting from a position  $(x_i, y_i, z_i)$ :

- If the  $z$  coordinate is bigger than  $z_{max}$  (ball A) the ball is moved to a position  $A' = (x_i - \Delta x_{max}^t, y_i, z_i - z_{max}^t)$ .
- If the  $z$  coordinate of the centroid is less than zero (ball B), the ball is moved to a position  $B' = (x_i + \Delta x_{max}^t, y_i, z_i + z_{max}^t)$  if shearing in the  $XZ$  direction.

- If the  $x$  coordinate is bigger than  $x_{max}^t$ , as ball C, the ball is moved to a position  $C'$  with the same  $y$  and  $z$  coordinates as  $C$  but along the opposite boundary ( $x_i - x_{max}^t$ ). In this particular case it is considered that the ball needs to be moved when it protrudes the vertical boundary, not the inclined (sheared) boundary.

A similar approach is considered when contacts are identified across periodic boundaries. Figure 5.14 shows that the contact distance in the  $x$ -direction is measured relatively to the periodic cell deformation. A contact point between particles A and B is shown. As it can be seen the relative distance,  $x_{rel}$  is the same for both the real and the virtual contact.

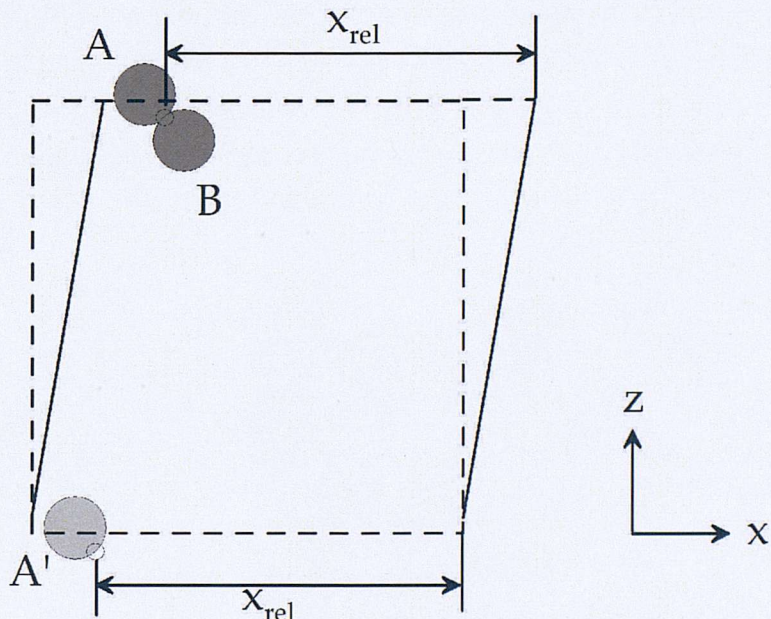


Figure 5.14: Contacts occurring across the horizontal boundaries

### 5.4.2 Contact detection

The principle of testing for contacts with particles located in the currently allocated bin as well as in its immediate neighbours is also used in DEM simulations involving principal stress rotation. However, further checks are required. For example, the particles with higher elevation should experience higher displacements in the  $x$ -direction during shearing in the  $XZ$ -direction (see Figure 5.13). Similar behaviour can be expected if shear deformations are introduced in different directions. As a

consequence, for simulations that present shear deformation, the area of influence in which the presence of inter-particle contacts are tested is bigger than in the case of the normal loading illustrated in Figure 5.2. Hence more bins are included in the contact identification process. This enlarged area of influence increases the computational cost of the simulations, but results in higher confidence in the results.

### 5.4.3 Code validation

The first attempt to validate the new development in the DEM code involved simple shear simulations for assemblies of equal spheres with cubic packing. Although an analytical solution for the failure of this assembly cannot be found, this packing is useful to understand the fundamental behaviour of the periodic cell when a shear deformation is simulated. The initial configuration of a cubic assembly is illustrated in Figure 5.15. It comprises a set of spheres contacting each other at their perpendicular contact points that coincide with the Cartesian axes.

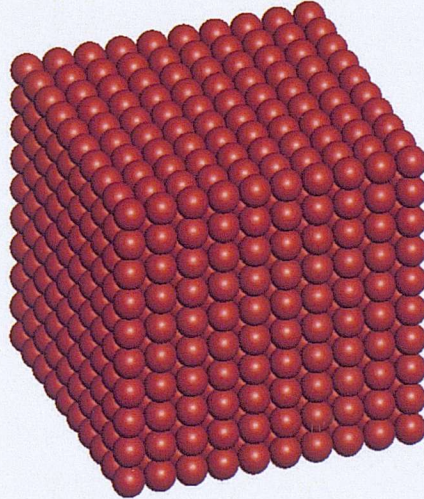


Figure 5.15: Initial arrangement of a cubic assembly of equally sized spheres

A DEM simulation on the assembly represented in Figure 5.15 was performed under simple shear conditions with the aim of assessing the particle displacements during shear. Due to the simplicity of the cubic packing, it is easy to predict how the deformation of the specimen should occur when a simple shear simulation is carried out.

This validation is therefore, entirely qualitative. Figure 5.16 illustrates the initial and deformed states of a cubic assembly when subjected to a shear deformation in the  $XZ$ -direction. The initial periodic cell dimensions were drawn in both diagrams. It can be seen that the specimen deforms as it is expected. If all the particles are considered as part of a continuum, the deformed shape of the single element would be as depicted by the dashed lines in the deformed state.

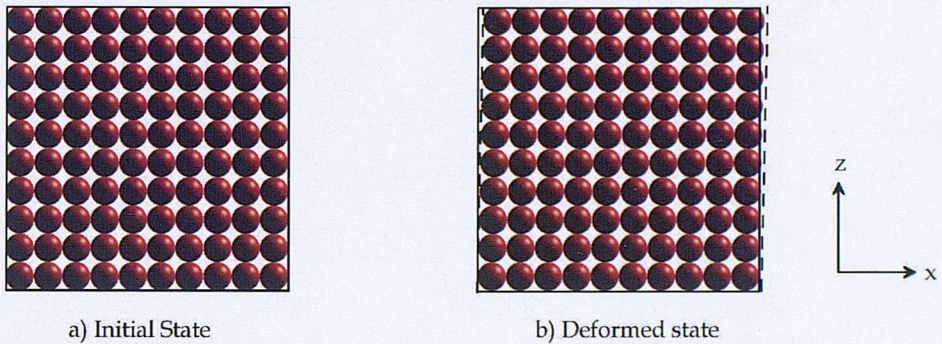


Figure 5.16: Initial and deformed states of a cubic assembly of equally sized spheres under simple shear conditions

Further analyses of the particle displacements for the cubic assembly can be obtained from Figure 5.17. In this figure, the displacements of each particle from the beginning to the end of the simulations are represented by arrows. The view of the  $XY$  plane indicates that all particles move in the  $x$ -direction, maintaining the plane strain condition in the  $y$ -direction. This is also evident in the view of the  $XZ$  plane. Additionally, in the view of the  $XZ$  plane, it can be seen that the particles with higher  $z$  coordinates move more than those with lower  $z$  coordinates. This kind of movement is expected as a result of the application of a shear stress.

An analytical validation can be performed following the study by Thornton (1979). His study considered different degrees of freedom to analyse the failure conditions of FCC assemblies, that is, the possibility of strain-increment and stress increment rotation about one or more axes. Intuitively, it is natural to compare DEM simulations involving stress rotation due to simple shear conditions with his derived solutions. Thornton (1979) considered the possibility of losing the  $T$  and  $U$  contacts as in the triaxial and plane strain conditions discussed above, but varying the shear components of the stress tensor to obtain an optimum solution involving a simple shear mechanism. This involved essentially an eigenvalue analysis. However, as pointed by Parkin (1981), the shear components (more specifically the inter-particle forces) used in the derivation of the stress tensor cannot be varied at will in an eigenvalue analy-

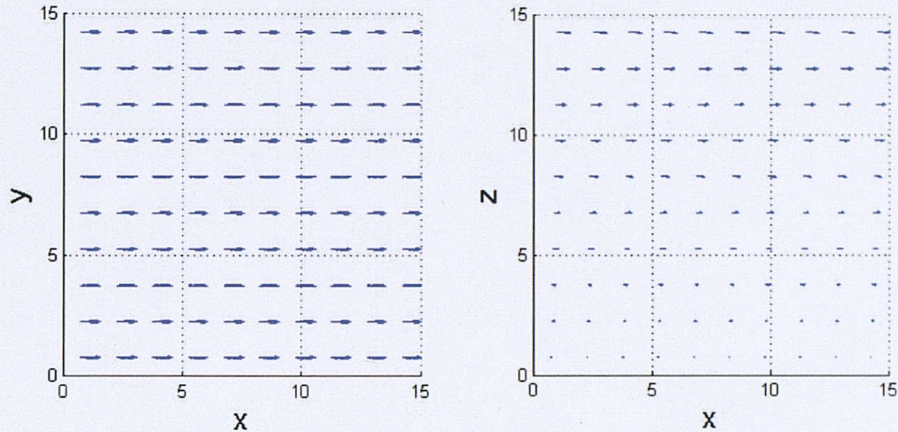


Figure 5.17: Total particle displacements of a cubic assembly of equally sized spheres under simple shear conditions

sis such as that performed by Thornton (1979). This led to a re-examination of the problem and the failure mechanism under simple shear conditions was re-described by Thornton (1981). Furthermore, a stress tensor at failure for such failure condition is not easy to calculate and could not be found in the literature. Consequently, the analytical validation of the simple shear conditions (involving principal stress rotation) is limited to the existence of a characteristic failure mechanism. In contrast to the triaxial and plane strain conditions, the derivation of principal stress ratios during failure for simple shear is non-trivial and cumbersome.

When the stress tensor is rotated about the  $y$  axis (i.e. the  $\tau_{xz}$  and  $\tau_{zx}$  components of the stress tensor are varied), the major principal stress orientations rotate in the  $XZ$ -plane, such as in the HCA tests. Referring to Figure 5.5, as stated by Parkin (1981) and Thornton (1981), the normal forces at the  $P$  and  $S$  contacts will be greater than the normal forces at the  $Q$  and  $R$  ( $p = s > q = r$ ). Under this conditions, separation must occur at the  $Q$  and  $R$  contacts, but not at the  $P$  and  $S$  contacts. Note that in this new failure mechanism the contacts at  $T$  and  $U$  are not lost, therefore the rotational case initially derived by Thornton (1979) is not valid. A schematic representation of this new failure mechanism is illustrated in Figure 5.18.

Considering Figure 5.18, the horizontal networks of contacts (in the  $x$  and  $y$  directions) always exist since the assembly cannot extend or contract in those directions. In the  $y$ -direction plane strain conditions impose that constraint. In the  $x$ -direction the particle displacements are due to the shear deformation only, hence, horizontal lines always have the same length. These horizontal dimensions remain constant

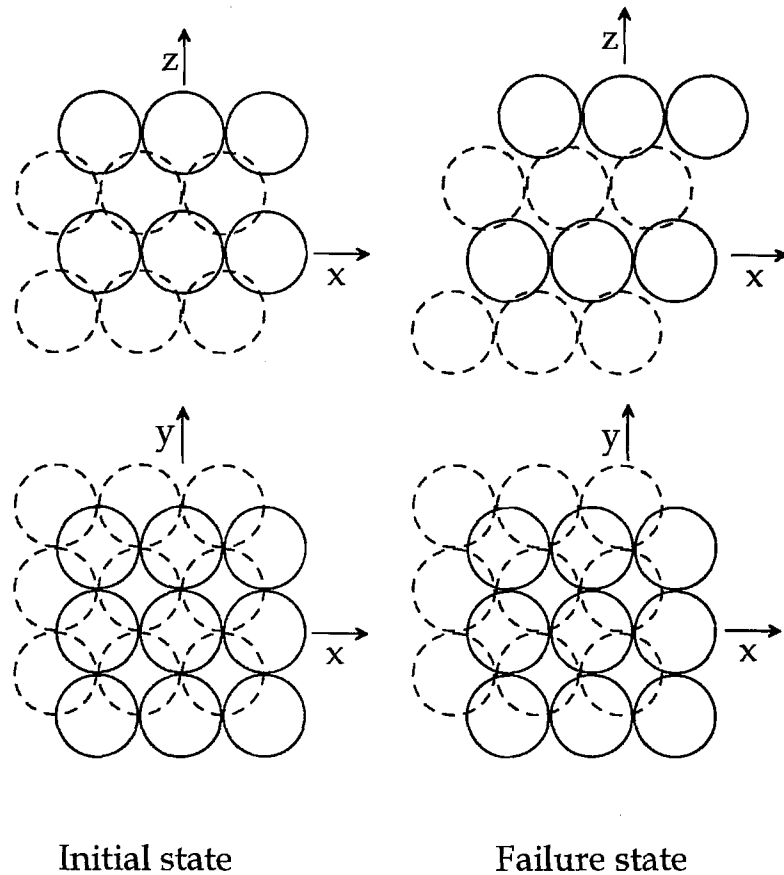


Figure 5.18: Schematic representation of the failure mechanism under simple shear conditions (Shear in the  $XZ$  direction)

independently of the  $z$  position of the particles. Due to that, the particles can only separate at the  $Q$  and  $R$  contacts, producing dilation in the  $z$ -direction.

For validation purposes, a series of DEM simulations involving simple shear conditions was performed. For the simulation results presented in Figure 5.19, an inter-particle friction coefficient of 0.3 was used. During shear, a strain rate tensor including a value for the  $\epsilon_{xz}$  component was defined. Additionally, a vertical stress of 200 kPa was applied to the specimen. This type of simulation replicates an experimental test that is normally carried out in a simple shear device. As it can be seen in Figure 5.19, the deformations in the  $y$  direction were restricted in order to attain plane strain conditions, and furthermore, the deformation in the  $x$ -direction is also zero. This confirms the impossibility of a failure mechanism involving the occurrence of gaps at the  $T$  and  $U$  contacts as initially analysed by Thornton (1979).

Note that the shear stress in Figure 5.19 is negative as it follows the convention defined in Chapter 4. This shear stress is equivalent to the application of torque in

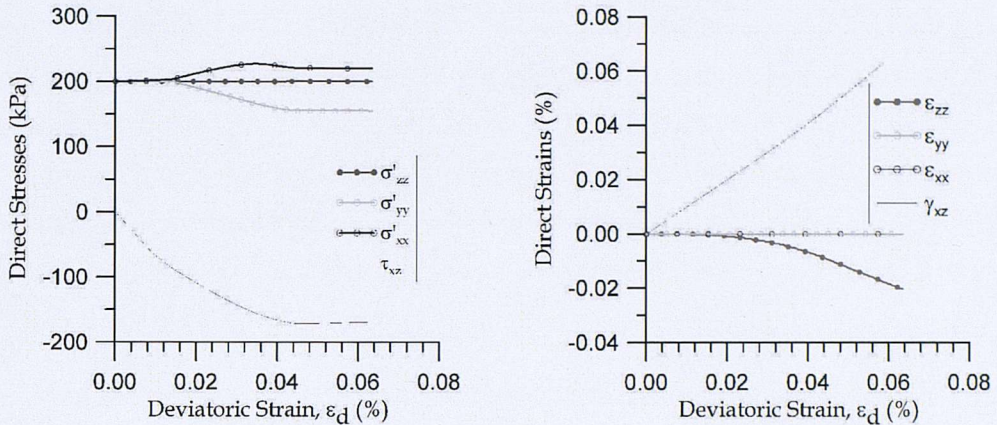


Figure 5.19: Direct stresses and strains for a typical DEM simulation of a FCC assembly under simple shear conditions

the anti-clockwise direction in the HCA tests described in the previous chapter.

The stress-strain data presented in Figure 5.19 includes the output results from a DEM simulation. As in the experiments, direct stresses are applied in the simulation according to the strain rate tensor, and the actual principal stresses and strains are calculated from these values. The calculated principal stresses and the coordination number for the same simulation described above are illustrated in Figure 5.20. It can be observed that the peak strength coincides with the occurrence of the failure mechanism as the coordination number reduces simultaneously with the presence of the maximum principal stress. The presence of the shear stress implies that the major principal stress is rotated approximately 45 degrees with respect to the vertical, although this orientation varies as shearing progresses.

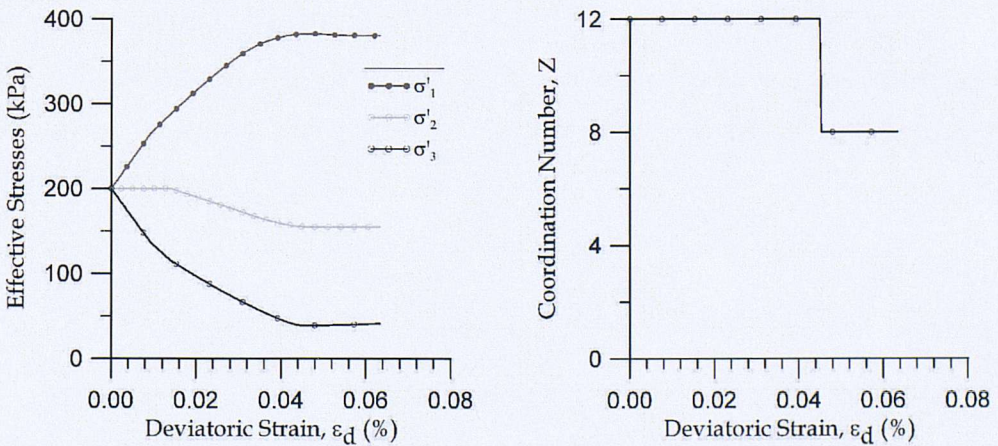


Figure 5.20: Effective stresses and coordination number for a typical DEM simulation of a FCC assembly under simple shear conditions

The nature of the failure mechanism is also confirmed by consideration of the contact force network which is represented in Figure 5.21 for a typical simulation. Clearly, the  $Q$  and  $R$  contacts are lost. As shown in Figure 5.20 the coordination number reduces from 12 to 8, corresponding to the loss of two  $Q$  contacts and two  $R$  contacts, as depicted schematically in Figure 5.18. Note that the  $XY$  plane shows no change in the contact force network because the contacts at  $P$  and  $S$  which still exist have  $x$  and  $y$  components.

These results demonstrate that the failure mechanism explained by Parkin (1981) and Thornton (1981) coincides with that observed in the DEM simulations. It is important to say that one of the reason why the previous research has not considered the derivation of the stress ratios at failure for such a mechanism is because it produces higher stress ratios than other possible mechanisms. The main objective of the works by Rennie (1959), Parkin (1965) and Thornton (1979), was to demonstrate the minimum stress ratios that would produce failure in FCC assemblies. In fact, Parkin (1965) mentioned the possibility of different failure mechanisms considering two broken contacts (different to T and U), and stated that they lead to higher strengths and therefore he did not discuss them. However, it is important to emphasize that the derivation of stress ratios at failure for the failure mechanism including the  $Q$  and  $R$  contacts is non-trivial and as pointed by Parkin (1981) it presents serious difficulties. Consequently, this derivation is considered to be out of the scope of this thesis.

For comparison purposes, considering a coefficient of inter-particle friction of 0.3, the maximum angles of shearing resistance are  $35.1^\circ$  and  $53.6^\circ$ , for the triaxial and simple shear conditions, respectively. This produces a difference of shearing strength of  $18.5^\circ$ . This difference is much higher than that found in the HCA experiments in Chapter 4. However, this can be expected for FCC assemblies as the initial structure is the densest possible packing, and furthermore, the contact normal distribution is extremely anisotropic.

## 5.5 New developments for the control of complex servo-controlled stress paths

Once the procedures that allow control of the periodic cell deformation were developed, it was necessary to implement new servo-controlled algorithms that allow to

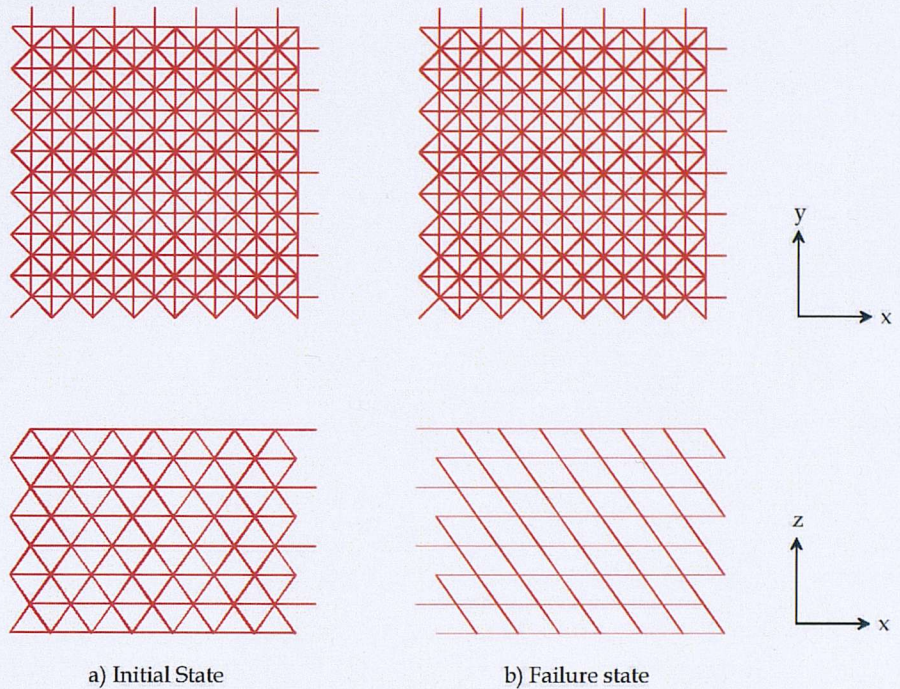


Figure 5.21: Contact force distribution for a DEM simulation of a FCC assembly under simple shear conditions

perform controlled stress paths. The aim was to be able to simulate traditional experimental stress paths such as those tested in the true triaxial and hollow cylinder apparatus but using the newly developed periodic cell.

The approach used to define the servo-control was consistent with that one described in Section 5.3. That is, the strain rate tensor was modified according to Equation 5.6. However, additional requirements were added to this procedure.

### Constant $b$ tests (True triaxial tests)

A constant  $b$  test is normally performed in a true triaxial device and involves normal loading only. As explained in Chapter 2, test samples are sheared under strain control in the vertical direction, while the other two perpendicular stresses are controlled. This control is aimed to keep constant values of  $p'$  and  $b$  during shearing.

The DEM servo-control is established in a similar manner. Referring to Equations 3.19, 3.20 and 3.21, and noting that  $\alpha = 0^\circ$  for constant  $b$  tests sheared in the vertical direction, it is clear that after the Mohr's circle interpretation, the following

equations can be established:

$$\sigma_z = p - t \left( \frac{2b - 1}{3} - \cos 2\alpha \right) \quad (5.18)$$

$$\sigma_y = p - t \left( \frac{2(1 - 2b)}{3} \right) \quad (5.19)$$

$$\sigma_x = p - t \left( \frac{2b - 1}{3} + \cos 2\alpha \right) \quad (5.20)$$

A sequential procedure is followed. A strain increment in the  $z$ -direction while keeping  $p$ ,  $b$  and  $\alpha$  constant produces an increment in the deviatoric stress  $t$  (see Equation 5.18) because  $\sigma_z$  increases. The change in  $\sigma_z$  produced by this strain increment can be easily measured in the DEM simulation. Therefore, a new value for  $t$  can be evaluated. This new value of  $t$  is then used in Equations 5.19 and 5.20 to find the required changes in the  $\sigma_y$  and  $\sigma_x$  stresses. This procedure is performed in each time-step of the DEM simulation, and the strain rate is modified in order to achieve the required stresses. In this way, constant  $b$  stress paths can be performed in DEM simulations.

### HCA tests

The approach to simulate HCA is similar to the one explained before for the true triaxial tests. However, an additional equation is required because the stress rotation that results from the introduction of a shear stress is required. The shear stress  $\tau_{zx}$  is given by the following equation:

$$\tau_{zx} = t \sin 2\alpha \quad (5.21)$$

Experimental HCA tests which involve principal stress rotation, as explained in Chapter 3 are commonly performed by introducing strain control in the applied torque. In the DEM simulation a similar approach is followed. Therefore, an initial shear strain increment is produced, which as a consequence produces an increment in the shear stress ( $\tau_{zx}$ ) in Equation 5.21. As the change in shear stress is measured in the DEM simulation, the change in  $t$  can be found from Equation 5.21. This

new value of  $t$  is used again in Equations 5.18, 5.19 and 5.20 in order to find the required stresses in the normal directions. Once again, this procedure is followed in each time-step to follow complex stress paths.

Note that this approach could also be applied including more complex combinations of normal and shear stresses. The possibilities to simulate any stress path that can be imagined could be easily implemented using the methods and procedures described in this chapter.

## **5.6 Summary**

This chapter has described the details of the numerical implementation of a periodic cell for DEM simulations. An entirely new algorithm was developed in order to perform DEM simulations involving principal stress rotation and additional improvements to the contact detection algorithm were incorporated in the DEM code. These developments make possible to simulate a wider range of stress paths than ever before. Most importantly, the simulations using these new algorithms are free from boundary effects. Hence, they are not affected by the presence of stress and strain non-uniformities.

All the above changes were validated analytically for triaxial, plane strain and simple shear conditions. The results of the validation included DEM simulations with varying input parameters.

New procedures that allow to follow identical stress paths to those experienced in HCA tests were also developed. These procedures involve the combination of different normal and shear stresses. Consequently, their implementation would have been impossible without the new developments proposed in this chapter. This is a new contribution that allows further insight to be gained on the behaviour of granular materials under complex loading conditions. This would not have been possible before. The fact that any stress path can be simulated free from boundary effect is a significant contribution that can enable further studies of the micro-mechanics of granular materials under complex loading conditions.

# Chapter 6

## DEM simulations under normal loading

### 6.1 Introduction

This chapter presents a series of DEM simulations that included normal loading only. Triaxial tests and constant  $b$  tests where  $p'$  is kept constant were simulated. Triaxial simulations and HCA tests where  $\alpha = 0^\circ$  is kept constant are compared with physical experiments carried out using glass ballotini. Both the macro-scale and micro-scale behaviour observed during the simulations are discussed in detail. All the simulations presented in this chapter are performed using periodic boundary conditions. Note that unless specifically stated, all the simulations presented in this chapter are performed using “medium” sized ballotini, which comprises particle diameters between 1.00 and 1.43 mm, as illustrated in Table 3.2.

It was mentioned in Chapter 2 that triaxial extension tests were a special case where  $\alpha = 90^\circ$  and  $b = 1.0$ . Although this is a specific case that can be performed under normal loading, DEM simulations where  $\alpha = 90^\circ$  are not discussed in this chapter. Further discussion of these simulations is presented in Chapter 7 where the influence of principal stress rotation on the behaviour of granular materials is studied.

Parameter	Description	SI	Units
$\nu$	Poisson's Ratio	0.22	-
$G$	Shear Modulus	28.68	GPa
$\rho$	Particle Density	2570	kg/m <sup>3</sup>

Table 6.1: Input Parameters for DEM Simulations

## 6.2 Input parameters

The essential input parameters for DEM simulations were highlighted in Chapter 3 and are presented in Table 6.1 for completeness. Note that in order to achieve resolution from the SI unit was not used in the DEM simulation input files. By adopting the mm as the unit of length the number of significant digits stored to memory was maximised.

In addition, the grain size distribution was discussed with reference to Figure 3.1. As noted in Chapter 3 all these input parameters are derived from physical experiments. Although the sensitivity of the DEM simulations to variations in these input parameters is discussed later in this chapter, it is important to highlight the following:

- In the DEM simulations, particles are simulated as perfect spheres. Although real particles have roundness bigger than 95%, they are not completely spherical.
- The determination of the shear modulus ( $G$ ) and the Poisson's ratio ( $\nu$ ) by Cavarretta (2009) involved curve fitting. It was found that the physical experiments fit the Hertzian contact law only after particle contacts have experienced some plastic deformation of the asperities.
- The experimental determination of the coefficient of friction is non-trivial and its value is inherently variable. The two values of  $\mu$  indicated in Table 6.1 were selected as representative values within the wide range provided by Cavarretta (2009).

The DEM simulations presented in this chapter were carried out using 4000 particles. Simulations with 2000 particles provide the same macro-scale results as the simulations with 4000 and 8000 particles. However, having 2000 particles does not provide a sample that is statistically representative for micro-scale analyses as concluded from analyses on quantification of fabric. In addition, comparing the simulations

## 6. DEM simulations under normal loading

---

Size (mm) $d_{50} = 0.6$ (Small)		Size (mm) $d_{50} = 1.1$ (Medium)		Size (mm) $d_{50} = 2.5$ (Big)	
No. Particles		No. Particles		No. Particles	
0.815	20	1.425	178	3.095	102
0.765	468	1.355	650	3.005	176
0.715	958	1.285	650	2.915	588
0.665	1086	1.215	650	2.820	882
0.615	1324	1.145	776	2.725	824
0.565	138	1.075	836	2.635	632
0.465	6	1.005	260	2.545	456
-	-	-	-	2.455	338

Table 6.2: Grain size distribution for specimens with 4000 particles

with 8000 and 4000 particles, the similarities in response meant that the higher computational cost of the 8000 particle simulations could not be justified.

Having experimentally found the grain size distribution, the input geometry for the simulations was created using seven or eight different sizes matching the previous gradings. In Table 6.2 the particle sizes used for the samples with 4000 particles are shown. This approach to replicate a grain size distribution using 6 different particle diameters was also used by Thornton (2000).

Apart from the physical input parameters, there are a few numerical input parameters that also need to be discussed. As for the physical input, parametric studies were performed to select an adequate value for these parameters and they are presented later in this chapter.

It is important to consider the time step used in the numerical integration. As discussed in Chapter 2, density scaling is not used for any of the simulations here presented. Care has been taken to select the maximum time step to avoid problems of numerical stability which are inherent to any finite difference integration scheme. Additionally, issues related to the contact detection algorithm must be avoided. If the time-step is too big during the simulation, then some contacts may be created and/or destroyed and not taken into account because the algorithm is based on a contact list updated frequently and only takes into account particles that are present in neighboring zones (see Chapter 5). Consequently, using a big time step some particles may come or go inside/outside the neighboring zone and are therefore not included in the contact list. For all simulations presented in this chapter the time step used was always less than 15% of the critical time step. This value is lower than the theoretical maximum recommended by O'Sullivan (2004).

## 6. DEM simulations under normal loading

The maximum strain rate used in the simulations was also selected in order to avoid contact detection issues that could result from a large particle displacement in a single time increment. Furthermore, if the simulations were run too quickly, the response observed would record dynamic stress waves moving through the system, rather than the quasi-static response sought. The maximum value of strain rate that was used in the DEM simulations was chosen after a study assessing the different stress-strain curves produced for different values of strain rate. This ensured that contact detection problems related with large particle displacements could be avoided.

### **6.3 Specimen generation**

The response of granular materials to applied loads and deformations is very sensitive to the material state. This state can be quantified by considering the current stress level and void ratio and relating them to the critical state line (e.g. Been & Jefferies 1985). Recognising this, in conventional experimental work to examine sand response, great care is taken to control specimen void ratio. For example, Vaid & Negussey (1988) and Tatsuoka et al. (1986) discuss various specimen preparation approaches for reconstituted sands. Therefore, if DEM is used to simulate granular material response, special care must be taken to control both the void ratio and the stress state.

There are many techniques to generate dense irregular arrangements of particles for DEM analyses (e.g Han et al. 2005, Bagi 1993, Jodrey & Tory 1985). However, the most common technique is to initially randomly generate a loose assembly of non-contacting particles. The density of the material is then increased either by isotropic compression or by gradually increasing the particle size (radius expansion). In both cases the process can be very tedious and precise control of the state (i.e. both the void ratio and the stress) is not trivial.

In this chapter, DEM simulations in which shearing starts from both isotropic and anisotropic stress states are presented. Consequently, the specimen generation approaches used for both of these cases are presented here. The influence of each of the generation approaches on the material fabric, i.e. coordination number and contact orientations, is also considered.

### 6.3.1 Specimen generation approach for isotropic stress states

Two specimen generation approaches were considered for this thesis: (i) the radial expansion approach and (ii) the isotropic compression approach. Both approaches started with an assembly of particles within a periodical cubical box. In each case the box contained an assembly of non-contacting spheres, generated randomly using the approach proposed by Jodrey & Tory (1985). The initial dimensions of this box were selected by considering the desired initial porosity of the specimen. For the higher porosity specimens a slightly larger initial box size was used in comparison with lower porosity specimens. In any case, the initial porosity must be sufficiently high to give freedom of movement to all the particles.

#### Radial expansion approach

If radial expansion was used, the external boundaries did not change their position, and the diameter of the particles was slowly increased during the DEM simulation. Using this approach, the simultaneous control of confining stress and void ratio was not very easy. Typically, when the required stress was reached, the corresponding required value of void ratio was not attained. On the other hand, the void ratio can only be specified with loss of stress control.

In order to investigate this problem, an additional series of simulations was performed. In these simulations, radial expansion was used until the assemblies achieved a stable state (i.e. when a constant coordination number is attained and there are no significant fluctuations in the measurement of stress), with a confining stress lower than the required stress. From that point, the isotropic compression approach was used to reach the desired value of 200 kPa. With this new methodology, better control of both void ratio and confining stress was achieved. However, the range of void ratios that could be obtained was typically smaller than the range illustrated in Figure 6.1 when the isotropic approach was used. Furthermore, the results were highly dependent on the confining stress reached at the stable state.

#### Isotropic compression approach

In the isotropic compression approach, the periodic boundaries, and hence the particles, were moved inwards at a constant strain rate. As the void ratio reduced and

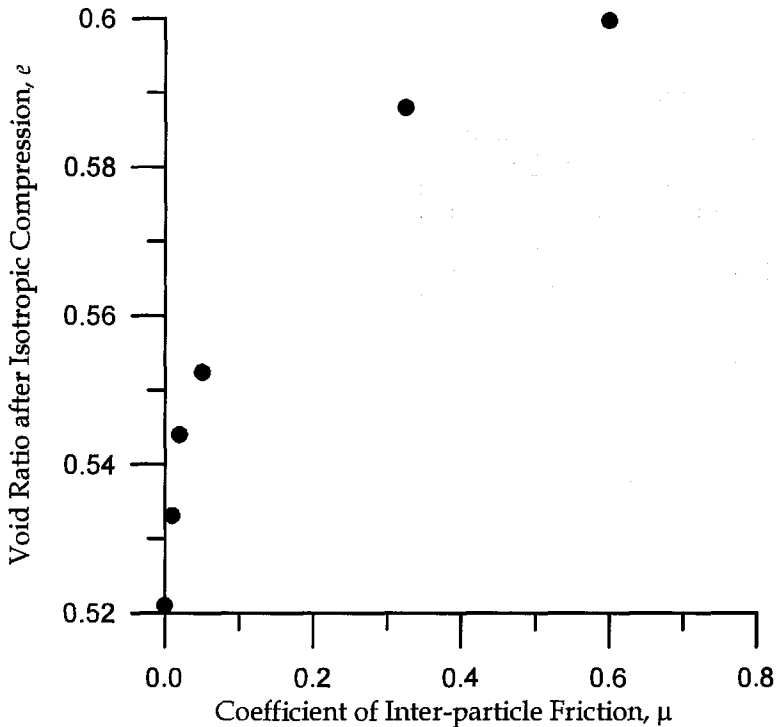


Figure 6.1: Values of initial void ratio after isotropic compression using different inter-particle friction coefficients

inter-particle contacts were created, the stress state could be measured. A servo-control algorithm was used to control the strain rate to monotonically converge to the required confining stress.

Using this approach the final void ratio of the specimen was easily controlled by changing the coefficient of inter-particle friction. The specimen void ratios following isotropic compression to a confining stress of 200 kPa for various inter-particle friction values are illustrated in Figure 6.1. Low values of friction allowed the formation of bigger number of contacts and denser specimens. An example of the initial and final states of a specimen generated using this approach is presented in Figure 6.2.

Note that the numerical void ratio values are consistent with the range found in physical experiments (see Tables 4.1 and 4.2). Furthermore, the stress level coincides with the confining pressure used in both triaxial and HCA tests. This fact gives confidence in the selected input parameters, but also allows direct comparison between simulations and experiments using real stresses and not in terms on stress ratio as used by numerous researchers (e.g. Cui & O'Sullivan 2006).

In order to be able to replicate the physical experiment it is necessary to use a specimen with the same initial void ratio as in the physical experiment. This is

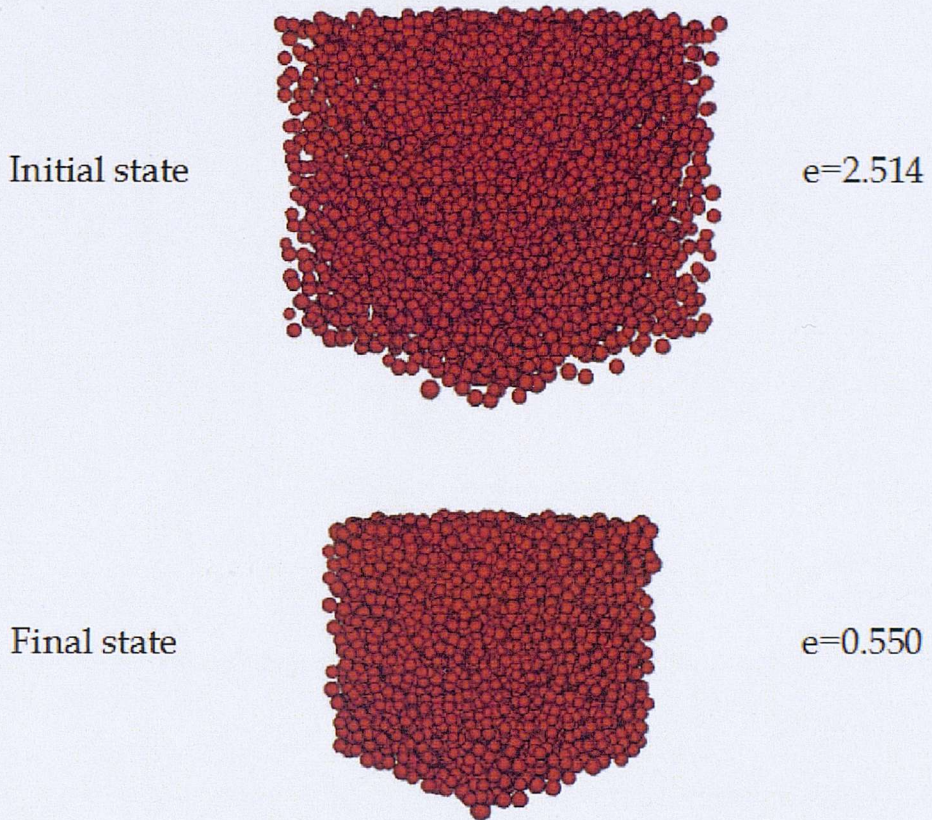


Figure 6.2: Example of a specimen generated with isotropic compression - Initial and final states ( $\mu = 0$ )

easily done using the results shown in Figure 6.1. Simply, the target void ratio is selected from that graph, and then a sample is isotropically compressed using the corresponding value for the coefficient of friction. Prior to shearing, the samples were assigned the same coefficient of inter-particle friction ( $\mu = 0.325$  and  $0.220$ ), chosen to be consistent with the measurements of Cavarretta (2009).

### 6.3.2 Specimen generation approach for anisotropic stress states

In many situations, soil samples are sheared starting from anisotropic stress states. For example, to replicate the HCA tests presented in Chapter 4, the specimen must be consolidated under  $K_0$  conditions prior to shearing. Experimentally, in a triaxial

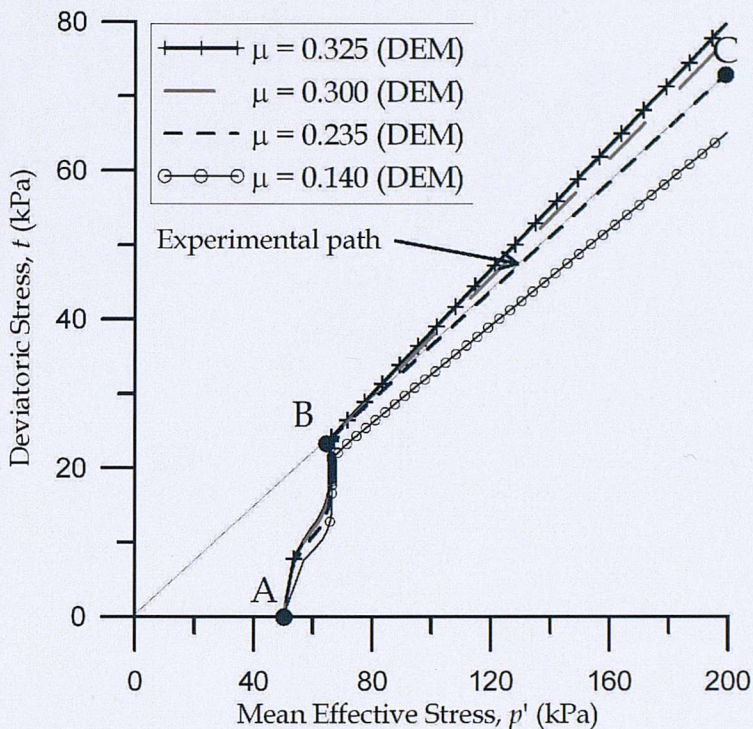


Figure 6.3: Anisotropic consolidation stress paths using different values of inter-particle friction

test, a  $K_0$  consolidation stress path is achieved by successive increments of axial stress and confining stress while maintaining no radial deformation. These increments of stress are relatively easily controlled in the laboratory with the help of a computer servo-control system. However, following a large number of axial stress and confining stress increments in DEM can be time consuming.

As a first attempt, a DEM simulation using the input parameters described in Table 6.1 and a coefficient of inter-particle friction of 0.325, was performed in order to replicate the experimental procedure. Referring to Figure 6.3, the specimen was initially isotropically consolidated to 50 kPa (point A), then the vertical stress was increased in order to reach the  $K_0$  line (point B). In the next step, the radial deformations were kept constant by keeping the vertical periodic boundaries stationary while the vertical strain was increased. Such a simulation gave a deviatoric stress slightly higher than the experimental one (point C). Consequently an iterative procedure using different values for the coefficient of inter-particle ( $\mu$ ) was followed. The required stress state was achieved when  $\mu = 0.235$  as illustrated in Figure 6.3.

It is interesting to note that the ideal  $K_0$  line was achieved using  $\mu = 0.235$ . It should be recommended that the value of  $\mu$  initially selected for the DEM simulations of HCA tests is 0.22. However, if a simulation using  $\mu = 0.22$  was performed,

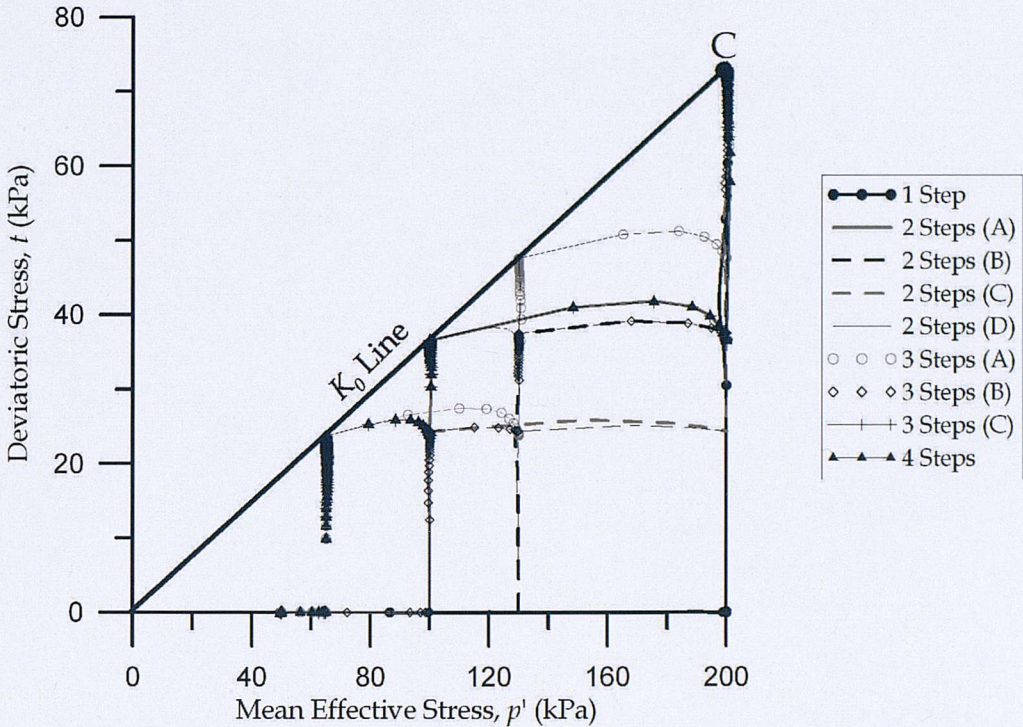


Figure 6.4: Achieving a specific anisotropic stress state with different stress paths

the resultant deviatoric stress level for  $p' = 200$  would be lower than the required ( $t = 72.77$  kPa). That is, a simulation using  $\mu = 0.22$  would appear in Figure 6.3 somewhere in between the simulations with  $\mu = 0.14$  and  $\mu = 0.235$ . As a consequence, a required increase in deviatoric stress would produce smaller radial strains.

Although the procedure for  $K_0$  consolidation described above is possible and successful, it is time consuming (a  $K_0$  consolidation procedure like that could last up to 3 days). Consequently, different consolidation stress paths were followed as illustrated in Figure 6.4 in order to achieve the same anisotropic stress state ( $p' = 200$  kPa,  $t = 72.77$  kPa). Note that for these stress paths a  $\mu$  value of 0.235 was used to provide a consistent comparison.

The aim behind the approach illustrated in Figure 6.4 was to compare the results of all the simulations in order to verify if the specimens could be anisotropically consolidated in a single step (i.e. isotropic compression up to 200 kPa followed by increase in  $t$  to 72.77 kPa). All the simulations were compared in terms of void ratio, coordination number ( $Z$ ) and magnitude of anisotropy ( $a$ ) as defined by Rothenburg & Bathurst (1989) and described in Chapter 2. The results of this comparison indicated maximum differences of 2% for both the coordination number and the magnitude of anisotropy ( $a$ ) for some of the stress paths, with an average

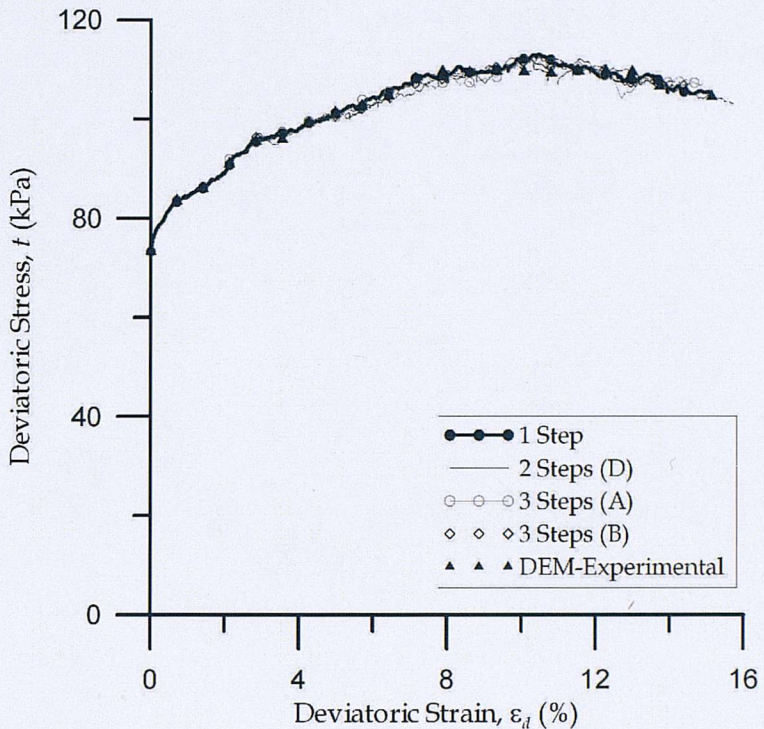


Figure 6.5: Stress-strain response for triaxial compression of anisotropically consolidated specimens using different approaches

of 0.248. The details of the comparison were presented by Barreto et al. (2008).

An extension of the previous study was to subject each of these specimens to triaxial compression in order to assess the effect of these minor differences in the macro- and micro-scale behaviour. The stress-strain response for triaxial simulations using the samples resulting from the anisotropic consolidation described above are shown in Figure 6.5. The specimen resulting from the simulation using  $\mu = 0.235$  in Figure 6.3 is labeled as “DEM-Experimental” in Figure 6.5.

Note that in Figure 6.5 only the stress paths that presented minor deviations in coordination number and magnitude of anisotropy are compared with the “DEM-Experimental” simulation, showing no difference with other simulations and is assumed to be theoretically valid. It is clearly observed that the minor differences in  $Z$  and  $a$  do not influence the subsequent macro-scale response during triaxial compression. Figure 6.6 also illustrates that there is no significant variation in the evolution of  $Z$  with deviatoric strain. Similar conclusions were derived from the development of  $a$ . Based on these results, it was decided that to reduce computational time, all the DEM simulations including  $K_0$  consolidation would be performed using a single step. That is, performing isotropic consolidation to  $p' = 200$  kPa, followed by an increase in  $t$  to 72.77 kPa while keeping  $p'$  constant.

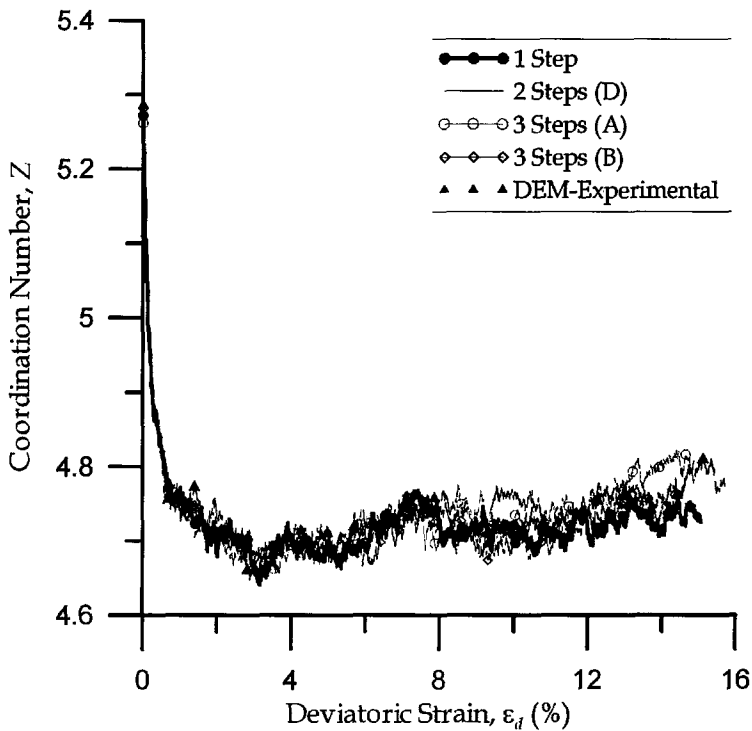


Figure 6.6: Evolution of the coordination number ( $Z$ ) for triaxial compression of anisotropically consolidated specimens using different approaches

## 6.4 Triaxial simulations

In this section the loading of granular materials under triaxial conditions is explored. Physical experiments of drained triaxial tests on glass ballotini are compared with DEM simulations using specimens with identical initial density. Only dry conditions are considered, as the certainty for the dry coefficient of inter-particle friction is bigger than for the wet case. This comparison is done for validation purposes. Once it is demonstrated that the DEM simulations coincide with the experiments, the sensitivity of different input parameters in the response of granular materials is evaluated.

### 6.4.1 Experimental validation

The validation of DEM codes was discussed in Chapter 5 where the importance of analytical validation was highlighted. Another way of validating a DEM code is by comparison with experimental tests on samples of spherical particles with random distributions. This section includes a limited number of conventional triaxial tests on glass ballotini and compares them with DEM simulations on specimens with a

## 6. DEM simulations under normal loading

---

random geometrical distribution of particles, but using the grain size distribution and input parameters described in Table 6.1.

Two physical experiments were performed for this validation. Both tests followed the triaxial testing procedures described in Chapters 3 and 4. The tests differed only in the initial void ratio prior to shearing.

As mentioned before, two values were selected for coefficient of inter-particle friction for glass ballotini. They were 0.220 and 0.325. Note however, that there is slight uncertainty in the experimental determination of the coefficient of inter-particle friction. Cavarretta (2009) highlights that the values for the coefficient of inter-particle friction under dry conditions vary between 0.084 and 0.351, the reported mean for 27 measurements was 0.157 with a standard deviation of 0.071. In conclusion, the first selected value for friction (0.220), although higher than the mean, is below the mean plus a standard deviation. For the case of the submerged (wet) coefficient of inter-particle friction, the number of measurements is only 6 and they vary between 0.079 and 0.284 (mean = 0.133; standard deviation = 0.076).

Recognising this variability, the second value which approaches the maximum limit of values was selected. Note that Cavarretta (2009) also stated that the results are likely to be affected by the humidity conditions where the tests were carried out. This difference however, is not very relevant to the results presented in this thesis since all the experiments that are compared with DEM simulations were performed under dry conditions.

It is important to emphasize that the range of variability for the dry value of inter-particle friction is high. In fact, the maximum value (0.351) is larger than the value of 0.325 selected. Additionally, in some of the simulations presented in this chapter, a  $\mu$  value of 0.14 is used based on the range of measurements suggested by Cavarretta (2009). It is for this reason that a parametric study assessing the effect of the coefficient of inter-particle friction was performed.

Figure 6.7 shows the stress-strain curves for the experiments and DEM simulations used for validation. All the DEM simulations illustrated in the Figure were performed with the same initial void ratio that was measured in the physical experiments prior to shearing ( $e = 0.600$ ). The only difference between simulations is the value of inter-particle friction ( $\mu$ ) assigned to the particles. It is clear that the experimental response is bounded by the values of  $\mu$  used in the simulations. Although the differences between numerical and experimental results are reasonable, it is evident that more confidence in the estimation of the value of  $\mu$  is required in

## 6. DEM simulations under normal loading

order to obtain a better match. It must be emphasized that in the DEM simulations all particles are assigned a unique value of  $\mu$ . This may not be the case in real experiments where this value can vary from sphere to sphere. However, O'Sullivan (2002) stated that 2D DEM simulations using a variable friction were not affected in comparison to simulations using a single value. Consequently, it is more likely that the differences can be attributed to the fact that the particles experimentally tested are not completely spherical, therefore particle geometry effects may be responsible for part of the difference found.

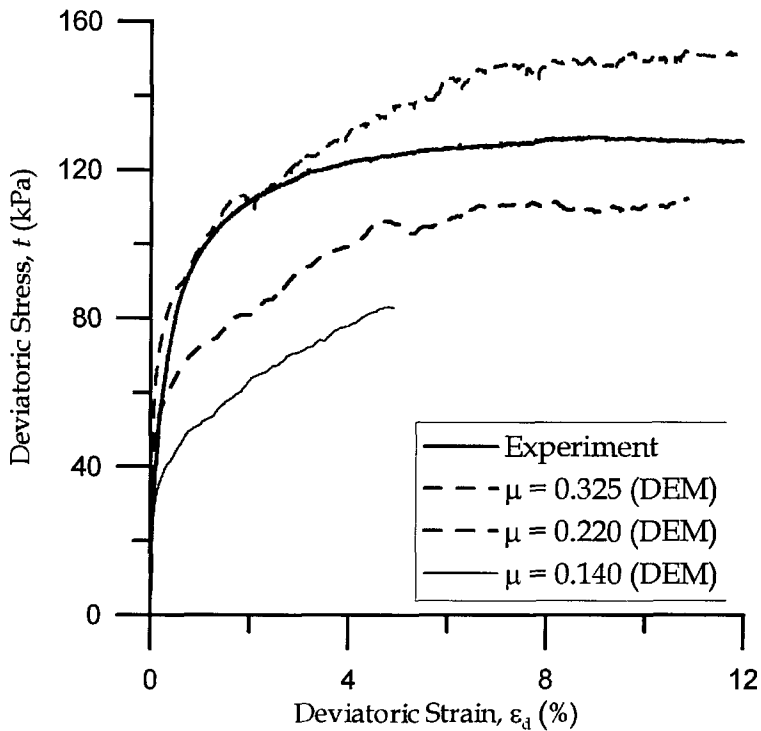


Figure 6.7: Comparison between experimental and numerical results of triaxial tests on glass ballotini - Stress-strain response

One of the advantages of the distinct element method is that it allows assessment of the effect of many parameters using an identical sample. This is impossible to do experimentally. More complex granular materials can include complex particle shapes and contact mechanisms. Consequently, if DEM results are used after fitting experimental to a DEM simulation without experimental measurement of the input parameters, it is not clear how reliable the extrapolation to different loading situations can be. Additionally, conclusions about micro-mechanics are questionable if only experimental tests are used.

Figure 6.8 shows the comparison between experimental tests and DEM simulations in terms of the volumetric response. It is evident that the agreement is not as good as

## 6. DEM simulations under normal loading

---

in terms of the stress-strain curves. The experimental dilation is significantly higher than in the simulations. Note however, that both, experiments and simulations experience a slight initial contraction, coinciding at very small strains, followed by the extensive dilation. The differences at larger deviatoric strain values may be a consequence of the particle geometry. The Hertzian model on the other hand, uses spherical particles and models a single contact point. Hence, the response of the DEM simulations can be stiffer.

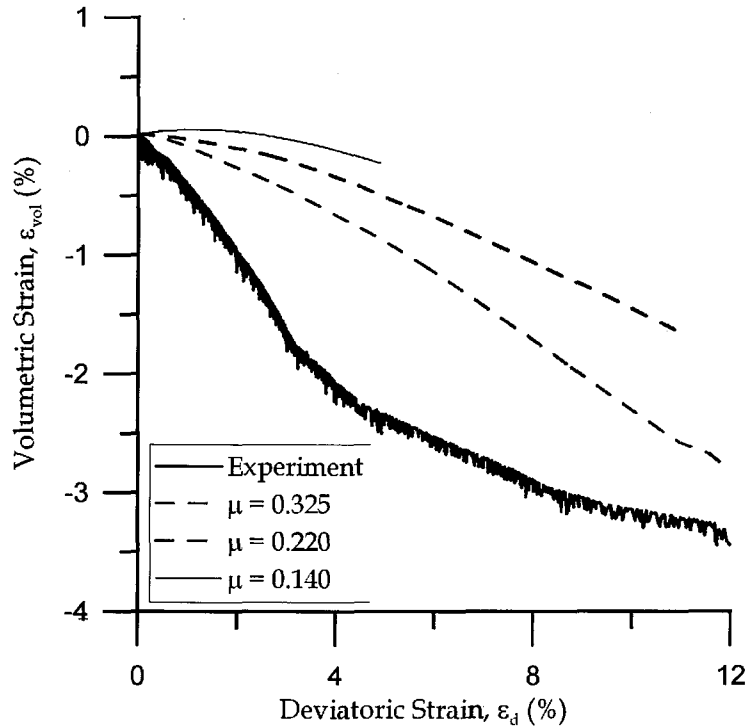


Figure 6.8: Comparison between experimental and numerical results of triaxial tests on glass ballotini - Volumetric response

It must be mentioned however, that the fact that the Hertzian model does not always replicate the volumetric response if the stress-strain curves are matched has been recognized for a long time. In fact, Ko & Scott (1967), without DEM simulations, showed that a modification of Hertz theory is required to explain the volumetric strain of a real granular soil under hydrostatic stresses, so that the numbers appear in reasonable agreement. In addition, experiments performed by Cavarretta (2009) have demonstrated experimentally, that initially the contact response between two particles is very soft, and then it stiffens with a Hertz-like behaviour at higher contact forces.

On the other hand, if the volumetric responses were replicated, a disagreement in the stress-strain curves would possibly appear. It is now believed that the Hertzian

## 6. DEM simulations under normal loading

model can be improved if plastic deformation at the contacts is considered. Other possible reason for the mismatch between experiments and simulations (in terms of volumetric strains) is the subjective assumptions that are often required in the experimental calculation of volumetric strains as described in Chapter 4. Further research is however needed in order to get conclusive results related to this issue.

### **6.4.2 Sensitivity analyses**

Since the DEM simulations have been validated against physical experiments, the influence of different input parameters in the triaxial response can be evaluated. This section includes physical input parameters and numerical input parameters as briefly discussed in Section 6.2.

#### **Effect of the coefficient of inter-particle friction**

Figure 6.7 clearly showed that the coefficient of inter-particle friction has a significant effect on the macro-scale response of granular materials under triaxial compression. Further simulations were performed in order to evaluate the micro-mechanical parameters affecting the macro-scale response. A specimen with an initial void ratio of 0.529 was sheared with varying coefficient of inter-particle friction ( $\mu$ ). The stress-strain response of this set of simulations is presented in Figure 6.9. It must be noted that the simulation with  $\mu = 0.00$  was difficult to perform. As its stress-strain response clearly indicates, the simulation is very unstable and it was very challenging to reach a high value of deviatoric strain.

Nevertheless, it is evident from Figure 6.9 that a higher value of  $\mu$  leads to a higher value of mobilised deviatoric stress, and also a more dilative response. It is interesting to note that although all simulations have the same initial density, the lowest values of  $\mu$  experienced a slight degree of compression at the beginning of shearing, while simulations with the highest values of  $\mu$  experienced a totally dilative response. Also note that the coefficient of friction has an effect on the rate of dilation. High values of  $\mu$  are related to slightly higher rates of dilation in comparison to low friction values.

Figure 6.10a) shows the development of the octahedral stiffness ( $G_{oct}$ ) during shearing for different  $\mu$  values. Figure 6.10b) illustrates how the octahedral stiffness at 0.01% of deviatoric strain changes with an increase in the value of inter-particle

## 6. DEM simulations under normal loading

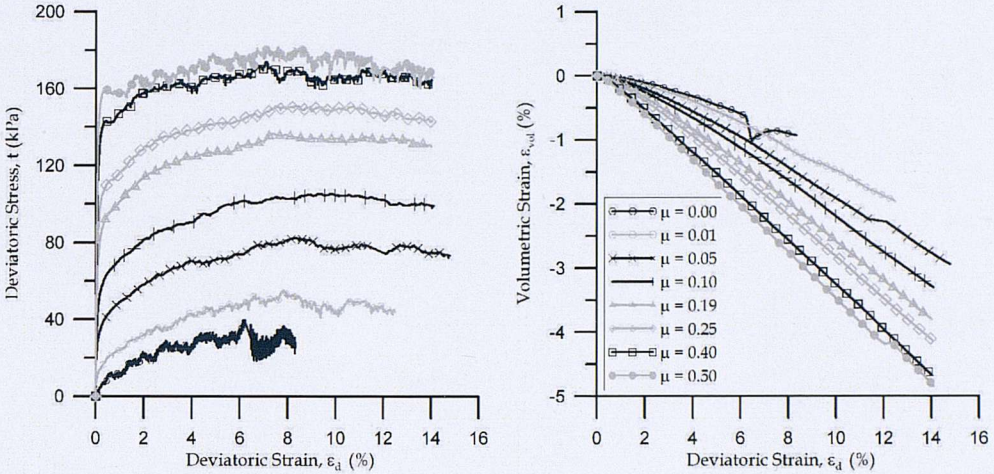


Figure 6.9: Effect of  $\mu$  on triaxial compression - Stress-strain response

friction. The obtained range of initial stiffnesses is very wide and clearly dependant on the value of  $\mu$ . The highest value of  $\mu$  presents the highest stiffness. It is also observed that the higher values of  $\mu$  ( $\geq 0.19$ ) tend to converge to a common value for the maximum shear stiffness at very small strain levels. Note that the simulation with  $\mu = 0.00$  has a limited stiffness and, as illustrated in Figure 6.9, a limited resistance. This result ( $\mu = 0.0$ ) is in disagreement with the results by Thornton (2000), but agrees with results of simulations performed by Ng (2008). It must be emphasized however, that Thornton (2000) also states that his simulations with zero friction were difficult to perform and that his published results represent an average of all his simulations. This may imply that some of his simulations had in fact some reduced resistance.

The results illustrated in Figure 6.10 highlight the significance of the inter-particle friction on the shear stiffness. During shearing with low values of  $\mu$  the material yields in the shear direction at the contact points more easily than when high friction is present. Low values of friction imply that particles start to slide once a lower value of the tangential force is achieved. High values of  $\mu$  evidently imply that a higher tangential force must be achieved for the particles to slide.

Before discussing the evolution of several micro-mechanical parameters during shearing, it is important to illustrate the effect of the coefficient of inter-particle friction on the mobilised angle of shearing resistance at peak. This is represented in Figure 6.11. As expected, the value of  $\phi'_{peak}$  increases with an increasing value of  $\mu$ . Note the similarities between Figure 6.11 and Figure 6.10. These trends coincide with that observed by many researchers in both experimental and numerical studies, but

## 6. DEM simulations under normal loading

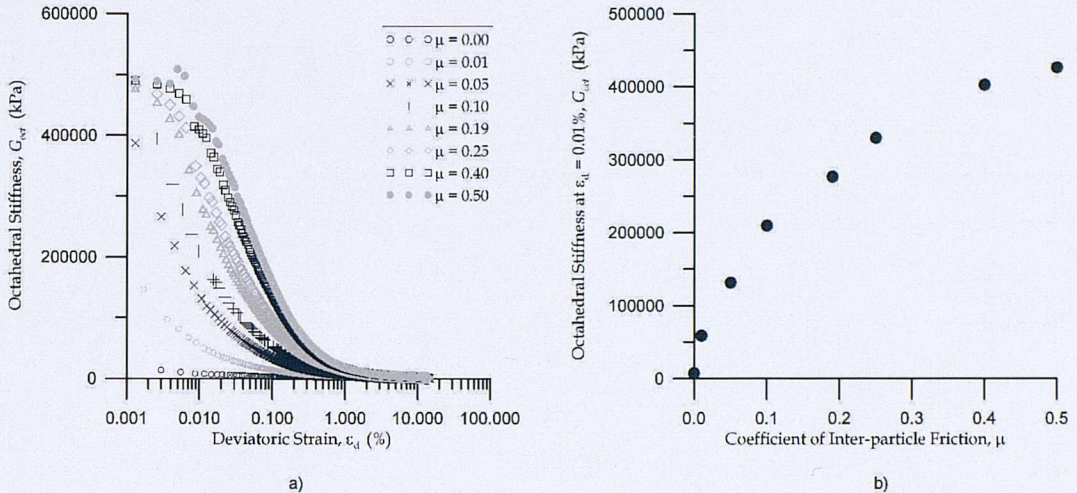


Figure 6.10: Effect of  $\mu$  on triaxial compression - Differences in shear stiffness

as discussed in Chapter 4, disagrees with the experimental studies of Skinner (1974).

In order to gain further insight into the particle-scale interactions underlying the macro-scale behaviour, the evolution of several micro-mechanical parameters during shearing was studied. Figure 6.12 illustrates the evolution of the coordination number ( $Z$ ) during shearing.  $Z$  is a measure of the average number of contacts per particle. It is evident that independently of the value of  $\mu$ , all simulations seem to achieve a constant value of  $Z$  at high values of deviatoric strains. Note that all simulations started from the same initial density, which implies the same number of contacts (as illustrated in Figure 6.12). However, the simulations with lower values of  $\mu$  experience a much smaller change in  $Z$  value over the initial 2% of strain compared to the simulations with higher values of  $\mu$ . Furthermore, the simulations with high values of  $\mu$  seem to reach a constant  $Z$  value at successively larger values of deviatoric strain.

All the observations above coincide with the observations related to the macro-scale behaviour. Comparing Figures 6.9 and 6.12 the greatest change in  $Z$  for the highest  $\mu$  has to be accompanied by the highest dilation, and the lowest volumetric strain is matched with the lowest change in the value of  $Z$ . These results imply that the higher the value of friction, the lower the number of contacts required to achieve a stable configuration of particles. Also note that although it seems to be a constant value of  $Z$ , this does not correspond to a constant value of volumetric strains as observed in Figure 6.9.

Figure 6.13 illustrates two different stages in the contact forces for two DEM simu-

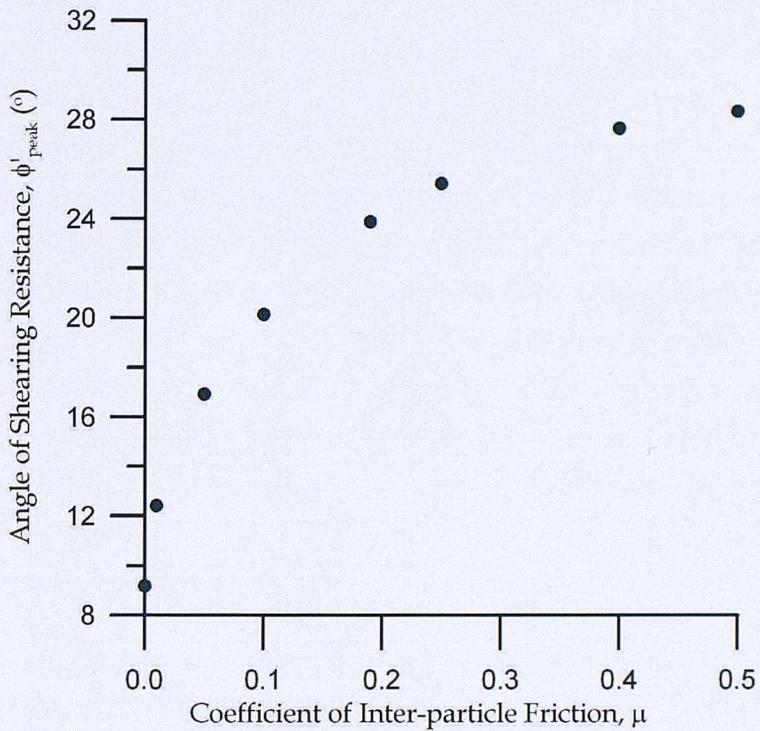


Figure 6.11: Effect of  $\mu$  on  $\phi'$

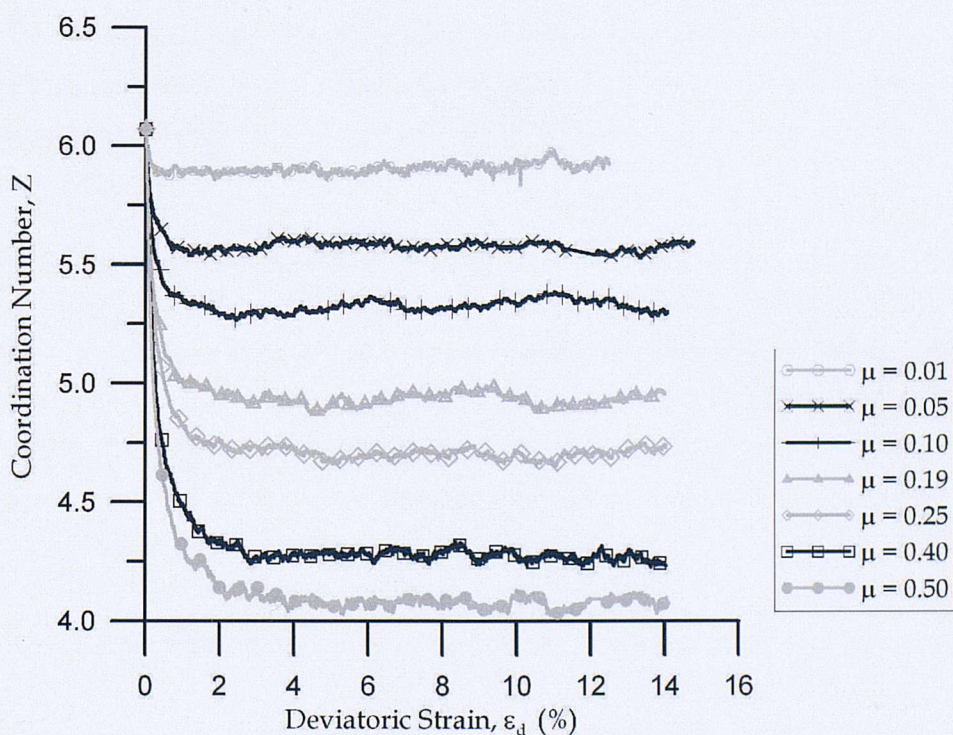


Figure 6.12: Effect of  $\mu$  on triaxial compression - Evolution of  $Z$

## 6. DEM simulations under normal loading

---

lations with different values of  $\mu$ . In these plots, contact normal forces are plotted connecting the centroids of particles in contact. The thickness of the contact force is proportional to its magnitude, the thicker the line, the stronger the force. For clarity in the interpretation of results, only the forces that are bigger than the average magnitude are drawn. In addition, the forces with magnitude bigger than the average plus one standard deviation are plotted in red, while the smaller forces are blue. The plots presented in Figure 6.13 correspond to three-dimensional slices with 3 mm thickness. The location of the slices is given by the coordinates indicated in the lowest part of the Figure. The first row of plots corresponds to the initial state of the specimens which is the same for the two simulations presented in the figure ( $\mu = 0.00$  and  $0.50$ ). The second row of plots includes the slices for the simulation with  $\mu = 0.00$  at the moment when the peak value of shearing resistance was reached, while the third row does the same for the simulation with  $\mu = 0.50$ .

It is evident that for the simulation with  $\mu = 0.50$  there is a greater heterogeneity in the contact force network than for the case with  $\mu = 0.00$ . When  $\mu = 0.50$  there appears to be a small number of highly stressed load chains, while in the  $\mu = 0.00$  case the heterogeneity in contact force is less marked. This is related to the fact that high values of friction experience a high amount of dilation during shearing. Additionally, it is observed that, in comparison to the initial state, the contact forces at the peak state are orientated towards the direction of the major principal stress ( $z$ -direction). This is a fact that is more evident in the simulation with  $\mu = 0.50$ , indicating that this simulation may have developed an internal structure that is more anisotropic.

The difference in anisotropy for these two values of friction is represented using polar histograms in Figure 6.14. These histograms represent the concentration of contact forces in each direction when all contact forces are projected onto the XZ plane. Clearly, at the start of shearing the distribution of contact normals is isotropic as the number of contact normal is approximately equal in all directions. In contrast, at the peak state the simulations with both values of  $\mu$  have an anisotropic distribution. Concentration of forces in the vertical direction is evident for both specimens. Note however that for the simulation using  $\mu = 0.50$  the number of contact forces providing lateral support has been reduced in comparison to the simulation with  $\mu = 0.00$ .

The anisotropy of the different specimens was quantified in order to validate the hypothesis described above. The deviatoric fabric ( $\Phi_d$ ) is calculated as:

## 6. DEM simulations under normal loading

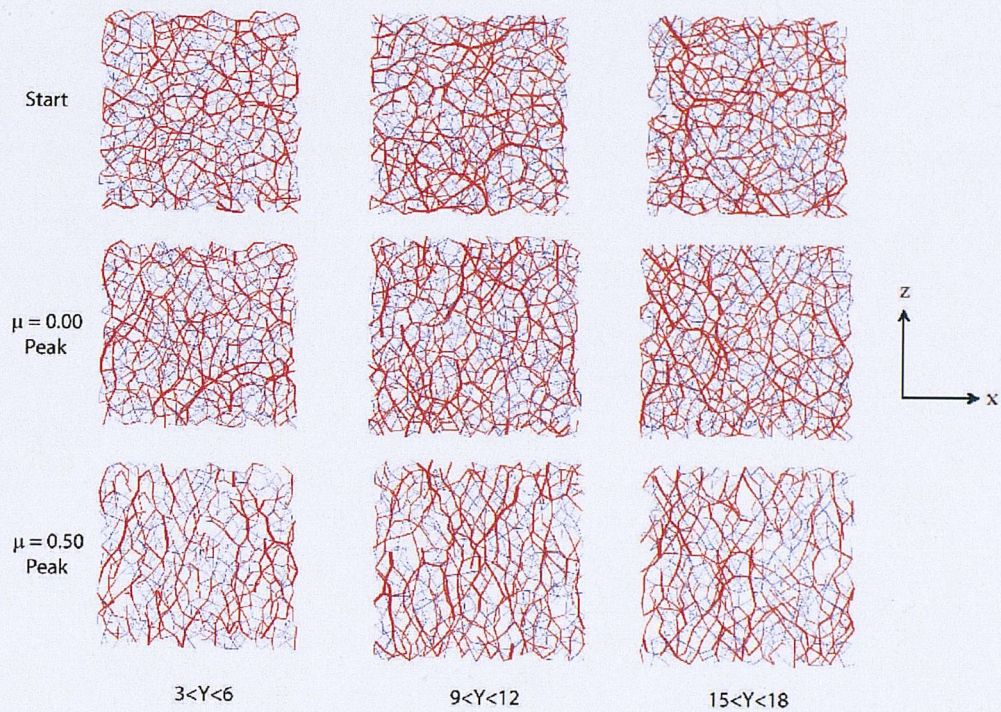


Figure 6.13: Effect of  $\mu$  on triaxial compression - Contact forces for three vertical slices through the DEM specimen

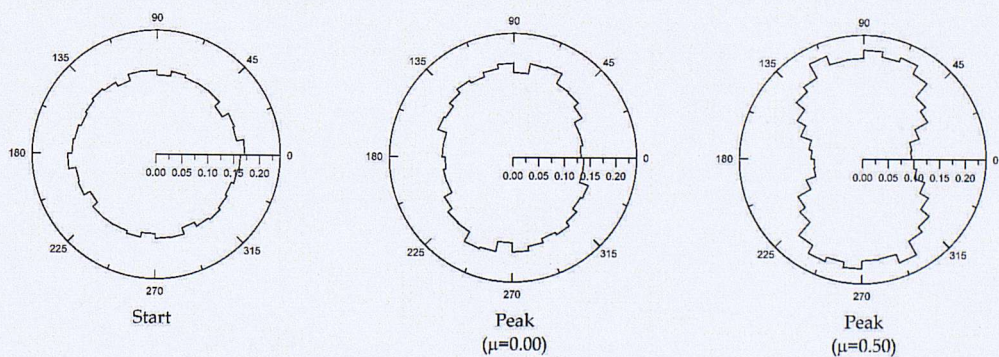


Figure 6.14: Effect of  $\mu$  on triaxial compression - Polar histograms of contact forces in the XZ plane at the start of shearing and at peak

$$\Phi_d = \Phi_1 - \Phi_3 \quad (6.1)$$

where  $\Phi_1$  and  $\Phi_3$  are the eigenvalues of the fabric tensor defined by Equation 2.16. This approach was also used by Thornton (2000). In the calculation all the contact forces, and not only those that are bigger than the average magnitude, are included.

The evolution of the deviatoric fabric is illustrated in Figure 6.15 for a selected number of simulations. Evidently, the deviatoric fabric response resembles the stress-strain response presented in Figure 6.9. Furthermore, it validates the fact observed in Figure 6.13 that the simulations with higher values of  $\mu$  develop internal structures with a fabric that is much more anisotropic.

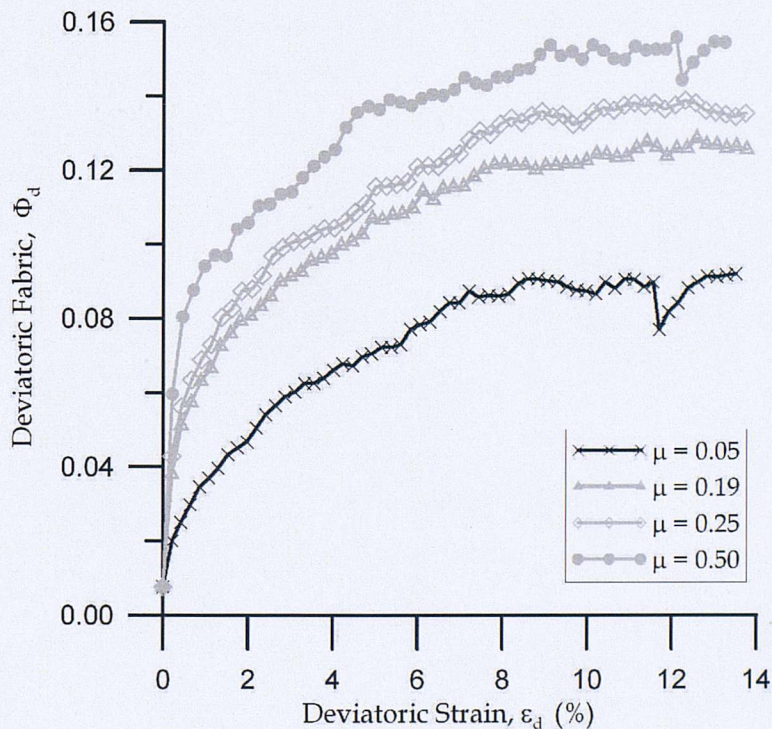


Figure 6.15: Effect of  $\mu$  on triaxial compression - Evolution of the deviatoric fabric

### Effect of the initial density

As mentioned in Section 6.3, different initial densities can be achieved if the value of  $\mu$  is modified during isotropic compression. Low values of  $\mu$  result in higher densities than when high values of  $\mu$  are used. This approach was used to evaluate the effect of the different initial density under triaxial compression. While the initial densities

## 6. DEM simulations under normal loading

---

for the simulations here presented were different, the value of  $\mu$ , and the other input parameters were equal for all the simulations. The coefficient of inter-particle friction used for these simulations was 0.220.

The stress-strain curves resulting from this analysis can be observed in Figure 6.16. The simulations presented include two limiting cases; one simulation which was isotropically compressed with zero friction ( $e_0 = 0.529$ ) giving the densest specimen, and a simulation compressed with  $\mu = 0.5$  in order to obtain a “loose” specimen ( $e_0 = 0.59$ ).

Referring to Figure 6.16 it can be seen that the densest samples develop a higher maximum angle of mobilised shearing resistance. This fact has been observed in many studies by different researchers and it is widely accepted. It is also clear that the densest specimens developed a higher dilation. Furthermore the specimens that were less dense experienced a clear amount of initial contraction before extensive dilation. Note that although limiting cases for the values of friction were used during specimen generation, all the samples followed the expected trend for dense samples, as all of them dilated. This may be caused by the specific grain size distribution, in fact, in Chapter 4 it was also observed that in both triaxial and HCA tests, the samples behaved as dense samples. However, further research is needed to clarify this matter.

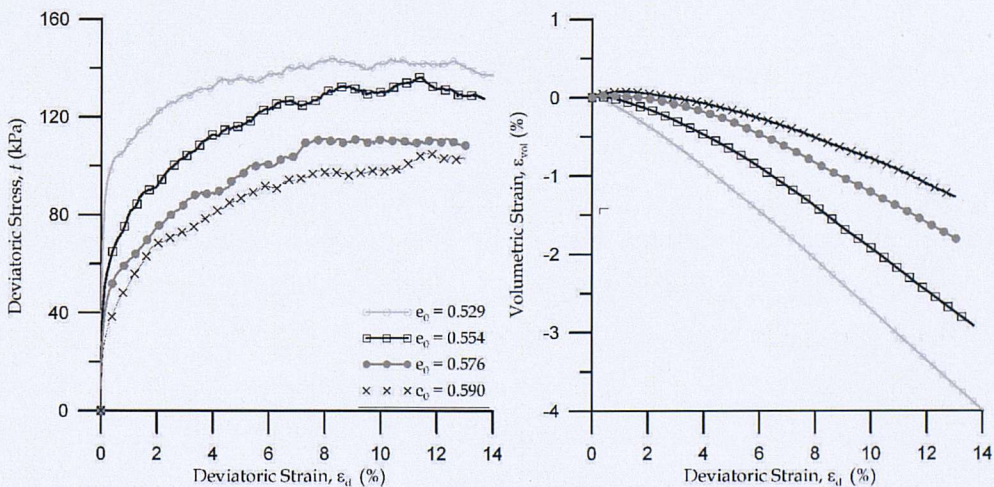


Figure 6.16: Effect of initial density on triaxial compression - Stress-strain response

At the particle scale, Figure 6.17 illustrates that independent of the initial density, all simulations converge to a constant value of coordination number ( $Z$ ), which is a manifestation of the existence of a critical state. However, this critical state is not evident in the volumetric strain response. At this point it is interesting to note that

## 6. DEM simulations under normal loading

---

the loosest specimen experienced an increase in  $Z$  in order to achieve that “critical”  $Z$  value. On the other hand, the simulation with ( $e_0 = 0.576$ ) did not change its coordination number in a significant manner during shearing. This evidences the existence of a possible stability requirement or percolation threshold for a specific value of inter-particle friction.

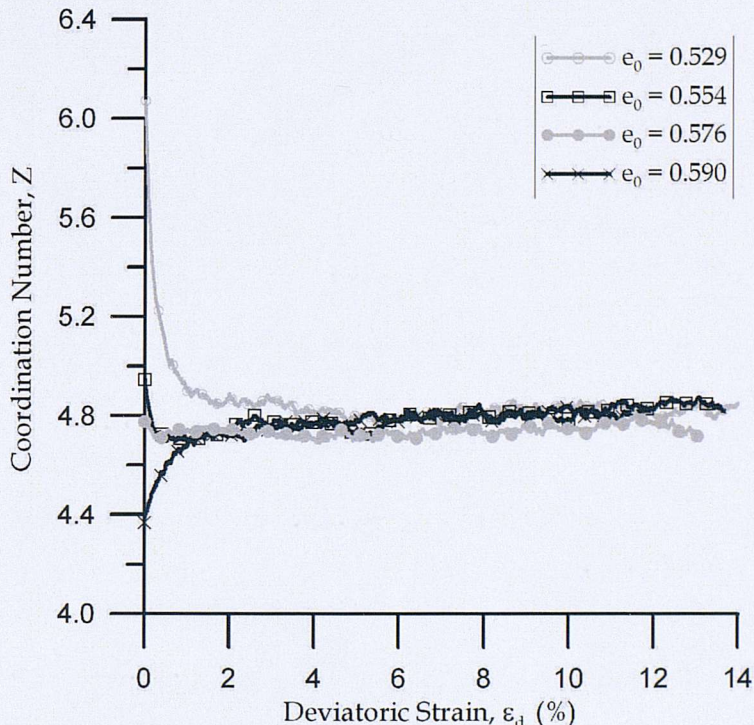


Figure 6.17: Effect of initial density on triaxial compression - Evolution of  $Z$

In a similar way to that shown in the previous section, the evolution of the deviatoric fabric was analysed in terms of the effects of the initial density. Figure 6.18 illustrates that the densest specimen develops the greatest anisotropy. This coincides with the conclusions of the previous section. When the effects of the coefficient of inter-particle friction were assessed, it was shown that the most anisotropic fabric was developed for the highest value of  $\mu$ , which simultaneously experienced the highest dilation. In terms of the initial density, the densest specimen experiencing the highest dilation, developed the most anisotropic fabric.

### Effect of the grain size and grain size distribution

In Chapter 4, some HCA tests performed to assess the effect of the different particle sizes produced a surprising result. It was expected that the tests using “big” ballotini

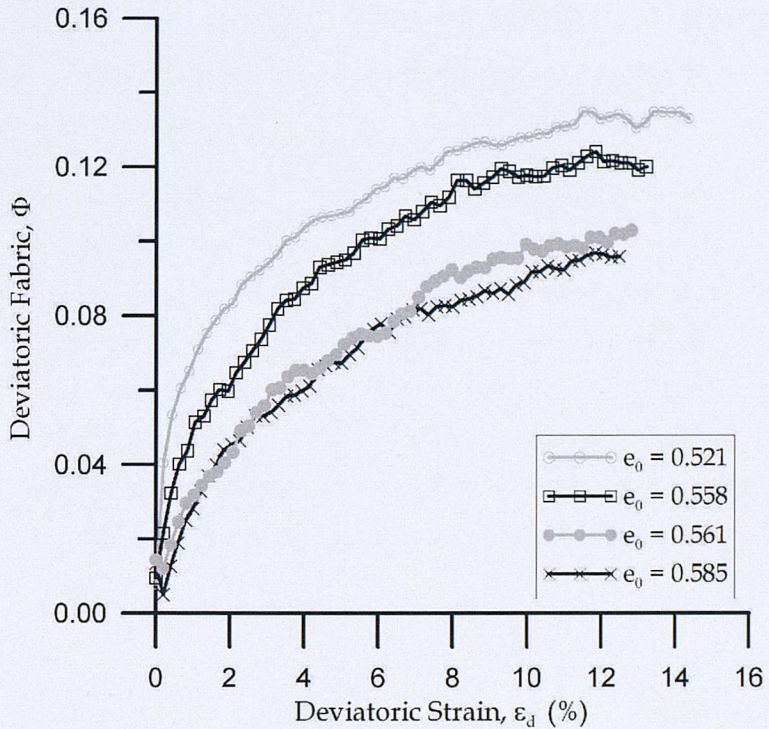


Figure 6.18: Effect of initial density on triaxial compression - Evolution of the deviatoric fabric

would show a very stiff response due to significant boundary effects produced by a reduced number of particles across the thickness of the sample. That result was indeed obtained as observed in Figure 4.15. Since all tests had equal initial void ratio it was expected that the tests on “medium” and “small” ballotini would behave in identical manner. Although both tests resulted in the same value of  $\phi'_{peak}$ , the response of the test in “small” ballotini was stiffer than for the “medium” ballotini. It was then hypothesized that this difference was a result of the different grain size distributions. Specifically, it was stated that both samples despite having very uniform sizes, they had very different range of sizes (i.e. the difference between the biggest and smallest particle size for each sample were proportionally different). The aim of the simulations presented in this section is to examine this hypothesis.

Two simulations were performed using  $\mu = 0.22$ . The initial void ratio for both simulations was 0.554. However, the simulations differed in the grain size distribution used. The simulations used the grain size distributions experimentally measured for both the “small” and “medium” particle sizes. These distributions were replicated using the distribution of particles detailed in Table 6.2, to investigate the effect of the particle size on the response. Since these simulations were performed using a periodic cell, they effect of particle size is isolated in the infinite space. Therefore,

## 6. DEM simulations under normal loading

---

the observed results are dependant only on the particle size distribution and not the particle size. Note however, that to isolate these two effects from the physical experiments is not possible.

Figure 6.19 shows the stress-strain response for both of these simulations. Clearly, both simulations mobilise the same peak angle of shearing resistance. Additionally, the stress-strain response of the “small” sized ballotini was stiffer than that of the “medium” sized ballotini. These phenomena also occurred in the experimental results. This validates the hypothesis first stated in Section 4.3.1 and gives further confidence in the results of both experiments and simulations even though it is recognised that the experiments are affected by other factors including particle shape and the presence of stress and strain non-uniformities.

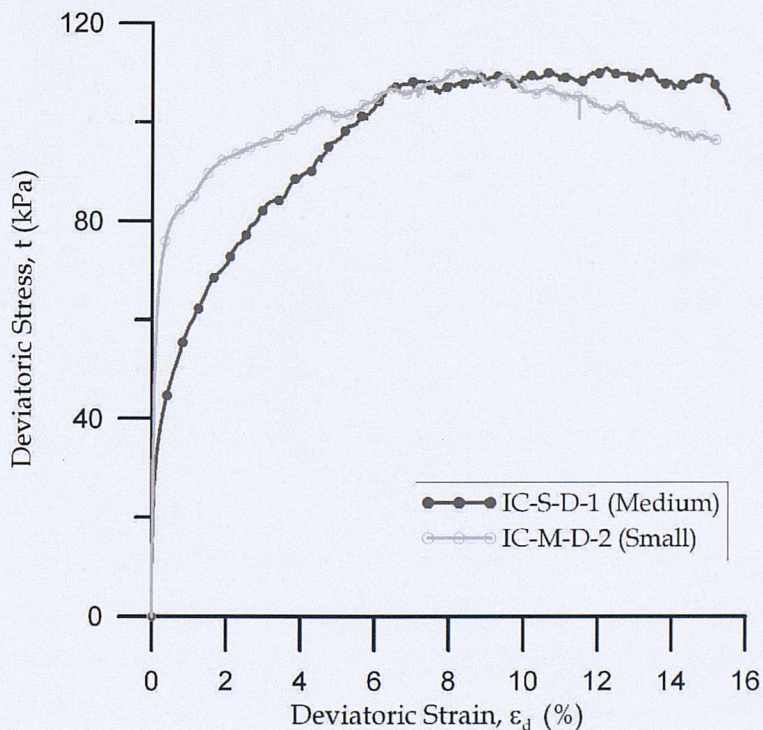


Figure 6.19: Effect of the grain size distribution on triaxial compression - Stress-strain response

### Effect of the elastic parameters - Poisson's ratio and Young's Module

As mentioned in Section 6.2, some assumptions were made when fitting the results of the experimental tests by Cavarretta (2009) to the Hertzian contact law by means of the elastic parameters (Poisson's ratio  $\nu$ , and Young's module  $E$ ). The aim of the sensitivity analyses presented in this section was to observe the possible difference

## 6. DEM simulations under normal loading

---

if the choice of parameters was varied. In this simulations the value of  $\mu$  used was 0.325.

The Poisson's ratio is the ratio of vertical and horizontal deformation when a body is subjected to a vertical load. In terms of such parameter, Figure 6.20 shows that there is no significant variation in the stress-strain development for the values chosen. Note that the choice of values for this parametric studies is wide and furthermore, the variation is bigger to that of the results presented by Cavaretta (2009). It was therefore concluded that the response was not affected by the value of the Poisson's ratio.

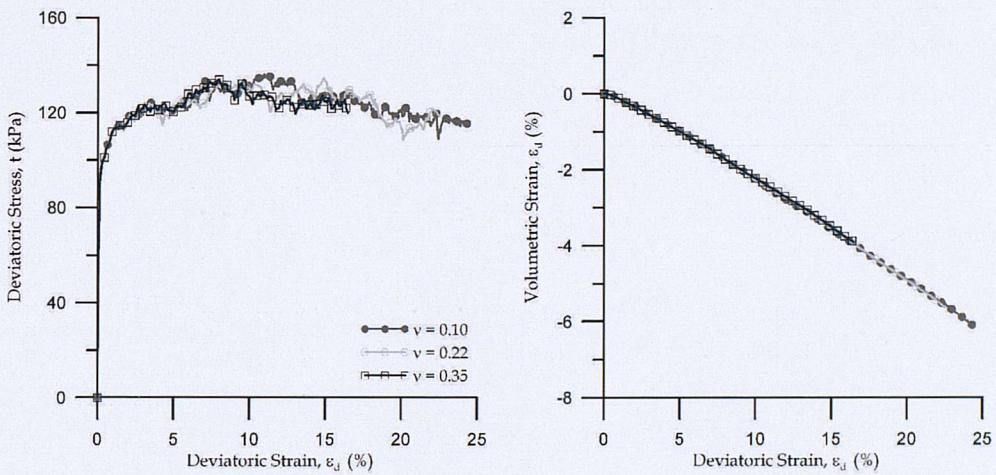


Figure 6.20: Effect of Poisson's ratio on triaxial compression - Stress-strain response

On the other hand, Figure 6.21 demonstrates that the simulations are not sensitive to a variation of Young's module between 50 and 90 GPa. Even at very small strain levels the difference is not significant. Note that although the range of variation for this parameters may seem low, the range of values chosen (i.e.  $50 \leq E \leq 90$ ) is bigger than the typical values used in the existing literature for DEM simulations of glass ballotini. Furthermore, the variation of the experimental measurements by Cavaretta (2009) is much lower than the interval of values used here.

The results presented here showed no variation due to the choice of elastic parameters. However, it is not concluded that these parameters have no influence in the response of granular materials. In fact, a variation in the Young's module of about one order of magnitude produces significantly different results. In anyway, choosing a value for the Young's module outside the range presented here (i.e. 50-90 GPa) could not be reasonably justified. Furthermore, it is expected that a difference can occur at very small strains levels which cannot be effectively modelled with the

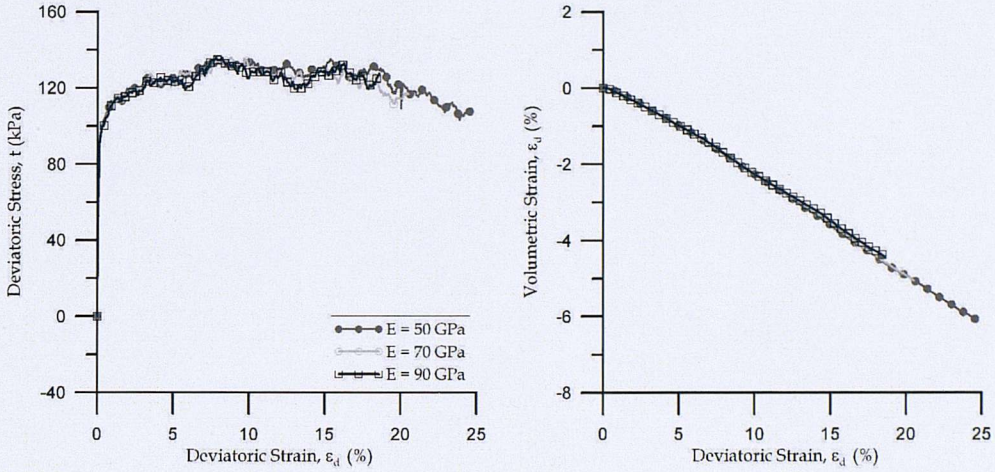


Figure 6.21: Effect of Young's module on triaxial compression - Stress-strain response

current contact model.

### Effect of the simulation strain rate

As mentioned in Chapter 2, the wrong choice of strain rate may cause problems with the contact detection algorithm. Furthermore, special care must be taken to avoid simulating a stress wave propagating through the media instead of the quasi-static response sought.

In simple terms, it can be observed from Figure 6.22 that while the two smallest values for the strain rate produce identical stress-strain responses, the biggest value (0.2) generated a significantly different response in both the deviatoric stress and the volumetric strain development. Consequently the maximum strain rate used in any of the simulations presented in this thesis is  $0.1 [T^{-1}]$ . No density scaling has been used to decrease the running time of the DEM simulations.

### Effect of using different time-step values

The choice of the fraction of the critical time-step used in the simulations may produce the same problems as the wrong choice of simulation strain rate in terms of the contact detection algorithm. Additionally, the fraction of critical time step used may produce numerical instabilities that are inherent to any finite difference integration scheme.

## 6. DEM simulations under normal loading

---

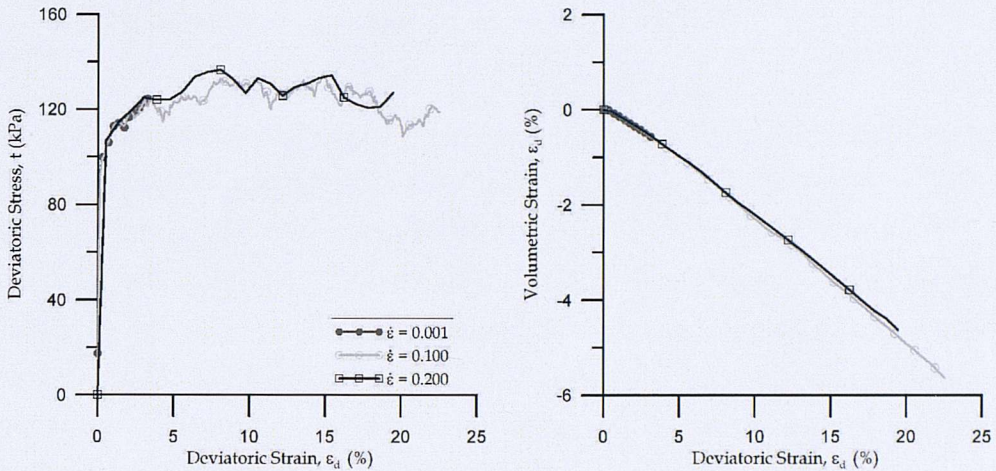


Figure 6.22: Effect of the strain rate on triaxial compression - Stress-strain response

The stress-strain response shown in Figure 6.23 illustrates that while the two smallest values for the fraction of the critical time step used are lying on top of each other, there is a slight difference in the response when the value of 0.20 was used. Furthermore, the simulation using  $\alpha_{\Delta t} = 0.20$  failed and could not be continued because one of the particles was detected outside of the initially specified geometric boundaries. This single difference was used as the only argument to decide on the use of the value of 0.10 as the most effective way to perform the simulations. Although a value of 0.15 could have been used, 0.10 was chosen in order to have the certainty that when simulations were performed following different stress paths to triaxial compression the simulations would be still valid.

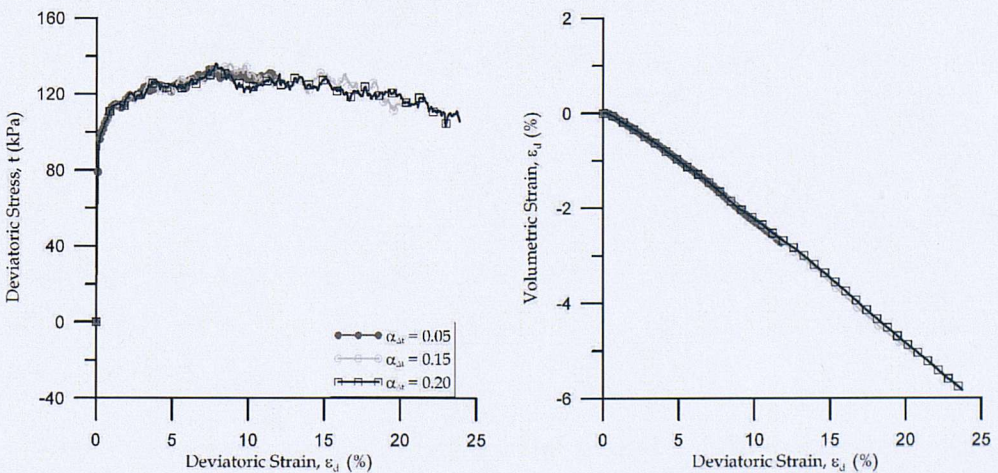


Figure 6.23: Effect of the time step on triaxial compression - Stress-strain response

## 6.5 Constant $b$ tests

A series of constant  $b$  tests was performed following the algorithms described in Chapter 5. Essentially, these are simulations in which  $p' = 200$  kPa,  $\alpha = 0^\circ$  and  $b$  are kept constant while sheared under strain control in the vertical direction. Different values of inter-particle friction ( $\mu$ ) and initial densities were used. In addition, two different consolidation histories were replicated; one involves isotropic consolidation and the other anisotropic consolidation using the  $K_0$  coefficient experimentally determined in Chapter 4. Simulations of isotropically consolidated specimens allow to situate the results of this thesis into the context of previous similar research. The anisotropically consolidated specimens on the other hand, are useful for comparison purposes as they can be analysed in contrast to the physical experiments presented in Chapter 4.

### 6.5.1 Isotropically consolidated specimens

#### Macro-scale behaviour

For the simulations initially presented here, an initial void ratio of 0.554 was used. The coefficient of inter-particle friction ( $\mu$ ) was 0.22. The specimens are isotropically consolidated until a confining stress of 200 kPa is achieved. Subsequently, they are sheared while keeping constant values of the intermediate stress ratio  $b$ . Simulations are carried out using  $b$  values varying in the range between 0.0 (as triaxial compression) and 1.0 (as in triaxial extension) with constant values of  $p' (= 200$  kPa) and  $\alpha = 0^\circ$ .

Figure 6.24 shows the stress-strain response for a set of constant  $b$  tests, with  $\mu = 0.22$  and  $e_0 = 0.554$ . Distinctive peaks can be identified for each of the simulations and a similar volumetric response is observed for all the  $b$  values. A variable of interest in terms of volumetric response is the development of axial strain in the intermediate direction ( $\epsilon_2$ ).

Figure 6.25 illustrates the evolution of this variable for different  $b$  values. It can be seen that  $\epsilon_2$  is dilative for all simulations between triaxial compression ( $b = 0.0$ ) and plane strain ( $b = 0.4$ ). However, it becomes compressive after plane strain towards triaxial extension ( $b = 1.0$ ). Also note that the simulation with  $b = 0.4$  seems to be very close to the limiting case of plane strain where  $\epsilon_2 = 0$ .

## 6. DEM simulations under normal loading

---

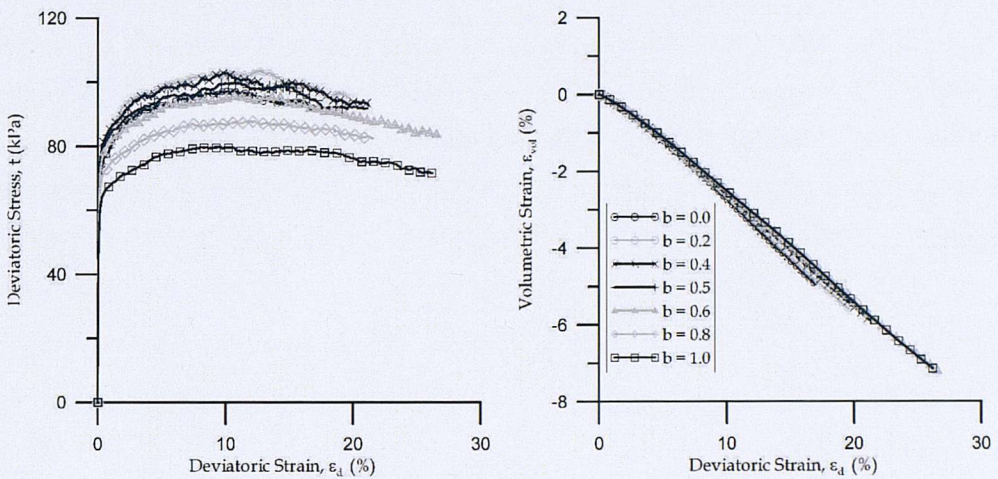


Figure 6.24: Effect of the intermediate stress ratio  $b$  - Stress-strain response

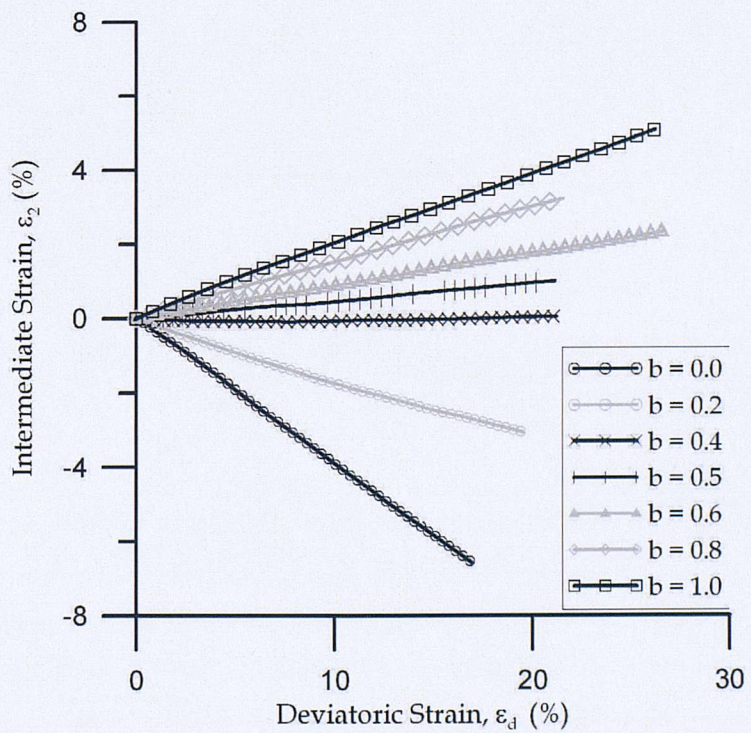


Figure 6.25: Effect of the intermediate stress ratio  $b$  - Development of intermediate strain ( $\epsilon_2$ )

## 6. DEM simulations under normal loading

---

The mobilised peak angle of shearing resistance is a parameter of interest as it can be compared with published results. Figure 6.26 presents these results. It is clear that the trends and range of variation agree with numerical and experimental data published by the different researchers described in Chapter 2. Following the approach suggested by Thornton & Sun (1993) and Ng (2004b), the results were fitted to the Lade & Duncan (1973) model introduced in Chapter 2 and a parameter  $\eta = 8.83$  was found. The failure states predicted using the model agree well with the simulation results, proving the effectiveness of the model.

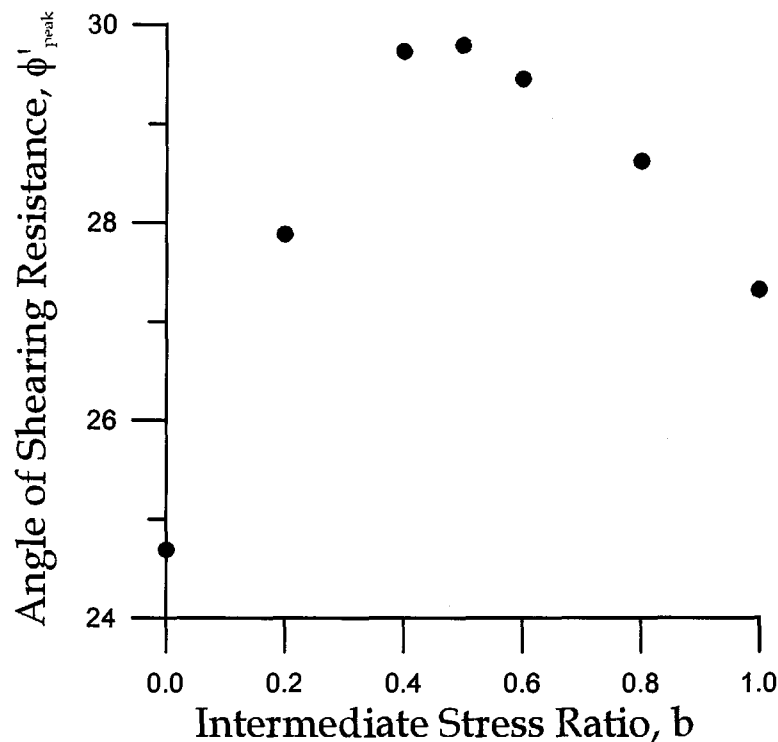


Figure 6.26: Effect of the intermediate stress ratio  $b$  on the angle of shearing resistance ( $\phi'$ )

Figure 6.27 presents the same results of Figure 6.26 in the generalised stress plane. In this Figure the typical shape of the failure envelope that the Lade & Duncan (1973) model can represent is clearly observed. Note that only one sector of the  $\pi$ -plane is used. This is because these simulations will be later compared with  $K_0$  consolidated simulations and the experimental results discussed in Chapter 4. As a further comparison, refer to Figure 2.31 where a similar trend can be observed.

Although Figure 6.28 shows that all specimens have similar stiffness, it is clear that the maximum  $G_{oct}$  was measured for the simulations with highest values of  $\phi'$  (i.e.  $b = 0.4$  and  $0.5$ ). It must be noted however, that due to the possibility of yielding of

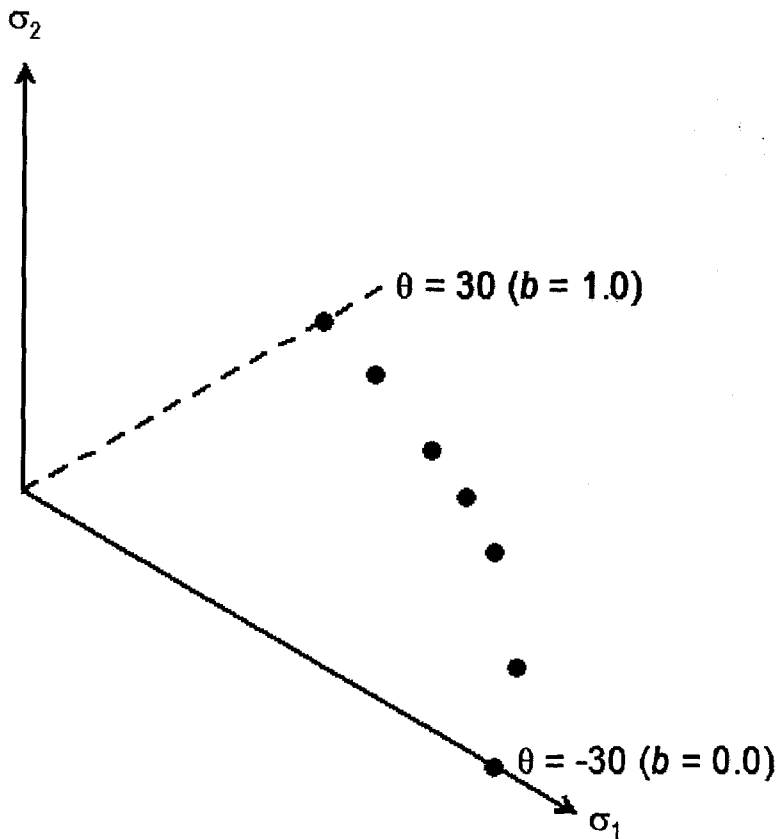


Figure 6.27: Effect of the intermediate stress ratio  $b$  on the angle of shearing resistance ( $\phi'$ )

the contact asperities as observed by ?, more accurate contact models are required in order to simulate the behaviour of these assemblies at very small strain levels. That would provide further understanding on the influence of  $b$  on the response of granular materials.

### Micro-scale results

Intuitively, since there are marked differences in the shearing resistance for the different  $b$  values, a significant difference in the average number of contacts per particle would be expected. Figure 6.29 shows that there are differences in the coordination number. However, they are not significant.

It is of particular interest to assess if there are differences in the anisotropy of soil fabric that could explain the differences observed in the macro-scale behaviour. For this set of simulations, the approach proposed by Rothenburg & Bathurst (1989) is not

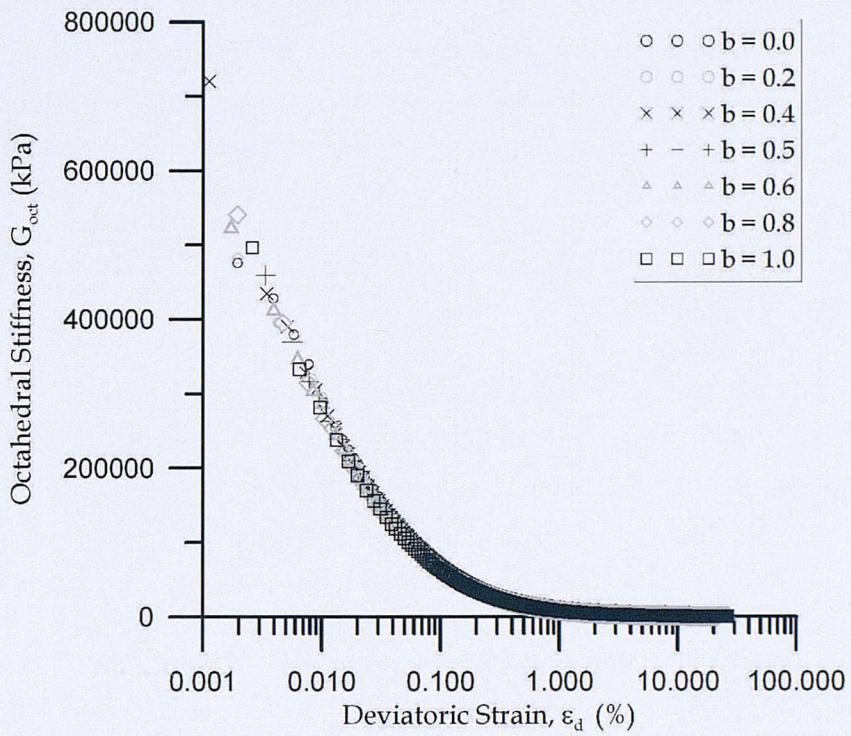


Figure 6.28: Effect of the intermediate stress ratio  $b$  on the octahedral stiffness

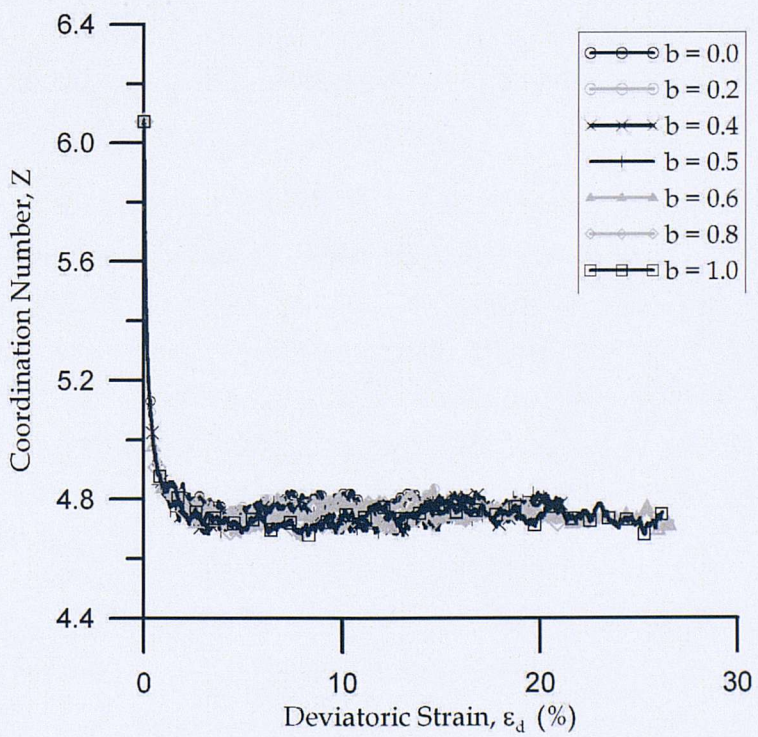


Figure 6.29: Effect of the intermediate stress ratio  $b$  on  $Z$

## 6. DEM simulations under normal loading

---

recommended because the simulations are three-dimensional while their approach is two-dimensional. The deviatoric fabric proposed by Thornton (2000) ( $\Phi_d = \Phi_1 - \Phi_3$ ) cannot be used as it does not consider the influence of  $\Phi_2$ . A more generalised approach is proposed here to define the deviatoric fabric as:

$$\Phi_d = \frac{1}{\sqrt{(2)}} \left[ (\Phi_1 - \Phi_2)^2 + (\Phi_2 - \Phi_3)^2 + (\Phi_1 - \Phi_3)^2 \right]^{0.5} \quad (6.2)$$

where  $\Phi_1$ ,  $\Phi_2$  and  $\Phi_3$  are the eigenvalues of the fabric tensor defined in Equation 2.16. Note that Equation 6.2 is a more general expression that equals the expression presented by Thornton (2000) if  $\Phi_2 = \Phi_3$  (i.e. during axi-symmetric loading conditions). Furthermore, this equation represents a multiple of the second invariant of the fabric tensor.

Figure 6.30 presents the evolution of the deviatoric fabric calculated using Equation 6.2 including all the contact forces existent within the DEM specimens. Although the deviatoric fabric is very similar for all the simulations, the maximum and minimum levels of  $\Phi_d$  can be identified. It is clear that the most anisotropic fabric is present in the simulation with  $b = 0.5$  and the lowest for the simulation with  $b = 0.0$ . If studied in detail, the trend observed in the deviatoric fabric is the same as for the stress-strain response. This allows us to conclude that the difference in shear strength observed in the macro-scale response is a manifestation of the development of fabric anisotropy during shearing.

Another way of representing the effect of the intermediate stress ratio on the fabric states was proposed by Thornton (2000). Thornton (2000) suggested that the eigenvalues of the fabric tensor at failure could be plotted in a generalised plane that is analogous to the generalised stress plane. Such approach is also followed here and is illustrated in Figure 6.31. A clear trend between the value of  $b$  and a fabric surface can be identified. Thornton (2000) suggested that this set of fabric states can be fitted to an inverted Lade & Duncan (1973) failure criterion given for an equation as indicated below:

$$\frac{3\Phi_1^3}{2\Phi_1\Phi_2 - 3\Phi_3} = \eta' \quad (6.3)$$

where  $\eta'$  is a model constant and  $\Phi_1$ ,  $\Phi_2$  and  $\Phi_3$  are the eigenvalues of the fabric tensor at failure. Comparing the results from Figure 6.27 and Figure 6.31 it can be

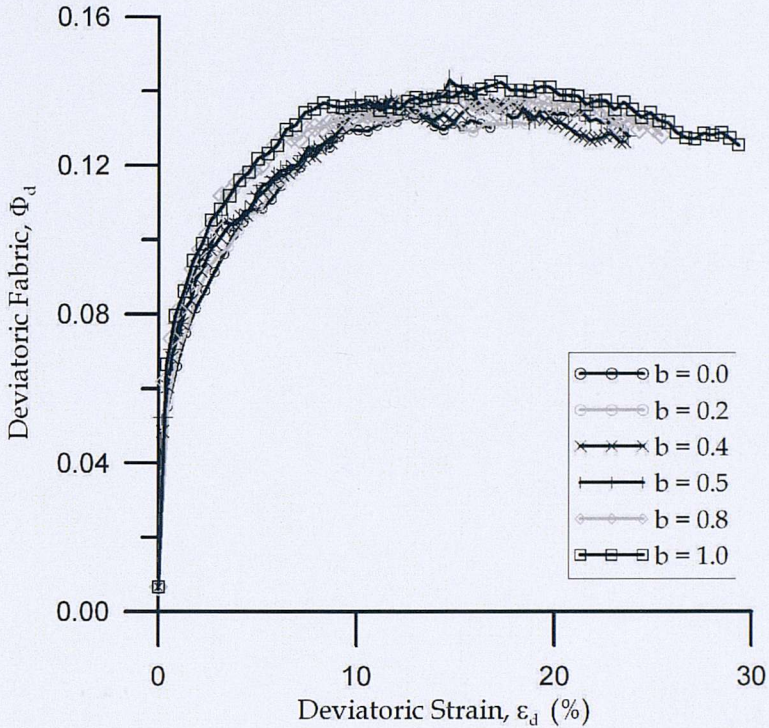


Figure 6.30: Effect of the intermediate stress ratio  $b$  on  $\Phi_d$

seen that the results replicate such a model and their trends agree with that found by Thornton (2000).

The use of the deviatoric fabric is an extremely useful tool to evaluate the evolution of soil anisotropy. However, the visual representation of these changes is, in some cases self-explanatory. Figure 6.32 illustrates these changes looking into sections of the DEM specimens at the initial and peak states. On the top of the figure, the view in the three planes at the start of shearing is presented and is equal for all the constant  $b$  simulations. Then, by rows, the views of the three planes at the peak states for  $b = 0.0, 0.5$  and  $1.0$  are shown. These simulations were selected as they are the extreme cases in terms of the peak angle of shearing resistance. Referring to the state of the force network at the start, it is clear that the distribution of contact forces is random and isotropic. This is also confirmed by any of the measurements used to quantify anisotropy (i.e.  $a \approx 0.00$  as defined by Rothenburg & Bathurst (1989)). On the other hand, at the peak states there are distinctive features for each of the simulations. The simulation with  $b = 0.0$  presents an isotropic distribution in the XY plane but less marked than at the beginning of the simulations. In contrast, the force network in the YZ and XZ planes shows a significant concentration of strong forces in the vertical direction. These features are also observed for the simulation

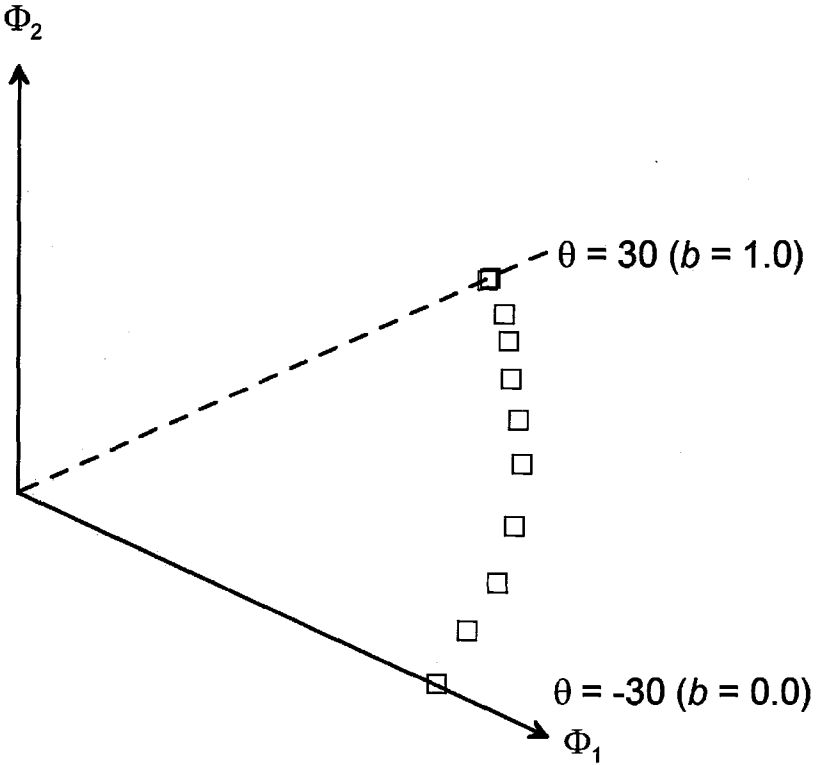


Figure 6.31: Effect of the intermediate stress ratio  $b$  on the fabric tensor at failure

with  $b = 0.5$ . However, the concentration of forces in the vertical direction is more localised for this case. The simulation with  $b = 1.0$  differs from the rest because the alignment of strong forces is clearly observed in the XY and XZ directions. Note that the preferred orientations of the contact forces distributions coincides with the directions of the principal stresses.

Figure 6.33 illustrates the polar histograms of normal contact force orientation at peak state for  $b = 0.0, 0.5$  and  $0.1$ . For the different cases it is clear that the majority of forces are orientated in the vertical direction. Furthermore, it is clear that the number of contact forces acting in the  $x$ -direction are remarkably similar for all cases. An increase of forces in the  $y$ -direction is expected due to the increase of  $b$ . It is then concluded that the number of forces orthogonal to the main force carrying loading columns is having an influence in the shearing strength.

The amount of particle rotation is another micro-mechanical quantity that is easily assessed from DEM simulations. Particle rotation is often used as an indicator for the presence of shear bands. However, strain localisation is not identifiable due to

## 6. DEM simulations under normal loading

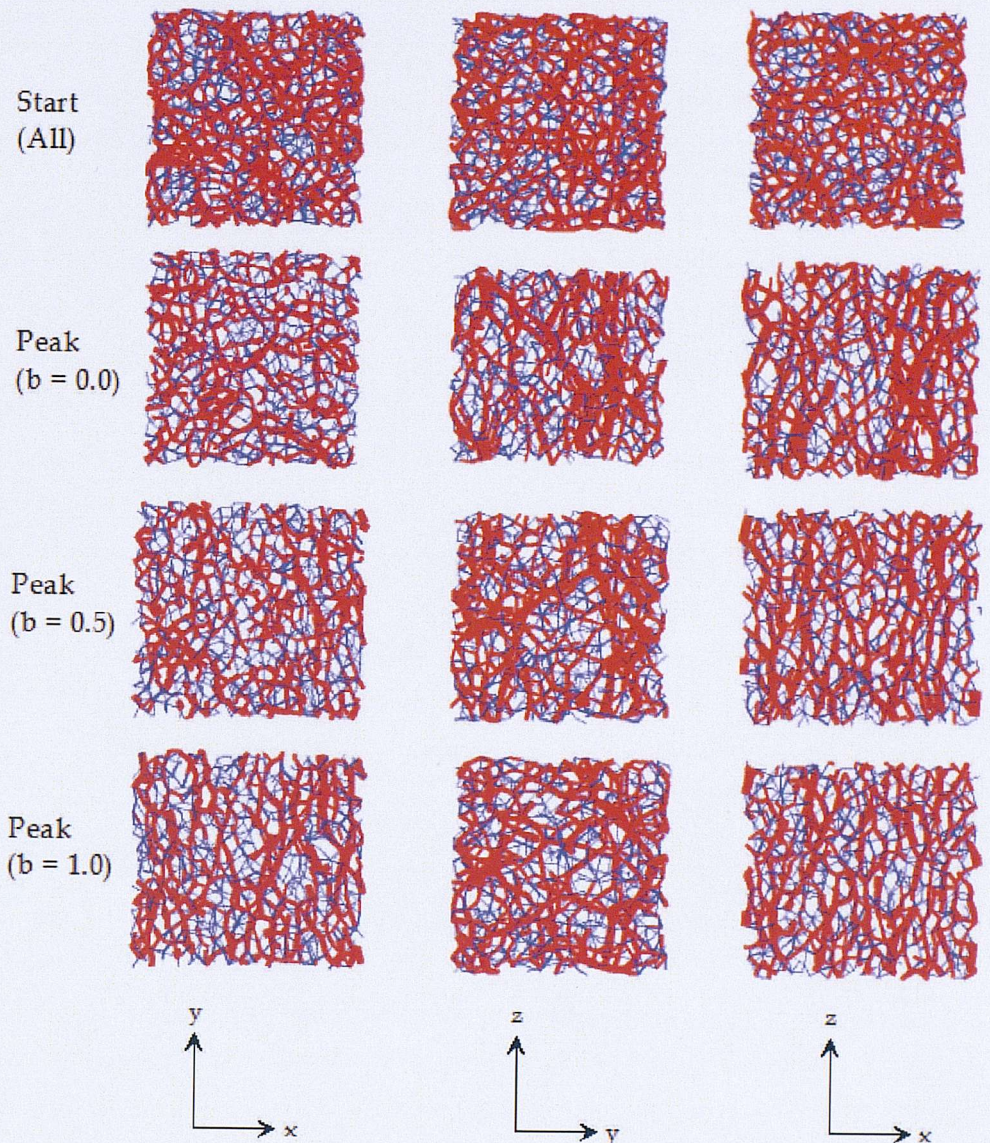


Figure 6.32: Effect of the intermediate stress ratio on the contact force network

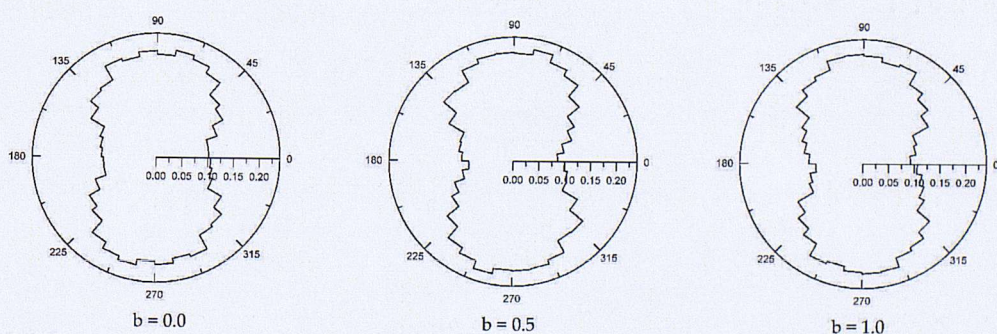


Figure 6.33: Effect of  $b$  on the concentration of contact force networks in the XZ plane

## 6. DEM simulations under normal loading

the continuity of the strain field and the lack of boundary effects when periodic boundaries are used. Nevertheless, it is interesting to highlight the differences of the level of particle rotation for these three DEM simulations, which represent extreme cases regarding the effects of the intermediate stress ratio.

Figure 6.34 shows the amount of particle rotation from the beginning of shearing until the peak shear strength was reached for the constant  $b$  tests with  $b = 0.0$ ,  $0.5$  and  $1.0$ . The color bar indicates that the darker the color of the spheres, the bigger the amount of rotation that they have experienced. Referring to the particle rotation in the XY plane (left column on Figure 6.34), it is clear that the rotation reduces as the  $b$  value increases. This trend is also observable when rotation in the XZ plane is analysed, however, the differences are more significant in this plane. Note that there are very reduced levels of particle rotation on the simulation with  $b = 1.0$  in comparison with the other two. Lastly, it is important to emphasize that the rotation in the YZ plane is different from that in the XZ plane. This is another manifestation of the anisotropic response of the material since both of these planes are related with particle movements in the vertical plane, which is where the direction of  $\sigma_1$  is located.

### **Effect of the coefficient of inter-particle friction**

It was observed in Section 6.4 that the triaxial compression behaviour was significantly affected by  $\mu$ . The aim of this section is to estimate the influence of varying the value of inter-particle friction on simulations of constant  $b$  tests. Note that such study is very difficult to perform in an experimental manner, therefore it has not been done before. On the other hand, it is an issue that has not been explored numerically either (using DEM). It can be observed from Figure 6.35 that an increase in  $\mu$  tends to increase the difference in strength between triaxial compression and plane strain. However, the tendency to reduce the shearing resistance from plane strain towards triaxial extension is observed even for very high values of  $\mu$  ( $= 0.7$ ).

The results are also plotted in the generalised stress plane in Figure 6.36. Note that for high values of inter-particle friction (higher shear resistance), the shape of the failure envelope becomes less round, whether it tends to become triangular as postulated by Lade & Duncan (1973) is unclear. However, referring to Figure 2.16 it is clear that extremely unrealistic values of  $\mu$  would be needed to obtain a completely triangular shape as the one with  $\eta = 10^5$  in the model proposed by Lade & Duncan (1973). Possibly, this theoretical response can be achieved if particle

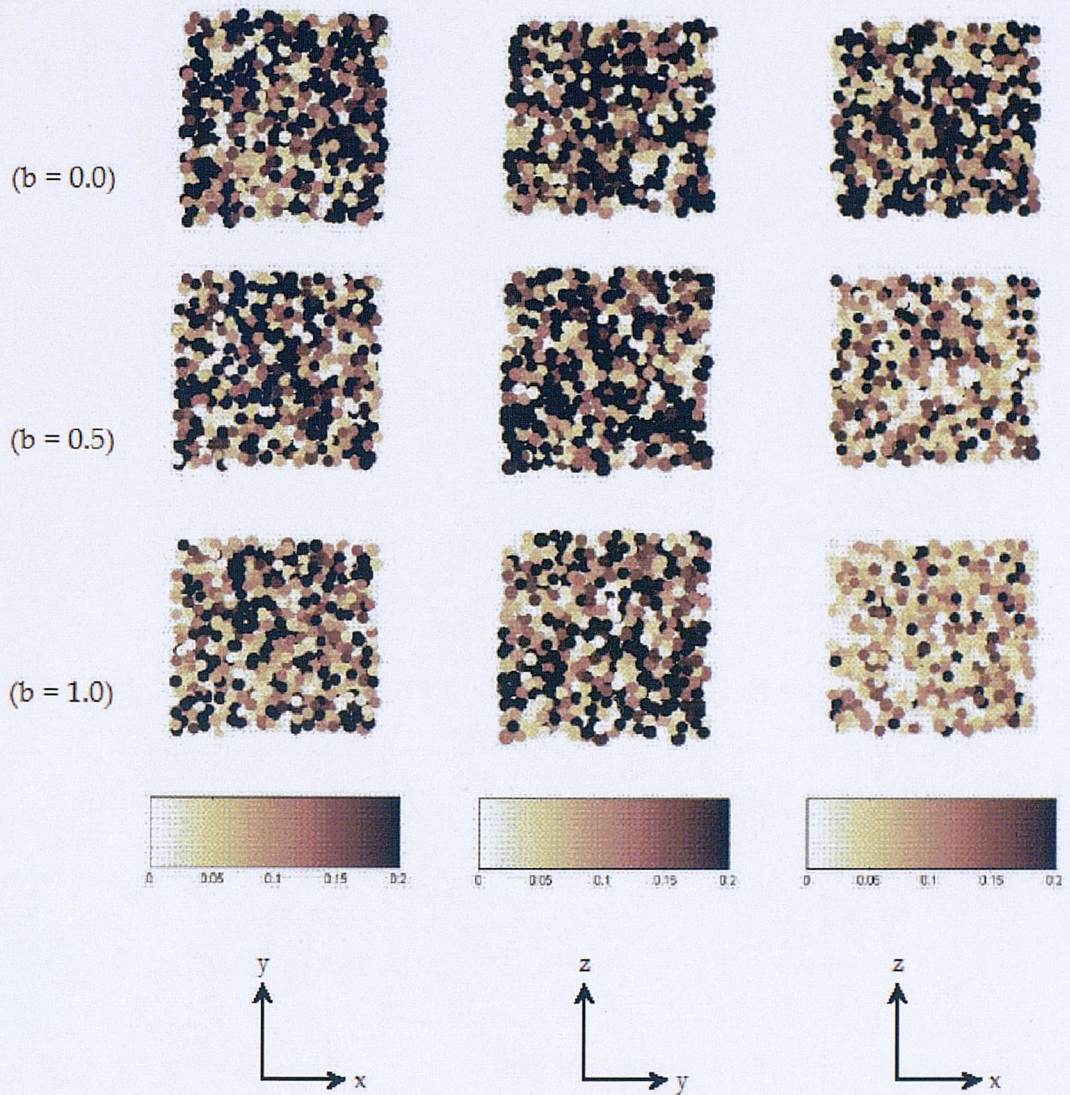


Figure 6.34: Effect of the intermediate stress ratio on particle rotation

shape is taken into consideration, but certainly it is not possible to obtain it using spherical particles in DEM simulations unless very unrealistic values of  $\mu$  are used.

The trends observed in the micro-scale analysis of the effects of friction on the different constant  $b$  tests were very similar to those described in the previous two sections. Additionally, analyses performed to evaluate the evolution of the deviatoric fabric confirmed that the simulations with the highest shear strengths had the highest level of anisotropy. It must be emphasized however that the level of anisotropy is dependent on many factors. Anisotropy was clearly observed in the contact force networks and at the level of particle rotations. It was observed that such anisotropy is also affected by the value of inter-particle friction and the initial density as described in the next section.

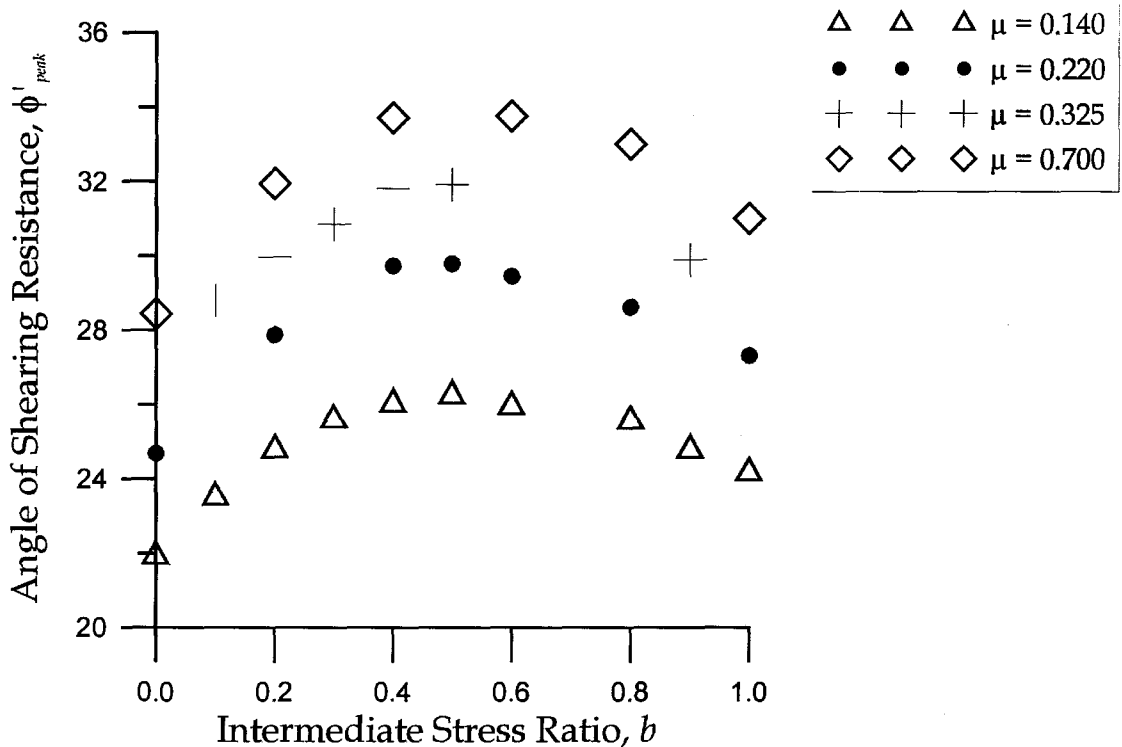


Figure 6.35: Effect of the coefficient of inter-particle friction on the shearing resistance of constant  $b$  tests

### Effect of the initial density

A series of constant  $b$  tests was performed to assess the influence of the initial density on the behaviour of granular materials under different intermediate stress ratios. Figure 6.37 shows the different failure envelopes for two sets of constant  $b$  tests with different initial densities on the generalised stress plane. For these simulations, the value of  $\mu$  was 0.22, and the initial void ratios were 0.529 and 0.554. As expected, the densest samples produced the highest shear resistances.

The same detailed macro- and micro-scale analyses were performed for these simulations. The conclusions derived from them are in agreement with those explained in the previous sections.

### 6.5.2 Anisotropically consolidated specimens ( $K_0$ )

In Chapter 4 two HCA experiments including normal loading were described. Those tests were performed using  $\alpha = 0^\circ$ ,  $p' = 200$ , and  $b$  values of 0.0 and 0.5. Furthermore, it was demonstrated that the tests carried out in the LICHCA involved a

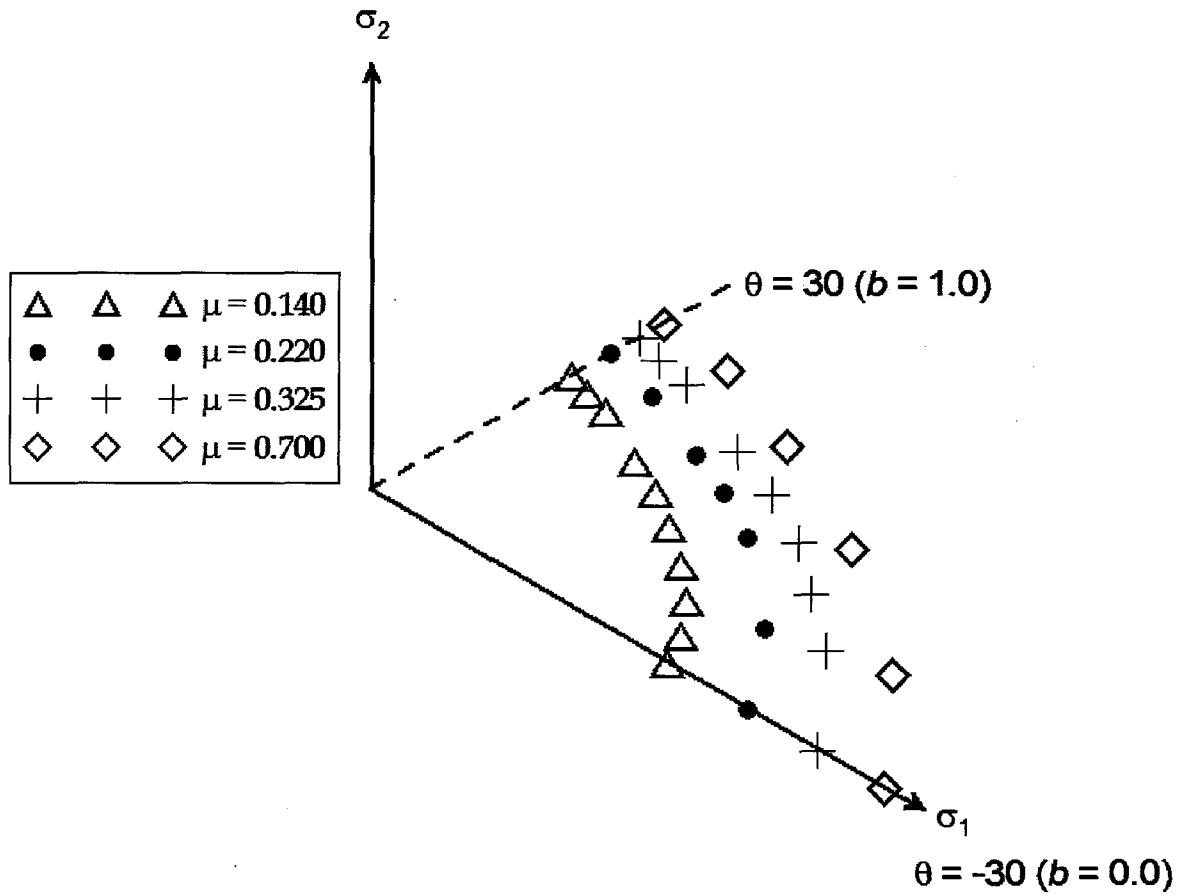


Figure 6.36: Changes in the failure envelope in relation to the coefficient of inter-particle friction

reduced level of stress and strain non-uniformities. It was shown that in agreement with previous finite element numerical analyses the most non-homogeneous case occurred when  $\alpha = 0^\circ$  and  $b = 0.5$ . Consequently, it is of primary interest to compare tests LIC-M-D-1 ( $\alpha = 0^\circ$ ,  $b = 0.5$ ) and LIC-M-D-2 ( $\alpha = 0^\circ$ ,  $b = 0.0$ ) with DEM simulations. These physical experiments, and the DEM simulations intended to replicate the experimental results, differ from the previous section because they were anisotropically consolidated prior to shearing. Additionally, simulations including a  $b$  value different from 0.0 also include a  $b$ -change stage, in the same way as in the physical experiments.

### Experimental validation

For validation purposes, the DEM simulations presented here were performed with the same initial void ratio as the physical experiments. Furthermore, the input pa-

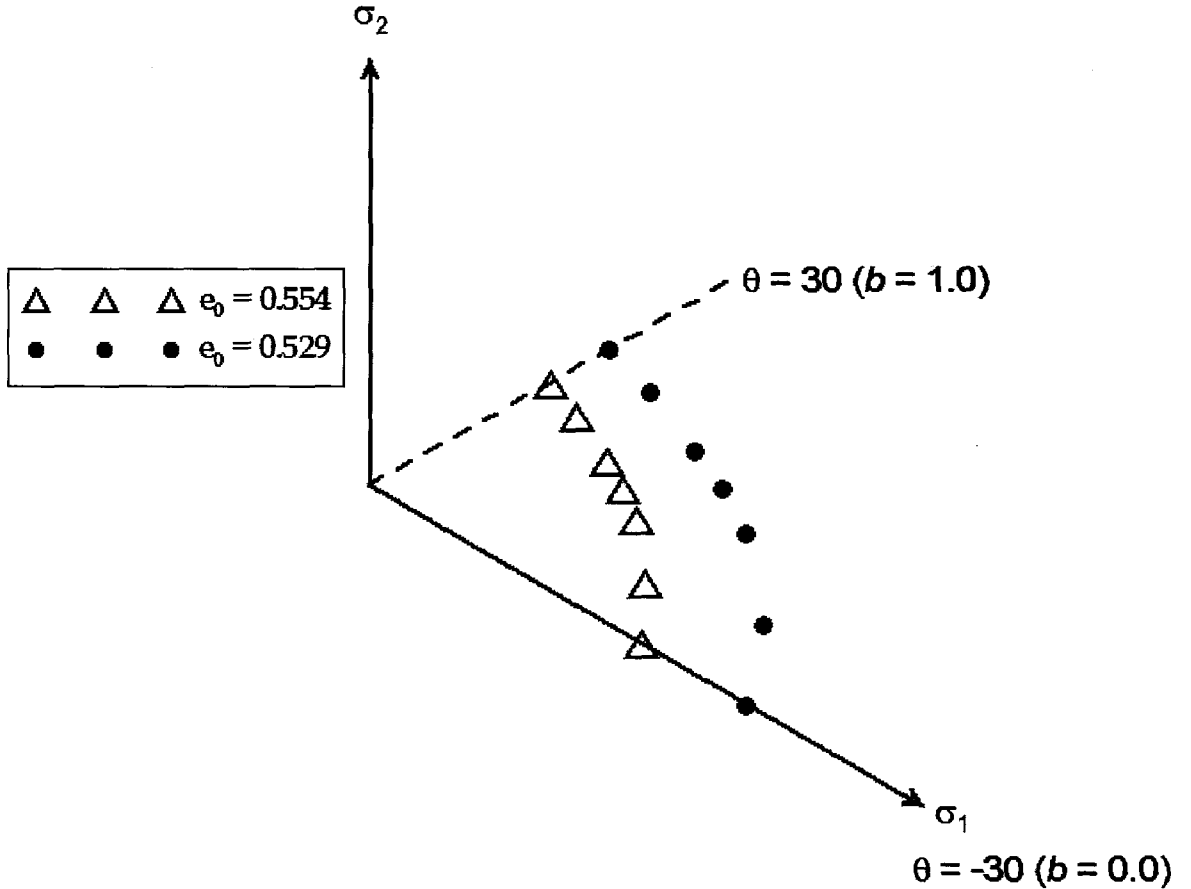


Figure 6.37: Effect of the initial density on constant  $b$  tests

rameters coincide with those experimentally measured. Figure 6.38 shows the DEM simulations with  $b$  values of 0.0 and 0.5 after following the same consolidation stress paths as in the experiments. The results of these simulations must be compared with the effects of  $b$  observed in Figure 4.20. The tendency is on reasonable agreements, at least in a qualitative manner because the stress-strain response of the simulation with  $b = 0.5$  lies above the one with  $b = 0.0$ . Direct comparison between DEM simulations and LICHCA experiments can be observed in Figures 6.39 and 6.40.

Referring to Figures 6.39 and 6.40, even though the initial stiffness of both DEM and experiments is very similar, the shear strength mobilised is higher in the experiments than in the simulations. These figures show simulations using two coefficients of friction that are within the measured range of values by Cavarretta (2009) (i.e.  $\mu = 0.220$  and  $0.325$ ). In addition a DEM simulation that has a better agreement with the physical experiments is also illustrated ( $\mu = 0.7$ ). This highlights the sensitivity to this parameter, which was also present in the comparison for triaxial compression tests. However, choosing an inter-particle friction of 0.7 is unrealistic

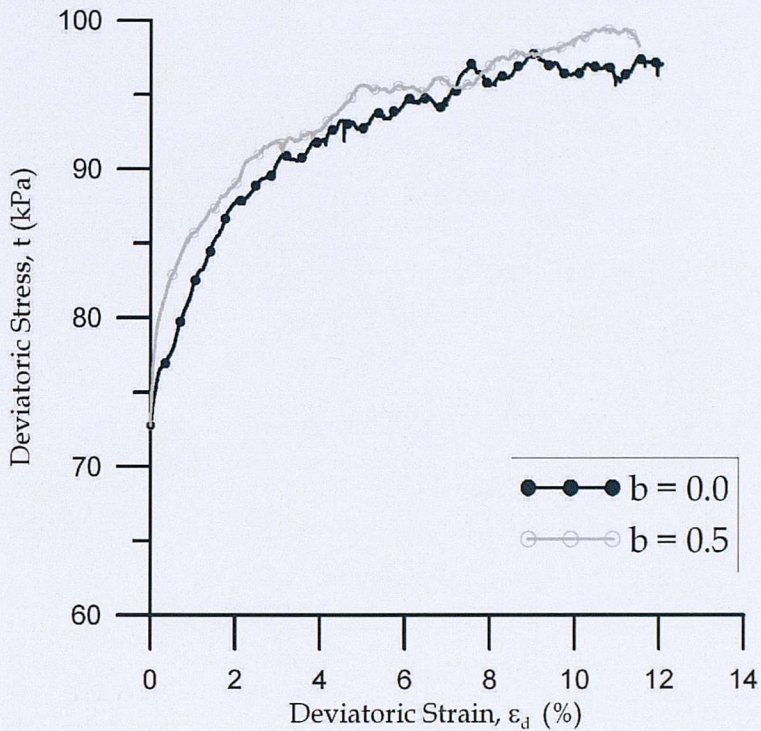


Figure 6.38: DEM simulations of HCA tests under different intermediate stress ratio

and cannot be justified.

Considering the simulations with  $b = 0.5$  and using  $\mu = 0.22$ , the differences in the peak value of  $\phi'$  is maximum  $4.45^\circ$  and it is  $6.54^\circ$  when  $\mu = 0.14$ . Recall that this is the most non-homogeneous case in terms of stress and strain and some of this difference can be attributed to that. Note however, that the experimental variation of similar tests performed by Lade et al. (2008) (see Figure 3.35) under the same conditions had even higher variation in the angle of shearing resistance (up to  $10^\circ$ ). On the other hand referring to the simulations with  $b = 0.0$ , the differences are  $2.45^\circ$  and  $4.10^\circ$  for  $\mu = 0.22$  and  $\mu = 0.14$ . These differences as expected, are lower than in the case of  $b = 0.5$  since the level of non-uniformities is less significant for these stress conditions. In summary, in spite of the visually marked difference of stress-strain response observed in Figures 6.39 and 6.40 between experiments and simulations, it is believed that these differences are reasonable considering the amount of experimental evidence and certainty of the input parameters available.

Apart from the presence of stress and strain non-uniformities and the uncertainty of the coefficient of inter-particle friction, there are other factors that may be contributing to the differences between experiments and simulations in a more considerable manner. These factors might have a more significant influence since the level of

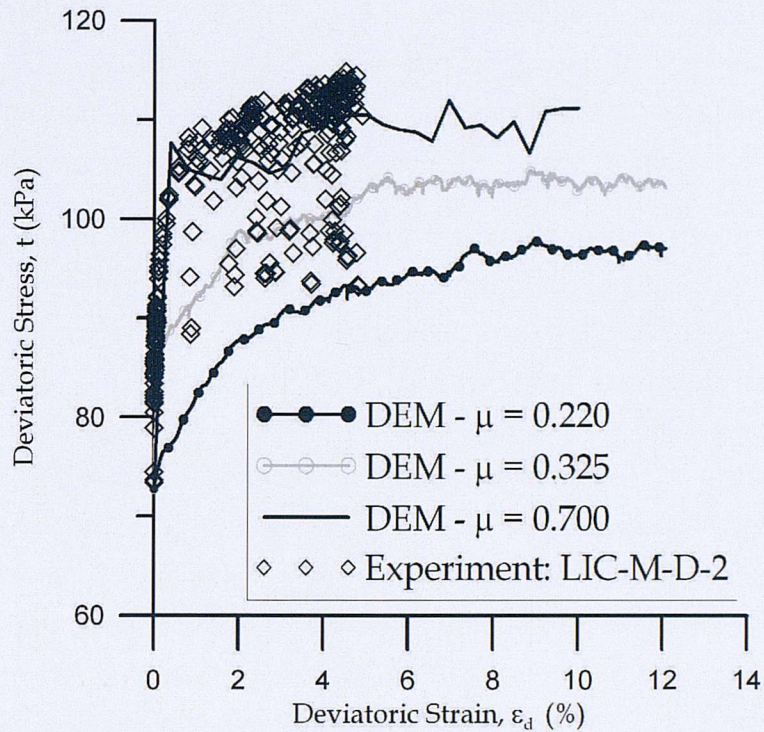


Figure 6.39: Comparison of DEM simulations and LICHCA tests with  $\alpha = 0^\circ$  and  $b = 0.0$

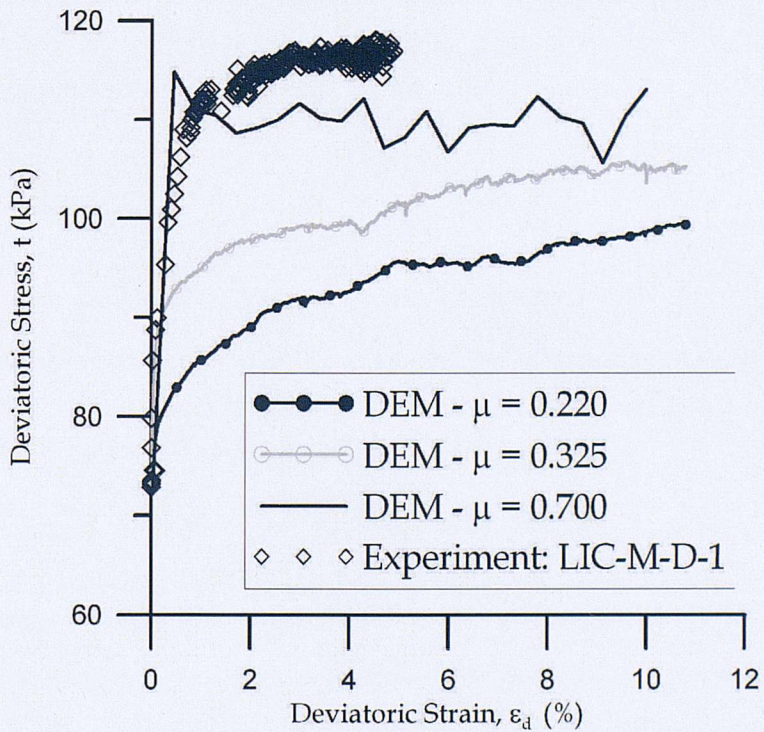


Figure 6.40: Comparison of DEM simulations and LICHCA tests with  $\alpha = 0^\circ$  and  $b = 0.5$

## 6. DEM simulations under normal loading

non-uniformities in the LICHCA was reduced with the change in the height of the sample. One of these factors is particle shape and it was also discussed for the triaxial compression scenario. Another factor that may affect the response of the DEM simulations is the lack of gravitational forces in the use of the periodic boundaries.

Gravitational forces are not normally included when periodic boundaries are used since a continuous particle movement in the direction of the body force would be unavoidable and unrealistic. It may be possible to introduce displacement gradients in the periodic cell simulations in order to take this effect into consideration, however this is out of the scope of this thesis. The fact that gravity may account responsible for differences between DEM simulations and experiments is related with sample preparation. As discussed in Chapter 2, it is widely recognised that sand samples prepared through air pluviation provide an inherently anisotropic structure. This inherent anisotropy occurs in addition to the induced anisotropy that is produced during  $K_0$  consolidation. In contrast to the physical experiments, the DEM simulations as performed in this thesis, can only provide the effects of induced anisotropy. The results shown in this chapter have demonstrated that the shear strength is definitely related to the magnitude of fabric anisotropy. As a consequence, simulations that are capable of reproducing inherent anisotropy in addition to induced anisotropy would probably provide more accurate results when compared to physical experiments. This hypothesis is partially proved with a small series of DEM simulations discussed in Chapter 7.

### **Macro-scale results**

Since the results of DEM simulations have been compared to physical experiments, it is interesting to assess the overall effect of the anisotropic consolidation in the constant  $b$  tests. The conclusions derived from the simulations presented here give further understanding of the effects of induced anisotropy.

Figure 6.41 illustrates the stress-strain response of a small set of constant  $b$  test DEM simulations. In this Figure, curves represented in black colour correspond to DEM simulations of specimens that were isotropically consolidated. For comparison purposes, the DEM simulations drawn in gray represent the results of specimens sheared after anisotropic consolidation ( $K_0$  consolidation) and a  $b$ -change stage where necessary. Note that this convention is used for all the following plots unless it is specifically stated.

## 6. DEM simulations under normal loading

---

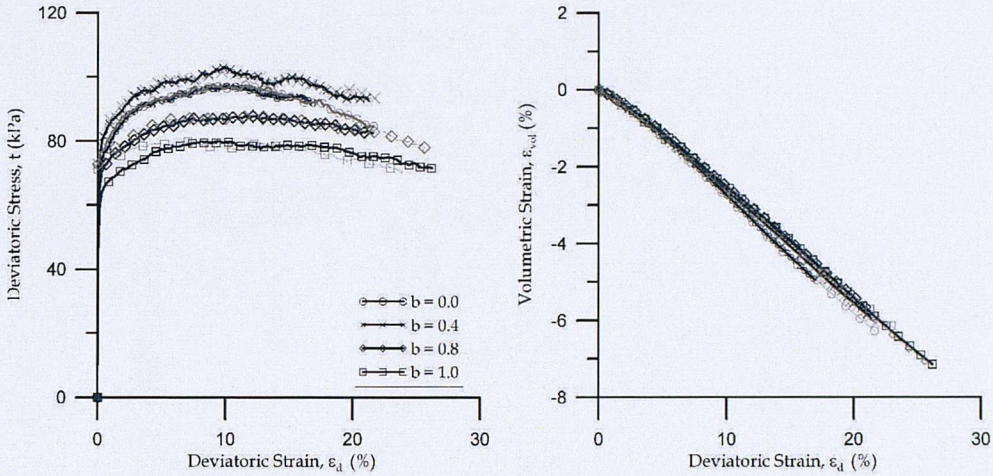


Figure 6.41: Effect of the intermediate stress ratio  $b$  - Comparison between the isotropically and  $K_0$  consolidated response

Referring to Figure 6.41 it is clear that both sets of simulations are very similar. However they are not identical. For certain  $b$ -values the stress-strain response of anisotropically consolidated specimens lies above the response of the isotropically compressed specimens. And in particular, the DEM simulations with  $b = 1.0$  has a very different stress-strain response. Also note that there are no significant differences in the volumetric strain development. For obvious reasons, the stress-strain response of anisotropically consolidated specimens starts with a deviatoric stress level of 72.77 kPa compared with the 0 kPa of the isotropic specimens.

Following the previous argument, and referring to Figure 6.42, it can be seen that the biggest difference in terms of the  $\phi'$  value occurs in the simulation closest to the plane strain conditions ( $b = 0.4$ ). This is perhaps the most clear and intuitive way to understand the effects of anisotropic consolidation. It is also interesting to note that for certain  $b$  values there were higher shear strengths in the anisotropic specimens, while in other cases the resistance of the isotropic specimens was higher. Similar conclusions can be derived from observations derived from Figure 6.43, which includes the shape of the failure envelopes for both sets of data in the generalised stress plane.

Since the stress-strain is so similar between the isotropically and anisotropically ( $K_0$ ) consolidated specimens, great differences in the evolution of the octahedral stiffness ( $G_{oct}$ ) were not expected. Note however, that although differences are insignificant enough to not being able to observe them in a plot, the anisotropically consolidated specimens showed a slightly lower initial stiffness. It is believed that this difference

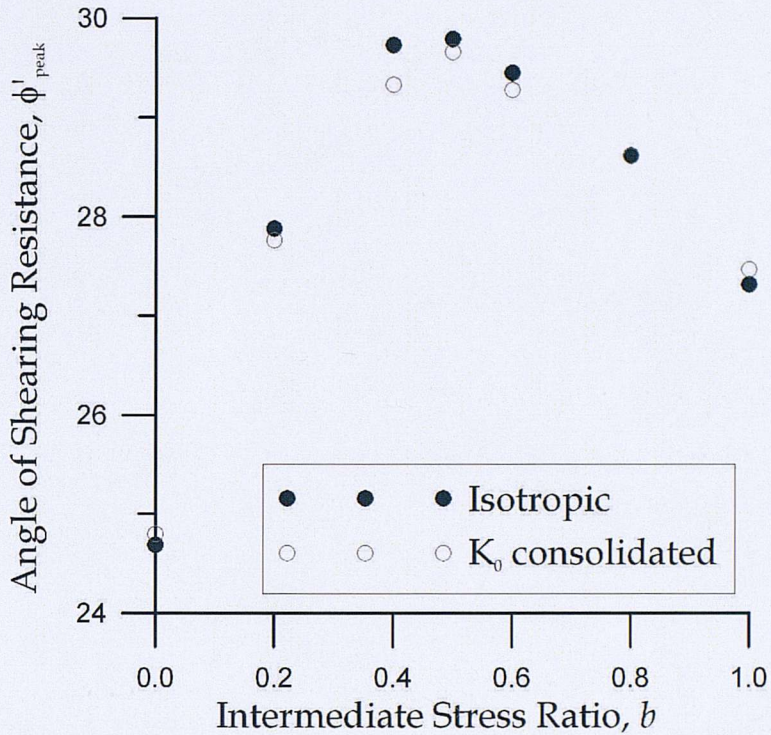


Figure 6.42: Effect of the intermediate stress ratio  $b$  on  $K_0$  consolidated specimens  
- Angle of shearing resistance ( $\phi'$ )

is caused due to the effect of the previous consolidation history of the  $K_0$  specimens.

### Micro-scale results

Starting with the micro-mechanical parameters, the evolution of the coordination number is presented in Figure 6.44. It is possible to see that in the case of anisotropically consolidated specimens the different  $b$  values do not produce marked differences in their critical  $Z$  values in opposition to the isotropic case (see Figure 6.29).

It is encouraging to know that the small differences in the macro-scale stress-strain behaviour can be explained in terms of the evolution of the deviatoric fabric. The trends illustrated in Figure 6.41 qualitatively match those observed in Figure 6.45. In particular and to ease the comparison, it is seen than the particular case with  $b = 1.0$  is precisely matched to the results observed in the stress-strain response. Note that the stress-strain curve in Figure 6.41 for  $b = 1.0$  can be distinguished in the same way in Figure 6.45.

A similar analysis to that performed in the isotropic case was performed to visually estimate differences in the contact force network for the two cases. However, dif-

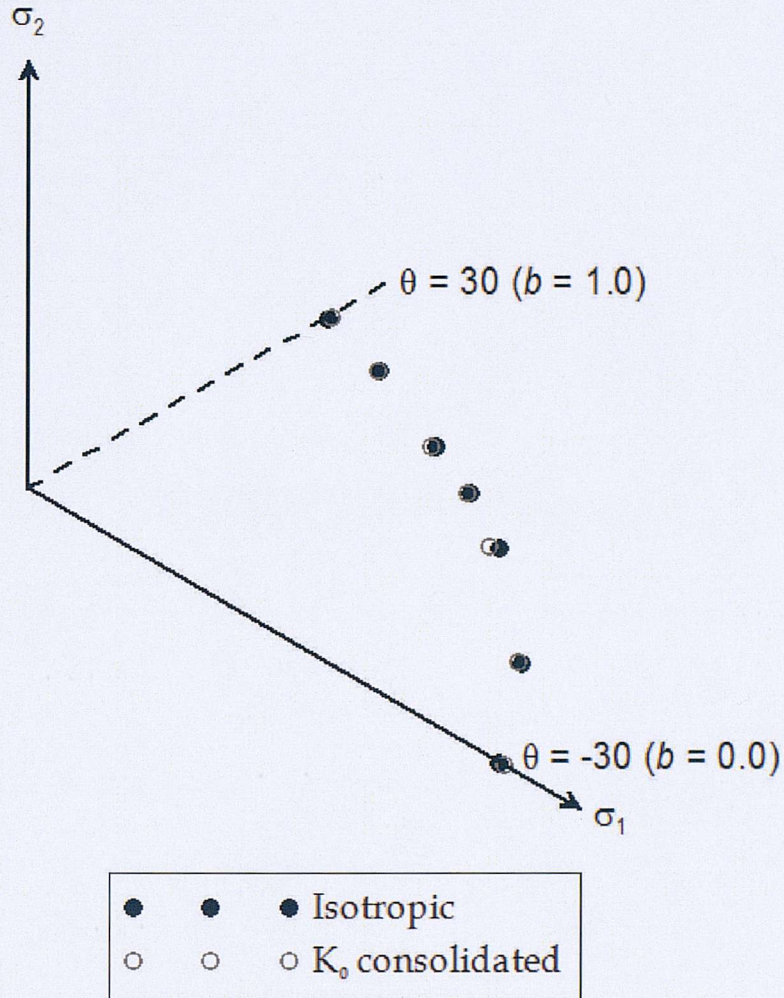


Figure 6.43: Effect of the intermediate stress ratio  $b$  on  $K_0$  consolidated specimens  
- Failure envelope in the  $\pi$ -plane

ferences where not visually identifiable. That is why these figures are not included here. The analysis of the contact force network is entirely quantitative and depends on the evolution of the deviatoric fabric.

It must be noted however that the load chains transmitting the deviatoric stress are aligned with the orientation of the major principal stress as clearly observed in Figure 6.32. The stability of these primary load carrying columns depends upon the lateral support provided by the orthogonal (or almost orthogonal) contacts that are orientated in the directions of the minor and intermediate principal stresses as schematically illustrated in Figure 6.46. As the intermediate stress ( $\sigma_2$ ) value increases, so too will the magnitude of the supporting compressive forces acting on the  $\sigma_2$  direction. The increase in these compressive forces effectively will increase the buckling resistance of the primary force chains. Detailed analysis of this mechanism

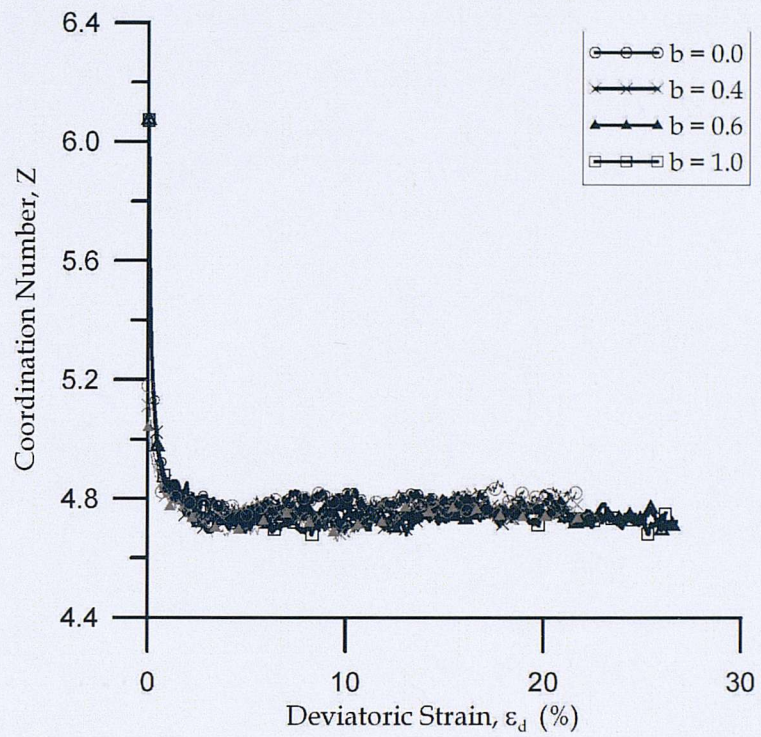


Figure 6.44: Effect of the intermediate stress ratio  $b$  on  $K_0$  consolidated specimens  
- Evolution of  $Z$

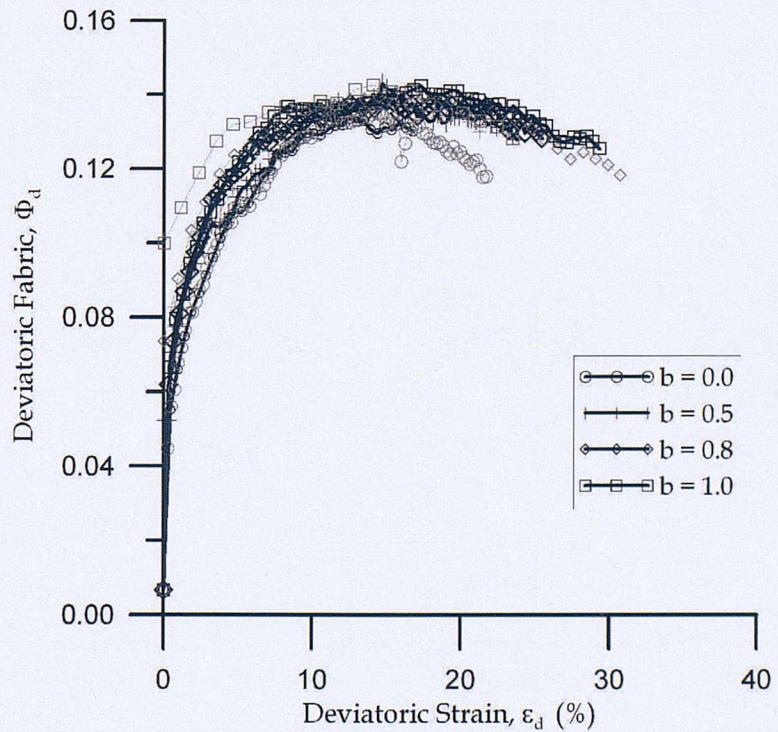


Figure 6.45: Effect of the intermediate stress ratio  $b$  on  $K_0$  consolidated specimens  
- Evolution of  $\Phi_d$

## 6. DEM simulations under normal loading

is non-trivial. Application of the analysis tools recently developed by Tordesillas & Muthuswamy (2009b) may be appropriate.

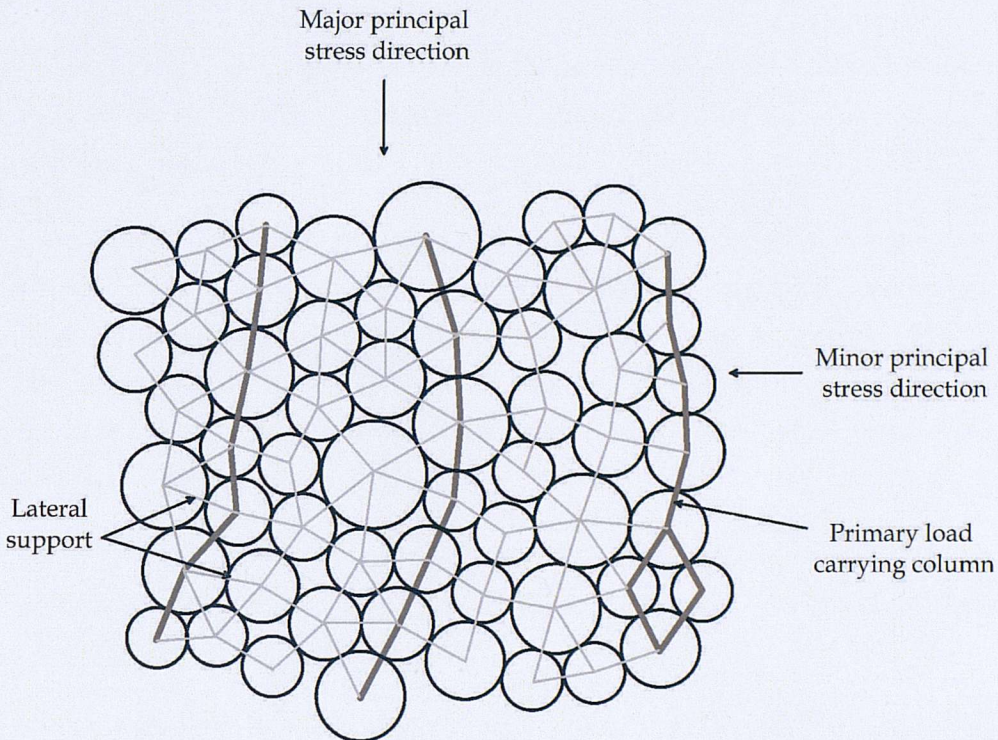


Figure 6.46: Schematic representation of main force carrying columns supported by lateral compressive stress that prevent chain buckling

In summary, DEM simulations show that the consolidation history affects the shearing behaviour of granular materials. Furthermore, the differences arise mainly due to the magnitude of anisotropy. Besides the magnitude of anisotropy is directly related to the relation between the main force loading carrying columns and the almost orthogonal forces providing lateral support that avoids the buckling of the main force chains.

## 6.6 Summary

This chapter discusses the macro- and micro-scale response of granular materials under different values of the intermediate stress ratio and involving normal loading with the major principal stress oriented in the vertical direction. The procedures to generate the DEM specimens are described in detail and the relevant DEM simulations are compared against physical experiments. A series of parametric studies were performed to assess the sensitivity of the simulations to many parameters, including

## 6. DEM simulations under normal loading

---

coefficient of inter-particle friction, initial density, elastic parameters and consolidation history. The key issues discussed in this chapter are summarised below:

- Different specimen generation techniques were assessed. Effective procedures to generate numerical specimens under initial specified stress states and porosities were proposed.
- Experimental results of both triaxial and HCA experiments are compared with DEM simulations, and it was demonstrated that they reasonably agree. It was postulated that the existing differences may be due to uncertainty in the input values (friction), lack of inherent anisotropy in DEM simulations, particle shape, presence of stress and strain non-uniformities in the HCA tests, amongst others.
- DEM simulations were used to prove that the range of sizes in the different grain size distributions are responsible for unexpected stress-strain behaviour of experimental HCA tests.
- It was shown that the macro-scale response of granular materials can be explained by underlying micro-scale interactions such as particle rotation, development of specific anisotropic soil structures and/or modification of contact force networks. Furthermore, it was illustrated that under certain  $b$  values the contribution of certain particle-scale interactions may be more dominant than others.

It was emphasized that the anisotropy of soil response can be qualitatively explained in terms of the relative contributions of main load carrying columns and the contacts forces that are orthogonal or almost orthogonal to these main force chains to provide lateral support. This dependence was clearly related to the magnitude of the intermediate stress ratio.

# Chapter 7

## DEM simulations involving principal stress rotation

### 7.1 Introduction

This chapter describes the results of DEM simulations including principal stress rotation. The algorithms implemented in the DEM code were described in Chapter 5, including their analytical validation. The validity of these new algorithms was also tested by simulating the response of isotropic specimens, and by comparing the results of simulations with experimental results on anisotropically consolidated specimens.

A detailed analysis of the macro- and micro-scale behaviour is described. Its results have allowed to propose a new fabric surface from which stress paths including  $\alpha$  and  $b$  could be interpreted and modelled.

The last part of the chapter describes some additional sets of simulations. The aim of these simulations is to understand the effects of the inherent anisotropy and demonstrate that the new DEM algorithms are able to simulate the existence of non-coaxial behaviour. The proposed fabric surface is also tested for different stress paths to those already analysed and the need for accurate and improved measures of fabric anisotropy is highlighted.

## 7.2 DEM simulations of hollow cylinder tests

This section presents the results of DEM simulations using periodic boundaries and the newly implemented algorithms as described in Chapter 5. The aim of these simulations is to demonstrate that the algorithms developed are able to replicate the observed experimental macro-scale behaviour of granular materials when subjected to shearing with the principal stresses oriented in different directions. Simulations on specimens isotropically and anisotropically ( $K_0$ ) consolidated are described. The behaviour of the anisotropically consolidated specimens is compared to the experimental results summarised in Chapter 4.

### 7.2.1 Isotropically consolidated specimens

In Chapter 2 it was mentioned that Arthur et al. (1981) used directional shear tests on cubical specimens deposited in the direction of the intermediate principal stress ( $\sigma_2$ ) and sheared with the major principal stress rotated at different directions measured on the plane perpendicular to the direction of deposition. Since their specimens were pluviated, they were inherently cross-anisotropic. However, when shearing over the plane of cross-anisotropy, the influence of the inherent anisotropy is eliminated when the principal stress direction is rotated in the plane perpendicular to the direction of deposition. Arthur et al. (1981) used this concept to demonstrate that the directional shear cell was performing correctly. Specimens tested with different principal stress orientations gave identical stress-strain response curves as it had been expected if the influence of the inherent anisotropy was removed.

The DEM simulations presented in this section are isotropically consolidated, therefore they have no inherent anisotropy. As a consequence, the principle used by Arthur et al. (1981) can be used to demonstrate that the newly implemented algorithms work in an appropriate manner when replicating HCA tests. When testing isotropic specimens with different major principal stress orientations, the same stress-strain response should be obtained.

The simulations presented in Figures 7.1, 7.2 and 7.3 correspond to specimens formed by 4000 spheres with the grain size distribution that corresponds to the “medium” sized ballotini. After isotropic compression up to 200 kPa, the stresses were modified to obtain a  $b$ -value of 0.5 and  $p' = 200$  kPa. Subsequently, the specimens were sheared while keeping  $b$ ,  $p'$  and  $\alpha$  constant. Note however, that as the legend in the figure indicates, each simulation was performed with a different  $\alpha$  value.

## 7. DEM simulations involving principal stress rotation

---

The stress-strain responses of some of these simulations are illustrated in Figure 7.1. Clearly, the curves overlap each other, and the same mobilised angle of shearing resistance is obtained for the different  $\alpha$  values. These results demonstrate that the DEM algorithms work in an adequate manner. Therefore, it provides confidence in the results obtained.

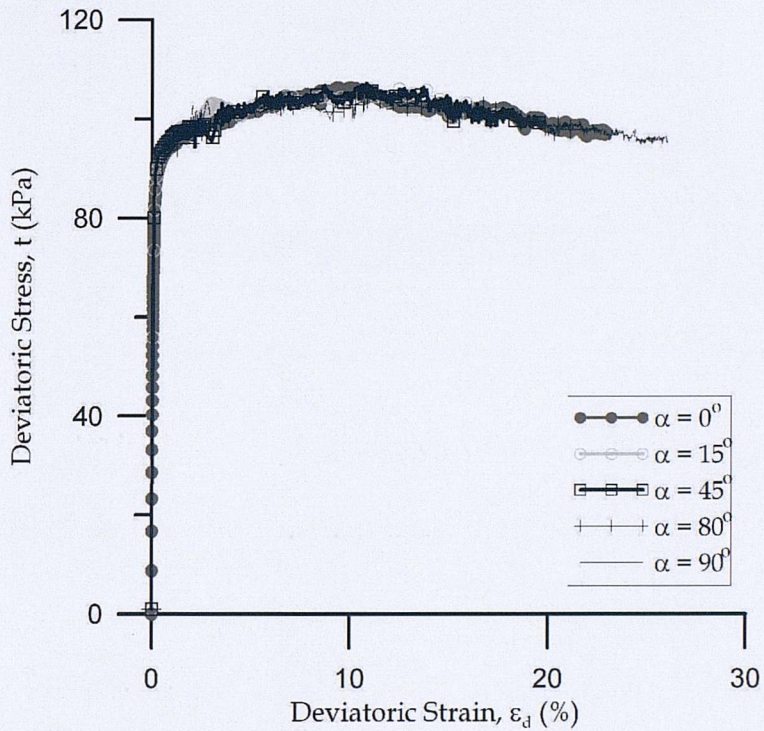


Figure 7.1: Stress-strain response for isotropically consolidated specimens sheared with different  $\alpha$  values

Simulations using periodic boundaries involving different principal stress orientations, as mentioned in Chapter 2, cannot be found in the literature. It is therefore interesting to discuss in a brief manner some micro-mechanical observations. The evolution of the coordination number ( $Z$ ) is presented in Figure 7.2. Since the stress-strain responses are all equal, and identical evolution of the coordination number would also be expected. This is clearly demonstrated in Figure 7.2.

It is interesting to observe that even though there is a total coincidence in the stress-strain response and the evolution of coordination number for all simulations, there is an influence of the major principal stress direction on the observed distribution of contact normal orientations. Figure 7.3 illustrates the contact normal distributions at peak shear strength for different  $\alpha$  values in the form of polar histograms. It is evident that the contacts are directed towards the orientation of the major principal stress. This is expected and it has been observed by many researchers both exper-

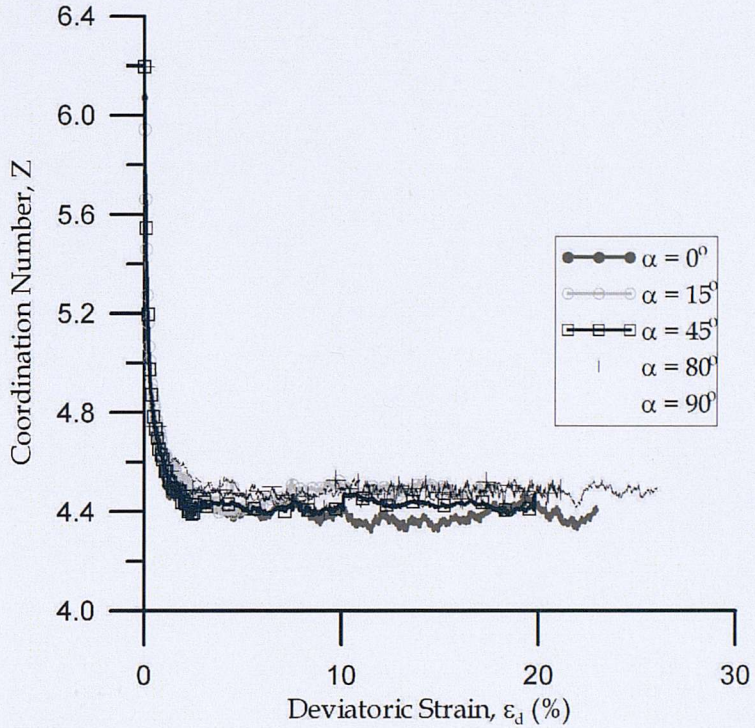


Figure 7.2: Evolution of the coordination number for isotropically consolidated specimens sheared with different  $\alpha$  values

imentally and numerically as described in Chapter 2. Note that the initial state for all these simulations was the same. In terms of the magnitude of anisotropy as defined by Rothenburg & Bathurst (1989), the initial state had an  $a$  value of 0.002 (i.e. isotropic) and a value at peak of 0.344. As explained before, the value of  $\theta_a$ , which describes the orientation of the major principal fabric, coincided with the orientation of the major principal stress in every case.

While only simulations using  $b = 0.5$  are presented here, similar observations were made for different  $b$  values including 0.0, 0.2, 0.8 and 1.0. Overall, while the angles of shearing resistance are not affected by the orientation of the major principal stress during shear, a sensitivity to the  $b$  value was observed. The dependence of the peak angle of shear resistance ( $\phi'_{peak}$ ) on the value of the intermediate stress ratio corresponded with the results presented in Figure 6.26.

### 7.2.2 Anisotropically ( $K_0$ ) consolidated specimens

Using the specimen generation approach described in Chapter 6, DEM simulations of anisotropically ( $K_0$ ) consolidated specimens are presented here for an assembly

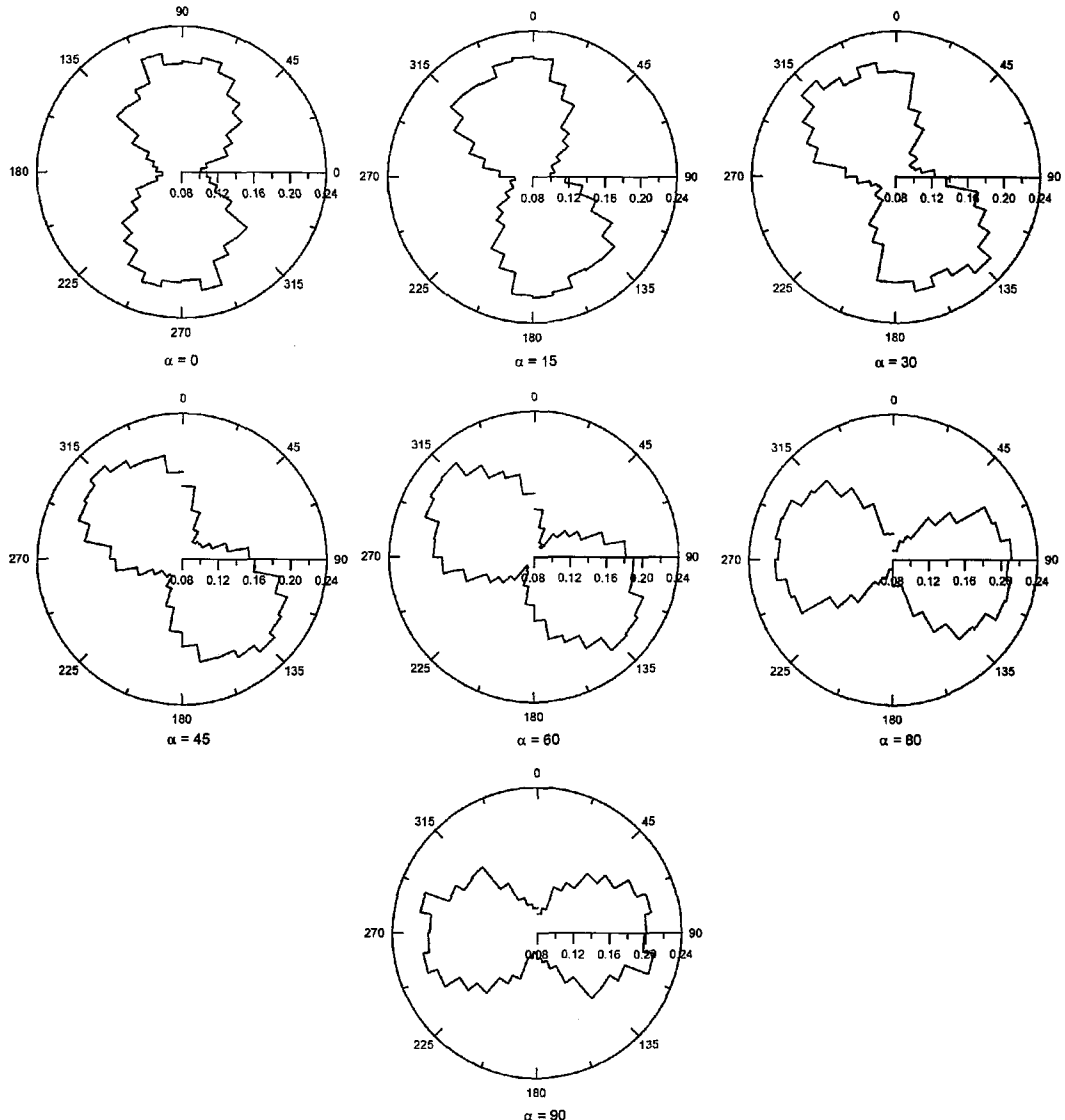


Figure 7.3: Polar distribution of contact forces in the  $XZ$ -plane

of 4000 spheres. The grain size distribution used corresponds to the “medium” sized ballotini. Experimental initial void ratios are equivalent to those in the DEM simulations, and furthermore, input parameters are measured experimentally, therefore results of LICHCA experiments are compared to simulations. The section also discusses macro- and micro-scale results for a set of simulations involving principal stress rotation.

### Experimental validation

As in previous chapters, it is important to compare the output of DEM simulations with the results of physical experiments. Figure 7.4 compares the stress-strain

responses for DEM simulations using different values of  $\mu$  with the experimental results from test LIC-M-D-3 ( $\alpha = 45^\circ$  and  $b = 0.5$ ). In this case, for ease of comparison, the stick-slip behaviour described in Chapter 4 has been removed from the behaviour. Therefore, the experimental stress-strain response is the envelope of the results presented in Figure 4.29.

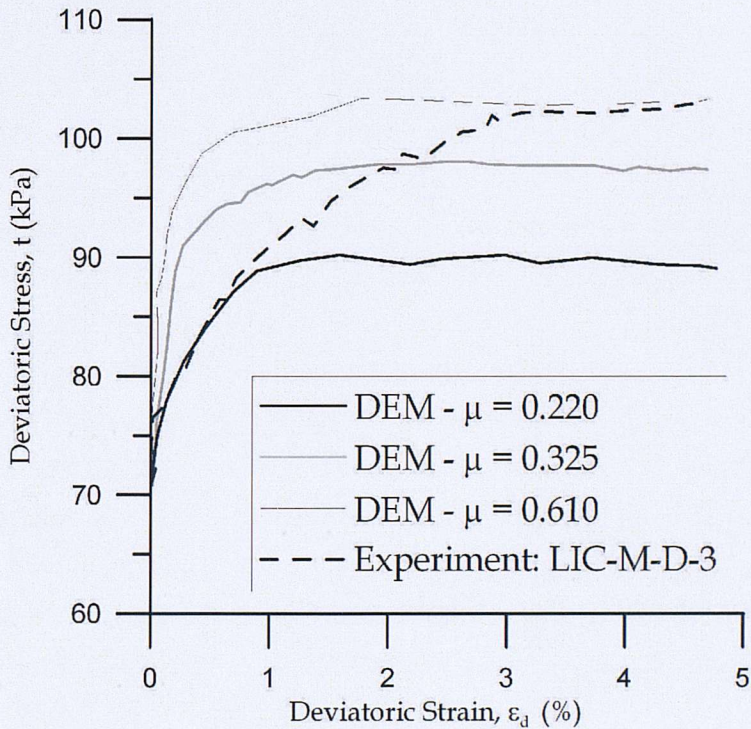


Figure 7.4: Comparison of experiment with DEM simulations - Stress-strain response for LICHCA test with  $\alpha = 45^\circ$  and  $b = 0.5$

Referring to Figure 7.4, it is clear that for the values of friction measured experimentally ( $\mu = 0.220$  and  $0.325$ ) the DEM simulations underestimate the experimental results. Note however that the initial response (up to  $2\%$  of  $\epsilon_d$ ) seems to be bounded by these two simulations. For completeness, Figure 7.4 also presents a DEM simulation that gives a reasonable match to the experimentally observed mobilised peak shear strength. In this case  $\mu$  was  $0.61$ . This high  $\mu$  value is clearly unrealistic and is not found in the experimental values measured by Cavarretta (2009). Furthermore, the initial stiffness of this simulation clearly overestimates the initial stiffness of the experiment.

In Chapter 4 physical tests on samples with two different aspect ratios under identical loading conditions ( $\alpha = 45^\circ$  and  $b = 0.5$ ) showed a stress-strain response that was almost identical. Consequently, it was concluded that this loading conditions were not largely affected by stress and strain non-uniformities. In Chapter 6 it was

proposed that experimental results seem to be affected by the presence of particle shape that cannot be simulated using spherical particles in the DEM simulations. These results give further confidence to that statement.

The data presented in Chapter 6 (normal loading, no stress rotation) also demonstrated that the experimental response in terms of peak angle of shearing resistance is underestimated by the DEM simulations. For these simulations the coefficient of inter-particle friction required to match the experiments was also unrealistically high. Furthermore, the value of  $\mu$  was 0.7 (normal loading) and was 0.61 for the simulation in Figure 7.4. This seems to confirm that although there are significant uncertainties in the  $\mu$  value, this uncertainty is not the source of discrepancy between the physical tests and the numerical results. The effects of non-uniformities were significantly reduced by increasing the aspect ratio of the physical experiments. It must therefore be concluded that the effect of particle shape is the most significant issue explaining the difference between the experiments and simulations. At this point is important to note that recent research performed by Dedecker (2009) has demonstrated that the shape of the particles also changes during shearing. These experimental observations have been confirmed recently at Imperial College using image analysis on “virgin” and sheared ballotini particles by Zhang (2009). Clearly, these observations introduce a more complex dimension into the issue of particle shape. Not only the simulated shape differs to the real particles, but also this shape changes as the tests progress.

The recent research of Ji et al. (2009) comparing DEM simulations and experiments on glass ballotini in an annular shear cell seems to confirm the effects of particle shape. In their study, Ji et al. (2009) observed that DEM simulations always underestimated the experimental results. Even when the coefficient of friction was unrealistically increased, the response could not be matched. It was found by Ji et al. (2009) that simulations and experiments could only agree if rolling friction was incorporated in the DEM simulations. These observations support the argument that particle shape plays a very important role in the physical experiments that is not simulated appropriately in the DEM simulations. If particle shape was included in the DEM simulations, the rotation of particles would be inhibited, increasing the mobilised shear strength. Incorporating rolling friction in the DEM simulations as proposed by Ji et al. (2009) has been frequently used in the literature and it is demonstrated that it inhibits particle rotation. Consequently, the shear strength is improved. However, this approach was not followed in this thesis as the rolling friction can not be measured. An additional consideration is that the

physical meaning of rolling friction is questionable. The rolling friction resistance is normally chosen arbitrarily.

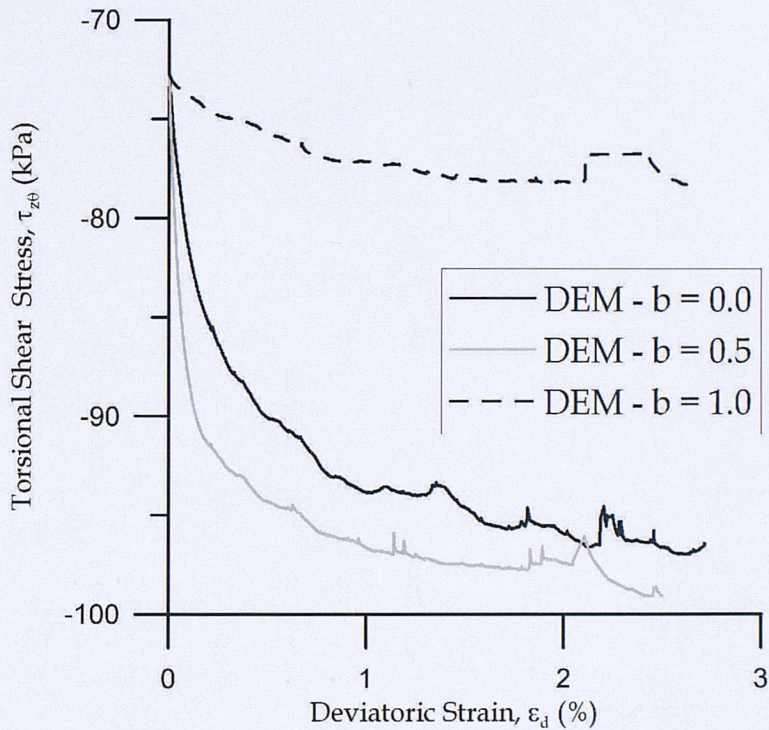


Figure 7.5: Evolution of torsional shear stress  $\tau_{z\theta}$  for DEM simulation with  $\alpha = 45^\circ$

It is important to note however, that the results of DEM simulations agree qualitatively with the physical experiments. Figure 7.5 illustrates the evolution of the torsional shear stress for three DEM simulations with different  $b$  values and  $\alpha = 45^\circ$ . When comparing this Figure 7.5 and Figure 4.23 which illustrates the same variables, the qualitative agreement is evident. In Figure 4.23 the highest (but smallest in magnitude) torsional shear stress occurs for the test with  $b = 1.0$  while the tests with  $b = 0.5$  and  $b = 1.0$  show a very similar torsional shear stress. The trend is the same in Figure 7.5.

### Macro-scale results

As the DEM simulations qualitatively agree with the physical experiments, it is interesting to study the effects of the principal stress rotation ( $\alpha$ ) on the behaviour of granular materials. This section presents a set of simulations with the same initial void ratio as in the physical experiments, a  $\mu$  value of 0.325, and an assembly of 4000 spheres. In the simulations shearing was performed with different values of  $\alpha$  while keeping  $b$  and  $p'$  constant.

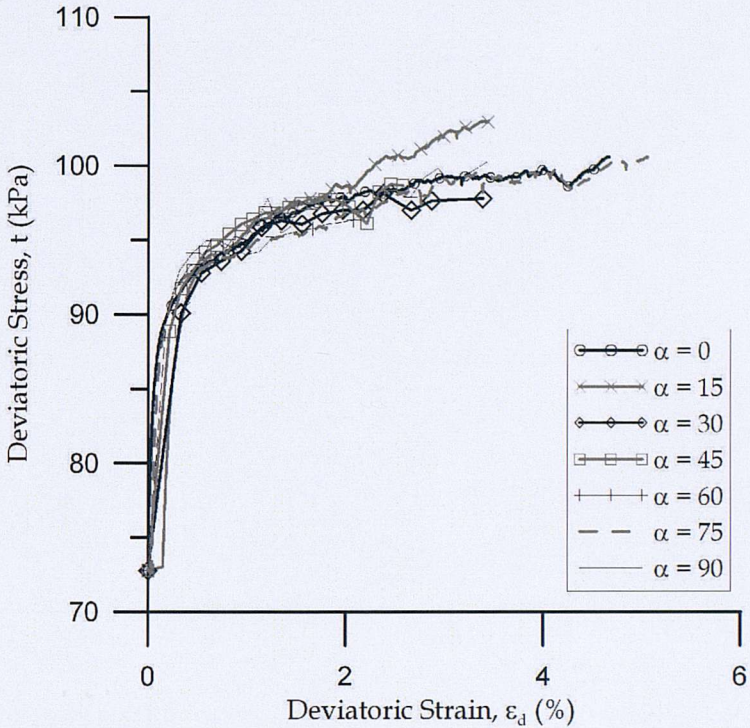


Figure 7.6: Stress-strain response for DEM simulations of anisotropically consolidated specimens sheared with  $b = 0.5$  and different  $\alpha$  values

Figure 7.6 shows the stress strain response for the anisotropically consolidated specimens, sheared with  $b = 0.5$  and different  $\alpha$  values. In comparison with Figure 7.1 which illustrated the response for the isotropic specimens, it is clear that in the case of the  $K_0$  consolidated specimens the curves do not lie on top of each other. From Figure 7.6, a trend can be observed in terms of the peak mobilised shear strength and the development of the octahedral stiffness. Similar trends were observed for different  $b$  values in the DEM simulations. Note that in Figure 7.6 a clear peak is observed only after 6% of the deviatoric strain (i.e. not in the figure) and at strain levels that could not be achieved experimentally for the LICHCA experiments. Nevertheless, the results qualitatively agree with the evidence found in the literature and described in Chapter 2.

The values for the peak value of the shear strength obtained for different loading conditions are presented in Figure 7.7. It is clear that the response is anisotropic and follows similar trends as the experiments described in this thesis and the available literature. In particular, it is seen that material is stronger when sheared in the vertical direction ( $\alpha = 0^\circ$ ) and that this strength is reduced as the principal stress orientation tends towards the horizontal. It must also be noted that the anisotropy is affected by the value of the intermediate stress ratio  $b$ . The difference between

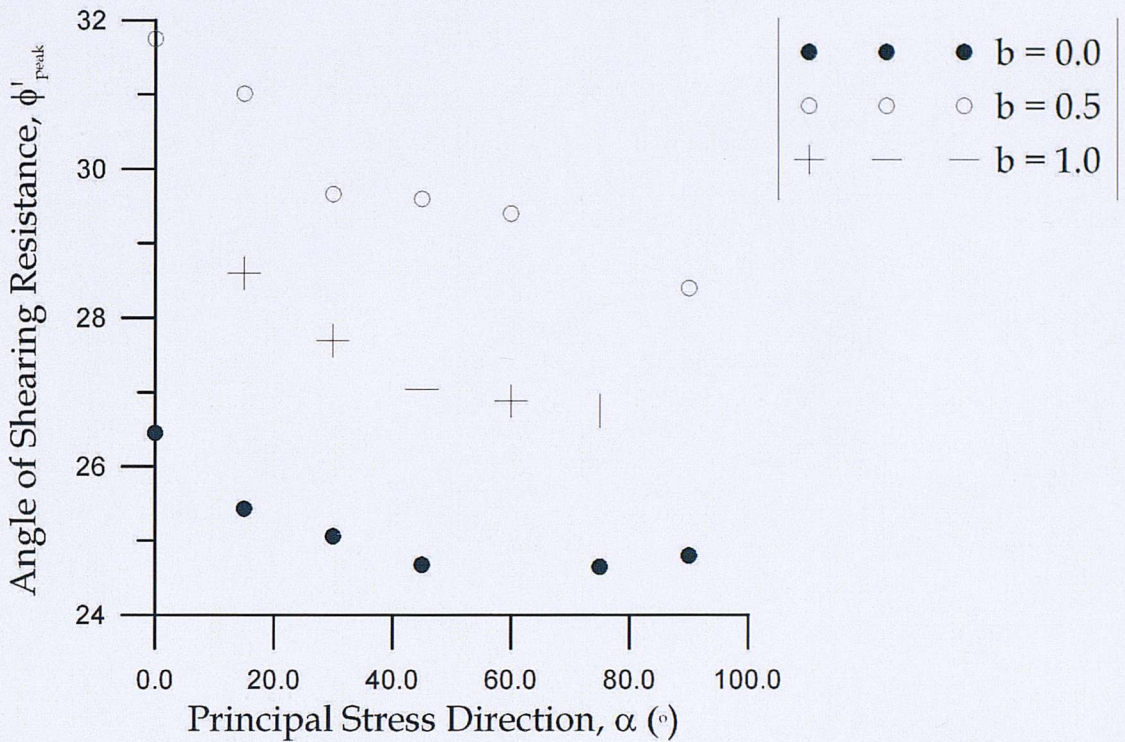


Figure 7.7: Peak shear strength for DEM simulations of anisotropically consolidated specimens sheared with different  $\alpha$  values

the maximum and minimum shear strengths is the greatest for the simulations with  $b = 0.5$ , and the least noticeable when  $b = 0.0$ . Furthermore, the results also show that the highest mobilised shear strength occurs close to the plane strain conditions ( $b \approx 0.5$ ) and the strength with  $b = 1.0$  is higher than with  $b = 0.0$ . These results agree with the results of the constant  $b$  tests described in Chapter 6 and also coincide with the experiments performed by Symes (1983) as observed in Figure 2.8.

Figure 7.8 presents the results given in Figure 7.7 in the deviatoric plane. It is evident from this figure that the orientation of the principal stresses modifies the strength envelope. The failure surface tends to shrink as the value of  $\alpha$  increases. Note however that the rate of decrease of this surface also depends on the value of the intermediate stress ratio. Referring to Figure 7.8 it can be seen that for  $b = 1.0$  the shrinkage of the failure surface is less than for  $b = 0.0$ . Therefore, the effects of  $b$  and  $\alpha$  cannot be treated separately.

Figure 7.9 includes the development of the octahedral stiffness for different  $\alpha$  values in simulations performed using  $b = 0.5$ . It is evident that the stiffness of the different specimens at small strains is different. The specimens sheared with the principal stress orientation close to the vertical are stiffer than the specimens sheared with

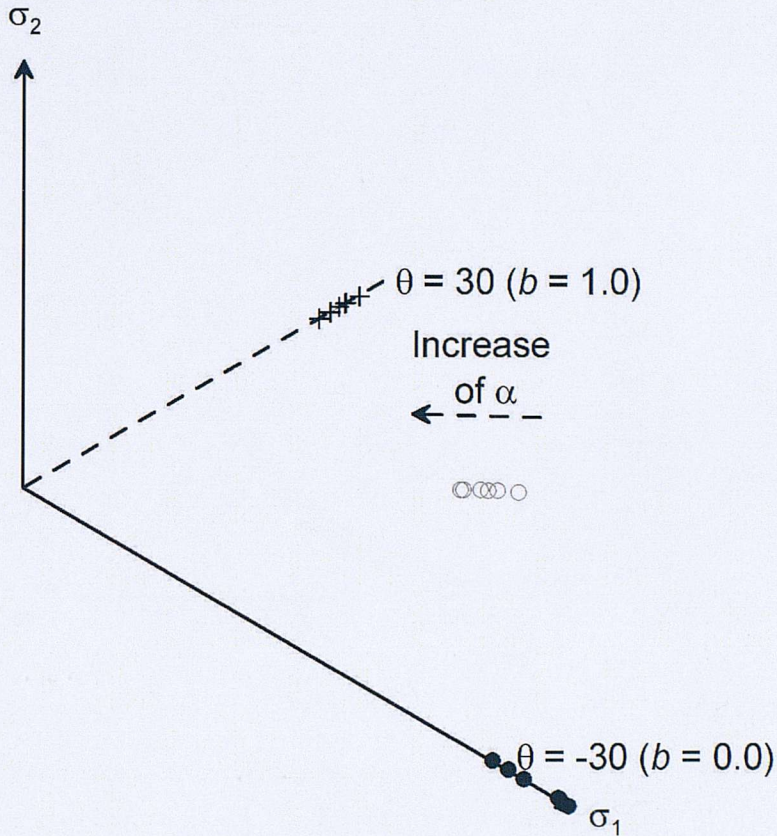


Figure 7.8: Effect of  $\alpha$  on  $K_0$  consolidated specimens - Failure envelope in the  $\pi$ -plane

the  $\alpha$  close to the horizontal direction. Similar trends were observed for the DEM simulations using  $b = 0.0$  and  $1.0$ . Once again, these results give further confidence to state that the DEM is successful to replicate the observed macro-scale behaviour of soils. The observations from these sets of simulations qualitatively coincide with the experimental results described in Chapter 2 and the results of the HCA experiments presented in Chapter 4.

### Micro-scale results

It is important to assess whether the observed macro-scale behaviour which was described in the previous section can be explained based on the particle scale interactions. To explore this, the evolution of the coordination number, the orientation of contact normals and the deviatoric fabric are analysed here.

Interestingly, Figure 7.10 illustrates that the orientation of the major principal stress

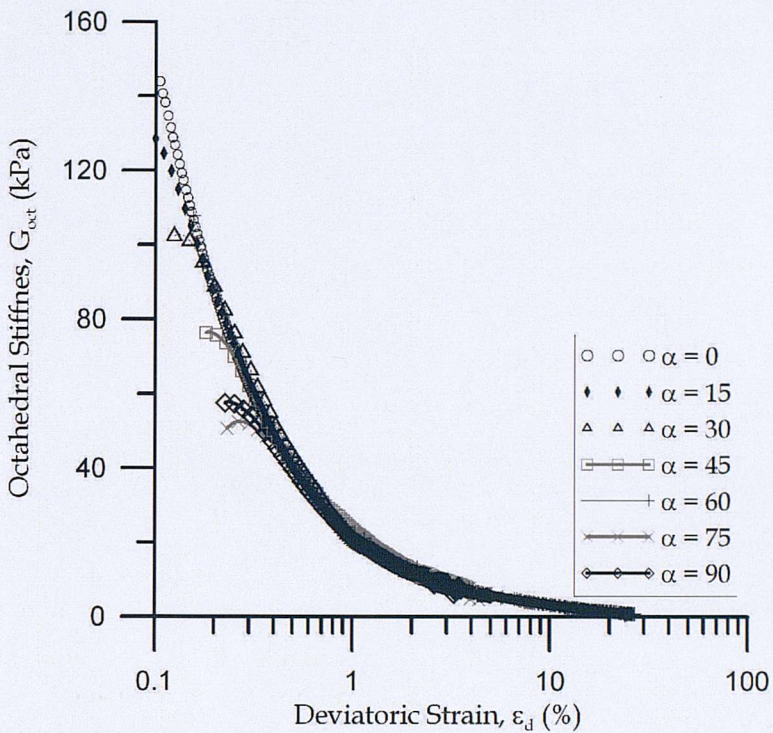


Figure 7.9: Effect of  $\alpha$  on  $K_0$  consolidated specimens - Development of octahedral stiffness (for  $b = 0.5$ )

does not affect the average number of contacts per particle. It is shown that independently of the value of  $\alpha$  the evolution of the coordination number for all DEM simulations with  $b = 0.5$  is the same. Similar observations could be derived if the results were plotted for the sets of simulations including  $b = 0.0$  and  $1.0$ . Note however that as discussed in Chapter 6, the value of  $b$  had a larger influence in this parameter. On the other hand,  $\alpha$  does not seem to have a significant influence in the average number of contacts.

Figure 7.11 includes the contact normal forces at the peak state for a set of DEM simulations with different  $\alpha$  values and  $b = 0.0$ . Slices with a thickness of 3 mm are presented for each of the orthogonal Cartesian planes. It can be observed that although in the  $XY$  and  $YZ$  planes the differences are difficult to see, the orientation of the large contact forces (in red) tends to align with the orientation of the major principal stress in the  $XZ$  plane.

As already stated, the influence of  $\alpha$  should not be considered in isolation from the effect of  $b$ . Figure 7.12 shows the normal contact force distribution for a set of simulations with  $\alpha = 45^\circ$  and different  $b$  values. Some differences can be observed when comparing the diagrams, however the differences are very difficult to visualise.

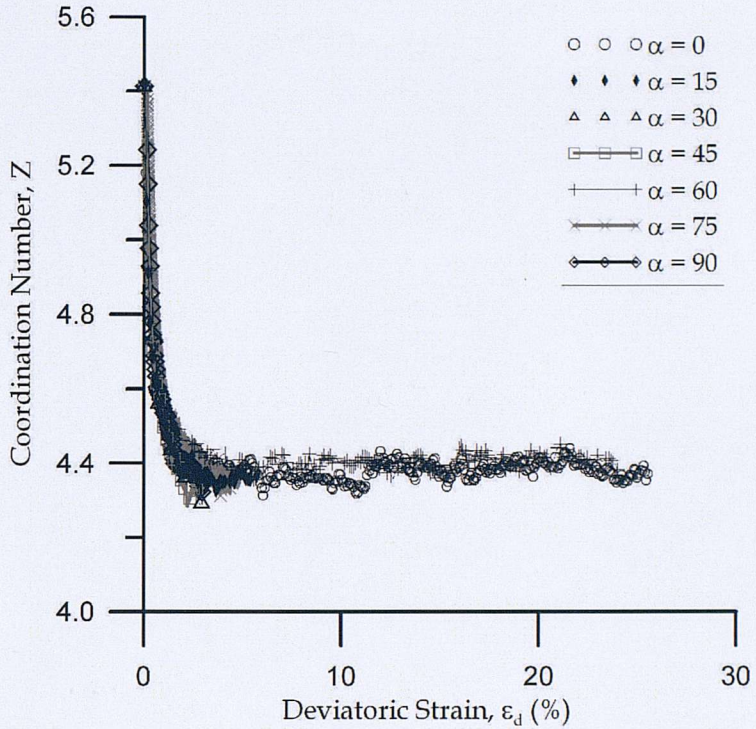


Figure 7.10: Effect of  $\alpha$  on  $K_0$  consolidated specimens - Evolution of coordination number (for  $b = 0.5$ )

With some effort it can be seen that  $b$  affects the magnitude of the contact forces. This is manifested by slightly different thicknesses in the networks of strong contact forces (in red). The difficulty of visualisation highlights the need for quantitative methods to describe soil fabric anisotropy.

As proposed by Rothenburg & Bathurst (1989) when the contact force distribution is represented in the form of polar histograms as in Figure 7.13 it can be quantified using the coefficients  $a$  and  $\theta_a$  from a Fourier series approximation. If Figure 7.13 is compared with Figure 7.3 it can be seen that slight differences can be observed. In particular, it can be observed that the polar histograms in Figure 7.13 are more anisotropic, this is confirmed by the presence of a bigger reduction of the concentration of contact forces in the minor principal direction. Quantitatively, this difference can also be derived from comparison of the magnitude of anisotropy  $a$ . For the isotropic simulations presented in Figure 7.3  $a = 0.344$ . In the  $K_0$  consolidated specimens from Figure 7.13  $a$  varies slightly for the different values of  $\alpha$  and has an average of 0.374. Note however that the differences for the different  $\alpha$  values are insignificant and can be attributed to the numerical accuracy of the Fourier approach.

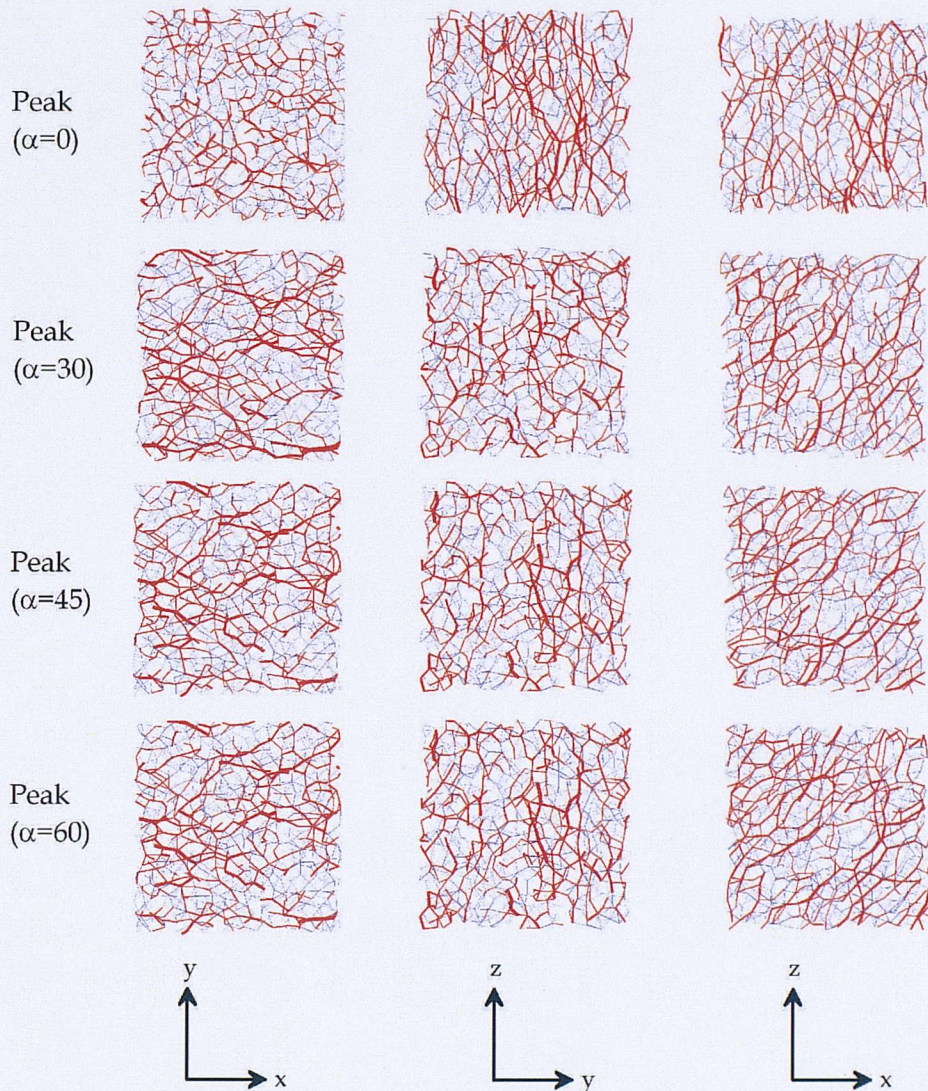


Figure 7.11: Effect of  $\alpha$  - Contact forces for three vertical slices through the DEM specimen (for  $b = 0.0$ )

Since the magnitude of  $a$  did not show significant differences at the peak condition as derived from the polar histograms, an analysis of the evolution of the deviatoric fabric  $\Phi_d$  was also performed. Figure 7.14 illustrates this evolution for a selected set of DEM simulations using  $b = 0.5$ . In Figure 7.14 the results for simulations with  $\alpha > 45^\circ$  have been omitted as they showed very similar results to the  $\alpha = 45^\circ$  case. This is coincident with the fact that the shear strength does not reduce significantly for this variation of  $\alpha$ .

Referring to Figure 7.14 it can be observed that there are marked differences for the different  $\alpha$  values. Of particular interest is the fact that the slowest increase on deviatoric fabric was obtained for the simulation with  $\alpha = 0$  which is the specimen

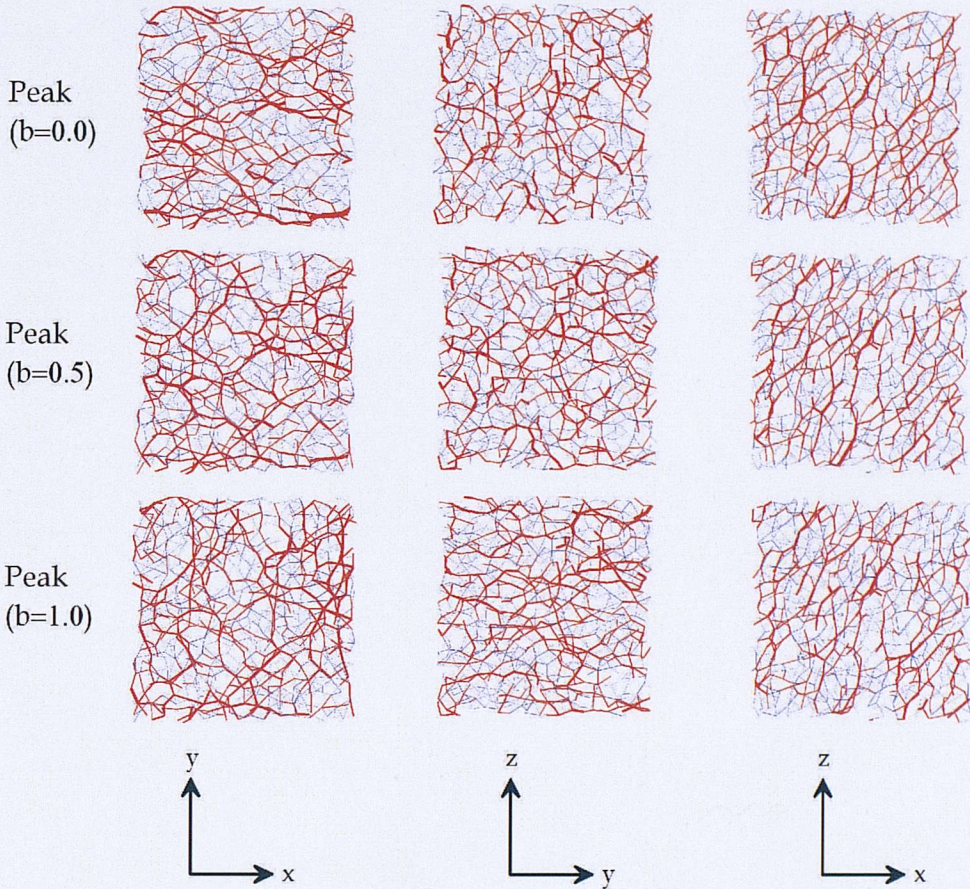


Figure 7.12: Effect of  $b$  on the anisotropic response - Contact forces for three vertical slices through the DEM specimen ( $\alpha = 45^\circ$ )

that experiences the highest mobilised strength. This fact was also observed in Chapter 6 in relation to the effect of  $b$  in the constant  $b$  tests using  $\alpha = 0$  (see Figure 6.30).

The observation above implies that the anisotropic response of granular materials is a manifestation of changes in the soil fabric. From the results obtained in this thesis, it may be proposed that the slowest change in deviatoric fabric is obtained for the lowest values of  $\alpha$  and for the  $b$  values close to the plane strain conditions for a logical reason. It can be hypothesized that for the constant  $b$  tests which are close to the plain strain conditions, the soil fabric is not very likely to change in a significant manner due to the deformation constraint imposed in the intermediate direction as discussed in Chapter 6.

The load chains transmitting the deviator stress are aligned with the orientation of the major principal stress. The stability of these primary load carrying columns

## 7. DEM simulations involving principal stress rotation

---

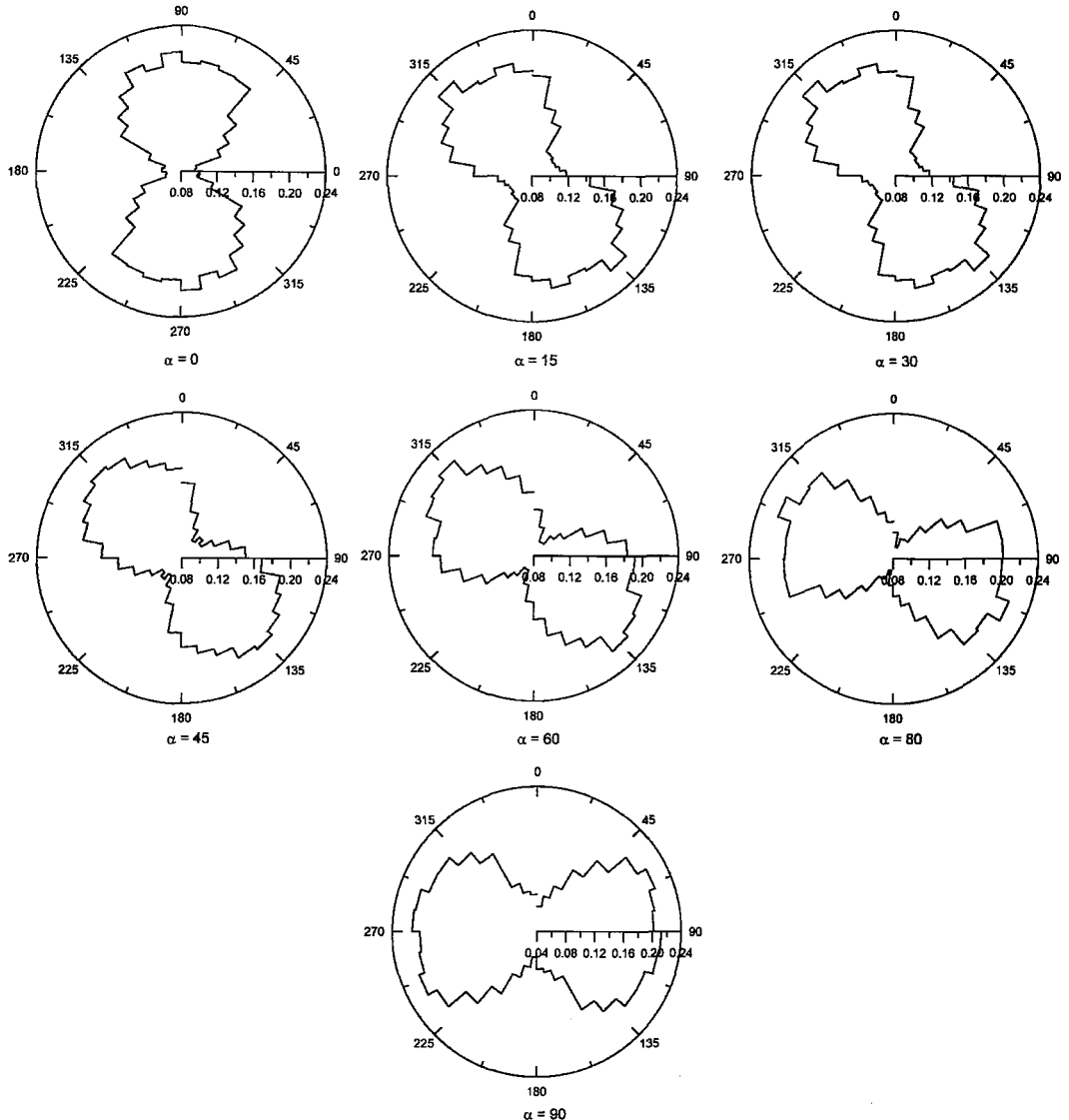


Figure 7.13: Polar distribution of contact forces in the  $XZ$ -plane for  $K_0$  consolidated specimens and  $b = 0.5$

depends upon the lateral support provided by the orthogonal (or almost orthogonal) contacts that are orientated in the directions of the minor and intermediate principal stresses (see Figure 6.46). As the intermediate stress ( $\sigma_2$ ) value increases, so too will the magnitude of the supporting compressive forces acting on the  $\sigma_2$  direction. The increase in these compressive forces effectively will increase the buckling resistance of the primary force chains. Detailed analysis of this mechanism is non-trivial. Application of the analysis tools recently developed by Tordesillas & Muthuswamy (2009b) may be appropriate.

The smallest deviatoric fabric change was observed in the simulations with the lowest values of  $\alpha$  because the primary load chains are already orientated in the  $\sigma_1$  direction,

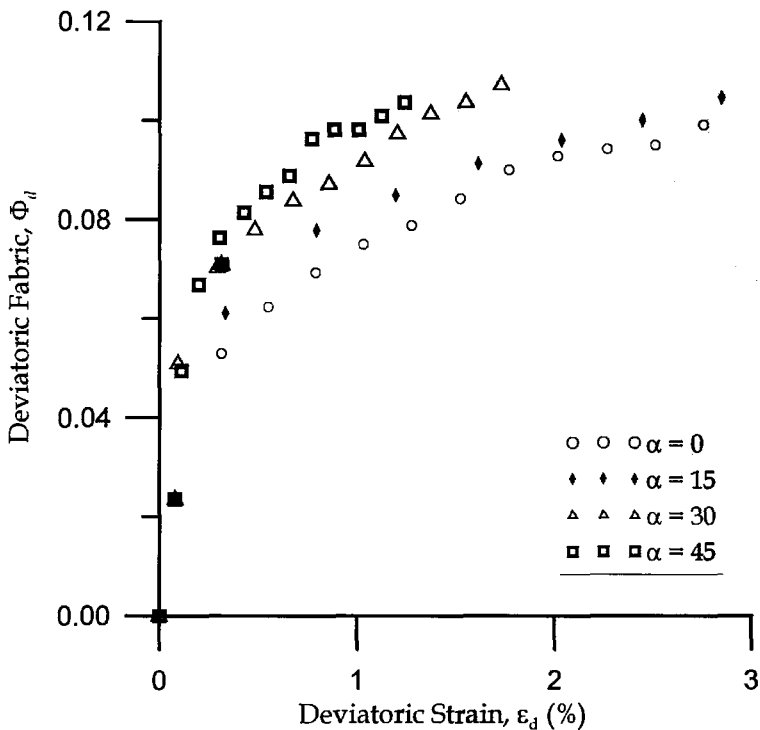


Figure 7.14: Effect of  $\alpha$  on  $K_0$  consolidated specimens - Evolution of the deviatoric fabric,  $\Phi_d$  (for  $b = 0.5$ )

therefore the specimen does not need to change its soil fabric in a significant way. In contrast, for specimens that were originally  $K_0$  consolidated and then sheared in a direction that is very different to that one experienced during consolidation, the original primary load chains will buckle/collapse as a new fabric develops, with the strong force network orientated towards the direction of  $\sigma_1$  to change the fabric radically (and quickly) in order to be able to withstand the applied stresses. The anisotropic response of granular materials is a consequence of the initial fabric prior to shearing and the need for substantial re-orientation of the contact network to reach the appropriate strong force network for the applied stresses. With high friction or high density values, soil fabrics that are anisotropic can remain in that condition in an easier manner than for lower density and friction values.

In the previous chapter it was demonstrated that the maximum magnitude of anisotropy, being quantified by the deviatoric fabric was increased as the inter-particle friction was increased. Similarly, it was observed that as the density increases the deviatoric fabric also increased. The hypothesis explained above does not contradict this observations. They are in fact complementary. Intuitively is not difficult to assume that for a specimen with a high density and an elevated inter-particle friction the soil fabric is less likely to change upon subsequent loading. A

higher density will impose a constraint in the possible movement of the particles, which in turn will inhibit the change of fabric. Furthermore, a higher friction enables the possibility of changing the orientation of the contact forces without a significant particle rearrangement. This is a consequence of the higher tangential forces that would be obtained for high values of  $\mu$ . Additionally, when  $\mu$  increases and the contact density increases, there is an increase in the buckling resistance of the strong force chains.

### 7.3 A new fabric surface to understand the behaviour of granular materials

In Chapter 2 it was mentioned that Thornton (2000) had described a fabric surface for constant  $b$  tests in the deviatoric plane. Thornton (2000) then used an inverted version of the failure model proposed by Lade & Duncan (1973) to quantify this fabric states. This was an useful model that could be used to quantify failure states depending on the deviatoric fabric states. However, this approach was formulated only for simulations in which  $\alpha = 0$ . (i.e. principal stress rotation is not accounted for).

In the previous section it has been shown that the magnitude of the deviatoric fabric is affected primarily by density, inter-particle friction, intermediate stress ratio  $b$  and the orientation of the principal stress  $\alpha$ . Since the changes of the deviatoric fabric can be directly related to the changes in these variables, a fabric surface or envelope depending on all these factors would be advisable for a better understanding and modelling of the behaviour of granular materials.

Two approaches could be used. A possible approach is to extend the method devised by Thornton (2000) and include the effects of principal stress rotation. Such an attempt is illustrated in Figure 7.15. Referring to this figure, it can be seen that the simulations with  $\alpha = 0$  do plot as an inverted Lade & Duncan (1973) failure criterion (see Chapter 6) when represented in terms of the deviatoric fabric at peak (data as squares). Clearly a pattern emerged when  $\alpha$  is included. It is observed for the tests varying  $\alpha$ , that the fabric surface shrinks as the value of  $\alpha$  increases. The effects of density and friction could also be included in this model by introducing expansion and contraction of the surfaces as these values change. This is very elegant approach since the deviatoric fabric space is analogue to the generalised stress space.

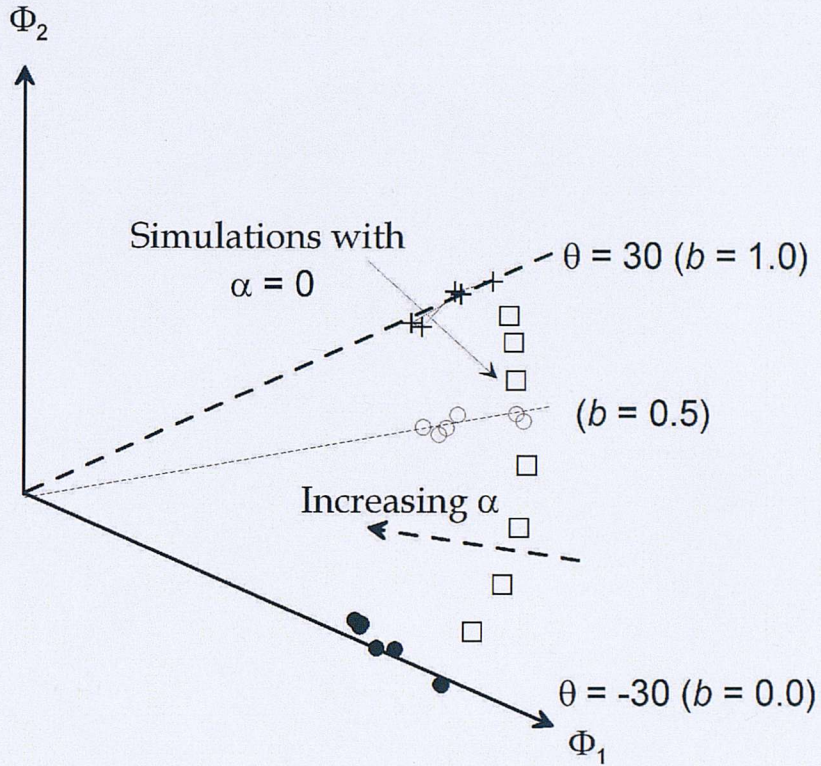
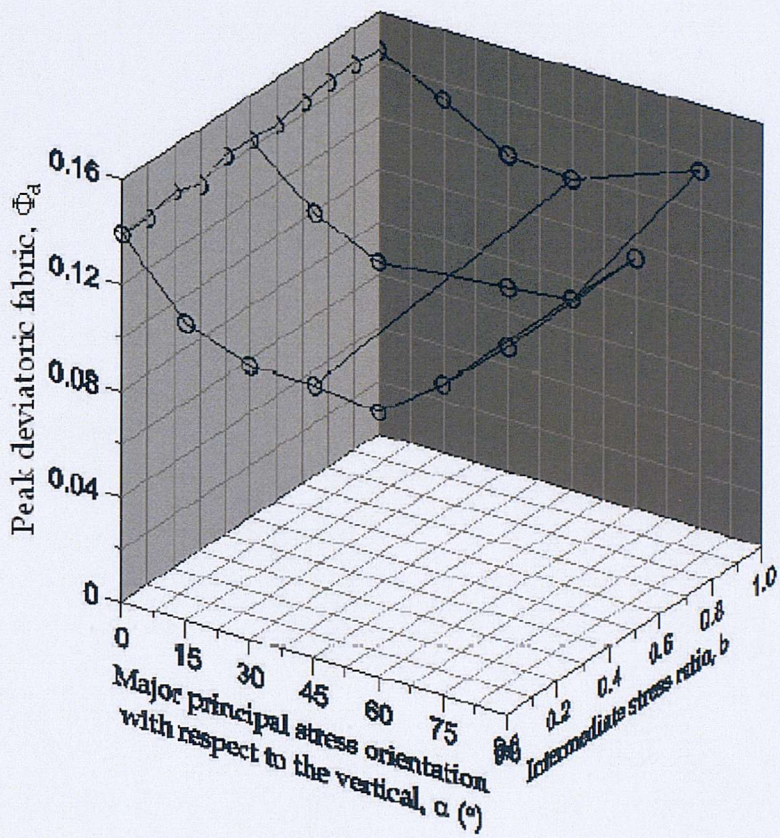


Figure 7.15: Deviatoric fabric in the generalised stress plane

A second, and new approach is proposed in this thesis and comprises a fabric surface in terms of  $b$ ,  $\alpha$  and the deviatoric fabric  $\Phi_d$ . The surface illustrated in Figure 7.16 was obtained using the set of simulations with  $\mu = 0.325$ . Clearly, in the  $\alpha$ - $b$ - $\Phi_d$  space a well defined fabric surface can be described. Equally, this surface can be shrunk or expanded with the corresponding change in density or inter-particle friction.

The proposed approach can be visualised as an alternative version of the surface proposed by Symes (1983). However, instead of the principal stress ratio, or the shearing strength the deviatoric fabric is used. This seems to be a valid approach because as already discussed shear strength can be explained in terms of deviatoric fabric. Furthermore, this surface must be seen as an ultimate boundary surface that limits the change in soil fabric for a specific granular material.

Both of the approaches described above can be successfully used to understand and model the behaviour of granular materials. The model proposed by Thornton (2000) requires the three principal values of the deviatoric fabric tensor in addition to the


 Figure 7.16: Newly proposed  $\alpha$ - $b$ - $\Phi_d$  space

density, friction,  $b$  and  $\alpha$ . The model presented here on the other hand, also requires the three principal values of the deviatoric fabric, but it puts these values together into the value of  $\Phi_d$ . This represents a reduction in the number of parameters that can ease the mathematical modelling of soil behaviour in terms of its fabric. This is advantageous if these parameters were to be incorporated into a constitutive model for example.

The potential for applicability of this fabric surface is significant, as it directly relates discrete interactions with macro-scale behaviour. Evidently, numerous additional simulations and experiments are required to test its validity. In particular, different grain size distributions and stress levels should be tested. The fact that the fabric surface could have a kinematic nature that relates directly to yielding is not discarded. However, more research is needed to confirm this assumption.

## 7.4 Effect of pre-shearing on the anisotropic response of granular materials

An effective way to produce an anisotropic structure is to pre-shear a specimen to a stress state close to failure and then reconsolidate it prior to the final shear. Such strategy is followed here for two DEM simulations. This process was adopted here as a means to replicate the inherent fabric in the physical tests (influenced by the deposition of particles under the action of gravity). An assembly of 4000 “medium” sized spheres was isotropically consolidated to 200 kPa and then sheared under triaxial compression until 6.7% deviatoric strain was reached. The specimen was then relaxed to an isotropic stress of 200 kPa. At this point two simulations were performed; both with  $p' = 200$  kPa and  $b = 0.0$ , but one was sheared with  $\alpha = 0^\circ$ , the other one with  $\alpha = 90^\circ$ . In this way two specimens, both with the same consolidation history were sheared with different orientations of the major principal stress.

A series of triaxial simulations informed the decision to shear to 6.7% prior to relaxation. At this strain level, following unloading to 200 kPa, the anisotropy of the samples was quantifiable. This anisotropy is clear in Figure 7.17 where a polar histogram of the contact normal distribution is illustrated. The magnitude of anisotropy ( $a$ ) as defined by Rothenburg & Bathurst (1989) can be used here since the specimens are axi-symmetric at this stage. After re-consolidation, and prior to final shearing  $a = 0.104$ . This value compares to  $a = 0.248$  which is produced after anisotropic  $K_0$  consolidation as described in Section 6.3.2.

While attempts were also made to achieve an anisotropic fabric using  $K_0$  consolidation, it was only after pre-shearing that specimens retained their anisotropic fabric during the relaxation. The difference in the two fabric arises when straining is introduced and the particles are forced to re-arrange. On the other hand, when the procedure is stress-controlled, the presence of high friction and low stress changes implies that the contact forces can re-orientate to withstand the stress state without significantly changing the arrangement between particles (i.e. the proportion of load transmitted by the normal and tangential components of the contact forces varies without significant re-orientation of contact normals orientations). Where  $K_0$  consolidation was used the anisotropy ( $a$ ) was only 0.002 when the sample stress was reduced to the isotropic state, while specimens after pre-shearing remained anisotropic when the stresses were relaxed.

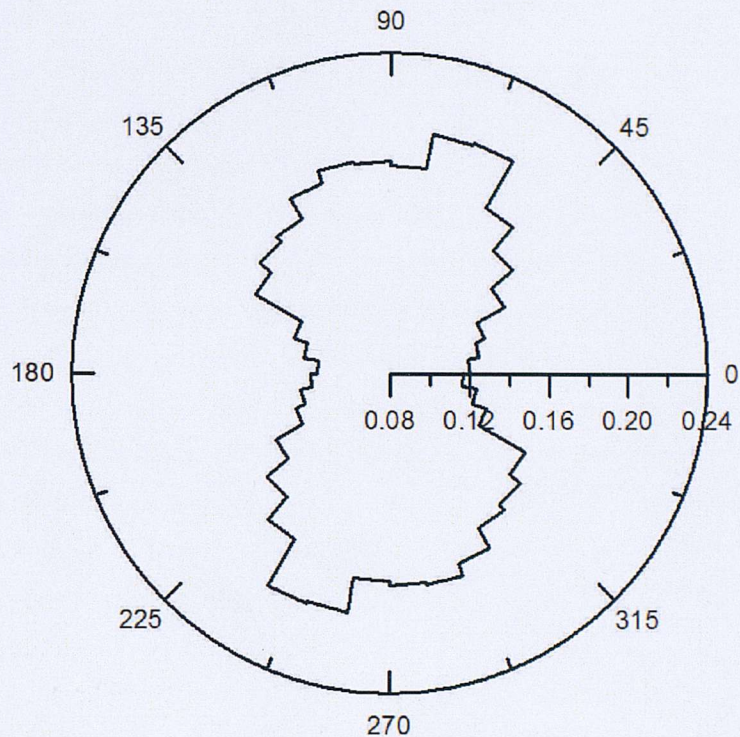


Figure 7.17: Magnitude of anisotropy ( $a$ ) after re-consolidation for simulations assessing the effects of inherent anisotropy

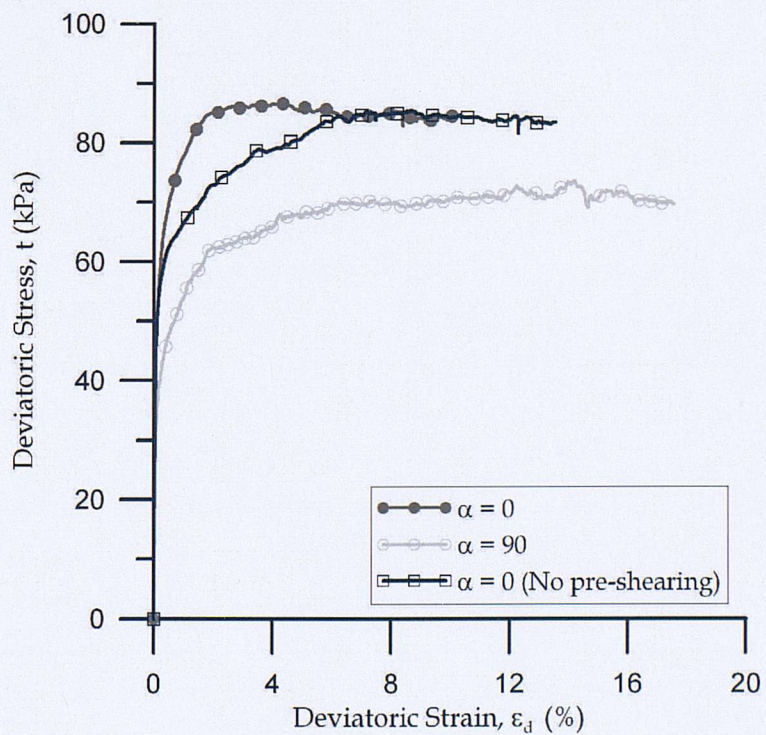


Figure 7.18: Influence of the inherent anisotropy in the stress-strain response for different major principal stress orientation

The influence of the inherent anisotropy on the material response is illustrated in Figure 7.18. It is clearly seen that the sample sheared with  $\alpha = 90^\circ$  is significantly weaker than the sample sheared with  $\alpha = 0^\circ$ . Furthermore, it can be observed that the response of the anisotropic (pre-sheared specimen) differs from the response of the isotropic specimen with the same initial conditions and stress path. It is evident that the anisotropic specimen is stiffer in the vertical direction ( $\alpha = 0^\circ$ ). Consequently, upon shearing it presents a higher shear strength when sheared with  $\alpha = 0^\circ$  than when sheared in the horizontal direction ( $\alpha = 90^\circ$ ). These numerical results qualitatively agree with both experimental results of Symes et al. (1982) (on Ham river sand) and the conclusions of Wong & Arthur (1985). Furthermore, these results also confirm that the mobilised shear strength is related to the way the soil fabric changes during shearing. Once again, a vertically pre-sheared specimen does not need to change its structure to withstand a vertical force. The vertical load carrying columns are in place to resist vertically applied loads, but when stressed horizontally, less developed force chains are loaded.

Referring to Figure 7.18, it can also be observed that for the simulations with  $\alpha = 0^\circ$ , although a strict critical state is not achieved, an apparent critical state can be inferred, where both specimens mobilise the same stresses. This similar large strain response suggests that during shearing the initial inherently anisotropic fabric is modified and tends to coincide for both specimens.

A similar study was performed by Yimsiri & Soga (2001) but considered soil behaviour sheared under undrained conditions. However, the conclusions derived from that study coincide with those derived here. The numerical results presented here confirm the hypothesis that the DEM simulations are under-estimating the shear resistance observed in the physical experiments because the effects of inherent anisotropy were not incorporated in the periodic cell implementation. If inherent anisotropy was included in the periodic cell simulations, the agreement between simulations and experiments would be greater. Numerical approaches to produce inherent anisotropy could be developed but they are beyond the scope of this thesis. Furthermore, it seems likely that the differences in particle shape (comparing simulations and experiments) are likely to have a more significant effect on the responses.

## 7.5 Influence of the initial structure on the development of non-coaxiality

It is widely recognized that the behaviour of granular materials can in some situations be non-coaxial. Experimental studies including the work of Gutierrez et al. (1991), demonstrate that the orientations of the strain and stress increments may not coincide. Thornton (2000) performed DEM simulations of a constant deviatoric strain test during shearing and showed that non-coaxial behaviour exists and that the extent of the non-coaxiality also depends on the stress path. Additionally, Thornton (1979) proved using an analytical approach that this non-coaxial behaviour is indeed a characteristic feature that might be observed in the behaviour of granular materials. Many researchers agree on the fact that this non-coaxiality is determined by the soil structure (fabric) generated during deposition.

In this section, DEM simulations using random and FCC assemblies confirm that these observations are also found in the simulations with the recently implemented algorithms. For comparison, a simple shear test simulation of an isotropically consolidated specimen is performed for both a FCC assembly, and an assembly with a random distribution of spheres of the same size. The purpose of this comparison was to show that the development of non-coaxiality is strongly dependant on the initial arrangement (fabric) of the particles in the assembly. A simple shear test is simulated, after isotropic consolidation (200 kPa), the specimens are sheared in the  $XZ$ -direction while a stress of 200 kPa is kept constant in the  $y$  and  $z$  directions.

Since we are concerned with the development of the orientation of the principal stress and strain, they are represented in Figure 7.19. Note that non-coaxiality is analysed by geotechnical engineers in terms of stress and strain increment directions. Furthermore, some researchers separate those increments in terms of elastic and plastic strains. Research performed by physicists additionally shows the development of principal stress and strain directions as illustrated in Figure 7.19. Referring to the stress and strain orientations for the random specimen, the results show the typical non-coaxial behaviour that is sometimes observed in granular materials. Although the principal stress and strain directions are similar, the strain orientation is initially ahead of the stress direction. However, as the level of strain increases, they tend to coincide. These results agree with the experimental results of Zdravkovic (1996) and the experiments from the present thesis. These results also agree with the recent numerical results of Tordesillas & Muthuswamy (2009a).

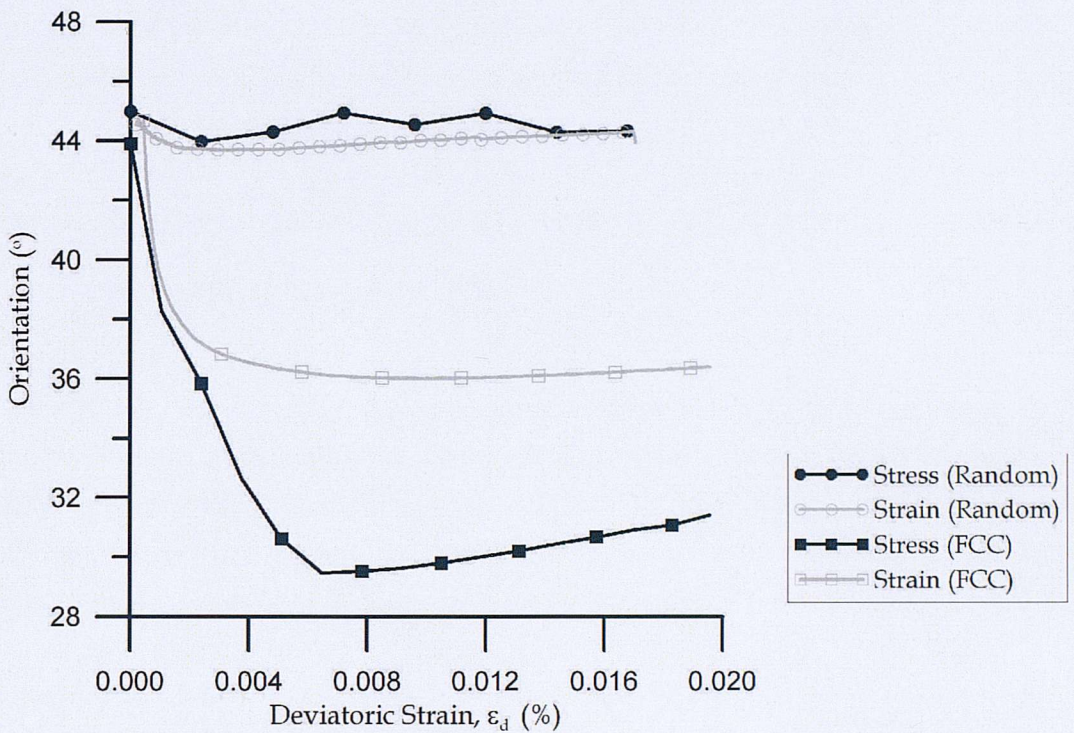


Figure 7.19: Influence of the initial fabric in the development of non-coaxiality

Concerning with the behaviour of the FCC assembly, both stress and strain directions appear to be tending towards a common value only at very large strains. However, it is evident that in opposition to the random specimen, the stress direction is ahead of the strain direction. These observations can be explained in relation to the initial fabric of the specimen. Initially the FCC fabric is in a highly stable state. A FCC assembly attains the minimum possible void ratio and the maximum attainable coordination number. Furthermore, this situation is homogeneous throughout the sample. During simple shear, the original FCC fabric tends to change, but due to the initial uniformity, particles take longer to re-arrange. In a FCC assembly the orientation of the principal stress can easily change without need for significant inter-particle contact re-arrangement. The direction of the principal strain however is highly dependant on the possibility of inter-particle contact re-arrangement. The ability to re-arrange inter-particle contact distribution in a FCC assembly is limited due to its high density and elevated number of inter-particle contacts with specific geometrical configuration.

As a conclusion, it has been demonstrated that the development of non-coaxiality is dependant on the initial fabric and furthermore, that it is possible to simulate this typical soil behaviour using the DEM algorithms recently implemented in the

code. Clearly, additional research is needed to provide further understanding of the micro-scale mechanisms underlying this macro-scale observations.

## 7.6 Stress path dependance of the response of granular materials

In this thesis, the behaviour of granular materials has been assessed in terms of a deviatoric plane with a constant mean effective stress of 200 kPa. By varying  $\alpha$  and  $b$  the whole area of the deviatoric plane has been explored. It is expected that under different values of  $p'$  similar behaviours could be observed. To assess the effect of different stress paths that include changes in the mean effective stress are paramount to confirm if a fabric boundary framework could be generalised for the widest set of loading conditions.

The simulations presented in this section are performed with the aim of assessing the influence of stress paths slightly different to those previously described. Some of these stress paths involve shearing under such conditions that the value of  $p'$  varies during shearing. These simulations could be directly compared to simulations with constant  $p'$  values.

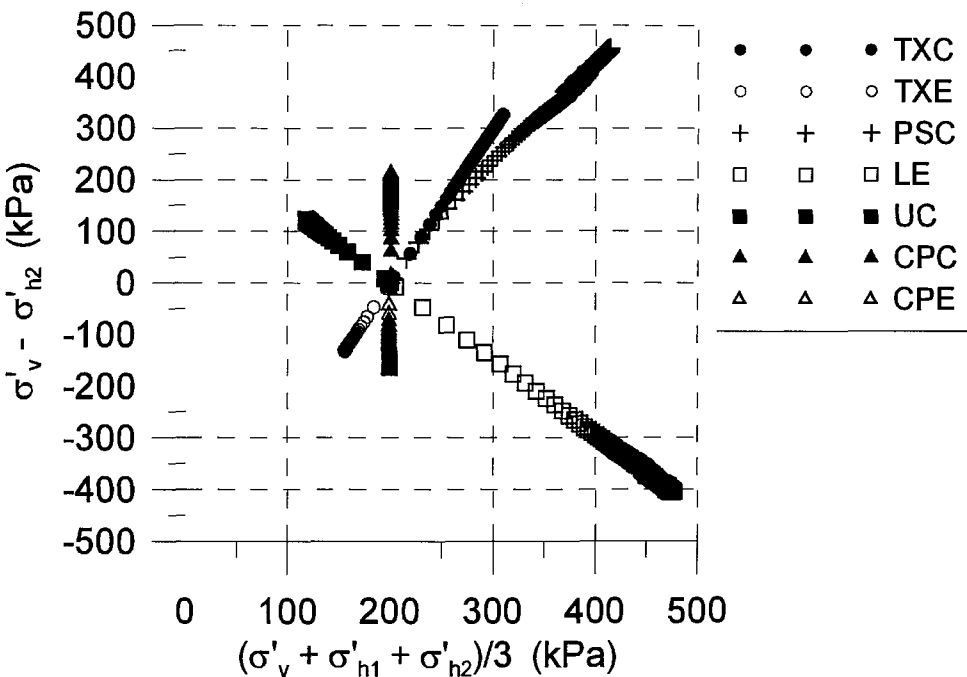


Figure 7.20: Shearing stress paths - Variable mean effective stress ( $\mu = 0.325$ )

## 7. DEM simulations involving principal stress rotation

A series of stress paths were performed on assemblies of “medium” sized spheres with 4000 particles, the same initial density, and  $\mu = 0.325$ . All stress paths included an initial isotropic consolidation to 200 kPa prior to shearing. The different stress paths evaluated in this study are illustrated in Figure 7.20. A brief description of each of the stress paths is as follows:

- **TXC** = Triaxial compression. Compression in the  $z$ -direction while  $\sigma_x = \sigma_y$ ,  $b = 0.0$ ,  $\alpha = 0^\circ$  and variable  $p'$ .
- **TXE** = Triaxial extension. Extension in the  $z$ -direction while  $\sigma_x = \sigma_y$ ,  $b = 1.0$ ,  $\alpha = 90^\circ$  and variable  $p'$ .
- **PSC** = Plane strain compression. Compression in the  $z$ -direction while  $\sigma_x$  is kept constant and  $\epsilon_y = 0$ .  $b \approx 0.4$ ,  $\alpha = 0^\circ$  and variable  $p'$ .
- **LE** = Loading extension. Compression in the  $x$  and  $y$ -directions while  $\sigma_z$  is kept constant.  $b = 1.0$ ,  $\alpha = 90^\circ$  and variable  $p'$ .
- **UC** = Unloading compression. Extension in the  $x$  and  $y$ -directions while  $\sigma_z$  is kept constant.  $b = 0.0$ ,  $\alpha = 0^\circ$  and variable  $p'$ .
- **CPC** = Constant  $p'$  compression. Compression in the  $z$ -direction while  $b = 0.0$ ,  $\alpha = 0^\circ$  and  $p'$  were kept constant.
- **CPE** = Constant  $p'$  extension. Compression in the  $z$ -direction while  $b = 1.0$ ,  $\alpha = 90^\circ$  and  $p'$  were kept constant.

As becomes apparent, the set of stress paths includes tests on a constant deviatoric plane, with different  $b$  and  $\alpha$  values as previously presented in this thesis (i.e. CPC and CPE). In addition, TXC, TXE, LE, UC and PSC simulations include a combination of variable  $p'$ ,  $\alpha$  and  $b$  values. In this manner, a comprehensive assessment of the influence of the stress path can be performed.

The stress-strain response for each of the stress paths is presented in Figure 7.21. The difference between the different stress paths is clear. Furthermore, the response can be inferred from the actual stress paths in Figure 7.20. As the magnitude of  $p'$  increases, the deviatoric stress required for failure also increases as the failure envelope in the generalised stress plane has a conical shape. In the same way, when the value of  $p'$  decreases, the radius of the conical shape reduces and a lower deviatoric stress is required for failure. Clearly, there seems to be a stress path

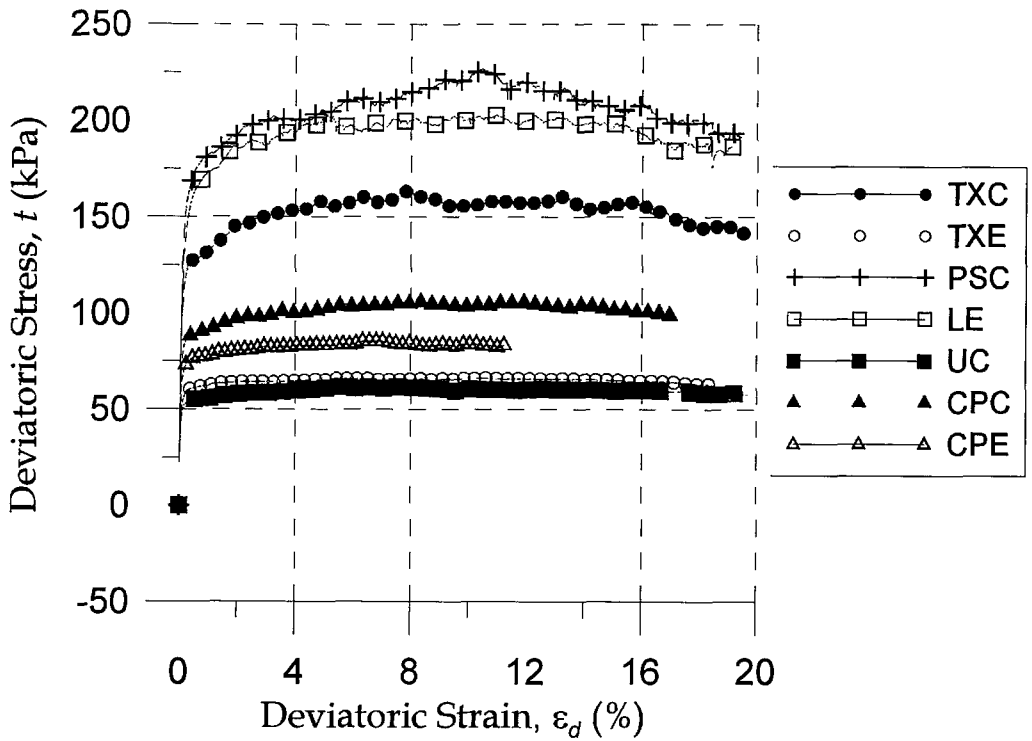


Figure 7.21: Influence of the stress path. Stress-strain response

dependance in terms of the value of the mean effective stress ( $p'$ ). Consequently, the stress-strain response can be normalized by the current value of  $p'$ . The result is illustrated in Figure 7.22.

Referring to Figure 7.22 it is evident that the stress paths have been now discriminated between extension, compression and plain strain. This can be expected. When the influence of  $p'$  is removed, all the extension paths (LE, CPE and TXE) become the same stress path with  $\alpha = 90^\circ$  and  $b = 1.0$  as described above. Similarly, all the compression paths (CPC, TXC and UC) become tests with  $b = 0.0$  and  $\alpha = 0^\circ$ . Although the PSC test is also a compression path, it differs from the other stress paths because its  $b$  value differs and it is approximately 0.4. The results presented in Figure 7.22 are then a result of the different  $b$  and  $\alpha$  values. These results coincide with earlier results presented in this thesis.

Particle-scale interactions affect the macro-scale response under different stress paths. For example, Figure 7.23 shows the evolution of the coordination number with deviatoric strain for the different stress paths. Although for all the stress paths it seems to be a critical coordination number around 4.4, there is a relationship between the stress-strain response from Figure 7.21 and Figure 7.23. From strongest to weakest, the different stress paths sequence is PSC-LE-TXC-CPC-CPE-TXE-UC. Careful

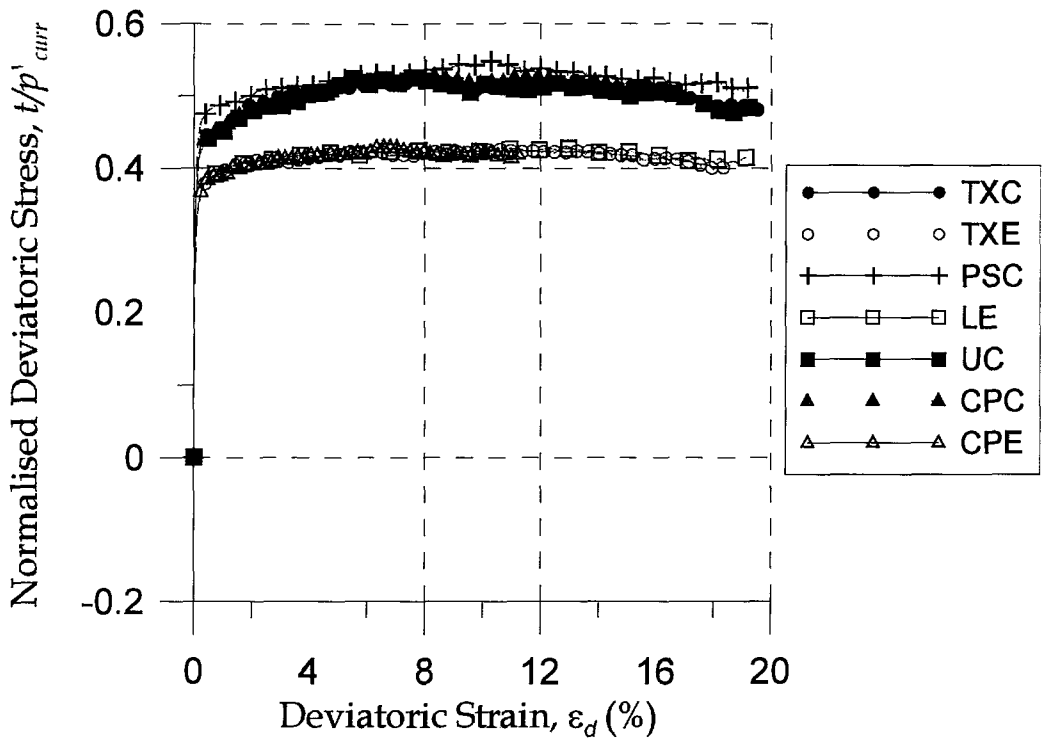


Figure 7.22: Influence of the stress path. Normalised stress-strain response

analysis of Figure 7.23 demonstrates that the same sequence can be observed at a level of deviatoric strain of about 6%, which coincides with the strain level for the peak strength of most of the stress paths. The strongest stress paths (i.e. PSC) also present the biggest number (average) of contacts per particle. Evidently, with a higher number of contacts, higher shear strengths can be mobilised. There is a combined effect of (possibly) an increase in the number of strong force chains and (more likely) an increase in the number of lateral supports preventing the buckling of the strong chains. Furthermore, the number of contacts that can develop seems to be affected by the stress path that is followed for each test. It should be expected that such changes in the number of contacts are also observed when the evolution of the soil fabric is quantified.

During a quantification of fabric, a geotechnical engineer should be interested in the orientation of the principal fabric in relation to the principal stresses, but also should be concerned about the magnitude of anisotropy in the soil fabric (i.e. the bias of contacts in each of the principal directions). For the set of simulations described above, the approaches proposed by Rothenburg & Bathurst (1989), which accounts for the direction of anisotropy ( $\theta_a$ ), and the method by Woodcock (1977) (which identifies the principal fabric orientations based on the eigenvectors of the fabric

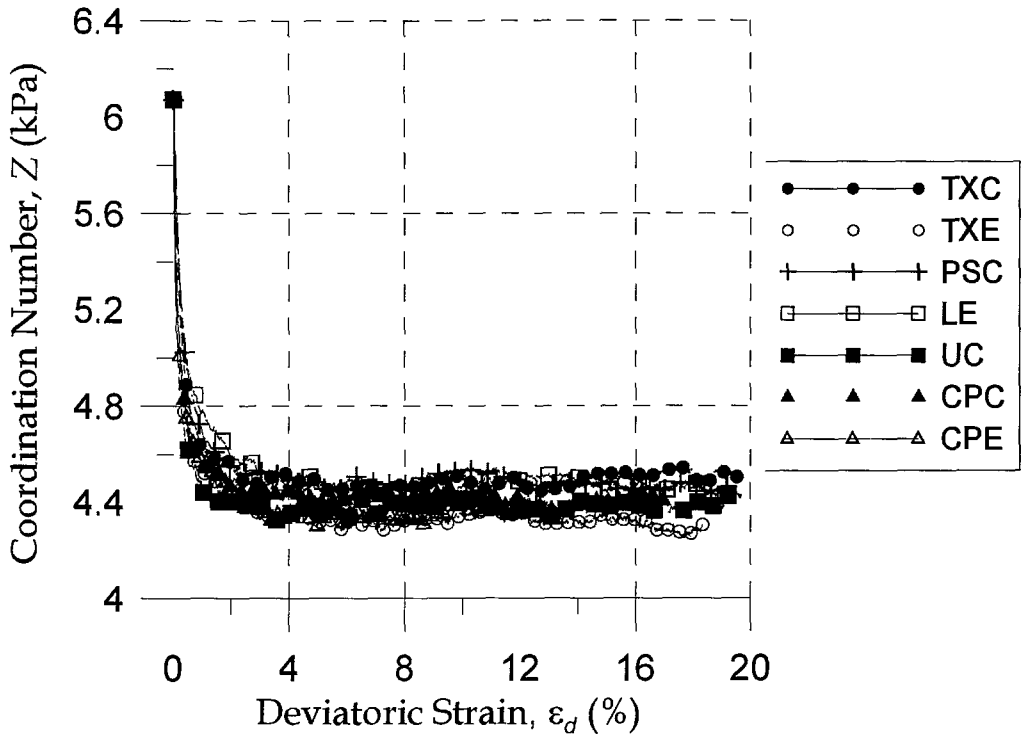


Figure 7.23: Influence of the stress path. Evolution of coordination number

tensor) were compared. In terms of the orientations, these methods provided the same answers. As it would be expected, the principal fabric was always orientated towards the major principal stress direction.

In relation to the magnitude of anisotropy, three measuring parameters were compared: i) the magnitude of anisotropy ( $a$ ) as defined by Rothenburg & Bathurst (1992), ii) the strength factor ( $C$ ) as proposed by Woodcock (1977) and iii) the new deviatoric fabric ( $\Phi_d$ ) parameter proposed in Equation 6.2.

The results for the magnitude of anisotropy ( $a$ ) considering different amounts of inter-particle contacts are illustrated in Figure 7.24. Three situations are considered. In the first case all the contacts are used, then only the contacts transmitting more than the average force, finally only the contacts exceeding the average force plus one standard deviation are considered. It is clear that as consideration is restricted to only the contacts transmitting the largest forces, the magnitude of anisotropy increases. This is a clear indication that the largest contact forces are more likely to be orientated in a direction that is close to the major principal stress orientation. As mentioned in Chapter 2, similar quantitative measures of soil fabric anisotropy have been used as input for continuum constitutive models (i.e. Yang et al. (2008b)). This study demonstrates that one must be careful when quantifying soil fabric. Using

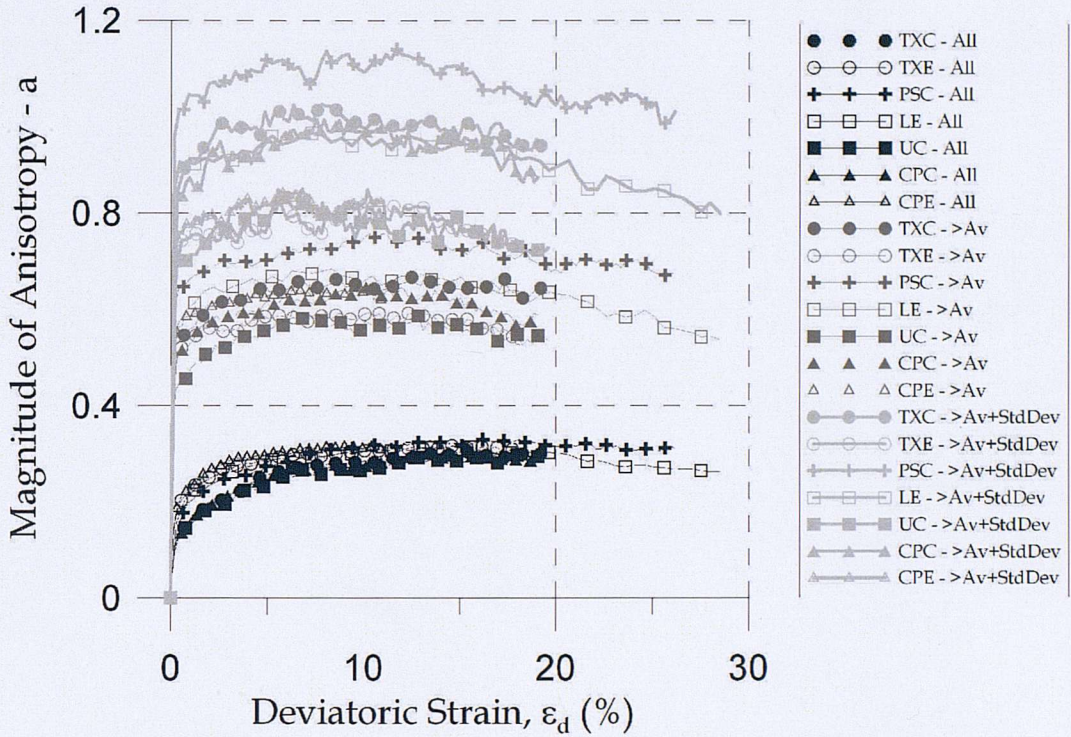


Figure 7.24: Influence of the stress path. Evolution of the magnitude of anisotropy ( $a$ )- All cases

only a portion of the contact forces with no scientific basis should be avoided. It must be emphasized that similar trends were observed for the strength factor ( $C$ ) and the deviatoric fabric ( $\Phi_d$ ).

It is obvious from Figure 7.24, that the shape of the curves representing the evolution of anisotropy roughly coincides with the shape of the stress-strain response given in Figures 7.21 and 7.22. An useful measure of the magnitude of anisotropy would be expected to give not only the shape but also the same sequence as in the stress-strain response. In that way, the ideal fabric quantification should provide a sequence (strongest to weakest) as PSC-LE-TXC-CPC-CPE-TXE-UC. In the opposite case, this measure should at least separate between plane strain (PSC), compression and extension tests in the order presented in Figure 7.22.

Figure 7.25 illustrates the evolution of  $a$  but including only the analysis for all forces and for the forces with magnitude bigger than the average plus a standard deviation. When all the forces are used,  $a$  is able to discriminate between plane strain, compression and extension tests. However, the figure indicates that compression tests are more anisotropic than the extension tests. That clearly contradicts the trend in Figure 7.22, and might be caused by the fact that  $a$  is a two-dimensional parameter

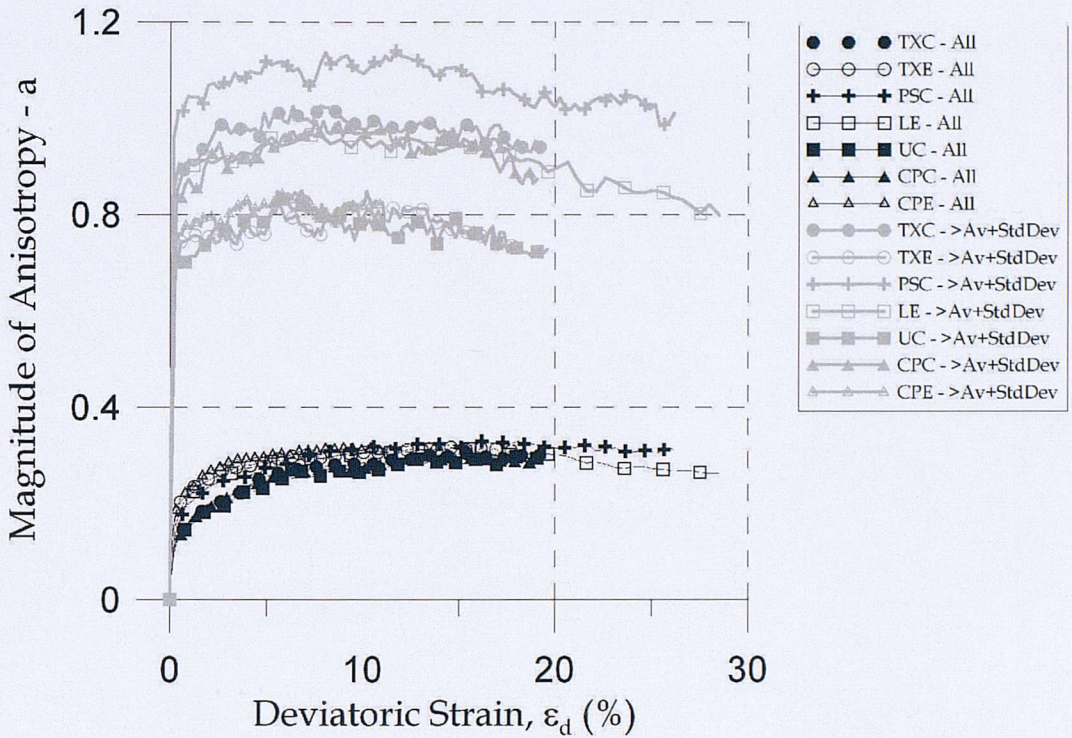


Figure 7.25: Influence of the stress path. Evolution of the magnitude of anisotropy (a)

being used to analyse three-dimensional data. Note however, that when only the very strong forces are used, the same trend as in Figure 7.21 is reproduced. That confirms that the strong forces do provide the strongest contribution for the stress tensor. The issue of how to separate strong forces and which threshold to consider is still unresolved.

In a similar manner, Figure 7.26 includes the analysis performed for the strength factor  $C$  (see Section 2.8). Even though this is a three-dimensional approach, the results are not an improvement over those obtained with the approach proposed by Rothenburg & Bathurst (1992). Clearly, for any number of contact forces considered, the evolution of  $C$  discriminates between plane strain, compression and extension but in the incorrect order. Furthermore, it can be seen that the approach is unsuccessful to reproduce the shape of the stress-strain curves for the stress paths which involve compression. From Figure 7.26, if used without caution, it could be inferred that compression stress paths do not develop fabric anisotropy. That is necessarily false.

The third analysis, for the deviatoric fabric is presented in Figure 7.27. If the plane strain test (PSC) were excluded from the analysis, this approach would be the most successful. Clearly, the approach discriminates between extension and compression

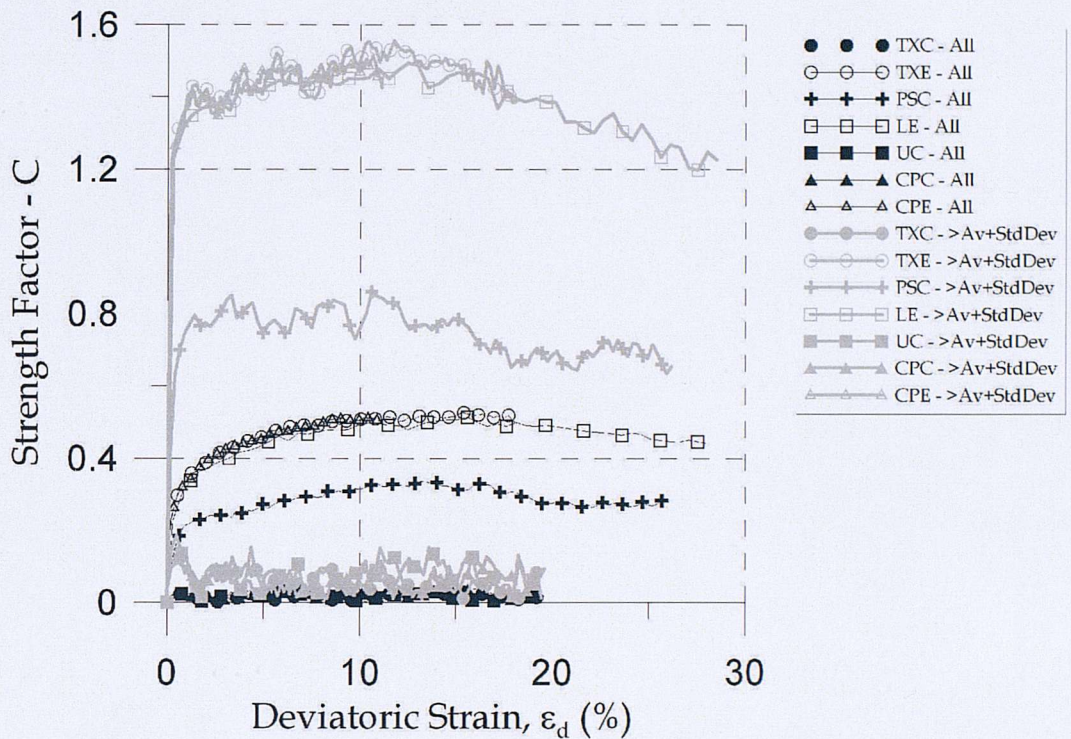


Figure 7.26: Influence of the stress path. Evolution of the strength factor ( $C$ )

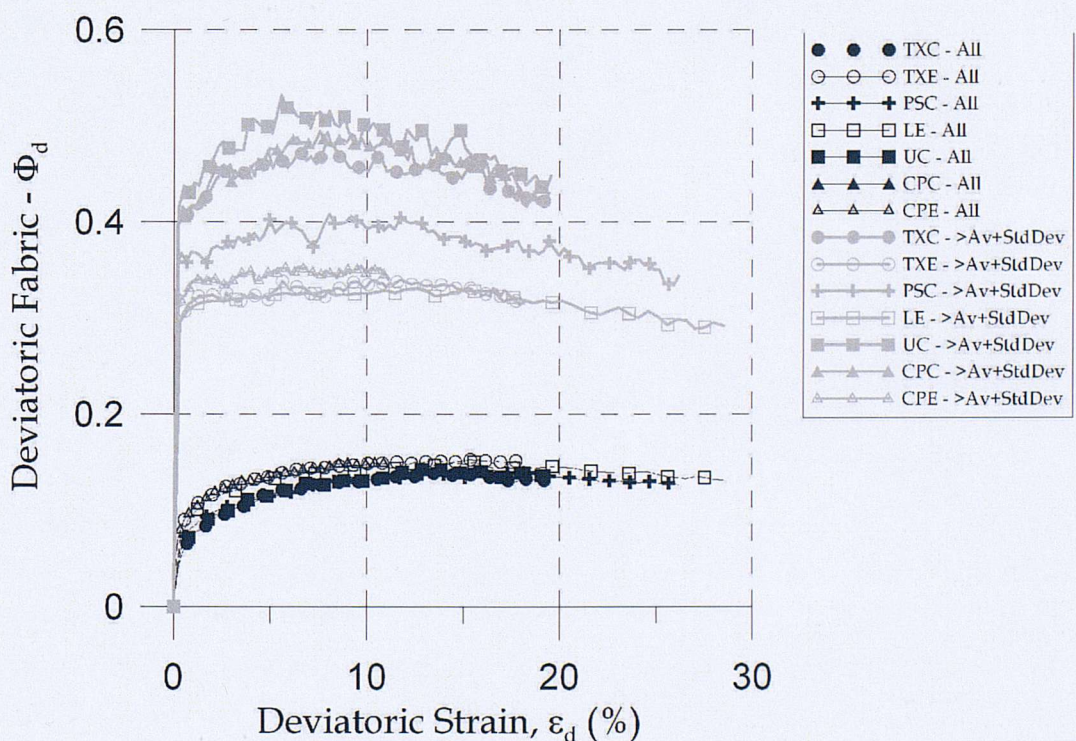


Figure 7.27: Influence of the stress path. Evolution of the deviatoric fabric ( $\Phi_d$ )

paths while the compression paths are stronger. However, this only happens when strong forces are considered.

A similar analysis to the one described above was also performed for an assembly of spheres in a much looser density state. It was found that for the loosest specimen, the approaches were even more unsuccessful since for some parameters, not even the shape of the stress-strain response could be reproduced. For example, considering the deviatoric fabric ( $\Phi_d$ ), the evolution considering all forces is illustrated in Figure 7.28. Clearly, the evolution of fabric anisotropy cannot be correlated in an easy way to the stress-strain response.

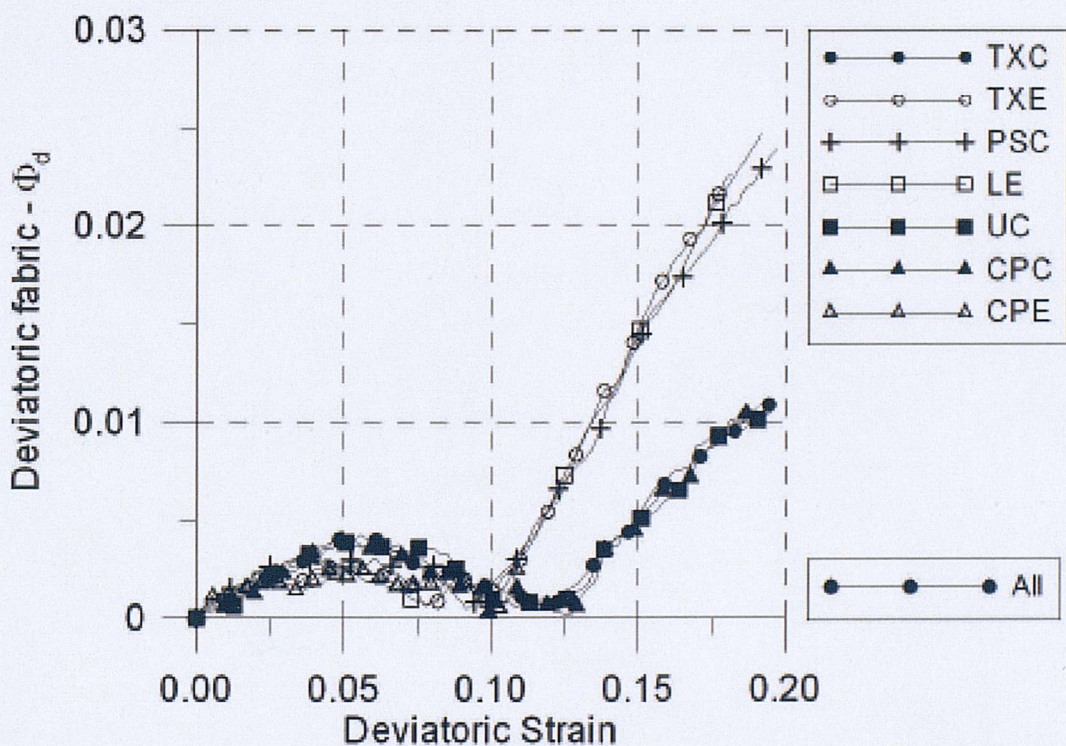


Figure 7.28: Influence of the stress path. Evolution of the deviatoric fabric ( $\Phi_d$ ) for a loose specimen (Barreto et al. 2009)

The possibility of using the second invariant of the fabric tensor (i.e. without the multiple of  $\frac{1}{\sqrt{2}}$ ), as well as other multiples of this parameter as an anisotropic descriptor were also explored (see Figure 7.29). It was found that these measures may affect the shape of the evolution of fabric anisotropy a little. However, the problems described above remain the same (i.e. the descriptors may be able to replicate the shape of the stress-strain response, but not in the appropriate sequence). In Figure 7.29 the following fabric descriptors were used:

$$\Phi_A = \Phi_d = \frac{1}{\sqrt{2}} \sqrt{(\Phi_1 - \Phi_2)^2 + (\Phi_2 - \Phi_3)^2 + (\Phi_1 - \Phi_3)^2} \quad (7.1)$$

$$\Phi_B = \frac{1}{\sqrt{6}} \sqrt{(\Phi_1 - \Phi_2)^2 + (\Phi_2 - \Phi_3)^2 + (\Phi_1 - \Phi_3)^2} \quad (7.2)$$

$$\Phi_C = \frac{1}{\sqrt{2}} [(\Phi_1 - \Phi_2)^2 + (\Phi_2 - \Phi_3)^2 + (\Phi_1 - \Phi_3)^2] \quad (7.3)$$

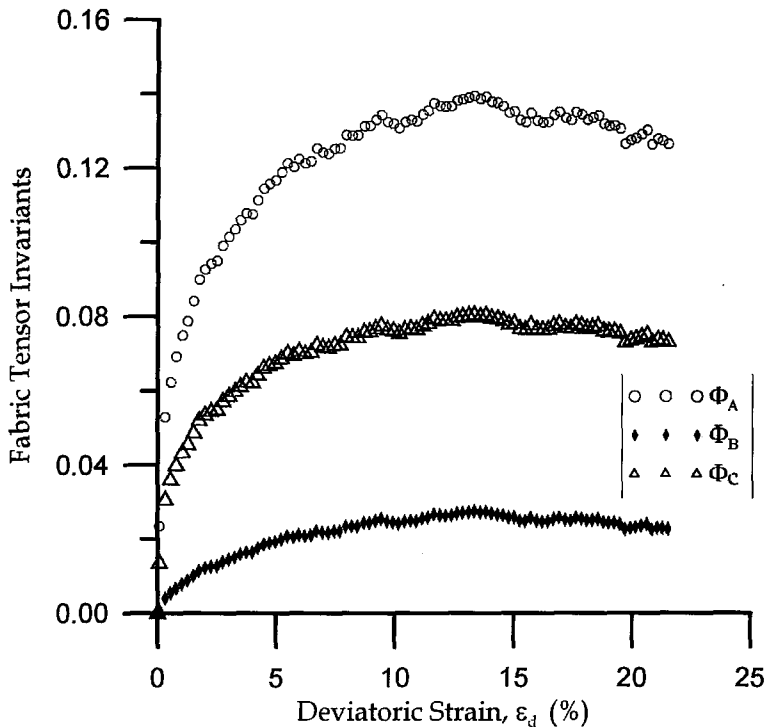


Figure 7.29: Different variations and multiples of the fabric invariant to quantify anisotropy

Whether the results presented above are particular cases due to the particular density states, or due to the very uniform grain size distribution, or a combination of more variables needs of further research. However, the analyses above clearly indicated that when different stress paths in the generalised stress plane are considered, there is no single measure of the fabric anisotropy that is entirely able to correlate with the stress-strain response. This highlights the need for improved parameters for the quantification of anisotropy. Additionally, it was evident that care must be taken if it is decided to consider only the “strong” forces, because there no clear scientific indication that allows separating strong forces from the weaker ones.

The results obtained from this study are important since they demonstrate that an improved measure of soil fabric is needed in order to firmly establish a fabric boundary framework. Note however, that the fabric surface proposed seems to work very well in the deviatoric plane under constant  $p'$  conditions. Therefore, different and complex loading conditions are already supported by such a framework. Better tools to analyse the topology of the contact force network are required. These tools should, most likely draw on the emerging science of networks (e.g. Watts (2003)).

## **7.7 Summary**

This chapter has demonstrated that DEM is able to replicate the behaviour of granular materials under stress rotation. The effects of  $b$  and  $\alpha$  on the macro-scale behaviour have been related to the evolution of the deviatoric fabric. As a consequence, a new fabric surface for interpretation and understanding of soil behaviour was proposed.

The possibility of modelling the effects of inherent anisotropy and the existence of non-coaxial behaviour have been also discussed. The dependance of this phenomena on the fabric has been highlighted.

In addition, after evaluating different methods for the quantification of fabric, it has been highlighted than accurate and improved measures of fabric anisotropy are required to completely understand and model soil behaviour under generalised 3D conditions.

# **Chapter 8**

## **Advanced modelling of hollow cylinder tests**

### **8.1 Introduction**

An extension of the axi-symmetric environment proposed by Cui (2006) was implemented for the results presented in this chapter. This environment allows to test a section of the HCA specimen with any desired angle between two circumferential periodic boundaries, while maintaining a continuous network of contact forces in the horizontal direction. Stress-controlled membranes were also implemented in order to simulate the latex membrane present in numerical experiments. The top and bottom platens which are used for the application of vertical stresses and torque are also included in the environment as rigid boundaries.

In this chapter, the details of each of the components of the axi-symmetric environment are described in terms of their particular implementation and validation. After the non-trivial issue of specimen generation is discussed, some examples of simulations using the newly implemented environment are presented.

### **8.2 Circumferential (vertical) periodic boundaries**

The work by Cui (2006), which served as a basis for the developments described in this chapter, used a Cartesian framework. This Cartesian framework could be adopted as one quadrant ( $90^\circ$  section) was considered in the analysis. This meant

that the usual rectangular box system could be used for the contact detection algorithm (see Section 5.3.1). In this thesis the circumferential periodic boundary concept is generalised so it can be used for any angle between periodic boundaries ( $\theta_b$ ). This generalisation is essential for DEM simulations of realistic HCA tests including boundary conditions. However, it can also be applied to other axi-symmetric systems (i.e. CPT tests). Calculations assuming an initial void ratio of 0.570 and a mean particle diameter of 1.1 mm produce approximately 4 million particles for the ICHCA and double that number for the LICHCA. DEM simulations using a section of 10 degrees on the other hand, require approximately 200.000 particles for the LICHCA and half this number for the ICHCA. These numbers are estimates, obviously there will be variations on these quantities depending on the density of the numerical specimens. Although simulations including 200.000 particles are very expensive in computational terms, they represent a radical improvement in relation to the 4 million that would be initially required to produce an accurate simulation of the LICHCA test.

Cui (2006) adopted the orthogonal boundary system as implementation is relatively straightforward, in comparison with the general case. Figure 8.1 defines the angle between circumferential (vertical) boundaries to be  $\theta_b$ , while the polar angle of each particle in a DEM simulation is defined by  $\theta_p$ .

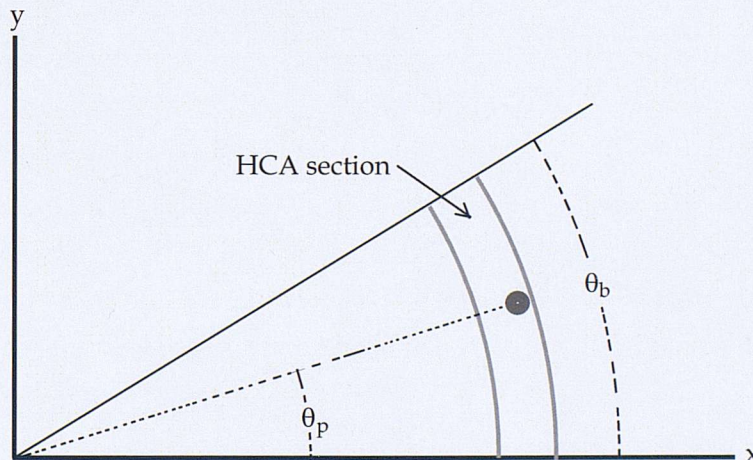


Figure 8.1: Definition of angles for the generalised axi-symmetric environment

For her 90°, Cui (2006) could use the following straightforward rotation tensor to rotate particles and coordinates in the clockwise direction from the  $x$  to  $y$  axis:

$$\theta_{xy} = \begin{bmatrix} 0 & -1 \\ 1 & 0 \end{bmatrix} \quad (8.1)$$

while rotating particles from  $y$  to  $x$  axis used a second rotation tensor:

$$\theta_{yx} = \begin{bmatrix} 0 & 1 \\ -1 & 0 \end{bmatrix} \quad (8.2)$$

However, these rotation tensors are proposed here in a more general manner. For the clockwise direction:

$$\theta_1 = \begin{bmatrix} \cos(\theta_b) & -\sin(\theta_b) \\ \sin(\theta_b) & \cos(\theta_b) \end{bmatrix} \quad (8.3)$$

while for anti-clockwise direction the tensor is given by:

$$\theta_2 = \begin{bmatrix} \cos(-\theta_b) & -\sin(-\theta_b) \\ \sin(-\theta_b) & \cos(-\theta_b) \end{bmatrix} \quad (8.4)$$

Figure 8.2 schematically represents an example of results for the generalised approach. In the figure, the red particles are examples of spheres located in the proximity of the circumferential periodic boundaries. Each of these spheres has a corresponding contact force. Although the centroid of the particles is not protruding for any of these spheres, virtual balls are represented in both the horizontal axis (green spheres) and the inclined axis (blue spheres) as aid in the visualisation of the rotated contact forces. The rotation of particles when they protrude through the boundaries uses the same approach and could be represented in the same way. This figure clearly demonstrates the effectiveness of the approach. Also note that particle overlap is evident in the figure, also as an aid in the analysis of the figure, but this would not be allowed to occur in a DEM simulation due to extremely high magnitude of inter-particle contact forces.

When this approach is used, although only a portion of a cylindrical specimen is simulated, it should effectively replicate a full specimen. This fact can be verified with reference to Figure 8.3. This figure illustrates the particles simulated for two sections, using  $\theta_b$  of 45 and 60 degrees. In Figures 8.3 b) and d) the full section

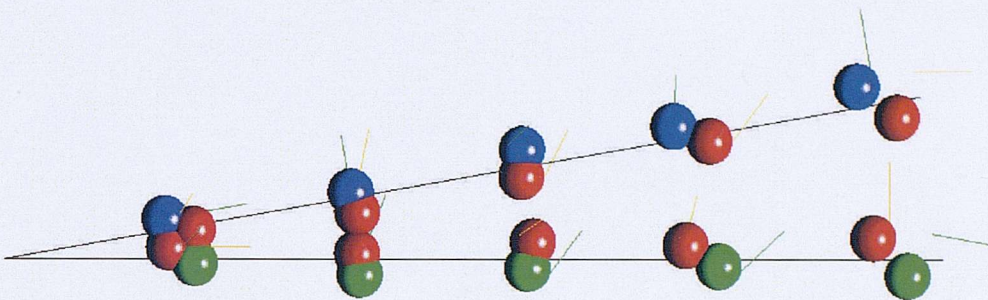


Figure 8.2: Rotation of particles protruding circumferential periodic boundaries and their corresponding inter-particle contact forces

simulated for a two-dimensional section is represented. Figures 8.3 a) and c) demonstrate that the section highlighted can be subsequently rotated to represent the full cylindrical specimen.

The use of circumferential periodic boundaries ensures a continuous network of particle to particle contacts can develop in the system. This continuity in the contact force network is important to accurately replicate soil element tests and for the development of arching effects. An illustration of the continuity of the force chain networks is shown in Figure 8.4 for a 2D simulation using  $\theta_b = 90^\circ$ . Figure 8.4 shows three different sections. First, the simulated section which has an angle of 90 degrees. Due to existence of the vertical circumferential periodic boundaries, when simulating a quadrant ( $\theta_b = 90^\circ$ ) continuity of forces is established for particles with contacts across periodic boundaries. A full (rotated) specimen is also shown. This specimen is the result of rotating the simulated section three times in order to form the full specimen. It can be confirmed in the insert showing a closer view of the point where sections meet that the network of forces is indeed continuous. An algorithm failing to produce a continuous network of inter-particle forces would not be able to produce the perfect match of force networks shown in the insert.

As mentioned before, Cui et al. (2007a) used orthogonal circumferential periodic boundaries ( $\theta_b = 90^\circ$ ) to simulate triaxial tests. This was done in order to simplify the contact force calculations along the periodic boundaries. When  $\theta_b = 90^\circ$ ,  $x$  and  $y$  are the axes for a periodic boundary pair. If a particle  $A$  (coordinates  $x = x_A$ ,  $y = y_A$ ,  $z = z_A$ ) protrudes from boundary  $o - x$ , then an image particle  $A'$  is introduced adjacent to the  $o - y$  boundary at the corresponding location ( $x = -y_A$ ,  $y = x_A$ ,  $z = z_A$ ). Particles protruding from the boundary  $o - y$  are handled in a

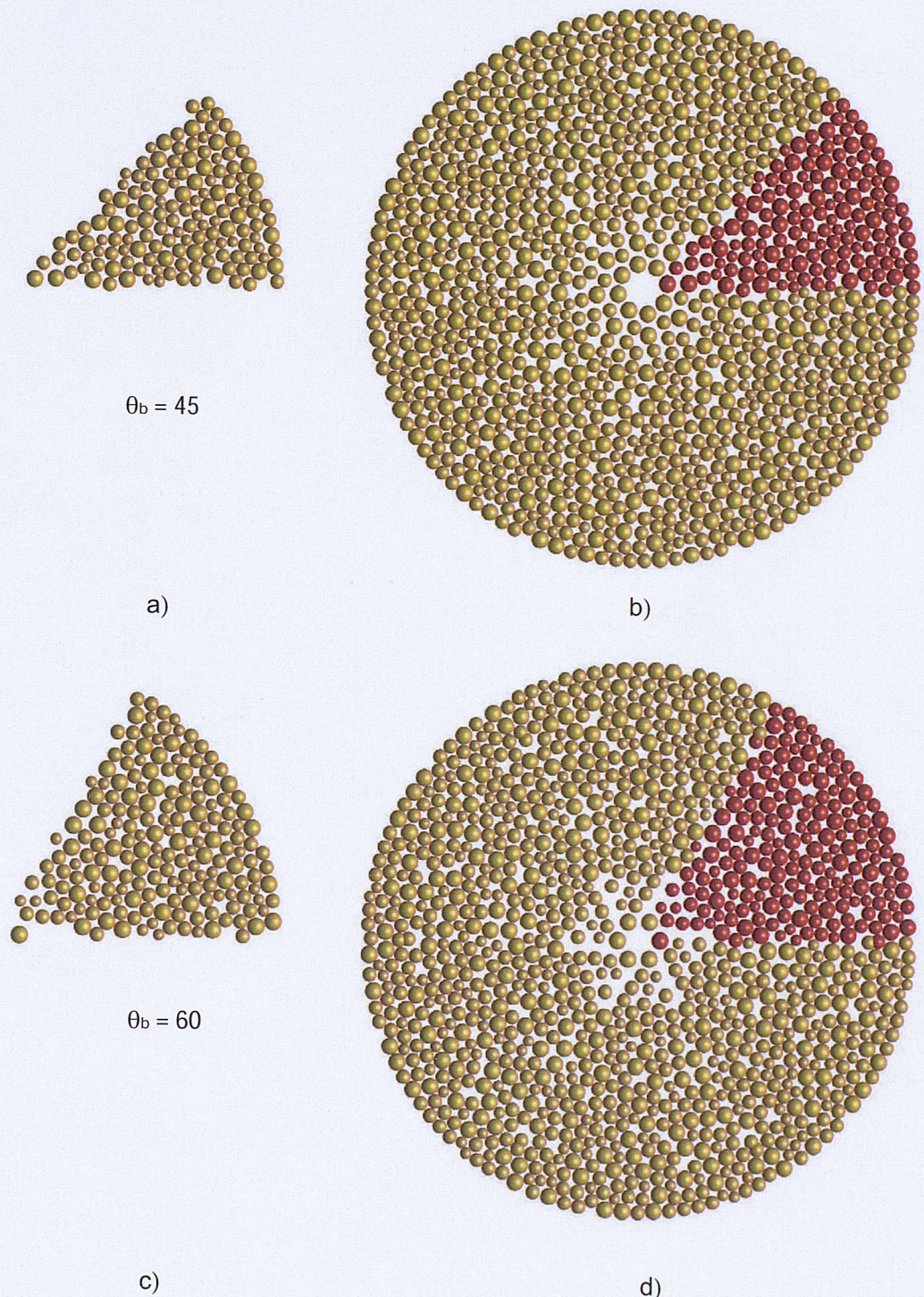


Figure 8.3: Simulation specimens using different angles between circumferential periodic boundaries

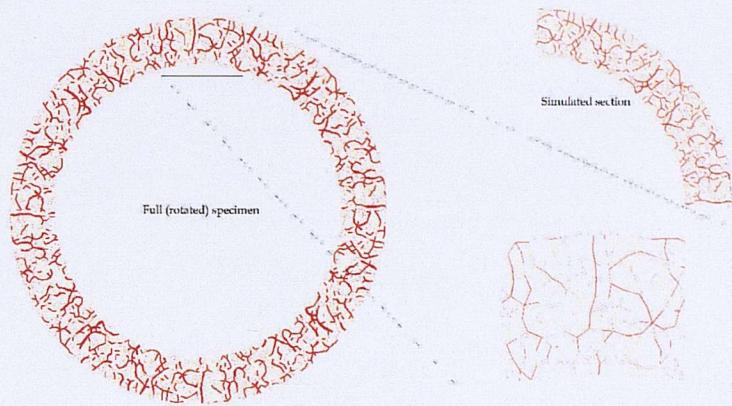


Figure 8.4: Continuity of force chain networks in a 2D simulation

similar way. This is illustrated in Figure 8.5 and is the result of using the rotation tensors defined in Equations 8.1 and 8.2 to rotate the particles.

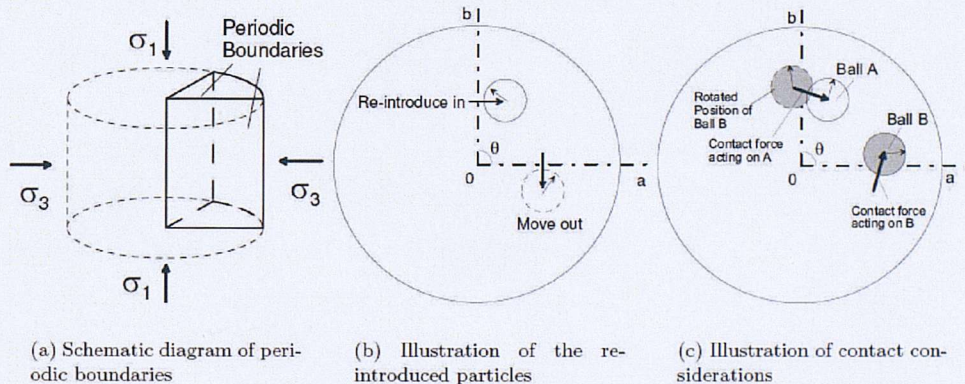


Figure 8.5: Rotation of particles and contact forces when  $\theta_b = 90^\circ$  (Cui et al. 2007a)

Additionally, a system of indexing was developed by Cui et al. (2007a) in the code to differentiate between real balls, the virtual balls protruding from the  $o-x$  boundary and the virtual balls protruding from the  $o-y$  boundary. This virtual ball approach was selected for facility of extension to various angles between periodic boundaries and it is used in the generalised scheme introduced for this thesis. It is very important to avoid double calculation of the contact forces where both contacting balls protrude from the periodic boundaries. In the case where a real ball itself is associated with its own virtual ball, when a contact force is calculated between the real ball and another virtual ball along a periodic boundary, the calculated force is applied

to the real ball only.

Note however, that with the introduction of a generalised axi-symmetric environment, issues arise in relation to the contact detection algorithm and may have been intuitively observed by the reader while observing Figure 8.2. The issues that needed to be solved included (i) how to determine the current box where the particle has been currently binned, (ii) how to find the neighbouring boxes that need to be used for contact detection for interior boxes and (iii) how to find the neighbouring boxes for particles close to vertical periodic boundaries.

Two different options were considered to tackle these challenges. Option 1 (Figure 8.6) was aimed at reducing the number of boxes involved in the simulation. Using this approach a grid is created covering only the particle system. There are therefore a different number of grid boxes in each row, and the grid indices of each box cannot be directly calculated from the particle coordinates. Rather an additional array mapping the ball indices to grid indices is required.

In this manner only the boxes influenced by the DEM simulation are included for the issues related to contact detection. The red box represents the box allocated to the current ball, and the green box represents the complement box which must be identified when looking for inter-particle contacts across periodic boundaries. The boxes that must be checked for contact detection are then identified at the beginning of the simulation. Since the algorithm depends on the coordinates of the corners and vertices defining the environment, there is no need to calculate box numbers every time the reboxing is updated. However, this approach had a potential disadvantage. It comprises an extensive use of memory, and also introduces new equations to compare the ball coordinates against the coordinates of the corners and vertices of the proposed environment.

Option 2 is illustrated in Figure 8.7. This figure includes the complement boxes that require to be inspected for contact detection. This option has got the advantage of using the existing Cartesian grid. The grid indices can easily be determined. Each grid is identified as being interior, periodic in the  $x$  axis, or periodic in the inclined axis. In this second option it is easy to determine the box number depending on the angle  $\theta_p$  (see Figure 8.1) used during the simulation.

There are three cases used for axi-symmetric rotation of particles and contact forces across vertical periodic boundaries. First, and considering the definitions represented in Figure 8.1, based on the  $x$  and  $y$  coordinates of each particle, the polar angle for the particle  $\theta_p$  is calculated. If  $\theta_p < 0$ , then a rotation tensor of the form

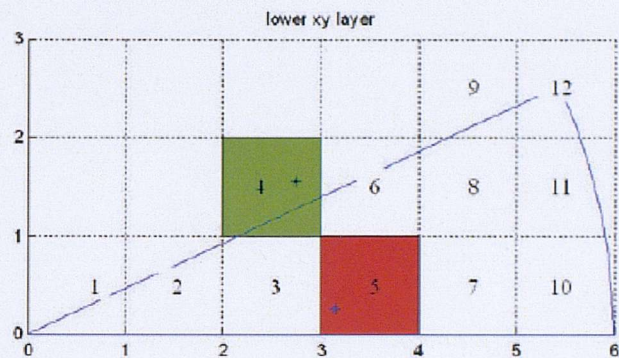


Figure 8.6: Reboxing algorithm for generalised DEM axi-symmetric environment - Option 1

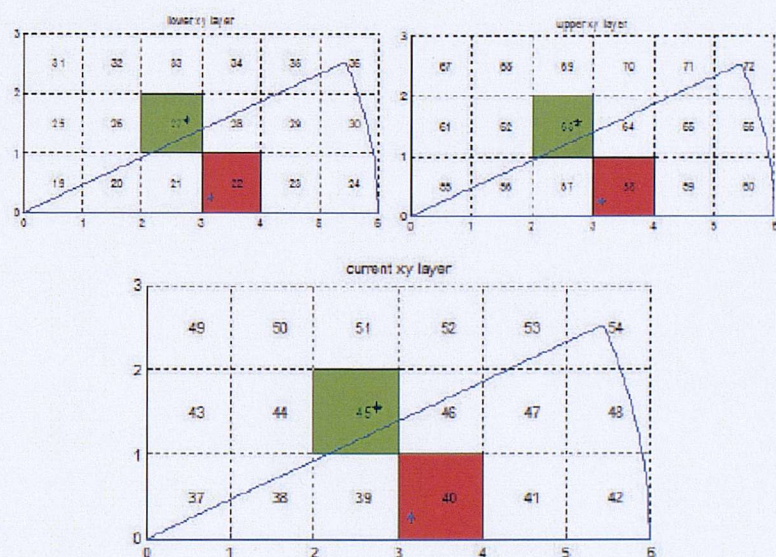


Figure 8.7: Reboxing algorithm for generalised DEM axi-symmetric environment - Option 2

$\theta_1$  is used to calculate the rotated position of the particle and associated forces in the opposite boundary. If  $0 < \theta_p < \theta_b$  then the particle centroid is not protruding the periodic boundary and no further action is required. Finally, if  $\theta_p > \theta_b$ , then the rotation tensor  $\theta_2$  is used to calculate position of new particles in the opposite boundary.

### 8.3 Flexible boundaries

A key consideration for DEM simulations of physical laboratory tests is to model the flexible latex membrane. A number of researchers have implemented the stress-controlled numerical membrane for three-dimensional DEM simulations (O'Sullivan 2002, Powrie et al. 2005, Cui 2006, Evans & Zhao 2008). The numerical membrane proposed by Cui (2006) for triaxial test simulations was developed based on the original concept of O'Sullivan (2002). In Cui's implementation, the flexible boundary algorithm required linking between the DEM code and MATLAB, making computation less efficient. One of the objectives of this thesis was to incorporate a stress-controlled membrane subroutine within the used DEM code, being independent of MATLAB, in order to improve efficiency.

Note that the implementation proposed here follows the more general axi-symmetric environment described above. It works for any angular axi-symmetric section opposite to the quarter of a cylindrical specimen that was used by Cui (2006). In addition, for the implementation of HCA tests, not only an external flexible boundary is used, but also an internal stress-controlled membrane.

The concept of the stress-controlled membrane subroutine implemented for this thesis is based in the concepts of Cui (2006) and O'Sullivan (2002). In summary, the starting point of this implementation involves the identification of the boundary balls. The coordinates of the membrane of boundary balls are then translated onto a two dimensional projection plane. Voronoi polygons surrounding the centroids of the membrane balls on the projection plane are then generated. The areas of these Voronoi polygons are then calculated. The forces applied on each of these boundary balls in order to maintain the required confining pressure are the product of the required confining pressure and the Voronoi polygon area. Further details of these algorithms are described in this section.

To ease the calculation procedures, the sample must be positioned with the centre of the axi-symmetric section at the origin of the Cartesian plane, and the specimen

being aligned with the vertical  $z$ -axis. The identification of membrane balls is based on a zone containing balls that can possibly form part of the membrane. First, the outermost ball is identified. The membrane zone has a thickness  $d$  as illustrated in Figure 8.8. The coordinates of the balls within the specimen are compared against the location of the membrane zone. If a ball is located within the membrane zone, it is subjected to a further check to determine if they have radial contacts. A ball can only be part of the membrane if it has no contact with another ball that is further away from the centre of the sample. Therefore, a zone for radial contact check is defined (see Figure 8.9). The radius of the specimen  $R$  is then calculated as the average distance between the membrane ball locations and the  $z$ -axis plus their ball radii.

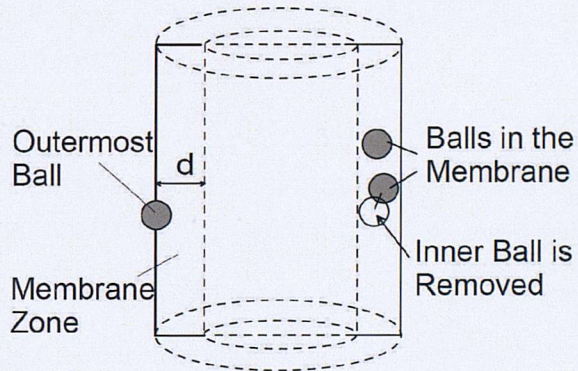


Figure 8.8: Definition of the membrane zone and identification of membrane balls (Cui et al. 2007a)

Once the membrane balls are identified, the confining pressure is maintained by applying the appropriate magnitude of forces on the membrane balls. The magnitude of the forces are calculated by determining the area of the Voronoi polygons created based on the centroid of the membrane balls. To do that, the membrane zone is unfolded and the coordinates of the membrane balls are projected onto a 2D projection plane. The Voronoi diagram is then created on the projection plane. An illustration of this process is presented in Figure 8.10. This figure shows the Voronoi diagram for the outer and inner membranes of a HCA simulation using an specimen of reduced height.

If the Voronoi diagram is generated considering only the Voronoi polygons, close to the top and bottom platens and in areas close to the circumferential periodic boundaries, some of the points could be vertices with infinite coordinates. In order to solve this problem, Cui (2006) proposed two different approaches to deal with

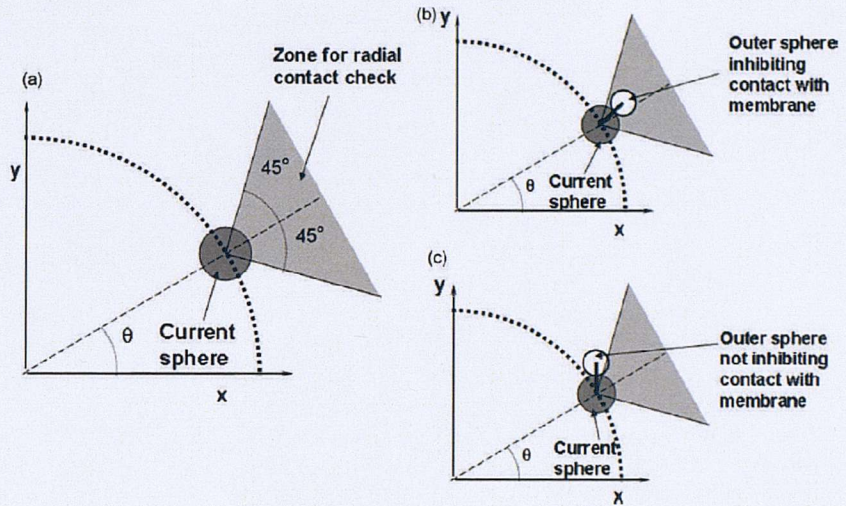


Figure 8.9: Additional check to ensure that a particle can be considered as a membrane ball (Cheung & O'Sullivan 2008)

this issue. In the case of top and bottom boundaries, virtual points are created. In the areas close to the ends of the projection plane (lateral boundaries) a different approach is used.

The projection plane that defines the Voronoi points is found using the following expressions:

$$x' = \theta_p * R \quad (8.5)$$

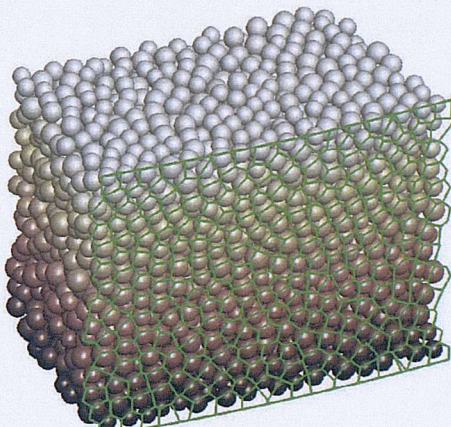
$$z' = z \quad (8.6)$$

where  $R$  is the polar radius of the surface and  $\theta_p$  is the polar angle of each membrane ball evaluated as

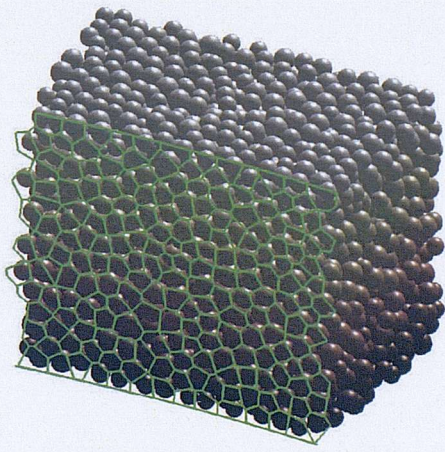
$$\theta_p = \arccos \left( \frac{x}{\sqrt{x^2 + y^2}} \right) \quad (8.7)$$

where  $x$  and  $y$  are the coordinates of the particle centroid.

For the areas close to the top and bottom boundaries, extra points are introduced at a vertical distance of 3 particle radii, with horizontal intervals of  $2r$  to eliminate problems with the infinite rays of the Voronoi tessellation. For the lateral bound-



Outer Membrane



Inner Membrane

Figure 8.10: Voronoi diagram for the simulation of flexible membranes - DEM simulation

aries, if the distance between one particle and one periodic boundary is smaller than  $3r$ , a virtual point is introduced outside the other periodic boundary at a distance  $d_2 = 2r$ . This points are illustrated in Figure 8.11, together with the infinite rays that result from the Voronoi tessellation if the extra points proposed by Cui (2006) were not considered. With careful observation, it can be seen that the Voronoi diagram also keeps the periodic nature of the circumferential boundaries. If copies of the Voronoi diagram are sketched subsequently and next to each other, a perfect full cylindrical membrane could be represented.

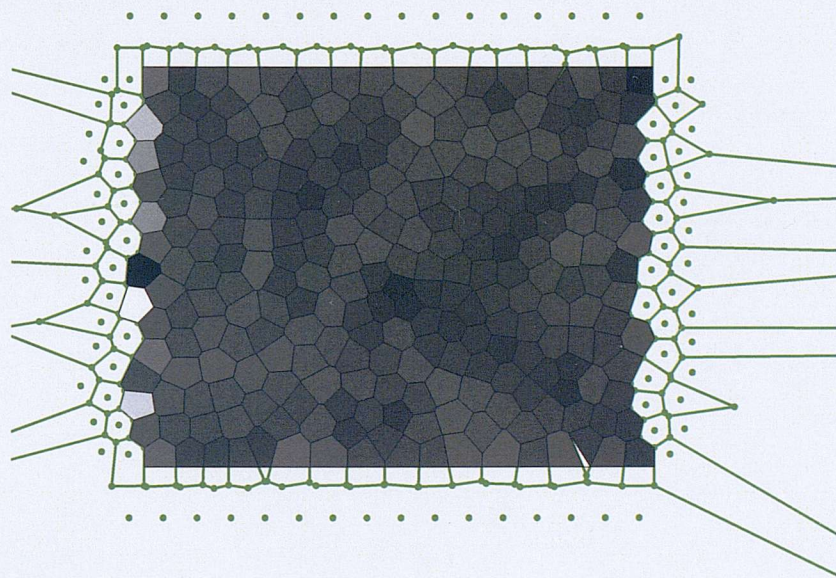


Figure 8.11: Projected Voronoi diagram for the simulation of flexible membranes - DEM simulation

The Voronoi diagram can be calculated recognising that, as discussed by Shewchuk (2002), for a given set of points  $p_i$ , the Voronoi diagram divides the space into regions  $V_i$  in such a way that the region  $V_i$  is the space closer to  $p_i$  than to any other point. For a cylindrical boundary, the polar coordinates of the boundary particles are projected onto a plane  $S'$  which is obtained by unfolding the cylindrical surface  $S$  going through the centre of the membrane zone as described above. Considering implementation, the computation of the Voronoi diagram is complex and it is performed with an additional subroutine incorporated in the DEM code based on the FORTRAN version of a program called *TABLE – VORONOI*. This was done to

## 8. Advanced modelling of hollow cylinder tests

avoid calling MATLAB from the DEM code as it was previously performed by Cui (2006) and O’Sullivan (2002).

*TABLE – VORONOI* is a program distributed under the GNU license and developed by Burkardt (2004) based on the work of Joe (1991). This program, available in both the C++ and FORTRAN languages computes the Delaunay triangulation and then, analyzing that Delaunay information, it works out the location of the Voronoi vertices, and their specific arrangement around each of the original data nodes which for this thesis are represented by the coordinates of the membrane balls. This recent implementation avoids the use of MATLAB as in the previous implementation by Cui (2006), hence the computational performance was significantly improved. For comparison purposes, a series of identical simulations was performed using both the old and new versions of the code. Improvements between 15 - 20% were observed in terms of computational time.

Having the coordinates of the Voronoi diagram, the areas of the Voronoi polygons that correspond to each of the membrane balls can be calculated as:

$$A_v = \frac{1}{2} \sum_{i=1}^n x'_{i-1} z'_i - x'_i z'_{i-1} \quad (8.8)$$

where  $n$  is the number of vertices of the polygon, and  $x'$  and  $z'$  represent the coordinates of the projected coordinates of the vertices of the Voronoi polygons. The applied forces for the membrane balls are then calculated using:

$$F_{ap} = A_v \sigma_{conf} \quad (8.9)$$

where  $F_{ap}$  is the magnitude of the applied force and  $\sigma_{conf}$  is the required confining pressure. A check is always carried out to compare the theoretical area of the projection plane and the sum of areas from all Voronoi polygons to ensure accurate results.

Note that this approach was validated by Cui (2006) simulating physical experiments on FCC assemblies described by Rowe (1962). For this thesis, the same validation procedure was adopted and a maximum error of 6% was found between experiments and simulations using a full specimen and a 90 degree specimen. The results agreed with those found by Cui (2006). This not only validates the flexible membrane algorithm, but also the generalised axi-symmetric environment. Further validation

of this approach has been provided by Cheung & O’Sullivan (2008) who implemented a numerical membrane into the commercial software PFC3D (Itasca 1998) using the C++ version of *TABLE – VORONOI* developed by Burkardt (2004).

Note that as the numerical specimen deforms (i.e. bulges as in the triaxial test), the geometrical configuration of the membrane changes and the Voronoi diagram must be checked and updated. The frequency of updating the membrane depends on the displacements of the balls within the specimen. At each cycle of calculation, a check is performed on the specimen to assess whether the numerical membrane conditions need to be updated. This is carried out by tracking the incremental displacements of all the balls within the specimen since the last updated numerical membrane. If the incremental displacement is bigger than a pre-defined tolerance, then an update is required.

One of the disadvantages of using this kind of flexible membrane is that the specimen must be consolidated to a required confining stress using rigid boundaries which are then removed and replaced by the flexible boundary conditions. These introduced several complications in the generation of HCA specimens for realistic simulations, as discussed later in this chapter.

Note that the stress-controlled membrane implemented by Cui (2006) and O’Sullivan (2002) has been used under constant value conditions (i.e. axi-symmetric compression of cylindrical specimens where the radial stresses remain constant during shearing). It has been shown in Chapters 4, 6 and 7 that the radial stress may change under different HCA stress paths. The effectiveness of the numerical implementation of this boundary condition still needs to be investigated under such conditions.

## 8.4 Rigid boundaries

Rigid horizontal boundaries were used in the newly implemented axi-symmetric environment to replicate the rigid platens that contain the porous stones in the LICHCA and ICHCA. New developments were included in order to provide the necessary control that is required to simulate HCA tests including vertical stresses as well as the application of torque as described in Chapter 3.

Translation of rigid boundaries is not new in DEM research, neither is the rotation of rigid boundaries. However, the rotation of rigid boundaries as in the HCA experiments required new code development. The rotation of the top rigid boundary was

necessary in order to replicate the application of torque in the HCA tests through the top rigid platen. Although the calculation of the rotation of a plane determined by three points with respect to the origin of the Cartesian axes is trivial, validation of the procedure was performed and it is described in Section 8.6.1.

Tilting tests of particles of glass ballotini over a porous stone were performed. This would allow introduction of accurate input parameters for the realistic DEM simulations as the friction of particles against the boundaries is different to the inter-particle friction. A total of 350 tests were performed. The number of measurements is significantly bigger than those performed by Cavarretta (2009) for the inter-particle friction. In spite of the easier methodology, the unsophisticated equipment and the increased number of tests, the results produced no improvement in terms of accuracy and precision of the results. An average particle-boundary friction coefficient of 0.33 was found. The standard deviation however, was 0.083, a higher value than that published by Cavarretta (2009) for inter-particle friction. This confirms the uncertainty resulting from the measurement of coefficients of friction. How this uncertainty can affect the results has been already discussed in Chapter 6.

## 8.5 Specimen generation

After the individual components of the generalised axi-symmetric environment were implemented and preliminary validated, it was of interest to generate a set of numerical specimens that could be used for the realistic DEM simulations of HCA experiments. As in the case of the periodic boundary simulations presented in Chapter 6 and 7, sample generation was expected to be non-trivial and several approaches were also attempted.

### 8.5.1 Two-dimensional simulations

Initially, for computational efficiency and ease of visualisation, some preliminary two-dimensional simulations were performed. These simulations used different grain size distributions which included a mono-disperse specimen (equal particle sizes), a poly-disperse specimen (with the grain size distribution of the “medium” sized ballotini), and a specimen with grain size distribution generated by the commercial software PFC3D (Itasca 1998). For example, Figure 8.12 illustrates the initial configuration of a mono-disperse specimen (top) and a specimen with a grain size

distribution defined by the commercial software PFC2D (bottom). It can be observed that in the specimen with a grain size distribution there are a number of particles whose sizes are clearly different than the rest. Note that for these cases only a quadrant of the whole specimen was simulated and is highlighted in Figure 8.12. In addition to the grain size distribution, different values of inter-particle friction were used. Furthermore, two approaches to vary the stress were considered. In the first case, the specimen was compressed to an isotropic stress state by reducing the radius of the outer circular rigid boundary while keeping the inner circular rigid boundary stationary. In the second approach the same method was used, but the outer boundary was immobile, therefore the sample was compressed from within.

Of primary interest was to confirm that the contact force network simulated with just a section was continuous. Figure 8.13 shows two illustrations of force chains in a two-dimensional annular sample of uniform spheres after compression. This is equivalent to a disk specimen as movement is restricted to the *XY*-plane. Both plots correspond to simulations of a mono-disperse specimen of spheres all located in the same plane. However, only the top image was obtained simulating the whole specimen. The illustration in the bottom was obtained from a simulation using only a quadrant of the whole specimen (i.e. a 90° section). In order to represent the whole specimen the contact forces were subsequently rotated in MATLAB to obtain the representation of the whole specimen. Note that the contact force network of the simulated quadrant is continuous and demonstrates once again the appropriate performance of the circumferential periodic boundaries. It is also clearly observed that in both cases crystallization occurs due to equal size of the particles. Furthermore, it is easy to observe that in both cases there exists areas with higher concentrations of stresses, evidenced by thicker chains of forces. Contact forces plotted in red correspond to forces bigger than the average magnitude of the contact forces and the thickness of the forces is proportional to the force magnitude. Stresses are obtained by local integration and averaging of contact forces. A non-uniform distribution of stresses is therefore evident and similar in both scenarios.

A similar comparison between the simulation of the whole specimen and sections with different angles (i.e. 15, 30, 45, 60 and 75 degrees) was performed to confirm the observations described above. A continuous contact force network was observed for all of these cases, as well as the non-uniform stress distribution and the occurrence of crystallized areas.

Once the effectiveness of the periodic boundary algorithm to simulate just a section of the specimen was confirmed, a detailed set of simulations was performed in order

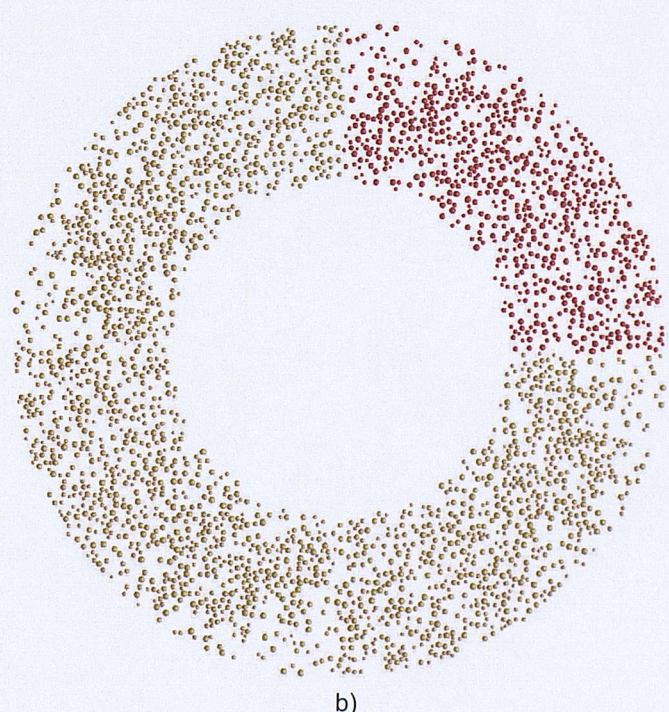
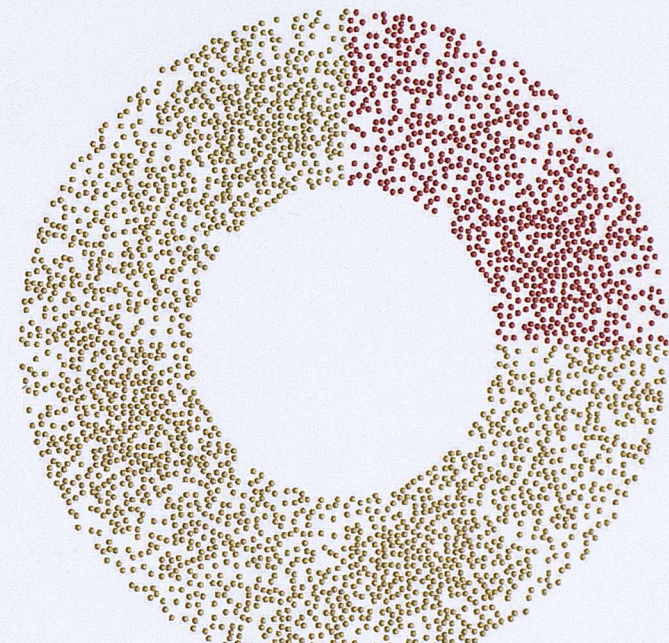


Figure 8.12: Initial configuration of specimens with a) uniform and b) non-uniform grain size distributions - Simulated section is highlighted

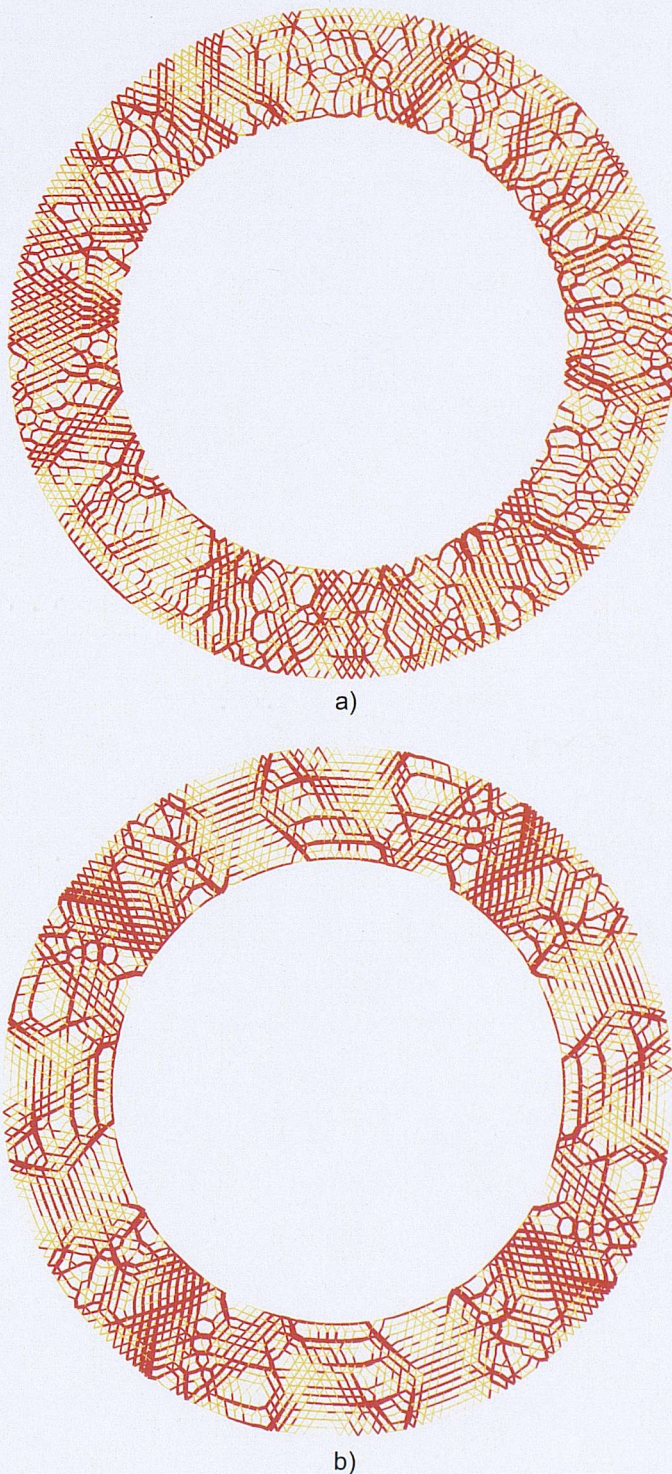


Figure 8.13: Comparison between section simulated partially (bottom) and in full (top) after compression

to obtain information for a specimen generation procedure that could be used for the realistic HCA (3D) simulations. As observed in the case of the simulation using periodic boundaries in Chapter 6, it was expected that a variation in the coefficient of inter-particle friction would produce a variation in the resulting void ratio obtained prior to shearing. Figure 8.14 shows instantaneous images of subsequent stages during the compression (in the inwards direction) of a mono-disperse specimen with a coefficient of inter-particle friction of 0.22. The specimen initially had no inter-particle contacts (as shown in Figure 8.12), and was compressed by reducing the radius of an outer circular rigid boundary while an inner circular rigid boundary remained stationary. The simulation was performed using a quadrant of the whole specimen (i.e. 90°) in order to have a significant number of particles (approximately 750) during the simulation, while having the capability of testing the axi-symmetric environment.

Referring to Figure 8.14 several observations can be made. First, it is clear that the network of contact forces starts in the areas which first contact the rigid boundary under movement. It is also clear that a higher concentration of stresses is produced in areas where the population of spheres is the highest (i.e. concentrated clusters of red contact forces). As the outer boundary radius is reduced more particles get together. Simultaneously, particles close to the inner boundary do not interact due to the slow strain rate (first interaction in inner boundary can be seen in Figure 8.14g). It must be highlighted the evidence of arching effects during compression. Arching is observed in the strong contact force network in red located circumferentially and adjacent to the outer boundary in Figures 8.14f), g) and i). Note that the arch in Figure 8.14g) is broken only after some support in the inner boundary (Figure 8.14h) is achieved. Finally, Figure 8.14i) shows a crystallized structure, a non-uniform distribution of stresses, but also the presence of a strong arch adjacent to the outer rigid boundary. The quadrant section in Figure 8.14j) illustrates the contact force network at the end of the simulation.

The use of a coefficient of inter-particle friction as indicated above produces a specimen with a low density. It was necessary to explore the possibility of using zero friction to obtain a denser specimen. Consequently an identical simulation was performed but with  $\mu = 0.00$ . The results in the form of the evolution of contact forces are illustrated in Figure 8.15. By comparison of Figures 8.14 and 8.15 it is evident that the arch formed with no friction is significantly stronger (thicker) and when it is broken, its failure is very brittle as confirmed by the disappearance of many of the inter-particle contacts. This is particularly observed in the transition from

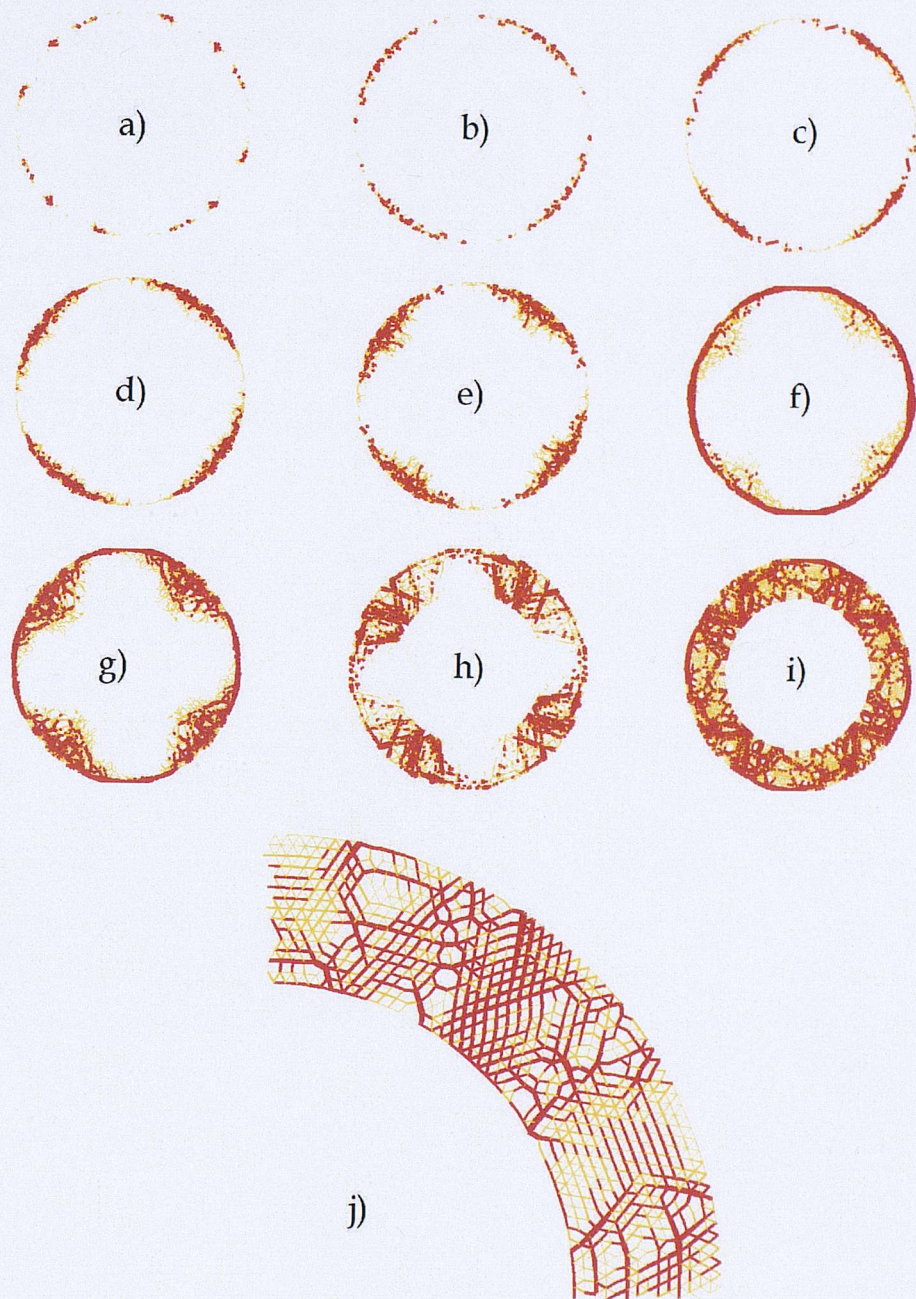


Figure 8.14: Arching effects in simulation with uniform specimen and  $\mu = 0.22$

## 8. Advanced modelling of hollow cylinder tests

Figure 8.15d) to Figure 8.15e). Furthermore, at the final stage of the simulation, as clearly observed in Figure 8.15i), the arching effects can be observed all along the specimen and not only in the area adjacent to the rigid boundary under movement. Note that crystallization and non-uniform distribution of stresses are also present in the simulation with the absence of friction.

Having found the dominance of the arching effects in the cases above, it was thought that the main cause of these effects was related to the grain size distribution. Therefore, a second set of simulations using  $\mu = 0.22$  and  $0.00$  was performed but using a grain size distribution with a wide range of particle sizes. The initial specimen is illustrated in Figure 8.12b). The resulting sequence of contact forces for both cases are presented in Figures 8.16 and 8.17 (cases with friction and no friction, respectively). Although some arching effects can be noticed for both cases, they are not as evident as in the case of the mono-disperse specimens. Note however, by comparison of Figures 8.16 and 8.17 that the greatest formation of arches occurred for the case with higher value of friction. This happened in contrast with the result of the mono-disperse case where the biggest arching effects occurred for the frictionless spheres.

Further research is needed to fully understand the sources of arching effects in granular materials. The occurrence and formation of arches has been a topic of study for physicists and engineers working both experimentally and numerically on the jamming of granular materials in silos (Zuriguel et al. 2003, Chen et al. 2005). However, a consensus about this is not clear. For example, it has been observed by Janda et al. (2008) that the variation in the grain size distribution does not have a big influence on arching, and considered that friction between particles plays a greater role.

Since the realistic HCA simulations had to replicate physical experiments in “medium” sized ballotini it was appropriate to perform some simulations using the grain size distribution equivalent to the “medium” sized ballotini. This grain size distribution was very uniform, but still had a range of sizes, it was expected that the result would be half way between the results for mono-disperse and poly-disperse specimen’s results described above. Figure 8.18 shows the distribution of the contact forces of a full specimen ( $360^\circ$ ) section using  $\mu = 0.22$ . Although it is not very evident, it can be observed that this grain size distribution is also prone to some crystallization. However, the distribution of stresses was moderately uniform and the presence of arching effects was reduced.

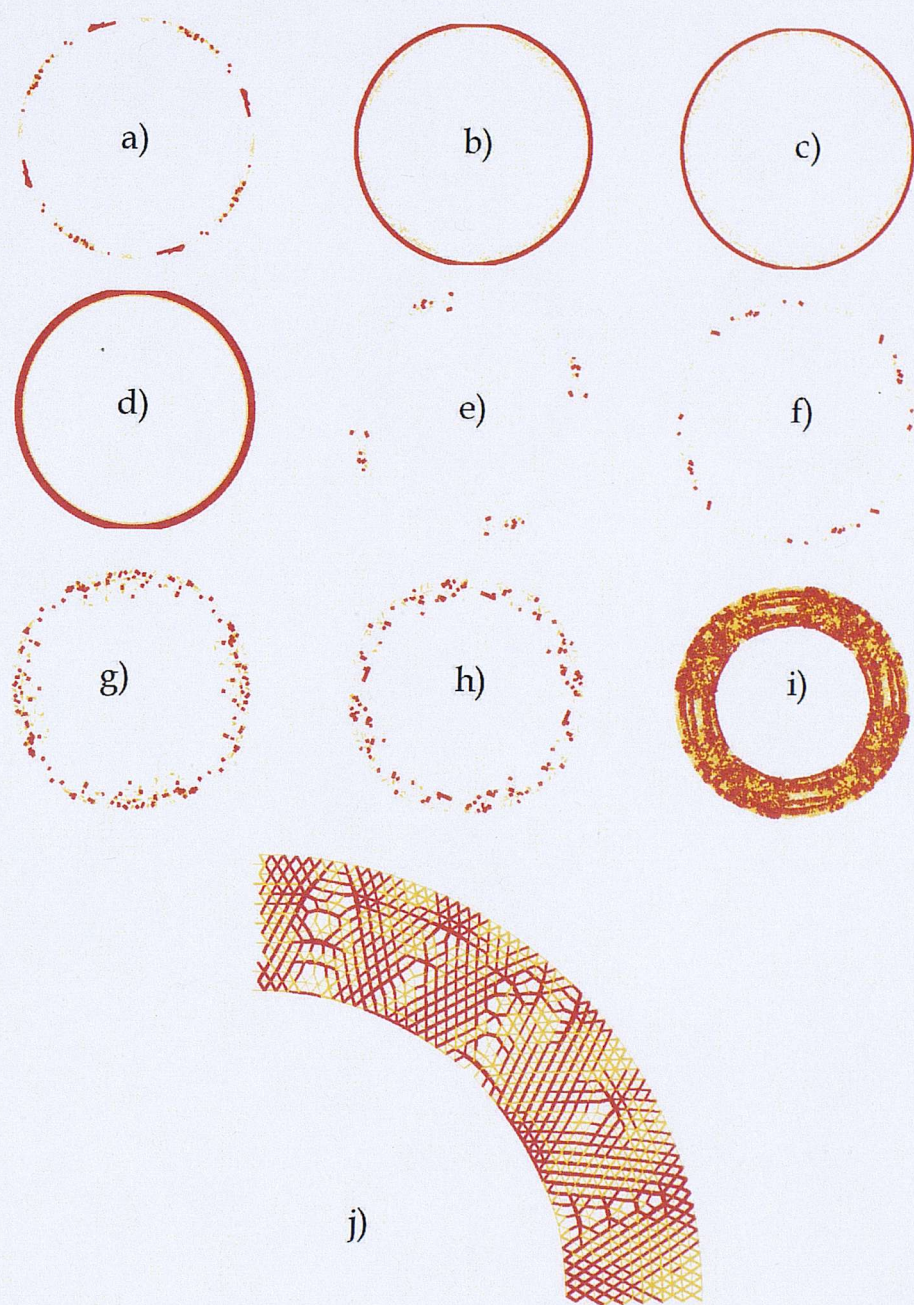


Figure 8.15: Arching effects in simulation with uniform specimen and  $\mu = 0.00$

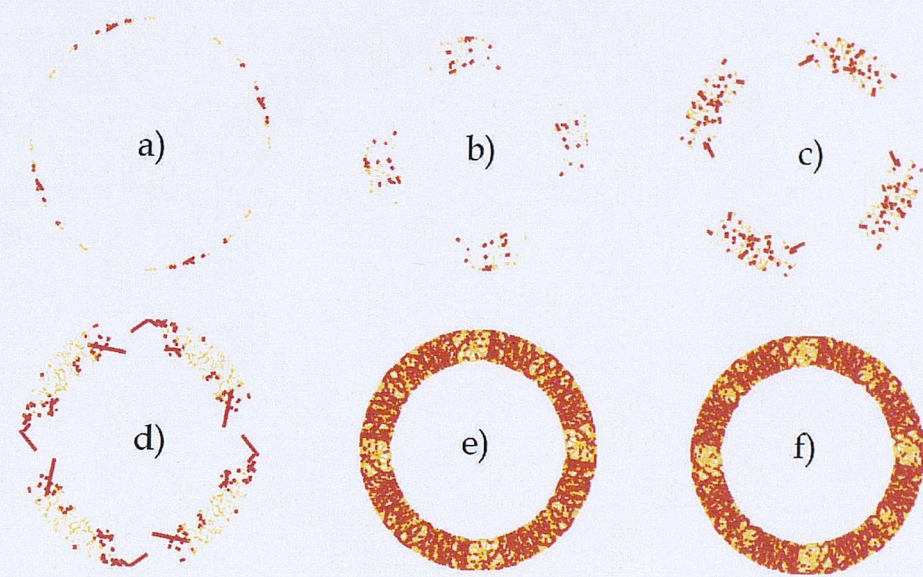


Figure 8.16: Absence of arching effects in simulation with non-uniform specimen and  $\mu = 0.22$

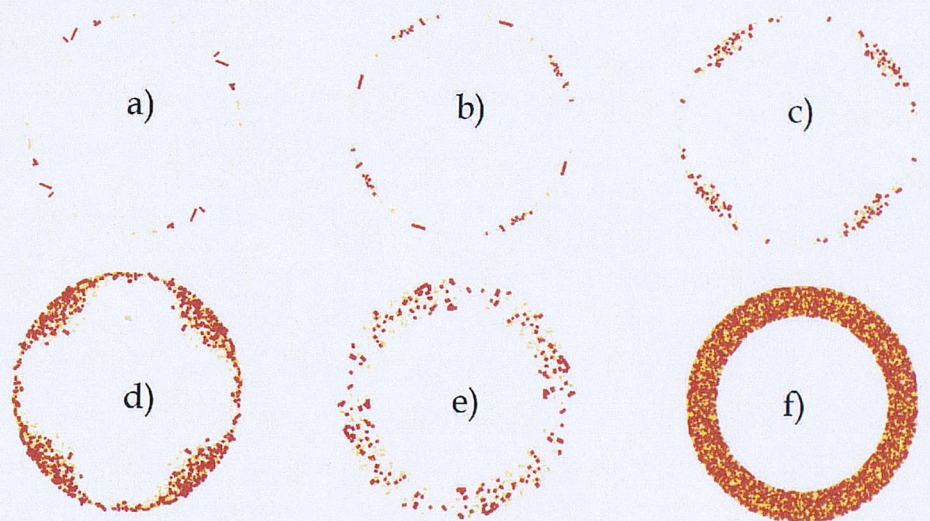


Figure 8.17: Absence of arching effects in simulation with non-uniform specimen and  $\mu = 0.00$

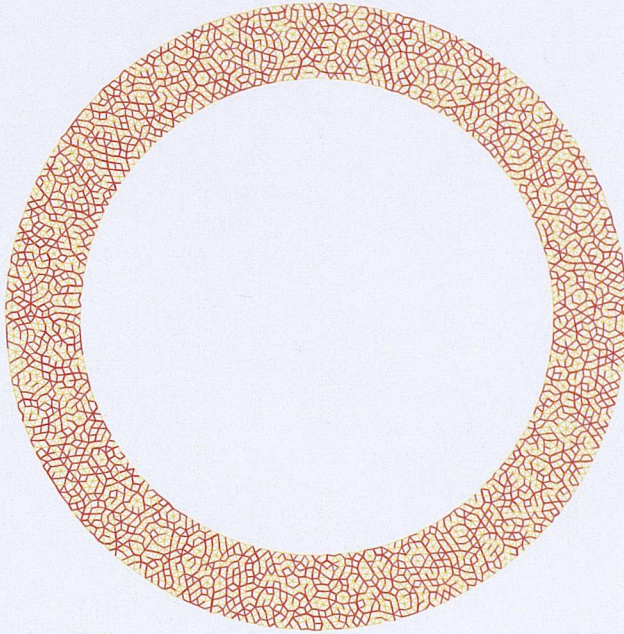


Figure 8.18: Arching effects in simulation with “medium” sized distribution specimen and  $\mu = 0.22$

As a final attempt, it was thought that the radius of curvature of the inner rigid boundary was smaller, therefore a reduction on the arching effects could be observed. However, as indicated in Figure 8.19, from a simulation using “medium” sized ballotini,  $\mu = 0.22$  and a quadrant section, all the effects of arching, non-homogeneity and crystallization were also observed.

As explained in Chapter 3 in Equations 3.23 to 3.26, the control of the physical experiments is based on the stress on the outer and inner boundaries. Consequently, when performing the realistic DEM simulations the control would have to be performed in the same way. Therefore, the evolution of the average radial force on the outer rigid boundary during compression of the different cases described above was of particular interest. Figure 8.20 shows the evolution of the radial force for the simulation of the frictionless mono-disperse specimen (i.e. the case where the arching effects were the most evident). It is observed that the radial force evolution is dominated by gradual increases in the magnitude of the force followed by sharp and sudden reductions. Detailed comparison of the time of occurrence of these reductions in force with the graphical evidence of destruction of arches as in Figure 8.15 demonstrates that these reductions correspond to the moment in which the arch



Figure 8.19: Absence of arching effects in simulation “medium” sized distribution specimen,  $\mu = 0.22$  and compressed from the inner boundary

collapses. In Figure 8.20 the time in which the arch from Figure 8.15d) collapsed is labelled as “d)”. In this figure, the simulation time in the  $x$ -axis indicate the internal computer time and not the real duration of the simulation. This convention is used in other figures described in this Chapter. Figure 8.20 also confirms the brittle nature of the failure of the arch commented before.

The observations from Figure 8.20 are of significant importance. The control of simulations must be done via servo-controlled algorithms for the boundary stresses. Clearly, a stress state can occur under different states of particle arrangement. One or several of these states can occur due to influence of very strong arches that introduce non-uniformity in the stress distribution. It would be desirable that the measurement of the stress was the result of the contribution of the whole mass and not only due to strong chains forming arches. Therefore, it was thought that different approaches were needed for specimen generation for the “realistic” DEM simulations in which a section of the specimen is simulated.

To conclude this section it is important to recall the discussion about stick-slip behaviour on Chapter 4. The 2D simulations above are probably the simplest case

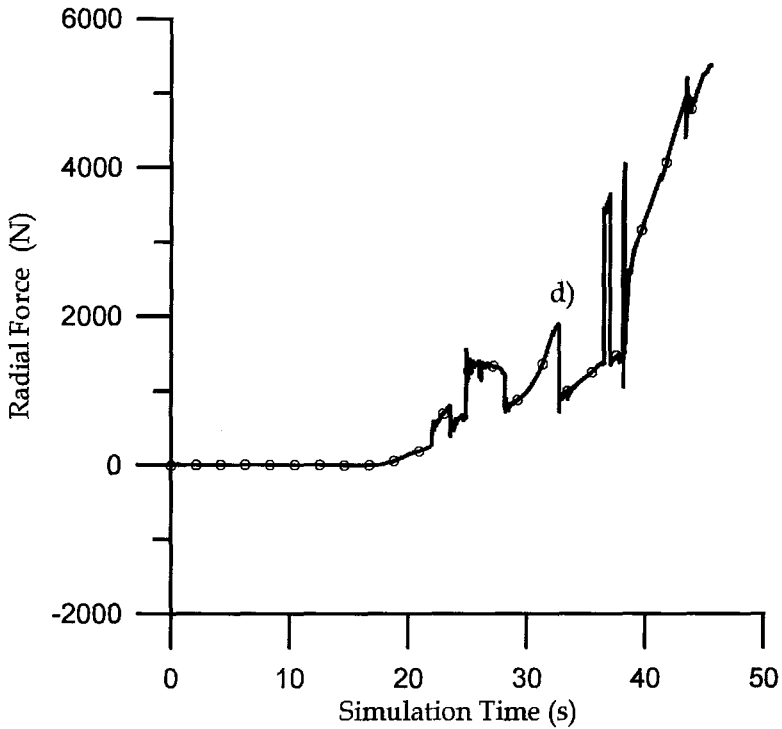


Figure 8.20: Evolution of radial force on outer rigid boundary during compression

to verify the existence of stick-slip and provide a further possible explanation for it. It has been postulated by Tordesillas & Muthuswamy (2009b) that stick-slip events correspond to sudden chain force buckling events, the results illustrated in Figure 8.20 seem to support that hypothesis. It must be added however that since stick-slip behaviour was not evident in the periodic cell simulations of Chapter 6, the boundary conditions must be also included in the discussion of this topic. Evidently, further research is needed for a valid and justified confirmation.

### 8.5.2 Three-dimensional attempts

In addition to the problems related to arching and non-uniformities in the stress distribution, generating a specimen for the realistic HCA simulations using the approaches followed in the previous section would be intractable due to the time needed to complete the simulations. This section presents a new three-dimensional approach for the generation of realistic HCA specimens.

As starting point, the procedure takes as a basis the isotropically consolidated specimens obtained for the periodic cell simulations as described in Section 6.3. Obviously, these specimens have a cubic shape and for the realistic HCA simulations a

different geometrical form is required. However, not only a different shape but also a bigger number of particles is introduced. To generate the HCA sections several cubic blocks are put together and then trimmed to the original HCA shape. An example of this initial state is represented in Figure 8.21. Clearly, the approach is successful to obtain an adequate shape of the generated specimens.

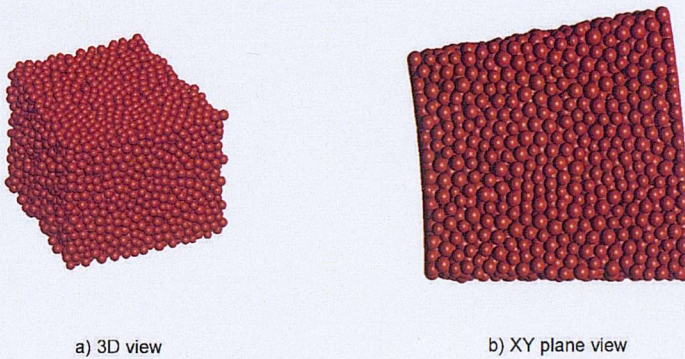


Figure 8.21: Example of generation for initial configuration of realistic HCA specimens

One of the intrinsic complications of the implementation of the numerical membrane for stress-controlled boundaries is that it requires a stable configuration before its activation. Cui (2006) and O’Sullivan (2002) described that the specimens should be consolidated to the required stress state using rigid boundaries. Once the desired stress state is reached, the rigid boundaries are deleted and replaced by the flexible boundary. Naturally, the same procedure was attempted for the realistic HCA simulations, an extensive number of simulations using rigid boundaries was performed in the search for an isotropic stress state upon which the flexible membrane could be activated.

The first attempts were of course, performed using a very reduced number of particles. However, these tests were fundamental to provide understanding of the specimen generation process and the particle scale interactions occurring in the HCA apparatuses. A first simulation used a 10 degree section with internal and outer radius equivalent to the physical LICHCA and ICHCA specimens (i.e. 100 and 125 mm). However, the sample height used for these specimens was only 18 mm. The specimens were surrounded by rigid circular boundaries in the outer and inner faces, as well as rigid planar boundaries at the top and bottom of the specimen. Periodic circumferential boundaries were used in the remaining boundaries in order to establish a continuous network of inter-particle forces as in the physical experiments. No friction was used between particles or between particles and boundaries.

Being consistent with both the physical experiments and the simulations presented in Chapter 6, the target stress state was to obtain an isotropic condition of 200 kPa. Figure 8.22 shows the evolution of the different boundary stresses. As a reference, the results illustrated in Figure 8.22 were obtained after approximately one week, and only 5241 particles were simulated. A particularly small time-step, as well as a very low strain-rate were chosen after a parametric study assessing the stability of the simulation. Since the coefficient of friction was 0.00, a value of damping of 10% was introduced to reduce particle oscillation in the simulation as well as to reduce the computational time.

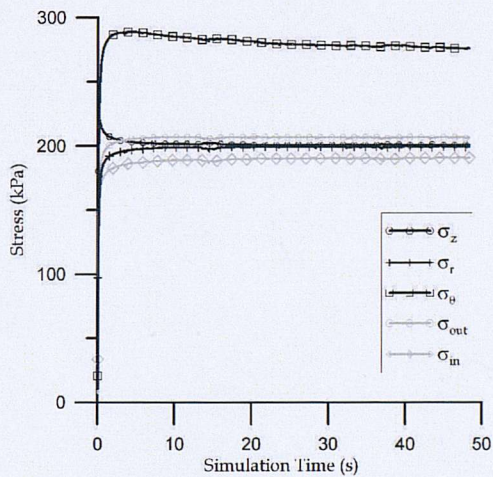


Figure 8.22: Evolution of boundary stresses

In Figure 8.22 the stresses in the outer, inner and horizontal ( $\sigma_{out}$ ,  $\sigma_{in}$  and  $\sigma_z$ ) boundaries is calculated using the forces acting on the boundary. The radial and circumferential ( $\sigma_r$  and  $\sigma_{theta}$ ) stresses are calculated in the same way as in the HCA experiments (i.e. Equations 3.2 and 3.3). It can be seen that both the vertical ( $\sigma_z$ ) and radial ( $\sigma_r$ ) stresses achieve a value of 200 kPa. A constant coordination number is also reached (not plotted in the figure). However, the circumferential stress ( $\sigma_\theta$ ) is not equally successful. These stresses are calculated in the same way as in the physical experiments. Naturally, the difference in  $\sigma_\theta$  occurs due to the difference in the outer and inner stresses in the rigid circular boundaries observed in Figure 8.22.

It was hypothesized that the difference between inner and outer stresses could be occurring due to the very specific boundary conditions used for the simulation and/or the presence of arching effects. Consequently, an extensive parametric study was performed to assess the effect of these geometric boundary conditions. Different sample thicknesses, sample heights and section angles were used with the same objective, the isotropic consolidation up to 200 kPa. Clearly, the success of the

approach depended on being able to achieve an equal stress in the outer and inner rigid circular boundaries. Although different coefficients of inter-particle friction were used, the friction between boundaries and particles was always neglected (i.e.  $\mu_{ball-wall} = 0.0$ ). It must be noted however, that the simulations using an inter-particle friction bigger than 0.0 behaved in a similar manner to those with frictionless particles, but achieved an equilibrium state much faster.

### Effect of sample thickness

Sample thicknesses of 15, 25 and 35 mm were used with a sample height of 18 mm,  $\mu = 0.325$  and a section of 10 degrees. Note that the thickness of 25 mm is equivalent to the real LICHCA and ICHCA apparatuses. The thickness of 35 mm, on the other hand, was selected in order to have a number of particles across the sample thickness that was big enough in accordance to the discussions of possible constraint in Chapter 4. After trying to compress the sample to an isotropic stress state of 200 kPa, the results shown in Figure 8.23 were obtained.

With reference to Figure 8.23 it is clearly seen that once again, the vertical stress and the average radial stress achieved were 200 kPa. However, the circumferential stress significantly differed depending on the differences between the outer and inner stresses along the rigid circular boundaries. It is clear from Figure 8.23b) that the thickest sample was the closest to the desired isotropic stress state. Furthermore, revision of Figure 8.23c) indicates that the stress in the outer boundary was particularly close for the thickest specimen. However, the effect of the change of thickness on the development of a higher inner stress was not as significant as in the case for the outer stress.

It is also interesting to note that the final coordination number was very close for all the three specimens, but also depended on the sample thickness. Furthermore, it is important to highlight that the coordination number achieved (around 4.4) was very close to the critical coordination number achieved during shearing in the simulations described in Chapter 6 ( $Z=4.45$ ) for the same coefficient of inter-particle friction. This clearly indicates a stability requirement for the assemblies, however, in the case of the realistic HCA simulations it occurs during the specimen generation stage. Whether this phenomenon is caused by the boundary conditions or due to particularities of the generation approach, the evidence is not conclusive.

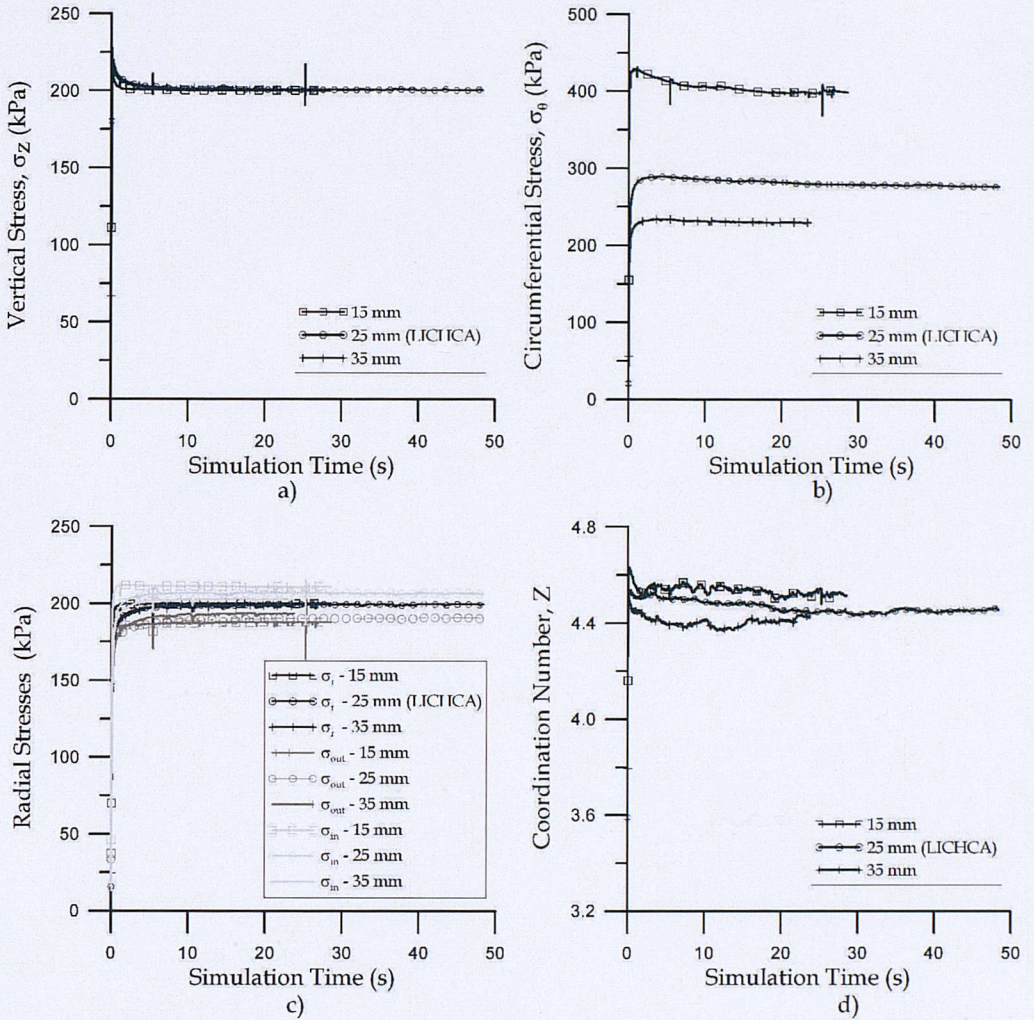


Figure 8.23: Effect of variable thickness on the stress distribution and coordination number

### Effect of section angle

Intuitively, it was expected that section used for the simulation of the whole specimen would have an effect on the simulated response. In the same way that experiments are affected by the number of particles along the thickness of the sample, the number of particles between circumferential boundaries were expected too to have an effect. Simulations using a sample height of 25 mm,  $\mu = 0.325$  and angles of 5, 10 and 15° were performed. The results are illustrated in Figure 8.24.

Referring to Figure 8.24, there is a difference between the section angles used in the simulations. Concerning the vertical stress (see Figure 8.24a), it is clear that the expected value of 200 kPa was achieved for all the simulations. Similar observations can be deducted in relation to the average radial stress and the coordination num-

## 8. Advanced modelling of hollow cylinder tests

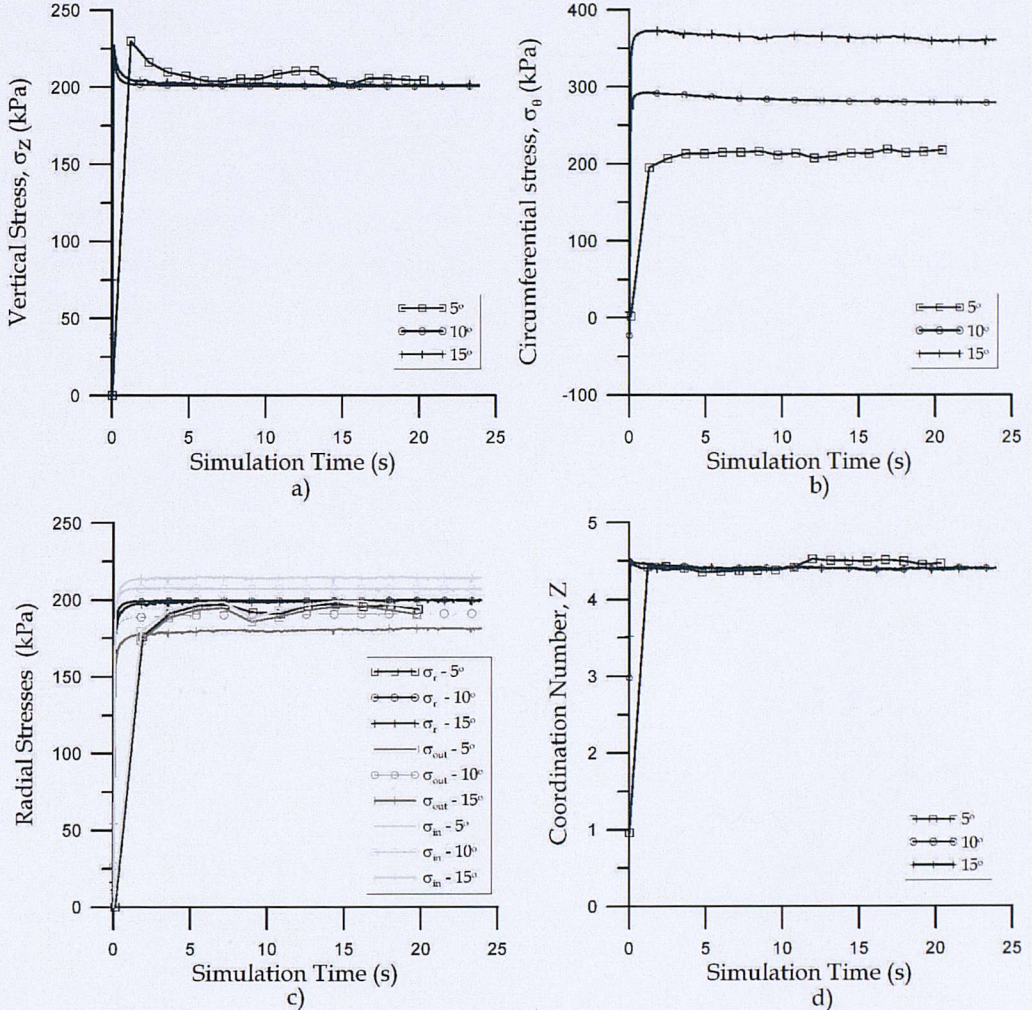


Figure 8.24: Effect of section angle on the stress distribution and coordination number

ber. These observations are coincident with those stated in the previous section. However, it was surprising to observe that the smallest section ( $5^\circ$ ) was the closest to desired isotropic state. Both the inner and outer pressures were very similar and very close to 200 kPa, and as a consequence, the circumferential stress was also very close to 200 kPa. Note that in Figure 8.24d) there is a tendency to approach the required 200 kPa as the section angle reduces. The reasons for this behaviour still need to be understood. But it was of particular interest to observe if these conditions could be equally maintained if a specimen with realistic height was used (i.e. 250 mm for the ICHCA and 500 mm for the LICHCA).

### Effect of sample height

The challenge of assessing the effects of the sample height is determined by the significant increase in the number of particles that must be included in the simulations. Once again, a  $5^\circ$  section was used with a sample thickness of 25 mm and  $\mu = 0.325$ . Three different sample heights were tested: 25, 50 and 250 mm, which included 3897, 7794 and 39594 particles, respectively. Note that the sample height of 250 mm corresponds to the dimensions of the ICHCA. The results obtained are shown in Figure 8.25.

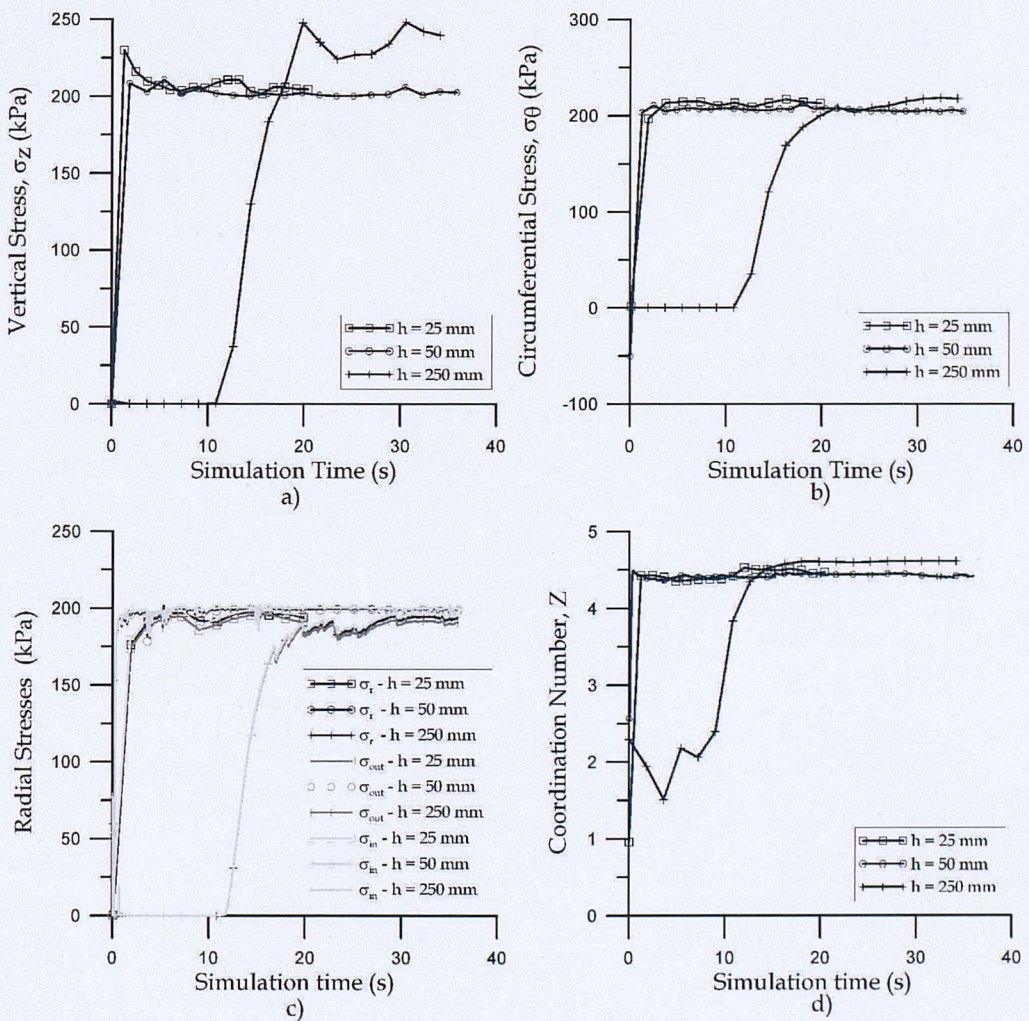


Figure 8.25: Effect of the height of the sample on the stress distribution and coordination number

Referring to Figure 8.25 it is important to note that in all the graphs there seems to be a delayed response on the specimen with 250 mm height. This is a result of a necessary reduction in the simulation time-step in order to avoid contact detection

problems encountered when the same time-step as in the other simulations was used. Apart from the evident “delay”, the most concerning effect of this change of time step is the duration of the simulations. The simulation presented here for  $h = 250$  mm took approximately 8 weeks, while the same simulation with frictionless spheres took about 12 weeks. Preliminary attempts with  $h = 500$  mm whose results are presented later experienced an even more significant increase in the computation time.

The observations of the results from Figure 8.25 are encouraging. Similar trends were observed in terms of vertical, radial and circumferential stresses. It must be noted however, that an increased duration would be needed to bring the simulation with  $h = 250$  mm to an equivalent point compared to the other two simulations. A duration of 11 weeks was required to bring a specimen with  $h = 500$  mm to a similar stress state. Note however, that this specimen was generated from the final state of the simulation with  $h = 250$  mm. Nevertheless, similar trends are clear. The vertical stress shows a rapid increment and a subsequent reduction thereafter. Similarly, the average radial and circumferential stresses are close to the 200 kPa, and the outer and inner pressures are very similar. The evolution of the coordination number on the other hand, is a bit higher for the simulation with  $h = 250$  mm, but it is expected to reduce if the simulation had continued and the vertical stress had approached its final value of 200 kPa.

The above results are clearly computationally expensive. Even though they cannot be considered conclusive, they are encouraging and give confidence in the methodology used.

It has been shown that a generalised axi-symmetric environment can be used successfully. However, further improvements and validation must be carried out in order to be able to implement the numerical membrane in this environment. The use of the stress-controlled membrane increases the computational cost as further calculations are required during each time-step. The need for increased computational power and/or parallel processing to be implemented into the DEM code is evident.

## 8.6 Simulation control for realistic axi-symmetric HCA specimens

Apart from the circumferential periodic boundaries and the stress-controlled membrane, realistic HCA simulations must be able to translate and rotate the top rigid boundary. The translation of the rigid boundary is a standardised procedure for DEM simulations of triaxial experiments for example. The torque application however, is entirely new and is essential for the introduction of principal stress rotation. On the other hand, realistic DEM simulations of HCA experiments need modified algorithms in order to follow the same stress paths as the physical experiments. This section describes those procedures.

### 8.6.1 Method for application of torque

As explained in Chapter 3, the introduction of the shear stress that allows the rotation of the orientation of the principal stresses is performed via a torque applied at the rigid top platen. This methodology is followed in the same way in the realistic DEM simulations. In order to introduce a torque the simulated rigid top platen rotates about the vertical axis of the Cartesian coordinate system.

The rigid boundary is mapped as any plane with the coordinates of three points. One of the points used to describe the boundary is located at the origin of the  $XZ$  plane at the specified height of the boundary. The other two points are then used to specify the rotation of the boundary at the required strain rate defined by a rotation tensor and servo-control algorithms similar to those described in Chapter 5.

The easiest way to validate the performance of such approach is to fix a single particle to the boundary via a very high coefficient of friction between the particle and the boundary, and also the inclusion of a body force in the direction perpendicular to the boundary. As a consequence the rotation of the centroid of the particle can be tracked as the boundary is rotated. Figure 8.26 illustrates this approach and demonstrates its effective performance for a single particle simulation (i.e. the figure was plotted with actual DEM data).

Figure 8.26 illustrates that the control points (2, 3) rotate around the vertical axis where the other control point (1) is located. Similarly it is shown that the tracked movement of the particle A is coincident with the movement of the control

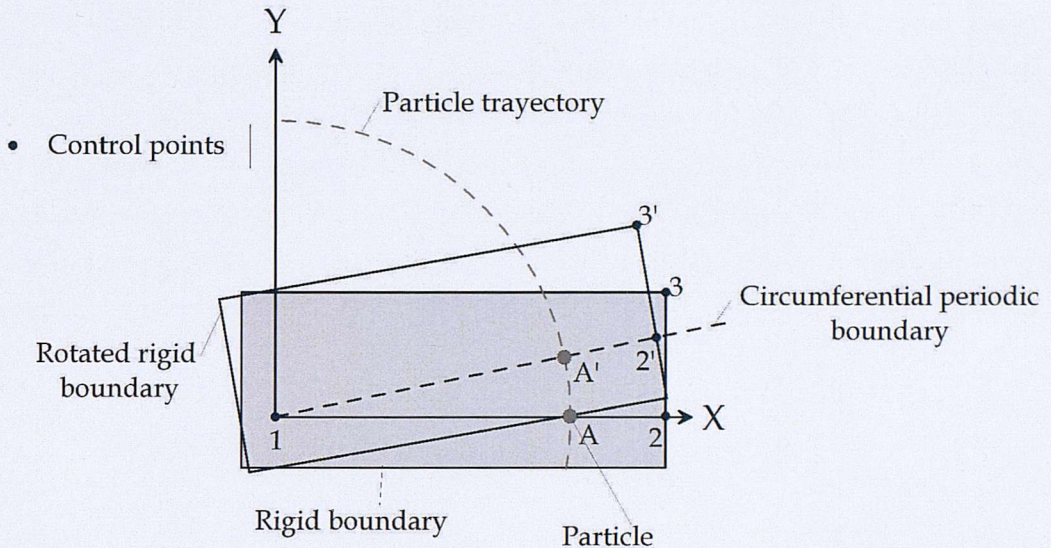


Figure 8.26: Single particle simulation to validate the approach to rotate the rigid top platen and allow the application of torque

points. Figure 8.26 also highlights another issue. The figure shows a HCA section of  $\theta_b = 10^\circ$ . Particle A was originally placed over the  $x$ -axis with the corresponding height to touch the rigid boundary. After a rotation of 10 degrees, where A' is drawn, the particle protrudes and appears again at position A. This also serves as an additional validation for the vertical periodic boundaries. Furthermore, the rigid boundary is represented as a rectangle that extends towards the negative portion of the  $x$  and  $y$ -axes. This is required for realistic simulations, otherwise the particles close to the  $x$ -axis would be free to fly above the boundary. That is because a boundary placed with an edge along the  $x$ -axis when rotated would leave a gap between the rigid boundary and the vertical periodic boundary where the particles are free to move.

The other issue that requires consideration for the application of torque is to investigate the detailed boundary conditions required along the rigid platen. As mentioned in Chapter 3, different approaches have been devised for the application of torque in physical experiments. Porovic (1995) and Nishimura (2005) used blades that penetrated the sample at the boundary. Lade et al. (2008) used particles of the sand tested glued to the boundary. Finally, the LICHCA uses an enlarged section (flares) in the vicinity of the boundary with a porous stone. For the realistic DEM simu-

lations an enlarged area of contact has not been included, while particles could be also “glued” to the boundary. Also groups of joined small particles or further rigid boundaries could be simulated as blades. The influence of these different boundary conditions was not investigated in this thesis but is a potential avenue for further research. However, to accurately reproduce the physical experiments, the coefficient of friction between the boundary and the particles was extensively measured via tilt tests whose results were mentioned before.

### 8.6.2 Control algorithms

The control of the realistic DEM simulations is similar to the experimental procedure described in Section 3.3.2 and opposite to the algorithms presented in Chapter 5 that used stresses resolved in the Cartesian coordinates, the realistic simulations are controlled as in the physical experiments, using stresses in cylindrical coordinates (i.e.  $z, r, \theta$ ).

The control parameters for the simulations as indicated below, remain the same:

$$b = \frac{\sigma_2 - \sigma_3}{\sigma_1 - \sigma_3} \quad (8.10)$$

$$t = \frac{\sigma_1 - \sigma_3}{2} \quad (8.11)$$

$$p = \frac{1}{3} (\sigma_1 + \sigma_2 + \sigma_3) \quad (8.12)$$

$$\alpha = \frac{1}{2} \arctan \left( \frac{2\tau_{z\theta}}{\sigma_z - \sigma_\theta} \right) \quad (8.13)$$

The target stresses for each increment of the stress path are calculated in the same manner as in the physical experiments:

$$\sigma_z = p - t \left( \frac{2b - 1}{3} - \cos 2\alpha \right) \quad (8.14)$$

$$\sigma_r = p - t \left( \frac{2(1 - 2b)}{3} \right) \quad (8.15)$$

$$\sigma_\theta = p - t \left( \frac{2b - 1}{3} + \cos 2\alpha \right) \quad (8.16)$$

$$\tau_{z\theta} = t \sin 2\alpha \quad (8.17)$$

At this stage, for the physical experiments, the axial force ( $W$ ), the torque ( $M_T$ ) and the inner and outer pressures ( $p_i$  and  $p_o$ ) were calculated and applied as explained in Chapter 3. The realistic DEM simulations follow the same procedure as the servo-controlling algorithms are implemented in terms of these imposed loads. Note that this step was not required in the simulations with cubical periodic boundaries because the control was performed in terms of the target stresses directly, and Cartesian coordinates were used.

As a consequence, as in the experiments, the stress paths can be followed under stress or strain control. At each time step the axial stress (or shear stress) is incremented under strain control. Subsequently, the shear stress (or deviatoric stress) changes and the corresponding required radial and circumferential stresses can be calculated such that constant values of  $p$ ,  $b$  and  $\alpha$  can be maintained. Knowing the required values for the radial and circumferential stresses, the required values for the internal and external pressures can be determined. This calculation cycle is performed in every time step of the DEM simulation.

## 8.7 Preliminary results using rigid boundaries

This section discusses a set of preliminary realistic DEM simulations of HCA tests. Simulations with both axial load and torque are described.

### 8.7.1 DEM simulation with axial translation of the top boundary

A preliminary set of simulations was performed to demonstrate the capabilities of the axi-symmetric environment to replicate HCA tests. For that purpose, simulations with a sample height of 25 mm, and a section angle of 10 degrees were carried out. Although it was demonstrated in the previous section that these specimens could not be isotropically consolidated in a successful manner, this specimens have a reduced

## 8. Advanced modelling of hollow cylinder tests

---

number of particles, allowing to perform the simulations in less time, and their results are sufficient to demonstrate the validity of the axi-symmetric environment.

The first simulation of this type was intended to shear the sample by translating the top boundary in a strain-controlled way while adjusting the inner and outer pressures to keep the radial and circumferential stresses constant and  $\mu = 0.325$ . This stress path replicates the form in which a triaxial tests would be performed in the HCA and it is not a HCA stress path that has been tested in the current study. However, it allows to visualise the main features of capabilities of the newly implemented environment.

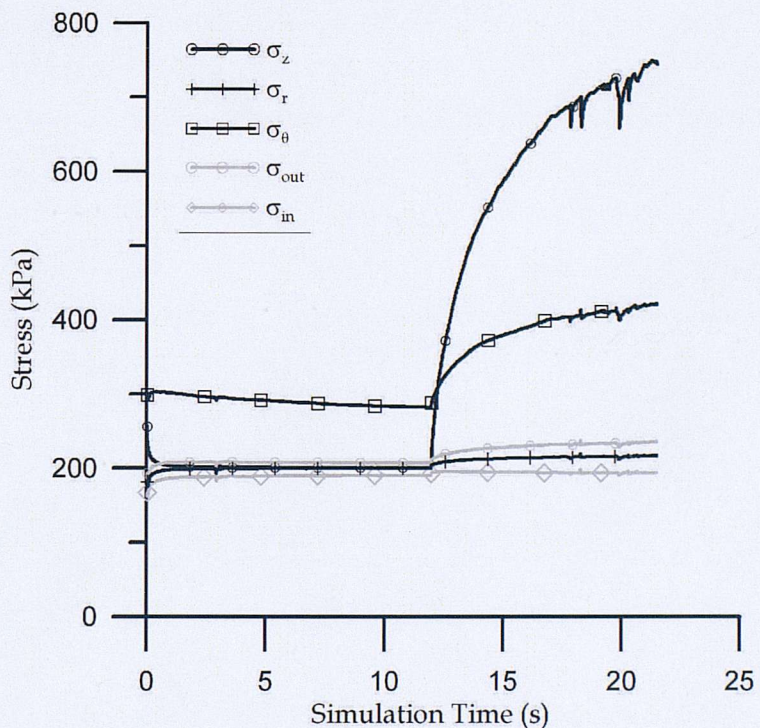


Figure 8.27: Stress-strain response of triaxial compression of a HCA specimen with  $h = 25$  mm

Figure 8.27 shows the stress-strain response for this particular stress path. As expected due to unsuccessful isotropic consolidation the initial stresses prior to shearing are not entirely isotropic. However, the evolution of the stresses demonstrate the possibility of shearing a sample by translation of the top rigid platen. Also note that upon start of shearing (i.e. when  $\sigma_z$  starts to increase) the values of the internal and outer stresses change in a different manner. As mentioned before, this simulation was intended to keep these stresses constant during shearing. This result suggested that it was necessary to have a different gain factor for the servo-control algorithms of each of the boundaries. This has been already implemented, and it has been

possible to maintain equal pressures for longer. However this makes the trial and error process (to find the appropriate gain parameters) for every simulation longer and more complicated.

### 8.7.2 DEM simulation with rotation of the top boundary to simulate application of torque

A second simulation, that intended to show the capabilities of the axi-symmetric environment for the application of torque was performed. Note that although the application of torque is not axi-symmetric, what was tested is the DEM environment. A specimen height of 25 mm,  $\mu = 0.325$  and rigid boundaries were used for this simulation. As in the case above, the stress-controlled membrane was not included for this simulation. After the “isotropic consolidation”, the objective was to maintain the external and internal pressures at a constant value while the top boundary was rotated around the vertical axis to allow for the application of torque. Note that this type of simulation is similar to the more common simple shear test.

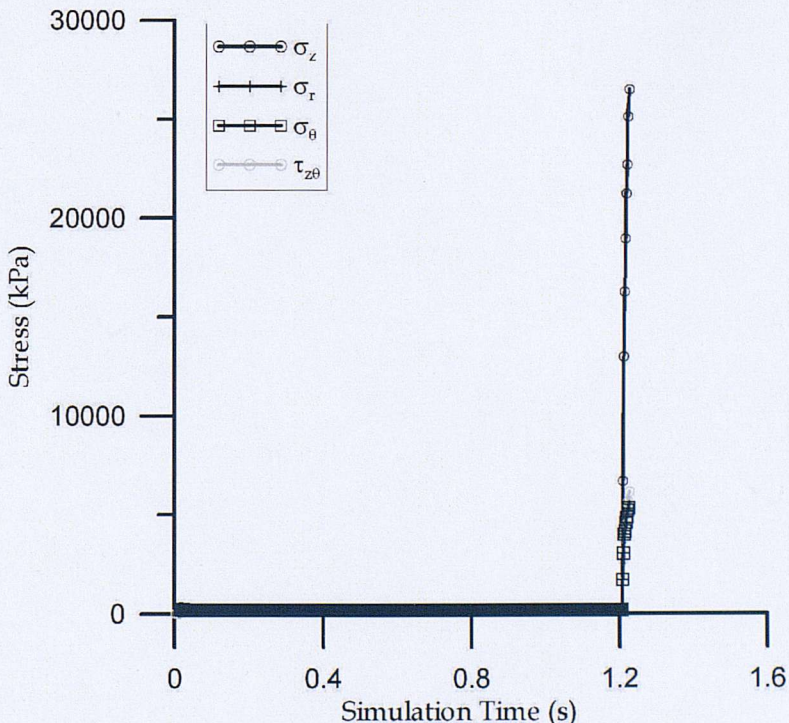


Figure 8.28: Stress-strain response during application of torque for a HCA specimen with  $h = 25$  mm

Figure 8.28 shows the evolution of stresses for the simulation. As it would be expected an increase in the shear stress and the vertical stress is observed. However,

this stress levels are unrealistically high. This is due to a very high strain rate of rotation applied during shear, and this is also the cause of the simulation failing at the point illustrated. The sudden and significant increase in the radial and circumferential stresses also demonstrate the lack of calibration in the shear strain rate and the corresponding gain factor for the servo-control algorithm of the boundary stresses. Nevertheless, the results show that it is possible to simulate HCA tests (including torque) using the DEM axi-symmetric environment.

Figure 8.29 shows the state of the contact force network at the end point of the simulation discussed above. Clearly a higher value of shear strain would be desirable for this kind of observation. However, it can be seen that the contact forces in the middle area (highlighted on the figure) of the  $r\theta$ -plane view are slightly inclined with respect to the vertical direction. The distribution of stresses is not uniform, as it would be expected from a simulation on a specimen of reduced height. However, the inclination of the contact network is the result of the principal stress rotation produced by the application of torque.

It has been demonstrated that DEM, and in particular an axi-symmetric environment can aid the understanding of the micro-scale mechanics governing the macro-scale response of granular materials under principal stress rotation. However, the need for higher computational efficiency is clear.

### 8.7.3 Some observations about non-uniformities in HCA testing

Figure 8.30 illustrates the evolution of contact forces for the simulation in which the top boundary was axially translated. It is important to discuss some features about the distribution of these networks. Referring to the conditions at the start of shearing, it is clear that there is a high concentration of heavily loaded particles in the radial direction. This is visible in both the  $rz$  and  $r\theta$  plane views. This is a result of the reduced number of particles across the sample thickness, since fewer particles must carry the same stress than in the vertical direction. Nevertheless, it is also evident that the distribution of contact forces is not uniform. There is a reduced population of strong contact forces in the top-right and bottom left corners of the  $rz$ -plane view. Similarly, an area of weaker forces seems to occur at the bottom of the  $r\theta$ -plane view.

In relation to the situation at the end of the shearing stage, a completely different

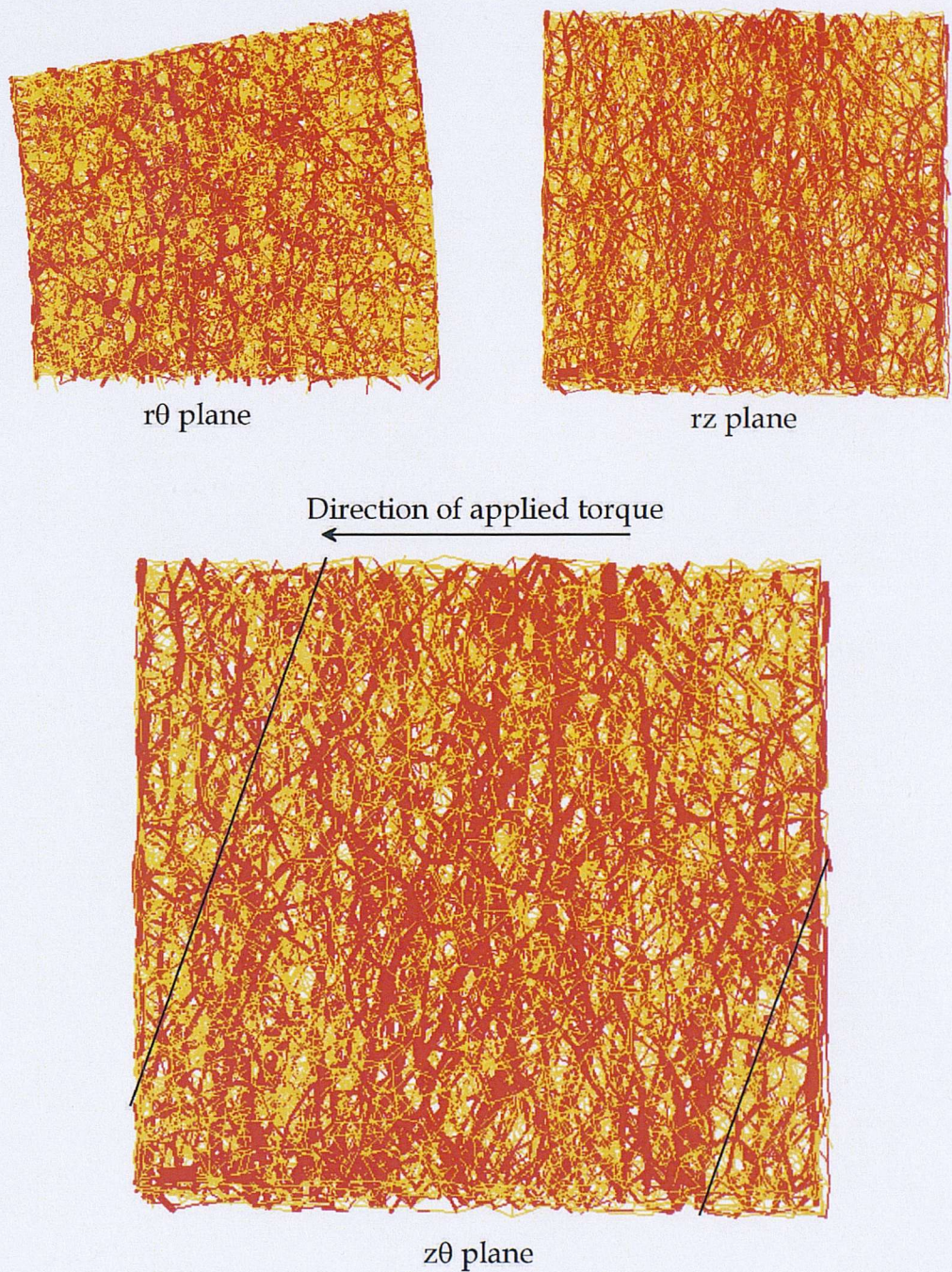


Figure 8.29: Evolution of contact forces during application of torque on a HCA specimen with  $h = 25$  mm

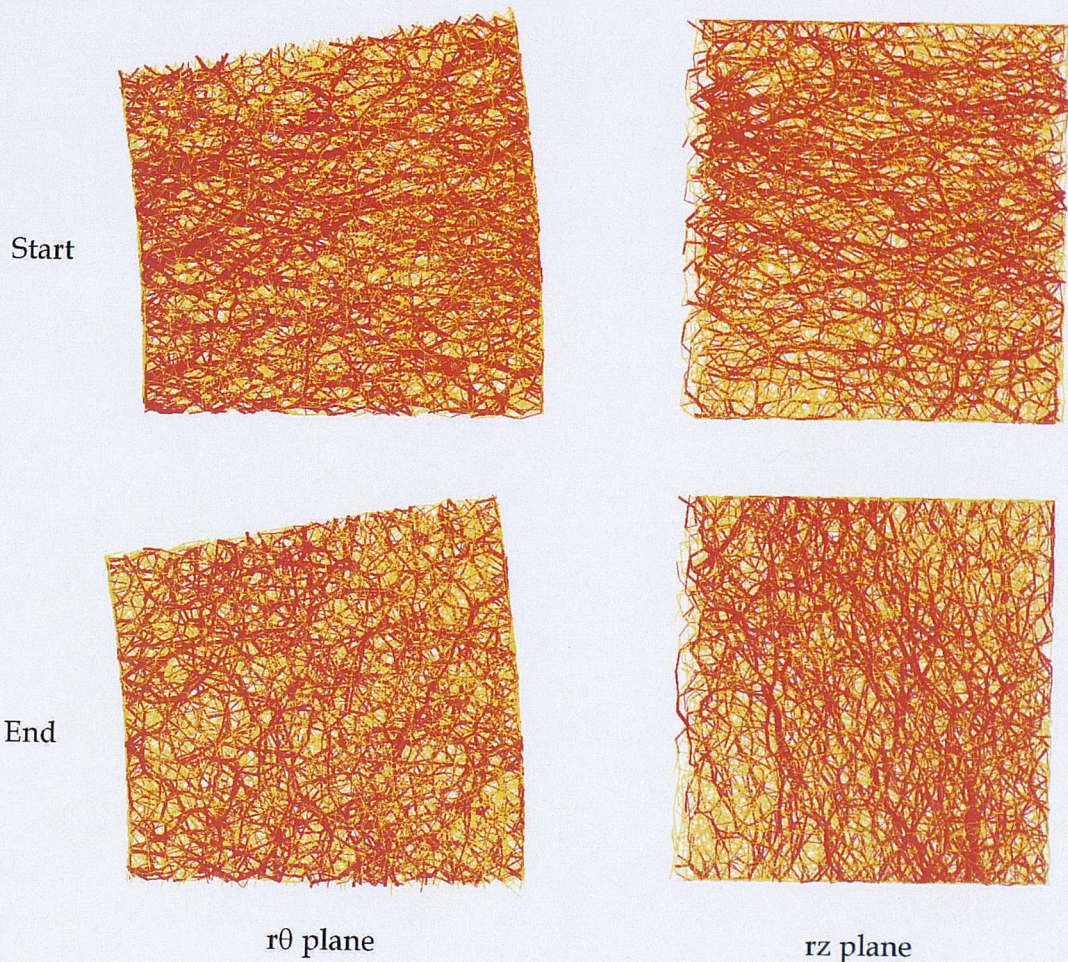


Figure 8.30: Evolution of contact forces during triaxial compression of a HCA specimen with  $h = 25$  mm

picture has arisen, which is even more non-uniform. This is in agreement with the FE numerical studies summarized in Chapter 3. Clearly, the majority of strong force chains have orientated vertically to withstand the major principal stress as it would be expected. Note however that the distribution is not homogeneous as it was observed in the periodic cell simulations of Chapter 6. The contact forces in the  $rz$ -plane view seem to leave weaker areas in the top right and bottom left corners of the specimen. This distribution is not far from that one observed in the continuum analysis by Hight et al. (1983) and illustrated in Figure 3.22.

At this point it is also interesting to compare Figures 8.31 and 3.21. Figure 8.31 illustrates the contact forces of a HCA specimen with  $h = 500$  mm in the  $rz$ -plane. This contact force distribution is the result of the DEM simulation that was discussed in Figure 8.25 with  $h = 500$  mm. Although the simulation in Figure 8.25 was not sheared, Figures 8.31 and 3.21 are comparable because the vertical stress is higher than the radial and circumferential stresses and the value of  $p'$  is approximately 200 kPa. As a consequence, the stress state represented in Figure 8.31 is such as the one that would occur at the beginning of shear at a small strain level.

In the same way as in Figure 3.21, only half of the section is plotted due to its symmetry. Noting that the thickness of the contact forces is proportional to the magnitude of the contact forces, it is clear that there is a concentration of stresses in the vicinity of the rigid boundary (bottom of closer view), just as it was demonstrated in Figure 3.21 through FE analyses. Additionally, the middle portion of the specimen appears to be free of stress non-homogeneities. The results must be fully compared when the flexible boundary is used in the DEM simulations. The results are nevertheless, very encouraging. This will allow to further understand the causes and development of non-uniformities in HCA testing.

## 8.8 Summary

In this chapter the implementation of a new and generalised axi-symmetric environment for the DEM simulations of HCA tests was presented. Each of the components of the environments was discussed. Details of the implementation and validation of these different boundary conditions were summarised.

The issue of specimen generation allowed to study other related issues such as arching and the effects of the sample geometry on the results. Preliminary results of HCA

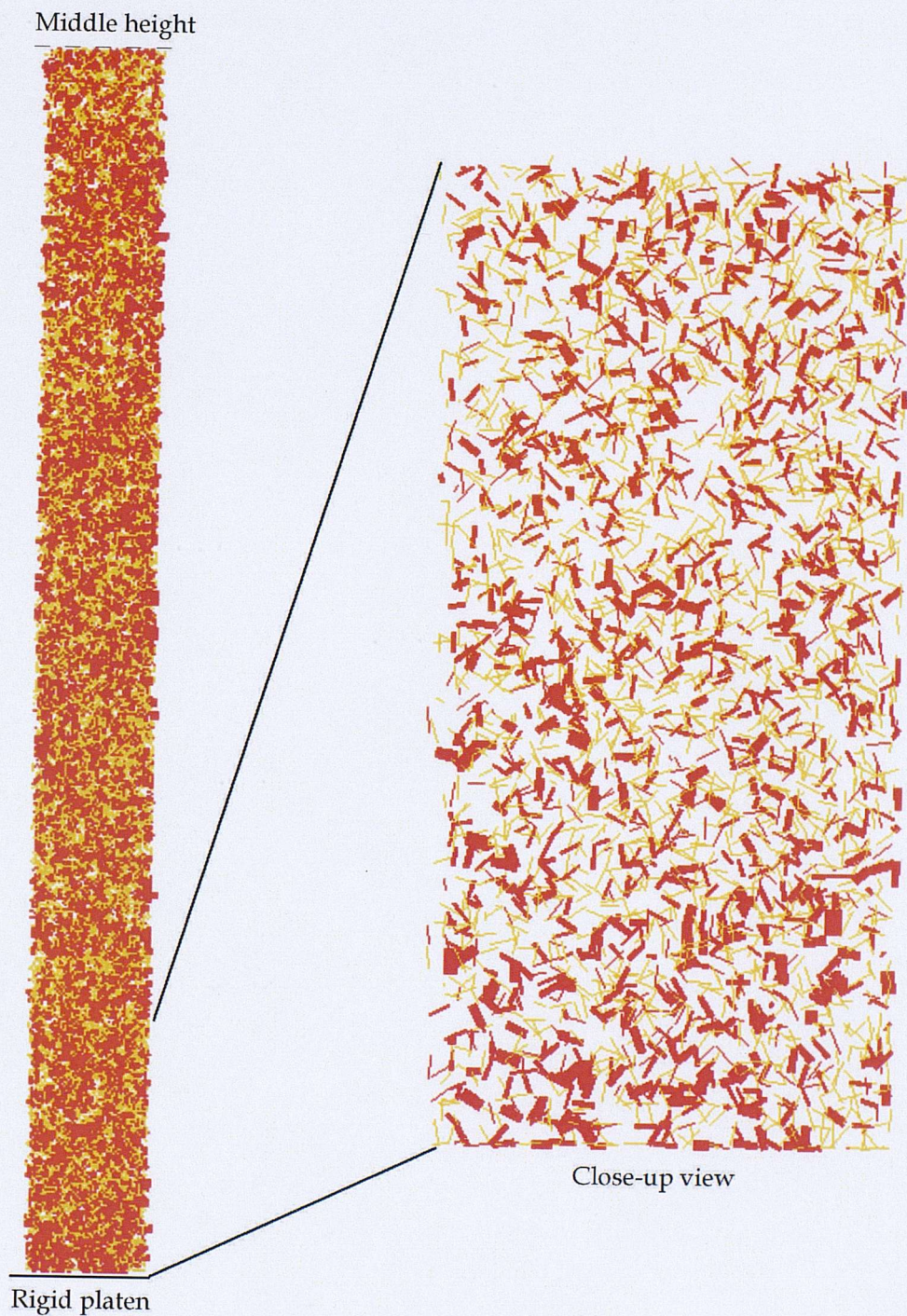


Figure 8.31: Distribution of contact forces in a HCA specimen with  $h = 500$  mm - Presence of stress non-uniformities

## 8. Advanced modelling of hollow cylinder tests

tests simulated using the axi-symmetric environment were presented. Not only the axial translation of the boundary but also the application of torque were described. These results also allowed to find some consistency between physical experiments, FE numerical analyses and DEM simulations in relation to the occurrence of non-uniformities.

The results of the preliminary simulations demonstrated that it is possible to simulate any stress path. However, more computational power or parallelisation of the code are necessary to obtain faster results. However, the potential of such approach and the need for further research are clearly indicated.



# Chapter 9

## Conclusions

### 9.1 Summary

The main objective of the current research project was to advance understanding of the particle scale interactions that underly the observed three dimensional nature of soil response. To achieve this aim, experimental results of HCA tests on glass ballotini were compared with DEM simulations that follow identical stress paths. Glass ballotini were used so that the DEM model could capture the geometrical and physical characteristics of the constituent particles. The results presented confirm that DEM is capable of reproducing the observed material behaviour, at least in a qualitative manner. The DEM simulations provided data to examine the particle scale mechanics.

Prior to embarking on the HCA testing programme, a preliminary set of triaxial experiments was performed in order to assess the testing conditions for HCA samples, and to characterise the behaviour of the glass ballotini. Both the bulk material properties were measured, as well as the particle characteristics required for input into the DEM simulations.

It was decided to test the HCA samples under dry and drained conditions. The experimental program was designed to assess the effect of the intermediate stress ratio ( $b$ ) and the principal stress rotation ( $\alpha$ ) on the material response. Two specimen geometries, with different aspect ratios were considered to experimentally assess the effects and sources of stress and strain non-uniformities during HCA testing. The sensitivity of the material response to the particle size distributions and the mean particle sizes were also evaluated.

## 9. Conclusions

---

The physical experiments were then simulated using DEM. Periodic boundaries can apply general stress states free from boundary effects were used. Quantitative validation of the DEM code was achieved using simulations of tests on uniform spheres with a lattice (FCC) packing. The comparison of DEM simulations and experiments qualitatively agreed. In addition, numerous parametric studies were performed to further understand the micro-mechanics of granular materials that underly the observed macro-scale response.

Finally, a generalised DEM axi-symmetric environment was developed and validated. The potential to use this system was demonstrated by considering the issues related to specimen generation. Preliminary examples of simulations of HCA tests using realistic boundary conditions were also presented.

## **9.2 Findings**

This work included both HCA experiments and three-dimensional DEM simulations of the response of granular materials under generalised stress conditions. A summary of the contributions presented in Chapters 3 to 8 was included at the end of each chapter. In this section the main findings presented in each chapter are combined here to give a general overview of the conclusions of this research project.

### **9.2.1 Experimental results**

#### **Triaxial tests**

It was found experimentally that the shear strength and stiffness characteristics of glass ballotini were affected by variations in the coefficient of inter-particle friction. This conclusion was derived on the basis of triaxial compression tests on submerged and dry ballotini and informed by these experimentally observed differences in values of inter-particle friction for dry and submerged glass ballotini particles were reported by Cavarretta (2009).

Volumetric strains can be estimated from local measurements of the sample deformation obtained from the radial strain belt, and making some assumptions about the mode of deformation of the sample. A direct comparison between the volumetric response of triaxial specimens calculated by different methods demonstrated that

## 9. Conclusions

---

the assessment of the volumetric response is dependent on the assumptions made about the mode of deformation of the sample. Consequently, it was considered that these results were partly subjective.

Triaxial tests under different testing conditions (i.e. dry and submerged) helped to decide that the HCA should be performed under dry conditions. This conclusion was based in the following arguments:

- The measurement of inter-particle friction is easier under dry conditions.
- The dry tests seemed to be less affected by stick-slip behaviour
- The volumetric response of dry specimens was bigger, a fact that would be an advantage in presence of the current resolution of the instrumentation in the ICHCA and LICHCA

During the experimental determination of the  $K_0$  coefficient it was confirmed that the formula by Jaky (1944) underestimates the value of this coefficient for glass ballotini.

### **HCA tests**

The aspect ratio (height/outer diameter ratio) of the ICHCA was increased from 1 to 2 by increasing its height. The new HCA apparatus with aspect ratio of 2 was denoted as the LICHCA. This change reduced the effect of stress and strain non-uniformities on the response observed in the experiments. The increase in height was justified by extensive previous research using finite element methods. Although the continuum analyses used for this assessment were performed using undrained stress paths, the conclusions were experimentally confirmed for drained conditions in this research.

As a result of the HCA enlargement, a consistent sample preparation method was devised in order to systematically compare tests under dry and saturated conditions for different sample geometries. The method proved to be successful in reproducing equal void ratios for different particle size distributions, sample sizes and testing equipment.

Several options were used in an attempt to improve the resolution of the proximity transducers for radial strain measurement. It was concluded that the most accurate way was to use foil targets stuck to the latex membrane using vacuum grease.

## 9. Conclusions

---

The effects of the particle size distribution were assessed experimentally. HCA tests demonstrated that samples of “medium” sized ballotini were slightly stiffer than the “small” sized ballotini. This difference was caused by slight differences in the particle size distribution between the two specimens.

ICHCA experiments performed using different particle size distributions with different mean diameters proved that for an average particle size of 1.1 mm, the results are accurate. A very stiff response was obtained for the “big”, 2.5 mm ballotini. Similarly in this test the formation of shear bands which was observed in the other tests (“medium” and “small” ballotini) was inhibited. The reduced number of particles across the specimen wall imposed a constraint in the movement of the particles. It was concluded that this result may differ for other granular materials with more complex particle shapes, which have a complex contact response (e.g. moments are transmitted at the contact point).

The presence of stick-slip may be related to the sudden local collapse of load carrying columns between grains. It was clear that the magnitude of the stick-slip stress fluctuations was significantly bigger for the tests where the major principal stress orientated 45 degrees with respect to the vertical. This observation could be explained by the fact that the  $K_0$  consolidated specimens develop an internal structure orientated in the vertical direction. Therefore, when sheared at a different inclination, a significant reorientation of the internal structure of the material must take place.

### **9.2.2 Numerical results - Implementation**

#### **Periodic boundaries**

An entirely new algorithm was developed in order to perform DEM simulations involving principal stress rotation using periodic boundaries. Additional improvements to the contact detection algorithm were necessary to achieve this. The inclusion of principal stress rotation into DEM simulations using periodic boundaries is a fundamental advance. It makes possible to simulate a wider range of stress paths than before.

This new implementation was validated analytically for triaxial, plane strain and simple shear conditions. The results of the validation included DEM simulations with varying input parameters.

## 9. Conclusions

---

In addition, new procedures that allow to follow identical stress paths to those experienced in HCA tests were also developed. These procedures involve the combination of different normal and shear stresses.

### **Realistic boundaries**

The axi-symmetric environment that uses vertical circumferential periodic boundaries was extended. In addition to the 90 degree quadrants used by Cui (2006), this new environment can now be used for any angular section. The possible applications of such environment are enormous. The application is however limited to problems involving axi-symmetric conditions (i.e. pile driving, CPT testing, etc.)

A new algorithm that allows to simulate a stress controlled membrane, as the latex membranes in experimental tests was incorporated into the DEM code. This is an improvement over previous versions of the code. The calculation of Voronoi diagrams is currently performed without the need of linking external software (i.e. MATLAB) for this calculation. As a result, the processing times for simulations using this type of boundaries were significantly reduced. In addition, algorithms to control DEM simulations of HCA tests using this realistic boundaries were also incorporated into the DEM code.

### **9.2.3 Numerical results - DEM simulations**

Simulation of tests on uniform spheres with lattice (FCC) packing validated the DEM code. However, the DEM simulations and experiments agreed only qualitatively. The differences between the experiments and the DEM simulations are most likely due to the effect of differences on particle shape. The possibility that differences in the inherent anisotropy and the presence of stress and strain non-uniformities in the experiments further contributed to the discrepancy was explored. These issues were considered in a series parametric studies that considered various input parameters and stress conditions on the response. The main findings of these numerical studies are summarised below.

#### **Input parameters**

In contrast to most published combined DEM and experimental studies, no macro-scale calibration or curve fitting was used in this study. Instead, the input param-

## 9. Conclusions

---

eters necessary to replicate physical tests were selected following physical experiments. The numerical input parameters including shearing strain rate and size of the time step were carefully selected based on the results of parametric studies. Density scaling was not used. Therefore actual stresses rather than stress ratios could be compared.

### **Specimen generation**

Algorithms to generate numerical specimens that could be sheared from both isotropic and anisotropic stress states were required. Previous research did not consider the generation of specimens with initial anisotropic stress states in detail. In this thesis an approach that starts from an initial isotropic stress state is used. Any anisotropic stress state can be achieved by increasing the magnitude of the deviatoric stress while the mean effective stress is kept constant. It was demonstrated that this method produced specimens with identical response as those which were produced by simulating  $K_0$  consolidation in the same way as in the laboratory experiments.

### **Results from parametric studies**

The 3D stress paths considered in this research included triaxial tests, constant  $b$  tests and HCA tests. No prior published study had considered as broad a range of loading conditions.

The coefficient of friction had a significant influence on the observed response of granular materials. The shear strength was most significantly affected, however the volumetric response, the octahedral stiffness, the critical coordination number and the heterogeneity of contact forces were all sensitive to this parameter. Sensitivity of the failure surface location on the deviatoric plane was identified in relation to the inter-particle friction.

Friction was found to have a measurable effect on the degradation of soil stiffness. Higher inter-particle friction seems to facilitate establishment of stronger contact force networks, and allows a broader range of stress conditions to be sustained without the need of massive particle re-arrangement. The increase in the resistance at a given contact provided by a higher friction value appears to mean that a smaller number of contacts is required to withstand a certain stress level. While a constant (critical) value of coordination number was found for all simulations, this “critical”

## 9. Conclusions

---

state did not correspond to constant volume conditions, or a constant deviatoric fabric.

Additional studies to validate the newly implemented axi-symmetric environment also showed the importance of friction on the behaviour of granular materials. It was evident that when rigid circular boundaries were used for HCA specimen generation, the coefficient of friction had an effect on the arching effect, i.e. the development of strong force chains orientated in the circumferential direction. It was demonstrated that the uniformity of the grain size interacts with the coefficient of friction to promote or inhibit arching.

A second parameter that affected the response of granular material was the initial density. While different volumetric responses and shear strengths were observed (as it would be expected) samples that differed only in their initial densities produced the same “critical” coordination number.

A variation in the elastic parameters of the particles ( $E$  and  $\nu$ ) demonstrated that for the strain levels studied, the macro-scale response was insensitive to these values. Further research should consider the sensitivity of the small strain response to these parameters.

Tests in which the intermediate stress ratio ( $b$ ) was varied while maintaining the principal stress rotation ( $\alpha$ ) constant were considered. Although significant variations in stiffness were not observed (for the strain levels under consideration), the shear strength, the volumetric strain, and the evolution of the deviatoric fabric did vary significantly. The global deformation constraint imposed during plane strain conditions is thought to be the main factor affecting the variables mentioned above.

The effect of the stress history or initial stress anisotropy was also assessed for the simulations evaluating the influence of  $b$ .  $K_0$  consolidated samples were slightly softer than their isotropic counterparts. Similarly, the evolution of deviatoric fabric was affected by this stress history.

When the effects of principal stress rotation  $\alpha$  were studied, as it would be expected, the different principal stress orientations had no influence on the stress-strain response or micro-mechanical characteristics of isotropically consolidated specimens. This observation contributed to the numerical validation of the DEM algorithms necessary to simulate this loading conditions.

In contrast to the isotropically consolidated specimens, the  $K_0$  consolidated specimens were found to be affected by the orientation of the principal stress during shear-

ing. The extent of the sensitivity of the strength, stiffness and micro-mechanical parameters (with exception of the critical coordination number) to the  $\alpha$  value depended on the  $b$  value considered. The need to treat the effects of  $\alpha$  and  $b$  in an unified manner was thus highlighted.

### 9.2.4 Evolution of soil fabric

Each macro- or micro-scale observation on the behaviour of granular materials in the parametric studies could be explained in terms of the evolution of the soil fabric. Based upon previous research we know that within soil a system of major load carrying columns or strong force chains exists. The “weaker” load chains orthogonal to the strong force chains provide lateral support. A variation in the  $b$  value influences the magnitude of the lateral support provided in the direction of the intermediate principal stress. The potential to buckle in the  $\sigma_2$  direction is at its minimum point under plain strain conditions ( $b \approx 0.4$ ). This explains why the maximum deviatoric stress is mobilised in the plain strain case. Similar observations can be made if a pre-shearing stage or  $K_0$  consolidation acts to generate a network of strong force chains in a given direction. When this material is loaded so that the deviatoric stress is transmitted along these relatively stable, pre-existing load carrying columns it is stronger than when the less stable networks available to transmit stress in other directions are loaded. The lateral support provided by the force chains orientated in the  $\sigma_2$  direction varies with  $b$ , and this in turn influences the extent of the sensitivity of the response to changes in  $\alpha$ .

Additionally, it was shown that fabric failure states could be identified and plotted in a generalised fabric space. This fabric space is analogue to the generalised stress space. An elegant way of visualising a fabric envelope surface in the deviatoric plane was proposed. This fabric surface resembles an inverted Lade & Duncan (1973) failure criterion. The model was qualitatively extended to capture the effect of changes in  $\alpha$  value.

A second fabric surface was proposed in the  $\alpha$ - $b$ - $\Phi_d$  space. This surface is analogous and complementary to the shear strength surface proposed by Symes (1983) in terms of  $\alpha$ ,  $b$  and  $\phi'_{peak}$ . Therefore it was proposed as a limit boundary surface for the fabric states. It may be possible to extend the model to capture the kinematic nature of fabric response. These methods for describing soil fabric can be invaluable for understanding the micro-mechanics of soil behaviour that underly the observed

macro-scale behaviour. Such frameworks could be the base for the generation of input parameters to be used in continuum constitutive models.

While some progress was made towards explaining soil behaviour in terms of changes of soil fabric, further research is needed to accurately quantify the changes in soil fabric. An assessment of several methods for quantification of soil fabric was performed for all the stress paths tested in the present study. Describing fabric changes under stress paths where the mean effective stress ( $p'$ ) varies is particularly challenging.

### **9.3 Suggestions for further research**

The research presented in this thesis involved both experimental and numerical work, and suggestions for further research are presented in relation to each of these two aspects.

#### **9.3.1 Experimental research**

The scope of the current research was limited as the behaviour of anisotropic characteristics at small strain levels could not be accurately measured experimentally. Consequently, the improvement of the local instrumentation for the measure of volumetric changes is recommended. As a minimum requirement, the proximity transducers should be replaced by LVDT transducers appropriately deployed in the internal and external faces of the soil specimen.

The extension of the ram in order to allow larger strain levels to be attained for the LICHCA specimens would help to deepen the experimental understanding of anisotropic soil behaviour. An increase in the size of the air/water pressure interfaces used for the control of the internal and external pressures in the HCA would improve the control of the experiments.

Previous research performed at Imperial College using the ICHCA and LICHCA apparatuses has been performed under a mean effective stress of 200 kPa. The use of different stress levels would help to further understand the dependence of the anisotropic properties on different stress levels.

The results presented in this thesis showed that the grain size distribution has an effect on the behaviour of granular materials. In particular, it was hypothesized

that the value of the  $K_0$  coefficient may be affected. Some influence on the stick-slip behaviour was also observed. These topics merit further experimental investigation.

In addition to the issues above, improved methods for the accurate determination of the coefficient of inter-particle friction are desirable. In conjunction with improved numerical contact models it is possible to provide a quantitative agreement between simulations and experiments.

### **9.3.2 Numerical research**

#### **Boundary effects**

The literature review presented in Chapter 2 highlighted the lack of consensus amongst the experimental interpretations of the effect of the intermediate stress ratio  $b$  on the peak angle of shearing resistance. While there was a consensus in the fact that the resistance increases as  $b$  changes from triaxial compression ( $b = 0.0$ ) towards a maximum around plain strain conditions ( $b \approx 0.4$ ), opinions divide on what happens in the transition from plane strain conditions to triaxial extension ( $b = 1.0$ ). These different interpretations depend on the boundary conditions used in each of the apparatuses. The boundary conditions used in the experimental apparatuses (true triaxial/HCA) are a combination of rigid platens and flexible boundaries. DEM simulations with ideal periodic boundaries allow these issues to be explored on identical specimens, without the experimental boundary issues. Furthermore, the different boundary configurations can be simulated and its results compared to simulations free from boundary effects.

Boundary effects on HCA tests can also be easily evaluated using DEM, and in particular the axi-symmetric environment implemented in Chapter 8. This is, in fact, the obvious and natural continuation of this research project. The micro-mechanical sources of strain and stress non-uniformities can provide further insight into what is really happening at a particulate level in HCA experiments. The sources and effects of the stress and strain non-uniformities can be studied, as well as the effects of different boundary conditions for the application of torque (i.e. enlarged section as in the LICHCA, blades for the transmission of torque, or particles glued to the boundary). Note that the development of more efficient methods for DEM specimen generation would be useful to attain this goal.

### Improvement of DEM algorithms

The implementation of a more sophisticated contact model would also enable to study particle-scale interactions that affect small strain behaviour. This could provide further insight in the micro-mechanical mechanisms that underly the kinematic yielding in soil behaviour.

DEM simulations with large numbers of particles are computationally expensive. It is believed that a significant advancement could be achieved if the code was modified so it is possible to run it under parallel processing.

### Dependance of complex soil behaviour on the evolution of soil fabric

This thesis demonstrated that many of the observations of soil behaviour can be explained in terms of quantifiable changes of soil fabric. However, current methods to quantify fabric anisotropy in 3D are limited. In this regard improvement in statistical quantification of fabric are required, as well as better methods to visualise three-dimensional DEM data. It may be possible to develop methods to describe the topology of contact force networks using the emerging science of networks. Future approaches should consider both the normal and tangential contact forces.

The nature of the fabric boundary surface proposed here for the interpretation and modelling of soil fabric could have a kinematic nature. Since the evolution of soil fabric is directly related to the stress-strain behaviour, kinematic fabric yielding surfaces associated with real soil behaviour may exist. To advance understanding of yielding the number of sliding contacts during the simulations should be monitored. The fraction of sliding contacts could resolve even more the significance of friction during yielding. In addition, the nature of yielding could be further understood if small probes in the generalised stress space were simulated in the same way as they are performed in physical experiments.

DEM is analogue to the finite element method in the sense that particle centroids are nodes of the finite element mesh, and the inter-particle contacts would be the actual finite elements. This means that stiffness matrix could be built for subsequent time steps, during a DEM simulation. As this stiffness matrix would change with the creation/destruction and re-arrangement of inter-particle contacts, it could be also compared to the evolution of the fabric tensor.

## 9. Conclusions

### **Further possibilities for DEM research**

There is further scope to advance understanding of soil yielding and non-coaxial behaviour. These issues remain incompletely understood, and developing research in these areas is a natural continuation of the current study.

The effects of the grain size distributions could be investigated systematically using DEM. Possible research directions include transitional soil behaviour and the effect of internal erosion in critical state behaviour. DEM provides the possibility of exploring the influence of the intermediate stress ratio and the orientation of the principal stress on the critical state. The effects of  $\alpha$  on critical state have not been studied to date due to the impossibility of achieving large strains in the equipment available (i.e. hollow cylinder and directional shear cell).

Finally, in relation the results from the present research, it is clear that the main issue to consider in further studies is the use of more realistic particles. Future studies should better model the particle geometries and possibly also include particle damage/crushing.

# References

- Ackerley, S. K., Hellings, J. E. & Jardine, R. J. (1987), 'Discussion: A new device for measuring local axial strains on triaxial specimens', *Géotechnique* **37**(3), 413–417.
- Adjemian, F. & Evesque, P. (2004), 'Experimental study of stick-slip behaviour', *International Journal for Numerical and Analytical Methods in Geomechanics* **28**, 501–530.
- Arthur, J. R. F. (1972), New techniques to measure new parameters, in 'Proceedings of the Roscoe Memorial Symposium', Foulis & Co, p. Unknown.
- Arthur, J. R. F., Bekenstein, S., Germaine, J. T. & Ladd, C. C. (1981), *Laboratory Shear Strength of Soil*, number STP 740, American Society for Testing and Materials, chapter Stress Path Tests with Controlled Rotation of Principal Stress Directions, pp. 516–540.
- Arthur, J. R. F., Chua, K. S. & Dunstan, T. (1977), 'Induced anisotropy in a sand', *Géotechnique* **27**(1), 13–30.
- Arthur, J. R. F. & Menzies, B. K. (1972), 'Inherent anisotropy in a sand', *Géotechnique* **22**(1), 115–128.
- Bagi, K. (1993), 'Quasi-static numerical model from micro-level analysis of granular assemblies', *Mechanics of Materials* **16**(1-2), 101–110.
- Barreto, D., O'Sullivan, C. & Zdravkovic, L. (2008), Specimen generation approaches for dem simulations, in S. E. Burns, P. W. Mayne & J. C. Santamarina, eds, 'Deformational Characteristics of Geomaterials', Vol. 2, IOS Press.
- Barreto, D., O'Sullivan, C. & Zdravkovic, L. (2009), Quantifying the evolution of soil fabric under different stress paths, in M. Nakagawa & S. Luding, eds, 'Powders and Grains 2009 - Proceedings of the 6th International Conference on Micromechanics of Granular Media', American Institute of Physics, pp. 181–184.

## REFERENCES

---

- Been, K. & Jefferies, M. G. (1985), 'A state parameter for sands', *Géotechnique* **35**(2), 99–112.
- Bishop, A. W. (1953), The effect of stress history on the relation between phi and porosity in sand, in 'Proceedings of the 3rd International Conference on Soil Mechanics', Vol. I, pp. 100–105.
- Bishop, A. W. & Henkel, D. J. (1962), *Test measurement of soil properties in the triaxial test*, 2nd edn, Arnold.
- Bishop, A. W. & Wesley, L. D. (1975), 'A hydraulic triaxial apparatus for controlled stress path testing', *Géotechnique* **25**(4), 657–670.
- Bjerrum, L. & Landva, A. (1966), 'Direct simple-shear tests on a norwegian quick clay', *Géotechnique* **16**(1), 1–20.
- Burkardt, J. (2004), Fortran90 code: table-voronoi.  
<http://people.sc.fsu.edu/~burkardt/f-src/table-voronoi/table-voronoi.html>.
- Burland, J. B. & Symes, M. (1982), 'A simple axial displacement gauge for use in the triaxial apparatus', *Géotechnique* **32**(1), 62–65.
- Carl-Zeiss-Microlmaging (2007), *Axiovision User's Guide - Release 4.6.3*, Gottingen.
- Casagrande, A. & Carrillo, N. (1944), Shear failure of anisotropic materials, in 'Proceedings of the Boston Society of Civil Engineers', pp. 74–87.
- Cavarretta, I. (2009), The influence of particle characteristics on the engineering behaviour of granular materials, PhD thesis, University of London.
- Chang, C. S., Sundaram, S. S. & Misra, A. (1989), 'Initial moduli of particulated mass with frictional contacts', *International Journal for Numerical and Analytical Methods in Geomechanics* **13**(6), 629–644.
- Chen, J. F., Rotter, J. M., Ooi, J. & Zhong, Z. (2005), 'Flow pattern measurement in a full scale silo containing iron ore', *Chemical Engineering Science* **11**, 3029–3041.
- Cheung, G. & O'Sullivan, C. (2008), 'Effective simulation of flexible lateral boundaries in two- and three-dimensional dem simulations', *Particuology* **6**(6), 483–500.
- Cornforth, D. H. (1964), 'Some experiments on the influence of strain conditions on the strength of sand', *Géotechnique* **14**(2), 143–167.

## REFERENCES

---

- Cui, L. (2006), Developing a virtual test environment for granular materials using discrete element modelling, PhD thesis, University College Dublin.
- Cui, L. & O'Sullivan, C. (2005), Development of a mixed boundary environment for axi-symmetric dem analyses, in 'Powders & Grains 2005: Proceedings of the 5th International Conference on Powders and Grains 2005', Vol. 1, pp. 301–305.
- Cui, L. & O'Sullivan, C. (2006), 'Exploring the macro- and micro-scale response of an idealised granular material in the direct shear apparatus', *Géotechnique* **56**(7), 455–468.
- Cui, L., O'Sullivan, C. & O'Neill (2007a), 'An analysis of the triaxial apparatus using a mixed boundary three-dimensional discrete element model', *Géotechnique* **57**(10), 831–844.
- Cui, L., O'Sullivan, C. & O'Neill, S. (2007b), Coupling dem simulations and physical tests to study the load-unload response of an ideal granular material, in 'Proceedings of Discrete Element Methods 07 - Brisbane, Australia'.
- Cummins, D. (2008), The influence of different micro- and macro- parameters in the response of granular materials subjected to 3d stress conditions, Master's thesis, Imperial College London.
- Cundall, P. A. & Strack, O. D. L. (1979a), 'A discrete numerical model for granular assemblies', *Géotechnique* **29**(1), 47–65.
- Cundall, P. A. & Strack, O. D. L. (1979b), The distinct element method as a tool for research in granular media, part ii, Technical report, University of Minnesota.
- Daramola, O. (1978), The influence of stress-history on the deformation of a sand, PhD thesis, University of London.
- Dedecker, C. (2009), 'Personal communication'.
- Evans, T. M. & Zhao, X. (2008), A discrete numerical study of the effect of loading conditions on granular material response, in S. E. Burns, P. W. Mayne & J. C. Santamarina, eds, 'Proceedings of the 4th International Symposium on Defromation Characteristics of Geomaterials, IS Atlanta', Vol. 2, pp. 907–914.
- Foundoukos, M. (2006), Investigation of soil anisotropy using a hollow cylinder apparatus and numerical analysis, PhD thesis, University of London.

## REFERENCES

---

- Fukushima, S. & Tatsuoka, F. (1982), Deformation and strength of sand in torsional simple shear, in 'Proceedings IUTAM Conference on Deformation and Failure of Granular Materials, Delft', pp. 371–379.
- Gens, A. & Potts, D. M. (1984), 'Formulation of the quasi-axisymmetric boundary value problems for finite element analyses', *Engineering Computations* **1**(2), 144–150.
- Green, G. E. (1971), Strength and deformation of sand measured in an independent stress control cell, in 'Proceedings of the Roscoe Memorial Symposium, Cambridge, England', G. T. Foulis and Co. Ltd, pp. 285–323.
- Green, G. E. & Reades, D. W. (1975), 'Boundary conditions, anisotropy and sample shape effects on the stress-strain behaviour of sand in triaxial compression and plane strain', *Géotechnique* **25**(2), 333–356.
- Guo, P. (2008), 'Modified direct shear test for anisotropic strength of sand', *Journal of Geotechnical and Geoenvironmental Engineering, ASCE* **134**(9), 1311–1318.
- Gutierrez, M., Ishihara, K. & Towhata, I. (1991), 'Flow theory for sand during rotation of principal stress direction', *Soils and Foundations* **31**(4), 121–132.
- Han, K., Feng, Y. T. & Owen, O. R. J. (2005), 'Sphere packing with a geometric based compression algorithm', *Powder Technology* **155**, 33–41.
- Hardin, B. O. (1978), 'The nature of stress-strain behaviour of soils', *Earthquake engineering and soil mechanics* **1**, 3–90.
- Haruyama, M. (1969), 'Effect of surface roughness on the shear characteristics of granular materials', *Soils and Foundations* **9**(4), 48–67.
- Haruyama, M. (1981), 'Anisotropic deformation-strength characteristics of an assembly of spherical particles under three dimensional stresses', *Soils and Foundations* **21**(4), 41–55.
- Hight, D. W., Gens, A. & Symes, M. J. (1983), 'The development of a new hollow cylinder apparatus for investigating the effects of principal stress rotation in soils', *Géotechnique* **33**(4), 355–383.
- Ishibashi, I., Chen, Y.-C. & Chen, M.-T. (1991), 'Anisotropic behaviour of ottawa sand in comparison with glass spheres', *Soils and Foundations* **31**(1), 145–155.

## REFERENCES

---

- Itasca (1998), *PFC2D 2.00 Particle Flow Code in Two Dimensions*, Minneapolis Minnesota.
- Jaky, J. (1944), *Talajmechanika*, Budapest.
- James, J. P. (1967), Stress-displacement relationship for sand subjected to passive pressure, PhD thesis, University of Manchester.
- Jamiolkowski, M., Leroueil, S. & Lo Presti, D. C. F. (1991), Design parameters from theory to practice, in 'Geo-Coast '91 Conference', Yokohama.
- Janda, A., Zuriguel, I., Garcimartin, A., Pugnaloni, L. A. & Maza, D. (2008), 'Jamming and critical outlet size in the discharge of a two-dimensional silo', *Europhysics Letters* **84**(4), 44002–44007.
- Ji, S., Hanes, D. M. & Shen, H. H. (2009), 'Comparisons of physical experiment and discrete element simulations of sheared granular materials in an annular shear cell', *Mechanics of Materials* **41**(6), 764–776.
- Jodrey, W. S. & Tory, E. M. (1985), 'Computer simulation of close random packing of equal spheres', *Physical Review A (General Physics)* **32**(4), 2347–2351.
- Joe, B. (1991), 'Geompack - a software package for the generation of meshes using geometric algorithms', *Advances in Engineering Software* **13**, 325–331.
- Jovicic, V., Coop, M. R. & Simic, M. (1996), 'Objective criteria for determining gmax from bender element tests', *Géotechnique* **46**(2), 357–362.
- Kharchaf, M. (1988), *Constitutive equations for granular non-cohesive soils*, Balkema, Rotterdam, chapter On effects of sample height in hollow cylinder tests, pp. 41–45.
- Ko, H. Y. & Scott, R. F. (1967), 'Deformation of sand in hydrostatic compression', *Journal of the Soil Mechanics and Foundations Division, ASCE* **137**, 283.
- Kramer, S. L., Sivaneswaran, N. & Davis, R. O. (1990), 'Analysis of membrane penetration in triaxial test', *Journal of Engineering Mechanics, ASCE* **116**(4), 773–789.
- Kuerbis, R. & Vaid, Y. P. (1968), 'Sand sample preparation: the slurry deposition method', *Soils and Foundations* **28**(4), 107–118.
- Kuwano, R. (1999), The stiffness and yielding anisotropy of sand, PhD thesis, University of London.

## REFERENCES

---

- Kuwano, R., Conolly, T. M. & Jardine, R. J. (2000), 'Anisotropic stiffness measurements in a stress-path triaxial cell', *Geotechnical Testing Journal* **23**(2), 74–84.
- Kwan, M. W. (2007), The influence of particle roughness on the behaviour of an ideal soil, Master's thesis, Imperial College of Science, Technology and Medicine.
- Lade, P. V. (1981), Torsion shear apparatus for soil testing, in 'Laboratory Shear Strength of Soil', Vol. STP740, pp. 145–163.
- Lade, P. V. (1988), *Constitutive equations for granular non-cohesive soils*, Balkema, Rotterdam, chapter Double hardening constitutive model for soils, parameter determination and prediction for two sands, pp. 367–382.
- Lade, P. V. & Duncan, J. M. (1973), 'Cubical triaxial tests on cohesionless soil', *Journal of the Soil Mechanics and Foundations Division, ASCE* **99**(10), 793–812.
- Lade, P. V., Nam, J. & Hong, W. P. (2008), 'Shear banding and cross-anisotropic behaviour observed in laboratory sand tests with stress rotation', *Canadian Geotechnical Journal* **45**(1), 74–84.
- Lam, W. & Tatsuoka, F. (1988), 'Effects of initial anisotropic fabric and  $\sigma_2$  on strength and deformation characteristics of sand', *Soils and Foundations* **28**(1), 89–106.
- Lin, X. & Ng, T. T. (1997), 'A three-dimensional discrete element model using arrays of ellipsoids', *Géotechnique* **47**(2), 319–329.
- Lo Presti, D. C. F., Pedroni, S. & Crippa, V. (1992), 'Maximum dry density of cohesionless soils by pluviation and by astm d 4523-83: A comparative study', *Geotechnical Testing Journal* **15**(2), 180–189.
- Mahdi, T. & Dafalias, Y. (2008), 'Sanisand: Simple anisotropic sand plasticity model', *International Journal for Numerical and Analytical Methods in Geomechanics* **32**(8), 915–948.
- Marachi, N. D., Duncan, J. M., Chan, C. K. & Seed (1981), *Laboratory Shear Strength of Soil*, number STP 740, American Society for Testing and Materials, chapter Plane-Strain Testing of Sand, pp. 294–302.
- Menkiti, O. C. (1995), Behaviour of clay and clayey-sand, with particular reference to principal stress rotation, PhD thesis, University of London.

## REFERENCES

---

- Mindlin, R. D. & Deresiewicz, H. (1953), 'Elastic spheres in contact under varying oblique forces', *Journal of Applied Mechanics* **20**, 327–344.
- Minh, A. M. (2006), An investigation of the stress-strain-strength characteristics of an Eocene clay, PhD thesis, University of London.
- Miura, K., Miura, S. & Toki, S. (1986), 'Deformation behaviour of anisotropic dense sand under principal stress axes rotation', *Soils and Foundations* **26**(1), 36–52.
- Miura, K. & Toki, S. (1982), 'A sample preparation method and its effect on static and cyclic deformation strength properties of sand', *Soils and Foundations* **22**(1), 61–77.
- Miura, K., Toki, S. & Tanizawa, F. (1984), 'Cone penetration characteristics and its correlation to static and cyclic deformation - strength behaviors of anisotropic sand', *Soils and Foundations* **24**(2), 58–74.
- Munjiza, A. & Andrews, K. R. F. (1998), 'Nbs contact detection algorithm for bodies of similar size', *International Journal for Numerical Methods in Engineering* **43**, 131–149.
- Ng, T. T. (2000), Fabric study of an ellipsoidal array at large strain, in '14th Engineering Mechanics Conference', pp. 1–5.
- Ng, T. T. (2001), 'Fabric evolution of ellipsoidal arrays with different particle shapes', *Journal of Engineering Mechanics* **127**(10), 994–999.
- Ng, T. T. (2004a), 'Behavior of ellipsoids of two sizes', *Journal of Geotechnical and Geoenvironmental Engineering, ASCE* **130**(10), 1077–1083.
- Ng, T. T. (2004b), 'Macro- and micro-behaviors of granular materials under different sample preparation methods and stress paths', *International Journal of Solids and Structures* **41**(21), 5871–5884.
- Ng, T. T. (2005), 'Behavior of gravity deposited granular material under different stress paths', *Canadian Geotechnical Journal* **42**(6), 1644–1655.
- Ng, T. T. (2008), Personal communication.
- Nishimura, S. (2005), Laboratory study on anisotropy of natural London clay, PhD thesis, University of London.
- Oda, M. (1972a), 'Initial fabrics and their relations to mechanical properties of granular material', *Soils and Foundations* **12**(1), 16–36.

## REFERENCES

---

- Oda, M. (1972b), 'The mechanism of fabric changes during compressional deformation of sand', *Soils and Foundations* **12**(2), 1–18.
- Oda, M., Koishikawa, I. & Higuchi, T. (1978), 'Experimental study of anisotropic shear strength of sand by plane strain test', *Soils and Foundations* **18**(1), 25–38.
- Oda, M. & Konishi, J. (1974), 'Microscopic deformation mechanism of granular material in simple shear', *Soils and Foundations* **14**(4), 25–38.
- Okamoto, M. & Fityus, S. (2006), *Geomechanics and Geotechnics of Particulate Media*, Taylor and Francis Group, London, chapter An evaluation of the dry pluviation preparation technique applied to silica sand samples, pp. 33–39.
- Okochi, Y. & Tatsuoka, F. (1984), 'Some factors affecting  $k_0$ -values of sand measured in triaxial cell', *Soils and Foundations* **24**(3), 52–68.
- O'Sullivan, C. (2002), The application of discrete element modeling to finite deformation problems in geomechanics, PhD thesis, University of California, Berkeley.
- O'Sullivan, C. (2004), 'Selecting a suitable time step for discrete element simulations that use the central difference time integration scheme', *Engineering Computations* **21**(2/3/4), 278–303.
- O'Sullivan, C., Bray, J. D. & Li, S. (2003a), 'Modified shear spring formulation for discontinuous deformation analysis of particulate media', *Journal of Engineering Mechanics, ASCE* **129**, 830–834.
- O'Sullivan, C., Bray, J. D. & Li, S. (2003b), 'A new approach for calculating strain for particulate media', *International Journal for Numerical and Analytical Methods in Geomechanics* **27**(10), 859–877.
- Parikh, P. V. (1967), The shearing behaviour of sand under axisymmetric loading, PhD thesis, University of Manchester.
- Parkin, A. K. (1965), 'On the strength of packed spheres', *Journal of the Australian Mathematical Society* **5**, 443–452.
- Parkin, A. K. (1981), 'Discussion: The conditions for failure of a face-centred cubic array of uniform rigid spheres', *Géotechnique* **31**(4), 559–560.
- Pennington, D. S., Nash, D. F. T. & Lings, M. L. (2001), 'Horizontally mounted bender elements for measuring anisotropic shear moduli in triaxial clay specimens', *Geotechnical Testing Journal* **24**(2), 133–144.

## REFERENCES

---

- Porovic, E. (1995), Investigation of soil behaviour using a resonant-column torsional-shear hollow cylinder apparatus, PhD thesis, University of London.
- Potts, D. M., Dounias, G. T. & Vaughan, P. R. (1987), 'Finite element analysis of the direct shear box', *Géotechnique* **37**(1), 11–23.
- Potts, D. M. & Zdravkovic, L. (1999), *Finite element analysis in geotechnical engineering: Theory*, Thomas Telford.
- Powrie, W., Ni, Q., Harkness, R. M. & Zhang, X. (2005), 'Numerical modelling of plane strain tests on sands using a particulate approach', *Géotechnique* **55**(4), 297–306.
- Pradel, D., Ishihara, K. & Gutierrez, M. (1990), 'Yielding and flow of sand under principal stress axes rotation', *Soils and Foundations* **30**(1), 87–99.
- Pradhan, T. B. S., Tatsuoka, F. & Horii, N. (1988), 'Simple shear testing on sand in a torsional shear apparatus', *Soils and Foundations* **28**(2), 95–112.
- Reades, D. W. & Green, G. E. (1976), 'Independent stress control and triaxial extension tests on sand', *Géotechnique* **26**(4), 551–576.
- Rennie, B. C. (1959), 'On the strength of sand', *Journal of the Australian Mathematical Society* **1**, 71–79.
- Rolo, R. (2003), The anisotropic stress-strain-strength behaviour of brittle sediments, PhD thesis, University of London.
- Roscoe, K. H. (1953), An apparatus for the application of simple shear to soil samples, Vol. 1, pp. 186–191.
- Rothenburg, L. & Bathurst, R. J. (1989), 'Analytical study of induced anisotropy in idealized granular materials', *Géotechnique* **39**(4), 127–170.
- Rothenburg, L. & Bathurst, R. J. (1992), 'Micromechanical features of granular assemblies with planar elliptical particles', *Géotechnique* **42**(1), 601–614.
- Rowe, P. W. (1962), 'The stress-dilatancy relation from static equilibrium of an assembly of particles in contact', *Proceedings of the Royal Society of London, A: Mathematical, Physical and Engineering Sciences* **269**, 500–527.
- Saada, A. & Townsend, F. (1981), State-of-the-art, laboratory strength testing of soils, in 'Laboratory Shear Strength of Soil', Vol. STP740, pp. 7–77.

## REFERENCES

---

- Satake, M. (1982), Fabric tensor in granular materials, *in* 'Proceedings IUTAM Conference on Deformation and Failure of Granular Materials, Delft', pp. 63–67.
- Sayao, A. & Vaid, Y. P. (1991), 'A critical assessment of stress nonuniformities in hollow cylinder tests specimens', *Soils and Foundations* **31**(1), 60–72.
- Shapiro, S. & Yamamuro, J. A. (2003), 'Effects of silt on three-dimensional stressstrain behavior of loose sand', *Journal of Geotechnical and Geoenvironmental Engineering, ASCE* **129**(1), 1–11.
- Shewchuk, J. R. (2002), 'Delaunay refinement algorithms for triangular mesh generation', *Computational Geometry: Theory and Applications* **22**(1-3), 21–74.
- Shibuya, S. (1985), Undrained behaviour of granular materials under principal stress rotation, PhD thesis, University of London.
- Skinner, A. E. (1974), The effect of high pore water pressures on the mechanical behaviour of sediments, PhD thesis, University of London.
- Smith, P. R. (1974), The properties of high compressibility clay with special reference to construction on soft ground, PhD thesis, University of London.
- Stroud, M. A. (1970), The behaviour of sand at low stress levels in the simple shear apparatus, PhD thesis, Cambridge University.
- Sutherland, H. B. & Mesdary, M. S. (1969), The influence of the intermediate principal stress on the strength of sand, *in* 'Proceedings of the 7th International Conference on Soil Mechanics and Foundation Engineering, Mexico City, Mexico', Vol. I, pp. 391–399.
- Symes, M. J., Gens, A. & Hight, D. W. (1988), 'Drained principal stress rotation in saturated sand', *Géotechnique* **38**(1), 59–81.
- Symes, M. J., Hight, D. W. & Gens, A. (1982), Investigating anisotropy and the effects of principal stress rotation and of the intermediate principal stress using a hollow cylinder apparatus, *in* 'Proceedings IUTAM Conference on Deformation and Failure of Granular Materials, Delft', pp. 441–448.
- Symes, M. J. P. R. (1983), Rotation of principal stresses in sand, PhD thesis, University of London.
- Takahashi, A. (2003), Development of control/data acquisition program for hollow cylinder apparatus, Internal report, Imperial College London.

## REFERENCES

---

- Tatsuoka, F., Ochi, K., Fujii, S. & Okamoto, M. (1986), 'Cyclic undrained triaxial and torsional shear strength of sands for different sample preparation methods', *Soils and Foundations* **26**(3), 23–41.
- Thornton, C. (1979), 'The conditions for failure of a face-centered cubic array of uniform rigid spheres', *Géotechnique* **29**(4), 441–459.
- Thornton, C. (1981), 'Discussion: The conditions for failure of a face-centred cubic array of uniform rigid spheres', *Géotechnique* **31**(4), 560–561.
- Thornton, C. (2000), 'Numerical simulations of deviatoric shear deformation of granular media', *Géotechnique* **50**(1), 43–53.
- Thornton, C. & Sun, G. (1993), Axisymmetric compression of 3d polydisperse systems of spheres, in C. Thornton, ed., 'Powders and Grains 93', A.A. Balkema, Rotterdam, pp. 129–134.
- Thornton, C. & Zhang, L. (2001), A dem comparison of different shear testing devices, in Y. Kishino, ed., 'Powders and Grains 2001', Swets and Zeitlinger, pp. 183–190.
- Toll, D. (1988), *TRIAX - a computer program for controlling triaxial stress path tests*.
- Tordesillas, A. & Muthuswamy, M. (2009a), 'Noncoaxiality and force chain evolution', *International Journal of Engineering Science In Press*.
- Tordesillas, A. & Muthuswamy, M. (2009b), 'On the modeling of confined buckling of force chains', *Journal of the Mechanics and Physics of Solids* **57**(4), 706–727.
- Tsunekawa, H. & Iwashita, K. (1993), Numerical simulation of triaxial test using two and three dimensional dem, in Y. Kishino, ed., 'Powders and Grains 01', A.A. Balkema, Rotterdam, pp. 177–182.
- Vaid, Y. P. & Negussey, D. (1988), 'Preparation of reconstituted sand specimens', *ASTM STP 977*.
- Vaid, Y. P., Sayao, A. & Negussey, D. (1990), 'Generalized stress-path-dependent soil behaviour with a new hollow cylinder torsional apparatus', *Canadian Geotechnical Journal* **27**(5), 601–616.
- Wang, Q. & Lade, P. V. (2001), 'Shear banding in true triaxial tests and its effect on failure in sand', *Journal of Geotechnical and Geoenvironmental Engineering, ASCE* **127**(8), 754–761.

## REFERENCES

---

- Watson, G. (1966), 'The statistics of orientation data', *Journal of Geology* **74**, 786–797.
- Watts, D. J. (2003), *Six degrees: the science of a connected age*, W. W. Norton and Company Inc.
- Whittle, A. J. & Kavvadas, M. J. (1994), 'Formulation of mit-e3 constitutive model for overconsolidated clays', *Journal of Geotechnical Engineering* **120**(1), 173–198.
- Wijewickreme, D. & Vaid, Y. P. (1991), 'Stress nonuniformities in hollow cylinder torsional specimens', *Geotechnical Testing Journal, ASTM* **14**(4), 349–362.
- Williams, J. R., Perkins, E. & Cook, B. (2003), 'A contact algorithm for partitioning n arbitrary sized objects', *Engineering Computations* **21**(2/3/4), 235–248.
- Wong, R. K. S. & Arthur, J. R. F. (1985), 'Induced and inherent anisotropy in sand', *Géotechnique* **35**(4), 471–481.
- Woodcock, N. H. (1977), 'Specification of fabric shapes using an eigenvalue method', *Geological Society of America Bulletin* **88**(9), 1231–1236.
- Wu, M. (2008), Experimental study of the influence of interparticle friction on the response of granular materials, Master's thesis, Imperial College of Science, Technology and Medicine.
- Yamada, Y. & Ishihara, K. (1979), 'Anisotropic deformation characteristics of sand under three dimensional stress conditions', *Soils and Foundations* **19**(2), 79–94.
- Yang, Z. X., Li, X. S. & Yang, J. (2007), 'Undrained anisotropy and rotational shear in granular soil', *Géotechnique* **57**(4), 371–384.
- Yang, Z. X., Li, X. S. & Yang, J. (2008a), 'Interpretation of torsional shear results for non-linear stress-strain relationship', *International Journal for Numerical and Analytical Methods in Geomechanics* **32**(10), 1247–1266.
- Yang, Z. X., Li, X. S. & Yang, J. (2008b), 'Quantifying and modelling fabric anisotropy of granular soils', *Géotechnique* **58**(4), 237–248.
- Yimsiri, S. & Soga, K. (2001), Effects of soil fabric on undrained behavior of sands, in S. Prakash, ed., 'Fourth International Conference on Recent Advances in Geotechnical Earthquake Engineering and Soil Dynamics', San Diego, California.

## REFERENCES

---

- Yimsiri, S. & Soga, K. (2008), Dem study of effects of soil fabric on anisotropic behavior of sands, *in* S. E. Burns, P. W. Mayne & J. C. Santamarina, eds, 'Proceedings of the 4th International Symposium on Defromation Characteristics of Geomaterials, IS Atlanta', Vol. 1, pp. 613–620.
- Yu, P. & Richart, F. E. (1984), 'Stress ratio effects on shear modulus of dry sand', *Journal of Geotechnical Engineering, ASCE* **110**(3), 331–345.
- Zdravkovic, L. (1996), The stress-strain-strength anisotropy of a granular medium under general stress conditions, PhD thesis, University of London.
- Zdravkovic, L. & Jardine, R. J. (1997), 'Some anisotropic stiffness characteristics of a silt under general stress conditions', *Géotechnique* **47**(3), 407–438.
- Zdravkovic, L. & Potts, D. M. (2005), Finite element investigation of non-uniformities in hollow cylinder experiments, *in* M. Barla & G. Barla, eds, 'Proceedings of the 11th International Conference on Computer Methods and Advances in Geomechanics, IACMAG, Italy', Vol. 2, pp. 251–258.
- Zhang, X. (2009), 'Personal communication'.
- Zuriguel, I., Pugnaloni, L. A., Garcimartin, A. & Maza, D. (2003), 'Jamming during the discharge of grains from a silo described as a percolating transition', *Physical Review E - Statistical, Nonlinear, and Soft Matter Physics* **68**(3), 303011–303014.